

Dipartimento di / Department of

Material Science

Dottorato di Ricerca in / PhD program Material Science and Nanotechnology
Ciclo / Cycle XXIX

Curriculum in (se presente / if it is)

STUDIES OF DIFFERENT ADMINISTRATION ROUTES OF ENGINEERED COLLOIDAL NANOPARTICLES

Cognome / Surname Santini Nome / Name Benedetta

Matricola / Registration number 787804

Tutore / Tutor: Miriam Colombo

Cotutore / Co-tutor:
(se presente / if there is one)

Supervisor:
(se presente / if there is one)

Coordinatore / Coordinator: Prof. G. Brivio

ANNO ACCADEMICO / ACADEMIC YEAR 2016

Contents

List of publications	1
Abbreviations	3
Chapter 1 Background	
1.1. Nanotechnology and biomedicine	4
1.2. Nanoparticles	6
1.2.1. What and why?	6
1.2.2. Structural properties	7
1.2.3. Diagnostic and therapeutic applications	8
1.2.4. Classification and functionalization	11
1.3. Administration routes	13
1.3.1. Intravenous injection	14
1.3.2. Oral administration	15
1.3.3. Inhalational administration	15
1.3.4. Topical administration	16
1.4. Drugs and dosage forms	18
Bibliography	20
Chapter 2 Aim of the thesis	23
Chapter 3 Results and Discussion	
3.1. Topical administration of iron oxide nanoparticles	30
3.1.1. Introduction	30
3.1.2. Iron oxide nanoparticles	32
3.1.3. Investigation of PMNP penetration through the human skin	33
3.1.4. Interaction with skin-localized cells of innate immunity in living mice	35
3.1.5. Formulation study of PMNP semi-solid preparation	37
3.1.6. <i>In vitro</i> permeation studies	39
Bibliography	42

3.2. Oral administration of polymeric nanoparticles containing insulin	44
3.2.1. Introduction	44
3.2.2. Nanoparticles synthesis and characterization	46
3.2.3. Core preparation and characterization	47
3.2.4. <i>In vitro</i> studies of cores	49
3.2.5. Preparation and characterization of coated pellets	49
3.2.6. <i>In vivo</i> hypoglycaemic effect	51
Bibliography	53
3.3. Targeted gold nanoparticles loaded with everolimus for inhalational administration	55
3.3.1. Introduction	55
3.3.2. Synthesis and characterization of anti-human CD44-functionalized GNPs loaded with everolimus	56
3.3.3. <i>In vitro</i> drug release kinetics	58
3.3.4. Cell characterization	59
3.3.5. CD44 expression on normal and pathologic epithelia	60
3.3.6. Expression of the mammalian target of everolimus, mTOR, in MCs	61
3.3.7. GNP-HCe cell uptake	61
3.3.8. Effect of GNP-HCes on MC proliferation and apoptosis	62
3.3.9. Effect of GNP-HCes on inflammatory cells	64
3.3.10. Effect of GNP-HCes on bronchial epithelial cell line	65
Bibliography	66
3.4. Nanoformulation of an antiretroviral drug able to cross the blood brain barrier (BBB) after intravenous injection	68
3.4.1. Introduction	68
3.4.2. Nanoparticles synthesis and characterization	69
3.4.3. Nanoconjugated enfuvirtide crosses the <i>in vitro</i> BBB model	69
3.4.4. <i>In vivo</i> brain targeting and trans-BBB delivery of nanoconjugated enfuvirtide	74
3.4.5. Fate of PMNP in RBMVECs	78
Bibliography	81

Chapter 4 Outlook

4.1. Conclusion	83
Bibliography	86
Appendix	87
Bibliography	88
Publications	90

List of publications

During the course of the PhD, a number of publications have been made, which are based on the work presented in this thesis. All of them are listed here for reference, while those that are directly related to the content of this work are included in the last section of the thesis.

1. Santini B., Musazzi U.M., Selmin F., Marini V., Corsi F., Allevi R., Ferretti A.M., Prospero D., Cilurzo F., Colombo M. and Minghetti P.
“Impact of semi-solid formulations on skin penetration of iron oxide nanoparticles”
Journal of Nanobiotechnology, **2017**
I contributed to this work with the nanoparticles synthesis, characterization and functionalization. I was also interested in the nanoparticles formulation and the set up of the Franz Diffusion Cell experiments.
2. Santini B., Zanoni I., Marzi R., Cigni C., Bedoni M., Gramatica F., Palugan L., Corsi F., Granucci F. and Colombo M.
“Cream formulation impact on topical administration of engineered colloidal nanoparticles”
PLoS One, **2015**
I contributed to this work with the nanoparticles synthesis, characterization and functionalization. I was also interested in the nanoparticles formulation, semi-solid formulation characterization and I coordinated the *in vitro* permeation experiments.
3. Salvioni L., Fiandra L., Del Curto MD., Mazzucchelli S., Allevi R., Truffi M., Sorrentino L., Santini B., Cerea M., Palugan L., Corsi F. and Colombo M.
“Oral delivery of insulin via polyethylene imine-based nanoparticles for colonic release allows glycemic control in diabetic rats” Pharmacol Res. **2016**
I contributed to this work with the nanoparticles synthesis, characterization and functionalization.
4. Cova E., Colombo M., Inghilleri S., Morosini M., Miserere S., Peñaranda-Avila J., Santini B., Magni S., Gramatica F., Prospero D. and Meloni F.;
“Antibody-engineered nanoparticles selectively inhibit mesenchymal cells isolated from patients with chronic lung allograft dysfunction” Nanomedicine UK, **2015**
I contributed to this work with the nanoparticles synthesis, characterization and functionalization.
5. Fiandra L., Colombo M., Mazzucchelli S., Truffi M., Santini B., Allevi R., Nebuloni M., Capetti A., Rizzardini G., Prospero D., Corsi F.;
“Nanoformulation of antiretroviral drugs enhances their penetration across the blood brain barrier in mice” Nanomedicine, **2015**
contributed to this work with the nanoparticles synthesis, characterization and functionalization.
6. Verderio P., Avvakumova S., Alessio G., Bellini M., Colombo M., Galbiati E., Mazzucchelli S., Avila JP., Santini B., Prospero D.;;
“Delivering colloidal nanoparticles to mammalian cells: a nano-bio interface perspective”.
Review. Adv Healthc Mater, **2014**
7. Daaboul GG., Gagni P., Benussi L., Bettotti P., Ciani M., Cretich M., Freedman DS., Ghidoni R., Ozkumur AY., Piotto C., Prospero D., Santini B., Ünlü MS., Chiari M.;

"Digital Detection of Exosomes by Interferometric Imaging" Scientific Report, **2016**

I contributed to this work with the exosomes characterization using NTA instrument (Nanosight).

8. Benussi L., Ciani M., Tonoli E., Morbin M., Palamara L., Albani D., Fusco F., Forloni G., Glionna M., Baco M., Paterlini A., Fostinelli S., Santini B., Galbiati E., Gagni P., Cretich M., Binetti G., Tagliavini F., Prosperi D., Chiari M., Ghidoni R.;

"Loss of exosomes in progranulin-associated frontotemporal dementia" Neurobiol Aging, **2016**

I contributed to this work with the exosomes characterization using NTA instrument (Nanosight).

9. Gagni P., Cretich M., Benussi L., Tonoli E., Ciani M., Ghidoni R., Santini B., Galbiati E., Prosperi D., Chiari M.;

"Combined mass quantitation and phenotyping of intact extracellular vesicles by a microarray platform" Anal Chim Acta, **2016**

I contributed to this work with the vesicles characterization using NTA instrument (Nanosight).

Abbreviations

NPs = nanoparticles
Cet = cetomacrogol
CMC = sodium carboxymethyl cellulose
CP = carboxypolymethylene
 D_h = hydrodynamic diameter of nanoparticle
DLS = dynamic light scattering
HE = human epidermis
HEC = hydroxyethyl cellulose
IONs = iron oxide nanoparticles
O/W = oil in water
PDI = poly dispersity index
MNP = iron oxide nanoparticles
PMNP = iron oxide nanoparticles coated by a poly-(isobutylene-*alt*-maleic anhydride)
 Q_{24} = amount of iron permeated in 24 h
 Q_{ret} = amount of iron retained in 24 h
 r_2 = relaxivity
RKM = membrane based on regenerated keratin
SC = stratum corneum
 T_2 = relaxation time
VE = viable epidermis
 ξ = zeta-potential
MRI = magnetic resonance imaging
PMA = poly-(isobutylene-*alt*-maleic anhydride)
FDCs = franz diffusion cell
ICP-OES = inductively coupled plasma optical emission spectrometry
TEM = transmission electron microscope
SEM = scanning electron microscope
HPMC = hydroxypropyl methylcellulose
NI = insulin-containing nanoparticles
PEI = polyethylene imine
GNPs = gold nanoparticles
GNP@PMA = gold nanoparticles coated by a poly-(isobutylene-*alt*-maleic anhydride)
FITC = fluorescein isothiocyanate
BOS = bronchiolitis obliterans syndrome
TEER = transepithelial/transendothelial electrical resistance
BBB = blood brain barrier
FI = fluorescence intensity
Enf = enfuvirtide
A = astrocyte
E = endothelial cell
RBC = red blood cells
NTA = nanoparticles tracking analysis
EVs = extracellular vesicles

Chapter 1

Background

1.1. Nanotechnology & Biomedicine

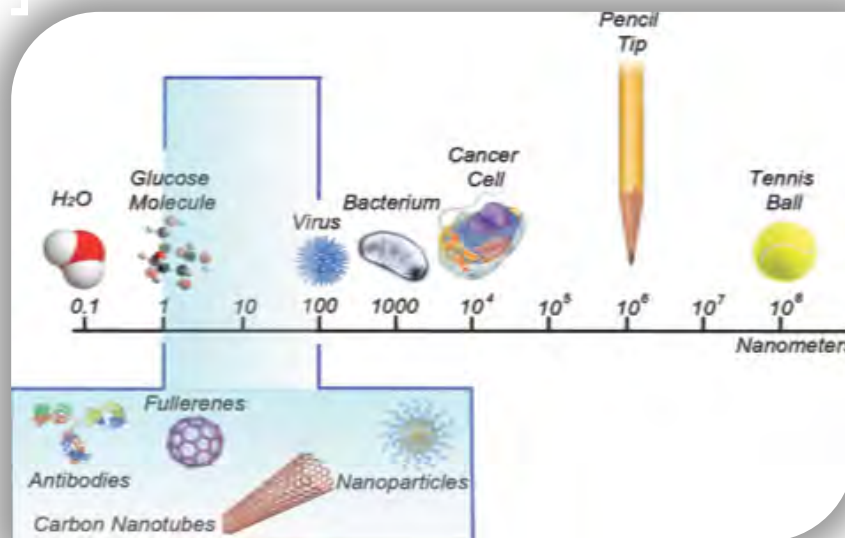


Figure 1.1. Nano-scale and some object dimensions as reference.

Nanotechnology is a multidisciplinary science able to control and manipulate the materials at the atomic and molecular level on a scale below the micrometre (1-100 nm range) and it's able to design devices in that dimension. In that range the objects have excellent properties that are absent in large scale and, at the same time, they allow a space saving and a proper control of the material properties without changing the chemical composition. In the recent years nanotechnology has been established as an emerging tool for biomedicine with its outstanding potential applications both in diagnosis and therapy^{1,2}.

Nanotechnology in general presents many revolutionary opportunities in several clinical pathologies: a lot are the studies about inflammatory diseases^{3,4,5}, neurodegenerative disorders^{6,7}, vaccines^{8,9} but, probably, cancer represents the most engaging challenge^{10,11,12}.

Cancer is a complex disease, which requires a series of action starting from diagnosis till therapy and it's a major killer disease of the last years. The early detection is fundamental and it can completely change the scenario of the treatment of most cancers; the therapy usually is

based on multi-drug approach with heavy side effects and often without eradicating the disease.

The nanotechnology features allow to ameliorate both these aspects: to be an innovative detector for an earlier diagnosis and a promising vehicle for a more selective and, therefore, a more effective and safe treatment of the tumours.

Pharmaceutical nanotechnology covers the applications of nanotechnology to pharmacy as nanomaterials, and as devices like drug delivery, diagnostic, imaging and biosensor.

In this context nanoparticles (NPs) represent one of the most interesting and studied fields of nanotechnology with the aim to overcome some of the limits of the conventional medicine¹⁰.

So far the US Food and Drug Administration (FDA) have approved various nanotechnology products for clinical use and many are under clinic and preclinic development¹³⁻¹⁶.

1.2. Nanoparticles

1.2.1. What and why?

The nanoparticles represent a new frontier for medicine. Typically, they are objects in the nano-scale designed to overcome pharmacological limitation included low drug bioavailability or insufficient targeting efficiency. They can be defined “theranostic agents” since they can be a single agent with the combination of diagnostic and therapeutic capabilities¹⁷. They are synthesized in many different ways: they can be organic, inorganic or hybrid and depending on their nature the nanoparticles have different chemical-physical properties such as high electron density and strong optical absorption (e.g., gold nanoparticles), superparamagnetic features (e.g., iron oxide nanoparticles), and photoluminescence (e.g., quantum dots).

The nanoparticles are presented as a new tool to overcome some problems concerning the deliver of therapeutic compounds like poor biodistribution, limited effectiveness, undesirable side effects, lack of selectivity, poor concentration in target tissue, rapid degradation and clearance.

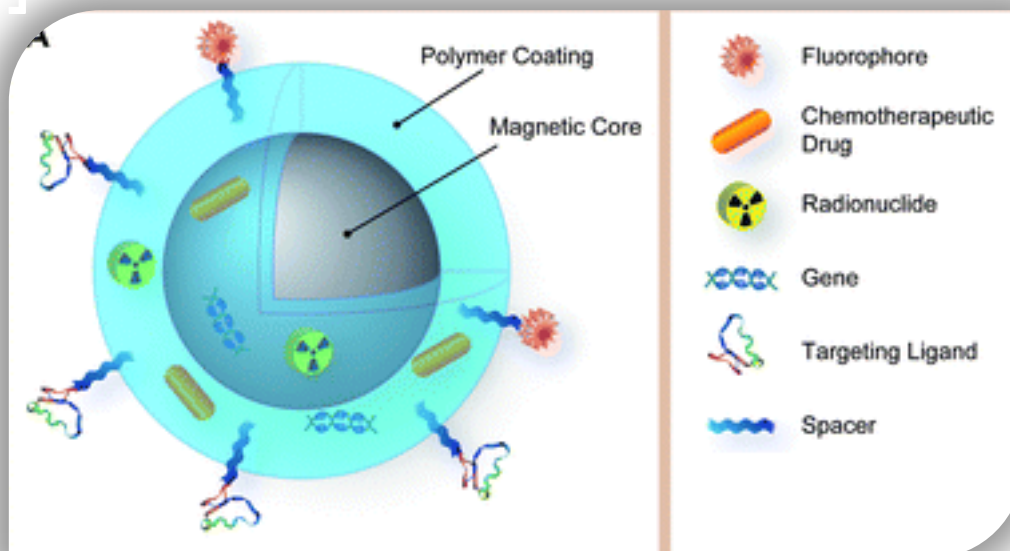


Figure 1.2. Schematic representation of multifunctional nanoparticle.

(Image taken from Zhang et al)¹⁸.

1.2.2. Structural properties

To be used as a promising device it's essential to consider and control some nanoparticles parameters:

- The **size** and the **architecture**: they are the most important characteristics that guarantee some chemical/physical properties of the materials and the readily interaction with the biomolecules. Therefore, most of the biological processes occur in the nanometre range so the nanoparticles can be the ideal candidate for biological interactions.
- The **surface area-volume ratio**: it's another significant feature, which determines the interaction with the biological interfaces: in fact constant volume but different shape can attribute different properties to the particles. So, it's essential working with monodispersed nanoparticles to have a proper control of the activities.
- The **effective surface charge**: it's another key aspect that ensures the stability of the nanoparticles suspension over time and at different cellular pH values^{19,20}. It determines the state of aggregation that is a crucial aspect that can cause the failure of the treatment. Also, the charge is a parameter that influences the immunity system: positively charged nanoparticles generate a higher immune response compared to neutral or negatively charged nanoparticles formulations.
- **Toxicity**: for *in vivo* studies NPs have to be safe for the biological environment.

Based on these remarks, the nanoparticles have many applications both in diagnosis and therapy.

1.2.3. Diagnostic and therapeutic applications

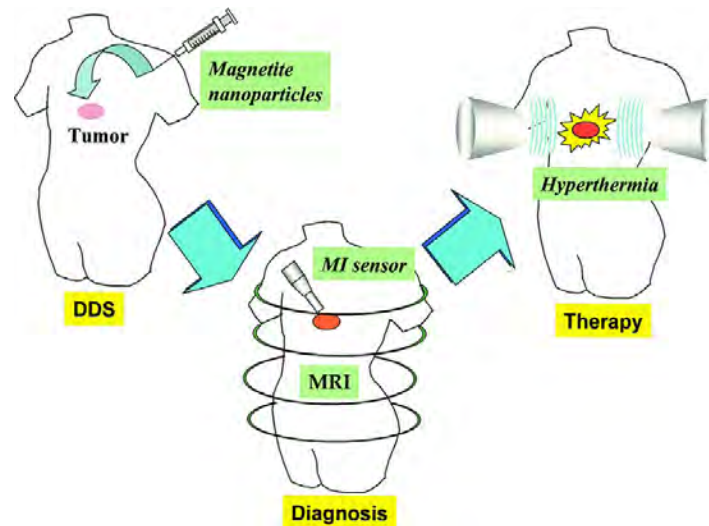


Figure 1.3. Explanation of the principal therapeutic and diagnostic strategies of the nanoparticles.

The principal nanoparticles application in diagnosis is:

- **MRI (Magnetic Resonance Imaging):** the injection to the patient of superparamagnetic nanoparticles as a contrast agent allows having a signal from vases or damaged organs. For this task, gadolinium or iron oxide nanoparticles with a core size around 10 nm are used.



Figure 1.4. MRI images of rat brain glioma before and 20 minutes after injection of gadolinium nanoparticles²¹.

The therapeutic applications of the nanoparticles are:

- **Hyperthermia:** this therapy is based on the characteristic of the cancer cells that don't survive at high temperature (42-43°C). For this reason iron oxide nanoparticles are used to selectively heat the tumour tissue ensuring uniform temperature diffusion and a selective cancer cells death.
- **Drug delivery systems:** NPs are designed to deliver the drug to the target by a site/time/speed-controlled release, preventing also the early degradation. (e.g. iron oxide nanoparticles, lipids NPs, liposomes, PLGA, ferritin, etc). Fig 1.5 shows an example of a liposome as drug delivery system.

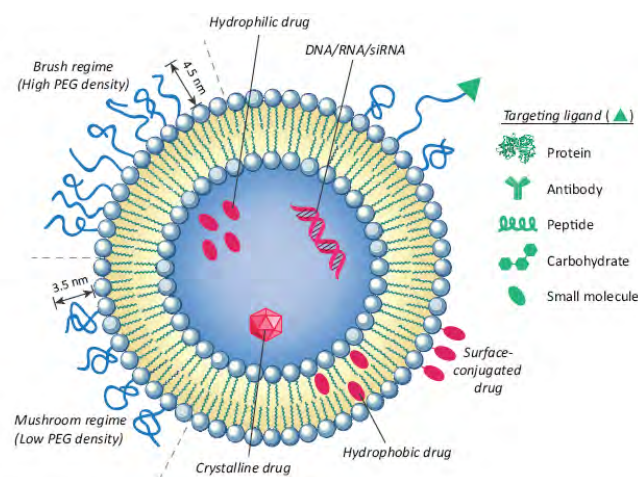


Figure 1.5. Structural and design consideration for liposome as drug delivery system.

(Image taken from Çağdaş et al)²².

These systems can overcome some drawbacks of active molecules such as hydrophobicity, early degradation, not controlled release, etc, which limit therapeutic efficacy.

- **Regenerative medicine:** it is proposed to replace cells, tissues or organs to the normal function in many degenerative disorders. NPs can be the intelligent promoter of the natural biological process such as molecular recognition, bio-adhesion, stimulation of growing processes and cell differentiation. The nanoparticles can offer

the delivery of proteins, peptides and genes to mimic these natural biological mechanisms.

1.2.4. Nanoparticles classification and functionalization

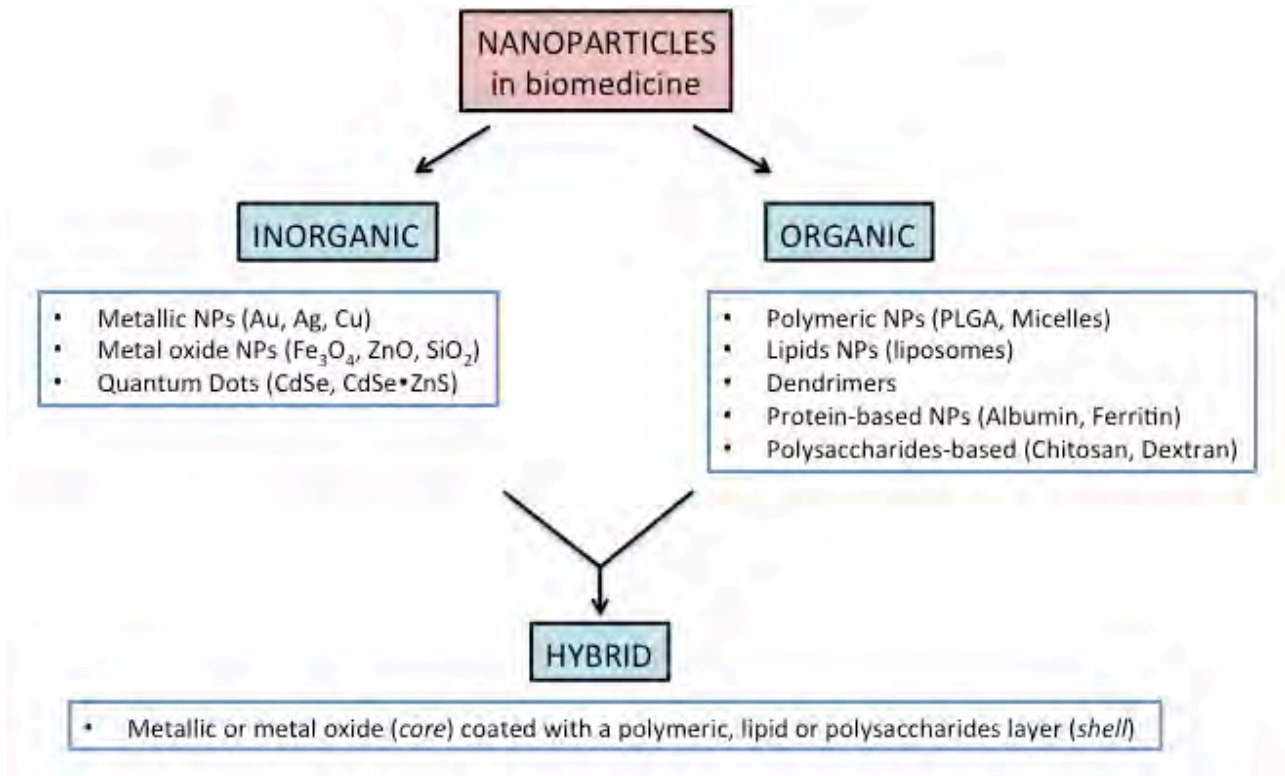


Figure 1.6. Nanoparticles classification scheme.

In recent years it's continually growing the number of the NPs' synthesis and thus the number of the existing types. As Fig 1.6. shows, from a macroscopic point of view, the nanoparticles can be classified in two big categories: **inorganic** and **organic**.

In the inorganic group, among the metallic nanoparticles, there are important biosensors, imaging and photothermal therapy devices, (Au and Ag nanoparticles), characterized by the surface resonance plasmon; it's also known the antimicrobial activity of the Ag nanoparticles. The metal oxide nanoparticles are used as drug delivery systems (SiO_2 , Fe_3O_4 nanoparticles) and as contrast agents for MRI (Fe_3O_4 nanoparticles).

Quantum Dots (CdSe, CdSe-Zn), semiconductor nanocrystals with unique size dependent optical and electronic properties originated from quantum size effect, have a dimension between 2 and 10 nm and they are the nanoparticles of choice for bioimaging and biosensing.

The organic class shows a plethora of nanoparticles used, mainly, as drug delivery systems (PLGA, liposomes, chitosan, albumin nanoparticles) with the aim to have a proper control of the drug release without introduce not biocompatible agents.

Nanoparticles with mixed nature is the new challenge: **hybrid** nanoparticles show both the organic and inorganic components to create a multi-effective device based on a core/shell system. A lot are the examples of this strategy: for example iron oxide or gold nanoparticles covered with an amphiphilic polymer. They are made by a metallic core, which is the source of the physic signal, and by a shell, usually made by lipids or polymers, which allows the stability at physiological pH and the surface functionalization with molecules of biological interest. This system can guarantee detection and selective therapy at the same time.

The functionalized nanoparticles can be used for intravenous administration since they can be easily localized as molecular imaging agents and they can be selective for the biological target. The principal molecules used for the functionalization are antibodies, oligosaccharides, proteins, peptides and small targeting ligands.

Many are the processes involved in the nanoparticles conjugation: covalent bonds have been developed to exploit the presence of amine, carboxylic, aldehyde and thiol groups on the NPs surface.

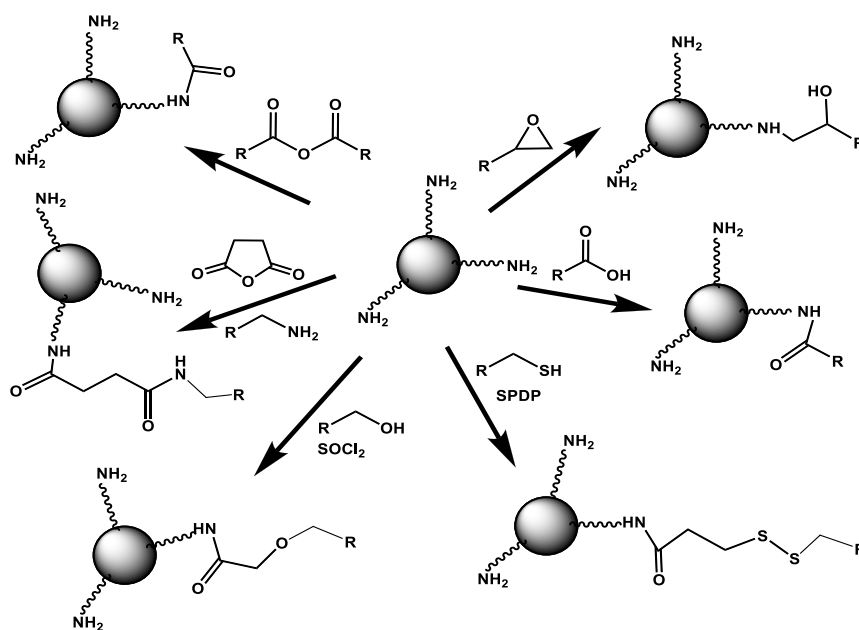


Figure 1.7. Different strategies for the nanoparticles functionalization: functionalization of a nanoparticle with amino group on its surface.

1.3. Administration routes

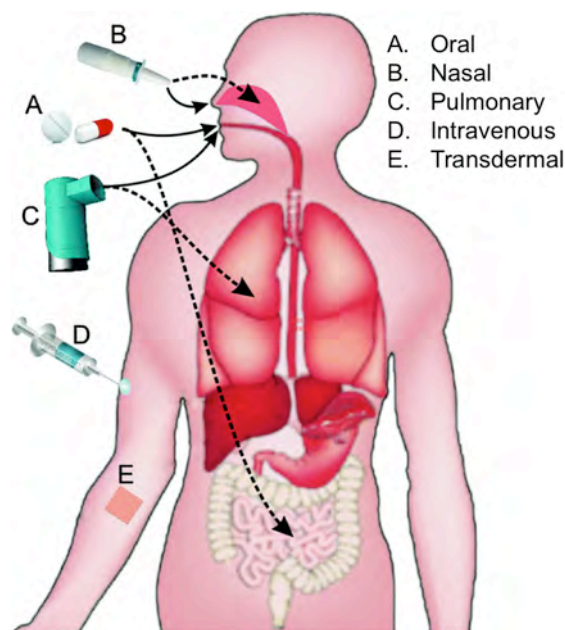


Fig 1.8. The more studied routes of nanoparticles administration.

The success of a pharmacological treatment depends not only on the nature of the drug or its dose but also on the technological and biopharmaceutical features of formulation. For example, if the drug is a protein or a nucleic acid, new technological strategies are required in order to optimize the efficacy, minimize side effects and to increase the compliance of the patient. Each administration route involves different pharmacokinetic and pharmacodynamics mechanisms that need a nanoparticle design suitable for the expected target. So far, the principal diagnostic and therapeutic applications of the nanoparticles view their administration by intravenous injection due to the possibility of this administration route to have a total and immediate bioavailability of the NPs²³. At the same time, the intravenous administration could not be the election way for the treatment of local diseases, since the NPs' systemic distribution can cause more side effects compared with a local administration route.

For these reasons, the administration routes alternatives to the intravenous one are gaining increasing interest in nanomedicine^{24,25}.

The factors involved in the NPs absorption by different administration routes could be classified in two categories: the biological environment and the physical-chemical aspects of the nanoparticles.

For the first one it's necessary to consider the mechanism of absorption (diffusion, pinocytosis, transcellular-intracellular way), through the different structures involved (the skin with its different layers, intestinal epithelium, olfactory mucosa and olfactory nerve), the distribution in the systemic circulation and, sometimes, in the lymphatic one, the metabolism and elimination.

The second ones affect the shape, size, surface, charge, functionalization of the nanoparticles and the presence of stabilising molecules (e.g. polyethylene glycol) or absorption enhancer (e.g. sodium glycocholate).

Nanomedicine is meant to improve the therapeutic performance and in the last years many strategies have been involved²⁶.

Therefore, to obtain a better drug efficacy and a less invasive application, it's very interesting and useful studying other NPs administration routes, alternative to the intravenous one.

1.3.1. Intravenous injection

The first approaches of the nanomedicine entail the nanoparticles administration by intravenous injection.

The principal advantages of this route are related to pharmacokinetics: the absence of the absorption phase guarantees the total and immediate bioavailability of the drug. So, the dose can be the minimum required and also it can be administered to unconscious patients. However, it's known that intravenous injection implicates low compliance by patients and also it's necessary a sterile equipment, a skilled staff, and, if on one hand the immediate efficacy is a big benefit, on the other hand it can cause more side effects such as allergic reactions, infections or overdose.

Once the NPs reach the systemic circulation they can be bind by opsonine and thus catch by endocytosis/phagocytosis in monocytes and macrophages.

The blood is a complex fluid, carrying on a lot of enzymes, proteins, leucocytes, amino acids, hormones, lipids so it's necessary to set up appropriate nano-devices bypassing aggregation phenomena²⁷.

Nanoparticles are small enough to cross the blood barriers to give a better cellular uptake. In particular, the blood brain barrier (BBB) is the most selective barrier and it represents the

principal obstacle to the targeting of central nervous system's (CNS) diseases²⁸. This barrier is a complex structure and it consists of endothelial cells connected with tight junctions, which strictly limit the passage of molecules. The capability of the nanoparticles to cross the BBB is a matter of debate and can allow some drugs, typically unable to arrive to the CNS, to cross the BBB and to be effective for many CNS diseases²⁹.

1.3.2. Oral administration

Among the reasons that make unique the oral administration, there is the minimal invasive procedure, with a generally high compliance, and the possibility to cure gastro-intestinal diseases (e.g., IBD) by specific drug delivery systems³⁰. The oral formulation of many drugs, also, could revolutionize the life of patients with chronic diseases who must be injected daily³¹.

Obviously, a non-total absorption of the nanoparticles, mainly due to their dimensions, represents a limit of this administration route and it can cause a non-total bioavailability of the drug. In this scenario the nanoparticles design and functionalization could be an interesting perspective.

The studies about the nanoparticles destiny in the gastro-intestinal tract are numerous³², and they show the oral route is applicable by the fact that NPs can be absorbed, they can be useful for a local release of the drug and are stable in the different gastro-intestinal tracts.

In general, the NPs uptake in gastro-intestinal tract is based on three different ways:

1. Transcytosis by M cells
2. Intracellular uptake by epithelial cells of the intestinal mucosa
3. Uptake by Peyer plaques

1.3.3. Inhalational administration

Currently, the inhalation therapy is used to administer drugs in the respiratory system for a local effect: for example the treatment of asthma, bronchitis and cystic fibrosis. However, the lungs could give a systemic effect. The principal advantage of this administration route is the high superficial area of absorption (140 m²), extremely vascularized, that allows a quick and predictable transport of the drug. The hepatic first pass effect is also avoided and there isn't the enzymatic degradation typical of the gastrointestinal tract. For these reasons this administration route allows the drug administration at lower dose than the oral one with

fewer side effects. All the deeper structures of the respiratory system are characterized by a dense network of blood capillaries useful for the gas exchange with the blood. There is also a strong defence structure: lymphocytes cells, mainly macrophages, are able to neutralize germs and extraneous particles reached in depth.

The inhalation bioavailability requires a respirable drug form: so the stability, dissolution speed, permeation through the membranes, bio-stability and the deposition site are key aspects³³.

The drug amount and the deposition site into the lungs depend on the physic properties of the aerosol like particles size, shape, charge, density, hygroscopicity and on the patient characteristics like lung geometry, sex, age and the way of breathing.

Furthermore, for a pulmonary treatment, an aerosol nano-formulation could be an innovative strategy for the therapy of lung diseases with low side effects and more specific drug delivery³⁴.

1.3.4. Topical administration

The skin is an organ that performs a lot of function like protection from external agents, thermoregulation, sensoriality, breathing, secretion, antimicrobial defence. To front all these activities the skin is composed by three different layers with different roles: starting from the external surface there is the epidermis, then the dermis and the deeper layer is the hypodermis. The epidermis is mainly composed by the stratum corneum, a layer rich of keratin that limits the penetration through the skin. Nanoparticles capability to cross this dermal barrier is an open challenge and it is still matter of debate^{35,36}. The chemical-physical parameters that influence this passage are: size, surface area, hydrophilicity/lipophilicity grade of the NPs and the vehicle in which they are dispersed.

Based on their characteristics, the molecules prefer different mechanism of transport:

- Hydrophilic molecule with a low molecular weight: intercellular way
- Hydrophilic molecule with a high molecular weight: cutaneous shunts
- Hydrophobic molecule with a low molecular weight: intracellular way
- Hydrophobic molecule with a high molecular weight: intercellular way

A new and interesting aspect can be the formulation where the nanoparticles are dispersed: for example hydrogels or creams can improve the NPs permeation.

Nanoparticles designed for a cutaneous application are mainly created for a local treatment but it's possible also their systemic diffusion by the lymphatic circle³⁷⁻⁴⁰.

1.4. Drugs and dosage forms

The drug is a substance with a pharmaceutical activity used for diagnosis, prevention and treatment of disease. A dosage form of a drug is a product suited for the administration to the patient by various routes for diagnosis or therapy. The drug administration is possible by dosage forms manufactured with the use of auxiliary substances or excipients, which are determinants for the dosage forms preparation and performances. These substances don't have pharmacological activity but they can alter the release profile, the action site, and thus change the drug availability, the characteristics and the efficacy of the drug³³.



Figure 1.9. Solid dosage forms.

The dosage form is the presentation of the drug after the transformation that makes it suitable for a specific administration route. In fact, to be delivered, the drug should be treated in the appropriate way for the selected administration route and it should be carried on a suitable specific dosage form: capsules, tablets, suspensions, suppositories, sprays, etc.

The dosage forms are classified in different ways:

A. Depending on the physic form:

- **semisolids** (creams, gels, etc)
- **solids** (tablets, powders, etc)
- **liquids** (solutions, etc)
- **gas**;

B. Depending on the administration route:

- **oral**

- **intravenous**
- **ocular**
- **parenteral**
- **topical**, etc

C. Depending on the type of the drug release:

- **conventional release dosage form:** the drug release depends on its molecular characteristics, so it's an immediate release.
- **modified release dosage form:** the speed and the release site are modified by peculiar preparation methods and, in particular, the drug release can be:
 1. Extended (the release is slower than the conventional one)
 2. Retarded (the release is delayed with respect to the administration time)
 3. Repeated (the release is sequentially repeated)

D. Depending on the unit of the dosage form:

- **single unit dosage form:** unitary subdivision of the dose.
- **multiple dose dosage form:** it's provided a measurement of the prescribed dose by the patient. They can be solutions, powders or syrups. The benefit can be the possibility to adapt the dose to each patient but the principal disadvantage is the not accurate measurement.

E. Depending on the volume (exclusively for the parenteral):

- **large-volume parenteral dosage form:** infusions and injections with a volume >100mL.
- **small-volume parenteral dosage form:** infusions and injections with a volume <100mL.

The pharmacopoeia also mentions other dosage forms for a specific use: **ear, nasal, ophthalmic, inhalator, rectal, vaginal and parenteral preparations.**

The science evolution and the use of new materials allow a remarkable progress in terms of drugs formulation, trying to adapt the pharmaceutical technology to the new therapeutic needs^{41,42}. Therefore, a lot are the formulations with a modified release or that ones which use new mirco- and nano-vehicles. The pharmaceutical technologies are continuously improving the development of new medical treatments and a multidisciplinary approach could be the key of more efficient therapies⁴³.

Bibliography

1. Dufort, S., Sancey, L. & Coll, J.-L. Physico-chemical parameters that govern nanoparticles fate also dictate rules for their molecular evolution. *Adv. Drug Deliv. Rev.* **64**, 179–189 (2012).
2. Haun, J. B., Devaraj, N. K., Hilderbrand, S. A., Lee, H. & Weissleder, R. Bioorthogonal chemistry amplifies nanoparticle binding and enhances the sensitivity of cell detection. *Nat. Nanotechnol.* **5**, 660–665 (2010).
3. Roy, K., Kanwar, R. K. & Kanwar, J. R. Molecular targets in arthritis and recent trends in nanotherapy. *Int. J. Nanomedicine* **10**, 5407–5420 (2015).
4. Guo, J., Jiang, X. & Gui, S. RNA interference-based nanosystems for inflammatory bowel disease therapy. *Int. J. Nanomedicine* **11**, 5287–5310 (2016).
5. Takedatsu, H., Mitsuyama, K. & Torimura, T. Nanomedicine and drug delivery strategies for treatment of inflammatory bowel disease. *World J. Gastroenterol.* **21**, 11343–11352 (2015).
6. Vio, V., Marchant, M. J., Araya, E. & Kogan, M. J. Metal nanoparticles for the treatment and diagnosis of neurodegenerative brain diseases. *Curr. Pharm. Des.* (2017).
7. Di Martino, P. *et al.* Nano-medicine improving the bioavailability of small molecules for the prevention of neurodegenerative diseases. *Curr. Pharm. Des.* (2016).
8. Torres-Sangiao, E., Holban, A. M. & Gestal, M. C. Advanced Nanobiomaterials: Vaccines, Diagnosis and Treatment of Infectious Diseases. *Mol. Basel Switz.* **21**, (2016).
9. Salatin, S. *et al.* Hydrogel nanoparticles and nanocomposites for nasal drug/vaccine delivery. *Arch. Pharm. Res.* **39**, 1181–1192 (2016).
10. Schroeder, A. *et al.* Treating metastatic cancer with nanotechnology. *Nat. Rev. Cancer* **12**, 39–50 (2011).
11. Ferrari, M. Cancer nanotechnology: opportunities and challenges. *Nat. Rev. Cancer* **5**, 161–171 (2005).
12. Blanco, E. *et al.* Nanomedicine in cancer therapy: innovative trends and prospects. *Cancer Sci.* **102**, 1247–1252 (2011).
13. Drugs@FDA: FDA Approved Drug Products. Available at: <http://www.accessdata.fda.gov/scripts/cder/daf/>. (Accessed: 30th January 2017)
14. Lammers, T., Kiessling, F., Hennink, W. E. & Storm, G. Drug targeting to tumors: principles, pitfalls and (pre-) clinical progress. *J. Control. Release Off. J. Control. Release Soc.* **161**, 175–187 (2012).

15. Davis, M. E., Chen, Z. G. & Shin, D. M. Nanoparticle therapeutics: an emerging treatment modality for cancer. *Nat. Rev. Drug Discov.* **7**, 771–782 (2008).
16. Farokhzad, O. C. & Langer, R. Impact of Nanotechnology on Drug Delivery. *ACS Nano* **3**, 16–20 (2009).
17. Shubayev, V. I., Pisanic, T. R. & Jin, S. Magnetic nanoparticles for theragnostics. *Adv. Drug Deliv. Rev.* **61**, 467–477 (2009).
18. Fang, C. & Zhang, M. Multifunctional magnetic nanoparticles for medical imaging applications. *J. Mater. Chem.* **19**, 6258–6266 (2009).
19. Albanese, A., Tang, P. S. & Chan, W. C. W. The effect of nanoparticle size, shape, and surface chemistry on biological systems. *Annu. Rev. Biomed. Eng.* **14**, 1–16 (2012).
20. Florez, L. *et al.* How shape influences uptake: interactions of anisotropic polymer nanoparticles and human mesenchymal stem cells. *Small Weinh. Bergstr. Ger.* **8**, 2222–2230 (2012).
21. Brain tumour localisation and destruction facilitated by gadolinium-based nanoparticles in microbeam radiation therapy. Available at: http://www.esrf.eu/news/spotlight/spotlight162/index_html. (Accessed: 30th January 2017)
22. Çağdaş, M., Sezer, A. D. & Bucak, S. Liposomes as Potential Drug Carrier Systems for Drug Delivery. (2014). doi:10.5772/58459
23. Barenholz, Y. (Chezy). Doxil® — The first FDA-approved nano-drug: Lessons learned. *J. Controlled Release* **160**, 117–134 (2012).
24. Weissleder, R., Bogdanov, A., Neuwelt, E. A. & Papisov, M. Long-circulating iron oxides for MR imaging. *Adv. Drug Deliv. Rev.* **16**, 321–334 (1995).
25. Baroli, B. Penetration of nanoparticles and nanomaterials in the skin: fiction or reality? *J. Pharm. Sci.* **99**, 21–50 (2010).
26. Emerich, D. F. & Thanos, C. G. Targeted nanoparticle-based drug delivery and diagnosis. *J. Drug Target.* **15**, 163–183 (2007).
27. Jokerst, J. V., Lobovkina, T., Zare, R. N. & Gambhir, S. S. Nanoparticle PEGylation for imaging and therapy. *Nanomed.* **6**, 715–728 (2011).
28. Hersh, D. S. *et al.* Evolving Drug Delivery Strategies to Overcome the Blood Brain Barrier. *Curr. Pharm. Des.* **22**, 1177–1193 (2016).
29. Bhowmik, A., Khan, R. & Ghosh, M. K. Blood Brain Barrier: A Challenge for Effectual Therapy of Brain Tumors. *BioMed Res. Int.* **2015**, (2015).
30. Govindarajan, A., Lakshmanan, P. M., Sarawagi, R. & Prabhakaran, V. Evaluation of date

syrup as an oral negative contrast agent for MRCP. *AJR Am. J. Roentgenol.* **203**, 1001–1005 (2014).

31. Rekha, M. R. & Sharma, C. P. Oral delivery of therapeutic protein/peptide for diabetes--future perspectives. *Int. J. Pharm.* **440**, 48–62 (2013).
32. Florence, A. T. Issues in Oral Nanoparticle Drug Carrier Uptake and Targeting. *J. Drug Target.* **12**, 65–70 (2004).
33. Team, M. S. Principi di tecnologie farmaceutiche - Paolo Colombo.
<http://www.mondadoristore.it/> Available at: <http://www.mondadoristore.it/Principi-tecnologie-Paolo-Colombo/eai978880808683/>. (Accessed: 15th February 2017)
34. Menon, J. U. *et al.* Polymeric nanoparticles for pulmonary protein and DNA delivery. *Acta Biomater.* **10**, 2643–2652 (2014).
35. Roberts, M. S. *et al.* Topical and cutaneous delivery using nanosystems. *J. Control. Release Off. J. Control. Release Soc.* **247**, 86–105 (2016).
36. DeLouise, L. A. Applications of nanotechnology in dermatology. *J. Invest. Dermatol.* **132**, 964–975 (2012).
37. Labouta, H. I., el-Khordagui, L. K., Kraus, T. & Schneider, M. Mechanism and determinants of nanoparticle penetration through human skin. *Nanoscale* **3**, 4989–4999 (2011).
38. Mortensen, L. J. *et al.* Quantification of quantum dot murine skin penetration with UVR barrier impairment. *Nanotoxicology* **7**, (2013).
39. Filipe, P. *et al.* Stratum Corneum Is an Effective Barrier to TiO₂ and ZnO Nanoparticle Percutaneous Absorption. *Skin Pharmacol. Physiol.* **22**, 266–275 (2009).
40. Ryman-Rasmussen, J. P., Riviere, J. E. & Monteiro-Riviere, N. A. Penetration of intact skin by quantum dots with diverse physicochemical properties. *Toxicol. Sci. Off. J. Soc. Toxicol.* **91**, 159–165 (2006).
41. Maroni, A. *et al.* In vitro and in vivo evaluation of an oral multiple-unit formulation for colonic delivery of insulin. *Eur. J. Pharm. Biopharm. Off. J. Arbeitsgemeinschaft Pharm. Verfahrenstechnik EV* **108**, 76–82 (2016).
42. Del Curto, M. D. *et al.* Erodible time-dependent colon delivery systems with improved efficiency in delaying the onset of drug release. *J. Pharm. Sci.* **103**, 3585–3593 (2014).
43. Yin, L., Wang, Y., Wang, C. & Feng, M. Nano-reservoir Bioadhesive Tablets Enhance Protein Drug Permeability Across the Small Intestine. *AAPS PharmSciTech* (2017).

doi:10.1208/s12249-016-0709-6

Chapter 2

Aim of the thesis

The aim of this thesis is to investigate the destiny of different kind of engineered colloidal nanoparticles (NPs) administered by different administration routes. In particular, the peculiarity of this work is the focus on both the nanotechnological and the technological-formulative aspects in order to develop new nanovehicle-based treatments with a better pharmaceutical performance compared to the drugs currently on the marketplace.

To obtain satisfactory pharmacokinetics profiles the nanoparticles should be able to interact with the biological structures like membranes, cytoplasm, nucleus, internal organelles and, therefore, they should have a good colloidal stability in aqueous environment.

All types of nanoparticles used for this project are characterized in terms of size, shape, weight and surface charge.

The administration routes that I have investigated in my work are:

- A. TOPICAL ADMINISTRATION
- B. ORAL ADMINISTRATION
- C. INHALATIONAL ADMINISTRATION
- D. INTRAVENOUS ADMINISTRATION

So far, nanotechnology has produced many different types of nanoparticles: for each considered treatment, a specific type of nanoparticle and a suitable dosage form is designed.

A) TOPICAL ADMINISTRATION OF IRON OXIDE NANOPARTICLES

To the best of my knowledge, the studies about the nanoparticles skin permeation and penetration are few and with heterogeneous results, mainly due to the type, shape, size and stability of the employed nanoparticles¹⁻⁷.

My purpose is to design and develop iron oxide nanoparticles coated with an amphiphilic polymer and formulated in highly stable suspensions or incorporated into semi-solids, to cross the skin in order to be used for loco-regional therapeutic treatments.

Iron oxide nanoparticles are particularly interesting since they have been already used in several medical areas, including therapeutics and diagnostics and their safety profile is already known.

They are ideal candidates as contrast agents for magnetic resonance imaging and magnetic force-assisted drug delivery systems.

Once the NPs suspension skin passage is assessed, the nanoparticles are loaded into different semi-solid formulations (creams and gels) to test the possible NPs permeation improvement.

In vitro experiments are performed on human abdominal skin and *in vivo* study in mice is set up to evaluate the NPs biodistribution after subcutaneous injection in comparison to topical administration.

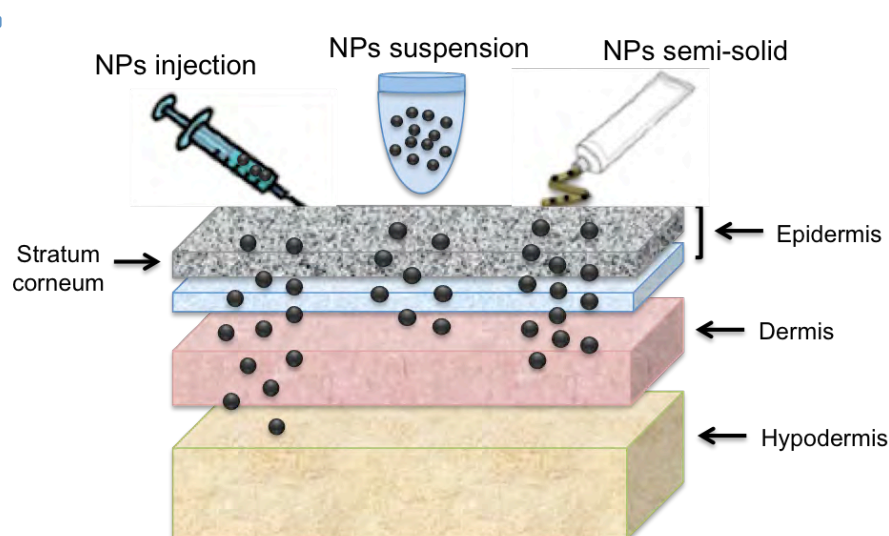


Figure 2.1. Skin layers and different NPs administration routes for skin permeation study.

B) ORAL ADMINISTRATION OF POLYMERIC NANOPARTICLES CONTAINING INSULIN

Several research studies have been focused on the development of novel formulations for the oral administration of insulin⁸⁻¹⁰. This could be a big benefit for diabetic patients who are daily subjected to intravenous injection. For this reason, insulin-containing nanoparticles are loaded into pellet cores and orally administered to diabetic rats. The pellets are an oral multiple-unit dosage form, which guarantee more homogeneous distribution in the gastrointestinal tract and less inter- and intra-individual variations. The nanoparticles proposed are polyethylene imine-based nanoparticles, selected for the positive charge that can allow more adhesion in intestinal tract, due to the negative charges of the mucins, glycoproteins present in large quantity in the mucus. NPs are incorporated by extrusion and spheronization technology into cores with an absorption enhancer and they are going to be subsequently coated with two overlapping layers and a gastrointestinal film. A triple coating of the NPs is developed for the retarded release of insulin into the distal intestine, characterized by relatively low proteolytic activity and high residence intervals of time. The nanotechnology science and the knowledge of the solid pharmaceutical forms allow building a novel nanoformulation, multiple-unit colon release system, i.e. pellets, as a possible oral nanocarrier for insulin.

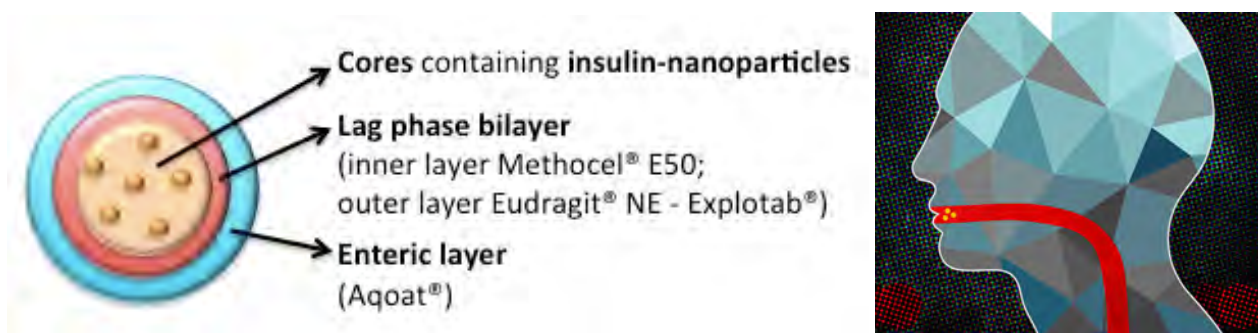


Figure 2.2. Pellet for oral delivery formulated with polyethylene imine-based nanoparticles.

C) TARGETED GOLD NANOPARTICLES LOADED WITH EVEROLIMUS FOR INHALATIONAL ADMINISTRATION

The aim of this project is a preliminary study of gold nanoparticles (GNPs) for the treatment of bronchiolitis obliterans syndrome (BOS), a typical chronic lung allograft dysfunction. Gold nanoparticles are an interesting nanomaterial characterized by their unique-size dependent electron and optical properties combined with a great potential as drug-delivery vehicles for biomedical applications¹¹⁻¹³. The GNPs are covered with an amphiphilic polymer and they are designed to be loaded with an immunosuppressant drug (everolimus) in the hydrophobic section and functionalized on the surface with a monoclonal antibody selective for the receptor expressed by mesenchymal cells, which are responsible of the pathology. This project wants to test the capability of functionalized GNPs to be a selective and efficient drug delivery system and future perspectives interest the *in vivo* administration by inhalation of GNPs on animal models of obliterative bronchiolitis.

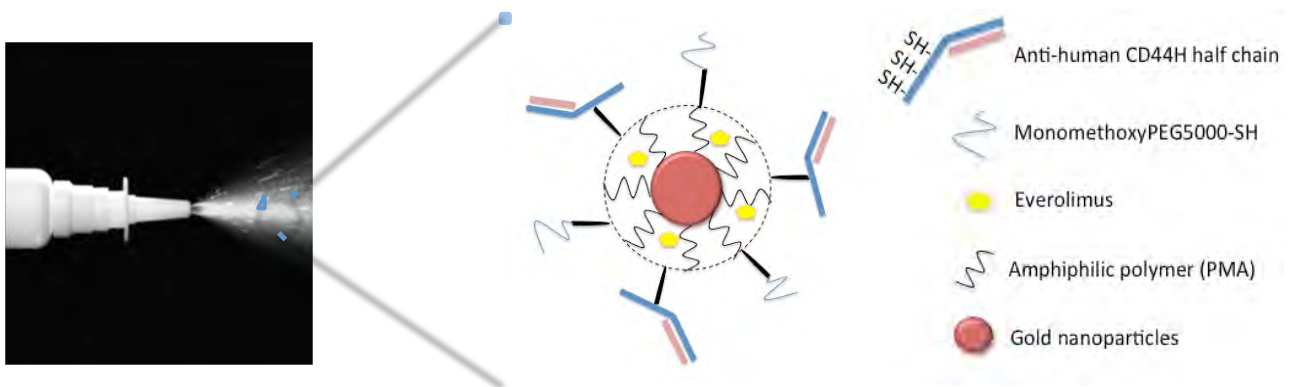


Figure 2.3. Functionalized gold nanoparticles for pulmonary targeting.

D) NANOFORMULATION OF AN ANTIRETROVIRAL DRUG ABLE TO CROSS THE BLOOD BRAIN BARRIER (BBB) AFTER INTRAVENOUS INJECTION

The blood brain barrier (BBB) is a poorly crossable endothelium by most drugs and for their inability to reach the central nervous system (CNS) most are the neurodegenerative disorders, which don't have effective therapies¹⁴⁻¹⁶.

For example, some peptides, potentially useful for the CNS diseases treatment, are unable to arrive to the cerebrospinal fluid after intravenous injection¹⁷.

To overcome this limit, I inject iron oxide nanoparticles conjugated with a peptide by intravenous administration to improve the peptide passage to the CNS. Iron oxide nanoparticles are coated with an amphiphilic polymer, which allows the NPs surface functionalization with the peptide and at the same time the conjugation with a dye. In this way it's possible to follow the NPs' destiny and the possible peptide translocation across the BBB.

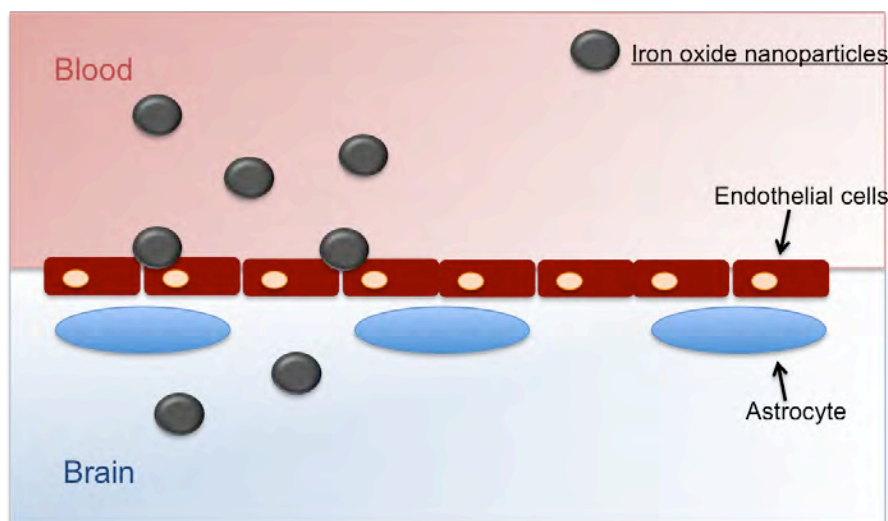


Figure 2.4. BBB passage of iron oxide nanoparticles.

Bibliography

1. Schneider, M., Stracke, F., Hansen, S. & Schaefer, U. F. Nanoparticles and their interactions with the dermal barrier. *Dermatoendocrinol.* 1, 197–206 (2009).
2. Baroli, B. *et al.* Penetration of metallic nanoparticles in human full-thickness skin. *J. Invest. Dermatol.* 127, 1701–1712 (2007).
3. Laresse, F. F. *et al.* Human skin penetration of silver nanoparticles through intact and damaged skin. *Toxicology* 255, 33–37 (2009).
4. Tak, Y. K., Pal, S., Naoghare, P. K., Rangasamy, S. & Song, J. M. Shape-Dependent Skin Penetration of Silver Nanoparticles: Does It Really Matter? *Sci. Rep.* 5, 16908 (2015).
5. Wang, L. & Wang, J. Skin penetration of inorganic and metallic nanoparticles. *J. Shanghai Jiaotong Univ. Sci.* 19, 691–697 (2014).
6. Baroli, B. Penetration of nanoparticles and nanomaterials in the skin: fiction or reality? *J. Pharm. Sci.* 99, 21–50 (2010).
7. Labouta, H. I. & Schneider, M. Interaction of inorganic nanoparticles with the skin barrier: current status and critical review. *Nanomedicine Nanotechnol. Biol. Med.* 9, 39–54 (2013).
8. Patel, M. M. Colon targeting: an emerging frontier for oral insulin delivery. *Expert Opin. Drug Deliv.* 10, 731–739 (2013).
9. Bayat, A. *et al.* Nanoparticles of quaternized chitosan derivatives as a carrier for colon delivery of insulin: ex vivo and in vivo studies. *Int. J. Pharm.* 356, 259–266 (2008).
10. Damgé, C., Reis, C. P. & Maincent, P. Nanoparticle strategies for the oral delivery of insulin. *Expert Opin. Drug Deliv.* 5, 45–68 (2008).
11. Giljohann, D. A. *et al.* Gold nanoparticles for biology and medicine. *Angew. Chem. Int. Ed Engl.* 49, 3280–3294 (2010).
12. Ghosh, P., Han, G., De, M., Kim, C. K. & Rotello, V. M. Gold nanoparticles in delivery applications. *Adv. Drug Deliv. Rev.* 60, 1307–1315 (2008).
13. Cogley, C. M., Chen, J., Cho, E. C., Wang, L. V. & Xia, Y. Gold nanostructures: a class of multifunctional materials for biomedical applications. *Chem. Soc. Rev.* 40, 44–56 (2011).
14. Ballabh, P., Braun, A. & Nedergaard, M. The blood-brain barrier: an overview: structure, regulation, and clinical implications. *Neurobiol. Dis.* 16, 1–13 (2004).
15. Domínguez, A., Álvarez, A., Suárez-Merino, B. & Goñi-de-Cerio, F. [Neurological disorders and the blood-brain barrier. Strategies and limitations for drug delivery to the brain]. *Rev. Neurol.* 58, 213–224 (2014).

16. Vries, H. E. de, Kuiper, J., Boer, A. G. de, Berkel, T. J. C. V. & Breimer, D. D. The Blood-Brain Barrier in Neuroinflammatory Diseases. *Pharmacol. Rev.* 49, 143–156 (1997).
17. Saraiva, C. *et al.* Nanoparticle-mediated brain drug delivery: Overcoming blood–brain barrier to treat neurodegenerative diseases. *J. Controlled Release* 235, 34–47 (2016).

Chapter 3

Results and discussion

3.1. TOPICAL ADMINISTRATION OF IRON OXIDE NANOPARTICLES

3.1.1. Introduction

The skin is the organ responsible of the thermoregulation, breathing and defence so it's difficult to deliver a drug into the skin layers at the desired depth, overcoming the *stratum corneum* (SC), which is the principal skin barrier¹.

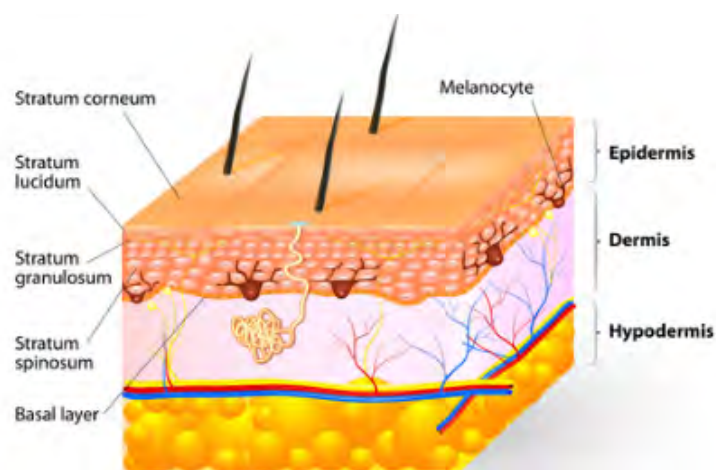


Figure 3.1.1. Human skin section.

Also, drug topical administration remains a challenge for the difficulties to adjust the skin penetration and to determine and reproduce the exact amount of the delivered drug into the skin layers.

There is a great interest in nanoparticles delivery of diagnostic and therapeutic into the skin because it represents a new opportunity to improve the treatment of loco-regional diseases and a lot of papers have been published investigating the skin penetration of many types of nanoparticles²⁻⁷. There are studies of topical application of TiO₂, Fe₃O₄, Au, Ag NPs and quantum dots with controversial conclusions⁸.

Until now, the NPs topical applications have mainly focused on skin cancer imaging and targeting therapeutics, vaccine delivery, antimicrobials and cosmetics⁹ and some of them are under clinical assessment or are going to be commercialized¹⁰.

To be useful in therapeutic applications, nanoparticles must be able to penetrate the skin barrier and be detected into the skin layers without adverse side effects.

Topical administration of NPs can be used to optimize the loco-regional treatment: a lower dosage results in an higher concentration of the drug at the target tissue, reducing systemic side effects with a better patient compliance^{11,12}. This strategy could be very useful to front failed cutaneous treatment with drugs characterized by low bioavailability due to instability, poor solubility, poor absorption and enzymatic degradation.

Looking at the critical points of the NPs cutaneous delivery, size, shape, surface properties and interactions with biological structures of the skin are crucial aspects.

It's known by literature that only the NPs smaller than 40nm are able to penetrate through the *stratum corneum* while 10nm-NPs are able to permeate the epidermis (HE)^{3,7}. To overcome SC, NPs can use different ways: the intercellular route, the trans-cellular one or the hair follicles.

Furthermore, the NPs permeation performance depends also on the composition and the physicochemical properties of the semi-solid formulation required to obtain a suitable cutaneous product. To my knowledge, creams formulations have never been exploited to improve the NPs absorption.

In the present works, iron oxide nanoparticles (MNP) coated by poly-(isobutylene-*alt*-maleic anhydride) (PMNP) are selected to test their skin permeation capability and to follow their fate into the skin layers. MNP represent a big promise for medical application since they are used as oral gastrointestinal contrast agents in MRI (i.e. Gastromark® and Ferumoxsil-containing products), they can be efficient drug delivery systems and, therefore, their safety profile is already known¹³⁻¹⁵.

However, the potential toxicity of colloidal nanoparticles remains an open question since most intravenously administered compounds approved by Food and Drug Administration (FDA) have been withdrawn from the marketplace¹⁶. Anyway, recent studies demonstrate that a "bio-friendly" surface coating can reduce the oxidative stress responsible of the toxicological effects improving the NPs stability in biological environment^{17,18}.

This study is discussed in two published papers.

In the first paper *in vitro* and *in vivo* experiments are set up: in the *in vitro* tests the penetration of PMNP colloidal suspension through human skin is compared with that one of the same nanoparticles developed in a water-in-oil (w/o) cream formulation, which consists of small droplets of water dispersed in a continuous oily phase; in the *in vivo* experiment a subcutaneous injection in mice of fluorescent PMNP is compared with the PMNP-cream treatment to investigate the NPs biodistribution.

The second paper shows the effect of different semi-solid formulations (creams and hydrogels) on PMNP skin permeation and *in vitro* tests highlight the incidence of the semi-solid vector in the NPs permeation. Indeed, the stability of the NPs in a vehicle is a critical factor that could affect the efficacy of their topical administration. For this reason, a systematic study of the interaction between the physicochemical features of PMNP and the different semi-solid formulations is carried out.

3.1.2. Iron oxide nanoparticles

Iron oxide nanoparticles are synthesized by solvothermal decomposition in organic solvent¹⁹. Starting from organometallic precursors, at high temperature and in presence of stabilizing surfactants, 12.0 ± 1.2 nm average diameter monodisperse nanoparticles (MNP) are prepared. To have a stable suspension in a physiological environment, a water phase transfer of nanoparticles is needed. To this aim, MNP are coated with an amphiphilic polymer (PMA), obtained by reacting poly-(isobutylene-*alt*-maleic anhydride) with an amount of dodecylamine sufficient to reach with 75% of anhydride groups²⁰. In this process the oleic acid (surfactant) of the MNP is intercalated with the hydrophobic alkyl chains of the PMA, which exhibits the hydrophilic backbone on the external water phase.

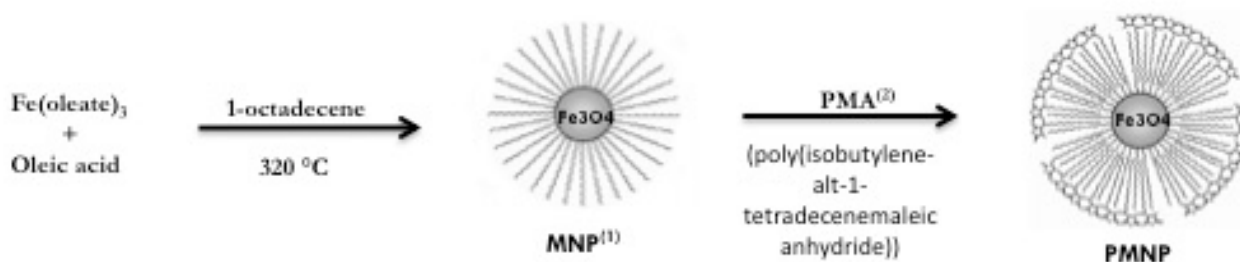


Figure 3.1.2. MNP synthesis and coating with PMA (PMNP).

The obtained coating exhibits peculiar advantages:

1. Colloidal stability in biological environment.
2. Surface functionalization with drugs or targeting molecules.
3. Improved NPs passage through hydrophilic-hydrophobic skin layers.
4. Ameliorated cream formulation homogeneity.

Based on these remarks, PMNP are a hybrid system that can provide MR imaging and drug delivery at the same time. Indeed, the magnetic *core* is the source of the magnetic signal and the *shell* guarantees the drug loading and the surface functionalization for the selective target. The resulting nano-system has a hydrodynamic diameter of 23.2 ± 2.0 nm, a ζ -potential of -64.80 ± 4.91 and it's stable and monodisperse in size. To evaluate their potential activity as magnetic resonance imaging contrast enhancer, the value of decreasing concentrations of PMNP in water is measured and it is $186 \text{ mM}^{-1} \text{ s}^{-1}$ at 0.47 T. This value is higher than the negative contrast power of agents currently available in approved clinical diagnostic practice (r_2 of Ferumxtyol is $83 \text{ mM}^{-1} \text{ s}^{-1}$ at 0.47 T).

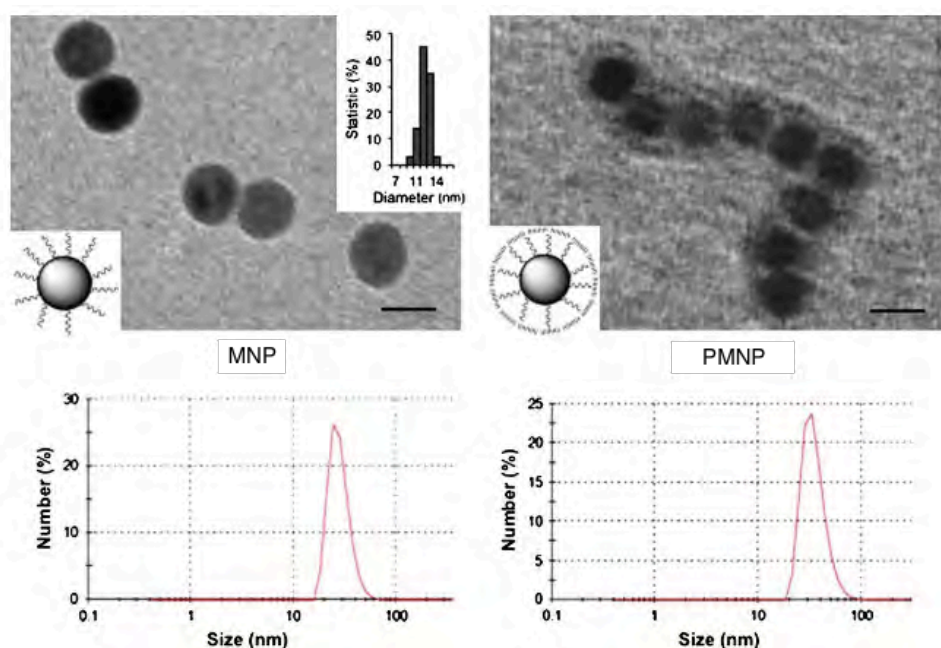


Figure 3.1.3. Transmission Electron Microscopy (TEM) and Dynamic Light Scattering (DLS) of MNP and PMNP. Scale bars 10nm. (Data taken from Santini et al)²¹.

For *in vivo* studies, PMNP are labelled with a dye (CFSE) using the bifunctional diamino-linker 2,2-(ethylenedioxy)-bis(ethylamine) (EDBE) previously activated by *N*-(3-dimethylaminopropyl)-*N'*-ethylcarbodiimide (EDC).

3.1.3. Investigation of PMNP penetration through the human skin.

In vitro skin permeation studies are carried out using human skin after verifying the morphological integrity of all the skin layers: the used skin is composed by *stratum corneum*, epidermis and dermis. The permeation experiment is conducted testing in parallel the PMNP suspension and the PMNP w/o cream in the Franz Diffusion Cell (FDCs). The two formulations are added in the donor compartment and samples of the receptor fluid, filled with PBS, are taken at various time intervals (1-3-5-7-24 h) and they are measured by ICP-OES to quantify the amount of iron normalized with that one present in the control samples. At the end of exposure time (24h) the skin treated with the two PMNP formulations are analysed by transmission (TEM) and scanning electron microscopies (SEM).

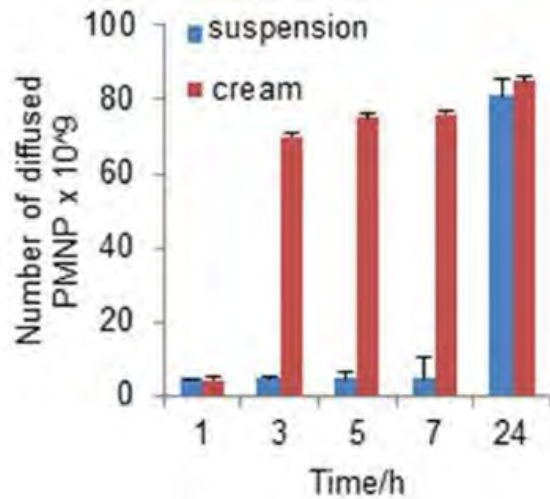


Figure 3.1.4. *In vitro* diffusion results of PMNP colloidal suspension and PMNP w/o cream. (Data taken from Santini et al)²².

.At the first sampling times it's evident the difference in terms of diffusion between the permeated PMNP of the suspension and that ones mixed with the cream: the cream formulation gives accelerated and homogeneous nanoparticle permeation. Moreover, the cream can give skin hydration and occlusive effect, which are factors determinants the PMNP's permeation. Figure 3.1.4., at 24h, shows no significant difference between cream and suspension administration, since the cream allows the reduction of the penetration and diffusion times.

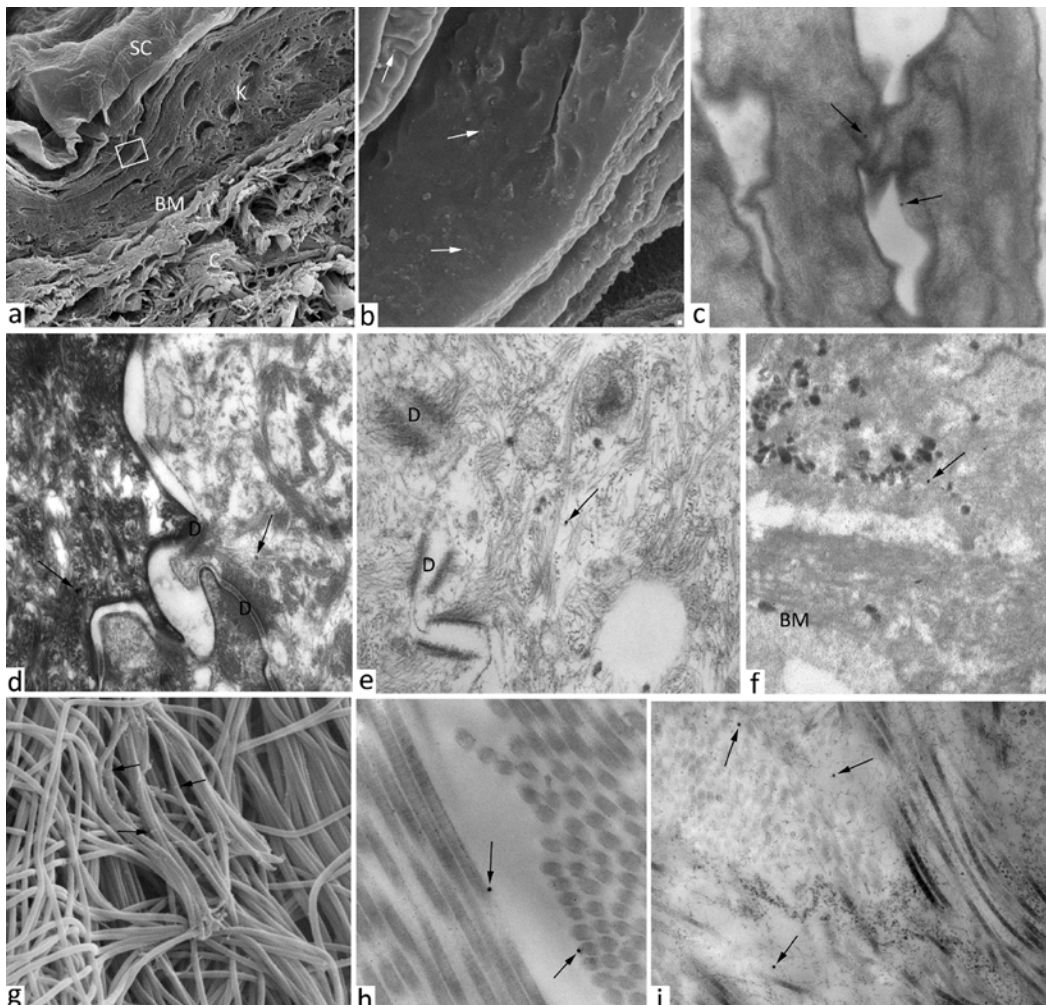


Figure 3.1.5. TEM and SEM images of treated skin.
(Data taken from Santini et al)²².

Also, TEM and SEM images (Figure 3.1.5., a-i) show PMNP intradermal delivery across the intact skin layers: there are no significant differences between the two formulations in terms of permeation mechanism and amount of penetrated NPs after 24h. PMNP are found in all the skin layers. Furthermore, PMNP are observed among corneocytes and across epidermis cells and this provides evidence that they use both the intercellular and intracellular pathway, even if the follicular pathway should be the easiest way to occur for large molecules. In all the TEM and SEM images PMNP maintain their individuality and they don't aggregate.

3.1.4. Interaction with skin-localized cells of innate immunity in living mice.

PMNP incorporation by cutaneous cells is evaluated in mouse models. Two different nanoparticles administration are performed: the sub-cutaneous injection of PMNP-CFSE and the topical application of the PMNP-CFSE cream. The cream is applied to the skin of previously shaved C57BL/6 mice (1 cm²), after 24h the mice are sacrificed and treated skin is analysed by flow cytometry after having obtained single cell suspensions. The draining lymph nodes are also analysed to consider the lymphatic transport. Skin cells of hematopoietic and non-hematopoietic origin are identified as CD45-positive and negative, respectively.

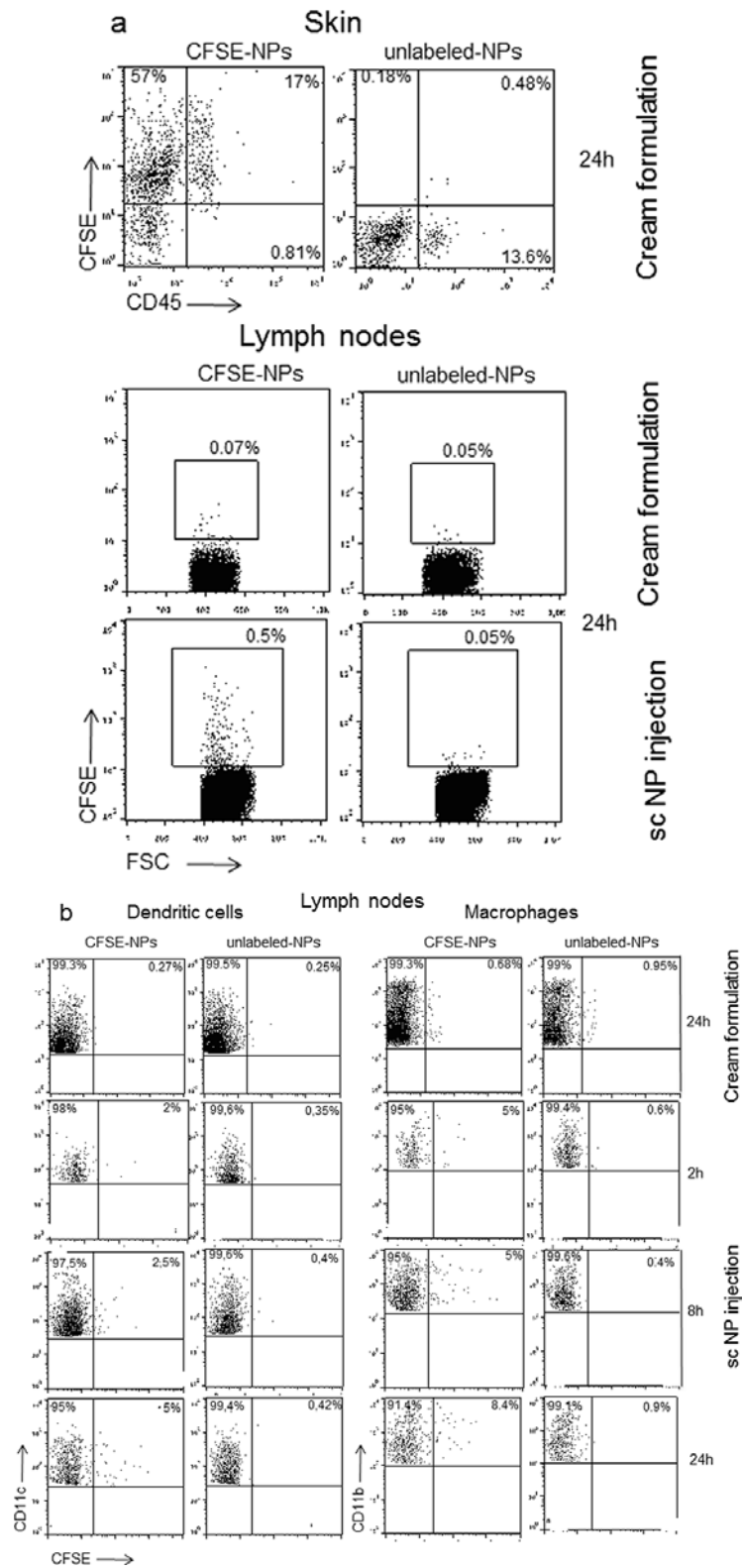


Figure 3.1.6. Cytofluorimetric analysis of PMNP uptake by mouse skin and lymph node cells. (Data taken from Santini et al)²².

Starting from the upper panels in Figure 3.1.6., skin CD45-positive and negative cells show CFSE incorporation. Most of the skin cells uptake PMNP nanoparticles administered with the cream formulation. In the lower panel the uptake of CFSE-positive cells in the lymph nodes are shown and, only with subcutaneous PMNP administration, nanoparticles-positive cells can be detected. Since no positive staining is observed in the draining lymph nodes, nanoparticles administered with cream formulations remained confined to the skin.

3.1.5. Formulation study of PMNP semi-solid preparations.

The second work aims to investigate the impact of five different semi-solid formulations on the physical stability of nanoparticles and on the *in vitro* penetration through HE.

PMNP are loaded in three hydrogels and two hydrophilic creams. The hydrogels used are hydroxyethyl cellulose (HEC), sodium carboxymethyl cellulose (CMC) and carbomer 974P (CP); the creams used are cetomacrogol cream (Cet) and a cold cream (SEP).

The physical stability of PMNP loaded into the semi-solid formulations is determined by two methods: low-field pulsed NMR and dynamic light scattering (DLS). The first technique provides information on the magnetic properties of nanoparticles, which are influenced by deviation in structure, surface composition, concentration and mobility. The second one allows to analyse the NPs hydrodynamic diameter, their possible aggregation phenomena and the surface charge. Both these techniques can give information about the physical stability of the NPs loaded into the semi-solids.

All the results of the PMNP semi-solid formulations are compared with that ones of the aqueous suspension.

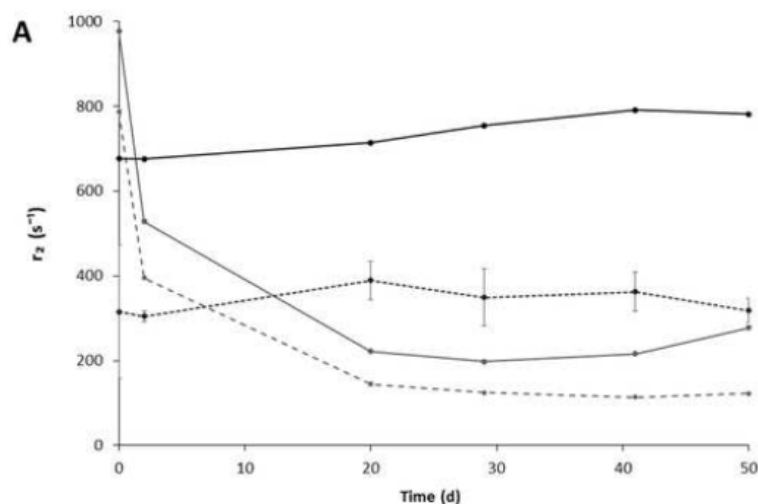


Figure 3.1.7. Variation of the r^2 of PMNP loaded in HEC (grey, solid line), CMC (grey, dash line) and CP (black, solid line) hydrogels, compared with the water suspension of PMNP (black, dash line). (Data taken from Santini et al)²¹.

Starting from the low-field pulsed NMR analysis, the measurement of the r^2 value of the nanoparticles in different media represents a sensitive parameter to control the interactions between the NPs and the formulation components. The r^2 value of the NPs in water doesn't significantly change within 50 days of storage at $25 \pm 2^\circ\text{C}$, confirming the PMNP water stability. The NPs dispersed in the two creams (Cet and Sep) have a similar trend so it can be assumed that NPs maintain their characteristics without losing stability. No changes are noticed also in the PMNP formulated in the CP hydrogel. Conversely, NPs dispersed in HEC and CMC hydrogels show a marked decrease of r^2 values after one day of storage, indicating a possible aggregation or alteration in size of iron oxide core.

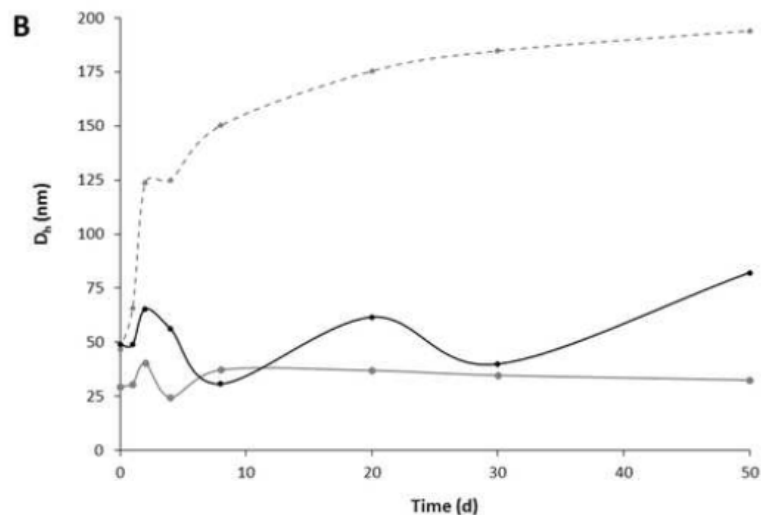


Figure 3.1.8. Variation of the hydrodynamic diameter (D_h) of PMNP loaded in HEC (grey, solid line), CMC (grey, dash line) and CP (black, solid line) hydrogels, compared with the water suspension of PMNP (black, dash line). (Data taken from Santini et al)²¹.

The DLS technique doesn't allow to directly analyse the NPs formulations: a prior sample dilution is required. Also, placebo hydrogels and o/w creams are analysed by DLS to evaluate possible interferences with the NPs signal. Looking at the measurements, DLS cannot be used to analyse the creams because the dispersed oily phase and the formulation viscosity don't allow to obtain correct and reproducible results. Based on these remarks, it's possible just to measure the three PMNP formulated into the hydrogels: NPs loaded into CP and HEC hydrogel appear stable; NPs loaded into CMC result unstable. These results confirm that ones of the low-field pulsed NMR except for the case of HEC. Probably, reversible NPs aggregates are not detectable by DLS due to the sample dilution.

Due to the physical instability of PMNP loaded in the CMC hydrogel, this vehicle is not considered for the permeability tests.

3.1.6. *In vitro* permeation studies

The permeation studies interest the amount of NPs permeated through HE and accumulated into SC and viable epidermis (VE) and the TEM – STEM/EDX images of the treated HE.

TEM images show the presence of nanoparticles both into the upper HE layers and near to the basal membrane of epidermis.

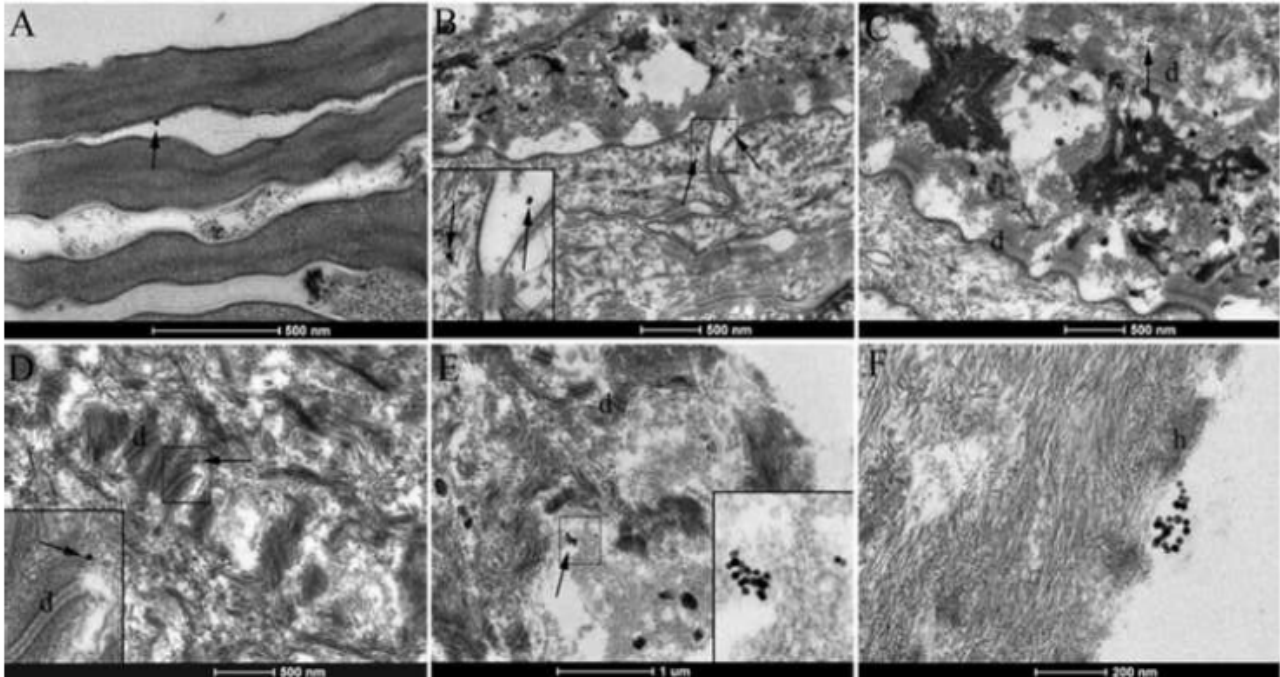


Figure 3.1.9. Transmission electron microscopy (TEM) images of skin samples treated with PMNP loaded into semi-solid formulations.

(Data taken from Santini et al)²¹.

As Figure 3.1.9. shows, the nanoparticles are found in *stratum corneum* (A), in *stratum lucidum* (B), in *stratum granulosum* (C), in *stratum spinosum* close to desmosomes (D), in *stratum basale* (E) and in proximity of desmosomes (F). It's also interesting notice in the Figure 3.1.9.B a nanoparticle into a cell of the *stratum lucidum* inside the cytoplasm.

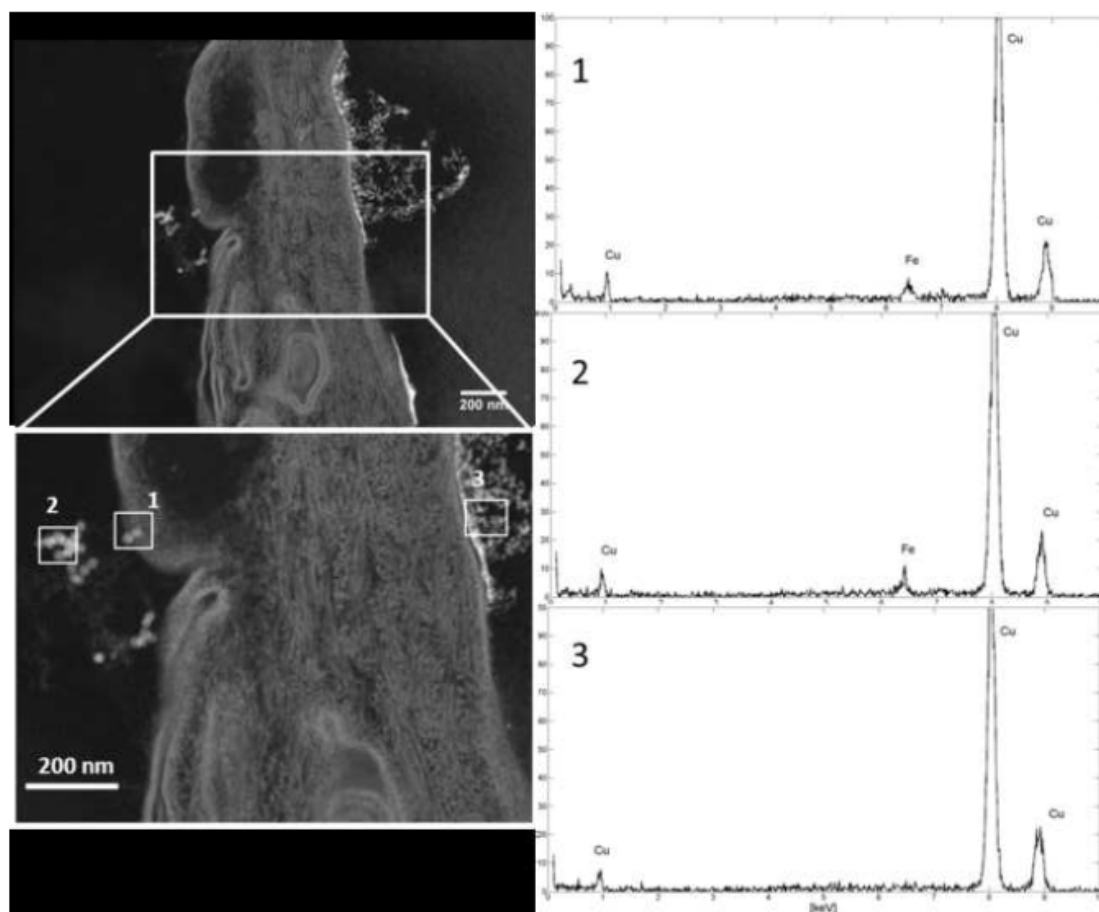


Figure 3.1.10. On the left, STEM images of HE treated with PMNP and its enlargement; in the right, EDX spectra of the highlighted white squares. (Data taken from Santini et al)²¹.

STEM analysis shows nanostructures close to the *stratum corneum* brighter than the other elements. The higher brilliance of the elements indicated by the white squares 1 and 2 in Figure 3.1.10. suggests that they are more electron dense and heavy than the other parts of the sample. This signal is analysed by EDX pointing the electron beam directly on these white spots to determine their elemental composition. The spectra reported on the right side of the STEM micrographs evidence the presence of the iron signals only in squares 1 and 2 of Figure 3.1.10., confirming that the nanoparticles are MNP. There are also two other peaks: a weak C-signal and a strong Cu-signal. Both of them are attributed to the epidermis.

The Franz diffusion cell allows to quantify the retained amounts (Q_{ret}) and the permeated amounts (Q_{24}) in SC and VE of aqueous suspension and semisolid preparations.

Formulation	Q_{ret}		Q_{24}		$Q_{ret}/Q_{24,HE}$
	A	N	A	N	
	$(\mu\text{g}/\text{cm}^2)$		$(\mu\text{g}/\text{cm}^2)$		
Water suspension	2.91±1.04	1.98±0.70	4.35±0.74	2.30±0.14	0.67
HEC hydrogel	1.73±0.34	1.18±0.23	3.48±0.30	1.84±0.16	0.50
CP hydrogel	4.70±0.25	3.19±0.17	7.22±2.40	3.83±1.27	0.65
Cet cream	1.98±0.57	1.34±0.39	10.51±2.46	5.57±1.30	0.19
Cold cream	5.30±0.74	3.60±0.50	8.05±4.50	4.26±2.39	0.66
Blank	1.47±0.08	1.00±0.05	1.89±0.26	1.00±0.14	-

normalize values with respect to blank (N) (mean ± SD; n=3).

Figure 3.1.11. Results of Q_{24} and Q_{ret} studies of aqueous suspensions and semisolid preparations containing 3 mg/mL of PMNP. (Data taken from Santini et al)²¹.

As Figure 3.1.11. shows, HE contains traces of iron due to the intense mitotic activity of VE²³ but after 24h of PMNP exposure the iron amount permeated through HE is double, suggesting the NPs capability to permeate the SC barrier and to concentrate into the VE.

The four semi-solid preparations have different trends in terms of skin penetration, highlighting the influence of the vehicle. All formulations significantly increase the permeated amount after 24h, except for the HEC hydrogel. CP hydrogel and cold cream are able to increase also the amount of PMNP retained into the HE.

The $Q_{ret}/Q_{24,HE}$ ratio of all the tested semi-solid formulations are similar to that of aqueous suspension (i.e., about 0.67), the permeated iron amount from the Cet cream is one order of magnitude higher than the relative retention data ($Q_{ret}/Q_{24,HE}$: 0.19), suggesting a higher tendency of PMNP to permeate than to be retained into the HE when they are loaded in the Cet cream.

Also, membranes based on regenerated keratins (RKM)²⁴, are used to verify the tendency of nanoparticles to diffuse through intracellular pathway of SC, because the permeation through RKM follows the affinity of NPs for the intracellular compartment of SC. The results show that $Q_{24,RKM}$ ($6.4 \pm 0.1 \mu\text{g}/\text{cm}^2$) is in accordance with the $Q_{24,HE}$ values.

On the other side, the $Q_{ret,RKM}$ ($28 \pm 5 \text{ ng}/\text{mg}$) is significantly lower than the value obtained through SC (p value: 0.024). Hence, it may be assumed that weak interactions occur between PMNP and keratins and PMNP diffuse preferentially through an intercellular pathway²⁵. TEM images confirm this hypothesis evidencing the presence of the NPs inly in the interstitial spaces among keratinocytes (Figure 3.1.9).

Bibliography

1. Elias, P. M. & Choi, E. H. Interactions among stratum corneum defensive functions. *Exp. Dermatol.* **14**, 719–726 (2005).
2. Schneider, M., Stracke, F., Hansen, S. & Schaefer, U. F. Nanoparticles and their interactions with the dermal barrier. *Dermatoendocrinol.* **1**, 197–206 (2009).
3. Baroli, B. *et al.* Penetration of metallic nanoparticles in human full-thickness skin. *J. Invest. Dermatol.* **127**, 1701–1712 (2007).
4. Larese, F. F. *et al.* Human skin penetration of silver nanoparticles through intact and damaged skin. *Toxicology* **255**, 33–37 (2009).
5. Tak, Y. K., Pal, S., Naoghare, P. K., Rangasamy, S. & Song, J. M. Shape-Dependent Skin Penetration of Silver Nanoparticles: Does It Really Matter? *Sci. Rep.* **5**, 16908 (2015).
6. Wang, L. & Wang, J. Skin penetration of inorganic and metallic nanoparticles. *J. Shanghai Jiaotong Univ. Sci.* **19**, 691–697 (2014).
7. Baroli, B. Penetration of nanoparticles and nanomaterials in the skin: fiction or reality? *J. Pharm. Sci.* **99**, 21–50 (2010).
8. Labouta, H. I. & Schneider, M. Interaction of inorganic nanoparticles with the skin barrier: current status and critical review. *Nanomedicine Nanotechnol. Biol. Med.* **9**, 39–54 (2013).
9. Roberts, M. *et al.* Topical and cutaneous delivery using nanosystems. *J. Controlled Release* **247**, 86–105 (2017).
10. DeLouise, L. A. Applications of nanotechnology in dermatology. *J. Invest. Dermatol.* **132**, 964–975 (2012).
11. Mathias, N. R. & Hussain, M. A. Non-invasive systemic drug delivery: developability considerations for alternate routes of administration. *J. Pharm. Sci.* **99**, 1–20 (2010).
12. Bolzinger, M.-A., Briançon, S., Pelletier, J. & Chevalier, Y. Penetration of drugs through skin, a complex rate-controlling membrane. *Curr. Opin. Colloid Interface Sci.* **17**, 156–165 (2012).
13. Weissleder, R., Bogdanov, A., Neuwelt, E. A. & Papisov, M. Long-circulating iron oxides for MR imaging. *Adv. Drug Deliv. Rev.* **16**, 321–334 (1995).
14. Wang, J. *et al.* Magnetic nanoparticles for MRI of brain tumors. *Curr. Pharm. Biotechnol.* **13**, 2403–2416 (2012).
15. Govindarajan, A., Lakshmanan, P. M., Sarawagi, R. & Prabhakaran, V. Evaluation of date syrup as an oral negative contrast agent for MRCP. *AJR Am. J. Roentgenol.* **203**, 1001–1005

(2014).

16. Bulte, J. W. M. In vivo MRI cell tracking: clinical studies. *AJR Am. J. Roentgenol.* **193**, 314–325 (2009).
17. Remya, N. S., Syama, S., Sabareeswaran, A. & Mohanan, P. V. Toxicity, toxicokinetics and biodistribution of dextran stabilized Iron oxide Nanoparticles for biomedical applications. *Int. J. Pharm.* **511**, 586–598 (2016).
18. Revia, R. A. & Zhang, M. Magnetite nanoparticles for cancer diagnosis, treatment, and treatment monitoring: recent advances. *Mater. Today Kidlington Engl.* **19**, 157–168 (2016).
19. Park, J. *et al.* Ultra-large-scale syntheses of monodisperse nanocrystals. *Nat. Mater.* **3**, 891–895 (2004).
20. Pellegrino, T. *et al.* Hydrophobic Nanocrystals Coated with an Amphiphilic Polymer Shell: A General Route to Water Soluble Nanocrystals. *Nano Lett.* **4**, 703–707 (2004).
21. Musazzi, U. M. *et al.* Impact of semi-solid formulations on skin penetration of iron oxide nanoparticles. *J. Nanobiotechnology* **15**, (2017).
22. Santini, B. *et al.* Cream Formulation Impact on Topical Administration of Engineered Colloidal Nanoparticles. *PLoS ONE* **10**, (2015).
23. Lansdown, A. B. G. Metal ions affecting the skin and eyes. *Met. Ions Life Sci.* **8**, 187–246 (2011).
24. Selmin, F., Cilurzo, F., Aluigi, A., Franzè, S. & Minghetti, P. Regenerated keratin membrane to match the in vitro drug diffusion through human epidermis. *Results Pharma Sci.* **2**, 72–78 (2012).
25. Prow, T. W. *et al.* Nanoparticles and microparticles for skin drug delivery. *Adv. Drug Deliv. Rev.* **63**, 470–491 (2011).

3.2. ORAL ADMINISTRATION OF POLYMERIC NANOPARTICLES CONTAINING INSULIN

3.2.1. Introduction

Type 1 diabetes is characterized by insufficient insulin secretion or its inadequate activity and the disease progression requires the introduction of exogenous insulin^{1,2}. Till now, the standard administration of insulin views the daily parenteral injection of the peptide, causing a significant reduction in quality of life and joining low compliance by the patient^{3,4}. Also, the subcutaneous injection of insulin doesn't allow a physiological distribution of the peptide as the physiological secretion; indeed, half of insulin produced by the pancreas is used for liver metabolism via the portal circulation, resulting in fine regulation of blood glucose levels and adequate metabolism of carbohydrates and proteins. For these reasons, the administration of insulin by alternative administration routes is matter of several research studies⁵. Particularly, the oral route is considered one of the most promising choices in order to have a better glucose regulation exploiting the liver first-pass metabolism of insulin, thus preventing the risks of fluctuating blood glucose levels and possibly the resulting morbidity due to chronic microvascular complications⁶. Still, the oral delivery of insulin remains an unmet need.

In this contest, the colon delivery is gaining increasing interest since it's characterized by specific properties such as low proteases activity, longer transit time, prolonged localization of insulin on the gut mucosa and greater responsiveness to permeation enhancers compared to the more proximal regions of the gastrointestinal tract. For these characteristics, the colon represents an interesting target for insulin oral delivery but, so far, an efficient drug delivery system is still not designed. From a general point of view, the oral delivery of insulin can be a big contribution to diabetic patients but it faces a principal trouble that is the low oral bioavailability of the peptide due to the degradation by proteases in the gastro-intestinal tract.

In the recent years, both nanomedicine and pharmaceutical technology have tried to design new systems able to improve the oral delivery of insulin.

The objective of this project is to evaluate the synergistic effect of these two branches of science in order to deliver a new efficient oral nano-system. One of the research aims of the nanoparticles-based vector is the protection of the drugs against chemical and enzymatic degradation with the possibility to improve the drug absorption by epithelia. The attempts to improve the oral delivery of insulin by NPs are few and it requires a nanovector suitable both for insulin incorporation and intestinal epithelium absorption after oral administration⁷⁻⁹. The NPs size and charge are the principal characteristics, which influence the insulin absorption by the enterocytes. In general small and positively charged NPs are absorbed more efficiently through the intestinal epithelium, because it is characterized by negative charges of mucins, glycoproteins present in large quantity in the mucus. A positively charged system has prolonged residence time and increases concentration gradient at the surface of the intestinal mucosa.

For the delivery of a nanosystem to the colon site, a solid dosage form, such as pellets or tablets, is required in order to allow the nanoparticles-containing insulin release in the desired site.

In my work, *in vitro* and *in vivo* studies are performed to test a novel nanoformulated, multiple-unit colon release system, i.e. coated pellets, as a possible nanocarrier for insulin.

The novelty of this approach is the evaluation of the synergistic effect of colon release, mucoadhesive nanoparticles and the presence of a permeation enhancer, sodium

glycocholate. In particular, this system is based on the benefits of this multiple-unit formulation and the consequent absorption pattern with the advantages of colloidal nanoparticles¹⁰. The pellets are an oral multiple-unit dosage form, which guarantees more homogeneous distribution in the gastro-intestinal tract and less inter- and intra-individual variations. They are made by a core, in which NPs are formulated with a absorption enhancer and by a triple coating consisting of a flexible film composed of a natural polymethacrylate Eudragit® NE and a superdisintegrant sodium starch glycolate Explotab®, added as a pore former, applied to a hydroxypropyl methylcellulose (HPMC) coating of reduced thickness in order to improve the efficiency of the erodible layer in delaying the drug liberation^{11,12}. An outer gastroresistant layer is also added in order to neutralize the variable residence time in the stomach of the coated dosage form and it allow its activation only following the entry into the duodenum. This time-dependent relies on the relative consistency of short intestinal transit time, the subsequent colon targeting and favouring the intestinal absorption of insulin at that level¹³.

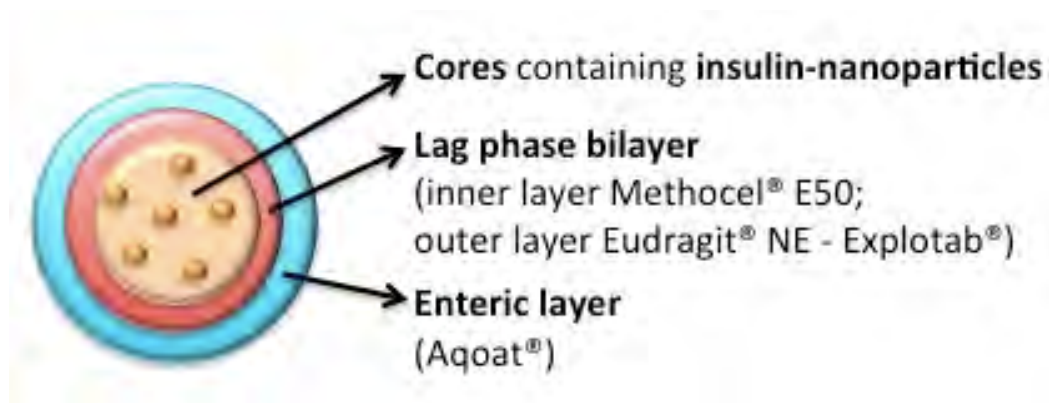


Figure 3.2.1. Structure of pellet containing insulin nanoparticles.

3.2.2. Nanoparticles synthesis and characterization

The polymeric nanoparticles are synthesized according to previously published preparation methods^{14,15}. The driving force of this synthesis is the opposite charge of polyethylene imine (PEI) and dextran sulphate resulting in the insulin incorporation into the polymeric matrix. Briefly, insulin and dextran sulphate solutions are added to the PEI solution under heating at 40°C. It is necessary to introduce some modification to the published protocol with the aim of scaling up the amount of synthesized NPs and reduce the amount of excipients to include in the final pellet formulation. The weight ratio between the two polymers is optimized in order to control the particle size and zinc sulphate solution is added dropwise to stabilize the nanoparticles (Figure 3.2.2.A).

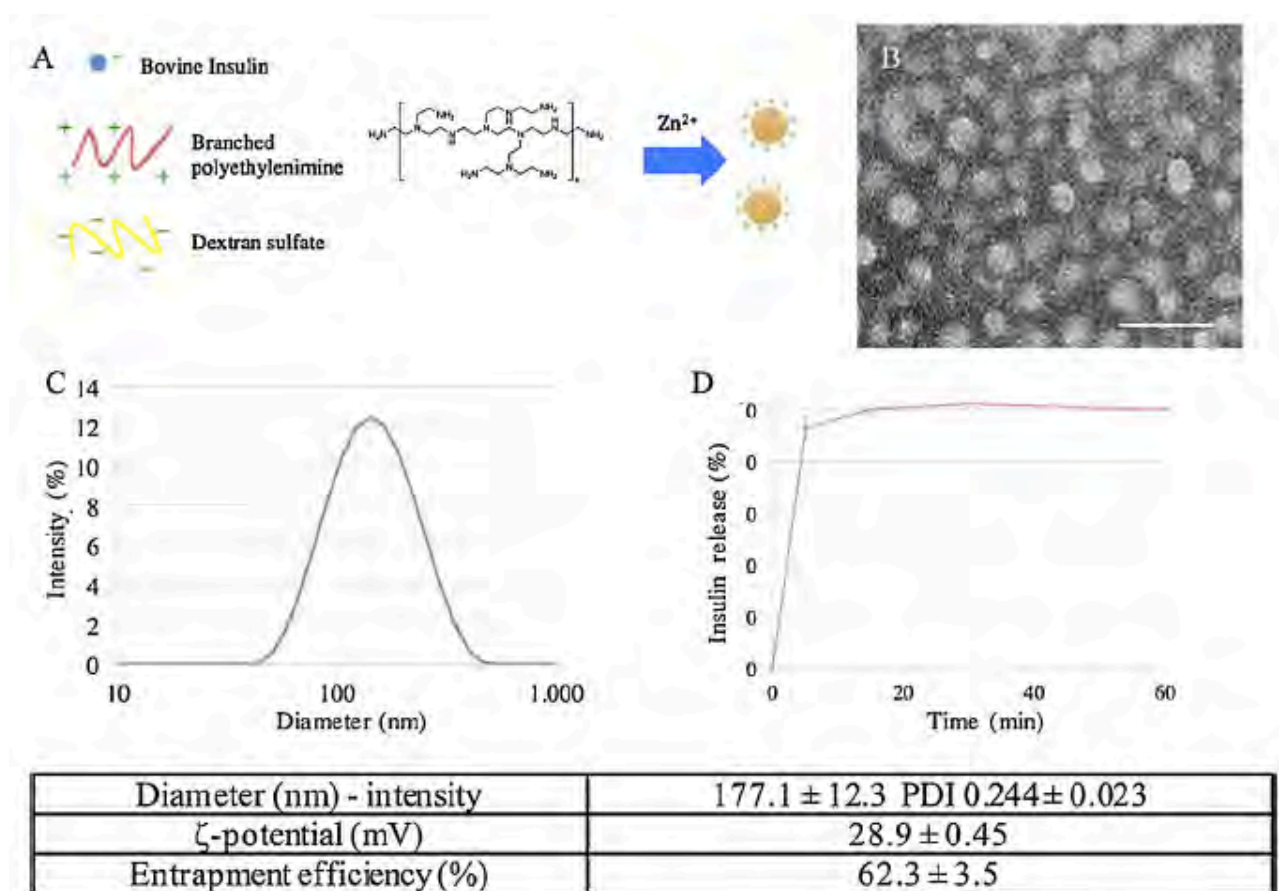


Figure 3.2.2. Schematic representation of insulin-containing nanoparticles (NI) synthesis (A). TEM image of NI, scale bar: 100 nm (B). Hydrodynamic size of NI measured by DLS (C). Dissolution profile of NI at 6.8 pH (mean ± SD, n=3) (D). (Data taken from Salvioni et al)¹⁶.

Another modification of the synthesis protocol interests the dialysis: NI are washed with deionized water instead of recommended 5% (w/v) mannitol solution. The amount of NI in the final dialyzed product is 72% of the starting amount. The obtained product, thanks to the modifications, results in 5-fold increase of insulin loading and in a 35-fold reduction of the material amount required to form the pellets. In this way, a concentrated colloidal suspension is obtained, more suitable for following pellets inclusion. Figure 3.2.2.B shows TEM images of spherical and nearly monodisperse 30 nm NI while, the hydrodynamic diameter (Figure 3.2.2.C) is 177 ± 12.3 nm, probably due to the high solvation efficiency of the polymeric matrix. The zeta potential is 28.9 ± 0.5 mV. The entrapment efficiency (EE%) determined after

extraction in acidic solution and measured by RP-HPLC is $62.3 \pm 3.5\%$, while the % of the degradation product A21-desamido insulin is $1.2 \pm 0.1\%$. Also, a release test is conducted and in 5 minutes there is over 90% of peptide dissolution at pH 6.8.

3.2.3. Core preparation and characterization

In order to achieve a prompt release of the nanoparticles at the desired site, an appropriate core formulation is designed.

Table 3.2.1. Compositions of cores under investigation.

Formulation	% (w/w)						
	Insulin	NI	Placebo NPs ^a	Avicel® CL611	Sodium glycocholate (NaGly)	Lactose	Explotab® CLV
PN01	---	---	50.0	50.0	---	---	---
PN02	---	---	50.0	26.4	---	15.7	7.9
PNI01	---	43.2	---	43.2	13.6	---	---
PNI02	---	43.2	---	22.7	13.6	13.8	6.7
PI02	2.3	---	---	39.1	23.4	23.7	11.5

^a The percentage refers to the solid nanoparticles. (Data taken from Salvioni et al)¹⁶.

A cellulose derivative, Avicel® CL611, a co-processed microcrystalline cellulose and sodium carboxymethyl cellulose, is identified as suitable spheronization agent due to the well-known advantages in terms of improved disintegration and dissolution performance over the traditional formulations based on microcrystalline cellulose¹⁷. Moreover, a superdisintegrant agent (Explotab® CLV) and a soluble diluent (lactose) are added in an alternative formulation in order to further improve the pursued fast-disintegration properties (Table 3.2.1.). Only in the case of pellets loaded with NI, sodium glycocholate (NaGly), an absorption enhancer with protease inhibition properties, is considered^{18,19}. The latter functional agent is indeed demonstrated to promote the oral absorption of a pancreatic hormone in rats administered with a minitablet formulation at 1:10 protein/adjuvant ratio²⁰. In addition, NaGly, due to its high solubility in aqueous media, could help to prevent the undesired matrix formation when pellets interact with water, thus possibly aiding their disintegration. Based on preliminary extrusion and spheronization trials, a 1:1 Avicel® CL611/placebo nanoparticles binary mixture is acknowledged as starting formulation suitable to lead to a dough with appropriate plasticity and pellets with adequate morphological characteristics (Table 3.2.1.). When insulin-containing formulations or all other systems containing Explotab® CLV and lactose are used, the process appears facilitated probably due to the concomitant decrease of nanoparticle amount and increase in the total solid mass attributable to the presence of the NaGly powder. In all cases, the possible issue associated with the large amount of colloidal suspension needs to obtain the required insulin dose for the *in vivo* studies, i.e. 4:1 w/w water vs. total solid mass, is overcome by adding the liquid in small aliquots and allowing the subsequent evaporation that limits the moisture content of the extrudable mass.

Table 3.2.2. Physico-chemical properties and process yield of cores prepared by extrusion and spheronization.

Batch	d_{geo} (μm)	σ_{geo} (μm)	AR	Yield (%)	Insulin recovery %	A21%
PN01	913	1.18	1.36 ± 0.18	59.9	-	-
PN02	804	1.21	1.38 ± 0.20	40.1	-	-
PNI01	809	1.21	1.21 ± 0.18	41.3	102.1 ± 1.6	1.8 ± 0.2
PNI02	1137	1.28	1.16 ± 0.10	61.9	88.8 ± 3.7	0.9 ± 0.3
PI02	1066	1.16	1.29 ± 0.15	74.4	91.8 ± 1.1	2.2 ± 0.3

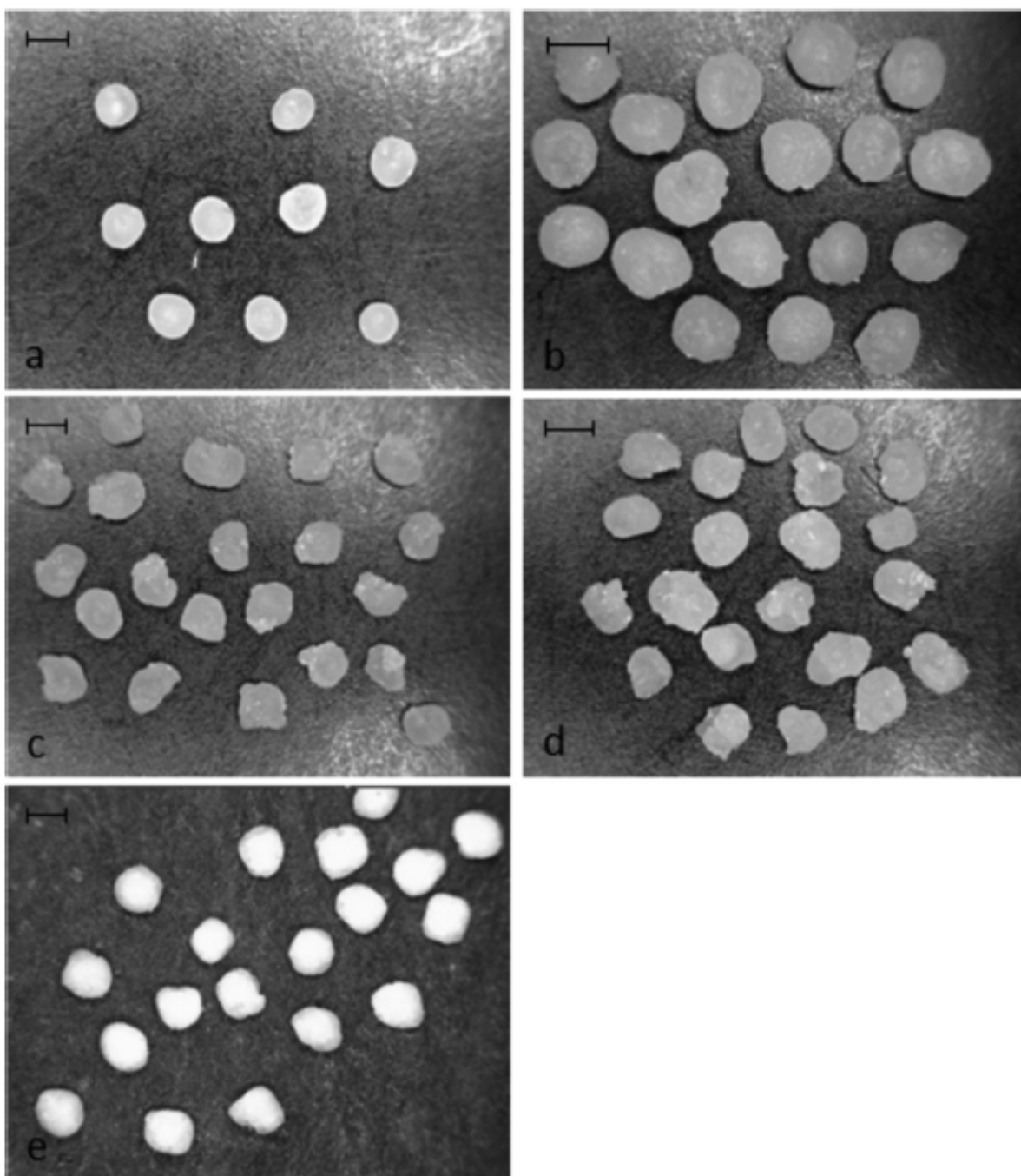


Figure 3.2.3. Digital photographs of core formulation under investigation: a)PN01, b)PN02, c)PNI01, d)PNI02 and e)PN02. Scale bar: 1 mm. (Data taken from Salvioni et al)¹⁶.

All the process yields are > 40% and, taking into account the low amounts of processed material, are considered satisfying. All batches show a mean particle size comprised within the desired 710–1400 μm range and a nearly spherical shape (Table 3.2.2, Figure 3.2.3). Only in the case of formulation batches PNI02 and PI02 a slightly higher mean diameter is observed. No differences in size or shape are observed between placebo and insulin-loaded pellets, which is not surprising considering that the final core product structure is not significantly affected by the low amount of protein payload within the colloidal suspension. The protein content in the pellets is $\geq 90\%$ of the theoretical amount and, despite the long wetting and evaporation phases, the % of A21 remains below the limits indicated in the monograph of bovine insulin reported of Pharm. Eur. 8th Ed., i.e. 3%. The overall results suggest that extrusion and spheronization might be a promising technology for loading a nanoparticle suspension into pellets.

3.2.4. *In vitro* studies of cores

Pellets containing the insulin-loaded nanoparticles are subjected to *in vitro* studies aiming to assess the disintegration and insulin release performances from the two different formulations. PNI02 formulation shows enhanced disintegration compared to PNI01, i.e. 26.4 vs. 10.8%. This behaviour can be ascribed to the presence of the superdisintegrant Explotab[®] and that of lactose acting as pore former compared to the formulation where the excipients are only Avicel[®] CL611. However, comparing such performance with that of a reference formulation containing paracetamol as analytical tracer instead of insulin nanoparticles and Avicel[®] CL611/lactose/Explotab[®] CLV in the same ratios as PNI02 formulation, a $\geq 75\%$ disintegration is obtained. It can be thus inferred that the presence of nanoparticles considerably contributes to the formation of a slow-eroding matrix. To confirm this result, re-dispersion studies are performed on batch PNI02, which appears the most promising system from *in vitro* disintegration and dissolution tests. These studies are setup in order to evaluate the presence of NI after exposure of the solid dosage form to aqueous fluids. Samples of this medium are collected and analysed by DLS. Nanoparticles with a mean diameter of 146.1 ± 1.0 nm ($n = 3$) are detected. Comparing the size of NI, before and after E-S process, it is noticed that the mean diameter is slightly lower than the initial value (177.1 ± 12.3 nm), although the size distribution appears to be maintained as evaluated by DLS polydispersity index (0.296 ± 0.005). To figure out the cause of this reduction, the same test is performed on 25 mg of a dried dough obtained by using the same components and operating conditions of the cores of PNI02 batch avoiding extrusion and spheronization steps. Also in this case, a decrease of mean diameter occurs, suggesting that it may depend on the mechanical stress during the dough formation. It can be thus inferred that cores under investigation might convey and liberate the colloidal system upon exposure to aqueous media.

3.2.5. Preparation and characterization of coated pellets

Pellets batches PNI02 and PI02 are selected as core formulations for preliminary *in vivo* testing on the basis of the *in vitro* results in terms of enhanced disintegration and dissolution properties. The cores are therefore coated either with a hydroalcoholic solution of Acoat[®] or in turn with a Methocel[®] E50-, Eudragit[®] NE/Explotab[®] CLV- and Acoat[®]- based formulations in order to prepare gastroresistant (G) and three-layer colonic (C) systems, respectively (Table 3.2.3.).

Table 3.2.3. Physico-technological characteristics of gastroresistant and three-layer colonic pellets.
(Data taken from Salvioni et al)¹⁶.

Formulations	d _m (µm)	SD (µm)	AR	Methocel® E50 mg/cm ²	Eudragit® NE-Explotab® CLV 20% mg/cm ²	Acoat® mg/cm ²
GPNI	1355	114	1.14	-	-	13.1
CPNI	1865	102	1.07	89.9	4.0	13.0
GPI	1392	121	1.25	-	-	11.9
CPI	2070	149	1.24	85.1	3.1	12.5

In the three-layer system, the hydrophilic layer based on Methocel® E50 is demonstrated to delay the drug release by a swelling/erosion mechanism, while the Eudragit® NE/Explotab® CLV film is aimed at prolonging the duration of the lag phase as imparted by the underlying HPMC coat. Finally, an outer gastroresistant film is added to the system to overcome the unpredictable gastric residence time of the system thus allowing its activation only at the duodenum and the consequent colonic release based on a time-dependent approach^{13,20}. The adopted process operative conditions and the coating levels need to achieve gastroresistance or a delayed release after a lag-phase suitable for colonic delivery are previously set up with an analogous formulation containing paracetamol as analytical tracer (data not shown). In particular, gastroresistance criteria are accomplished with an Acoat® coating level of 12–13 mg/cm². When using colonic systems, an *in vitro* lag time of approximately 60 min corresponded to 85–90 mg/cm² of Methocel® E50, 3.0–4.0 mg/cm² of Eudragit® NE-Explotab® CLV 20% and 12–13 mg/cm² of Acoat®²⁰. Particularly, a similar multiple-unit system with an *in vitro* lag phase of the latter duration shows an insulin peak in rats and a corresponding drop in blood glucose levels 6 h post-dose following oral administration. Based on typical gastrointestinal transit times reported in the literature for rats, the delivery system, after this lag time, is expected to be able to arrive, mostly intact, to the ileo-colonic region²¹. All coated batches show a mean particle size in the 1.3–2.1 mm range and coating levels in line with what expected based on preliminary set up results. The shape is closer to roundness than the starting cores, as a result of the subsequent coating steps. When subjected to *in vitro* release tests all formulation meet gastroresistance criteria (< 10% release after 2 h in 0.1 M HCl), albeit the release test is conducted under more vigorous stirring, performed by magnetic stirrer, compared to the compendial method (Figure 3.2.4).

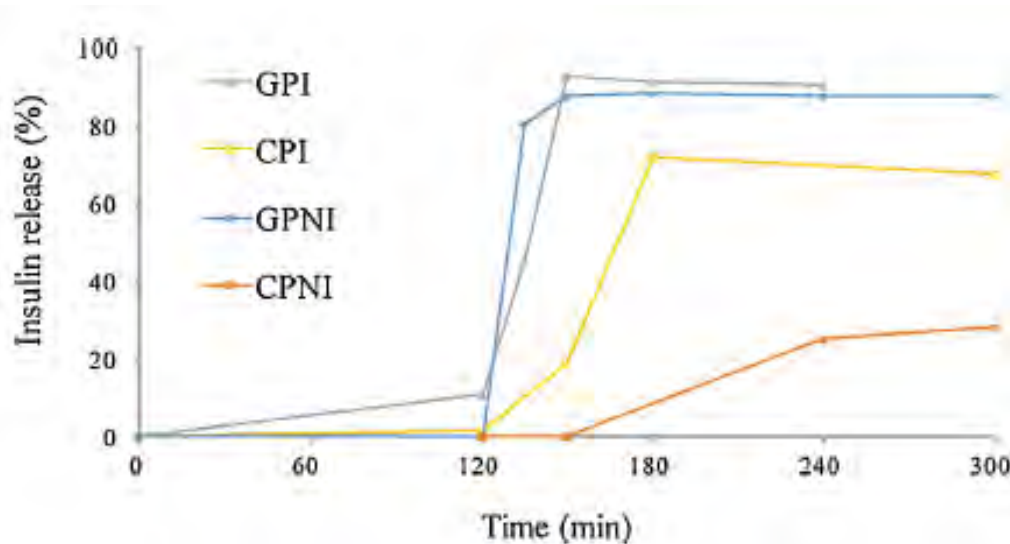


Figure 3.2.4. *In vitro* insulin release of coated pellets.
(Data taken from Salvioni et al)¹⁶.

When exposed to a pH 6.8 buffer, all enteric systems show a prompt release due to core disintegration following dissolution of the enteric coat. The three-layer colonic systems containing the NI show a lag-phase preceding the onset of release. The time corresponding to 10% release, $t_{10\%}$, is 65 min. Moreover, the CPI pellet formulation used as reference shows a shorter lag time that is demonstrated to be caused by the adopted release testing conditions (data not show).

3.2.6. *In vivo* hypoglycaemic effect

The NI loaded into the pellets are tested *in vivo* in diabetic rats. The rat model is chosen since the gastrointestinal transit time is comparable to that of humans²². The animals that reach stable glucose values in blood of at least 350 mg/dL following streptozotocin administration are subjected to one of the following treatments: 1) oral administration of 1.33 mg/kg insulin (OI) or as NI, 2) subcutaneous injection of 0.07 mg/kg insulin (SCI), 3) insertion through gastrostomy of different amounts of pellets in capsules (GPI, GPNI, CPI, CPNI) to allow administration of 1.33 mg/kg. A group of non-treated rats is used as control (NT).

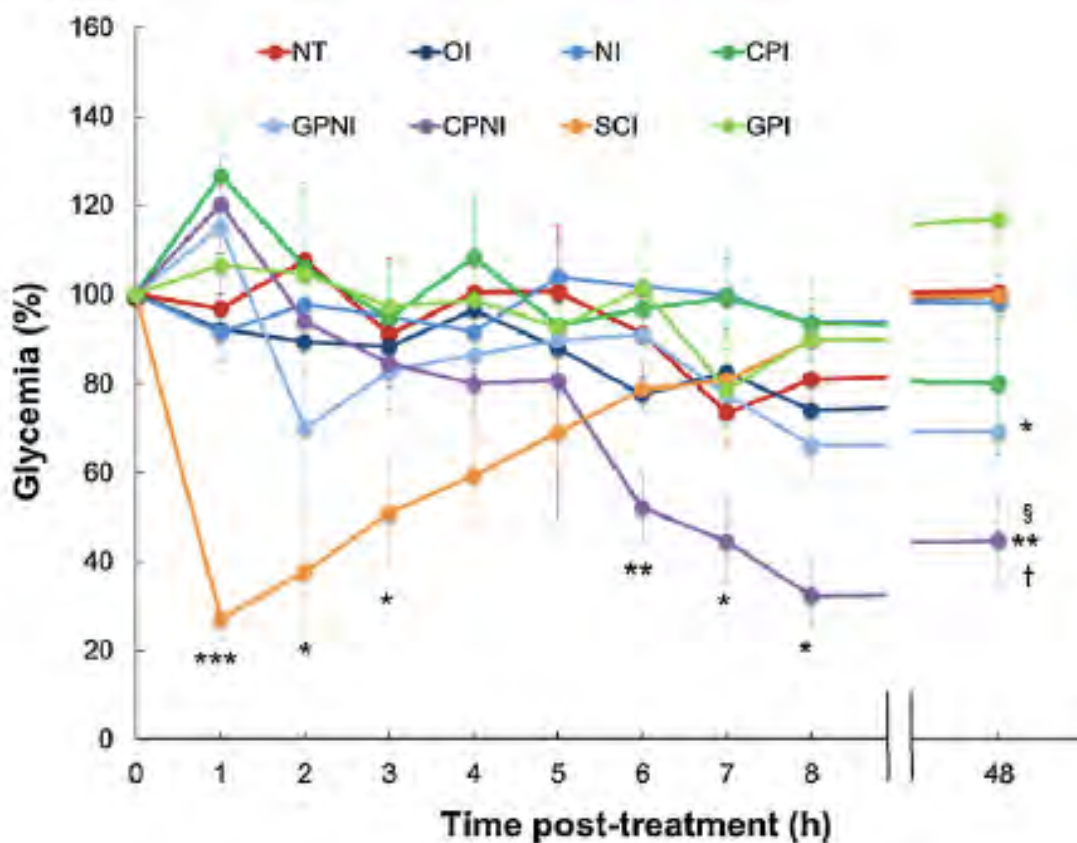


Figure 3.2.5. Time course of the *in vivo* activity of different insulin formulations, expressed as percentage variation of rat blood glucose levels after treatment. Diabetic rats are exposed to oral (OI) or subcutaneous (SCI) administration of insulin, oral administration of insulin nanoparticles (NI), or insertion through gastrotomy of capsules containing gastroresistant pellet-formulated insulin (GPI) or insulin-nanoparticles (GPNI), colon-release pellet-formulated insulin (CPI) or insulin-nanoparticles (CPNI); NT: untreated rats. Mean \pm SE of 3–6 animals for group. *** $p < 0.0005$; ** $p < 0.01$; * $p < 0.05$ vs NT; § $p < 0.0005$ vs OI, NI, GPI and SCI; † $p < 0.05$ vs GPNI and CPI (one tailed Student t-test). (Data taken from Salvioni et al)¹⁶.

Figure 3.2.5. shows the % variation of glycaemia from 1 to 48 h post-treatment. The base line for each experimental group is the mean value of blood glucose measured before the treatment, considered as 100%. In the first 8 h post-treatment, physiological oscillation of glucose blood levels is observed in NT rats, which however don't exceed 30% of the initial value. Orally administered insulin, either free or in NI, has no significant effect on blood glucose levels, while the subcutaneous injection of insulin causes a rapid and marked reduction of the glycaemia to 25% of the initial values at 1 h post-treatment. However, blood glucose levels return to the initial level when measured after 8 h. The treatment with GPI or GPNI doesn't show any significant effect on the glucose blood levels as compared to NT during the first 8 h. In contrast, the rat treatment with CPNI is able to induce an immediate, significant decrease in blood sugar levels as compared to the NT, with a significant fall in glycaemia, as much as 50% of the initial value, at 6 h post-treatment, and a subsequent further decrease of up to 30% at 8 h. On the other hand, the treatment with CPI doesn't exert any significant hypoglycaemic effect. At longer times (48 h), NT and SCI-, OI-, NI-, and GPI-administered rats have blood glucose equal the initial values, while in rats administered with CPNI the glucose concentration remains at 45% of the starting level and significantly different from those of all other experimental groups. At 48 h post-treatment, a slight decrease of glycaemia is observed upon administration of CPI, while in GPNI-treated rats glucose values become about 70% of initial values and significantly lower than those of controls.

Bibliography

1. Bailey, T. Options for combination therapy in type 2 diabetes: comparison of the ADA/EASD position statement and AACE/ACE algorithm. *Am. J. Med.* **126**, S10-20 (2013).
2. Dal, S. *et al.* Portal or subcutaneous insulin infusion: efficacy and impact on liver inflammation. *Fundam. Clin. Pharmacol.* **29**, 488–498 (2015).
3. Maroni, A., Zema, L., Del Curto, M. D., Foppoli, A. & Gazzaniga, A. Oral colon delivery of insulin with the aid of functional adjuvants. *Adv. Drug Deliv. Rev.* **64**, 540–556 (2012).
4. Rekha, M. R. & Sharma, C. P. Oral delivery of therapeutic protein/peptide for diabetes--future perspectives. *Int. J. Pharm.* **440**, 48–62 (2013).
5. Sousa, F., Castro, P., Fonte, P. & Sarmento, B. How to overcome the limitations of current insulin administration with new non-invasive delivery systems. *Ther. Deliv.* **6**, 83–94 (2015).
6. Patel, M. M. Colon targeting: an emerging frontier for oral insulin delivery. *Expert Opin. Drug Deliv.* **10**, 731–739 (2013).
7. Ensign, L. M., Cone, R. & Hanes, J. Oral drug delivery with polymeric nanoparticles: The gastrointestinal mucus barriers. *Adv. Drug Deliv. Rev.* **64**, 557–570 (2012).
8. Bayat, A. *et al.* Nanoparticles of quaternized chitosan derivatives as a carrier for colon delivery of insulin: ex vivo and in vivo studies. *Int. J. Pharm.* **356**, 259–266 (2008).
9. Damgé, C., Reis, C. P. & Maincent, P. Nanoparticle strategies for the oral delivery of insulin. *Expert Opin. Drug Deliv.* **5**, 45–68 (2008).
10. Palugan, L., Cerea, M., Zema, L., Gazzaniga, A. & Maroni, A. Coated pellets for oral colon delivery. *J. Drug Deliv. Sci. Technol.* **25**, 1–15 (2015).
11. Maroni, A. *et al.* Polymeric coatings for a multiple-unit pulsatile delivery system: Preliminary study on free and applied films. *Int. J. Pharm.* **440**, 256–263 (2013).
12. Del Curto, M. D. *et al.* Erodible time-dependent colon delivery systems with improved efficiency in delaying the onset of drug release. *J. Pharm. Sci.* **103**, 3585–3593 (2014).
13. Davis, S. S. The design and evaluation of controlled release systems for the gastrointestinal tract. *J. Controlled Release* **2**, 27–38 (1985).
14. Tiyaboonchai, W., Woiszwilllo, J., Sims, R. C. & Middaugh, C. R. Insulin containing polyethylenimine-dextran sulfate nanoparticles. *Int. J. Pharm.* **255**, 139–151 (2003).
15. Tiyaboonchai, W. & Limpeanchob, N. Formulation and characterization of amphotericin B-chitosan-dextran sulfate nanoparticles. *Int. J. Pharm.* **329**, 142–149 (2007).
16. Salvioni, L. *et al.* Oral delivery of insulin via polyethylene imine-based nanoparticles for

- colonic release allows glycemic control in diabetic rats. *Pharmacol. Res.* **110**, 122–130 (2016).
17. Di Pretoro, G., Zema, L., Gazzaniga, A., Rough, S. L. & Wilson, D. I. Extrusion-spheronisation of highly loaded 5-ASA multiparticulate dosage forms. *Int. J. Pharm.* **402**, 153–164 (2010).
 18. Yamamoto, A. *et al.* Effects of various protease inhibitors on the intestinal absorption and degradation of insulin in rats. *Pharm. Res.* **11**, 1496–1500 (1994).
 19. Tozaki, H. *et al.* Chitosan capsules for colon-specific drug delivery: improvement of insulin absorption from the rat colon. *J. Pharm. Sci.* **86**, 1016–1021 (1997).
 20. Maroni, A. *et al.* In vitro and in vivo evaluation of an oral multiple-unit formulation for colonic delivery of insulin. *Eur. J. Pharm. Biopharm. Off. J. Arbeitsgemeinschaft Pharm. Verfahrenstechnik EV* **108**, 76–82 (2016).
 21. Tuleu, C., Andrieux, C., Boy, P. & Chaumeil, J. C. Gastrointestinal transit of pellets in rats: effect of size and density. *Int. J. Pharm.* **180**, 123–131 (1999).
 22. DeSesso, J. M. & Jacobson, C. F. Anatomical and physiological parameters affecting gastrointestinal absorption in humans and rats. *Food Chem. Toxicol. Int. J. Publ. Br. Ind. Biol. Res. Assoc.* **39**, 209–228 (2001).

3.3. TARGETED GOLD NANOPARTICLES LOADED WITH EVEROLIMUS FOR INHALATIONAL ADMINISTRATION

3.3.1. Introduction

The local administration of drug remains a crucial goal for those therapies characterized by insufficient drug accumulation at target sites and systemic drug toxicity. Bronchiolitis obliterans syndrome (BOS) represents the most frequent chronic lung allograft dysfunction phenotype, which doesn't still have an effective therapy. This syndrome is characterized by a patchy submucosal fibrosis causing the total occlusion of tracts of bronchiolar lumen¹. In transplanted lung, BOS shows firstly an inflammatory phase, which is ultimately followed by an excessive and uncontrolled fibroproliferative phase of mesenchymal cells (MCs), thus leading to irreversible obliteration of airway lumen^{2,3}. At the moment, the therapy is based on the prevention/treatment of the inflammatory phase preceding fibrotic evolution and the use of "antifibrotic drug" targeting MCs but it's usually poorly effective⁴. The direct target of the drug into airways without additional systemic toxicity is still a promising strategy; in particular aerosolized agents can be the proper systems.

In this work, gold nanoparticles (GNPs) of 6 nm covered with an amphiphilic polymer, are functionalized with an antibody selective for CD44 and loaded with everolimus, an inhibitor of mTOR, also endowed with potent immunosuppressive activities, which is demonstrated to suppress the *in vitro* proliferation of fibroblast isolated from BOS patients⁵⁻⁷.

GNPs have unique optical and electronic properties owing to changes in the particle size, shape, surface chemistry and aggregation state^{8,9}. These nanoparticles can be used for several biomedical applications, among which the most common is drug delivery system^{10,11}. Indeed, they can physically adsorb the drugs on the particle surface or reversibly anchor them through a covalent bond^{12,13}.

In vitro experiments are set up in order to test both the selectivity and the efficacy of the functionalized nanocarrier on MCs. The future step will be their administration as aerosol spray.

In addition, a possible deleterious proinflammatory effect of our nanovectors is assessed. The activation of macrophages, the first innate defence line in lung, and neutrophils that exert a crucial role in BOS pathogenesis, is evaluated and excluded.

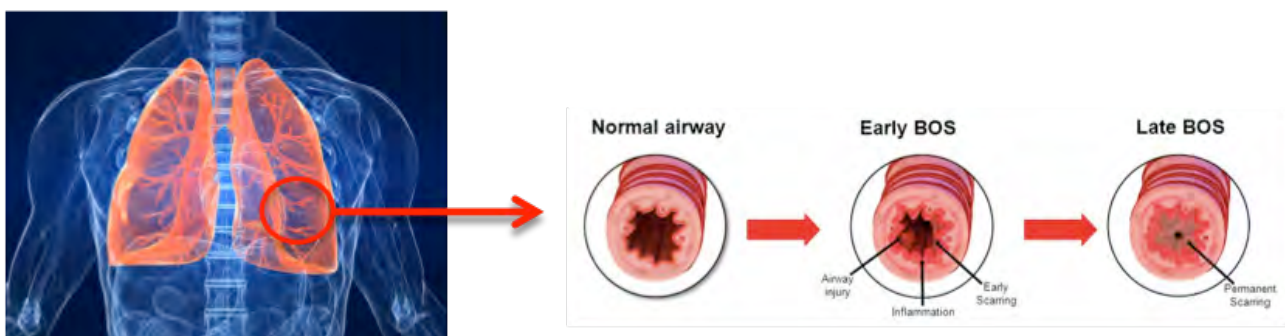


Figure 3.3.1. Representation of BOS progression.

3.3.2. Synthesis and characterization of anti-human CD44-functionalized GNPs loaded with everolimus

Gold nanoparticles of 6 nm are synthesized in organic solvent according to Brust method¹⁴. Briefly, AuCl_4^- is transferred from aqueous solution to toluene using tetraoctylammonium bromide as phase-transfer reagent and reduced with aqueous sodium borohydride in the presence of dodecanethiol. In the final step the product is dissolved in organic solvent. To make GNPs watersoluble, a phase transfer is needed. As for iron oxide nanoparticles used in the other projects, I cover gold nanoparticles with the amphiphilic polymer (PMA) obtained by condensation of poly-(isobutylene-*alt*-maleic anhydride) with an amount of dodecylamine sufficient to reach with 75% of anhydride groups (GNP@PMA)¹⁵. Thanks to the amphiphilic character of the PMA, GNPs are stabilized in water solution and suitable to be functionalized on the surface. Firstly, GNPs react with 1-ethyl-3-(dimethylaminopropyl)-carbodiimide, then with 2,2-(ethylenedioxy)bis(ethylamine) and next the nanoparticles are shaken in the presence of *N*-succinimidyl-3-[2-pyridyldithio]-propionate (SPDP). The resulting thiol-reactive PDP functionalities are exploited for the immobilization of two half-chain antibody portions (HCs) of the anti-human CD44 antibody and the residual thiol-reactive groups on the polymer are saturated with monomethoxy-PEG-thiol (5kDa), which acts as a colloidal stabilizer and reduces nonspecific interactions (GNP-HCs; hydrodynamic size = 47.3 ± 1.0 nm). As a control, I also synthesize fluorescently labelled GNP-PEGs (hydrodynamic size = 29.8 ± 2.4 nm).

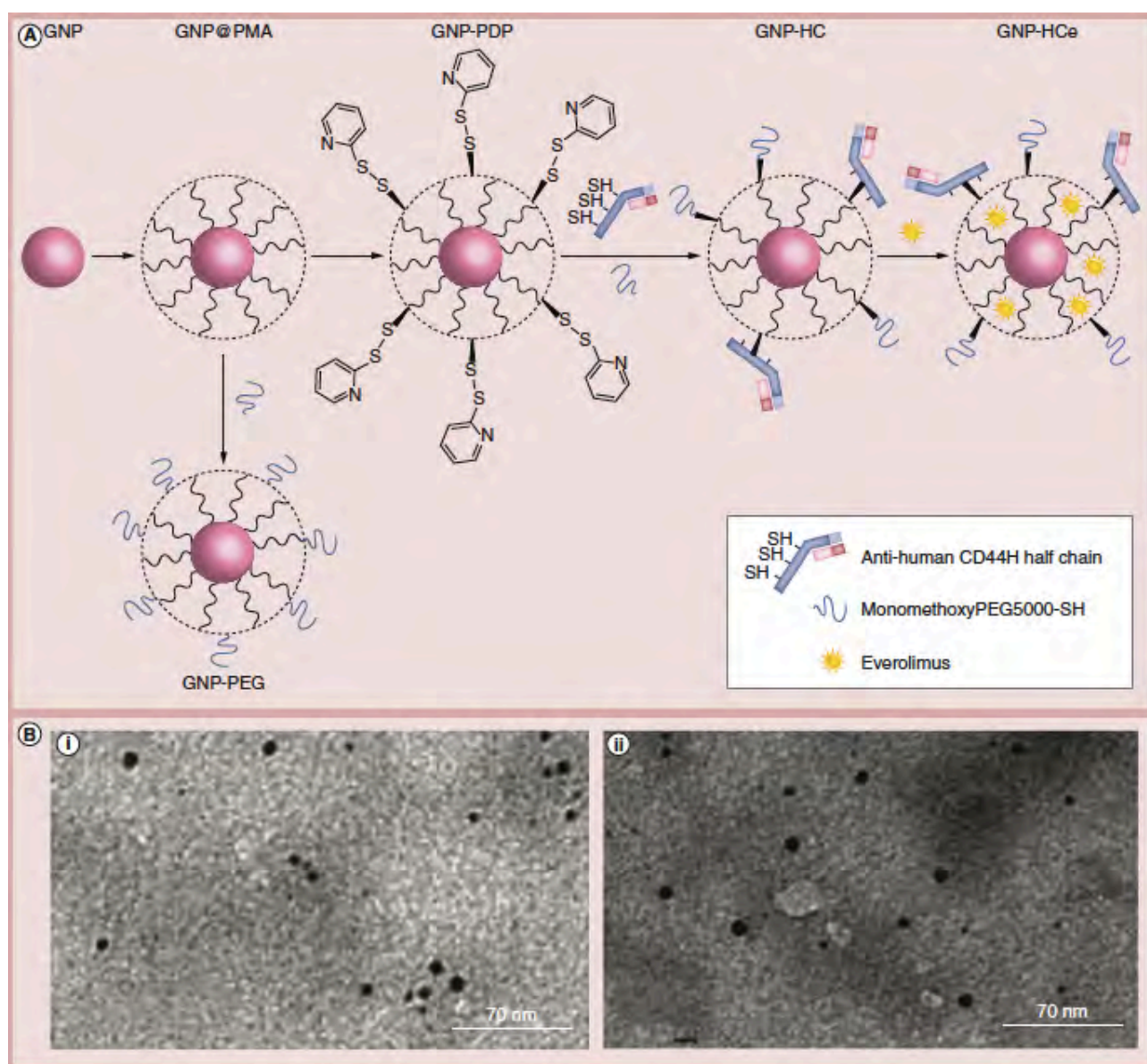


Figure 3.3.2. Synthesis of fully armed half-chain gold nanoparticles with everolimus, and PEGylated gold nanoparticles. **(A)** Hydrophobic GNPs are synthesized and coated with an amphiphilic polymer PMA. The resulting GNP@PMA are functionalized with *N*-succinimidyl-3-[2-pyridyldithio]-propionate (GNP-PDPs). The thiol-reactive PDP functionalities are exploited for the immobilization of heavy-chain CD44 monoclonal antibodies (GNP-HC) labelled with Alexa® (Invitrogen; CA, USA) Fluor 488 dye. As a control, I also synthesize fluorescently labelled, PEGylated GNPs. Finally, GNP-HCs are loaded with everolimus (GNP-HCe). **(B)** Transmission electron microscopy images show that **(i)** GNP-HCs and **(ii)** GNP-HCes exhibit the same hydrodynamic size. GNP: Gold nanoparticle; HC: Half chain; HCe: Half chain with everolimus; PDP: 2-pyridylthiopropionate. (Image taken from Cova et al)¹⁶.

The synthetic strategy is illustrated in Figure 3.3.2. Finally, GNP-HCs are loaded with everolimus by incubating overnight at 4°C (GNP-HCes) obtaining a loading efficiency of approximately 0.5 mg everolimus per mg of GNP-HCes. The hydrodynamic size measured by dynamic light scattering changes from 19.8 ± 2.6 nm (GNP@PMAs) to 47.3 ± 1.0 nm (GNP-HCs) and 46.7 ± 1.8 nm (GNP-HCes). Transmission electron microscope images confirm the colloidal stability of GNP-HCs and GNP-HCes in aqueous dispersion and show that no apparent changes in size and shape of the metal core are associated to the surface modifications of nanoparticles (Figure 3.3.2.). As expected, GNP-HCs and GNP-HCes exhibit the same hydrodynamic size, corroborating the hypothesis that everolimus incorporated inside the polymer shell basically doesn't affect the overall colloidal stability of nanoparticles.

3.3.3. *In vitro* drug release kinetics

Figure 3.3.3. illustrates the release of everolimus from GNP-HCes into PBS buffer (pH 7.4) containing 2% bovine serum albumin.

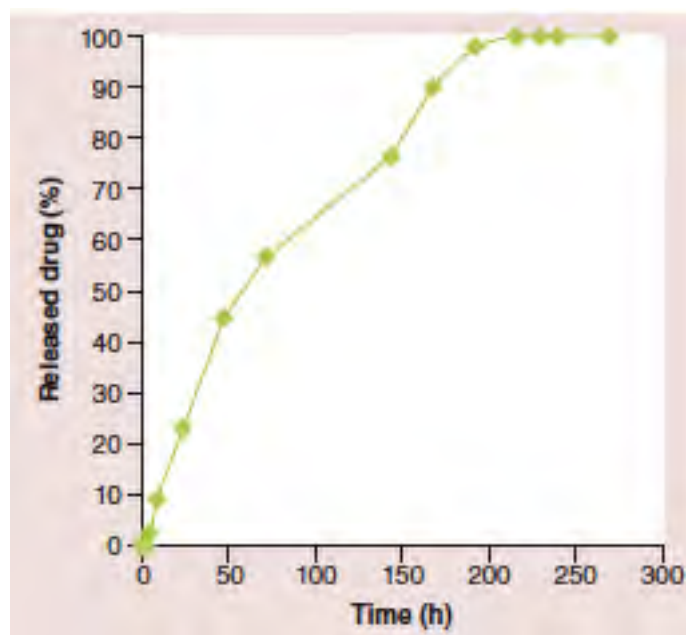


Figure 3.3.3. Curve of everolimus release from half-chain gold nanoparticles with everolimus into phosphate-buffered saline buffer. The loaded drug is released in a controlled way and 90% of half-chain gold nanoparticles with everolimus is dissolved in 8 days. A lag phase in everolimus release, approximately 3–5-h long, is recorded. (Data taken from Cova et al)¹⁶.

It could be noticed that the loaded drug is released in a controlled way and 90% of GNP-HCes are dissolved in 8 days. Surprisingly, the expected burst effect is not observed in this case, but a lag phase is detected. This retard in the everolimus release is approximately 3–5-h long and it could be ascribed to a sort of activation of the polymer due to the interaction with release medium; probably a process of PMA unfolding is necessary to permit the release of the entrapped drug. Based on these data, the drug release mechanism cannot be easily explained. For this reason, to interpret the release profile a Korsmeyer–Peppas model, suitable to describe different drug release profiles, is applied:

$$ft = atn \text{ (Equation 1)}$$

where ft is the cumulative percentage of drug released at time (t); a is a constant that incorporates structural and geometric characteristics of the drug dosage form; n is the release exponent, indicative of the drug release mechanism. To determine the exponent (n), the portion of the release curve where the amount of drug released after $t < 60\%$ is used¹⁷. Due to the presence of a lag time (l) in the first section of the release profile, a modified form of Korsmeyer–Peppas equation could be applied:

$$ft = a(t - l)n \text{ (Equation 2)}$$

Fitting the data of the percentage of released drug and considering data up to 60% (72 h), the resulting equation is:

$$ft = 0.1863(t - l)0.8765 (R2 = 0.9895) \text{ (Equation 3)}$$

It's interesting to note that exponent value is very close to 0.89, the value that, considering the structural and geometric characteristics of the dosage form, indicates a zero-order drug release. Equation fitting drug release data points using data up to 98% (192 h) is:

$$ft = 0.2719(t - l)0.7776 (R2 = 0.9813) \text{ (Equation 4)}$$

that surprisingly shows a very good fitting. Exponent value decreases with respect to the previous one, indicating a profile bending that is symptomatic of a moderate influence of drug amount remaining in the nanoparticles to the drug release rate.

3.3.4. Cell characterization

MCs are isolated only from 30% of BAL of patients and are characterized at the first culture passage. CD44 expression ranges between 84 and 99% of isolated cells (Figure 3.3.4.A), while the positivity for CD90 and CD105 varies more appreciably between 60–84 and 47–87%, respectively. The expression of these markers is reported in Table 1. Cells isolated from different patients are all negative for CD34 and CD45. No differences in marker expression are recordable between stable and BOS patients. The absence of the epithelial marker E-cadherin is assessed by immunocytochemical (ICC) experiments (data not shown). ICC also confirms the high percentage of CD44 positivity in all isolated MCs (Figure 3.3.4.B). 16HBE epithelial cells did not express CD44, as proved by flow cytometry experiments (data not shown).

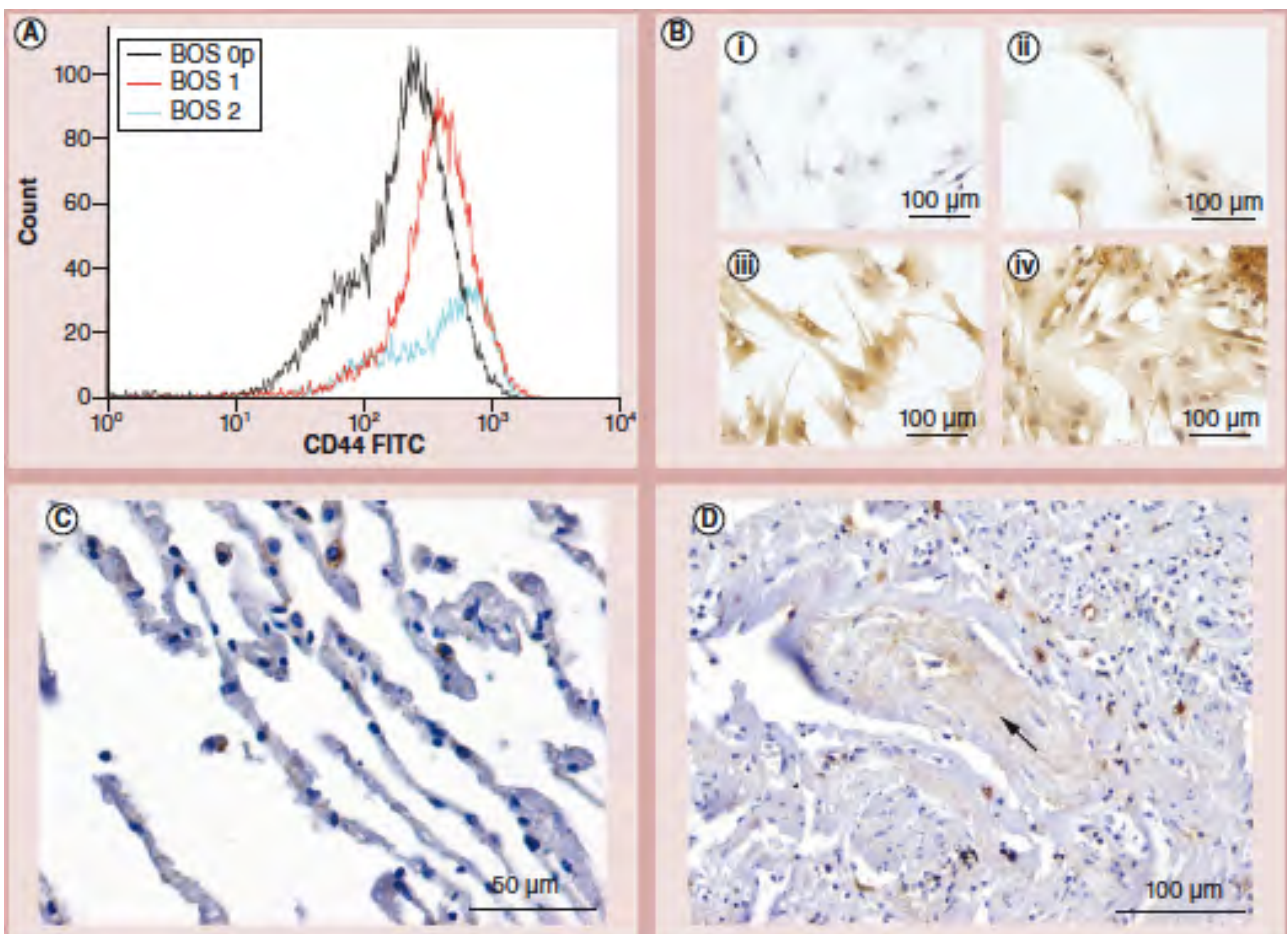


Figure 3.3.4. CD44 expression on mesenchymal cell surface, and in normal and bronchiolitis obliterans syndrome epithelia. CD44 is detected by (A) flow cytometry and (B) immunocytochemistry on the three cell lines used in the experiments; (i) negative control, (ii) BOS 0p, (iii) BOS 1 and (iv) BOS 2. Immunohistochemistry procedure demonstrates that (C) normal alveolar epithelia don't not express CD44, (D) while cells invading bronchiolar lumen, indicated by the arrow, from a patient retransplanted for BOS, are positive to CD44 monoclonal antibody. BOS: Bronchiolitis obliterans syndrome; FITC: Fluorescein isothiocyanate. (Images taken from Cova et al)¹⁶.

Table 1. Clinical features of enrolled patients and surface characterization of primary mesenchymal cells isolated from bronchoalveolar lavage.

Age ^a (years)	Transplant type, Indication	Lung function (%)	FU (months)	IS regimen	BAL (M/L/N/E [%])	MC	CD44	CD34	CD45	CD90	CD105
54	BLT, PAH	100	3	TAC, MMF, PRD	93/7/0/0	No					
58	BLT, COPD	93	7	TAC, MMF, PRD	93/6/1/0	Yes	++	-	-	++	++
41	BLT, COPD	30	153	CyA, EVR, PRD	56/26/15/3	No					
54	BLT, COPD	86	13	TAC, MMF, PRD	95/4/1/0	Yes	++	-	-	++	+
47	BLT, COPD	65 (AR2)	3	TAC, MMF, PRD	26/66/8/0	Yes	++	-	-	++	++
55	BLT, IPF	100	3	TAC, MMF, PRD	71/28/1/0	Yes	++	-	-	++	+
56	SLT, IPF	87	59	TAC, MMF, PRD	65/33/1/1	No					
35 ^a	SLT/fibrosis	80	288	TAC, PRD	68/31/1/0	Yes	++	-	-	++	++
38 ^a	SLT/IPF	89	25	TAC, MMF, PRD	61/12/27/0	Yes	++	-	-	++	++
45	SLT/IPF	69	20	TAC, MMF, PRD	43/5/46/6	No					
56	SLT/IPF	32	120	TAC, MMF, PRD	75/22/3/0	Yes	++	-	-	++	+
39	BLT/BOS	93	8	CyA, EVR, PRD	87/8/5/0	No					
24	BLT/CF	77	184	TAC, PRD, AZITR	95/4/1/0	No					
34	BLT/Bronch	63	105	TAC, PRD, AZITR	90/8/2/0	Yes	++	-	-	++	n.d.
27	SLT/LAM	85	214	CyA, EVR, PRD	29/31/38/2	No					
61	BLT/COPD	68	89	TAC, MMF, PRD	96/1/3/0	No					
56	SLT/IPF	81	110	TAC, MMF, PRD	90/5/5/0	No					
59 ^a	BLT/IPF	70	89	TAC, MMF, PRD	96/3/1/0	Yes	++	-	-	++	++
64	SLT/IPF (CMV)	100	3	TAC, MMF, PRD	93/7/0/0	Yes	++	-	-	+	+
36	BLT/CF	100	3	TAC, MMF, PRD	65/34/1/0	Yes	++	-	-	++	++
42	BLT/CF	100	41	TAC, MMF, PRD	82/14/4/0	No					
38	BLT/PAH	37	162	TAC, PRD, AZITR	71/5/24/0	Yes	++	-	-	+	+
48	SLT/IPF	82	51	TAC, MMF, PRD	91/7/2/0	No					
27	BLT/PAH	59	37	CyA, EVR, PRD	53/16/30/1	No					

^aAt lung transplantation.
^bThese rows are the patients whose cells have been used for the experiments with nanoparticles.
 - : Positive cells less than 10%; +: Positive cells between 10 and 50%; ++: Positive cells more than 50%; AR2: Acute cellular rejection grade 2; AZITR: Azithromycin; BAL: Bronchoalveolar lavage; BLT: Bilateral lung transplantation; BOS: Bronchiolitis obliterans syndrome; Bronch: Bronchiectasis; CF: Cystic fibrosis; CMV: Positive to cytomegalovirus; COPD: Chronic obstructive pulmonary disease; CyA: Cyclosporin; E: Eosinophil; EVR: Everolimus; FU: Length of follow-up at time of bronchoalveolar lavage sampling; IPF: Idiopathic pulmonary fibrosis; IS: Immunosuppression; L: Lymphocyte; LAM: Lymphangioleiomyomatosis; M: Macrophage; MC: Primary mesenchymal cell isolation from bronchoalveolar lavage; MMF: Mycophenolate mofetil; N: Neutrophil; n.d.: Not determined; PAH: Pulmonary arterial hypertension; PRD: Pirfenidone; SLT: Single lung transplantation; TAC: Tacrolimus.

3.3.5. CD44 expression on normal & pathologic epithelia

To avoid possible adverse effect of GNPs functionalized with the specific CD44 mAbs on epithelial cells, I evaluate the presence of the glycoprotein on the surface of bronchiolar epithelium. Immunohistochemical experiments demonstrate that normal, not-inflamed epithelia don't express CD44 (Figure 3.3.4.C) confirming the validity of the selected marker.

Positive reaction is evident in cells invading the bronchiolar lumen in specimens from a BOS patient who underwent retransplant (Figure 3.3.4.D).

3.3.6. Expression of the mammalian target of everolimus, mTOR, in MCs

I find that MCs isolated from BAL of lung transplant recipients express an active form of mTOR in the cytosol (Figure 3.3.5.A), stating the potential effectiveness of the selected drug in inhibiting MC proliferation.

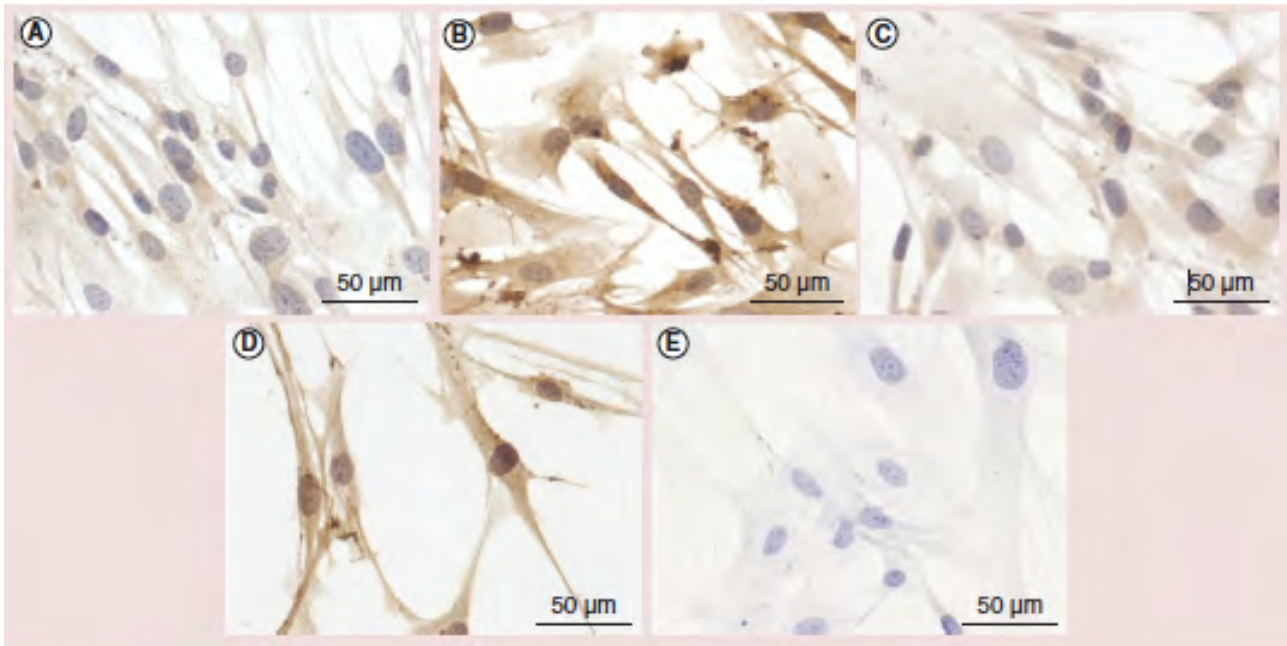


Figure 3.3.5. Expression of phospho-activated form of mTOR in mesenchymal cells. The expression is evaluated by immunocytochemistry in (A) untreated control cells, (B) cells treated with half-chain gold nanoparticles (GNPs) with everolimus, (C) cells treated with GNP-PEG and (D) anti-CD44 monoclonal antibody. The protein level in (A) untreated cells is similar in all cell lines. The expression of phosphoactivated form of mTOR is highly increased (B) 12 h after a 2-h incubation with half-chain GNPs with everolimus, (C) while no effect is detectable with GNP-PEG in the same experimental conditions. A stimulatory effect similar to that observed in half-chain GNPs with everolimus is present 12 h after a 2-h incubation with anti-CD44 monoclonal antibody (1:100). (E) Negative control reaction is shown. (Images taken from Cova et al)¹⁶.

3.3.7. GNP-HCe cell uptake

To evaluate nanoparticle uptake, experiments are performed adding GNP-HCes labelled with Alexa Fluor 488 fluorescent dye to the complete culture medium and observing their entrance from 15 min to 2 h. Internalization is detected by means of confocal microscopy along z-axis and by flow cytometry. Confocal microscopy images and scatter-plot analysis show that only HC-functionalized nanoparticles are able to enter into MCs within 1 h and remain inside, proving the uptake specificity (Figures 3.3.6.B & 3.3.6.D). By contrast, inert GNP-PEGs, marked with the same fluorochrome, are not captured by the cells even after 8 h incubation (Figures 3.3.6.A & 3.3.6.C). No differences are observed in particle uptake by different primary cells. For cell proliferation and apoptosis experiments, nanoparticles are left 2 h in culture to allow their full entrance into the cells.

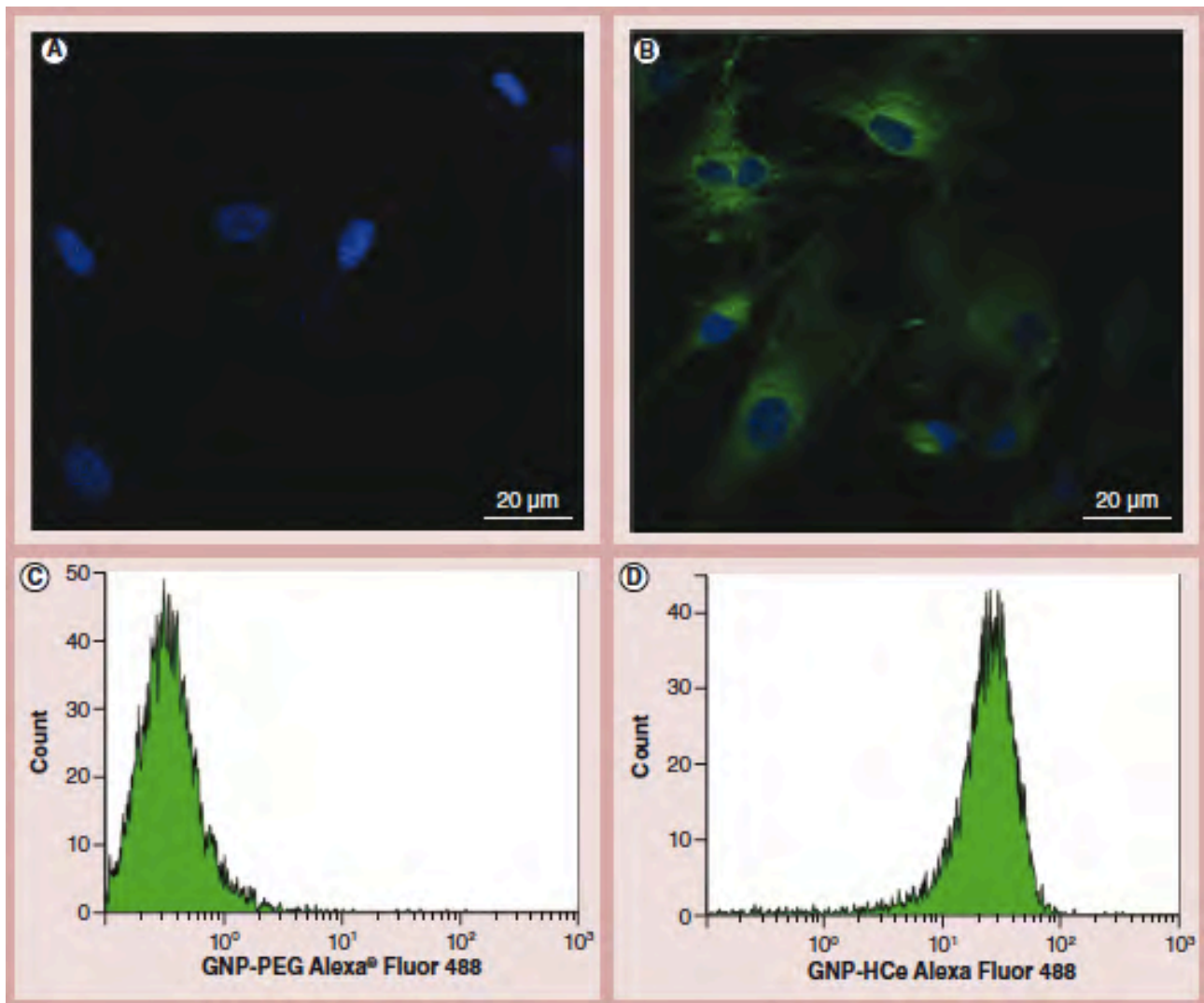


Figure 3.3.6. Half-chain gold nanoparticles with everolimus internalization in mesenchymal cells. To evaluate nanoparticle uptake and specificity, mesenchymal cells are incubated with GNP-HCe labeled with Alexa® (Invitrogen; CA, USA) Fluor 488 fluorescent dye. Internalization is detected by confocal microscopy along the z-axis and by flow cytometry. (B) Images show that only functionalized nanoparticles are able to enter into mesenchymal cells within 1 h. (D) Scatter plots confirm the positivity to fluorescence only in mesenchymal cells incubated with GNP-HCe. By contrast, (A & C) inert GNP-PEG, marked with the same fluorochrome, are not captured by the cells even after 8 h incubation. Original magnification: 60×. GNP: Gold nanoparticle; HCe: Half-chain with everolimus. (Images taken from Cova et al)¹⁶.

3.3.8. Effect of GNP-HCes on MC proliferation & apoptosis

The inhibitory effect of GNP-HCes on MCs is assayed either by evaluating the inhibition of the proliferation rate or the increase in the percentage of apoptotic cells. To detect a possible toxic effect of functionalized GNPs without everolimus (GNP-HCs) inside the cells, GNP-HCs are used as control under the same experimental conditions. As further control, CD44 mAb alone is used to exclude an unspecific action of the antibody linked to the GNP surface on cell proliferation.

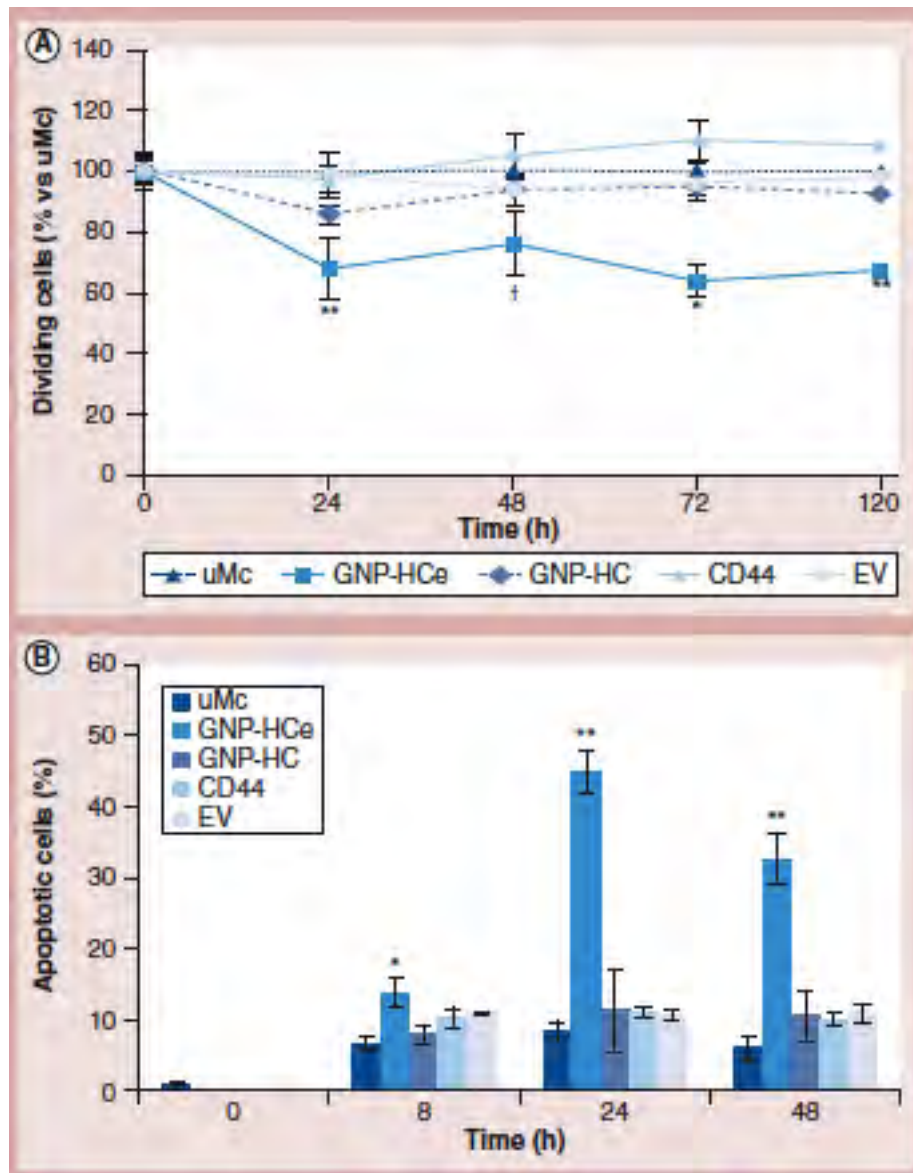


Figure 3.3.7. Effect of half-chain gold nanoparticles with everolimus on mesenchymal cell proliferation and apoptosis. * $p < 0.05$ versus uMc, GNP-HC, CD44 and EV. ** $p < 0.01$ versus uMc, GNP-HC, CD44 and EV. † $p < 0.05$ versus CD44. (A) The proliferation rate is evaluated by carboxy-fluorescein succinimidyl ester at 24, 48, 72 and 120 h after 2 h incubation with GNP-HCe, GNP-HC, CD44 and EV. The results are referred to normal proliferation rate of uMCs cultured in the same experimental conditions. (B) The apoptosis is evaluated by Annexin V incorporation at 8, 24 and 48 h after 2 h incubation with GNP-HCe, GNP-HC, CD44 and EV. The percentage of apoptotic cells is reported for uMCs cultured in the same experimental conditions. Curves and histograms are obtained from the means \pm standard error of three experiments. The error bars represent the standard error. EV: Everolimus; GNP: Gold nanoparticle; HC: Half chain; HCe: Half-chain with everolimus; uMC: Untreated mesenchymal cell. (Data taken from Cova et al)¹⁶.

MCs derived from three patients with different BOS grades (0, 1 and 2 p), are analyzed to estimate whether BOS severity could influence GNP-HCe effectiveness. The results show that GNP-HCes inhibit cell proliferation in all cells without significant differences between the three series. In particular, the effect of the drug is significant at 24, 72 and 120 h after incubation while, in all experiments, proliferation rate invariably shows a tendency to increase at 48 h (Figure 3.3.7.). As a result, no significant difference with control cells is detectable at this time point. Since this result is recovered in all MCs, I hypothesize that the interaction of CD44 mAb with CD44 could produce a remarkable biological effect, inducing

cell proliferation. Indeed, a slight although not significant, increase in growth rate is recorded following the treatment of MC with anti-CD44 mAb (Figure 3.3.7.). Accordingly, ICC experiments evidence an increased expression of mTOR after 12 h incubation with functionalized GNPs (both GNP-HCs and GNP-HCs) (Figure 3.3.5.B) or anti-CD44 mAb (Figure 3.3.5.D), while no change in mTOR expression is detectable in the presence of MCs treated with GNP-PEGs (Figure 3.3.5.C). In the same experimental conditions used for the treatment with GNP-HCs, everolimus doesn't significantly affect cell proliferation. Notably, the proliferation curve shows that the drug released by the uptaken GNP-HCs is effective overtime, as evidenced by the persistence of an inhibitory activity after 120 h from GNP incorporation and confirmed by *in vitro* drug release kinetic curve. MCs incubated with GNP-HCs or GNP-HCs are analyzed for Annexin V incorporation at 8, 24 and 48 h after GNP incubation. As further controls, I also study apoptosis in presence of CD44 mAb and everolimus. Figure 3.3.7.B shows a remarkable and significant increase of apoptosis: approximately 14% MC cells are apoptotic 8 h after GNP-HCe treatment. This percentage progressively increases up to approximately 42% after 24 h, and diminishes at 48 h. The effect is due to the release of everolimus inside the cells, since the incubation with GNP-HCs (without everolimus) and CD44 mAb alone induces as much apoptosis as control untreated MCs. Of note MC treatment with everolimus alone for 2 h is unable to induce apoptosis, demonstrating the superiority of the drug carrier.

3.3.9. Effect of GNP-HCs on inflammatory cells

The uptake of fluorescent nanoparticles by inflammatory cells is demonstrated by flow cytometry (data not shown).

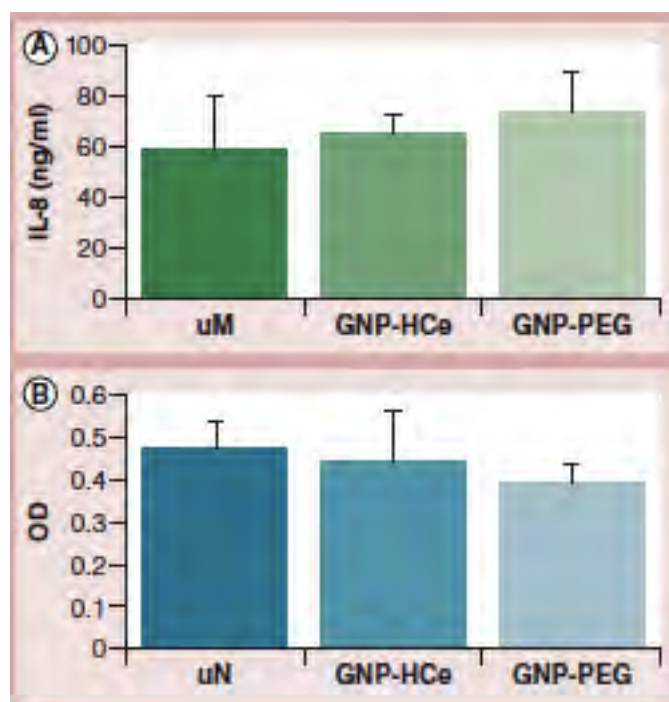


Figure 3.3.8. Effect of half-chain gold nanoparticles with everolimus on macrophage and neutrophil activation. (A) IL-8 secretion, evaluated by ELISA test and used to assay the macrophage activation, is not increased by 24 h incubation with GNP-HCe or GNP-PEG compared with untreated macrophages. (B) Elastase activity, evaluated by enzymatic assay to detect possible effects on neutrophils by incubation with GNP-HCe or GNP-PEG, is comparable to untreated neutrophils. The data represent the means \pm standard error of three experiments. The error bars represent the standard error. GNP: Gold nanoparticle; HCe: Half-chain with everolimus; OD: Optical density; uM: Untreated macrophage; uN: Untreated neutrophil.

(Data taken from Cova et al)¹⁶.

The results summarized in Figure 3.3.8. show that, after 24 h incubation, IL-8 secretion is not increased in the presence of GNP-HCes and GNP-PEGs (Figure 3.3.8.A). Furthermore, both GNPs with or without functionalization don't activate neutrophils (Figure 3.3.8.B).

3.3.10. Effect of GNP-HCes on bronchial epithelial cell line

In order to exclude a possible toxic effect of nanoparticles on epithelial cells, the apoptotic and proliferation rate in presence of functionalized (GNP-HCes and GNP-HCs) and non-functionalized (GNP-PEGs) nanoparticles are studied using the same experimental conditions and procedures. The results obtained by flow cytometry using Alexa Fluor 488 dye marked nanoparticles prove that 16HBE cells don't uptake either functionalized or nonfunctionalized nanoparticles from 1-h up to 8-h incubation. In addition, no significant differences are recorded in proliferation (GNP-PEGs: 100.8 ± 8.5 ; GNP-HCs: 93 ± 10.8 ; GNP-HCes: 93.8 ± 9.2 after 72 h from incubation and expressed as percentage vs untreated 16HBE cells) or apoptosis rate (untreated 16HBE: 12.5 ± 1.4 ; GNP-PEGs: 11.4 ± 1.3 ; GNP-HCs: 12.8 ± 1.3 ; GNP-HCes: 16.35 ± 1.7 after 24 h from incubation and expressed as percentage).

Bibliography

1. Todd, J. L. & Palmer, S. M. Bronchiolitis obliterans syndrome: the final frontier for lung transplantation. *Chest* **140**, 502–508 (2011).
2. Sato, M. & Keshavjee, S. Bronchiolitis obliterans syndrome: alloimmune-dependent and -independent injury with aberrant tissue remodeling. *Semin. Thorac. Cardiovasc. Surg.* **20**, 173–182 (2008).
3. Ramirez, A. M., Nunley, D. R., Rojas, M. & Roman, J. Activation of Tissue Remodeling Precedes Obliterative Bronchiolitis in Lung Transplant Recipients. *Biomark. Insights* **3**, 351–359 (2008).
4. Hayes, D. A review of bronchiolitis obliterans syndrome and therapeutic strategies. *J. Cardiothorac. Surg.* **6**, 92 (2011).
5. Bianco, R. *et al.* Inhibition of mTOR pathway by everolimus cooperates with EGFR inhibitors in human tumours sensitive and resistant to anti-EGFR drugs. *Br. J. Cancer* **98**, 923–930 (2008).
6. Azzola, A. *et al.* Everolimus and mycophenolate mofetil are potent inhibitors of fibroblast proliferation after lung transplantation. *Transplantation* **77**, 275–280 (2004).
7. Nashan, B. Review of the proliferation inhibitor everolimus. *Expert Opin. Investig. Drugs* **11**, 1845–1857 (2002).
8. Giljohann, D. A. *et al.* Gold nanoparticles for biology and medicine. *Angew. Chem. Int. Ed Engl.* **49**, 3280–3294 (2010).
9. Lu, Y. & Chen, W. Sub-nanometre sized metal clusters: from synthetic challenges to the unique property discoveries. *Chem. Soc. Rev.* **41**, 3594–3623 (2012).
10. Ghosh, P., Han, G., De, M., Kim, C. K. & Rotello, V. M. Gold nanoparticles in delivery applications. *Adv. Drug Deliv. Rev.* **60**, 1307–1315 (2008).
11. Cobley, C. M., Chen, J., Cho, E. C., Wang, L. V. & Xia, Y. Gold nanostructures: a class of multifunctional materials for biomedical applications. *Chem. Soc. Rev.* **40**, 44–56 (2011).
12. Sandhu, K. K., McIntosh, C. M., Simard, J. M., Smith, S. W. & Rotello, V. M. Gold Nanoparticle-Mediated Transfection of Mammalian Cells. *Bioconjug. Chem.* **13**, 3–6 (2002).
13. Rothrock, A. R., Donkers, R. L. & Schoenfisch, M. H. Synthesis of Nitric Oxide-Releasing Gold Nanoparticles. *J. Am. Chem. Soc.* **127**, 9362–9363 (2005).
14. Brust, M., Walker, M., Bethell, D., Schiffrin, D. J. & Whyman, R. Synthesis of thiol-derivatised gold nanoparticles in a two-phase Liquid–Liquid system. *J. Chem. Soc., Chem. Commun.* 801–802 (1994). doi:10.1039/C39940000801

15. Pellegrino, T. *et al.* Hydrophobic Nanocrystals Coated with an Amphiphilic Polymer Shell: A General Route to Water Soluble Nanocrystals. *Nano Lett.* **4**, 703–707 (2004).
16. Cova, E. *et al.* Antibody-engineered nanoparticles selectively inhibit mesenchymal cells isolated from patients with chronic lung allograft dysfunction. *Nanomed.* **10**, 9–23 (2015).
17. Costa, P. & Sousa Lobo, J. M. Modeling and comparison of dissolution profiles. *Eur. J. Pharm. Sci.* **13**, 123–133 (2001).

3.4. NANOFORMULATION OF AN ANTIRETROVIRAL DRUG ABLE TO CROSS THE BLOOD BRAIN BARRIER (BBB) AFTER INTRAVENOUS INJECTION

3.4.1. Introduction

The blood brain barrier (BBB) performs protection role of the brain from noxious agents. For this reason it's a very selective barrier and the delivery of therapeutics to the brain remains a big challenge^{1,2}. BBB is a very poorly crossable barrier by most drugs; consequently many neurodegenerative disorders or brain tumours don't still have effective therapies³⁻⁵. The barrier is made by astrocytes and endothelial cells connected by tight junctions which don't exist in normal circulation and limit the drug diffusion to the central nervous system (CNS)⁶. It's known in literature that only very small (<400 Da) and lipophilic molecules can diffuse through the BBB, while the crossing of lipid insoluble or larger hydrophilic molecules is very limited⁷.

Among the approaches to cross BBB, the nanotechnologies represents a new tool to improve the delivery of drugs and biological therapeutics⁸⁻¹⁰. Indeed, thanks to their size and physical-chemical properties, nanoparticles can allow drugs to reach the brain avoiding the damage of the barrier¹⁰.

Among the pathologies affecting CNS and still not curable, there is HIV, the human immunodeficiency virus that, unlike some other viruses, the human body can't get rid of completely. HIV-1 is responsible for the majority of Acquired Immune Deficiency Syndrome (AIDS) cases and it compartmentalizes in sanctuary sites, which include the genital tract, the gut-associated lymphoid tissue, the lymph nodes, tissue macrophages and the CNS. One of the principal obstacle to eradicate this pathology is represented by the difficulty to achieve therapeutic antiretroviral concentration in these sites^{11,12}. In particular, the CNS is considered one of the most important viral reservoirs. This is mainly due to the presence of macrophages that promote the inflammatory escalation with subsequent astrogliosis and neurodegeneration, thus establishing the so-called NeuroAIDS¹³, responsible for neurocognitive disorders with different grades of severity (AIDS dementia complex). So, a promising approach could be the delivering antiretroviral drugs in HIV sanctuaries preventing T-cell mediated delivery of the virus in the brain and interact directly with HIV-sensitive CD4+ cells inside these sites (*i.e.* microglial cells of brain)¹². The use of nanoparticles could allow antiretroviral drugs to effectively reach this reservoir¹³, preventing the replication of the virus and reducing the damages induced by the infection.

To this aim iron oxide nanoparticles (MNP) coated with PMA amphiphilic polymer (PMNP) are used to enhance the permeation of a peptide, called enfuvirtide (Enf), across the BBB both *in vitro* and *in vivo* models. This nanocarrier allows the covalent conjugation of the peptide on the nanoparticles surface and, at the same time, ensures the detection of the fluorescent nanosystem into the body. Enf (Fuzeon™ from Roche Laboratories Inc. and Trimeris Inc.) is a 36-amino acid peptide that targets multiple sites in gp41, a HIV glycoprotein responsible for the fusion with CD4+ cells¹⁴⁻¹⁶. Enfuvirtide inhibits HIV-1 mediated cell-cell fusion and transmission of cell-free virus while it does not have substantial activity against HIV-2¹⁸⁻²⁰.

Because of its unfavourable pharmacological profile, with a half-life of approximately 2h and a high molecular weight (4.5 kDa), Enf is particularly indicated to provide a proof of concept of the improved access of antiretroviral drug to HIV sanctuaries by nanoformulation. Indeed, Enf is not able to cross the BBB for its complex structure¹⁷, so I investigate the Enf-nanoconjugation to see the peptide passage to the brain.

3.4.2. Nanoparticles synthesis and characterization

Iron oxide nanoparticles (MNP) covered with PMA polymer (PMNP) are synthesized as described previously in project A. Then, these nanoparticles are characterized in size and shape by DLS and TEM (Figure 3.4.1.B): MNP have a hydrodynamic diameter of $18.8 \text{ nm} \pm 2.1$ in hexane. After the phase transfer, MNP maintain the original average crystal size (8 nm by TEM), and the final nanoparticles shape is uniformly spherical, with a hydrodynamic diameter of $23.9 \pm 2.0 \text{ nm}$ (PMNP in water) as determined by DLS. After drug conjugation, the nanoparticles size increases up to $35.2 \pm 2.2 \text{ nm}$. The pH value of the suspension is around 5.5 and the zeta potential obtained at this pH value is $-29.58 \pm 1.90 \text{ mV}$, likely suggesting a high stability of Enf-PMNP with minimal aggregation in water medium at this pH. Indeed a zeta potential value higher than $\pm 30 \text{ mV}$ is generally required for a colloiddally stable nanoparticle dispersion^{18,19}.

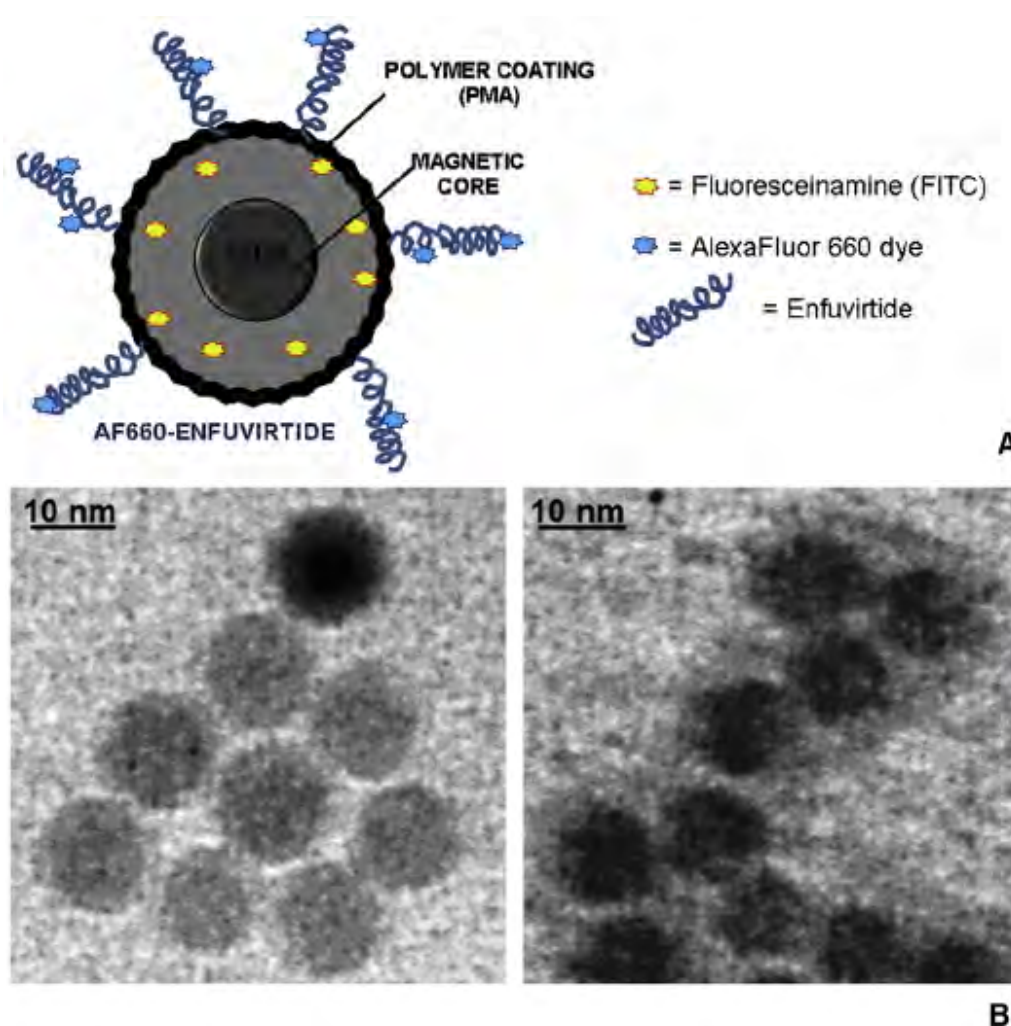


Figure 3.4.1. (A) Schematic representation of labelled Enf-PMNP. (B) TEM images of MNP in hexane (left) and PMNP in water (right). (Images taken from Fiandra et al)²⁰.

3.4.3. Nanoconjugated enfuvirtide crosses the *in vitro* BBB model

The efficiency of PMNP in increasing the trans-BBB permeation of Enf is first evaluated on an *in vitro* BBB model consisting of a double layer of astrocytes and RBMVECs. Before treatment, the integrity of our experimental model is validated by measuring the transepithelial/transendothelial electrical resistance (TEER) and by determining the trans-BBB apparent permeability of the Dextran 40. In all BBB models devoted to the subsequent experimental phase, I record a mean TEER value higher than $400\Omega\text{cm}^2$. BBB selectivity to the Dextran 40 labeled with FITC (FD40) is assessed in some additional inserts by measuring the trans-BBB flux over 3 h (Figure 3.4.2.).

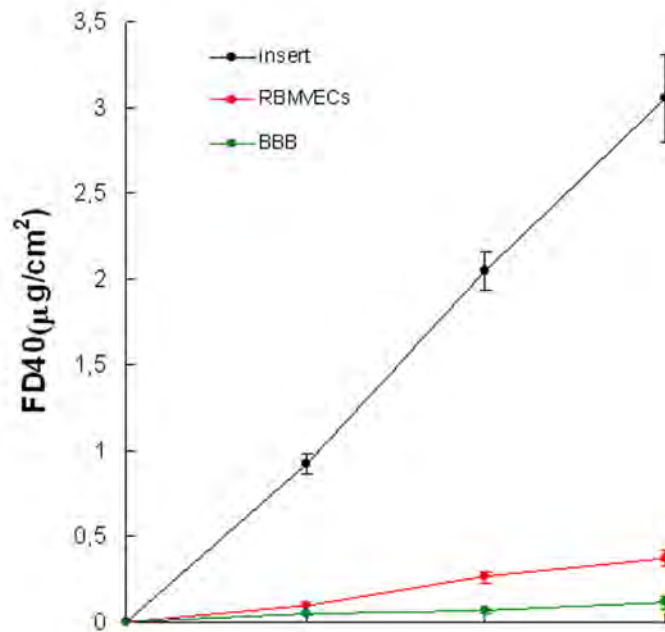


Figure 3.4.2. Time course of the FD40 (1 mg mL^{-1}) flux from the upper to the lower side of the BBB *in vitro* system, compared to that across the RBMVECs layer and the empty PET insert. Means \pm SE; n° inserts $s=3$. (Data taken from Fiandra et al)²⁰.

The resulting P_{app} ($0.10 \pm 0.03 \text{ } \mu\text{m} \text{ s}^{-1}$, mean \pm SE, $n = 6$) confirms the production of a very tight barrier. SEM observations show the presence of a uniform layer of endothelial cells (Figure 3.4.3.A), and TEM images clearly demonstrate that cells are connected by well-structured tight junctions (Figure 3.4.3.B).

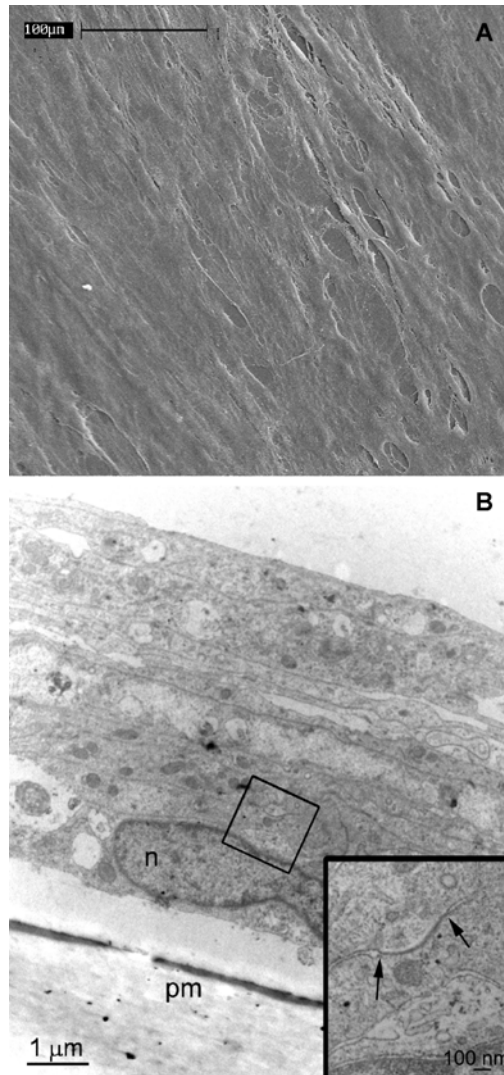


Figure 3.4.3. RBMVECs on PET membrane analysed by SEM (A) and TEM (B). n = nucleus; pm = PET insert; arrows indicate the tight junction between two adjacent cells (insert of panel B). (Images taken from Fiandra et al)²⁰.

The permeability of Enf, PMNP and Enf-PMNP across the BBB model is determined by labeling the peptide and the nanoparticle with AF660 and FITC, respectively (Figure 3.4.1.A). The nanoparticle suspensions are added in the upper chamber of the experimental apparatus and their passage through the BBB model is assessed after 4 and 7 h of incubation by measuring their fluorescence intensity (FI) into the lower chamber. I find that only a small fraction of free Enf is able to cross the BBB *in vitro*: after 4 h, Enf FI in the lower chamber is about 0,15 % of Enf FI added in the upper chamber, and the percentage increase of FI in the lower chamber over the subsequent 3 h of incubation is 30% (Figure 3.4.4.A). Conjugation of Enf to the nanoparticle don't significantly affect its FI in the lower chamber within the first four hours, but it is able to greatly increase its permeation across the BBB (by over 170%) between 4 and 7 h of incubation (Figure 3.4.4.A). Surprisingly, the percentage increase of the FITC FI in the lower chamber calculated between 4 and 7 h, which is associated to PMNP permeation across the BBB, is only 10%, and therefore much lower than that of the conjugated peptide in the same time span (Figure 3.4.4.B). The great difference between the % increase in lower chamber of AF660 (conjugated to Enf) and FITC (conjugated to PMNP) after incubation with the Enf-PMNP nanocomplex strongly suggests that the two components don't have the same fate when crossing the BBB, and that they likely dissociate into the barrier to be processed

separately. The permeation of PMNP through the BBB is also assessed by measuring the iron content in the solution collected by the lower chamber by ICP-OES: I find that the percentage increase of iron recorded between 4 and 7 h is only 1.84 ± 0.04 (mean \pm SE, $n = 8$) for both PMNP and Enf-PMNP. Then, I measure the FI of the three formulations in the lower chamber of the BBB apparatus after 24 h of incubation. I observe that the Enf trans-BBB permeation is enhanced between 7 and 24 h of incubation by 175% (Figure 3.4.4.A), likely because of increased leakage of the RBMVEC barrier over the time. However, the effect of the nanocomplexation on the permeation of Enf across the BBB is still remarkable: the percentage increase of AF660 FI in the lower chamber between 7 and 24 h of exposure to Enf-PMNP reaches 745% (Figure 3.4.4.A). By contrast, the percentage increase of FITC FI in the lower chamber is about 20% for both PMNP and Enf-PMNP (Figure 3.4.4.B), thus underlining a discrepancy between the FI recorded for Enf and PMNP after incubation of the BBB with Enf-PMNP. The percentage increase of iron content in the lower chamber between 7 and 24 h is still negligible and comparable for both conjugated and unconjugated nanoparticles ($1.89\% \pm 0.03$, mean \pm SE, $n = 8$). In parallel, I perform a confocal microscopy analysis of the upper side of the insert after 7 h of incubation with Enf or Enf-PMNP. Figure 3.4.4.C shows that while free Enf is not internalized by the RBMVECs, the conjugation of the peptide to the nanoparticles allows it to deeply enter into the cells, confirming the enhanced permeability of Enf when nanoconjugated. The merge image of the cells incubated with Enf-PMNP reveals that the AF660 and the FITC fluorescence are mostly non-overlapping (Figure 3.4.4.C & 3.4.4.D). These image data, combined with the great difference in the trans-BBB permeation rate observed between the two components, strongly suggest that a dissociation of the peptide from the nanoparticle might have occurred in the endothelial layer.

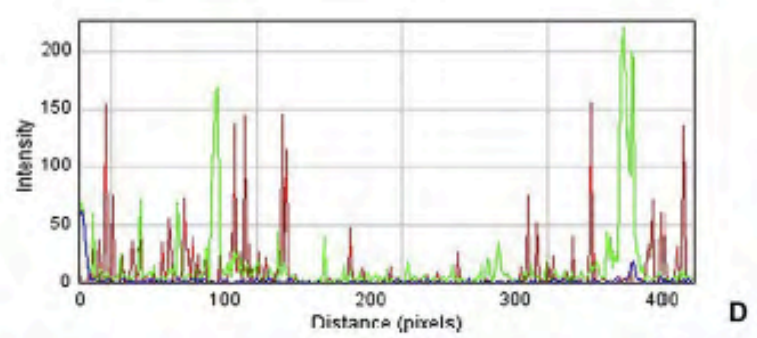
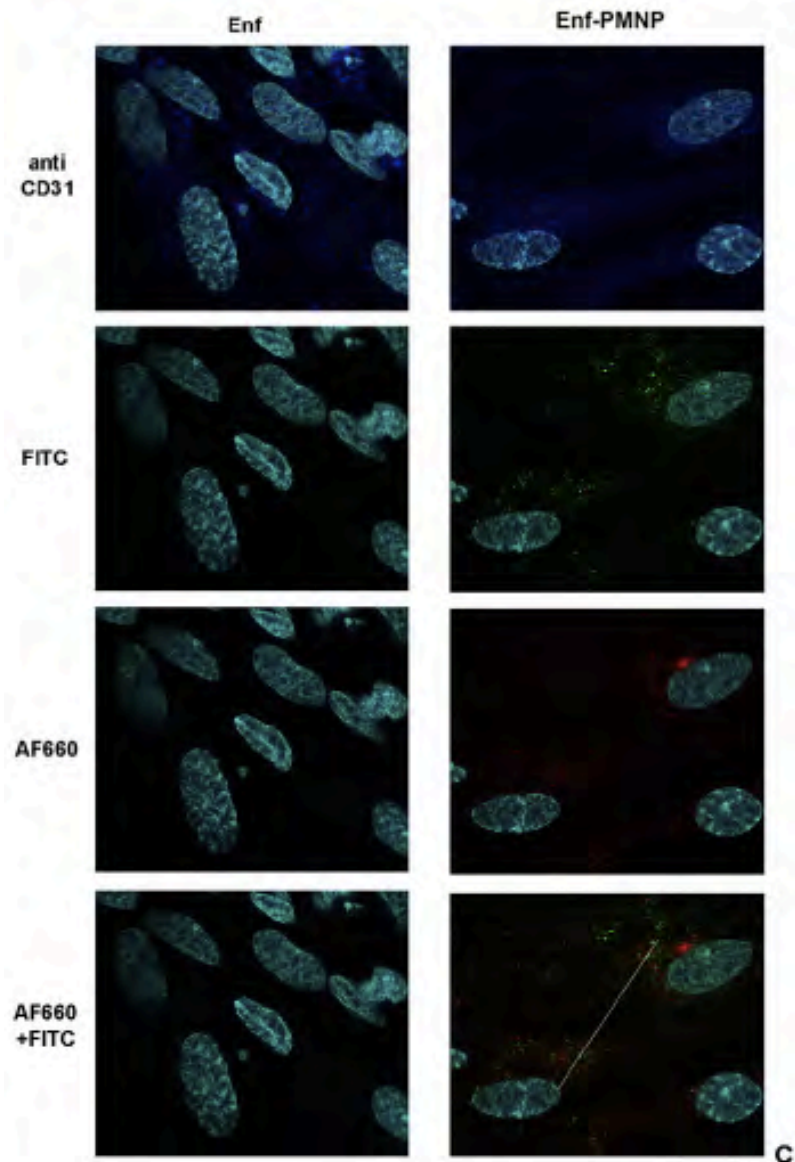
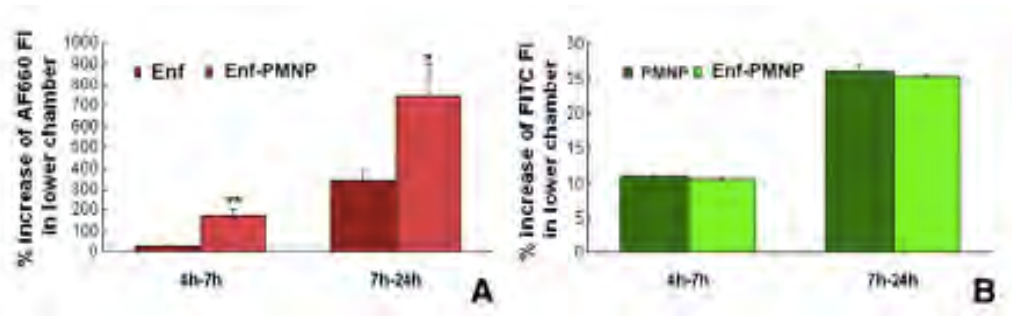


Figure 3.4.4. Percentage (%) increase of FI of free or conjugated (AF660)Enf (A) or (FITC)PMNP (B) in the lower chamber of the BBB *in vitro* system calculated between 4 and 7 h, and 7 and 24 h, from the addition of labelled Enf, PNMP and Enf-PMNP into the upper chamber. Mean \pm SE of 4 replicates; $**P < 0,001$ and $*P < 0,05$, Enf-PMNP vs Enf (Student's *t* test) (C) Confocal laser-scanning micrographs (single optical sections) of RBMVECs after 7 h of incubation with free Enf or Enf-PMNP. Enf and PMNP are labelled with AF660 (red) and FITC (green) respectively; nuclei are stained with DAPI (cyan) and endothelial cells are immunodecorated with anti-CD31 antibody (blue); scale bar: 10 μ m. (D) Overlay of the signal intensity plots of Enf and PMNP along a one-pixel line covering a cytoplasmic portion of the cells. (Data taken from Fiandra et al)²⁰.

3.4.4. *In vivo* brain targeting and trans-BBB delivery of nanoconjugated enfuvirtide

Trans-BBB permeation of PMNP conjugated with Enf is then assessed *in vivo* in Balb/c mice intravenously injected with free Enf or with the same peptide conjugated to nanoparticles. I decide to follow the bioavailability and biodistribution of Enf, by labeling the peptide with AF660 whose efficiency as *in vivo* probe has been previously reported in mice^{21,22}. Firstly, plasma concentration of free or conjugated Enf is monitored at 30 min, 1 h and 6 h after injection in eight different animals for each experimental condition, to verify the effect of nanoconstruct on peptide bioavailability. I observe a maximal concentration of both free or conjugated drug in the blood stream within 1 h postinjection and a strong decrease over the following hours, up to negligible levels at 6 h postinjection. Moreover, Enf concentration in plasma appears reduced by conjugation to PMNP and therefore less available for the potentially infected organs, including brains (Figure 3.4.5.).

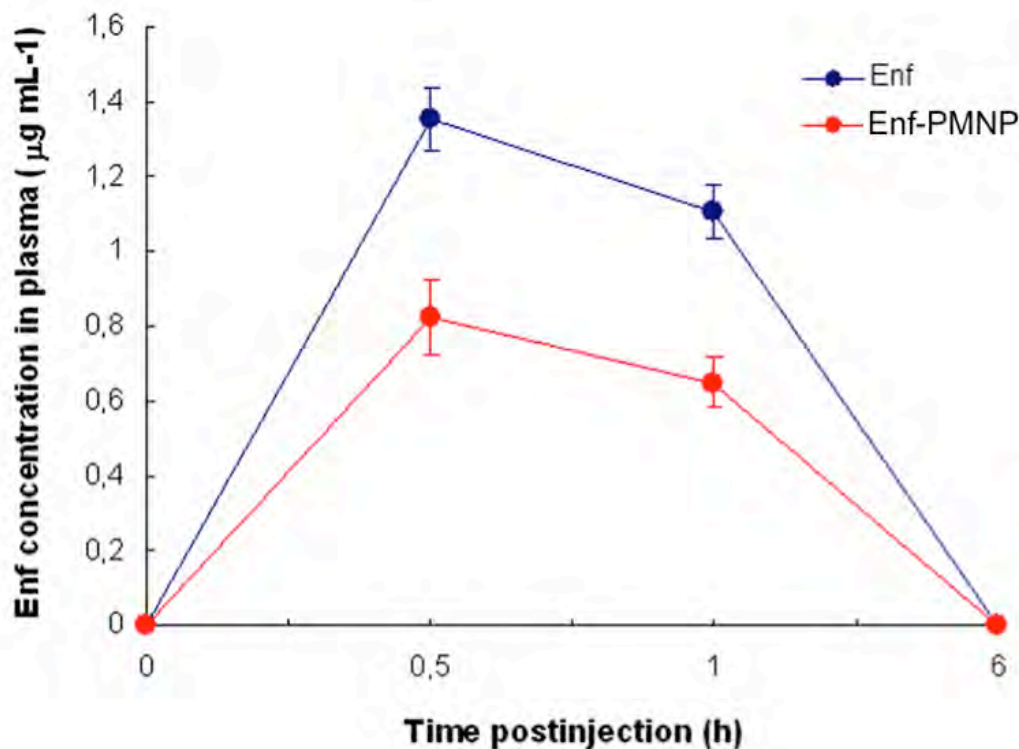


Figure 3.4.5. Time course of the plasma concentration of free or nanoconjugated (AF660) Enf (0.2 μ g g⁻¹ body weight), after i.v. injection in mice. Means \pm SE of 8 animals. (Data taken from Fiandra et al)²⁰.

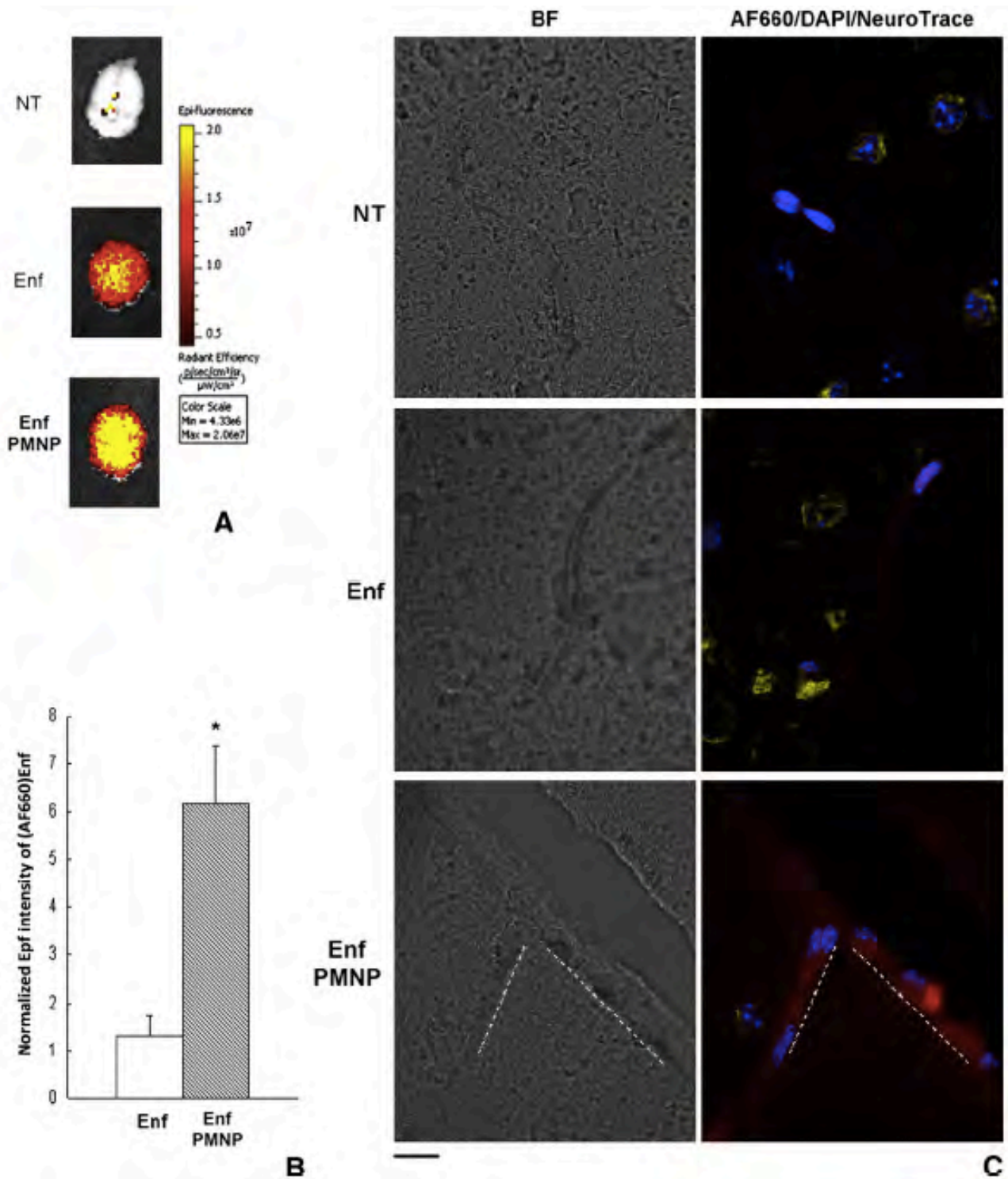


Figure 3.4.6. Analysis of brains isolated from non-treated mice (NT) or mice exposed for 1 h to free or conjugated AF660-labeled enfuvirtide. (A) Epf images of isolated brains, where Epf intensity is expressed as radiant efficiency. (B) Averaged Epf intensity of isolated brains where Epf values have been normalized on fluorescence intensity of injected solution in order to keep into account the differences in intrinsic fluorescence emission for each preparation; mean \pm SE of 9 different brains for each experimental condition; * $P < 0,01$ (Student's t test). (C) Confocal laser-scanning micrographs (single optical sections) of brain cryosections; images from control animals (NT) or from animals treated with free or nanocomplexed enfuvirtide (red) have been overlaid on the corresponding images reporting nuclei (blue) and neuronal cytoplasm (yellow), counterstained with DAPI and NeuroTrace 530/615, respectively (right column); brightfield (BF) images are reported on the left; dashed lines highlight the vessel boundaries; bar: 10 μm . (Data taken from Fiandra et al)²⁰.

Other mice are injected with Enf or Enf-PMNP (nine for each experimental condition) to be sacrificed at 1 h postinjection, together with three untreated animals (controls). Fluorescence imaging of dissected brains reveals a significant accumulation of both free and nanoformulated Enf in this organ at 1 h postinjection, as pointed out by the strong Epf signal not observed in the brain of non-treated mice (Figure 3.4.6.A), feasibly due to the peptide content in the blood circulation of brain. Nevertheless, Epf intensity associated with nanoformulated Enf is stronger than that of free Enf (Figure 3.4.6.A & 3.4.6.B), thus suggesting a higher accumulation of the nanoformulated peptide in this organ despite its lower bioavailability. To determine if the observed increased concentration of Enf in the brain is really associated to an increased permeation of the drug across BBB by effect of the nanocomplexation, I analyze the interaction of Enf and Enf-PMNP with BBB cells and their localization in the perivascular space. Cryosections of mice brains excised 1 h postinjection of Enf or Enf-PMNP are analyzed by confocal microscopy. Figure 3.4.6.C shows enhanced fluorescence intensity in brain capillaries in samples treated with the nanoconjugated Enf when compared to the free peptide, where instead fluorescence is only slightly higher than control autofluorescence. In addition, nanocomplexation of Enf induces a spreading of fluorescence outside the boundaries of the vessel. To confirm the efficacy of PMNP in driving Enf into the endothelial cells of brain capillaries and finally exerting an efficient trans-BBB permeation of the drug, I inject mice with PMNP, Enf or Enf-PMNP (three mice for each experimental condition) and analyse the localization of the different compounds in brain sections after 1 h from injection, by means of the differential labeling of Enf and PMNP with AF660 and FITC, respectively (Figure 3.4.7.).

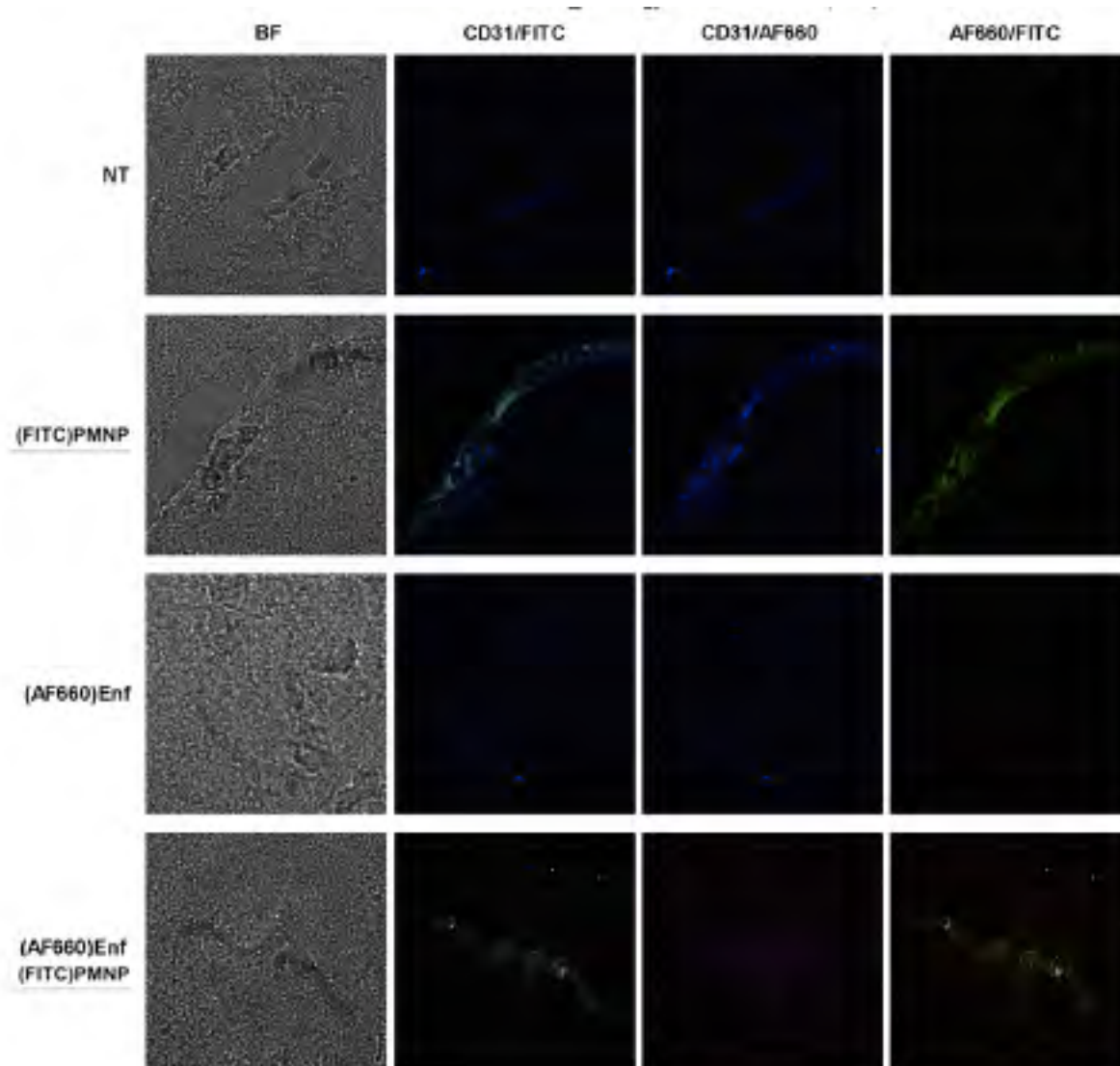


Figure 3.4.7. Confocal laser-scanning micrographs (single optical sections) of brain cryosections from non-treated mice (NT) or mice exposed for 1 h to (AF660)Enf, (FITC)PMNP or (AF660)Enf-PMNP(FITC); conjugated or free AF660-Enf (red) and FITC-PMNP (green) have been overlaid each other and with CD-31 stained endothelial cells (blue); brightfield (BF) images are reported on the left; bar: 10 μ m. (Images taken from Fiandra et al)²⁰.

Immunodecoration of the endothelial cells with anti-CD31 antibody reveals a huge intracellular accumulation for PMNP. As expected, the ability of free Enf to enter BBB endothelial cells and reach brain parenchyma is negligible, while conjugation of the peptide to the nanoparticles allows it to cross the barrier. Merge between Enf and PMNP signals in samples treated with Enf-PMNP clearly shows that only the peptide is able to diffuse outside the BBB, while nanoparticles are restricted to the vessel endothelium. This result, in agreement with *in vitro* observations, further suggests the dissociation of the nanocomplex within endothelial cells, with subsequent excretion of Enf. The systemic toxicity of administered formulations is then assessed by histopathological examination of brain, liver, kidneys, spleen, and lungs isolated 1 h after Enf, PMNP or Enf-PMNP injection. Analysis is performed on organs specimens from three different animals for each experimental condition. No histological lesions are observed in the analysed organs (Figure 3.4.8.).

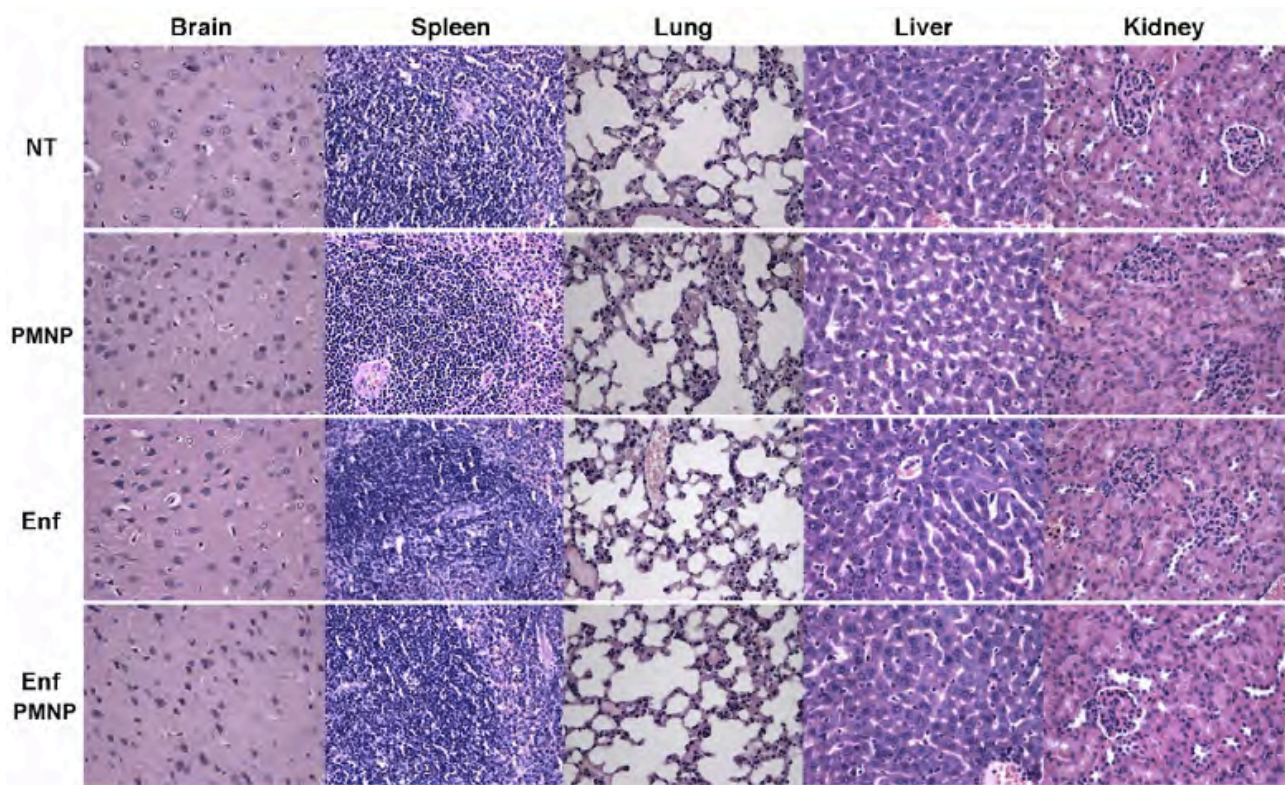


Figure 3.4.8. Histopathological analysis of brain, spleen, lung, liver and kidney dissected from non-treated (NT) mice, or from mice injected with PMNP, Enf and Enf-PMNP. Hematoxylin-eosin, OM \times 40. (Images taken from Fiandra et al)²⁰.

3.4.5. Fate of PMNP in RBMVECs

The mechanism of PMNP entry and trafficking into the RBMVECs is investigated by TEM analysis on BBB-bearing inserts after 4, 7 or 24 h from the addition of Enf-PMNP in the upper chamber. Figure 3.4.9.A shows that, at 4 h of incubation, nanoparticles are either attached to the plasma membrane of the endothelial cells or internalized in the cytosol. The lack of membrane invaginations and the presence of free nanoparticles in the cytoplasm suggest that a non-endocytotic mechanism is involved in the internalization of PMNP by RBMVECs, as confirmed also by TEM images of brain samples exposed *in vivo* to the nanocomplex (Figure 3.4.10.). Macropinocytosis rafts are also visible where a large number of nanoparticles came in contact with the cellular membrane. Once internalized, PMNP accumulate into large cellular compartments (Figure 3.4.9.A & 3.4.9.B), and after 24 h of incubation, they are also detected into lysosomes (Figure 3.4.9.C). The same result is obtained by incubating the cells with the unconjugated PMNP.

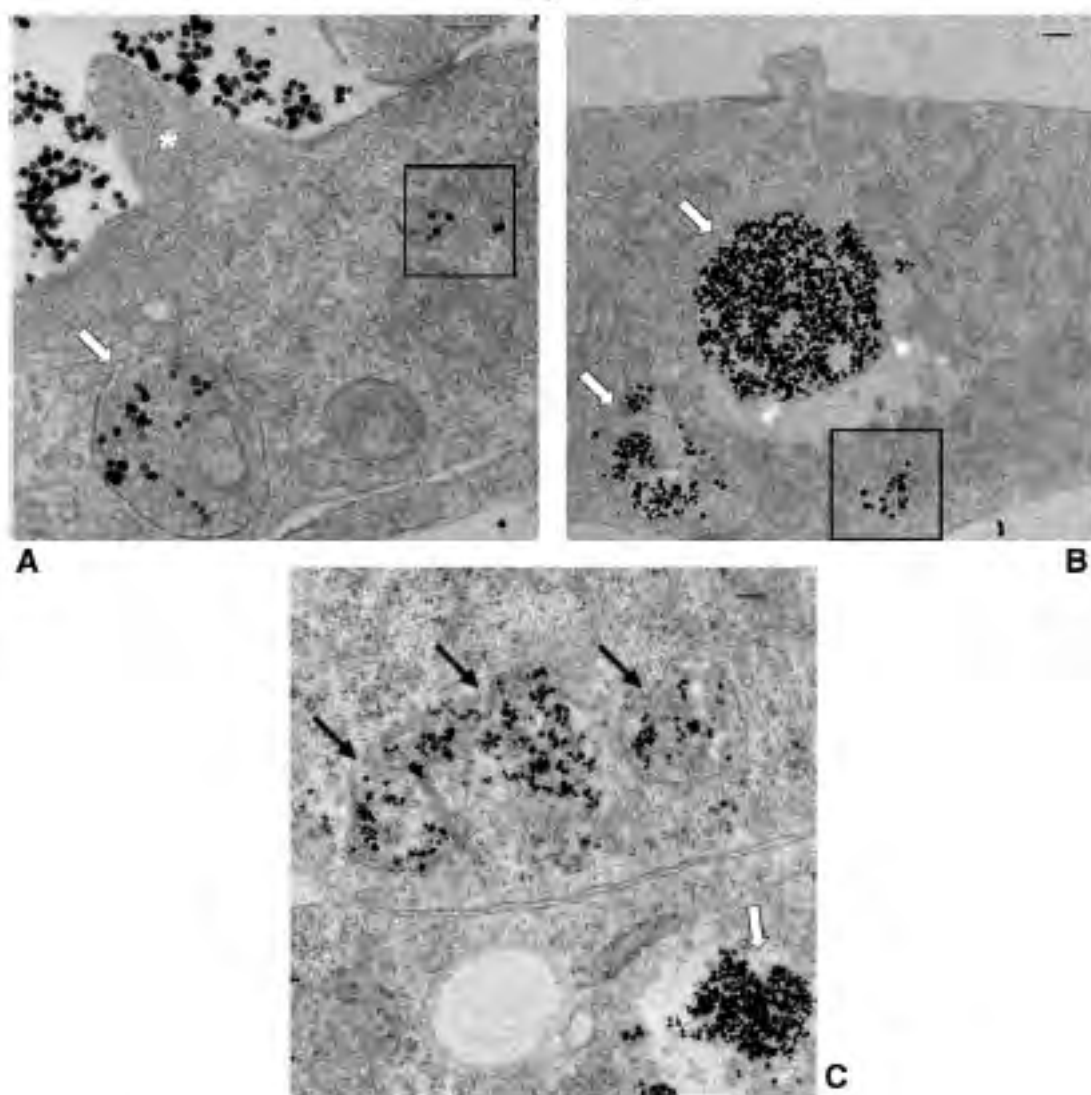


Figure 3.4.9. TEM images of RBMVECs in a BBB *in vitro* model exposed to 0.1 mg Enf-PMNP for 4 h (A), 7 h (B) and 24 h (C). PMNP are localized in big cell compartments (white arrows), in lysosomes (black arrows) or free into the cytosol (boxes); asterisk indicates a macropinocytosis raft; bars: 100 nm. (Images taken from Fiandra et al)²⁰.

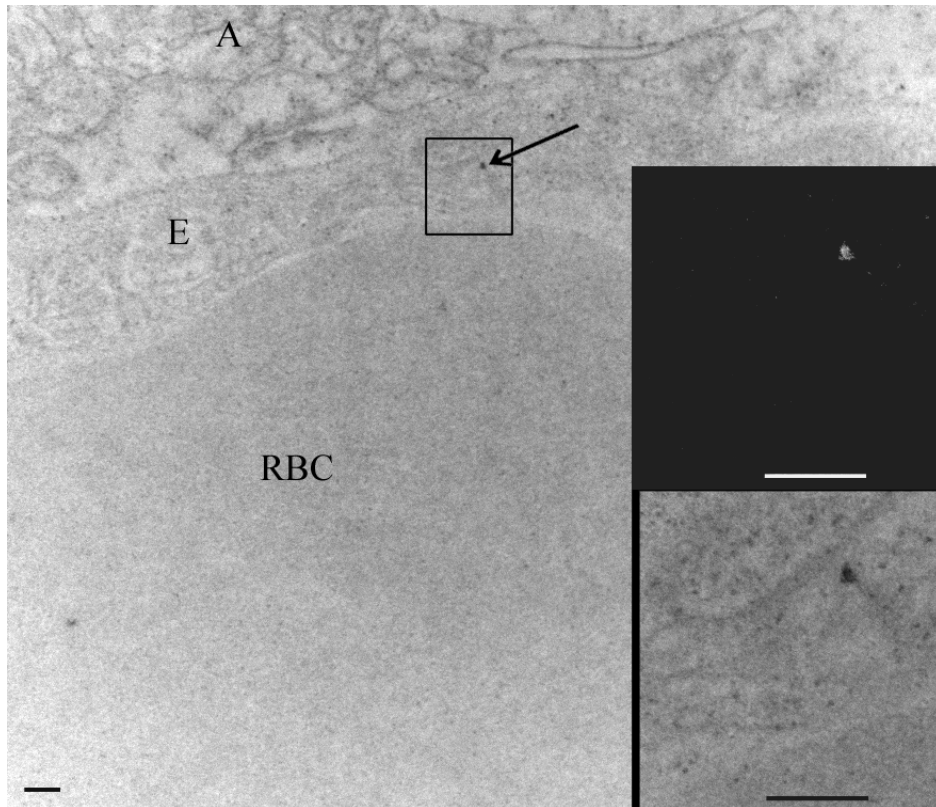


Figure 3.4.10. TEM image of a mouse brain isolated at 1 h postinjection of Enf-PMNP ($12.5 \mu\text{g g}^{-1}$ body weight). The nanoparticle is evidenced by the arrow. A: astrocyte; E: endothelial cell, RBC: red blood cells. In inserts is reported the correspondent higher magnification image (down) and its digital dark field (up). Bars: 100 nm. (Data taken from Fiandra et al)²⁰.

Bibliography

1. Ballabh, P., Braun, A. & Nedergaard, M. The blood-brain barrier: an overview: structure, regulation, and clinical implications. *Neurobiol. Dis.* **16**, 1–13 (2004).
2. Abbott, N. J., Patabendige, A. A. K., Dolman, D. E. M., Yusof, S. R. & Begley, D. J. Structure and function of the blood–brain barrier. *Neurobiol. Dis.* **37**, 13–25 (2010).
3. Domínguez, A., Álvarez, A., Suárez-Merino, B. & Goñi-de-Cerio, F. [Neurological disorders and the blood-brain barrier. Strategies and limitations for drug delivery to the brain]. *Rev. Neurol.* **58**, 213–224 (2014).
4. Iorio, A. L. *et al.* Blood-Brain Barrier and Breast Cancer Resistance Protein: A Limit to the Therapy of CNS Tumors and Neurodegenerative Diseases. *Anticancer Agents Med. Chem.* **16**, 810–815 (2016).
5. Vries, H. E. de, Kuiper, J., Boer, A. G. de, Berkel, T. J. C. V. & Breimer, D. D. The Blood-Brain Barrier in Neuroinflammatory Diseases. *Pharmacol. Rev.* **49**, 143–156 (1997).
6. Abbott, N. J. Blood-brain barrier structure and function and the challenges for CNS drug delivery. *J. Inherit. Metab. Dis.* **36**, 437–449 (2013).
7. Banks, W. A. Characteristics of compounds that cross the blood-brain barrier. *BMC Neurol.* **9**, S3 (2009).
8. Jain, K. K. Nanobiotechnology-based strategies for crossing the blood-brain barrier. *Nanomed.* **7**, 1225–1233 (2012).
9. Saraiva, C. *et al.* Nanoparticle-mediated brain drug delivery: Overcoming blood–brain barrier to treat neurodegenerative diseases. *J. Controlled Release* **235**, 34–47 (2016).
10. Grabrucker, A. M. *et al.* Nanoparticle transport across the blood brain barrier. *Tissue Barriers* **4**, (2016).
11. HIV-1 genital shedding in HIV-infected patients randomized to second-line lopinavir/ritonavir monotherapy versus tenofovir/lamivudine/lopinavir/ritonavir. *ResearchGate* Available at: https://www.researchgate.net/publication/262045976_HIV-1_genital_shedding_in_HIV-infected_patients_randomized_to_second-line_lopinavirritonavir_monotherapy_versus_tenofovir_lamivudine_lopinavirritonavir. (Accessed: 7th March 2017)
12. Kramer-Hämmerle, S., Rothenaigner, I., Wolff, H., Bell, J. E. & Brack-Werner, R. Cells of the central nervous system as targets and reservoirs of the human immunodeficiency virus. *Virus Res.* **111**, 194–213 (2005).
13. Mahajan, S. D. *et al.* Enhancing the delivery of anti retroviral drug ‘Saquinavir’ across

- the blood brain barrier using nanoparticles. *Curr. HIV Res.* **8**, 396–404 (2010).
14. Dando, T. M. & Perry, C. M. Enfuvirtide. *Drugs* **63**, 2755-2766-2768 (2003).
 15. Patel, I. H., Zhang, X., Nieforth, K., Salgo, M. & Buss, N. Pharmacokinetics, pharmacodynamics and drug interaction potential of enfuvirtide. *Clin. Pharmacokinet.* **44**, 175–186 (2005).
 16. Liu, S. *et al.* Different from the HIV fusion inhibitor C34, the anti-HIV drug Fuzeon (T-20) inhibits HIV-1 entry by targeting multiple sites in gp41 and gp120. *J. Biol. Chem.* **280**, 11259–11273 (2005).
 17. Price, R. W. *et al.* Enfuvirtide Cerebrospinal Fluid (CSF) Pharmacokinetics and Potential Use in Defining CSF HIV-1 Origin. *Antivir. Ther.* **13**, 369–374 (2008).
 18. Bazylińska, U., Kulbacka, J. & Wilk, K. A. Dicephalic ionic surfactants in fabrication of biocompatible nanoemulsions: Factors influencing droplet size and stability. *Colloids Surf. Physicochem. Eng. Asp.* **460**, 312–320 (2014).
 19. Alkilany, A. M. *et al.* Colloidal stability of citrate and mercaptoacetic acid capped gold nanoparticles upon lyophilization: effect of capping ligand attachment and type of cryoprotectants. *Langmuir ACS J. Surf. Colloids* **30**, 13799–13808 (2014).
 20. Fiandra, L. *et al.* Nanoformulation of antiretroviral drugs enhances their penetration across the blood brain barrier in mice. *Nanomedicine Nanotechnol. Biol. Med.* **11**, 1387–1397 (2015).
 21. Fiandra, L. *et al.* Assessing the In Vivo Targeting Efficiency of Multifunctional Nanoconstructs Bearing Antibody-Derived Ligands. *ACS Nano* **7**, 6092–6102 (2013).
 22. Zaharoff, D. A., Hance, K. W., Rogers, C. J., Schlom, J. & Greiner, J. W. Intratumoral immunotherapy of established solid tumors with chitosan/IL-12. *J. Immunother. Hagerstown Md* **1997** **33**, 697–705 (2010).

Chapter 4

Outlook

4.1 Conclusion

The main aim of this work was to investigate the possibility to administer engineered colloidal nanoparticles by different routes in alternative to the intravenous one: topical, oral, and inhalational. Indeed, the local administration of drugs is a critical issue when the therapy is characterized by insufficient drug accumulation at target sites and systemic drug toxicity. Nanoparticles, with their peculiar physico-chemical properties along with the choice of the administration route represent a promising solution in order to improve the therapeutic efficacy and subsequent target selectivity whilst reducing the side effects owing to their size in addition to the versatility of surface functionalization approaches.

Since the use of different administration routes in a clinical perspective is of great importance, I studied the effect of different formulations on the interaction between the NPs and the biological environment in order to explore their potential application in biomedicine.

Finding the best way to administer a drug makes the difference in a therapy and allows to optimize the efficacy of the treatment. Particularly, the routes investigated in this work were selected based on specific reasons: the topical route could be exploited for local skin treatments giving higher drug accumulation at the target tissue minimising the systemic side effects and drugs metabolism; the oral way is the administration route which enjoys the best compliance of the patient resulting in a less invasive, more safe administration of the proper dose; the inhalational route represents a favourable choice to selectively administer the drug into the deeper lung tissues, allowing systemic diffusion without hepatic metabolism as it is characterized by a rich vascularization. Regarding the blood brain barrier passage, the intravenous injection is selected to test the nanoparticles capability to cross the BBB once they are immediately injected in the systemic circle.

Nanotechnology provides a plethora of different kinds of nanoparticles: for my project, I selected different types of them in order to have a biological application, therapeutic efficacy, target selectivity and possibility to check where the nanoparticles are distributed once they are administered by a specific administration route. For these reasons, iron oxide nanoparticles were selected for the topical routes because of their stability in suspension, they can be functionalized on the surface and they can be easily localized in the skin by TEM and ICP analysis. Thanks to their excellent colloidal stability they were also chosen for the BBB passage after intravenous administration and they also provides the possibility to be simultaneously functionalized with dyes and drugs. For the inhalational way, I selected gold nanoparticles due to their excellent colloidal stability necessary to achieve optimal nanoparticle nebulization.

Differently from the project listed above, for the oral route I tested polymeric nanoparticles essentially due to their biocompatible matrix, as the administration of insulin requires frequent and chronic administration of the peptide, which could be hardly achieved with colloidal nanocarriers. In addition, polyethylenimine-based nanoparticles were strongly positively charged resulting in a more efficient absorption through the intestinal epithelium, characterized by negative charges of mucins.

As regard to the investigation of the topical administration, iron oxide nanoparticles coated with an amphiphilic polymer (PMNP) are able to permeate and penetrate the human skin. An

in vitro permeation analysis carried out through intact human skin Franz Diffusion Cell suggests that PMNP loaded in a w/o cream induce an increased, faster and more regular penetration of nanoparticles in comparison to the nanoparticle aqueous suspension as such. However, probably due to the amphiphilic character of the polymer coating, nanoparticles formulated in suspension exhibit an intrinsic enhanced propensity to penetrate through the different human skin layers in accordance with similar data reported in previous literature¹.

In vivo treatment in mice with these nanoparticles shows their uptake by the dermal resident immune cells and, when administered in the form of nano-cream suspension, nanoparticles remain confined within the thin skin layers of mice, as no migration to the draining lymph nodes is observed. The results obtained in this study are promising for the development of nano-cream for the local skin treatment, without a systemic diffusion of the nanovehicle. The PMNP core/shell system can be a carrier to deliver drugs encapsulated in the hydrophobic shell or covalently linked to the nanoparticles surface for the topical route.

Furthermore, PMNP are loaded in different semi-solid vehicles in order to see any differences in terms of NPs permeation performance and in general the tested semi-solids don't affect the NPs permeation profile only if they maintain their stability over time. Low-field pulsed NMR allows to assess the physical stability of PMNP loaded into semi-solids. All the tested semi-solid formulations (hydroxyethyl cellulose, sodium carboxymethyl cellulose, carbomer 974P, cetomacrogol cream and a cold cream) influence the PMNP penetration through the epidermis; the cetomacrogol cream allows the highest permeation and the lowest retained amount while cold creams and carbomer hydrogels favour the nanoparticle accumulation into the skin membrane. This makes nano-cream very promising for application in local therapies: the results suggest that these two very basic formulations are suitable to be conveniently used to administer PMNP topically in order to improve the efficiency of colloidal nanoparticles in penetrating the skin layers.

In a landscape where oral formulation of insulin is still missing, I propose a new approach for the oral administration of insulin targeting the colon as release and absorption site. The synergistic effect, due to the nanoformulation of insulin and the encapsulation in a triple-layer pellet system for colon-release delivery, results in a significant and long-lasting hypoglycaemic effect. This multi-tasking delivery system represents a new promising strategy for orally administered insulin, prolonged hypoglycaemic activity and a more physiological insulin metabolism.

The functionalization of gold nanoparticle (GNP) with an antibody selective for CD44 and the loading with everolimus, a potent immunosuppressive drug, demonstrate the capability of this nanosystem to significantly inhibit mesenchymal cell proliferation *in vitro*, which is responsible of the fibrotic phenomenon of bronchiolitis obliterans syndrome (BOS). Specifically engineered GNPs show both target selectivity and good therapeutic efficacy, offering the possibility to administer functionalized drug-loaded GNPs by aerosolization without raising a further inflammatory response. Indeed, the future perspective of this project, already in progress in the laboratory, will be the *in vivo* administration by inhalation of GNPs to test their safety in mice and their efficacy in animal models of obliterative bronchiolitis.

Iron oxide nanoparticles coated with the amphiphilic polymer (PMNP) are also tested for the blood-brain barrier (BBB) penetration by intravenous injection. To this aim, an anti-retroviral peptide, enfuvirtide (Enf), is chosen as proof of concept to test its capability to cross the BBB when conjugated to the PMNP. Indeed, Enf is not able to cross the BBB by itself for its complex structure as the 98% of the antiretroviral drugs². In the present project PMNP

demonstrate to be promising drug delivery system to the central nervous system (CNS) for antiretroviral drugs, by taking advantage of their intrinsic propensity to cross the BBB. An *in vitro* increased permeation of nanoformulated-Enf across BBB up to 170% after 3h of incubation. Moreover, conjugated enfuvirtide shows increased epifluorescent intensity in mice brain, as result of its huge CNS accumulation. Once into the cell, PMNP are isolated by huge endosome-like compartments and then directed to lysosomes. The data indicate that Enf dissociated from PMNP in the endothelial cells to be efficiently excreted in the outside environment.

In conclusion, this is the first documented experience of a nanotechnological engineering of the complex antiretroviral drug enfuvirtide, which confers to this large peptide the capability to cross the BBB. Whether and how the propensity of Enf nanoconjugate to cross the BBB could affect the viral replication in the CNS sanctuary remain to be established, and further studies will be performed to assess the antiviral efficacy of Enf after trans-BBB permeation.

Overall, the accomplishment of the four different tasks explored within this thesis work suggests that colloidal nanoparticles are well suited to be formulated through different routes well beyond the conventional intravenous administration.

In particular, the topical, the oral and the intravenous administrations focus on very challenging results since they offer a finished dosage form available for clinical use. At the same time, even if the inhalational way didn't get to a finished pharmaceutical form, it achieved very promising preliminary results for the treatment of fibrotic phenomena in bronchiolitis obliterans syndrome.

My results contribute to expand the potential of the use of colloidal nanoparticles in pharmacological studies, reducing the gap between preclinical investigation and an actual clinical translation.

Bibliography

1. Baroli, B. Penetration of nanoparticles and nanomaterials in the skin: fiction or reality? *J. Pharm. Sci.* **99**, 21–50 (2010).
2. Sagar, V., Pilakka-Kanthikeel, S., Pottathil, R., Saxena, S. K. & Nair, M. Towards nanomedicines for neuroAIDS. *Rev. Med. Virol.* **24**, 103–124 (2014).

APPENDIX

During the PhD course I had the possibility to acquire expertise with Nanoparticles Tracking Analysis (NTA) instrument (Nanosight), which offers information about nanoparticles size distribution and concentration. In collaboration with different research groups, I used this instrument to characterize a specific type of nanoparticles, which are extracellular vesicles (EVs) or exosomes.

The interest towards these vesicles is exponentially growing because they are involved in intercellular communication¹⁻³ and serving reservoirs for biomarkers for tumors⁴ and they have also a great potential for liquid biopsy development, possibly replacing many costly and invasive tissue biopsies^{5,6}. Exosomes, which are membranous nanovesicles, are actively released by cells and have been attributed to roles in cell-cell communication, cancer metastasis, and early disease diagnostics. Indeed, the presence of exosomes in circulating bodily fluids, including blood⁷, urine⁸ and saliva⁹, suggests that minimally-invasive diagnosis of a number of diseases can be achieved through detection of these vesicles¹⁰⁻¹³. In particular, EVs carry molecular and proteomic cargo from their tumour cell of origin¹⁴ and, regarding the neurological disorders, there is increasing evidence that deregulation of EVs secretion plays a pathological role in neurodegenerative diseases such as Alzheimer's disease and Frontotemporal dementia¹⁵⁻¹⁹. The limited utility of exosomes in diagnostics is mainly due to difficulties in specifically characterizing them using a scalable phenotyping method and for these reasons there is still not a method of election to characterize them. The small size (30–100 nm) along with low refractive index contrast of exosomes makes direct characterization and phenotypical classification very difficult because they are too small to be accurately sized by conventional methods such as optical microscopy and flow cytometry without labels.

The efforts in development of new tools for analysis of exosomes have led to a number of innovative technologies with potential clinical applications. In the few recently commercialized nanoparticle detection technologies that are typically utilized in characterization of exosomes, my interest is to focus on the Nanoparticle Tracking Analysis (NTA) instrument. NTA analyses samples containing diluted nanoparticles suspensions which are illuminated by a monochromatic laser beam at 532 nm to register a 60 second video taken with a mean frame rate of 30 frames/s. The NTA software (version 3.0, NanoSight) is optimized to first identify and then track each particle on a frame-by-frame basis, and its Brownian movement is tracked and measured from frame to frame. Particle size is determined applying the two-dimensional Stokes–Einstein equation based on the velocity of particle movement²⁰. From each video, the mean, mode, and median particles size are used to calculate samples concentration expressed in nanoparticles/mL.

In this way it's possible to count the vesicles contained in the samples but it's necessary to compare the results with that ones obtained with other detection methods. Indeed NTA is not able to offer qualitative information about the nature of the vesicles and the number of counted particles could be altered for the presence of other aggregates (i.e. protein aggregates, lipids) and not only exosomes.

The contribution of my work for these collaboration projects results in a number of three publications (in the list of publications are the papers number 7, 8, 9). Each one regards a specific issue with the aim of using exosomes for diagnostic or therapeutic applications.

Bibliography

1. Valadi, H. *et al.* Exosome-mediated transfer of mRNAs and microRNAs is a novel mechanism of genetic exchange between cells. *Nat. Cell Biol.* **9**, 654–659 (2007).
2. Raposo, G. & Stoorvogel, W. Extracellular vesicles: Exosomes, microvesicles, and friends. *J Cell Biol* **200**, 373–383 (2013).
3. Tetta, C., Ghigo, E., Silengo, L., Deregibus, M. C. & Camussi, G. Extracellular vesicles as an emerging mechanism of cell-to-cell communication. *Endocrine* **44**, 11–19 (2013).
4. Hood, J. L., San, R. S. & Wickline, S. A. Exosomes Released by Melanoma Cells Prepare Sentinel Lymph Nodes for Tumor Metastasis. *Cancer Res.* **71**, 3792–3801 (2011).
5. Robbins, P. D. & Morelli, A. E. Regulation of immune responses by extracellular vesicles. *Nat. Rev. Immunol.* **14**, 195–208 (2014).
6. Yoshioka, Y. *et al.* Ultra-sensitive liquid biopsy of circulating extracellular vesicles using ExoScreen. *Nat. Commun.* **5**, 3591 (2014).
7. Orozco, A. F. & Lewis, D. E. Flow cytometric analysis of circulating microparticles in plasma. *Cytom. Part J. Int. Soc. Anal. Cytol.* **77**, 502–514 (2010).
8. Gonzales, P. A. *et al.* Large-scale proteomics and phosphoproteomics of urinary exosomes. *J. Am. Soc. Nephrol. JASN* **20**, 363–379 (2009).
9. Sharma, S., Gillespie, B. M., Palanisamy, V. & Gimzewski, J. K. Quantitative Nanostructural and Single-Molecule Force Spectroscopy Biomolecular Analysis of Human-Saliva-Derived Exosomes. *Langmuir* **27**, 14394–14400 (2011).
10. Skog, J. *et al.* Glioblastoma microvesicles transport RNA and proteins that promote tumour growth and provide diagnostic biomarkers. *Nat. Cell Biol.* **10**, 1470–1476 (2008).
11. Lv, L.-L. *et al.* MicroRNA-29c in urinary exosome/microvesicle as a biomarker of renal fibrosis. *Am. J. Physiol. - Ren. Physiol.* **305**, F1220–F1227 (2013).

12. Alvarez, S. *et al.* Urinary exosomes as a source of kidney dysfunction biomarker in renal transplantation. *Transplant. Proc.* **45**, 3719–3723 (2013).
13. Duijvesz, D., Luiders, T., Bangma, C. H. & Jenster, G. Exosomes as biomarker treasure chests for prostate cancer. *Eur. Urol.* **59**, 823–831 (2011).
14. Brock, G., Castellanos-Rizaldos, E., Hu, L., Coticchia, C. & Skog, J. Liquid biopsy for cancer screening, patient stratification and monitoring. *Transl. Cancer Res.* **4**, 280–290 (2015).
15. Ghidoni, R., Paterlini, A. & Benussi, L. Circulating progranulin as a biomarker for neurodegenerative diseases. *Am. J. Neurodegener. Dis.* **1**, 180–190 (2012).
16. Joshi, R. S., Tanpure, R. S., Singh, R. K., Gupta, V. S. & Giri, A. P. Resistance through inhibition: ectopic expression of serine protease inhibitor offers stress tolerance via delayed senescence in yeast cell. *Biochem. Biophys. Res. Commun.* **452**, 361–368 (2014).
17. Joshi, P., Benussi, L., Furlan, R., Ghidoni, R. & Verderio, C. Extracellular Vesicles in Alzheimer's Disease: Friends or Foes? Focus on A β -Vesicle Interaction. *Int. J. Mol. Sci.* **16**, 4800–4813 (2015).
18. Rajendran, L. *et al.* Emerging Roles of Extracellular Vesicles in the Nervous System. *J. Neurosci.* **34**, 15482–15489 (2014).
19. Benussi, L. *et al.* Loss of exosomes in progranulin-associated frontotemporal dementia. *Neurobiol. Aging* **40**, 41–49 (2016).
20. Filipe, V., Hawe, A. & Jiskoot, W. Critical evaluation of Nanoparticle Tracking Analysis (NTA) by NanoSight for the measurement of nanoparticles and protein aggregates. *Pharm. Res.* **27**, 796–810 (2010).
21. Dragovic, R. A. *et al.* Sizing and phenotyping of cellular vesicles using Nanoparticle Tracking Analysis. *Nanomedicine Nanotechnol. Biol. Med.* **7**, 780–788 (2011).

RESEARCH ARTICLE

Cream Formulation Impact on Topical Administration of Engineered Colloidal Nanoparticles

Benedetta Santini¹✉, Ivan Zanoni^{1,2,6}✉, Roberta Marzi¹, Clara Cigni¹, Marzia Bedoni³, Furio Gramatica³, Luca Palugan⁴, Fabio Corsi⁵, Francesca Granucci^{1,6}, Miriam Colombo¹*

1 NanoBioLab, Dipartimento di Biotecnologie e Bioscienze, Università degli Studi di Milano-Bicocca, Milano, Italy, **2** Division of Gastroenterology, Boston Children's Hospital, Harvard Medical School, Boston, Massachusetts, United States of America, **3** Laboratorio di Nanomedicina e Biofotonica Clinica, Fondazione Don Carlo Gnocchi ONLUS, Milano, Italy, **4** Dipartimento di Scienze Farmaceutiche, Università degli Studi di Milano, Milano, Italy, **5** Dipartimento di Scienze Biomediche e Cliniche "Luigi Sacco", Università degli Studi di Milano, Milano, Italy, **6** Unit of Cell Signalling and Innate Immunity, Humanitas Clinical and Research Center, Rozzano, Milan, Italy

✉ These authors contributed equally to this work.

* miriam.colombo@unimib.it



OPEN ACCESS

Citation: Santini B, Zanoni I, Marzi R, Cigni C, Bedoni M, Gramatica F, et al. (2015) Cream Formulation Impact on Topical Administration of Engineered Colloidal Nanoparticles. PLoS ONE 10(5): e0126366. doi:10.1371/journal.pone.0126366

Academic Editor: Bing Xu, Brandeis University, UNITED STATES

Received: January 26, 2015

Accepted: April 1, 2015

Published: May 11, 2015

Copyright: © 2015 Santini et al. This is an open access article distributed under the terms of the [Creative Commons Attribution License](https://creativecommons.org/licenses/by/4.0/), which permits unrestricted use, distribution, and reproduction in any medium, provided the original author and source are credited.

Data Availability Statement: All relevant data are within the paper.

Funding: This work was supported by the following sources: Fondazione Regionale per la Ricerca Biomedica (FRRB), NanoMeDia Project (A.O. "L. Sacco" and Regione Lombardia); the Cariplo Foundation (Grant 2011-2096 and Grant 2010-0678), Associazione Italiana per la Ricerca sul Cancro (MFAG, Rif.13235).

Competing Interests: The authors have declared that no competing interests exist.

Abstract

In order to minimize the impact of systemic toxicity of drugs in the treatment of local acute and chronic inflammatory reactions, the achievement of reliable and efficient delivery of therapeutics in/through the skin is highly recommended. While the use of nanoparticles is now an established practice for drug intravenous targeted delivery, their transdermal penetration is still poorly understood and this important administration route remains almost unexplored. In the present study, we have synthesized magnetic (iron oxide) nanoparticles (MNP) coated with an amphiphilic polymer, developed a water-in-oil emulsion formulation for their topical administration and compared the skin penetration routes with the same nanoparticles deposited as a colloidal suspension. Transmission and scanning electron microscopies provided ultrastructural evidence that the amphiphilic nanoparticles (PMNP) cream formulation allowed the efficient penetration through all the skin layers with a controllable kinetics compared to suspension formulation. In addition to the preferential follicular pathway, also the intracellular and intercellular routes were involved. PMNP that crossed all skin layers were quantified by inductively coupled plasma mass spectrometry. The obtained data suggests that combining PMNP amphiphilic character with cream formulation improves the intradermal penetration of nanoparticles. While PMNP administration in living mice via aqueous suspension resulted in preferential nanoparticle capture by phagocytes and migration to draining lymph nodes, cream formulation favored uptake by all the analyzed dermis cell types, including hematopoietic and non-hematopoietic. Unlike aqueous suspension, cream formulation also favored the maintenance of nanoparticles in the dermal architecture avoiding their dispersion and migration to draining lymph nodes via afferent lymphatics.

Introduction

Nanomaterials, which size is included within 1–100 nm range, hold tremendous potential in biomedical applications thanks to the favorable combination of unique chemical and physical size-dependent properties [1,2]. In particular, nanoparticles can be designed in many different fashions and their clinical applications in drug delivery and diagnosis of human diseases are taken into consideration [3]. Among them, magnetite nanoparticles are ideal candidates as contrast agents for magnetic resonance imaging and magnetic force-assisted drug delivery systems [4]. It has been demonstrated several times that MNP are nontoxic at therapeutic dosages and the first MNP-based medical tools have already entered the marketplace [5] or are currently subjected to clinical trials [6].

Drug delivery nanosystems are meant to improve the biopharmaceutical properties of existing drugs that often exhibit a limited effectiveness in therapy. Such limitations include solid- and suspension-state instability, poor solubility and poor drug absorption that could lead to low bioavailability and insufficient targeting efficiency that could lead to unfavorable ratio between the amount of the administered drug and the concentration at the target tissue [7–9]. In order to optimize the loco-regional release of therapeutics, the topical route has been one of the most promising noninvasive delivery options, ameliorating patient compliance, improving the pharmacokinetics of degradable compounds and reducing frequently occurring side effects [10–12]. Nevertheless, drug topical administration remains a challenge in pharmaceuticals because of the difficulties to adjust the skin penetration and to determine and reproduce the exact amount of drug reaching the skin layers at the desired depth [13,14]. In fact, the conventional transdermal drug delivery methods are limited by skin barrier properties according to the “brick and mortar model” (*stratum corneum*) that prevents excessive water loss and offers an efficient protective tissue against exogenous chemical, physical and mechanical stimuli and pathogens [15].

In this scenario, the preparation of high quality engineered colloidal nanoparticles loaded with drugs and modified with targeting molecules to improve the localized therapeutic effect represents a promising new strategy to develop a novel generation of therapeutic agents [16]. Despite at the moment only few studies have been reported on transdermal penetration of colloidal nanoparticles, cutaneous administration is expected to raise interest in the next future to achieve more efficient loco-regional delivery [17–19]. However, most attempts have mainly exploited invasive and expensive enhancement techniques or electrical methods to improve the penetration of nanoparticles in the healthy skin, with controversial conclusions [20]. So far, very few examples have been reported using human skin as a model for ultrastructural investigations [17].

To our knowledge, cream formulations have never been exploited to improve the absorption of nanoparticles. Water-in-oil (w/o) creams, which consist of small droplets of water dispersed in a continuous oily phase, can be used to improve the cutaneous absorption of pharmaceutical agents and to facilitate their penetration through the skin layers [21].

In the present work, we have synthesized MNP coated with a pro-functional amphiphilic polymer and used them as a colloidal aqueous suspension or formulated in a w/o cream. These nanoparticles, termed PMNP, were found to be colloidally stable both in aqueous fluids and in a w/o cream formulation and thus particularly appropriate to gain information on the destiny of nanoparticles. PMNP were used to study penetration in human skin samples by ultrastructural analysis and to assess nanoparticle distribution in immune cells of dermis in living mice. Despite mice skin is remarkably thinner than human, localized cells of innate immunity behave very similarly for this reason living mice represent a good model in order to investigate the interaction between colloidal nanoparticles and dermal cytotypes.

Materials and Methods

Ethics Statement

We declare that all *in vivo* experiments were performed using protocols approved by the University of Milano-Bicocca Animal Care and Use Committee. Protocols were approved by the Italian Ministry of Health under the protocol number 11–2012. Consensus of the Ethical Committee “Niguarda Cà Granda” Hospital, Milan was obtained for the use of fresh human skin samples.

Mice and Reagents

All mice were bred on a C57BL/6 background and animals were housed under pathogen-free conditions. C57BL/6 mice were purchased from Charles River and were maintained in our animal facility at the University of Milano-Bicocca. Mice were housed in containment facilities of the animal facility and maintained on a regular 12:12 hour light:dark cycle with food and water *ad libitum*.

Fresh human skin samples were obtained by Bank Tissue after ethical committee consensus (Ethical Committee “Niguarda Cà Granda” Hospital, Milan). Cell culture medium and chemicals were purchased from EuroClone (Pero, Italy). All the antibodies (anti-CD11c, anti-CD11b, anti-CD19, anti-CD3, anti-CD45.2) used for fluorescence-activated cell sorting (FACS) analysis were purchased from BD Biosciences (San Diego, CA). For TEM images of the tissues, at the end of Franz Cell experiment, small portions of skin were fixed in 2.5% glutaraldehyde in 0.1 M phosphate buffer, pH 7.2 (Electron Microscopy Sciences, Hatfield, PA), for 2 h. After one rinse with phosphate buffer, specimens were post fixed in 1.5% osmium tetroxide (Electron Microscopy Sciences) for 2 h, dehydrated by 50, 70, 90, and 100% EtOH, and embedded in epoxy resin (PolyBed 812 Polysciences Inc., Warrington, PA).

Synthesis of PMNP and cream and suspension formulation. MNP were synthesized by solvothermal decomposition in octadecene from iron oleate precursor, as described previously [22]. MNP (10 mg) suspended in chloroform (5 mg mL⁻¹) were transferred to water phase by mixing with a 0.5 M solution of an amphiphilic polymer (poly(isobutylene-*alt*-1-tetradecene-maleic anhydride)) (PMA, 136 μ L) in 5 mL of sodium borate buffer (SBB, pH 12) [23]. The resulting PMA-coated nanoparticles (PMNP) were dispersible in aqueous media. For *in vivo* experiments green dye-labeled PMNP were synthesized using 5(6)-carboxyfluorescein diacetate N-succinimidyl ester (CFSE). After activation of the carboxylate groups of the PMA by 0.1 M EDC (6.5 μ L), 0.05 M 2,2-(ethylenedioxy)-bis(ethylamine) (EDBE, 2.5 μ L) was added and stirred 2 h. Next, nanoparticle dispersion was concentrated and washed twice with water. Subsequently, CFSE (1.8 mg dissolved in 180 μ L of dimethyl sulfoxide) was added to 8 mg of nanoparticles, stirred 2 h and washed twice with water. The amount of CFSE onto PMNP was determined by measuring fluorescence emission at 518 nm (λ_{ex} 491 nm).

For PMNP suspension, PMNP as synthesized are concentrated in Amicon tubes (50 kDa filter cutoff) (Millipore Corporation, Billerica, MA) by centrifuging at 3000 rpm in order to obtain the final concentration of 8 mg mL⁻¹ (5×10^{14} nanoparticles mL⁻¹). The PMNP cream formulation was obtained by addition of 8 mg PMNP or PMNP-CFSE to 1 g of w/o cream (Essex cream, Shering-Plough) according to the method of progressive dilution.

Dynamic light scattering (DLS) and zeta-potential measurements. DLS measurements were performed at 90° with a 90Plus Particle Size Analyzer from Brookhaven Instruments Corporation (Holtville, NY), working at 15 mW of a solid-state laser (λ 661 nm). Nanoparticles were dispersed in the solvent and sonicated in a S15H Elmasonic apparatus (Elma, Singen, Germany) before analysis. Final sample concentration used for measurements was 5 mg mL⁻¹.

Zeta-potential measurements were elaborated on the same instrument equipped with AQ-809 electrode and data were processed by ZetaPlus Software (Brookhaven Instruments Corporation, Holtsville, NY).

Transmission electron microscopy (TEM) of MNP and PMNP. For TEM analysis, MNP and PMNP were dispersed in hexane and water, respectively ($50 \mu\text{g mL}^{-1}$), and a drop of the resulting solution was placed on a Formvar/carbon-coated copper grid and air-dried. TEM images were obtained by a Zeiss EM-109 microscope (Oberkochen, Germany) operating at 80 kV.

Skin preparation. A central punch biopsy of full skin thickness (epidermis, dermis and partially hypodermis) for each specimen was reduced for Franz Diffusion Cell (FDC) analysis. After the reduction the specimens ($n = 2$, for each 4 experiments) were placed in Petri dishes, epidermis side-up and dermis submerged in PBS (0.1 M, pH 7.4), then were thawed at room temperature (RT) till the experimental set up.

Histological analysis. A fragment of each skin biopsy was fixed in 4% buffered formaldehyde solution (0.1 M PBS, pH 7.4) for 5 h at RT, thoroughly washed with PBS, dehydrated using graded ethanol, and embedded in paraffin. Paraffin serial sections were prepared at a thickness of 5 μm , deparaffinized, and stained with haematoxylin and eosin. All sections were analyzed using a Leica microscope (DM2500) equipped with a digital camera (Leica, Wetzlar, Germany).

Skin penetration study with Franz Diffusion Cell. FDCs were maintained at 32°C with thermostated water in the jacket surrounding the cells. Receptor chambers were filled with 5 mL PBS and stirred continuously using a magnetic stir bar. Human skin (epidermis side-up, facing the donor chamber) was mounted into FDC interface and the PMNP formulations (saturated NP cream $>10 \text{ mg cm}^{-2}$ or solution $>100 \mu\text{L cm}^{-2}$, volume 1 mL) were applied to the donor chambers on the basis of an infinite dose test. All the experimental conditions were studied to simulate the physiological condition of temperature, pH and moisture. At specific time intervals (1-3-5-7-24 h), 500 μL samples were withdrawn from the receptor chamber using a syringe and the same amount of fresh PBS was replaced in the same chamber at each time point. Statistical analysis was performed by means of two-tail t-student's test (Excel 2007, Microsoft, Redmond, WA), and the differences were considered statistically significant for $p < 0.05$.

Nanoparticles quantification by ICP analysis. For ICP-OES analysis, to 500 μL samples, collected at specific times from the receptor chambers, were added 3 mL of aqua regia and, after 72 h, the samples were diluted with 7 mL of distilled water. All samples were measured in triplicate with Optima 7000 DV ICP-OES (Perkin Elmer, Waltham, MA).

Skin fixation protocol for SEM and TEM analysis. After the fixation, longitudinal skin sections of 70–80 nm thicknesses were obtained by perpendicular cutting to avoid the tissue disruption and were examined by means of a transmission electron microscope (Zeiss EM109) (Zeiss, Oberkochen, Germany) operating at 80 kV. For SEM images of the tissues, at the end of Franz Cell experiment, small portions of skin were fixed in 2.5% glutaraldehyde in 0.1 M phosphate buffer pH 7.2 (Electron Microscopy Sciences, Hatfield, PA), for 24 h. After one rinse with phosphate buffer, specimens were dehydrated by 10, 25, 50, 75, and 100% EtOH, and dried with hexamethyldisilazane. The samples are carefully mounted on a stub and coated with a very thin film of Agar Auto Sputter Coater (Assing, Monterotondo, Italy) before SEM examination with Leica S420 Microscope operating at 15 Kv.

Isolation of skin cells. Cells were isolated as previously described [24]. Briefly, skin was isolated and digested for 45 min in a cocktail containing collagenase XI, hyaluronidase and DNase. 10% fetal bovine serum (FBS) was added to stop the reaction and cells were then stained to assess the percentage of different cell populations.

Flow Cytometry. Single cell suspensions were washed with ice-cold PBS and stained with the appropriate antibody for 30 min on ice, followed by ice-cold PBS washing. Staining was assessed with a FACS Calibur (Becton Dickinson).

Results and Discussion

Colloidal nanoparticles synthesis and characterization of and formulation in a w/o cream

Hydrophobic magnetite nanoparticles (MNP) were synthesized from organometallic precursors by solvothermal decomposition in octadecene [22]. The high temperature and the presence of stabilizing surfactants provided an optimal crystal nucleation and growth resulting in highly uniform and monodisperse nanoparticles with 12.0 ± 1.2 nm average diameter, as measured by TEM, that were suspended in chloroform by virtue of the oleate surfactant coating. A TEM image of MNPs is shown in Fig 1A. This feature was further confirmed by dynamic light scattering (DLS) analysis, which resulted in a hydrodynamic diameter of 19.0 ± 1.3 nm in hexane. To produce a stable suspension in a physiological environment, a water phase transfer of nanoparticles was needed. To this aim, MNP were coated with an amphiphilic polymer (PMA), obtained by reacting poly(isobutylene-*alt*-1-tetradecene-maleic anhydride) with an amount of dodecylamine sufficient to react with 75% of anhydride groups (Fig 1B) [24]. In MNP coating process, the hydrophobic alkyl chains intercalated between those of oleic acid, which acted as a surfactant (PMNP, 12.2 ± 1.8 nm, TEM measured diameter). The resulting nanoparticle suspension exhibited important advantages including: 1) a stable colloidal dispersion both in aqueous solution and physiological buffer; 2) the polymer coating can be easily functionalized with drugs or targeting molecules for future therapeutic applications; 3) the amphiphilic coating was expected to improve the nanoparticle penetration through both hydrophobic and hydrophilic skin layers; 4) the amphipathic character of the composite nanomaterial was suitable to obtain a homogenous cream nanoformulation. In this way, we developed a nanoparticle scaffold that could be formulated both in suspension (even at a PMNP concentration of 8 mg mL^{-1}) and in w/o cream, which might be useful for topical application. As expected, PMNP nanoparticles coated with PMA appeared a bit larger than MNP by themselves at DLS analysis (23.2 ± 2.0 nm) but were still stable and monodisperse in size. Beyond, the ζ -potential analysis showed a strongly negative surface charge in water ($\zeta = -55.98 \pm 3.18$ mV). To evaluate the potential of PMNP for future application as magnetic resonance imaging contrast enhancers, the value of decreasing concentrations of PMNP in water was $186 \text{ mM}^{-1}\text{s}^{-1}$ at 0.47 T. This value is higher than the negative contrast power of agents currently available in approved clinical diagnostic practice (r_2 of Ferumxtyol is $83 \text{ mM}^{-1}\text{s}^{-1}$ at 0.47 T). For *in vivo* studies, CFSE was conjugated to PMNP using the bifunctional diamino-linker 2,2-(ethylenedioxy)-bis(ethylamine) (EDBE) previously activated by *N*-(3-dimethylaminopropyl)-*N'*-ethylcarbodiimide (EDC). Both labeled and unlabeled PMNP were formulated in a cream, using the method of progressive dilution, in order to obtain a homogeneous preparation (Fig 1C). The maximum amount of PMNP included in 1 g of cream for biological experiments was 8 mg, used to test *in vitro* diffusion and *in vivo* absorption. Physical stability of the cream containing PMNP was also evaluated in order to test the stability of the final product. The organoleptic properties did not show any changes over two years examination.

Investigation of nanoparticle penetration through the human skin.

In order to investigate nanoparticles penetration applied with both types of formulations, through all skin layers, *in vitro* skin permeation studies were carried out using normal human

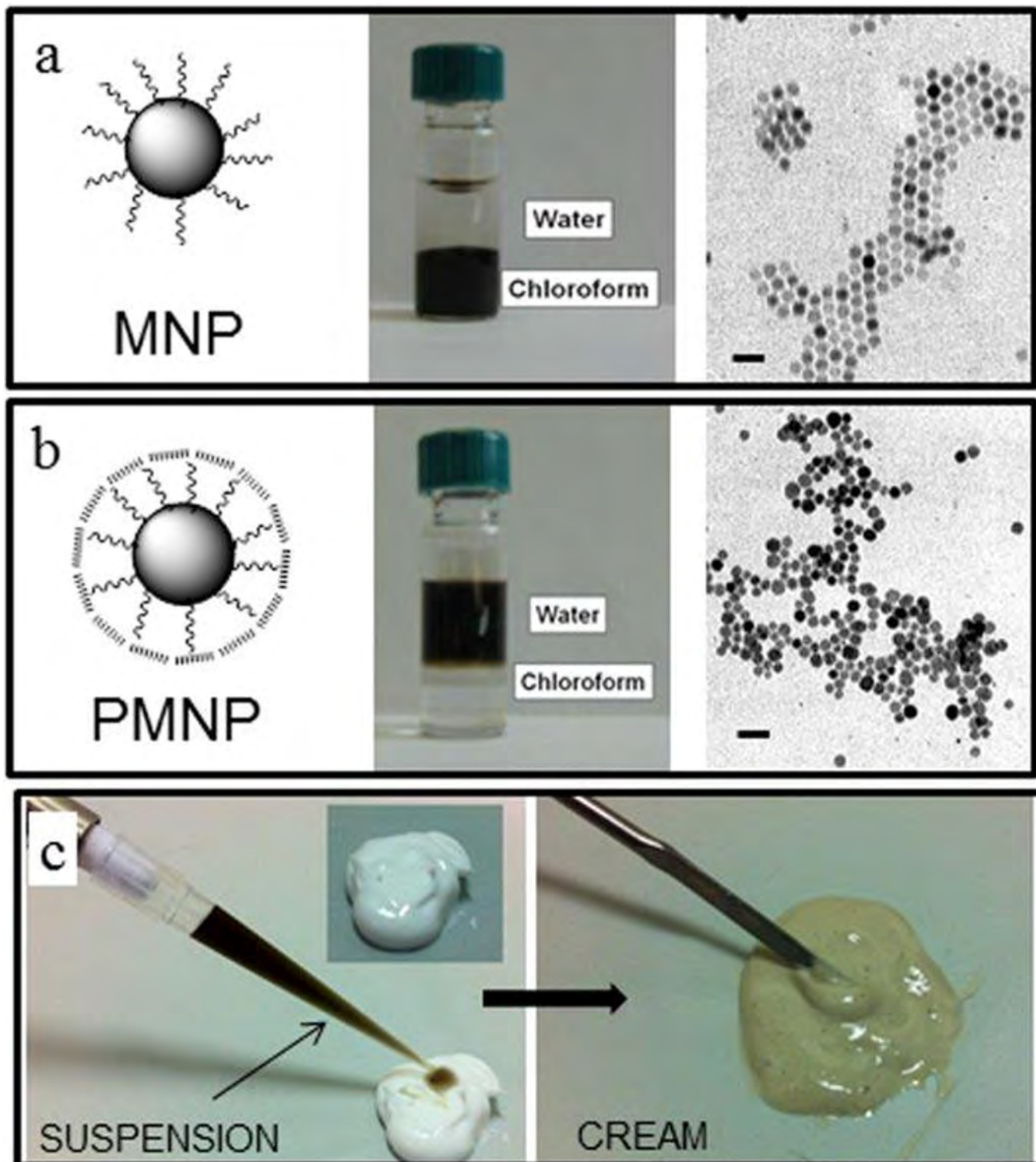


Fig 1. Fe_3O_4 nanoparticles (MNP, a) synthesized in organic solvent and transferred to a water solution using PMA amphiphilic polymer (PMNP, b). MNP and PMNP were highly monodisperse in size as it is shown by TEM images (scale bars = 40 nm.). Part of the highly concentrated PMNP suspension (8 mg mL^{-1}) was incorporated in a w/o cream (0.8 wt % concentration) (c).

doi:10.1371/journal.pone.0126366.g001

skin in FDCs. Before the penetration study, a histological analysis was performed in parallel on human skin biopsies to verify the morphological integrity of all skin layers. Histological examination of haematoxylin and eosin-stained skin sections revealed a regular histological appearance of epidermis and dermis (Fig 2A). A deep monolayer of well-preserved cubical and cylindrical cells (basal layer), an intermediate spinous layer, an upper granular layer, and outermost stratum corneum were always observed. Compact papillary and reticular dermis filled with blood vessels were also maintained.

After histological validation, nanoparticle permeation in different skin layers was analyzed by TEM and SEM. Receptor chambers were filled with PBS (5 mL) and PMNP were applied to the donor chambers. Samples of receptor fluid were taken at various time intervals (1-3-5-7-24 h) and the relevant PMNP concentrations in the receptor fluid were assessed measuring ICP-OES values normalized with values obtained by control samples. Next, nanoparticle permeation in different skin layers was analyzed by transmission and scanning electron microscopies. Fig 2B, at the end of skin exposure time (24 h), shows no significant difference between cream and suspension administration was observed in the amount of diffused nanoparticles through the human intact skin ($p > 0.05$); on the other hand, at previous sampling times (3, 5 and 7 h), the differences were significant ($p = 3.6 \times 10^{-9}$ at 3 h, $p = 4.0 \times 10^{-8}$ at 5 h, $p = 1.8 \times 10^{-6}$ at 7 h oppure $p = 3.6 \times 10^{-9}$, $p = 4.0 \times 10^{-8}$ and $p = 1.8 \times 10^{-6}$ respectively). This result can be explained by the physico-chemical properties of PMNP nanoparticles, which allowed the penetration from side to side of the skin barrier. In fact, the superficial amphiphile-like behavior of the polymer might favor the optimal permeation of both the hydrophobic and hydrophilic layers. The application of PMNP w/o cream formulation gave an accelerated and homogeneous nanoparticle permeation resulting in a reduction of the penetration and diffusion time, probably allowed by skin hydration and achieved by cream application. Moreover, the occlusive effect of the cream prevented the water evaporation and the loss of moisture promoting the nanoparticles penetration. Indeed, PMNP suspension required 24 h to equilibrate the penetration kinetics through the dermis.

Electron microscopy analysis of skin penetration

There is evidence that the major constrain for skin penetration is due to the *stratum corneum* barrier [12]. Three possible permeation routes have been identified including intracellular, intercellular, and follicular pathways. In principle, the latter should be considered the easiest way to occur for large molecules, due to the obvious preferential pathway along the follicular channels. However, in human skin, hair distribution represents only a small skin area fraction [14]. On the other hand, it is more difficult to discriminate between intracellular and intercellular routes. Fig 3 shows PMNP intradermal delivery across the intact skin layers observed by electron microscopy. Nanoparticles can be clearly distinguished in all skin layers, from the surface to deeper levels, both in cream and suspension formulations. No significant differences were detected between the two formulations in terms of permeation mechanism and amount of penetrated nanoparticles after 24 h. PMNP amphiphilic polymer coating confers nanoparticles both a hydrophobic character, useful for the penetration of waterproof corneocyte-based *stratum corneum*, and a hydrophilic propensity required for deeper viable epidermis permeation. TEM images suggest that nanoparticles penetrated mainly through intercellular pathway, as numerous nanoparticles can be distinguished across epidermis cells and through the whole skin thickness (Fig 3A–3C). However, the presence of PMNP among corneocytes provided direct evidence that the intracellular penetration pathway also occurred both in cream and in suspension (TEM images in Fig 3D and 3E). PMNP were also observed close to the basal membrane (Fig 3F). After epidermis penetration, nanoparticles reached the dermis layer,

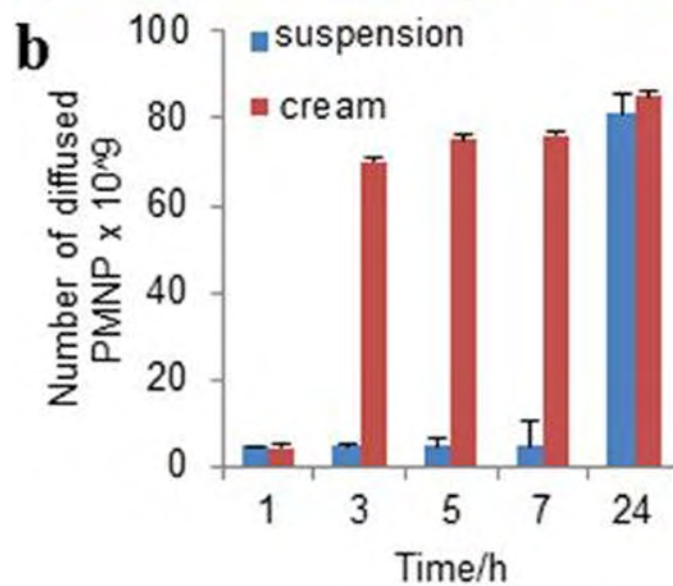
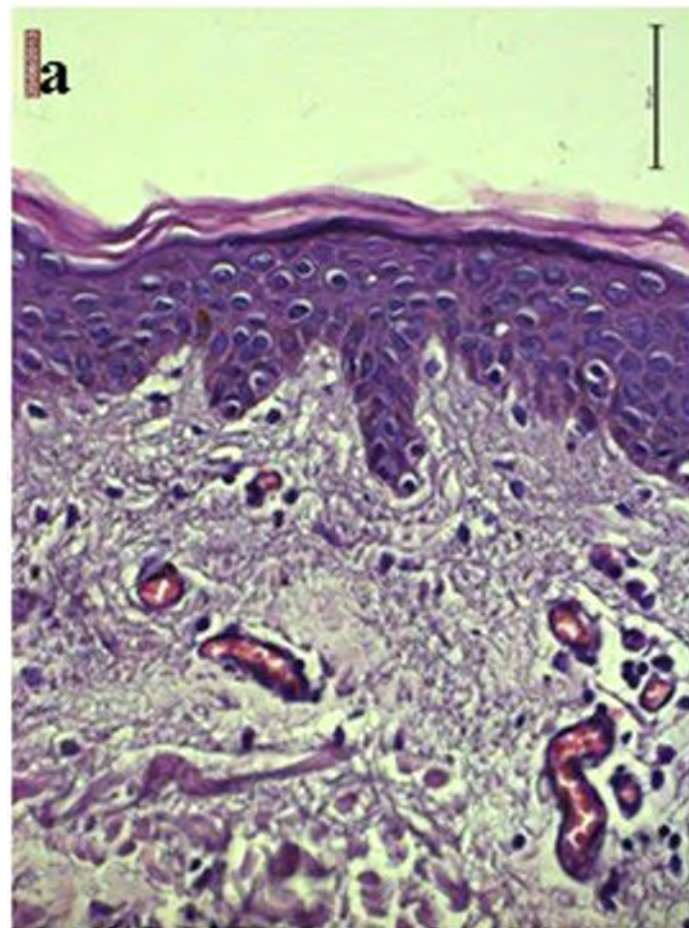


Fig 2. Histological microphotograph of normal human skin section. Haematoxylin and eosin staining (original magnification 40×) (a). *In vitro* diffusion studies of PMNP colloidal suspension or cream in human skin were carried out using Franz diffusion cells and diffused PMNP were quantified by ICP-OES analysis (b).

doi:10.1371/journal.pone.0126366.g002

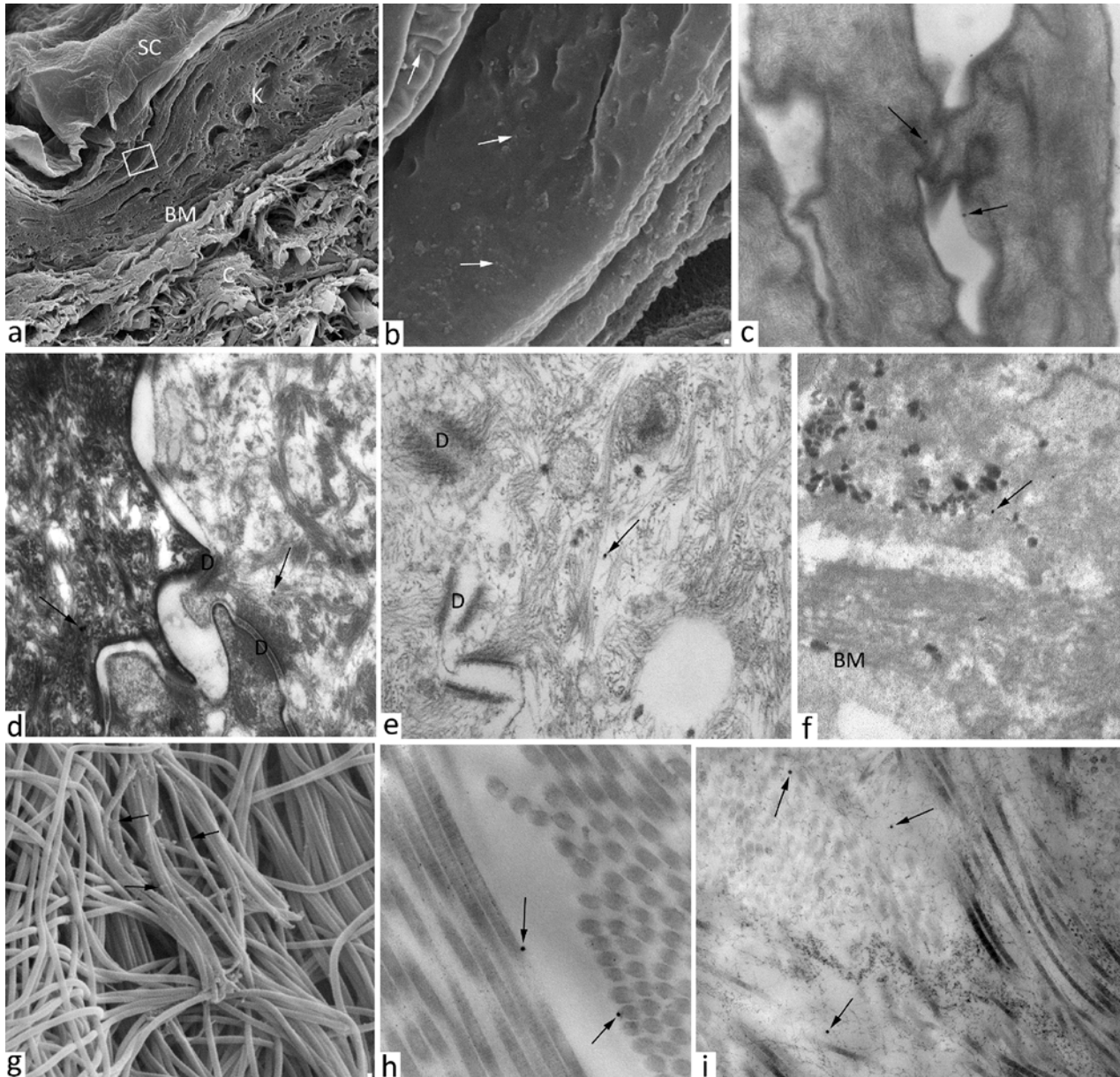


Fig 3. Images of skin samples treated with PMNPcream or suspension obtained with transmission and scanning electron microscopy. Selected micrographs show (a) SEM image of transversal skin section treated with PMNP solution for 24 h, SC = *stratum corneum*, K = keratinocytes, BM = basal membrane, C = collagen, (b) high magnification of Fig “a”, PMNP are detected on the surface of the keratinocytes (white arrows). TEM images of PMNP nanoparticles (black arrows) inside the corneocytes of the skin treated with cream (c, d) or suspension (e, f) PMNP nanoparticles in proximity of the basal membrane, D = desmosomes. (g, h) and (i) photomicrographs of PMNP nanoparticles (black arrows) intercalated between the collagen fibers of the dermis, (g) SEM image (h) and (i) TEM images.

doi:10.1371/journal.pone.0126366.g003

where they were detected in proximity to the collagen fibers (Fig 3G–3I). A large number of nanoparticles could be recovered in the dermis in higher concentration than expected from previous reports, probably due to the contribution of the amphiphilic polymer coating [20]. Another important observation was that, analyzing several dermis sections by TEM/SEM, nanoparticles maintained their individuality and did not aggregate. This result was confirmed by DLS analysis of the solution collected in the receptor chamber of the FDC, in which

nanoparticles in the 35–65 nm size range were recovered. This is consistent with the assumption that after passing through different skin layers, the biological identity of nanoparticles, including the formation of a thick protein corona, was expected to change by adsorbing various biological materials on their surface [7,24]. As control, we found the similar values measuring PMNP size after incubating them in fetal bovine serum media.

Interaction with skin-localized cells of innate immunity in living mice

Nanoparticles incorporation by cutaneous cells was evaluated in mouse models. Cream formulations of CFSE-conjugated PMNP were applied to the skin of previously shaved C57BL/6 mice (1 cm²). Mice were sacrificed 24 h later and treated skin was recovered and analyzed by flow cytometry after having obtained single cell suspensions. Draining lymph nodes were also analyzed to evaluate the possible transport of nanoparticle via the lymph. Skin cells of hematopoietic and non-hematopoietic origin were identified as CD45-positive and negative, respectively. As shown in Fig 4, both populations contained fluorescent cells, indicating that both groups of cells could incorporate PMNP nanoparticles. Since no positive staining could be observed in the draining lymph nodes (Fig 4A) interestingly, nanoparticles administered with cream formulations remained confined to the skin. It is known that sub-cutaneously (sc) inoculated substances reach the draining lymph nodes by entering the afferent lymphatics free or associated with dendritic cells [25]. In order to double check the detection of nanoparticle-positive cells in the lymph nodes, if present, we injected CFSE-conjugated PMNP sc in an aqueous suspension. As Fig 4A clearly shows, after sc administration, CFSE-positive cells could be clearly detected in the draining lymph nodes. Since macrophages and dendritic cells are the cells that preferentially uptake particulate antigens inside the lymph nodes, we also analyzed these two cell types in mice that treated with PMNP cream or PMNP in aqueous solution. In the draining lymph nodes of mice that received PMNP nanoparticle via sc administration CFSE-positive macrophages and dendritic cells could be detected starting from 2 h after treatment. On the other hand no positive cells could be detected in the lymph nodes of mice treated with PMNP cream (Fig 4B). This data suggests that cream formulations, thanks to the high lipidic concentration, permeabilize different cell types, including T and B-cells, macrophages, dendritic cells and mast cells, and non-hematopoietic cells (CD45-negative cells), and entrap the nanoparticles avoiding their dispersions. Otherwise, not being entrapped in a lipidic film, nanoparticles freely administered in aqueous suspensions have easy open access to the afferent lymphatics and to draining lymph nodes (Fig 5). These results indicate that cream formulations represent the ideal solution when a topical localized treatment is needed and different cell types have to be targeted.

Conclusions

In summary, in the present work we developed colloidal nanoparticles composed of an iron oxide nanocrystal core coated by a tightly bound amphiphilic polymer, formulated in a w/o cream able to permeate and penetrate the human skin. The same nanoparticles were also used for biological experiments in colloidal suspension as control. *In vitro* permeation analysis, carried out through intact human skin using Franz Diffusion Cell exhibited an increased, faster and more regular penetration of nanoparticles when formulated in cream in comparison to nanoparticle deposition as aqueous suspension. This makes nano-cream very promising for application in local therapies. However, probably due to the amphiphilic character of the polymer coating, nanoparticles formulated in suspension exhibited an intrinsic enhanced propensity to penetrate through the different human skin layers as well as results reported in previous literature [26]. *In vivo* treatment of living mice with these nanoparticles showed their uptake by the

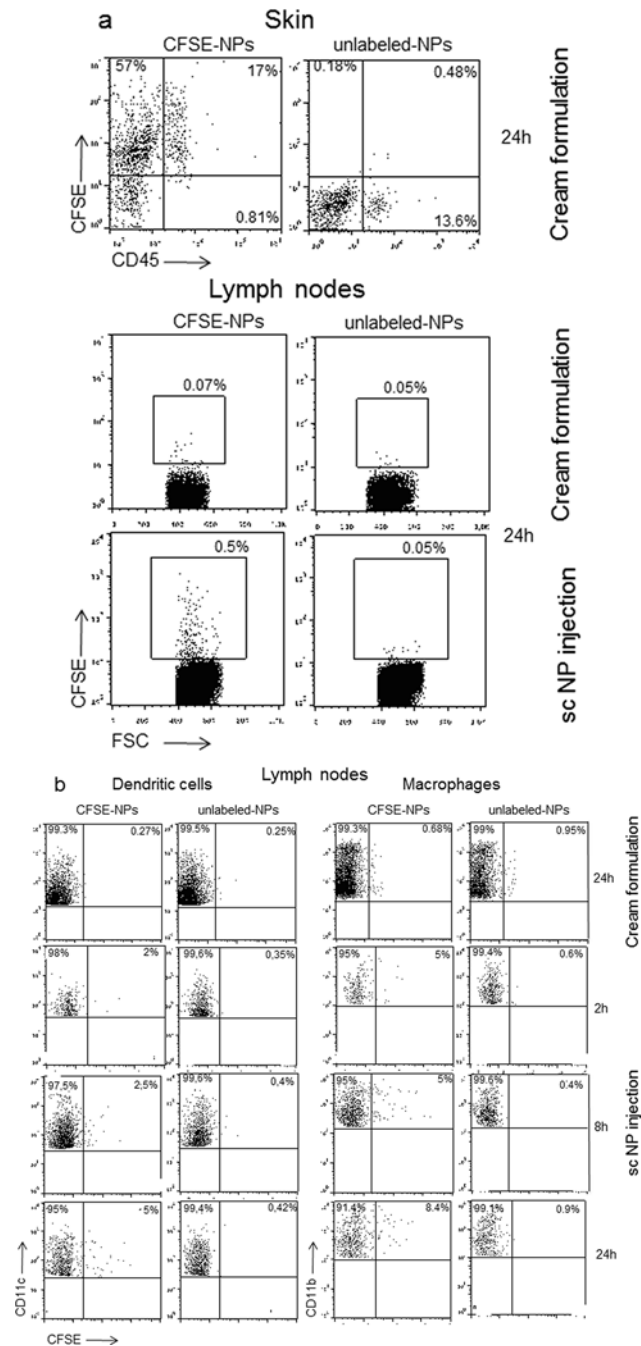


Fig 4. Cytofluorimetric analysis showing PMNP nanoparticles uptake by mouse skin and lymph node cells. PMNP suspension (a, upper panels). Skin CD45-positive and negative cells showing CFSE incorporation. Note that most of the skin cells uptake PMNP nanoparticles administered with the cream formulation. (a, lower panels) CFSE-positive cells in the lymph nodes of mice that received PMNP nanoparticles via cream formulation or via sc administration. Note that only with sc PMNP administration, nanoparticle-positive cells can be detected in the draining lymph nodes. (b) Lymph node macrophages and dendritic cells, identified as CD11b- and CD11c-positive cells respectively, showing CFSE incorporation. Note that only when PMNP are administered sc, CFSE positive macrophages and dendritic cells can be detected in the lymph nodes.

doi:10.1371/journal.pone.0126366.g004

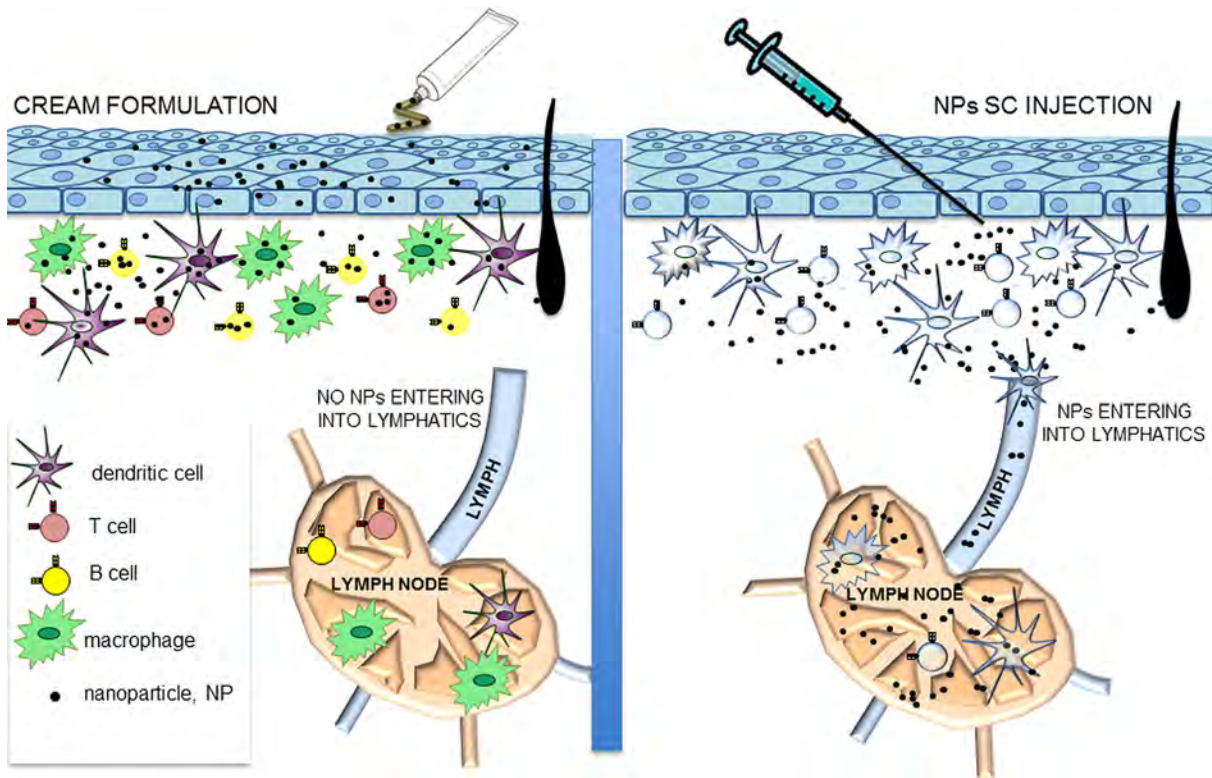


Fig 5. Fates of nanoparticles depending on the route of skin administration. Nanoparticle administered in a cream formulation are taken up by all the skin cell types and do not reach the draining lymph nodes. Nanoparticle administered with a sc injection in aqueous suspension are efficiently transported to the draining lymph nodes.

doi:10.1371/journal.pone.0126366.g005

dermal resident immune cells. In particular, when administered in the form of nano-cream suspension, nanoparticles remained confined within the thin skin layers of mice, as no migration to the draining lymph nodes could be observed. The results obtained in this study offer promise in the development of nano-cream for the rapid targeting of bioactive agents and drugs in the skin barriers. Such molecules could be encapsulated in the hydrophobic shell or covalently linked to the nanoparticle surface, supporting the topical route as a convenient alternative to the parenteral administration of anti-inflammatory and cytotoxic nanoconjugate drugs reducing systemic effect of toxic agents.

Acknowledgments

We thank R. Allevi (CMENA, University of Milano) for TEM and SEM images, M. Tringali (University of Milano-Bicocca) for ICP-OES analysis.

Author Contributions

Conceived and designed the experiments: MC F. Granucci F. Gramatica FC. Performed the experiments: BS IZ RM CC MB. Analyzed the data: MC LP MB IZ. Contributed reagents/materials/analysis tools: F. Granucci F. Gramatica. Wrote the paper: MC F. Granucci MB.

References

1. Haun JB, Devaraj NK, Hilderbrand SA, Lee H, Weissleder R. (2010) Bioorthogonal chemistry amplifies nanoparticle binding and enhances the sensitivity of cell detection. *Nat Nanotechnol* 5: 660–665. doi: [10.1038/nnano.2010.148](https://doi.org/10.1038/nnano.2010.148) PMID: [20676091](https://pubmed.ncbi.nlm.nih.gov/20676091/)
2. Prapainop K, Witter DP, Wentworth PA. (2012) Chemical approach for cell-specific targeting of nanomaterials, small molecule-initiated misfolding of nanoparticle corona proteins. *J Am Chem Soc* 134: 4100–4103. doi: [10.1021/ja300537u](https://doi.org/10.1021/ja300537u) PMID: [22339401](https://pubmed.ncbi.nlm.nih.gov/22339401/)
3. Schroeder A, Heller DA, Winslow MM, Dahlman JE, Pratt GW, Langer R, et al. (2012) Treating metastatic cancer with nanotechnology. *Nat Rev Cancer* 12: 39–50. doi: [10.1038/nrc3180](https://doi.org/10.1038/nrc3180) PMID: [22193407](https://pubmed.ncbi.nlm.nih.gov/22193407/)
4. Colombo M, Carregal-Romero S, Casula MF, Gutierrez L, Morales MP, Böhm IB, et al. (2012) Biological applications of magnetic nanoparticles. *Chem Soc Rev* 41: 4306–4334. doi: [10.1039/c2cs15337h](https://doi.org/10.1039/c2cs15337h) PMID: [22481569](https://pubmed.ncbi.nlm.nih.gov/22481569/)
5. Duncan R, Gaspar R. (2011) Nanomedicine(s) under the microscope. *Mol Pharmaceutics* 6: 2101–2141. doi: [10.1021/mp200394t](https://doi.org/10.1021/mp200394t) PMID: [21974749](https://pubmed.ncbi.nlm.nih.gov/21974749/)
6. Harisinghani MG, Barentsz J, Hahn PF, Deserno WM, Tabatabaei S, van de Kaa CH, et al. (2003) Non-invasive detection of clinically occult lymph node metastases in prostate cancer. *N Engl J Med* 348: 2491–2499. PMID: [12815134](https://pubmed.ncbi.nlm.nih.gov/12815134/)
7. Verderio P, Avvakumova S, Alessio G, Bellini M, Colombo M, Galbiati E, et al. (2014) Delivering colloidal nanoparticles to mammalian cells: a nano-bio interface perspective. *Adv Healthcare Mat* 7: 957–976.
8. Jain K, Mehra NK, Jain NK. (2014) Potentials and emerging trends in nanopharmacology. *Curr Opin Pharmacol* 15C: 97–106.
9. Avvakumova S, Colombo M, Tortora P, Prosperi D. (2014) Biotechnological approaches toward nanoparticle biofunctionalization. *Trends Biotechnol* 31: 11–20.
10. DeLouise LA. (2012) Applications of nanotechnology in dermatology. *J Invest Dermatol* 132: 964–975. doi: [10.1038/jid.2011.425](https://doi.org/10.1038/jid.2011.425) PMID: [22217738](https://pubmed.ncbi.nlm.nih.gov/22217738/)
11. Mathias NR, Hussain MA. (2010) Non-invasive systemic drug delivery: developability considerations for alternate routes of administration. *J Pharm Sci* 99: 1–20. doi: [10.1002/jps.21793](https://doi.org/10.1002/jps.21793) PMID: [19499570](https://pubmed.ncbi.nlm.nih.gov/19499570/)
12. Bolzinger MA, Briançon S, Pelletier J, Chevalier Y. (2012) Penetration of drugs through skin, a complex rate-controlling membrane. *Curr Opin Colloid Interface Sci* 17: 156–165.
13. Sonavane G, Tomoda K, Sano A, Ohshima H, Terada H, Makino K. (2008) In vitro permeation of gold nanoparticles through rat skin and rat intestine: Effect of particle size. *Colloids Surf B* 65: 1–10.
14. Labouta HI, El-Khordagui LK, Krausc T, Schneider M. (2011) Mechanism and determinants of nanoparticle penetration through human skin. *Nanoscale* 3: 4989–4999. doi: [10.1039/c1nr11109d](https://doi.org/10.1039/c1nr11109d) PMID: [22064944](https://pubmed.ncbi.nlm.nih.gov/22064944/)
15. Elias P M, Choi E H. (2005) Interactions among stratum corneum defensive functions. *Exp Dermatol* 14: 719–726. PMID: [16176279](https://pubmed.ncbi.nlm.nih.gov/16176279/)
16. Dufort S, Sancey L, Coll JL. (2012) Physico-chemical parameters that govern nanoparticles fate also dictate rules for their molecular evolution. *Adv Drug Deliv Rev* 64: 179–189. doi: [10.1016/j.addr.2011.09.009](https://doi.org/10.1016/j.addr.2011.09.009) PMID: [21983079](https://pubmed.ncbi.nlm.nih.gov/21983079/)
17. Vogt A, Combadiere B, Hadam S, Stieler KM, Lademann J, Schaefer H, et al. (2006) 40 nm, but not 750 or 1500 nm, nanoparticles enter epidermal CD1a+ cells after transcutaneous application on human skin. *J Invest Dermatol* 126: 1316–1322. PMID: [16614727](https://pubmed.ncbi.nlm.nih.gov/16614727/)
18. Desai P, Ram R, Patlolla Singh M. (2010) Interaction of nanoparticles and cell-penetrating peptides with skin for transdermal drug delivery. *Mol Membr Biol* 27: 247–259. doi: [10.3109/09687688.2010.522203](https://doi.org/10.3109/09687688.2010.522203) PMID: [21028936](https://pubmed.ncbi.nlm.nih.gov/21028936/)
19. Gratieri T, Schaefer U F, Jing L, Gao M, Kostka KH, Lopez RF, et al. (2010) Penetration of quantum dot particles through human skin. *J Biomed Nanotechnol* 6: 586–595. PMID: [21329051](https://pubmed.ncbi.nlm.nih.gov/21329051/)
20. Labouta HI, Schneider M. (2013) Interaction of inorganic nanoparticles with the skin barrier: current status and critical review. *Nanomedicine* 9: 39–54. doi: [10.1016/j.nano.2012.04.004](https://doi.org/10.1016/j.nano.2012.04.004) PMID: [22542824](https://pubmed.ncbi.nlm.nih.gov/22542824/)
21. Klein K. (2003) Formulating water-in-oil emulsions: a scary endeavor. *Cosmet Toiletries* 118: 24–25.
22. Park J, An K, Hwang Y, Park JG, Noh HJ, Kim JY, et al. (2004) Ultra-large-scale syntheses of monodisperse nanocrystals. *Nat Mat* 3: 891–895.
23. Pellegrino T, Manna L, Kudera S, Liedl T, Koktysh D, Rogach AL, et al. (2004) Hydrophobic nanocrystals coated with an amphiphilic polymer shell: A general route to water soluble nanocrystals. *Nano Lett* 4: 703–707.

24. Rosenblum MD, Gratz IK, Paw JS. (2011) Response to self antigen imprints regulatory memory in tissues. *Nature* 480: 538–542. doi: [10.1038/nature10664](https://doi.org/10.1038/nature10664) PMID: [22121024](https://pubmed.ncbi.nlm.nih.gov/22121024/)
25. Zanoni I, Ostuni R, Barresi S, Di Gioia M, Broggi A, Costa B, et al. (2012) CD14 and NFAT mediate lipopolysaccharide-induced skin edema formation in mice. *J Clin Invest* 122: 1747–1757. doi: [10.1172/JCI60688](https://doi.org/10.1172/JCI60688) PMID: [22466648](https://pubmed.ncbi.nlm.nih.gov/22466648/)
26. Baroli B (2010) Penetration of metallic nanoparticles in human full-thickness skin: fiction or reality? *J Invest Dermatol* 127: 1701–1712.

RESEARCH

Open Access



Impact of semi-solid formulations on skin penetration of iron oxide nanoparticles

Umberto M. Musazzi^{1†}, Benedetta Santini^{2†}, Francesca Selmin¹, Valentina Marini¹, Fabio Corsi³, Raffaele Allevi³, Anna M. Ferretti⁴, Davide Prosperi², Francesco Cilurzo¹, Miriam Colombo^{2*} and Paola Minghetti^{1*}

Abstract

Background: This work aimed to provide useful information on the incidence of the choice of formulation in semi-solid preparations of iron-oxide nanoparticles (IONs). The appropriate analytical methods to assess the IONs physical stability and the effect of the semi-solid preparations on IONs human skin penetration were discussed. The physical stability of IONs ($D_h = 31 \pm 4$ nm; $\zeta = -65 \pm 5$ mV) loaded in five semi-solid preparations (0.3% w/v), namely Carbopol gel (CP), hydroxyethyl cellulose gel (HEC), carboxymethylcellulose gel (CMC), cetomacrogol cream (Cet) and cold cream was assessed by combining DLS and low-field pulsed NMR data. The in vitro penetration of IONs was studied using human epidermis or isolated stratum corneum (SC).

Results: Reversible and irreversible IONs aggregates were evidenced only in HEC and CMC, respectively. IONs diffused massively through SC preferentially by an intercellular pathway, as assessed by transmission electron microscopy. The semi-solid preparations differently influenced the IONs penetration as compared to the aqueous suspension. Cet cream allowed the highest permeation and the lowest retained amount, while cold cream and CP favored the accumulation into the skin membrane.

Conclusion: Basic cutaneous semi-solid preparations could be used to administer IONs without affecting their permeation profile if they maintained their physical stability over time. This property is better discriminated by low-field pulsed NMR measurements than the commonly used DLS measurements.

Keywords: Iron oxide nanoparticles, Polymer coating, Semi-solid preparation, Skin penetration, Nanoparticle stability

Background

Skin is one of the focuses for research in drug delivery with many drugs being evaluated for transdermal or dermal administration. However, penetration and retention of drugs into the epidermis is not a simple task. Indeed, the outermost layer of the skin, the stratum corneum (SC), is a barrier both to water transport out of the body and to inward chemical permeation. In addition to the physical barriers, the clearance of capillaries in the dermis and the cutaneous metabolism via local phase I and

phase II metabolic enzymes can also reduce the local bio-availability of drugs [1]. Among the possible approaches to overcome these issues, nanocarriers represent a new opportunity to improve the treatment of loco-regional diseases. For instance, nanoparticle dispersions (e.g., vesicles) have been applied to transcutaneous delivery of drugs, with some of them being commercialized and many more under clinical assessment [2].

Metal-based nanoparticles provide new perspectives on particle absorption into/through the skin, since their particle size and shape could be tailored to favor the penetration of SC via the intercellular route [3–5]. Nevertheless, most of the studies hinge on the potential toxicity effect of the nanoparticles through the skin and the mechanism related to the interaction between nanoparticles and skin layers [6, 7]. Multifunctional colloidal nanoparticles have been designed to improve the delivery

*Correspondence: miriam.colombo@unimib.it; paola.minghetti@unimi.it

[†]Umberto M. Musazzi and Benedetta Santini contributed equally to this work

¹ Department of Pharmaceutical Sciences, Università degli Studi di Milano, via G. Colombo, 71, 20133 Milan, Italy

² Department of Biotechnology and Biosciences, Università degli Studi di Milano-Bicocca, Piazza della Scienza, 2, 20126 Milan, Italy

Full list of author information is available at the end of the article

of conventional drugs, peptides, vaccines or genes across biological barriers, including blood brain barrier, dermal, transdermal and intraocular delivery [8]. Among the plethora of metal-based colloidal nanoparticles, the use of iron oxide nanoparticles (IONs) appears of particular interest since they have been already used in several medical areas, including therapeutics and diagnostics, and, therefore, their safety profiles are already known [9, 10]. *In vitro* transdermal studies demonstrated that the IONs bearing antitumor drugs were able to penetrate the skin assisted by an applied magnetic field, suggesting a potential of IONs as drug delivery system for transdermal therapy of skin cancer [11].

However, the actual broad applicability of IONs in the clinical practice remains controversial due to contradictory evidence on potential toxicity of colloidal nanoparticles. Recent studies suggested that appropriate surface coating with “bio-friendly” materials might improve the nanoparticle stability in biological environment, reducing the oxidative stress mediated toxicological effects as well as immune and carcinogenic effects and preserving the physiological processes [12, 13].

Intravenous administration of colloidal nanoparticles is still matter of debate. Intravenous and oral administrations of IONs formulations have been approved for clinical use by the Food and Drug Administration (FDA) [14]. However, most intravenously administered compounds approved by FDA have been withdrawn from the marketplace [15], with the exception of some therapeutics indicated for the treatment of iron deficiency anemia in adults [16]. IONs for oral administration remain on the market for use as an oral gastrointestinal contrast agent in MR imaging (i.e., *Gastromark*[®] and *Ferumoxsil*-containing products) [17]. For these reasons, the skin penetration of IONs has been gaining increasing interest in nanomedicine [9, 18, 19]. It has been suggested that IONs with a diameter smaller than 40 nm were able to penetrate the intercellular space among keratinocytes of the SC [18] and 10 nm-IONs were able to penetrate the human epidermis (HE), without reaching the dermal layer [20]. In addition, the IONs polymer coating, which is required to obtain a colloidal solution stable both in water and in physiologic media, should be carefully selected since an isoelectric point similar to that of human skin would favor the formation of IONs clusters at the skin interface, preventing their permeation [20].

In a preliminary study, IONs coated by a poly-(isobutylene-alt-maleic anhydride) (PMA-IONs) were demonstrated to accumulate in *ex vivo* full-thickness human skin and in mice skin after topical application *in vivo* [21]. However, physicochemical attributes, such as size, surface charge, surface chemistry, and physical state of the nanoparticles are not the only critical

determinants for their skin permeation. Indeed, the diffusion performance relies also on the physicochemical properties and composition of the semi-solid formulation required to obtain a suitable cutaneous product. Such a vehicle includes other excipients to afford the lubricity and spreading properties, the desired residence time on skin and the patient compliance. Although the stability of IONs, or more in general of nanoparticles, in the vehicle has been one of the major critical factors that could affect the effectiveness of their topical administration, very few data were reported in literature. In particular, no systematic studies have been carried out to investigate the influence of semi-solid formulations on the physicochemical features of IONs and on their permeability across the human skin. Therefore, to rationalize the selection of a suitable vehicle for PMA-IONs administration, this work aimed to investigate the impact of semi-solid formulations (i.e., hydrogels and o/w creams) on the physical stability of nanoparticles and on the *in vitro* penetration through HE.

Results

Formulation study of PMA-IONs semi-solid preparations

The protocol adopted for the production of PMA-IONs allowed to obtain monodisperse nanoparticles with a strongly negative surface charge (Fig. 1; Table 1). PMA-IONs were loaded in three hydrogels, made of hydroxyethyl cellulose (HEC), sodium carboxymethyl cellulose (CMC) and carbomer 974P (CP), and two hydrophilic creams, namely a cetomacrogol (Cet) cream and a cold cream.

The physical stability of PMA-IONs loaded into the semi-solid formulations was determined according to two different methods, namely low-field pulsed NMR and dynamic light scattering (DLS), using the physicochemical features of the aqueous suspension as reference. The former technique was selected because it could provide direct characterization of the semi-solid preparation, while the latter allowed to assess the possible formation of nanoparticle aggregates or change in size.

Low-field pulsed NMR analysis provided information on the magnetic properties of nanoparticles, which are influenced by deviation in structure, surface composition, concentration and mobility. Hence, the measurement of the r_2 value of PMA-IONs was a sensitive parameter to characterize changes in the nanoparticles mobility in different media because its variation suggested the formation of interactions among the formulation components. As expected, the r_2 value of the nanoparticles suspension in aqueous solution did not significantly change within 50 days of storage at 25 ± 2 °C, confirming the stability of PMA-IONs in water. A similar trend was evident analyzing nanoparticles dispersed in both o/w cream

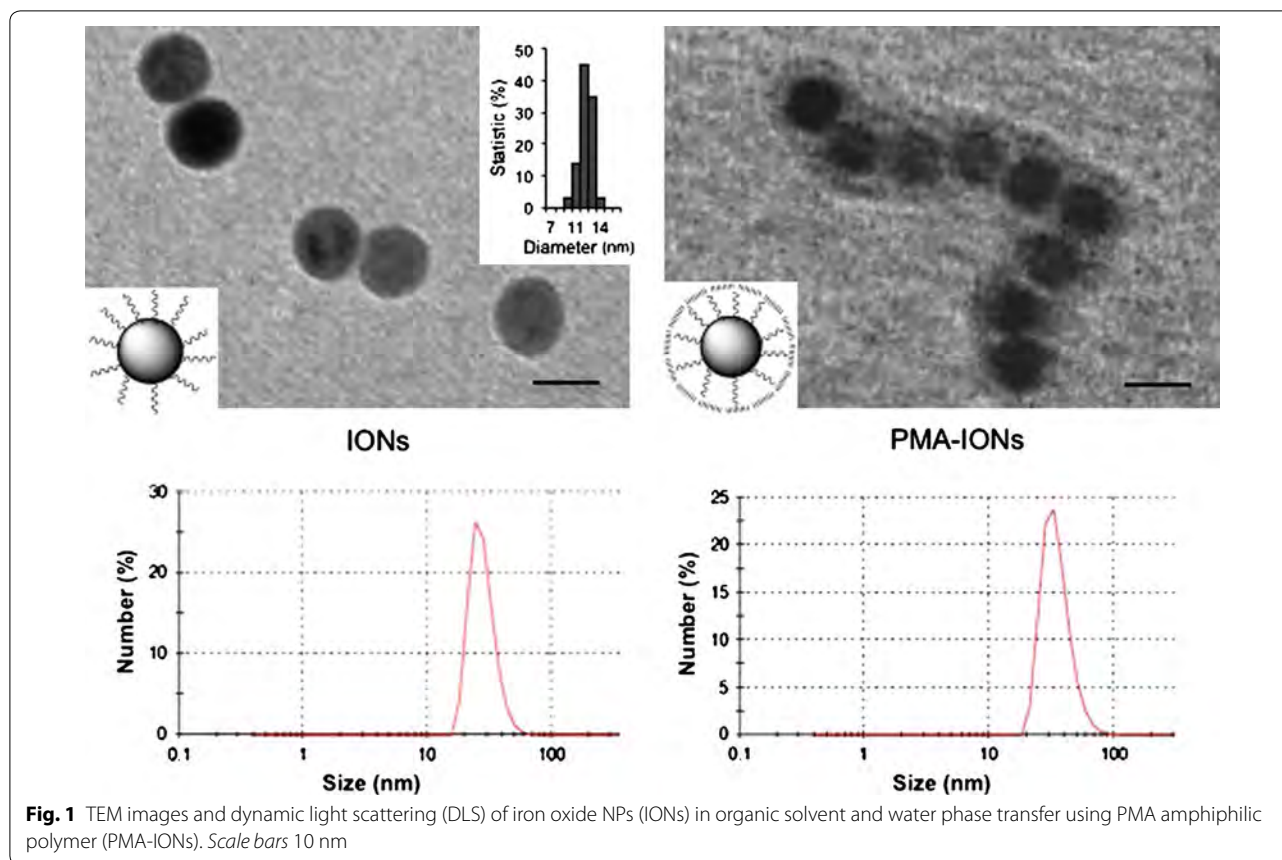


Table 1 Physical characterisation of PMA-IONs and PMA-IONs-loaded hydrogels (mean \pm SD, n = 3)

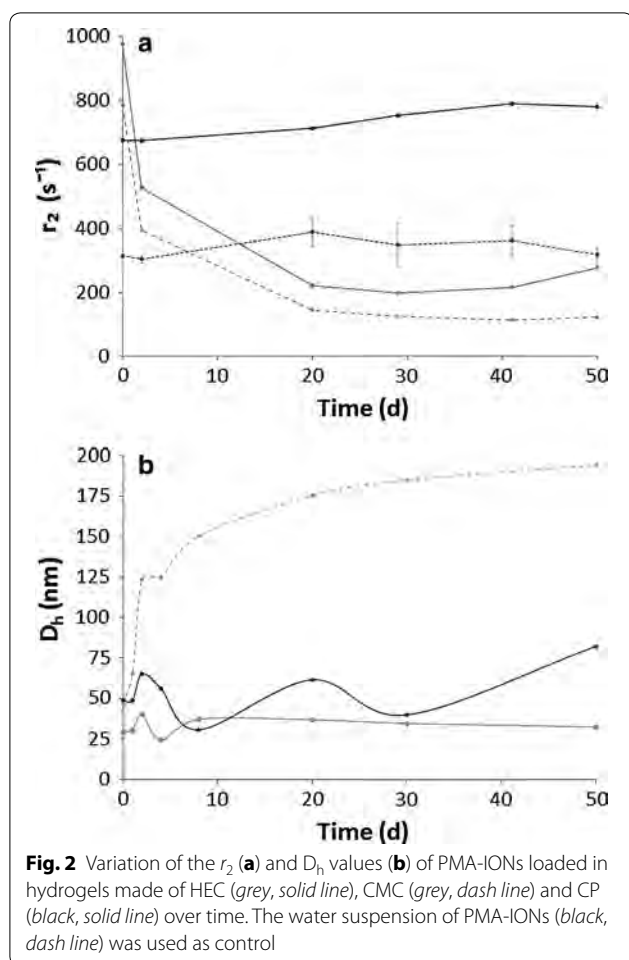
Formulation	D _h (nm)	PDI	ξ (mV)	pH
PMA-IONs	31 \pm 4	0.15 \pm 0.04	-64.80 \pm 4.91	7.0
HEC	29 \pm 15	0.44 \pm 0.05	-42.17 \pm 1.68	5.0
CMC	47 \pm 7	0.54 \pm 0.03	-79.77 \pm 2.00	6.5
CP	52 \pm 4	0.29 \pm 0.04	-72.83 \pm 5.25	6.0

HEC hydroxyethyl cellulose, CMC sodium carboxymethyl cellulose, CP carbomer 974P

compositions (Additional file 1). Consequently, it might be assumed that neither aggregation nor alteration in size of iron oxide core occurred within this time window, as well as no modification of surface coating was detected over the time. The same trend was measured in the CP hydrogel. Conversely, in the case of HEC or CMC hydrogels, a sharp decrease of r_2 values was noticed after one day of storage (Fig. 2a; Additional file 1). In particular, r_2 value of CMC decreased due to PMA-IONs aggregation followed by a precipitation that became visually noticeable after 30 days.

Unlike low-field pulsed NMR technique, DLS measurements could not be performed directly on the semi-solid

vehicles, but a prior sample dilution was required. Preliminarily, placebo hydrogels and o/w creams were analyzed by DLS to evaluate possible interferences. Adapting the protocol of sample preparation, DLS technique could be used only for analyzing hydrogels. On the contrary, it could not be exploited to verify the physical state of PMA-IONs incorporated into o/w creams because the dispersed oily phase and the formulation viscosity did not allow to obtain reproducible results, despite the dilution. As depicted in Fig. 2b, the DLS trends found for CMC and CP were almost superimposable during storage at 25 °C: PMA-IONs loaded in CMC hydrogel confirmed to be unstable, whereas the CP hydrogel appeared physically stable using both techniques. Contradictory results were found in the case HEC. Even if the low-field pulsed NMR evidenced instability of PMA-IONs in HEC hydrogel, no aggregates were noticed by DLS technique. These different patterns might be explained considering that the cellulose chains were able to promote the formation of reversible aggregates of PMA-IONs, which were not detectable by DLS due to the sample dilution. The formation of such reversible aggregates might be also in agreement with the very significant reduction of the absolute ξ values (Table 1), which did not undergo to significant



variations over the considered time period (Additional file 1).

Increasing the storage temperature at 40 °C, the trends in DLS data were confirmed, although in case of IONs loaded in CMC hydrogel physical instability was observed after 4 days of storage (Additional file 1).

Due to the physical instability of PMA-IONs loaded in the CMC hydrogel, such vehicle was not considered worthy for further investigations.

In vitro permeation studies

Transmission electron microscope (TEM) images showed the presence of nanoparticles both into the upper HE layers and near to the basal membrane of epidermis (Fig. 3). Indeed, after 24 h, PMA-IONs were found on the surface and close to the corneocytes, into the epidermis and near the basal membrane (Fig. 3). Figure 3F showed nanoparticles into a cell of the stratum lucidum inside the cytoplasm, while Fig. 3C showed nanoparticles close to desmosomes. Thus, even though PMA-IONs were present in the extracellular matrix, they showed also affinity for the proteins of the intercellular junctions.

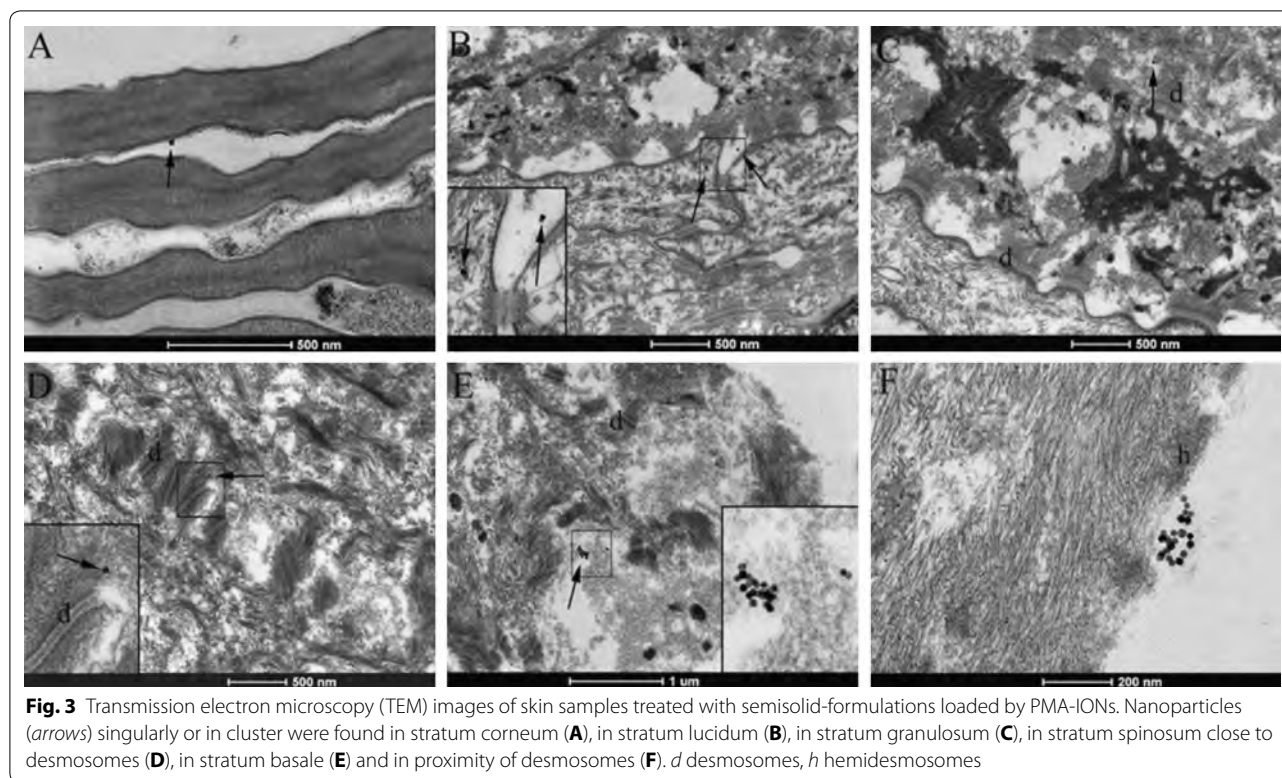
In order to identify correctly the nature of that nanoparticles revealed by the conventional TEM in the HE sample, the STEM/EDX analysis was also carried out [22]. The STEM images were collected in different sections of the same sample previously analyzed by conventional TEM. Also STEM showed images with high degree of details. In particular, STEM micrographs show nanostructures close to the stratum corneum brighter than the other elements. These white regular spots are indicated by the white squares 1 and 2 in Fig. 4 and another brighter area (Additional file 1). The higher brilliance of these elements suggests that they are more electron dense and heavy than the other parts of the sample, without providing information on their chemical composition. So, the EDX analysis was performed on these white spots pointing the electron beam directly on them to determine their elemental composition. The spectra reported on the right side of STEM micrographs evidenced the presence of the iron signals only in squares 1 and 2 of Fig. 4, confirming that the nanoparticles are IONs. The EDX spectra revealed also the presence of a weak C-signal and a strong Cu-signal, which was attributed to the epidermis and TEM grid used to support the analyzed section, respectively.

This result was in agreement with the in vitro permeation study. Indeed, after 24 h, the retained amounts of PMA-IONs in SC and VE, normalized by the weight of the epidermal layers, were 234 ± 101 and 308 ± 101 ng/mg, respectively (Table 2).

In addition, the iron amount permeated through HE after exposure to PMA-IONs for 24 h ($p < 0.01$) was doubled with respect to the pre-exposure HE, which was reported to contain traces of iron (Table 2) related to the intense mitotic activity of VE [23]. This finding suggested that PMA-IONs were able to permeate the SC barrier and to concentrate into the VE.

Membranes based on regenerated keratins (RKM) [24] were used to model the tendency of nanoparticles to diffuse through intracellular pathway of SC, because the lower the permeation through RKM, the higher the affinity of nanoparticles for the intracellular compartment of SC. The results showed that $Q_{24,RKM}$ ($6.4 \pm 0.1 \mu\text{g}/\text{cm}^2$) was in accordance with the $Q_{24,HE}$ values (Table 2).

On the other side, the $Q_{ret,RKM}$ ($28 \pm 5 \text{ ng}/\text{mg}$) was significantly lower than the value obtained through SC (p value: 0.024). Hence, it may be assumed that weak interactions occurred between PMA-IONs and keratins and that PMA-IONs diffused preferentially through an intercellular pathway [25]. This hypothesis was also in agreement with the TEM microphotographs evidencing the presence of nanoparticles only in the interstitial spaces among keratinocytes (Fig. 3).



The components of the four semi-solid vehicles differently influenced the skin penetration of PMA-IONS. With the exception of the HEC hydrogel, all formulations significantly increased the permeated amount after 24 h, while only CP hydrogel and cold cream were able to increase also the amount of PMA-IONS retained into the HE (Table 2). Although the $Q_{ret}/Q_{24,HE}$ ratio of all the tested semi-solid formulations were similar to that of aqueous suspension (i.e., about 0.67), the permeated iron amount from the Cet cream was one order of magnitude higher than the relative retention data ($Q_{ret}/Q_{24,HE}$: 0.19), suggesting a higher tendency of PMA-IONS to permeate than to be retained into the HE when they were loaded in the Cet cream.

Discussion

The permeation of nanoparticles through human skin is still matter of debate. Indeed, scientific evidence suggested that only those nanoparticles with size below the 6–7 nm limit were able to permeate the healthy skin through the lipidic trans-epidermal, whereas nanomaterials larger than 36 nm could be preferentially absorbed by the aqueous pores or trans-follicular routes [18].

PMA-IONS proposed in the current work exhibited a significant penetration through the human epidermis. Indeed, both TEM microscopy and permeation studies supported the evidence that PMA-IONS permeate

significantly through the SC and accumulated into the VE. This behavior resulted dissimilar from that described for two types of 10 nm-IONS stabilized with a different coating [20]. In both cases, the nanosystems permeated the SC without reaching the VE in a massive amount. Hypothesizing that PMA-IONS permeate human skin following the same concentration-gradient mechanism of smaller chemical molecules, such incongruities may be explained on the basis of the differences in the experimental protocols, e.g. the type of membrane model. The experimental results of PMA-IONS were performed using HE, whereas full-thickness human skin has been used as membrane model by Baroli and co-authors. As discussed by Cross and Roberts, HE can model an in vivo “infinite dermal perfusion”, where the penetrated solute is fully removed from below the epidermal-dermal junction [26]. On the contrary, no clearance of solute from the dermis is expected using full thickness skin, suggesting that such membrane can be a model of in vivo “infinite dermal vasoconstriction”. In this context, the permeation profile of PMA-IONS may be increased by using an “infinite dermal perfusion” model with respect to other models of cutaneous barrier.

Besides such differences in the experimental protocols, the incongruities between experimental and published results may be also explained by a different tendency to distribute and diffuse through SC due to the different

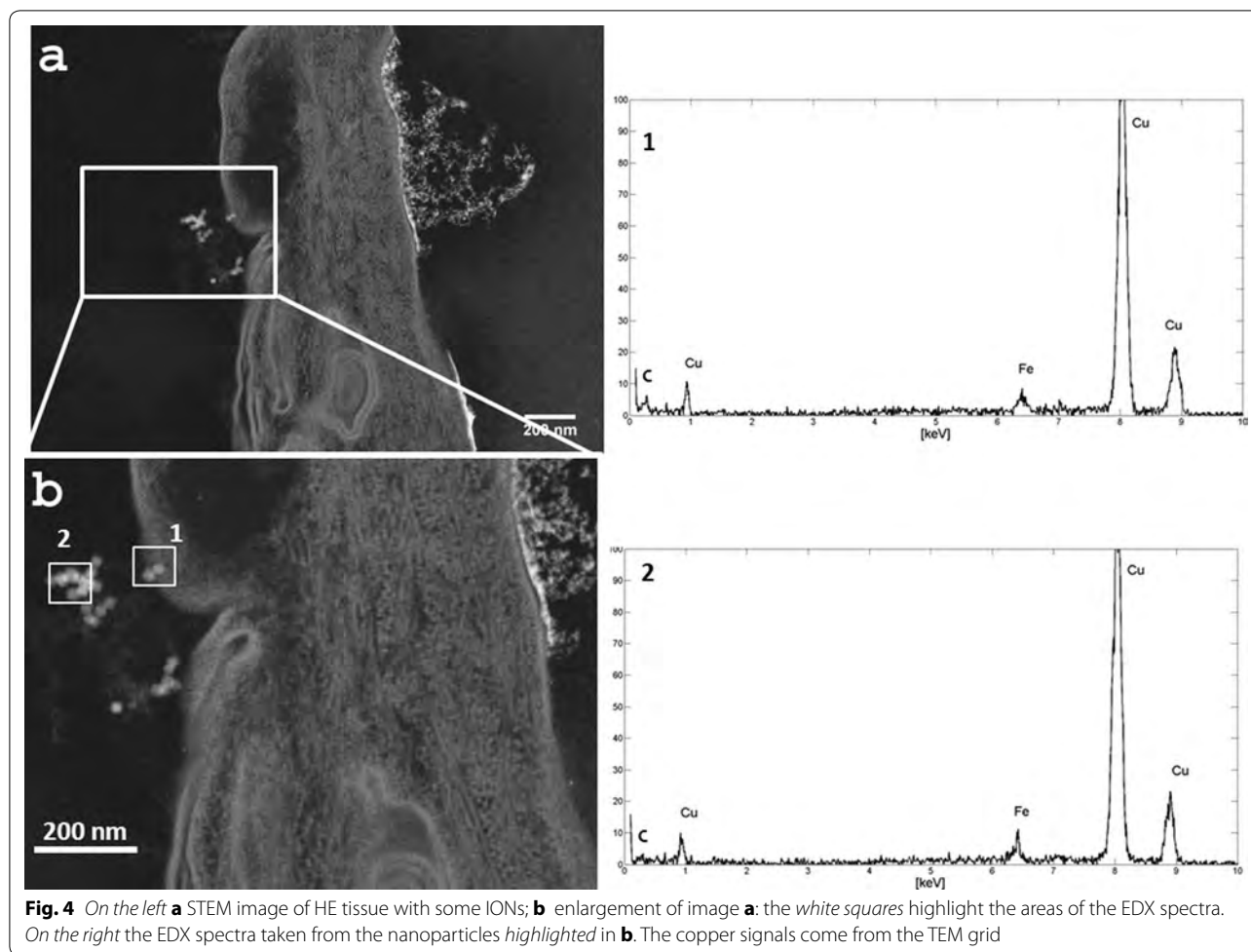


Table 2 Results of permeation (Q_{24}) and retention (Q_{ret}) studies of aqueous suspensions and semisolid preparations containing 3 mg/mL of PMA-IONs

Formulation	Q_{ret}		Q_{24}		$Q_{ret}/Q_{24,HE}$
	A ($\mu\text{g}/\text{cm}^2$)	N	A ($\mu\text{g}/\text{cm}^2$)	N	
Water suspension	2.91 ± 1.04	1.98 ± 0.70	4.35 ± 0.74	2.30 ± 0.14	0.67
HEC hydrogel	1.73 ± 0.34	1.18 ± 0.23	3.48 ± 0.30	1.84 ± 0.16	0.50
CP hydrogel	4.70 ± 0.25	3.19 ± 0.17	7.22 ± 2.40	3.83 ± 1.27	0.65
Cet cream	1.98 ± 0.57	1.34 ± 0.39	10.51 ± 2.46	5.57 ± 1.30	0.19
Cold cream	5.30 ± 0.74	3.60 ± 0.50	8.05 ± 4.50	4.26 ± 2.39	0.66
Blank	1.47 ± 0.08	1.00 ± 0.05	1.89 ± 0.26	1.00 ± 0.14	–

The data were reported as absolute values (A) or as normalize values with respect to blank (N) (mean \pm SD; n = 3)

HEC hydroxyethyl cellulose, CMC sodium carboxymethyl cellulose, CP carbomer 974P, Cet cetomacrogol

coating of IONs. The coated-IONs investigated by Baroli and co-authors were only stabilized in water by electrostatic interactions with sodium bis-(2-ethylhexyl) sulfosuccinate or tetramethylammonium hydroxide, whereas the use of PMA provided several advantages. Indeed, the amphiphilic property of PMA allowed to improve the

colloidal stability of nanoparticles at physiological pH and their surface functionalization taking advantage of the presence of activated carboxylic groups on the surface. Another important advantage of the amphiphilic coating was that it could improve the IONs incorporation into a semi-solid formulation, their permeation through

hydrophobic/hydrophilic biological environment and their penetration of SC by increasing their affinity for keratin or lipids present in the SC.

To make the topical administration of nanosystems clinically acceptable, they should be incorporated in semi-solid preparations, namely complex vehicles that potentially could affect their permeation performances. Exception made for HEC, the results demonstrated that all the tested semi-solid vehicles improved PMA-IONS penetration through HE (Table 2). It is worth mentioning the behavior of the Cet cream, which determined the highest permeation of PMA-IONS through HE and, at the same time, the lowest retained amount. These findings might suggest that the larger amount of surfactants used in its preparation, with respect to other tested formulations, influenced the affinity of PMA-IONS for HE, enhancing their permeation. Such evidence was also in agreement with previous published data obtained *in vivo* using a semi-solid base with a very similar composition [21]. Furthermore, the *in vitro* penetration results stressed how critical was the physical stability of nanoparticles in the semi-solid matrix for permeating through the skin. Indeed, the permeation of PMA-IONS loaded in HEC was significantly reduced in comparison to other formulations (Table 2). According to the r_2 values, PMA-IONS loaded in both HEC and CMC hydrogel changed their physical state within one week after preparation. Although such changes of their superficial properties were reversible (i.e., adsorption or weak interactions), both polymers caused a reduction of PMA-IONS penetration through human epidermis. Therefore, the selection of a suitable semi-solid vehicle for the nanosystems should be rationalized on the basis of their physical stability at short and long term. The modifications of the physical properties of PMA-IONS loaded in hydrogels and *o/w* creams were dependent on the formulation features. Thus, the application of a universal methodology to assess the physical stability of these systems could not be considered.

Our results demonstrated that DLS, which is routinely used for the characterization of liquid suspensions, was not the technique of election for semi-solid formulations since the physical status of nanoparticles could be affected by the necessary dilution of the sample. Moreover, DLS was not able to discriminate among particles deriving from the excipients used for the formulation and to be applied to opaque products such as creams due to the signal interferences of the large droplets of the dispersed phase, even if it was used in backscattering mode. To overcome this issue, low-field pulsed NMR, which exploits the magnetic properties of the superparamagnetic core of PMA-IONS, was conveniently proposed as an alternative to directly evidence changes of PMA-IONS

dispersed in semi-solid matrices. By the comparison of the two analytical techniques, a wider versatility of low-field pulsed NMR was clearly evidenced since it allowed the direct determination of the physical stability of paramagnetic nanoparticles in opaque vehicles and it did not require any sample dilution. Furthermore, the former technique was more sensitive since it was able to highlight also changes of PMA-IONS physical state that could affect their inability to penetrate the skin (e.g., HEC). As a matter of fact, the reduction of r_2 values in the HEC hydrogel provided a fast evidence of the instability of PMA-IONS, which was in agreement with the permeation data profile.

Conclusions

The current results support the use of superparamagnetic nanoparticles coated with PMA as a technological platform for drug delivery to human epidermis after topical administration. The loading of PMA-IONS in semi-solid vehicles did not affect their permeation profile only if they maintained their stability over time.

Considering that the physical state of PMA-IONS in semi-solid preparations was the most critical attribute for *in vitro* permeation performances, the selection of appropriate analytical methods was underlined. In particular, the overall results demonstrated that low-field pulsed NMR allowed to better discriminate the physical stability of superparamagnetic nanosystems in comparison to the conventionally utilized DLS measurements, due to the higher versatility and sensitivity. However, only these techniques provided a deeper insight into a very complex system, allowing to discriminate between irreversible and reversible changes in the physical states of paramagnetic nanosystems. All the tested semi-solid formulations influenced the PMA-IONS penetration through HE; the Cet cream allowed the highest permeation and the lowest retained amount while cold creams and CP hydrogels favored the nanoparticle accumulation into the skin membrane. These results suggest that these two very basic formulations are suitable to be conveniently used to administer PMA-IONS topically in order to improve the efficiency of colloidal nanoparticles in penetrating the skin layers.

Methods

Preparation of polymer coated superparamagnetic iron-oxide nanoparticles

PMA-IONS were prepared following previously reported procedures [27–29]. Briefly, iron oxide nanoparticles were synthesized by solvothermal decomposition at high temperature in octadecene from iron oleate precursor resulting in iron oxide core dispersed in chloroform with an average diameter of 12.21 ± 0.8 nm (i.e., IONs).

Afterward, 4 mg (0.43 nmols, determined by ICP measurements) of IONs were transferred to water phase by mixing with 136 μL of 0.5 M solution of an amphiphilic polymer [poly-(isobutylene-alt-1-tetradecenemaleic anhydride)], corresponding to 100 monomers. After evaporation under vacuum, 5 mL of pH 12 sodium borate buffer were added to the dried mixture to suspend the nanoparticles (i.e., PMA-IONs). PMA-IONs were twice washed in water. PMA-IONs were purified by electrophoresis gels as described elsewhere [30] and re-suspended in water at a final concentration of 3 mg/mL.

Preparation of topical semi-solid dosage forms containing PMA-IONs

All the semi-solid formulations were prepared with decreased water content, which was subsequently replaced by the aqueous nanoparticles dispersion at the PMA-IONs at 0.6% w/v concentration after the production. The final loading was fixed at 0.3% w/v. Briefly:

- Hydroxyethyl cellulose (HEC) hydrogel: 2.5% w/w HEC previously wet by 10% w/w glycerol was dispersed in distilled water heated at about 40 °C under magnetic stirring.
- Sodium carboxymethyl cellulose (CMC) hydrogel: 5% w/w CMC previously wet by 10% w/w glycerol was dispersed in distilled water heated at about 60 °C under magnetic stirring.
- Carboxypolymethylene (Carbomer 974P, CP) hydrogel: 0.8% w/w was dispersed in distilled water by a magnetic bar. Then, sodium EDTA and propylene glycol was added. Then, the mixture was neutralized by drop wise addition of a 10% w/v sodium hydroxide solution until the gel formation occurred. Amount of sodium hydroxide was adjusted to pH 7.
- Cetomacrogol (Cet) cream was prepared by heating both the oily (i.e., cetomacrogol 1000, cetostearyl alcohol, liquid paraffin and petrolatum) and aqueous phase at the temperature of about 60 °C. Afterwards, the aqueous phase was added to the oily phase under constant stirring.
- Cold cream was prepared by mixing 4% w/w Sepineo P600, 10% w/w almond oil and water.

In all cases, 0.025% w/v methyl-paraben and 0.075% w/v propyl-paraben were added to water in order to preserve form bacteria and mold contamination.

Storage stability of PMA-IONs loaded hydrogels and creams

PMA-IONs loaded hydrogels and creams were stored at 25 ± 3 and 40 ± 2 °C over a 2-month period. At pre-determined data points, the formulations were visually

inspected to evidence aggregate formations. The hydrodynamic diameter, zeta-potential and MRI relaxivity were also measured by DLS.

Morphology of IONs

The morphology of IONs was detected by TEM analysis, 50 $\mu\text{g}/\text{mL}$ of IONs were dispersed in hexane and 50 $\mu\text{g}/\text{mL}$ PMA-IONs were dispersed in water. A drop of the resulting solution was placed on a Formvar/carbon-coated copper grid and air-dried. TEM images were obtained by a Tecnai G2 Spirit microscope (Oregon, USA) operating at 120 kV.

Dynamic light scattering (DLS) and zeta-potential measurements

The mean hydrodynamic diameter of nanoparticle (D_h), PDI, and zeta-potential (ξ) were measured at 25 °C by DLS method. Aliquots of PMA-IONs suspensions and PMA-IONs-loaded semi-solid formulations were diluted 1:20 in HPLC-grade water, filtered with 0.22 μm nylon filter (VWR, USA) and analyzed by Zetasizer Nano ZS (Malvern Instruments Ltd, UK). According to the National Institute of Standards and Technology, a sample with a PDI < 0.05 is considered monodisperse [31].

Evaluation of PMA-IONs stability in the semi-solid dosage forms by MRI relaxivity measurement

The study of the variation of the PMA-IONs relaxation time in the semi-solid formulations was made by low-field pulsed NMR Spectrometer mq20 (Bruker The Minispec, Italy). Aliquots 1 mL of were analyzed in a glass vial at 40 °C; a magnetic field was applied and, once the stimulus was interrupted, T_2 relaxation time was measured. The relaxivity (r_2) of PMA-IONs was calculated according the following equation (Eq. 1):

$$r_2 = \frac{\left(\frac{1}{T_2}\right)_{\text{sample}} - \left(\frac{1}{T_2}\right)_{\text{control}}}{[\text{PMA} - \text{IONs}]} \quad (1)$$

where $(1/T_2)_{\text{sample}}$ was the inverse of relaxation time of the semisolid matrix containing PMA-IONs, $(1/T_2)_{\text{control}}$ the inverse of relaxation time of the placebo semisolid matrix and the [PMA-IONs] was the concentration of nanoparticles in the semisolid matrix.

All the formulations were analyzed at the nanoparticles concentration of 0.15% w/v. Each analysis was conducted after 0, 2, 20, 32, 41 and 48 days from preparation ($n = 3$).

In vitro penetration studies

In vitro permeation and retention studies were performed with the Franz diffusion cells using HE or SC, or a membrane based on regenerated keratin (RKM; 24).

HE was prepared from full-thickness skin following an internal standard procedure [32]. The SC and viable epidermis (VE) were obtained by incubating HE in a Petri dish with 10 mL of 0.005% trypsin in pH 7.4 PBS at 37 ± 1 °C for 18 h. The integrity of HE was checked before the permeation studies by measuring the electrical resistance of HE or SC [33].

The membrane was placed on the Franz diffusion cell whose receptor compartment was filled with degassed 0.9% w/v NaCl solution containing 0.01% w/v NaN_3 as preservative. The donor compartment was filled with 0.5 mL of aqueous suspension or formulations loaded with 3 mg/mL PMA-IONs. The system was kept at 32 ± 1 °C throughout all the experiment. At experiment end, the receptor phase was withdrawn and analyzed by ICP-OES for determining the iron amount permeated through the membrane after 24 h (Q_{24}).

Afterwards, the membrane was gently cleaned to eliminate the unabsorbed PMA-IONs. Subsequently, the sample was dried, weighted and analyzed by ICP-OES to quantify the iron amount retained into the membrane (Q_{ret}). The results were expressed as the average of parallel experiments, performed in triplicate. As discussed by Musazzi et al. [33], the $Q_{\text{ret}}/Q_{24, \text{HE}}$ ratio was calculated as parameter to estimate the affinity of PMA-IONs to be retained or to permeate through HE. The higher the $Q_{\text{ret}}/Q_{24, \text{HE}}$, the higher the retention affinity of nanoparticles.

Nanoparticles quantification by ICP analysis

For the ICP-OES analysis of the samples collected from the Franz diffusion cell receptor chambers, 3 mL of aqua regia were added to the samples and, after 72 h, the samples were diluted with 7 mL of distilled water. All samples were measured in triplicate with Optima 7000 DV ICP-OES (Perkin Elmer, Waltham, USA).

Epidermis fixation protocol and transmission electron microscopy (TEM) analysis

For the ultrastructural analysis a fragment of each skin specimen was fixed in 2.5% buffered glutaraldehyde, washed with buffer and post-fixed in 1.5% buffered OsO_4 at 4 °C for 2 h. The specimens were dehydrated in a graded series of alcohol solution and embedded in Epon. The sections were then stained with uranyl acetate and lead citrate and examined in a FEI Tecnai G2 Spirit microscope equipped with a digital camera (Oregon, USA). The obtained sections were deposited on Formvar/carbon-coated copper grid.

EDX analysis

The STEM image and energy dispersive X-ray analysis (EDX) were performed using a ZEISS LIBRA200FE

TEM equipped with an HAADF-STEM (high angular annular dark field scanning electron microscopy) and EDS—Oxford INCA Energy TEM 200. The EDX analysis was performed on the epithelial tissue exposed to the IONs for 24 h and prepared as described in the previous paragraph.

Additional file

Additional file 1. Additional tables and figures.

Abbreviations

Cet: cetomacrogol; CMC: sodium carboxymethyl cellulose; CP: carboxypoly-methylene; D_h : hydrodynamic diameter of nanoparticle; DLS: dynamic light scattering; HE: human epidermis; HEC: hydroxyethyl cellulose; IONs: iron oxide nanoparticles; o/w: oil in water; PDI: poly dispersity index; PMA-IONs: iron oxide nanoparticles coated by a poly-(isobutylene-*alt*-maleic anhydride); Q_{24} : amount of iron permeated in 24 h; Q_{ret} : amount of iron retained in 24 h; r_2 : relaxivity; RKM: membrane based on regenerated keratin; SC: stratum corneum; T_2 : relaxation time; VE: viable epidermis; ξ : zeta-potential.

Authors' contributions

UMM, BS, VM, AMF and RA performed experiments and helped in data acquisition. UMM, BS, FS, FC, DP, MC and PM designed experiments and gave intellectual input. All authors contributed in writing the manuscript. All authors read and approved the final manuscript.

Author details

¹ Department of Pharmaceutical Sciences, Università degli Studi di Milano, via G. Colombo, 71, 20133 Milan, Italy. ² Department of Biotechnology and Biosciences, Università degli Studi di Milano-Bicocca, Piazza della Scienza, 2, 20126 Milan, Italy. ³ Dipartimento di Scienze Biologiche e Cliniche, Università degli Studi di Milano, via G. B. Grassi, 74, 20157 Milan, Italy. ⁴ Lab. di Nanotecnologie, CNR-Istituto di Scienze e tecnologie Molecolari, via G. Fantoli 16/15, 20138 Milan, Italy.

Acknowledgements

We thank M. Tringali (University of Milano-Bicocca) for ICP-OES analysis.

Competing interests

The authors declare that they have no competing interests.

Availability of data and materials

All data generated or analysed during this study are included in this published article (and its Additional file 1).

Funding

This work was partly supported by the Fondazione Regionale per la Ricerca Biomedica (FRRB), Fondazione Cariplo-Regione Lombardia (Grant 2016-0886), and Academic Funding Unimib 2016.

Received: 27 July 2016 Accepted: 10 February 2017

Published online: 17 February 2017

References

- Esser C, Gotz C. Filling the gaps: need for research on cell-specific xenobiotic metabolism in the skin. *Arch Toxicol*. 2013. doi:10.1007/s00204-013-1031-7.
- DeLouise LA. Applications of nanotechnology in dermatology. *J Invest Dermatol*. 2012;132:964–5.
- Sonavane G, Tomoda K, Sano A, Ohshima H, Terada H, Makino K. In vitro permeation of gold nanoparticles through rat skin and rat intestine: effect of particle size. *Colloids Surf B Biointerfaces*. 2008;65(1):1–10.

4. Tak YK, Pal S, Naoghare PK, Rangasamy S, Song JM. Shape-dependent skin penetration of silver nanoparticles: does it really matter? *Sci Rep*. 2015;5:16908.
5. Labouta HI, Schneider M. Interaction of inorganic nanoparticles with the skin barrier: current status and critical review. *Nanomedicine*. 2013. doi:10.1016/j.nano.2012.04.004.
6. Samberg ME, Oldenburg SJ, Monteiro-Riviere NA. Evaluation of silver nanoparticle toxicity in skin in vivo and keratinocytes in vitro. *Environ Health Perspect*. 2010;118:407–13.
7. Wu J, Liu W, Xue C, Zhou S, Lan F, Bi L, Xu H, Yang X, Zeng F-D. Toxicity and penetration of TiO₂ nanoparticles in hairless mice and porcine skin after subchronic dermal exposure. *Toxicol Lett*. 2009;191(1):1–8.
8. Mahapatra AK, Murthy PN, Sannoju S, Mohapatra AK. Tiny technology proves big: a challenge at engineering, medicine and pharmaceutical sciences interface. *Crit Rev Ther Drug Carrier Syst*. 2014;31:1–47.
9. Weissleder R, Bogdanov A, Neuwelt EA, Papisov M. Long-circulating iron oxides for MR imaging. *Adv Drug Deliv Rev*. 1995;16:321–34.
10. Wang J, Huang Y, David AE, Chertok B, Zhang L, Yu F, Yang VC. Magnetic nanoparticles for MRI of brain tumors. *Curr Pharm Biotechnol*. 2012;562(13):2403–16.
11. Rao YF, Chen W, Liang XG, Huang YZ, Miao J, Liu L, Lou Y, Zhang XG, Wang B, Tang RK, Chen Z, Lu XY. Epirubicin-loaded superparamagnetic iron-oxide nanoparticles for transdermal delivery: cancer therapy by circumventing the skin barrier. *Small*. 2015;11(2):239–47.
12. Remya NS, Syama S, Sabareeswaran A, Mohanan PV. Toxicity, toxicokinetics and biodistribution of dextran stabilized Iron oxide Nanoparticles for biomedical applications. *Int J Pharm*. 2016;511(1):586–98.
13. Revia RA, Zhang M. Magnetite nanoparticles for cancer diagnosis, treatment, and treatment monitoring: recent advances. *Mater Today*. 2016;19(3):157–68.
14. Estelrich J, Sánchez-Martín MJ, Busquets MA. Nanoparticles in magnetic resonance imaging: from simple to dual contrast agents. *Int J Nanomedicine*. 2015;10:1727–41.
15. Bulte JW. In vivo MRI cell tracking: clinical studies. *Am J Roentgenol*. 2009;193(2):314–25.
16. Anselmo AC, Mitragotri S. Nanoparticles in clinic. *Bioeng Trans Med*. 2016;1:10–29.
17. Govindarajan A, Lakshmanan PM, Sarawagi R, Prabhakaran V. Evaluation of date syrup as an oral negative contrast agent for MRCP. *AJR Am J Roentgenol*. 2014;203(5):1001–5.
18. Baroli B. Penetration of nanoparticles and nanomaterials in the skin: fiction or reality? *J Pharm Sci*. 2010;99(1):21–50.
19. Prow TW, Grice JE, Lin LL, Faye R, Butler M, Becker W, Wurm EM, Yoong C, Robertson TA, Soyer HP, Roberts MS. Nanoparticles and microparticles for skin drug delivery. *Adv Drug Deliv Rev*. 2011;63(6):470–91.
20. Baroli B, Ennas MG, Loffredo F, Isola M, Pinna R, López-Quintela MA. Penetration of metallic nanoparticles in human full-thickness skin. *J Invest Dermatol*. 2007;127(7):1701–12.
21. Santini B, Zanoni I, Marzi R, Cigni C, Bedoni M, Gramatica F, Palunga L, Corsi F, Granucci F, Colombo M. Cream formulation impact on topical administration of engineered colloidal nanoparticles. *PLoS ONE*. 2015;10(5):e0126366.
22. Patri A, Umbreit T, Zheng J, Nagashima K, Goering P, Francke-Carroll S, Gordon E, Weaver J, Miller T, Sadrieh N, McNeil S, Stratmeyer M. Energy dispersive X-ray analysis of titanium dioxide nanoparticle distribution after intravenous and subcutaneous injection in mice. *J Appl Toxicol*. 2009;29:662–72.
23. Lansdown ABG. Metal ions affecting the skin and eyes. *Met Ions Life Sci*. 2011;8:187–246.
24. Selmin F, Cilurzo F, Aluigi A, Franzè S, Minghetti P. Regenerated keratin membrane to match the in vitro drug diffusion through human epidermis. *Results Pharma Sci*. 2012;2:72–8.
25. Prow TW, Grice JE, Lin LL, Faye R, Butler M, Becker W, Wurm EM, Yoong C, Robertson TA, Soyer HP, Roberts MS. Nanoparticles and microparticles for skin drug delivery. *Adv Drug Deliv Rev*. 2011;63(6):470–91.
26. Cross SE, Roberts MS. Use of in vitro human skin membranes to model and predict the effect of changing blood flow on the flux and retention of topically applied solutes. *J Pharm Sci*. 2008;97(8):3442–50.
27. Soliman MG, Pelaz B, Parak WJ, del Pino P. Phase transfer and polymer coating methods toward improving the stability of metallic nanoparticles for biological applications. *Chem Mater*. 2015;27(3):990–7.
28. Pellegrino T, Manna L, Kudera S, Liedl T, Koktysh D, Rogach AL, Keller S, Rädler J, Natile G, Parak WJ. Hydrophobic nanocrystals coated with an amphiphilic polymer shell: a general route to water soluble nanocrystals. *Nano Lett*. 2004;4(4):703–7.
29. Colombo M, Sommaruga S, Mazzucchelli S, Polito L, Verderio P, Galeffi P, Corsi F, Tortora P, Prosperi D. Site-specific conjugation of ScFvs antibodies to nanoparticles by bioorthogonal strain-promoted alkyne–nitrene cycloaddition. *Angew Chem Int Ed*. 2012;51(2):496–9.
30. Sperling RA, Pellegrino T, Li JK, Chang WH, Parak WJ. Electrophoretic separation of nanoparticles with a discrete number of functional groups. *Adv Funct Mater*. 2006;16(7):943–8.
31. HHackley V, Ferraris C. The use of nomenclature in dispersion science and technology. NIST Recommended Practice Guide. Washington, DC: National Institute of Standards and Technology (NIST); 2001
32. Cilurzo F, Vistoli G, Selmin F, Gennari CGM, Musazzi UM, Franzè S, Lo Monte M, Minghetti P. An insight into the skin penetration enhancement mechanism of N-methylpyrrolidone. *Mol Pharm*. 2014;11(3):1014–21.
33. Musazzi UM, Matera C, Dallanoce C, Vacondio F, De Amici M, Vistoli G, Cilurzo F, Minghetti P. On the selection of an opioid for local skin analgesia: structure-skin permeability relationships. *Int J Pharm*. 2015;489:177–85.



Oral delivery of insulin via polyethylene imine-based nanoparticles for colonic release allows glycemic control in diabetic rats



Lucia Salvioni^{a,1}, Luisa Fiandra^{b,1}, Maria Dorly Del Curto^{c,1}, Serena Mazzucchelli^b, Raffaele Allevi^b, Marta Truffi^b, Luca Sorrentino^b, Benedetta Santini^a, Matteo Cerea^c, Luca Palugan^{c,*}, Fabio Corsi^{b,*}, Miriam Colombo^{a,*}

^a Università degli Studi di Milano-Bicocca, NanoBioLab, Dipartimento di Biotecnologie e Bioscienze, piazza della Scienza 2, 20126 Milan, Italy

^b Università degli Studi di Milano, Dipartimento di Scienze Biomediche e Cliniche "L. Sacco", via G.B. Grassi 74, 20157 Milan, Italy

^c Università degli Studi di Milano, Dipartimento di Scienze Farmaceutiche, Sezione di Tecnologia e Legislazione Farmaceutiche "Maria Edvige Sangalli", via G. Colombo 71, 20133 Milan, Italy

ARTICLE INFO

Article history:

Received 14 April 2016

Received in revised form 10 May 2016

Accepted 10 May 2016

Available online 12 May 2016

Keywords:

Polymeric nanoparticles
Multiple-unit formulation
Insulin release
Peptide oral delivery
Type 1 diabetes

ABSTRACT

In this study, insulin-containing nanoparticles were loaded into pellet cores and orally administered to diabetic rats. Polyethylene imine-based nanoparticles, either placebo or loaded with insulin, were incorporated by extrusion and spheronization technology into cores that were subsequently coated with three overlapping layers and a gastroresistant film. The starting and coated systems were evaluated *in vitro* for their physico-technological characteristics, as well as disintegration and release performance. Nanoparticles-loaded cores showed homogeneous particle size distribution and shape. When a superdisintegrant and a soluble diluent were included in the composition enhanced disintegration and release performance were observed. The selected formulations, coated either with enteric or three-layer films, showed gastroresistant and release delayed behavior *in vitro*, respectively. The most promising formulations were finally tested for their hypoglycemic effect in diabetic rats. Only the nanoformulations loaded into the three-layer pellets were able to induce a significant hypoglycemic activity in diabetic rats. Our results suggest that this efficient activity could be attributed to a retarded release of insulin into the distal intestine, characterized by relatively low proteolytic activity and optimal absorption.

© 2016 Elsevier Ltd. All rights reserved.

1. Introduction

Current therapy for diabetes mellitus relies on a correct diet, physical exercise, and oral hypoglycemic agents [1]. In case of disease progression or in Type 1 diabetes, insufficient insulin secretion or inadequate activity need to be considered. Therefore, replacement with exogenous insulin becomes mandatory for survival [1,2]. Unfortunately, nowadays the only administration route available for insulin is parenteral which implies one or more daily injections, with a significant reduction in quality of life and, sometimes, poor patient adherence to therapy [3,4]. Moreover, administration of insulin by subcutaneous injection may induce peripheral hyperinsulinaemia and portal hypoinsulinaemia. Under normal conditions, half of insulin produced by the pancreas is used for liver metabolism

via the portal circulation, resulting in fine regulation of blood glucose levels and adequate metabolism of carbohydrates and proteins [2]. Thus, several research studies have been focused on the development of novel formulations of the hormone through alternative routes of administration [5]. Particularly, the oral route has been considered as possibly leading to a better glucose regulation exploiting the liver first-pass metabolism of insulin, thus preventing the risks of fluctuating blood glucose levels and possibly the resulting morbidity due to chronic microvascular complications [6]. Therefore, an oral formulation of insulin could revolutionize the management of insulin-dependent diabetic patients due to its potential clinical benefits. However, the oral bioavailability of insulin is very low and several efforts have been attempted to promote insulin bowel absorption, avoiding gastric or intestinal degradation by proteases. Such attempts included formulations with protease inhibitors and/or absorption enhancers or mucoadhesive systems. Still, oral delivery of insulin remains an unmet need [3]. As a result of this, colonic delivery and release of insulin has gained increasing interest by researchers because of the longer transit time, prolonged localization of insulin on the gut mucosa,

* Corresponding authors.

E-mail addresses: luca.palugan@unimi.it (L. Palugan), fabio.corsi@unimi.it (F. Corsi), miriam.colombo@unimib.it (M. Colombo).

¹ Equally contributed.

lower levels of proteases in the colon or mucosal P-glycoprotein and greater responsiveness to permeation enhancers compared to the more proximal regions of the gastrointestinal tract. Such features would point to the colon as an interesting target for insulin oral delivery but, so far, an efficient drug delivery system for this purpose is still missing [3,6,7–9].

A few attempts to improve the oral delivery of insulin by means of nanoparticle-based vectors have been reported [10–12]. Several nanoparticle (NP) types have been designed to protect biological drugs, including insulin, against chemical and enzymatic degradation and to enhance the intestinal absorption through paracellular and transcellular pathways [10,11]. Structural characteristics of nanoparticles, including size and surface charge, have been shown to influence the insulin absorption by the enterocytes. In general, small particles, provided with a positive charge are absorbed more efficiently through the intestinal epithelium. This is due to the interaction of NPs bearing positive charges with mucin residues that are negatively charged at physiological pH. The consequent prolonged residence time and increased concentration gradient at the surface of the intestinal mucosa might therefore promote protein absorption [3,11]. *Ex-vivo* and *in vivo* studies have also proven the potential of colloidal nanoparticles in increasing insulin absorption throughout the colonic region, but the lack of an appropriate delivery system that ensures their safe transit through the upper gastrointestinal tract strongly limits their usefulness [12,13]. Therefore, a solid dosage form, including pellets and tablets, which could host drug-loaded nanoparticles and possibly undergo a subsequent coating process, might represent a valuable strategy to enhance stability and provide release versatility of these colloidal systems administered via the oral route [6].

The objective of the present study was to prepare, characterize and evaluate both *in vitro* and *in vivo*, a novel nanoformulated, multiple-unit colon release system, *i.e.* coated pellets, as a possible oral nanocarrier for insulin. The novelty of this approach was the evaluation of the synergistic effect of colon release, muco-adhesive nanoparticles and the presence of a permeation enhancer, sodium glycocholate. The proposed multi-approach strategy combines the well-known benefits of this multiple-unit formulation in terms of reproducible transit time through the gastrointestinal tract, the consequent absorption pattern with the advantages of colloidal nanoparticles [14]. For this purpose, a recently proposed three-layer release technology platform was applied, consisting of a flexible film composed of a neutral polymethacrylate Eudragit® NE and a superdisintegrant sodium starch glycolate Explotab®, added as a pore former, applied to a hydroxypropyl methylcellulose (HPMC) coating of reduced thickness in order to improve the efficiency of the erodible layer in delaying the drug liberation [14–16]. An outer gastroresistant layer was also added in order to neutralize the variable residence time in the stomach of the coated dosage form and allow its activation only following the entry into the duodenum. This time-dependent relies on the relative consistency of short intestinal transit time, the subsequent colon targeting and favoring the intestinal absorption of insulin at that level [17].

2. Materials and methods

2.1. Materials

Bovine insulin (MW 5734 Da), polyethylene imine (MW 750 kDa), dextran sulfate (MW > 500 kDa), zinc sulfate, streptozotocin (STZ) and cellulose ester dialysis membrane tubing with a molecular weight cut-off (MWCO) of 1.000.000 Da (Spectra/Por® Biotech CE) were purchased from Sigma-Aldrich (St Louis, MO, US). All chemicals were used as received without further purification. Lactose was obtained from Prodotti Gianni (Milan, Italy). Micro-

crystalline cellulose co-processed with sodium carboxymethyl cellulose (Avicel® CL611) and hydroxypropyl methyl cellulose acetate succinate (Aqoat® LG, HPMCAS) were gifts from FMC Europe (Brussels, Belgium, distributed by IMCD Italia, Milan, Italy) and from Shin-Etsu (Tokyo, Japan, distributed by Seppic, Milan, Italy), respectively. Hydroxypropyl methylcellulose (Methocel® E50, HPMC) was kindly donated by Colorcon (Milano, Italy). Poly(ethylacrylate, methylmethacrylate) (2:1 monomer molar ratio) as 30% V:w aqueous dispersion (Eudragit® NE 30 D) of Evonik Röhm (Darmstadt, Germany) was a kind gift of Rofarma (Gaggiano, Italy). Polyethylene glycol (PEG 400) and size 4 hard-gelatin capsules were purchased from ACEF (Fiorenzuola D'Arda, Italy). Sodium glycocholate (NaGly) was obtained from and Tokyo Chemical Industry (Tokyo, Japan). Sodium starch glycolate (Explotab® CLV) was a gift from JRS Rettenmaier Italia (Castenedolo, Italy).

2.2. Synthesis of insulin-containing nanoparticles (nanoformulated insulin, NI)

22.1 mL of insulin solution (10 mg/mL in 0.01 M HCl), 10.8 mL of a 10% w/V dextran sulfate (DS) solution and 18.0 mL of 10 mM tris buffer, pH 9, were added under stirring (500 rpm) to 12.6 mL of polyethylene imine (PEI) solution (25% w/V). Afterwards, the mixture was heated at 40 °C and maintained under stirring because of its high viscosity and 7.8 mL zinc sulfate solution (2 M) were added, dropwise. As a result of the addition of the stabilizer, the formation of the nanoparticles took place and the viscosity of the solution decreased. The product was stirred for 15 min at 40 °C. The product was finally dialyzed in Milli-Q® water with cellulose ester dialysis membrane tubing with a molecular weight cut-off (MWCO) of 1.000.000 Da.

2.3. Synthesis of placebo nanoparticles (NPs)

22.1 mL of HCl 0.01 M, 10.8 mL of a 10% w/V DS solution and 18.0 mL of 10 mM tris buffer, pH 9, were added under stirring (500 rpm) to 12.6 mL of polyethylene imine (PEI) solution (25% w/V) and then treated as described above.

2.4. Nanoparticle characterization

2.4.1. Dynamic light scattering (DLS) and zeta potential measurements

The mean diameter and surface charge of the nanoparticles were assessed with a Zetasizer Nano ZS ZEN3600 from Malvern Instruments Ltd (Worcestershire, United Kingdom) operating at a light source wavelength of 633 nm and a fixed scattering angle of 173°. The sample concentration was chosen to keep attenuator values between 7 and 9. The refractive index of material was 1.524. The measurements were performed in triplicate, after dilution of the nanoparticles respectively with MilliQ® water and aqueous solution of sodium chloride (1 mM).

2.4.2. Transmission electron microscopy (TEM) analysis

Nanoparticles were visualized using 120 keV TEM (Jeol 1010, Tokyo, Japan). Two microliters of the sample, along with 2% w:V uranyl acetate solution, were deposited onto a piece of ultrathin 200-mesh copper grid (Ted-pella, Redding, CA, US) and left to dry in air before examination by TEM.

2.4.3. Determination of the entrapment efficiency (EE%) of insulin into the nanoparticles

The amount of insulin encapsulated into the nanoparticles was determined suspending the NI, corresponding to 30 µg/mL theoretical insulin concentration, in 0.05 M HCl and centrifuging at 12000 rpm for 20 min (ScanSpeed 1730R, Labogene, Lynge,

Denmark). After centrifugation, the amount of insulin in supernatant was measured by a reverse-phase, high-performance liquid chromatography (RP-HPLC) analysis with a method reported in Eur. Pharm. 8th Ed. for insulin and its degradation product A21-desamido insulin (A21) quantitation that was previously set-up [18]. Insulin quantitation was performed using a freshly prepared standard having identical insulin concentration and analyzed the same day of nanoparticles. The EE% is expressed as ratio percentage between the insulin amount in the suspension and the theoretical value of the insulin added.

2.4.4. In vitro insulin release from NI

In vitro release was assessed following incubation of the nanoparticle suspension containing theoretically 0.35 mg of insulin in 10 mL of 0.095 M phosphate buffer pH 6.8 prepared as indicated in the Eur. Pharm. 8th Ed. at 37 °C under stirring (MIX15eco, 2mag, München, Germany; 600 rpm). Bovine albumin (0.2% w/V) was added to the dissolution medium to avoid non-specific adsorption of insulin to glass surface. At pre-determined time intervals, 1 mL of medium was withdrawn, filtered by 0.2 µm polyethersulfone (PES) membrane (VWR) and acidified with 40 µL of 1 M HCl before the analysis by RP-HPLC as previously described. Dissolution studies were performed in triplicate.

2.5. Preparation and coating of cores

All cores were prepared by extrusion and spheronization (E-S) process.

Powders (9.2 g) were mixed in a mortar for 5 min. Nanoparticle suspensions, either placebo or loaded with insulin, (70 g) were then added in small aliquots to the powder blend under continuous mixing, in the same mortar, over a total period of 8 h; during that time the most of water could evaporate to allow the moisture content suitable to the next step. The room was maintained at 30 °C with 25% relative humidity. The resulting wetted mass was extruded through an 850 µm sieve. Spheronization was performed in a spheronizer (Nica™ S320, GEA, Düsseldorf, Germany) with a cross-hatched plate (400 rpm, 5 min). Pellets cores were finally dried in a static oven at 40 °C for 24 h. As a reference, a pellet formulation containing the non-encapsulated peptide was prepared by mixing insulin powder with Avicel® CL611, NaGly, lactose and Explotab® CLV (9.4 g) and adding deionized water (3.5 g). The E-S was then performed as for nanoparticles loaded formulations.

In order to obtain three-layer colonic systems, pellets were coated in a fluid bed (GCPG 1.1, Glatt®, Binzen, Germany). The following formulations were in turn sprayed: i) a hydro-alcoholic solution (1:9 w/w, water/ethanol) of Methocel® E50 (5% w/w) and PEG 400 (0.5% w/w) (10 g/min spray rate), ii) an aqueous suspension of Eudragit® NE 30D-Explotab® CLV (20% vs. solid Eudragit® NE) (1.4 g/min) and iii) a hydro-alcoholic solution (23% w/w, water/ethanol) of Aqoat® (5.8% w/w) (8 g/min). In the case of the coatings with the hydro-alcoholic solutions of both Methocel® E50 and Aqoat® the rotor insert was employed while for Eudragit® NE-based suspension a Wurster process was applied. In the case of gastroresistant formulations, pellets were directly coated with the hydro-alcoholic solution of Aqoat®, as previously described. The operating conditions for all coatings were: inlet air temperature, 40 °C; product temperature, 33–35 °C; airflow rate, 70 m³/h; nozzle diameter, 1.2 mm; spray pressure, 2.0 bar; final drying time at 40 °C, 5 min. A curing step in a static oven at 40 °C was performed on intermediate systems coated with Eudragit® NE-Explotab® CLV and final enteric formulations for 24 h and 2 h, respectively. In all process steps, placebo mini-tablets (weight 10.5 mg, diameter 2.5 mm, height 2.3 mm) were added in the process chamber to reach the minimum capacity of the fluid bed.

2.6. Pellets characterization

2.6.1. Particle size and shape analyses

Particle size distribution of the pellets was determined by a set of analytical sieves (500, 600, 710, 850, 1000, 1180, 1400, 1700, 2000 µm) piled in a sieve shaker (Endecotts, Octagon 200, London, United Kingdom) operated for 5 min at an amplitude of 4. Mean diameter and aspect ratio were determined using an image analysis system. Digital photomicrographs (n = 30, DinoCapture, Hsinchu, Taiwan) were analyzed by ImageJ software (Version 1.48, 19 April 2014, National Institute of Health, Bethesda, MD, US) that allow calculation of pellets dimensional and shape descriptors. The aspect ratio (AR) was calculated as follows:

$$\text{Aspect ratio (AR)} = \frac{\text{Major Axis}}{\text{Minor Axis}}$$

AR indicates the particle's fitted ellipse.

Yield% was calculated as ratio between the mass of obtained cores (500–2000 µm range) and the weighed amount of excipients.

2.6.2. Disintegration test

Disintegration test was performed in a dissolution apparatus 2: 300 mg of pellets in the 850–1000 µm range were poured in a vessel containing 1000 mL of pH 6.8 phosphate buffer (37.0 ± 0.5 °C), and stirred at 100 rpm for 30 min. Then, pellets retained by a 400 µm net were dried (40 °C, 24 h) and weighted; finally, the percentage of mass loss was calculated [19].

2.6.3. Insulin assay and in vitro release

In order to assess insulin content, approximately 10 mg of cores of pellets, exactly weighed, were added to 0.05 M HCl, stirred at 350 rpm for 10 min, sonicated for 10 min and centrifuged (12000 rpm, 20 min). The supernatant was analyzed by RP-HPLC analysis as described in section 2.4.3. *In vitro* release from nanoparticles, uncoated cores and coated pellets was assessed following incubation in 10 mL of phosphate buffer (pH = 6.8) containing 0.2% bovine albumin at 37 °C under stirring. At pre-determined time-points, 1 mL of medium was withdrawn and replaced with fresh buffer solution, centrifuged and analyzed by RP-HPLC as previously described in section 2.4.3. In the case of three-layer and gastroresistant formulations, coated pellets were tested in HCl 0.1 M for 2 h prior to the buffer stage.

2.6.4. Re-dispersion studies

25 mg of cores (PNI02) were incubated in 5 mL of 0.1 M HCl at 37 °C under stirring (600 rpm) for 5 h. After incubation, an aliquot (2 mL) was filtered with 0.45 µm membrane and analyzed by DLS. The choice of the medium is occurred by checking the non-influence of other excipients in analysis result and the stability of the nanoparticles in this solution. The study was conducted in triplicate.

2.7. In vivo studies

2.7.1. Diabetic rat model

For the *in vivo* experiments, Sprague Dawley rats, purchased by Charles River Laboratories (Calco, Italy), were maintained in a fully-equipped facility in appropriate cages and provided with a proper environment. Diabetes was induced by two intraperitoneal injections of 50 mg/kg streptozotocin diluted in 0.1 M sodium citrate buffer pH 4.5 (one injection per week for two weeks). Seven days after the first administration, all rats were weighted and glycaemia was measured by puncturing the tail vein with an 18-gauge needle and collecting the blood droplet in the test strip of a blood glucose meter (Contour Link, Bayer, Milan, Italy). After the first injection, around 40% of treated rats developed glycemic values

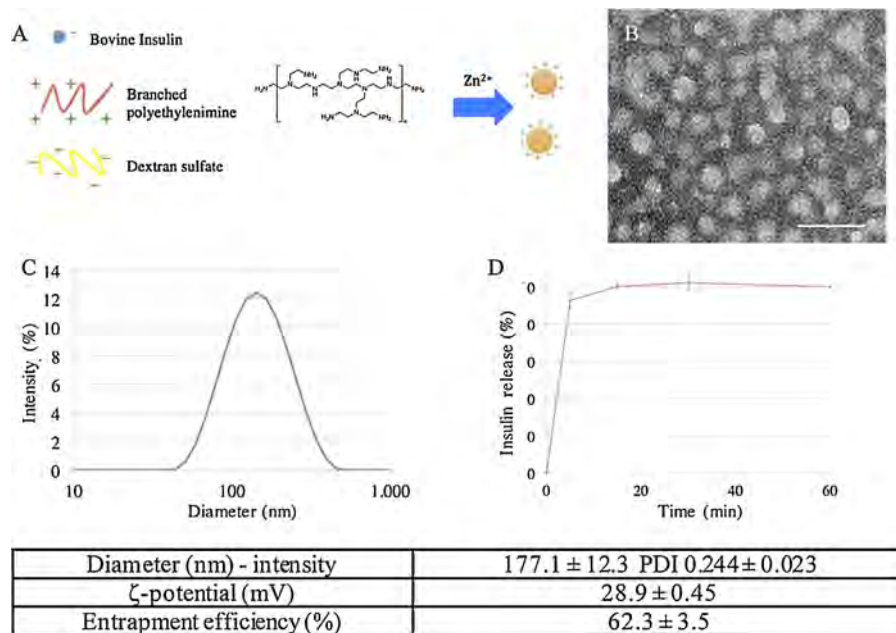


Fig. 1. Schematic representation of NI synthesis (A). TEM image of NI, scale bar: 100 nm (B). Hydrodynamic size of NI measured by DLS (C). Dissolution profile of NI at 6.8 pH (mean ± SD, n = 3) (D).

Table 1
Compositions of cores under investigation.

Formulation	% (w/w)						
	Insulin	NI ^a	Placebo NPs ^a	Avicel® CL611	Sodium glycocholate (NaGly)	Lactose	Explotab® CLV
PN01	–	–	50.0	50.0	–	–	–
PN02	–	–	50.0	26.4	–	15.7	7.9
PNI01	–	43.2	–	43.2	13.6	–	–
PNI02	–	43.2	–	22.7	13.6	13.8	6.7
PI02	2.3	–	–	39.1	23.4	23.7	11.5

^a The percentage refers to the solid nanoparticles.

over 350 mg/dL, indicative of diabetes onset [20]. All animals were treated again and, after further seven days, we obtained 75–80% of stably diabetic rats (glucose concentration ranging between 350 and 600 mg/dL).

2.7.2. Administration of insulin formulations to diabetic rats

Three groups of diabetic rats have been in turn injected subcutaneously with a solution of free insulin (n = 3, 0.07 mg/kg in phosphate buffer pH 6.8), and orally by gavage with a peptide solution (n = 5, 1.33 mg/kg in 10⁻³ M HCl) as well as with a nanoparticle formulation (n = 6, NI, 1.33 mg/kg). All other rats have undergone a surgical gastrostomy, upon anesthetization by intraperitoneal injection of 500 mg/kg of Avertin, for the insertion into the stomach of one capsule containing pellets formulations loaded with insulin (1.33 mg/kg): GPNI (n = 5, 53 mg), GPI (n = 3, 55 mg) CPNI (n = 4, 168 mg), CPI (n = 4, 63 mg). After insertion of the capsule, the stomach was sutured with 4-0 resorbable running suture, and the abdomen closed by 2-0 silk interrupted stitches. The gastrostomy procedure was chosen due to the impossibility to obtain a suitable oral administration of the free pellets in aqueous solution: low stability and high electrostatic interaction with the gavage tube were observed. One group of 5 rats was left untreated. The blood glucose levels were monitored by collecting blood droplets as described above at 1, 2, 3, 4, 5, 6, 7, 8, and 48 h post-treatment. Rats were used in accordance with an experimental protocol subjected to the direct approval of the Italian Ministry of Health.

3. Results

3.1. Nanoparticle synthesis and characterization

Insulin-loaded polymeric nanoparticles were synthesized according to previously published protocols with some modifications with the aim of scaling up the amount of synthesized nanoparticles and reduce the amount of excipients to include in the final pellet formulation [21,22]. Briefly, insulin and dextran sulfate solutions were added to a PEI solution under heating at 40 °C. The driving force for the formation of the nanoparticles was the opposite charges of PEI and dextran sulfate resulting in the insulin entrapment into the polymeric matrix. The weight ratio between the two polymers was optimized in order to control the particle size and zinc sulfate solution was added dropwise to stabilize the nanoparticles (Fig. 1A). The resulting insulin-containing nanoparticles (NI) were washed by dialysis against deionized water that was chosen as the dialysis medium instead of recommended 5% (w/v) mannitol solution [21]. The amount of NI in the final dialyzed product was 72% of the starting amount. Compared to previously reported preparation, bulky stabilizer exclusion, along with the 5-fold increase of insulin loading, resulted in a 35-fold reduction of the material amount required to form the pellets [21,22]. Furthermore, added solutions were at the minimum volumes needed to ensure the reagents solubility. With this adjustment, concentrated colloidal suspension was obtained, more suitable for following pellets inclusion.

Table 2
Physico-chemical properties and process yield of cores prepared by extrusion and spheronization.

Batch	d_{geo} (μm)	σ_{geo} (μm)	AR	Yield (%)	Insulin recovery%	A21%
PN01	913	1.18	1.36 ± 0.18	59.9	–	–
PN02	804	1.21	1.38 ± 0.20	40.1	–	–
PNI01	809	1.21	1.21 ± 0.18	41.3	102.1 ± 1.6	1.8 ± 0.2
PNI02	1137	1.28	1.16 ± 0.10	61.9	88.8 ± 3.7	0.9 ± 0.3
PI02	1066	1.16	1.29 ± 0.15	74.4	91.8 ± 1.1	2.2 ± 0.3

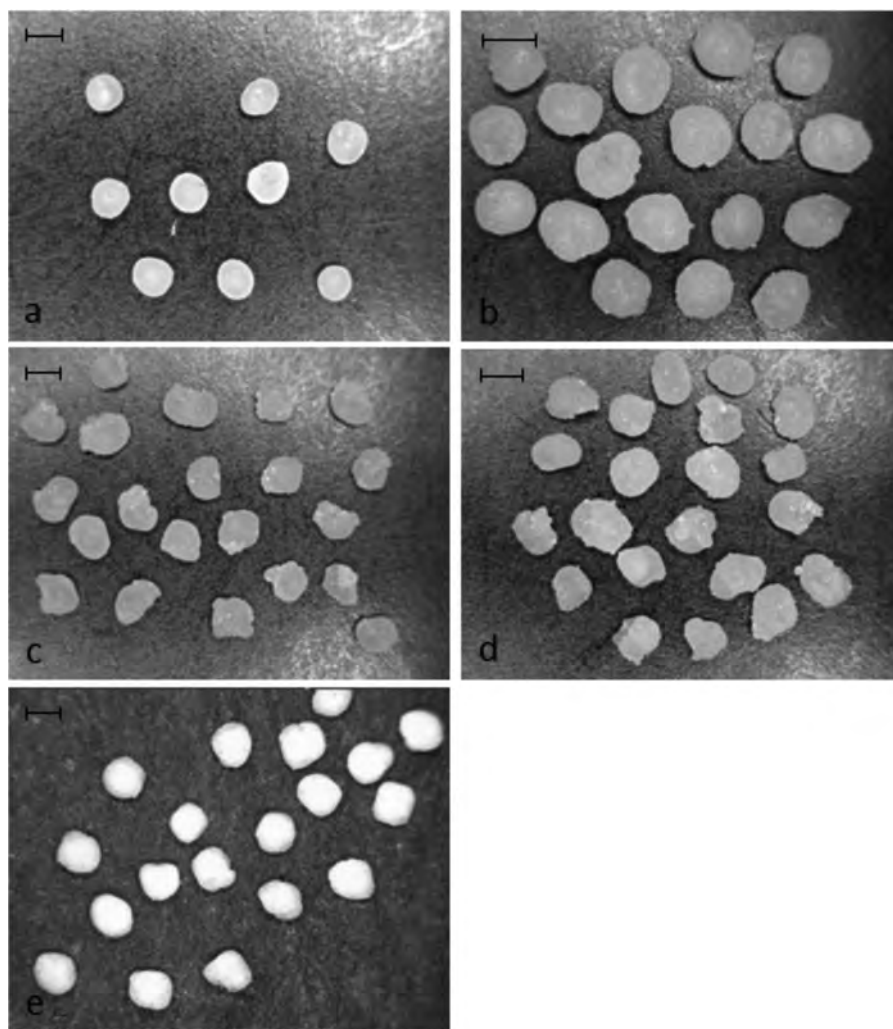


Fig. 2. Digital photographs of core formulation under investigation: a) PN01, b) PN02, c) PNI01, d) PNI02 and e) PI02. Scale bar: 1 mm.

Transmission electron microscopy (TEM) images of the negatively stained NI (Fig. 1B) showed spherical and nearly monodisperse 30 nm nanoparticles. However, the mean hydrodynamic size of NI as determined by DLS was 177.1 ± 12.3 nm, probably due to the high solvation efficiency of the polymeric matrix, and the zeta potential was $+28.9 \pm 0.5$ mV. The entrapment efficiency (EE%) determined after extraction in acidic solution and measured by RP-HPLC was $62.3 \pm 3.5\%$, while the % of the degradation product A21-desamido insulin was $1.2 \pm 0.1\%$. Although slightly lower than previous reports, EE% was in the range of interest to conduct the subsequent loading steps. In addition, the A21% levels below the limits reported in the bovine insulin monograph of the Pharm. Eur. 8th Ed. confirmed that no major hydrolytic degradation had occurred during the preparation of colloidal nanoparticles.

Insulin nanoparticles subjected to release test showed a fast peptide dissolution at pH 6.8 (over 90% within 5 min). This behav-

ior is consistent with that of similar nanoparticles reported in the literature [21].

3.2. Core preparation and characterization

In order to achieve a prompt release of the nanoparticles at the desired site, an appropriate core formulation was designed. A cellulose derivative, Avicel® CL611, a co-processed microcrystalline cellulose and sodium carboxymethyl cellulose, was identified as suitable spheronization agent due to the well-known advantages in terms of improved disintegration and dissolution performance over the traditional formulations based on microcrystalline cellulose [19,23]. Moreover, a superdisintegrant agent (Explotab® CLV) and a soluble diluent (lactose) were added in an alternative formulation in order to further improve the pursued fast-disintegration properties (Table 1). Only in the case of pellets loaded with NI, sodium

Table 3
Physico-technological characteristics of gastroresistant and three-layer colonic pellets.

Formulations	d_m (μm)	SD (μm)	AR	Methocel [®] E50 mg/cm ²	Eudragit [®] NE-Explotab [®] CLV 20% mg/cm ²	Acoat [®] mg/cm ²
GPNI	1355	114	1.14	–	–	13.1
CPNI	1865	102	1.07	89.9	4.0	13.0
GPI	1392	121	1.25	–	–	11.9
CPI	2070	149	1.24	85.1	3.1	12.5

glycocholate (NaGly), an absorption enhancer with protease inhibition properties, was considered [24,25]. The latter functional agent was indeed demonstrated to promote the oral absorption of a pancreatic hormone in rats administered with a minitab formulation at 1:10 protein/adjuvant ratio [26]. In addition, NaGly, due to its high solubility in aqueous media, could help to prevent the undesired matrix formation when pellets interact with water, thus possibly aiding their disintegration. Based on preliminary extrusion and spheronization trials, a 1:1 Avicel[®] CL611/placebo nanoparticles binary mixture was acknowledged as starting formulation suitable to lead to a dough with appropriate plasticity and pellets with adequate morphological characteristics (Table 1). When insulin-containing formulations or all other systems containing Explotab[®] CLV and lactose were used, the process appeared facilitated probably due to the concomitant decrease of nanoparticle amount and increase in the total solid mass attributable to the presence of the NaGly powder. In all cases, the possible issue associated with the large amount of colloidal suspension needed to obtain the required insulin dose for the *in vivo* studies, *i.e.* 4:1 w/w water vs. total solid mass, was overcome by adding the liquid in small aliquots and allowing the subsequent evaporation that limited the moisture content of the extrudable mass.

All the process yields were >40% and, taking into account the low amounts of processed material, were considered satisfying. All batches showed a mean particle size comprised within the desired 710–1400 μm range and a nearly spherical shape (Table 2, Fig. 2). Only in the case of formulation batches PNI02 and PI02 a slightly higher mean diameter was observed. No differences in size or shape were observed between placebo and insulin-loaded pellets, which was not surprising considering that the final core product structure was not significantly affected by the low amount of protein payload within the colloidal suspension.

The protein content in the pellets was $\geq 90\%$ of the theoretical amount and, despite the long wetting and evaporation phases, the % of A21 remained below the limits indicated in the monograph of bovine insulin reported of Pharm. Eur. 8th Ed., *i.e.* 3%. The overall results suggested that extrusion and spheronization might be a promising technology for loading a nanoparticle suspension into pellets.

3.2.1. *In vitro* studies on cores

Pellets containing the insulin-loaded nanoparticles were subjected to *in vitro* studies aiming to assess the disintegration and insulin release performances from the two different formulations.

PNI02 formulation showed enhanced disintegration compared to PNI01, *i.e.* 26.4 vs. 10.8%. This behavior could be ascribed to the presence of the superdisintegrant Explotab[®] and that of lactose acting as pore former compared to the formulation where the excipients were only Avicel[®] CL611. However, comparing such performance with that of a reference formulation containing paracetamol as analytical tracer instead of insulin nanoparticles and Avicel[®] CL611/lactose/Explotab[®] CLV in the same ratios as PNI02 formulation, a $\geq 75\%$ disintegration was obtained. It can be thus inferred that the presence of nanoparticles considerably contributed to the formation of a slow-eroding matrix.

To confirm this result, re-dispersion studies were performed on batch PNI02, which appeared the most promising system from *in vitro* disintegration and dissolution tests. These studies were set up in order to evaluate the presence of NI after exposure of the solid dosage form to aqueous fluids. Samples of this medium were collected and analyzed by DLS.

Nanoparticles with a mean diameter of 146.1 ± 1.0 nm ($n=3$) were detected. Comparing the size of NI, before and after E-S process, it was noticed that the mean diameter was slightly lower than the initial value (177.1 ± 12.3 nm), although the size distribution appeared to be maintained as evaluated by DLS polydispersity index (0.296 ± 0.005). To figure out the cause of this reduction, the same test was performed on 25 mg of a dried dough obtained by using the same components and operating conditions of the cores of PNI02 batch avoiding extrusion and spheronization steps. Also in this case, a decrease of mean diameter occurred, suggesting that it may depend on the mechanical stress during the dough formation. It can be thus inferred that cores under investigation might convey and liberate the colloidal system upon exposure to aqueous media.

3.2.2. Preparation and characterization of coated pellets

Pellets batches PNI02 and PI02 were selected as core formulations for preliminary *in vivo* testing on the basis of the *in vitro* results in terms of enhanced disintegration and dissolution properties. The cores were therefore coated either with a hydroalcoholic solution of Acoat[®] or in turn with a Methocel[®] E50-, Eudragit[®] NE/Explotab[®] CLV- and Acoat[®]- based formulations in order to prepare gastroresistant (G) and three-layer colonic (C) systems, respectively (Table 3). In the three-layer system, the hydrophilic layer based on Methocel[®] E50 was demonstrated to delay the drug release by a swelling/erosion mechanism, while the Eudragit[®] NE/Explotab[®] CLV film was aimed at prolonging the duration of the lag phase as imparted by the underlying HPMC coat. Finally, an outer gastroresistant film was added to the system to overcome the unpredictable gastric residence time of the system thus allowing its activation only at the duodenum and the consequent colonic release based on a time-dependent approach [17,26].

The adopted process operative conditions and the coating levels needed to achieve gastroresistance or a delayed release after a lag-phase suitable for colonic delivery were previously set up with an analogous formulation containing paracetamol as analytical tracer (data not shown). In particular, gastroresistance criteria were accomplished with an Acoat[®] coating level of 12–13 mg/cm². When using colonic systems, an *in vitro* lag time of approximately 60 min corresponded to 85–90 mg/cm² of Methocel[®] E50, 3.0–4.0 mg/cm² of Eudragit[®] NE-Explotab[®] CLV 20% and 12–13 mg/cm² of Acoat[®] [26]. Particularly, a similar multiple-unit system with an *in vitro* lag phase of the latter duration showed an insulin peak in rats and a corresponding drop in blood glucose levels 6 h post-dose following oral administration. Based on typical gastrointestinal transit times reported in the literature for rats, the delivery system, after this lag time, was expected to be able to arrive, mostly intact, to the ileo-colonic region [27].

All coated batches showed a mean particle size in the 1.3–2.1 mm range and coating levels in line with what expected based on pre-

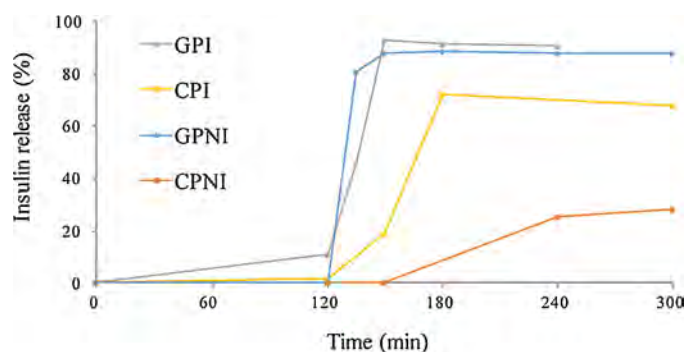


Fig. 3. *In vitro* insulin release of coated pellets.

liminary set up results. The shape was closer to roundness than the starting cores, as a result of the subsequent coating steps.

When subjected to *in vitro* release tests all formulation met gastroresistance criteria (<10% release after 2 h in 0.1 M HCl), albeit the release test was conducted under more vigorous stirring, performed by magnetic stirrer, compared to the compendial method (Fig. 3).

When exposed to a pH 6.8 buffer, all enteric systems showed a prompt release due to core disintegration following dissolution of the enteric coat. The three-layer colonic systems containing the NI showed a lag-phase preceding the onset of release. The time corresponding to 10% release, $t_{10\%}$, was 65 min. Moreover, the CPI pellet formulation used as reference showed a shorter lag time that was demonstrated to be caused by the adopted release testing conditions (data not show).

3.3. *In vivo* hypoglycemic effect

The NI loaded into the pellets were tested *in vivo* in diabetic rats. The rat model was chosen since the gastrointestinal transit time is comparable to that of humans [28]. The animals that reached stable glucose values in blood of at least 350 mg/dL following streptozotocin administration were subjected to one of the following treatments: 1) oral administration of 1.33 mg/kg insulin (OI) or as NI, 2) subcutaneous injection of 0.07 mg/kg insulin (SCI), 3) insertion through gastrostomy of different amounts of pellets in capsules (GPI, GPNI, CPI, CPNI) to allow administration of 1.33 mg/kg. A group of non-treated rats was used as control (NT). Fig. 4 shows the % variation of glycaemia from 1 to 48 h post-treatment. The baseline for each experimental group was the mean value of blood glucose measured before the treatment, considered as 100%. In the first 8 h post-treatment, physiological oscillation of glucose blood levels was observed in NT rats, which however did not exceed 30% of the initial value. Orally administered insulin, either free or in NI, had no significant effect on blood glucose levels, while the subcutaneous injection of insulin caused a rapid and marked reduction of the glycemia to 25% of the initial values at 1 h post-treatment. However, blood glucose levels returned to the initial level when measured after 8 h. The treatment with GPI or GPNI did not show any significant effect on the glucose blood levels as compared to NT during the first 8 h. In contrast, the rat treatment with CPNI was able to induce an immediate, significant decrease in blood sugar levels as compared to the NT, with a significant fall in glycaemia, as much as 50% of the initial value, at 6 h post-treatment, and a subsequent further decrease of up to 30% at 8 h. On the other hand, the treatment with CPI did not exert any significant hypoglycemic effect. At longer times (48 h), NT and SCI-, OI-, NI-, and GPI-administered rats had blood glucose equal the initial values, while in rats administered with CPNI the glucose concentration remained at 45% of the starting level and significantly different from those of all other

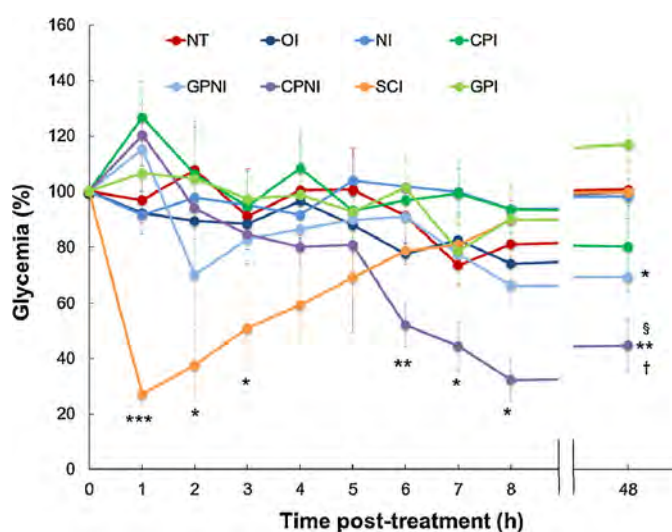


Fig. 4. Time course of the *in vivo* activity of different insulin formulations, expressed as percentage variation of rat blood glucose levels after treatment. Diabetic rats were exposed to oral (OI) or subcutaneous (SCI) administration of insulin, oral administration of insulin nanoparticles (NI), or insertion through gastrostomy of capsules containing gastroresistant pellet-formulated insulin (GPI) or insulin-nanoparticles (GPNI), colon-release pellet-formulated insulin (CPI) or insulin-nanoparticles (CPNI); NT: untreated rats. Mean \pm SE of 3–6 animals for group. *** $p < 0.0005$; ** $p < 0.01$; * $p < 0.05$ vs NT; § $p < 0.0005$ vs OI, NI, GPI and SCI; † $p < 0.05$ vs GPNI and CPI (one-tailed Student *t*-test).

experimental groups. At 48 h post-treatment, a slight decrease of glycaemia was observed upon administration of CPI, while in GPNI-treated rats glucose values became about 70% of initial values and significantly lower than those of controls.

4. Discussion

Preparation method of nanoparticles allows a considerable amount of insulin loaded and to a high concentration of nano-suspension: these factors are both favorable for the preparation of NI loaded pellets. Extrusion/spherulization of a formulation containing Avicel® CL611, lactose and Explotab® CLV wetted by nano-suspension leads to cores with technological and biopharmaceutical characteristics suitable for the following coating steps and for allowing a rapid NI release. Finally, *in vitro* performances of three layers coated pellets pledged a delayed release to promote colon targeting.

Orally administered insulin, either “free” or formulated in nanoparticles (NI) were not effective in reducing blood glucose levels in diabetic rats at 8 h after treatment. That was expected since insulin is rapidly degraded in the stomach. On the other hand, the subcutaneous injection of insulin, as used in clinical practice, caused a rapid and significant hypoglycemic effect with a subsequent gradual return to the initial blood glucose levels at 8 h. Curiously, at 1 h post-treatment all rats treated with the different capsules (GPI, GPNI, CPNI, or CPI) showed a temporary increase in blood glucose concentrations, possibly due to the effect of surgery and anesthesia, which is known to cause stress-related acute hyperglycaemia in fed rats [29]. The treatments with GPI or GPNI, enteric coated pellets which were supposed to release the nanoformulated insulin in small intestine, in the duodenum and the jejunum, did not significantly reduce the blood glucose levels as compared to NT in the first 8 h ($p > 0.05$). This may be due to the degradation of insulin by the high proteolytic activity of pancreatic peptidases but also to the effect of the insulin-degrading enzymes inside the cytosol of the small intestine enterocytes which can internalize the peptide by specific insulin receptors [30,31]. In contrast, the rat treatment

with CPNI induced a significant decrease in blood glucose levels as compared to the NT group. The reduction was significant at 6 h post-treatment with as much as 50% of the initial values, with a subsequent further decrease of up to 30% at 8 h. This result suggested that, unlike the gastroresistant pellet (GP) which releases the insulin into active small intestine, the three-layer colon-release pellet (CP) passed this tract without being degraded and released the NI in the distal part of the small intestine or in the colon. There are several reasons which make the colon as a desirable tract for insulin delivery and release: 1) the enzymatic activity, such as pancreatic endopeptidases, is remarkably lower and most of proteins, including insulin, would be available to intestinal absorption; 2) the microvilli are less developed in this tract as compared to the small intestine and their membrane-associated peptidases are limited making such microvilli more susceptible to permeation; 3) the P-glycoprotein is less expressed in colonic mucosa, and colon enterocytes and M-cells easily internalize nanoparticles; 4) there is a prolonged localization of insulin on the colonic mucosa due to slow transit time, thinner unstirred water layer (UWL) adjacent to mucosa, and slow turnover of colon mucosal film [5]. The lack of significant decrease in glycaemia of the rats treated with CPI indicates that the delivery of insulin as such to the colon by pellets is not sufficient to exert the hypoglycemic effect. A drug delivery system is required to properly address and release insulin to the colonic mucosa. Therefore, insulin nanoformulation plays a key role in reaching this goal. It has been demonstrated that polyethylenimine, as other cationic polymers (e.g. chitosans-CS), is able to loosen tight junctions (TJ) resulting in increased permeability of intestinal epithelium cells, which leads to paracellular permeation of molecules [32]. Many studies have already demonstrated the ability of different kinds of CS nanoparticles to increase the intestinal permeation of conjugated insulin through TJ opening [33]. In particular, Lin and colleagues suggested a mechanism for the paracellular transport of insulin to the blood circulation based on CS nanoparticles, whose stability and release of loaded insulin greatly depended on the environmental pH. In this model, the neutral pH, typical of the jejunum and the ileum, favors the degradation of the nanocomplex resulting in the complete release of CS and insulin. CS interaction with the TJ proteins enhances the paracellular pathway, promoting the absorption of greater amounts of insulin [34]. An equivalent mechanism could be suggested also for the NI released from pellets into the colon. Indeed, the pH values of this tract, from 6.5 in the ascending colon to 7 in the descending colon, could promote nanoparticle instability and cause the release of insulin (Fig. 1). Considering that the entire nanocomplex was not allowed to permeate across the TJ, even under the effect of paracellular enhancers, a few conclusions can be drawn: 1) the released NI undergoes degradation in the colon lumen; 2) the released insulin that is not subjected to significant proteolytic activity in this tract of the gut and the PEI fragments both reach the mucosal surface; 3) PEI is supposed to interact with the TJ and opens the paracellular pathway, thus promoting a significant insulin absorption [35]. In addition, the presence of sodium glycocholate, that is known to promote insulin passage through the colonic mucosa by different mechanisms, including the rearrangement of the phospholipid bilayer and increase of the relevant fluidity, could have a synergistic effect on the overall protein absorption.

At 48 h, NT and SCI-, OI-, NI-, and GPI-administered rats had the blood glucose values return to initial levels while in rats administered with CPNI the blood glucose levels remained persistently and significantly reduced, as compared to the initial values. Such a long-lasting effect could be ascribed to the mucoadhesive properties of the nanocomplex, involving ionic interactions between the positively charged PEI and the negative charges of the mucosal surface. It may be hypothesized that, even if most of the nanoparticles were degraded in the colon lumen, part of them still interacted with the

membrane-bound mucins on the intestinal epithelium, releasing the insulin beyond UWL, in the proximity of the absorptive cells. The UWL, forming a diffusion barrier between the luminal contents and the epithelium, probably maintained an adequate concentration of insulin in proximity of the enterocytes, allowing a prolonged insulin absorption over the whole period. On the contrary, most of the other administered formulations were eliminated previously. These results suggest a two-phase mechanism in rats administered with CPNI. During the first phase, a massive absorption of insulin takes place within the initial hours from the treatment (*i.e.* 6–8 h) as an effect of the rapid release of the drug from the nanoparticles into the colon lumen followed by the PEI-mediated opening of the paracellular route. During the second phase, a long-lasting absorption of the insulin released in proximity of the colon epithelium by the nanoparticles is triggered by active interaction with the negatively charged mucus layer.

At 48 h post-treatment, a slight decrease of blood glucose levels, not significantly different from that observed in NT and orally treated rats, was observed upon administration of CPI, while in GPNI-treated rats, glucose values were still about 70% of the initial values and significantly lower than those of controls. It is likely that the hypoglycemic effect could be attributed to the release of insulin by those nanoparticles which escaped luminal degradation and reached the mucosal surface. In this case, a certain amount of the protein, protected from the proteolytic activity due to the presence of the secretory mucin barrier [36], is still available for the intestinal absorption. This likely occurs through the PEI-activated paracellular pathway.

The colonic delivery of nanoformulated insulin holds a significant potential in clinical practice. This study provides the proof of the concept that the oral delivery of insulin targeted at colonic release and absorption may survive the hostile environments of gastric acidity or the peptidase rich small bowel. Moreover, blood glucose remained nearly half of the initial levels at 48 h post-administration of CPNI, thanks to slow and continuous release of insulin in the colon. This fact is particularly significant, since it may indicate that a prolonged control of glycaemia may be reached with a possible reduction in the overall insulin requirements of the patient resulting in a possible reduction in the number of daily injections. This would result in improved quality of life and potential reduction in long-term complications related to unstable glycemic control. Another goal reached by this novel insulin nanoformulation is the restoration of a physiological delivery of insulin into the portal vein, with a proper liver metabolism. This avoids fluctuating blood glucose levels and allows a more precise control of glycaemia. No fluctuation was observed in blood glucose levels of CPNI-treated rats, in favor of a progressive regular fall of the glycaemia [2,6]. In addition, a low between-subjects variability in blood glucose levels was observed in rats treated with CPNI, suggesting a reproducible response of glycaemia to this novel insulin nanoformulation. The clinical impact of this phenomenon could be important considering that, currently, a major limitation encountered in clinical and preclinical trials with oral insulin delivery so far was the highly variable response of glycemic control [37]. Furthermore, mimicking the physiological insulin circulation in the portal vein and the extraction by the liver, this formulation might obviate the drawbacks of insulin administered subcutaneously: systemic hyperinsulinemia with subsequent possible hypoglycaemia, local lipoatrophy with consequent day-to-day variability of subcutaneous absorption, weight gain, atherogenesis and enhanced lipogenesis. The peripheral administration of insulin is also implicated in the worsening of insulin resistance which makes the adjustment of insulin dosing difficult in, for instance, diabetes Type 2 patients.

Finally, hepatic insulin extraction after colon absorption as opposed to that after peripheral administration might improve

the liver inflammation and the oxidant production involved in the pathogenesis of hepatic steatosis. Therefore, the multitasking nanodevice described in this study for oral delivery of insulin is promising, although further research is needed to better clarify, for example, the efficacy in glycemic control immediately after a meal and the variations caused by oral insulin on various others metabolic and diabetes indicators, such as glucagon, insulin-like growth factor 1 (IGF-1), fructosamine and glycated hemoglobin.

5. Conclusion

Oral insulin delivery remains a clinical challenge, and despite a growing body of publications on this topic, there is still no oral formulation for insulin. In this study, a new approach for the oral administration of insulin is proposed targeting the colon as the release and absorption site. The synergistic effect due to the nanoformulation of insulin and the encapsulation in a triple-layer pellet system for colon-release delivery resulted in a significant and long-lasting hypoglycemic effect. The impact of our multitasking delivery system for oral insulin in controlling diabetes is clinically appealing, since it represents an oral route for insulin administration, with a prolonged hypoglycemic activity and a more physiological insulin metabolism. However, further research is needed to promote this novel nanoformulation into clinical trials.

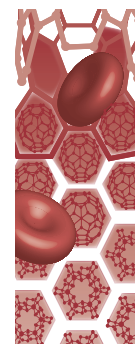
Acknowledgments

This work was supported by Fondazione Regionale per la Ricerca Biomedica (FRRB).

We thank Maurizio Bevilacqua, MD, head of Endocrinology Unit Hospital L.Sacco Milan for methodological support.

References

- [1] T. Bailey, Options for combination therapy in type 2 diabetes: comparison of the ADA/EASD position statement and AACE/ACE algorithm, *Am. J. Med.* 126 (2013) S10–20.
- [2] S. Dal, N. Jeandier, A. Schaschkow, A.H. Spizzo, E. Seyfritz, C. Sookharee, W. Bietiger, C. Péronet, F. Moreau, M. Pinget, E. Maillard, S. Sigris, Portal or subcutaneous insulin infusion: efficacy and impact on liver inflammation, *Fundam. Clin. Pharmacol.* 29 (2015) 488–498.
- [3] A. Maroni, L. Zema, M.D. Del Curto, A. Foppoli, A. Gazzaniga, Oral colon delivery of insulin with the aid of functional adjuvants, *Adv. Drug. Deliv. Rev.* 64 (2012) 540–556.
- [4] M.R. Rekha, C.P. Sharma, Oral delivery of therapeutic protein/peptide for diabetes-Future perspectives, *Int. J. Pharm.* 440 (2013) 48–62.
- [5] F. Sousa, P. Castro, P. Fonte, B. Sarmento, How to overcome the limitations of current insulin administration with new non-invasive delivery systems, *Ther. Deliv.* 6 (2015) 83–94.
- [6] M.M. Patel, Colon targeting: an emerging frontier for oral insulin delivery, *Exp. Opin. Drug Deliv.* 10 (2013) 731–739.
- [7] A. Gazzaniga, A. Maroni, M.E. Sangalli, L. Zema, Time-controlled oral delivery systems for colon targeting, *Exp. Opin. Drug Deliv.* 3 (2006) 583–597.
- [8] S. Haupt, A. Rubinstein, The colon as a possible target for orally administered peptide and protein drugs, *Crit. Rev. Ther. Drug Carr. Syst.* 19 (2002) 499–551.
- [9] S. Bourgeois, R. Harvey, E. Fattal, Polymer colon drug delivery systems and their application to peptides proteins, and nucleic acids, *Am. J. Drug Deliv.* 3 (2005) 171–204.
- [10] C. Dámge, C.P. Reis, P. Maincent, Nanoparticle strategies for the oral delivery of insulin, *Exp. Opin. Drug Deliv.* 5 (2008) 45–68.
- [11] L.M. Ensign, R. Cone, J. Hanes, Oral drug delivery with polymeric nanoparticles: the gastrointestinal mucus barriers, *Adv. Drug Deliv. Rev.* 64 (2012) 557–570.
- [12] A. Bayat, F.A. Dorkoosh, A.R. Dehpour, L. Moezi, B. Larijani, H.E. Junginger, M. Raffee-Tehrani, Nanoparticles of quaternized chitosan derivatives as a carrier for colon delivery of insulin: ex vivo and in vivo studies, *Int. J. Pharm.* 356 (2008) 259–266.
- [13] K. Cheng, L.Y. Lim, Insulin-loaded calcium pectinate nanoparticles: effects of pectin molecular weight and formulation pH, *Drug. Dev. Ind. Pharm.* 30 (2004) 359–367.
- [14] L. Palugan, M. Cerea, L. Zema, A. Gazzaniga, A. Maroni, Coated pellets for oral colon delivery, *J. Drug Deliv. Sci. Technol.* 25 (2015) 1–15.
- [15] A. Maroni, M.D. Del Curto, M. Cerea, L. Zema, A. Foppoli, A. Gazzaniga, Polymeric coatings for a multiple-unit pulsatile delivery system: preliminary study on free and applied films, *Int. J. Pharm.* 440 (2013) 256–263.
- [16] M.D. Del Curto, L. Palugan, A. Foppoli, L. Zema, A. Gazzaniga, A. Maroni, Erodible time-dependent colon delivery systems with improved efficiency in delaying the onset of drug release, *J. Pharm. Sci.* 103 (2014) 3585–3593.
- [17] S.S. Davis, The design and evaluation of controlled release systems for the gastrointestinal tract, *J. Control Release* 2 (1985) 27–38.
- [18] A. Maroni, M.D. Del Curto, M. Serratori, L. Zema, A. Foppoli, A. Gazzaniga, M.E. Sangalli Feasibility, stability and release performance of a time-dependent insulin delivery system intended for oral colon release, *Eur. J. Pharm. Biopharm.* 72 (2009) 246–251.
- [19] F. Casati, L. Palugan, G. Loreti, M.D. Del Curto, L. Zema, A. Gazzaniga, Co-processed microcrystalline cellulose and sodium carboxymethyl cellulose as spheronization aid for disintegrating pellets, in: 54th Simposio AFI, Rimini, 11–13 Giugno, 2014.
- [20] J.J. Lee, H.-Y. Yi, J.-W. Yang, J.-S. Shin, J.-H. Kwon, C.-W. Kim, Characterization of Streptozotocin-induced diabetic rats and pharmacodynamics of Insulin formulations, *Biosci. Biotechnol. Biochem.* 67 (2003) 2396–2401.
- [21] W. Tiyaboonchai, J. Woiszwillo, R.C. Sims, C.R. Middaugh, Insulin containing polyethylenimine-dextran sulfate nanoparticles, *Int. J. Pharm.* 255 (2003) 139–151.
- [22] W. Tiyaboonchai, J. Woiszwillo, C.R. Middaugh, Formulation and characterization of amphotericin B-polyrthylenimine-dextran sulfate nanoparticles, *J. Pharm. Sci.* 90 (2001) 902–914.
- [23] G. Di Pretoro, L. Zema, A. Gazzaniga, S.L. Rough, D. Wilson, Extrusion-spheronisation of highly loaded 5-ASA multiparticulate dosage forms, *Int. J. Pharm.* 402 (2010) 153–164.
- [24] A. Yamamoto, T. Taniguchi, K. Rikyu, T. Tsuji, T. Fujita, M. Murakami, S. Muranishi, Effects of various protease inhibitors on the intestinal absorption and degradation of insulin in rats, *Pharm. Res.* 11 (1994) 1496–1500.
- [25] H. Tozaki, J. Komoike, C. Tada, T. Maruyama, A. Terabe, T. Suzuki, A. Yamamoto, S. Muranishi, Chitosan capsule for colon-specific drug delivery: improvement of insulin absorption from the rat colon, *J. Pharm. Sci.* 86 (1997) 1016–1021.
- [26] A. Maroni, S. Salmaso, M.D. Del Curto, G. Loreti, P. Caliceti, A. Gazzaniga, Preliminary in vivo evaluation of an oral multiple-unit formulation for colonic delivery of insulin, in: 41st Annual Meeting & Exposition of the Controlled Release Society, Chicago, IL, USA, July 13–16, 2014.
- [27] C. Tuleu, C. Andrieux, P. Boy, J.C. Chaumeil, Gastrointestinal transit of pellets in rats: effect of size and density, *Int. J. Pharm.* 180 (1999) 123–131.
- [28] J.M. De Sessa, C.F. Jacobson, Anatomical and physiological parameters affecting gastrointestinal absorption in humans and rats, *Food Chem. Toxicol.* 39 (2001) 209–228.
- [29] J.K. Saha, J. Xia, J.M. Grondin, S.K. Engle, J.A. Jakubowski, Acute hyperglycemia induced by ketamine/xylazine anesthesia in rats: mechanisms and implications for preclinical models, *Exp. Biol. Med.* 230 (2005) 777–784.
- [30] J.P.F. Bai, L.L. Chang, Transepithelial transport of Insulin: i. Insulin degradation by insulin-degrading enzyme in small intestinal epithelium, *Pharm. Res.* 12 (1995) 1171–1175.
- [31] L.L. Chang, L.E. Stout, W.D. Wong, J.G. Buls, D.A. Rothenberger, W.T. Shier, R.L. Sorenson, J.P. Bai, Immunohistochemical localization of insulin-degrading enzyme along the rat intestine in the human colon adenocarcinoma cell line (Caco-2), and in human ileum, *J. Pharm. Sci.* 86 (1997) 116–119.
- [32] G. Ranaldi, I. Marigliano, I. Vespignani, G. Perozzi, Y.J. Sambuy, The effect of chitosan and other polycations on tight junction permeability in the human intestinal Caco-2 cell line, *Nutr. Biochem.* 13 (2002) 157–167.
- [33] G. Sharma, A.R. Sharma, J.-S. Nam, G. Priya, C. Doss, S.-S. Lee, C. Chakraborty, Nanoparticle based insulin delivery system: the next generation efficient therapy for Type 1 diabetes, *J. Nanobiotechnol.* 13 (2015) 74–87.
- [34] Y.H. Lin, C.T. Chen, H.F. Liang, A.R. Kulkarni, P.W. Lee, C.H. Chen, H.W. Sung, Novel nanoparticles for oral insulin delivery via the paracellular pathway, *Nanotechnology* 18 (2007) 105102.
- [35] A. Adson, P.S. Burton, T.J. Raub, C.L. Barsuhn, K.L. Audus, N.F. Ho, Passive diffusion of weak organic electrolytes across Caco-2 cell monolayers: uncoupling the contributions of hydrodynamic, transcellular, and paracellular barriers, *J. Pharm. Sci.* 84 (1995) 1197–1204.
- [36] G.J. Strous, J. Dekker, Mucin-type glycoproteins, *Crit. Rev. Biochem. Mol. Biol.* 27 (1992) 57–92.
- [37] E. Zijlstra, L. Heinemann, L. Plum-Mörschel, Oral insulin reloaded: a structured approach, *J. Diabet. Sci. Technol.* 8 (2014) 458–465.



Antibody-engineered nanoparticles selectively inhibit mesenchymal cells isolated from patients with chronic lung allograft dysfunction

Aims: Chronic lung allograft dysfunction represents the main cause of death after lung transplantation, and so far there is no effective therapy. Mesenchymal cells (MCs) are primarily responsible for fibrous obliteration of small airways typical of chronic lung allograft dysfunction. Here, we engineered gold nanoparticles containing a drug in the hydrophobic section to inhibit MCs, and exposing on the outer hydrophilic surface a monoclonal antibody targeting a MC-specific marker (half-chain gold nanoparticles with everolimus). **Materials & methods:** Half-chain gold nanoparticles with everolimus have been synthesized and incubated with MCs to evaluate the effect on proliferation and apoptosis. **Results & discussion:** Drug-loaded gold nanoparticles coated with the specific antibody were able to inhibit proliferation and induce apoptosis without stimulating an inflammatory response, as assessed by *in vitro* experiments. **Conclusion:** These findings demonstrate the effectiveness of our nanoparticles in inhibiting MCs and open new perspectives for a local treatment of chronic lung allograft dysfunction.

Original submitted 24 July 2013; Revised submitted 15 October 2013

Keywords: antifibrotic agent • bronchiolitis obliterans syndrome • chronic lung allograft dysfunction • mesenchymal cell • targeted drug-loaded nanoparticle

Background

Gold nanoparticles (GNPs) are among the most intensely studied nanomaterials due to their unique size-dependent electronic and optical properties [1,2] combined with a great potential in a broad range of biomedical applications [3–11], among which the most common is drug-delivery vehicles [12,13]. However, in order to be useful in biomedicine, GNPs need surface modification to enhance stability in a biological environment and functionalization to improve delivery and target selectivity [5]. When GNPs are used as drug carriers, the drug can be physically adsorbed on the metal surface [14], included inside internal cavities [15], or reversibly anchored through a covalent bond [16]. Furthermore, GNPs with size above 6–8 nm are generally believed to be acceptably safe materials [17–19].

Lung transplantation represents the ultimate treatment option for patients with end-stage pulmonary disease [20]. However, long-term graft and patient survival continue to be challenged by chronic lung allograft dysfunction, which accounts for more than 30% of deaths after the third postoperative year, and the 5-year survival after chronic lung allograft dysfunction onset is only 30–40% [21]. The most frequent chronic lung allograft dysfunction phenotype is represented by bronchiolitis obliterans syndrome (BOS), whose histological correlate is obliterans bronchiolitis, characterized by a patchy submucosal fibrosis causing total occlusion of tracts of bronchiolar lumen [22]. Although the exact pathogenesis of BOS is still unknown, it is believed that an insult to the epithelium precedes an amplification of

Emanuela Cova^{*1}, Miriam Colombo^{*2}, Simona Inghilleri¹, Monica Morosini¹, Simona Miserere¹, Jesus Peñaranda-Avila², Benedetta Santini², Davide Piloni¹, Sara Magni¹, Furio Gramatica³, Davide Prosperi^{*2,3} & Federica Meloni^{*1,4}

¹Clinica di Malattie dell'Apparato Respiratorio, IRCCS Fondazione Policlinico S Matteo, viale Golgi 19, 27100 Pavia, Italy

²Dipartimento di Biotecnologie e Bioscienze, Università di Milano-Bicocca, Piazza della Scienza 2, 20126 Milano, Italy

³Laboratorio di Biofisica e Nanomedicina, Polo Tecnologico, Fondazione Don Gnocchi IRCCS-ONLUS, via Capacelatro 66, 20148 Milan, Italy

⁴Dipartimento di Medicina Molecolare, Unità di Pneumologia, Università di Pavia, viale Golgi 19, 27100 Pavia, Italy

*Author for correspondence:

Tel.: +39 0382 501 007

Fax: +39 0382 422 704

f.meloni@smatteo.pv.it

[#]Authors contributed equally

both innate and adaptive immune responses. Chronic or recurrent exposure to several inflammatory triggers unbalance local response from graft tolerance to allo- or auto-immunity, mainly of the Th17 pattern, driving the typical neutrophilic inflammation of BOS [23–25]. Activated neutrophils can further damage the epithelium by releasing reactive oxygen species, chemokines, alarmins and metalloproteinases [26–28]. This inflammatory phase is ultimately followed by a fibroproliferative phase, leading to proliferation of mesenchymal cells (MCs) whose origin, from extrapulmonary or resident stem cells or epithelial mesenchymal transitional cells, is still in debate [29–31]. Although MC proliferation and extracellular matrix deposition are physiological processes in the reparative course, they appear excessive and uncontrolled in transplanted lungs, thus leading to irreversible obliteration of airway lumen [32,33]. From a clinical point of view, BOS is characterized by a reduction of the pulmonary function parameters and four stages, namely BOS 0p, 1, 2 and 3, have been defined based on the rate of airway obstruction [22]. Unfortunately, functional diagnosis is usually made in an advanced stage; thus, therapeutic strategies, founded either on the prevention/treatment of the inflammatory phase preceding fibrotic evolution or on the use of so called ‘antifibrotic drugs’ targeting MCs, are usually poorly effective [34]. Among the agents with antimitogen action, everolimus, an inhibitor of mTOR, also endowed with potent immunosuppressive activities, has been demonstrated to suppress the *in vitro* proliferation of fibroblast isolated from BOS patients [35–37]. Nevertheless, both treatment strategies (i.e., prevention of inflammatory phase and antiproliferative action) have shown poor clinical response, partly because limited by systemic drug toxicity and by insufficient drug accumulation at target sites [38–41]. Recently, innovative approaches based on the administration of aerosolized cyclosporine or tacrolimus along with systemic immunosuppression, resulted in a survival improvement and extended periods of BOS-free survival [42] or in an improvement in graft function and oxygenation [43]. Therefore, the local administration of drugs is still a promising strategy, possibly because it directly targets the pathogenic effectors into airways without additional systemic toxicity. However, many aerosolized agents may exert toxicity towards epithelial cells, thus perpetuating the vicious cycle of injury/repair [44]. The possibility of targeting a local drug delivery specifically to fibroblasts by inhalation of biocompatible GNPs might minimize epithelial damage and systemic toxicity compared with systemic administration of

everolimus, and may represent the best solution to fulfill the above claims.

Based on these remarks, we have designed this study aiming to develop a new nanovehicle-based treatment that could be delivered by local route, targeting MCs, the ultimate BOS effector [31,45]. In this work, we assayed the effect of GNPs loaded with everolimus on MCs, cultured from bronchial lavage (BAL) of patients affected by different grades of BOS. GNPs have been functionalized to specifically target CD44 expressed by primary MCs, in view of avoiding possible toxic effects on epithelial cells. In addition, a possible deleterious proinflammatory effect of our nanovectors has been assessed. The activation of macrophages, the first innate defense line in lung, and neutrophils that exert a crucial role in BOS pathogenesis, has been evaluated and excluded.

Materials & methods

Synthesis of everolimus-loaded fluorescent GNPs functionalized with anti-human CD44

Organic, soluble GNPs, with an average size of approximately 6 nm, synthesized according to the Brust protocol [46] were transferred from organic to aqueous solution undergoing a coating procedure with the amphiphilic polymer PMA, obtained by condensation of poly-(isobutylene-alt-maleic anhydride) and dodecylamine (25% anhydride, 75% C₁₂COOH) [47]. Nanogold coated with PMA (500 µl, 4 µM), was reacted with 1-ethyl-3-(3-dimethylaminopropyl)-carbodiimide (20 µl, 1 M) for 2 min, then 2,2-(ethylenedioxy)bis(ethylamine) (80 µl, 0.05 M) was added and stirred for 2 h. Next, the nanoparticle dispersion was concentrated and washed two additional times with water. Nanoparticles were shaken for 4 h in the presence of *N*-succinimidyl-3-[2-pyridyldithio]-propionate (500 µl, 10 mg ml⁻¹ in dimethyl sulfoxide), concentrated and washed twice with water (GNP 3-[2-pyridyldithio]-propionate [PDPs]). Next, lyophilized monoclonal anti-human CD44 (CD44 monoclonal antibody [mAb]; 400 µg) dissolved in phosphate-buffered saline (PBS) EDTA (0.5 ml) was added to the 2-mercaptoethanolamine kit (Thermo Scientific; NY, USA) and treated to reduce the disulfide bridges between the two heavy chains of IgG, obtaining the half-chain antibody portions (HCs). HC was immediately added to 100 µl of the thiol-reactive GNP-PDPs (3 µM) and incubated at room temperature for 1 h. The residual PDP functional groups were saturated with excess MeO-PEG5000-SH. The excess of chemicals and biological reagents was removed by dialysis and the GNP-HCs were collected. For the studies with cell

cultures, we used CD44 mAb labeled with Alexa Fluor® (Invitrogen; CA, USA) 488 dye. Everolimus dissolved in ethanol (50 µl, 10 µg ml⁻¹) was added to the GNP-HC solution (1 ml, 1 mg ml⁻¹) and incubated overnight at 4°C. Finally, the nanoparticles were concentrated at 3500 rpm for 10 min and washed with PBS. The amount of encapsulated drug was double-checked as described in the text.

Synthesis of fluorescent PEG-functionalized GNPs

FITC-labeled PMA (0.5 M) was obtained by reacting 0.5 M PMA (5 ml of in CHCl₃) overnight at room temperature with 1.0 M fluoresceinamine (0.5 ml) in ethanol. Next, it was reacted with GNPs as described above. A GNP@PMA solution (250 µl of 4 µM solution), was reacted with 1 M 1-ethyl-3-(3-dimethylaminopropyl)-carbodiimide (9.5 µl) for 2 min, then 27 µl of *O*-(2-aminoethyl)-*O*'-methyl-PEG (PEG2000-NH₂, MW 2000, 0.1 M in water) was added and stirred for 2 h. The excess of PEG was removed by concentration at 3500 rpm through 100 kDa Amicon® (Sigma-Aldrich; Milan, Italy) filters. The concentrated solution was washed twice in the same way and the nanoparticles were then recovered as a stock solution in PBS.

In vitro drug release

Half-chain gold nanoparticles with everolimus (GNP-HCes; ~2 mg) were placed within dialysis membranes (30 kDa MW cut-off), able to retain the nanoparticles and suitable for free diffusion of everolimus molecules, and dipped in 6 ml of PBS buffer (154 mM, pH 7.4), 2% bovine serum albumin was added as a natural protein surfactant in order to increase apparent solubility of everolimus up to approximately 600 mM to reproduce sink conditions during dissolution test. Dissolution medium was kept at 37 ± 0.5°C and magnetically stirred at 100 rpm. At predetermined time intervals, samples (1 ml) were analyzed with ultra violet light spectrophotometrically at 424 nm. The remaining part of dissolution medium was entirely withdrawn and replaced with 6 ml of fresh medium. Each experiment was conducted in triplicate.

Patients

From October 2011 to December 2012, 33 BAL samples were collected from 24 lung transplant recipients. Clinical features of these lung transplantation recipients are shown in Table 1. BOS diagnosis was made according to published criteria [48]. Enrolled patients received a standard triple-drug regimen consisting of cyclosporine or tacrolimus plus azathioprine or mycophenolate mofetil and low-dose steroids. All BOS 1 and BOS 2 patients had been classified as nonresponder to macrolides

after a 3-month course with 250 mg azitromycin every other day (failed to improve forced expiratory volume in 1 s >10%). Macrolide unresponsive patients, upon consent to treatment, were submitted to extracorporeal photophoresis, as previously published [49]. Each patient gave informed consent to the procedure.

Cell culture & isolation from BAL

MCs were isolated from BAL obtained following standard recommendations [50]. Two million cells were seeded in high-glucose DMEM with 10% fetal calf serum, and 100 units ml⁻¹ penicillin/streptomycin solution. Single foci of MCs formed between 7–28 days, and representing the only remained cells, were isolated and collected. Afterwards, they were characterized using a panel of antibodies and spread in new culture dishes. For the experiments, cells of three patients (BOS 0p, 1 and 2), between the second and fifth passage after isolation were used. A transformed primary cell line, 16HBE, retaining differentiated bronchial epithelial morphology and function [51] was used for the experiments as MCs. 16HBE cells were cultured in minimal essential medium with 10% fetal calf serum, and 100 units ml⁻¹ penicillin/streptomycin solution. For the experiments, GNP-HCes and GNP-HCs (150 nM) were added to the culture medium of MCs and 16HBE and left for 2 h at 37°C in 5% CO₂ incubator. As controls, the cells were incubated in full medium with the same experimental conditions. As further controls, MCs were treated with 1 µg/ml of CD44 mAb (clone 2C5, R&D System; MN, USA) or 0.003 µg/ml of everolimus. Preliminary experiments proved the unsuitability of both lower (100 nM) and higher (200 nM) concentrations of GNP-HCes, the first being too scarce to release enough everolimus and the second cytotoxic.

Cell characterization by flow cytometry

Surface phenotypes of all isolated MCs at first passage were evaluated using fluorochrome-labeled antibodies (CD44-FITC, CD105-FITC, CD90-PE, CD34-ECD and CD45-APC750 [Instrumentation Laboratory; Milan, Italy]) by flow cytometry (Navios™ [Beckman Coulter Inc.; CA, USA] Flow cytometer) and data analyzed using Kaluza® software (Beckman Coulter Inc.). The appropriate mouse immunoglobulin isotypes were used as control. 16HBE cells were assayed for CD44 expression only with the same method.

Immunocytochemical & immunohistochemical analyses

MCs, cultured on Lab-Tek® II Chamber Slides™ (Thermo Scientific), were fixed with 2% paraformaldehyde for 10 min and permeabilized

Table 1. Clinical features of enrolled patients and surface characterization of primary mesenchymal cells isolated from bronchoalveolar lavage.

Age [†] (years)	Transplant type, indication	Lung function (%)	FU (months)	IS regimen	BAL (M/L/N/E [%])	MC	CD44	CD34	CD45	CD90	CD105
54	BLT, PAH	100	3	TAC, MMF, PRD	93/7/0/0	No					
58	BLT,COPD	93	7	TAC, MMF, PRD	93/6/1/0	Yes	++	-	-	++	++
41	BLT,COPD	30	153	CyA, EVR, PRD	56/26/15/3	No					
54	BLT,COPD	86	13	TAC, MMF, PRD	95/4/1/0	Yes	++	-	-	++	+
47	BLT,COPD	65 (AR2)	3	TAC, MMF, PRD	26/66/8/0	Yes	++	-	-	++	++
55	BLT,IPF	100	3	TAC, MMF, PRD	71/28/1/0	Yes	++	-	-	++	+
56	SLT,IPF	87	59	TAC, MMF, PRD	65/33/1/1	No					
35 [‡]	SLT/fibrosis	80	288	TAC, PRD	68/31/1/0	Yes	++	-	-	++	++
38 [‡]	SLT/IPF	89	25	TAC, MMF, PRD	61/12/27/0	Yes	++	-	-	++	++
45	SLT/IPF	69	20	TAC, MMF, PRD	43/5/46/6	No					
56	SLT/IPF	32	120	TAC, MMF, PRD	75/22/3/0	Yes	++	-	-	++	+
39	BLT/BOS	93	8	CyA, EVR, PRD	87/8/5/0	No					
24	BLT/CF	77	184	TAC, PRD, AZITR	95/4/1/0	No					
34	BLT/Bronch	63	105	TAC, PRD, AZITR	90/8/2/0	Yes	++	-	-	++	n.d.
27	SLT/LAM	85	214	CyA, EVR, PRD	29/31/38/2	No					
61	BLT/COPD	68	89	TAC, MMF, PRD	96/1/3/0	No					
56	SLT/IPF	81	110	TAC, MMF, PRD	90/5/5/0	No					
59 [‡]	BLT/IPF	70	89	TAC, MMF, PRD	96/3/1/0	Yes	++	-	-	++	++
64	SLT/IPF	100 (CMV)	3	TAC, MMF, PRD	93/7/0/0	Yes	++	-	-	+	+
36	BLT/CF	100	3	TAC, MMF, PRD	65/34/1/0	Yes	++	-	-	++	++
42	BLT/CF	100	41	TAC, MMF, PRD	82/14/4/0	No					
38	BLT/PAH	37	162	TAC, PRD, AZITR	71/5/24/0	Yes	++	-	-	+	+
48	SLT/IPF	82	51	TAC, MMF, PRD	91/7/2/0	No					
27	BLT/PAH	59	37	CyA, EVR, PRD	53/16/30/1	No					

[†]At lung transplantation.

[‡]These rows are the patients whose cells have been used for the experiments with nanoparticles.

-: Positive cells less than 10%; +: Positive cells between 10 and 50%; ++: Positive cells more than 50%; AR2: Acute cellular rejection grade 2; AZITR: Azithromycin; BAL: Bronchoalveolar lavage; BLT: Bilateral lung transplantation; BOS: Bronchiolitis obliterans syndrome; Bronch: Bronchiectasis; CF: Cystic fibrosis; CMV: Positive to cytomegalovirus; COPD: Chronic obstructive pulmonary disease; CyA: Cyclosporin; E: Eosinophil; EVR: Everolimus; FU: Length of follow-up at time of bronchoalveolar lavage sampling; IPF: Idiopathic pulmonary fibrosis; IS: Immunosuppression; L: Lymphocyte; LAM: Lymphangiomyomatosis; M: Macrophage; MC: Primary mesenchymal cell isolation from bronchoalveolar lavage; MMF: Mycophenolate mofetil; N: Neutrophil; n.d.: Not determined; PAH: Pulmonary arterial hypertension; PRD: Pirfenidone; SLT: Single lung transplantation; TAC: Tacrolimus.

with 0.1% Triton™ (Sigma-Aldrich) X-100. Immunohistochemical analysis on human biopsies was performed on 4-µm thick paraffin sections incubated at 60°C overnight, deparaffinized and treated for 40 min in EDTA buffer for heat-mediated antigen retrieval. Afterwards, the slides with cells and biopsies were treated with blocking solution and incubated with the primary antibodies, CD44 mAb and anti-phospho-mTOR (rabbit monoclonal; clone 49F9 [Cell Signaling; IL, USA]). After inhibition of endogenous peroxidase, positive reaction was revealed using ImmPRESS™ detection system (Vector Laboratories

Inc.; CA, USA). Slides were counterstained with hematoxylin and eosin.

GNP-HCe cell uptake

GNP-HCe uptake was evaluated by confocal microscopy and flow cytometry. GNPs that were not functionalized (GNP-PEGs) were used to evaluate the uptake specificity. For confocal microscopy experiments, cells were seeded on collagen precoated glass slides and used at subconfluence. Entrance of GNP-HCes and GNP-PEGs was evaluated starting 15 min through 2 h at 37°C in medium. Then,

slides were fixed with 4% paraformaldehyde and incubated for 10 min with 0.1 M glycine in PBS solution. Samples were treated with a blocking solution and slides were stained with 4',6-diamidino-2-phenylindole solution. Microscopy analysis was performed using confocal laser microscope (Leica DM IRBE [Leica Microsystems; Milan, Italy]). For flow cytometry experiments (Navios Flow Cytometer), cells incubated 2 h with GNP-HCes or GNP-PEGs marked with Alexa Fluor 488 were trypsinized and analyzed.

Cell proliferation & apoptosis assays

Proliferation and apoptosis rate were evaluated by carboxy-fluorescein succinimidyl ester (BD Pharmingen; Milan, Italy) and annexin V (Molecular Probes, Life Technologies; Milan, Italy) by flow cytometry. Fluorescence of carboxy-fluorescein succinimidyl ester was evaluated at 24, 48, 72 and 120 h, while apoptosis rate was assayed at 8, 24 and 48 h after different treatments. Proliferation and

apoptosis were expressed as percentage of dividing and apoptotic cells, respectively.

Macrophage & neutrophil isolation

Macrophages were isolated from patients' BAL by adhesion procedure. Cells recovered from BAL were seeded in 24-well plates at concentration of 5×10^5 cells/well in Roswell Park Memorial Institute medium containing 10% heat-inactivated fetal calf serum for 2 h at 37°C to allow macrophage adhesion. For neutrophil isolation a buffy-coat sample was separated by gradient stratification with Lympholyte® (Cedarlane Laboratories; ON, Canada). After washing with PBS, the cells were resuspended in Roswell Park Memorial Institute media, counted with a Bürker chamber and used for the experiments.

Macrophage & neutrophil activation assay

The activation of macrophages was evaluated by assaying the release of IL-8 by ELISA procedure in the culture medium after 24 h incubation with

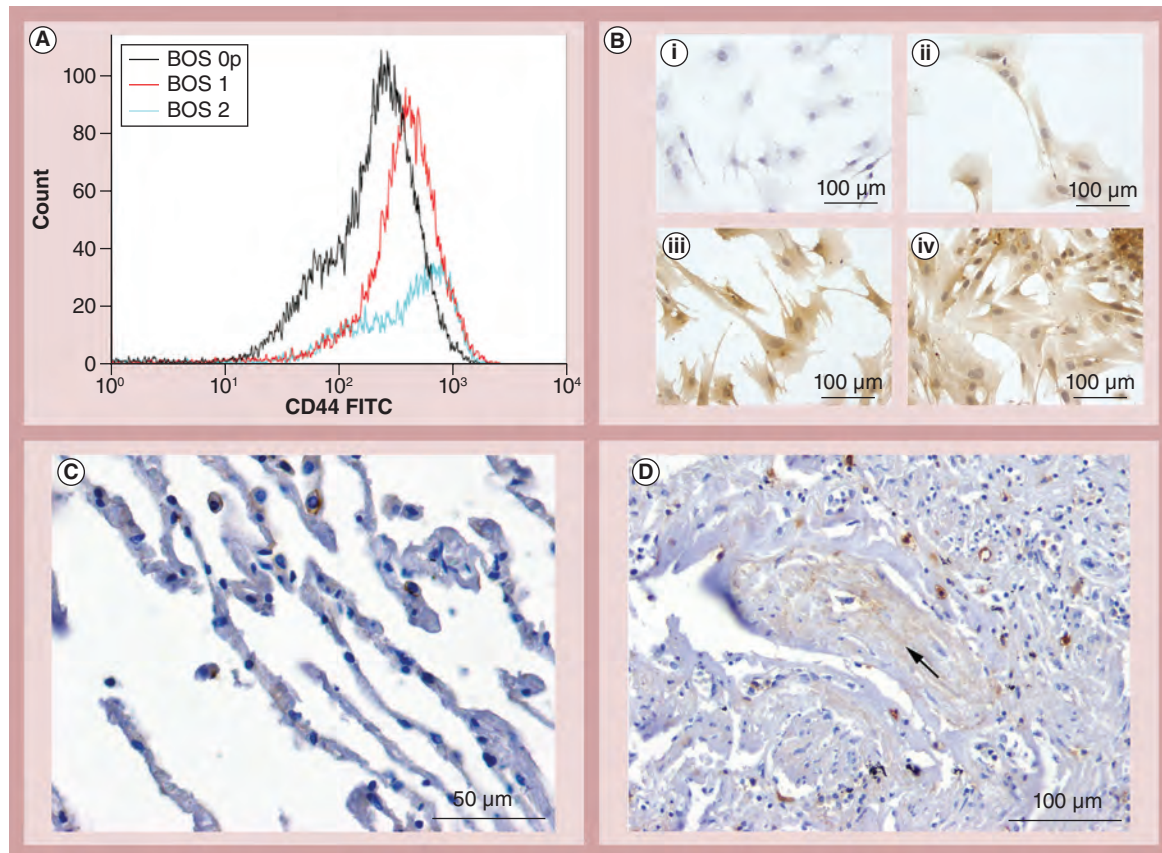


Figure 1. CD44 expression on mesenchymal cell surface, and in normal and bronchiolitis obliterans syndrome epithelia. CD44 was detected by (A) flow cytometry and (B) immunocytochemistry on the three cell lines used in the experiments; (i) negative control, (ii) BOS 0p, (iii) BOS 1 and (iv) BOS 2. Immunohistochemistry procedure demonstrated that (C) normal alveolar epithelia did not express CD44, (D) while cells invading bronchiolar lumen, indicated by the arrow, from a patient retransplanted for BOS, were positive to CD44 monoclonal antibody. BOS: Bronchiolitis obliterans syndrome; FITC: Fluorescein isothiocyanate.

GNP-HCes or GNP-PEGs. The amount of IL-8 in each sample was determined by ELISA. The activation of neutrophils was assayed evaluating the elastase release by enzymatic assay. Untreated macrophages and neutrophils were respectively used as control.

Statistical analysis

Statistical differences between untreated cells, cells treated with GNP-HCes, GNP-HCs, CD44 mAbs and everolimus were evaluated using ANOVA analysis. All analyses were carried out with Graph Prism 5.0 statistical program. A p-value <0.05 was considered statistically significant.

Results

Cell characterization

MCs were isolated only from 30% of BAL of patients and were characterized at the first culture passage. CD44 expression ranged between 84 and 99% of isolated cells (Figure 1A), while the positivity for CD90 and CD105 varied more appreciably between 60–84 and 47–87%, respectively. The expression of these markers is reported in Table 1. Cells isolated from different patients were all negative for CD34 and CD45. No differences in marker expression were recordable between stable and BOS patients. The absence of the epithelial marker E-cadherin was

assessed by immunocytochemical (ICC) experiments (data not shown). ICC also confirmed the high percentage of CD44 positivity in all isolated MCs (Figure 1B). 16HBE epithelial cells did not express CD44, as proved by flow cytometry experiments (data not shown).

CD44 expression on normal & pathologic epithelia

To avoid possible adverse effect of GNPs functionalized with the specific CD44 mAbs on epithelial cells, we evaluated the presence of the glycoprotein on the surface of bronchiolar epithelium. Immunohistochemical experiments demonstrated that normal, not-inflamed epithelia did not express CD44 (Figure 1C) confirming the validity of the selected marker. Positive reaction was evident in cells invading the bronchiolar lumen in specimens from a BOS patient who underwent retransplant (Figure 1D).

Expression of the mammalian target of everolimus, mTOR, in MCs

We found that MCs isolated from BAL of lung transplant recipients expressed an active form of mTOR in the cytosol (Figure 2A), stating the potential effectiveness of the selected drug in inhibiting MC proliferation.

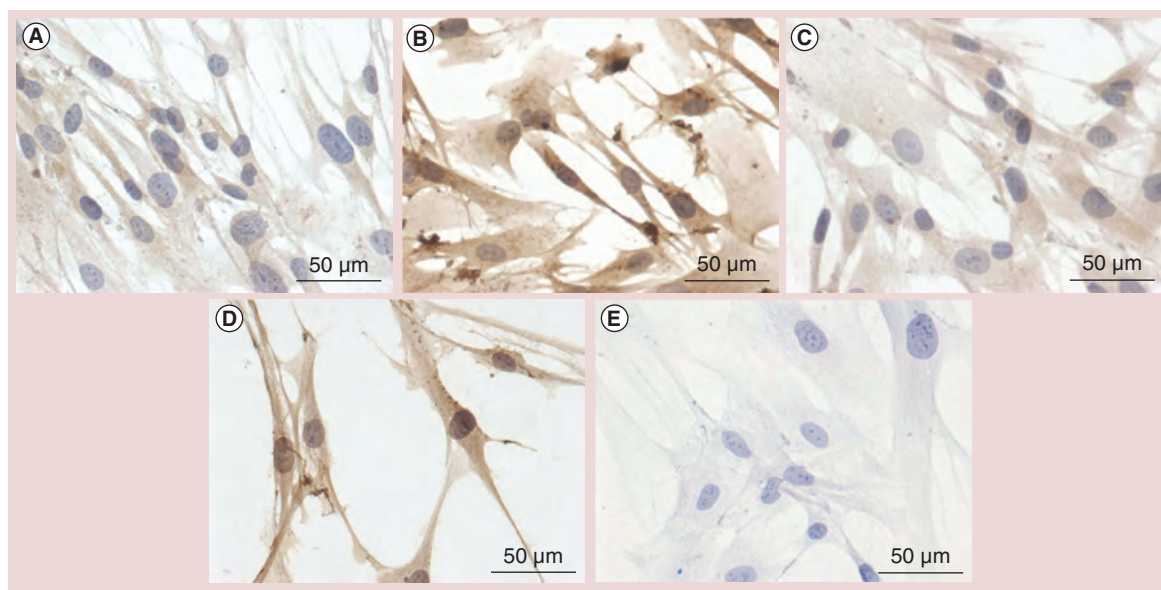


Figure 2. Expression of phospho-activated form of mTOR in mesenchymal cells. The expression was evaluated by immunocytochemistry in (A) untreated control cells, (B) cells treated with half-chain gold nanoparticles (GNPs) with everolimus, (C) cells treated with GNP-PEG and (D) anti-CD44 monoclonal antibody. The protein level in (A) untreated cells was similar in all cell lines. The expression of phosphoactivated form of mTOR was highly increased (B) 12 h after a 2-h incubation with half-chain GNPs with everolimus, (C) while no effect was detectable with GNP-PEG in the same experimental conditions. A stimulatory effect similar to that observed in half-chain GNPs with everolimus was present 12 h after a 2-h incubation with anti-CD44 monoclonal antibody (1:100). (E) Negative control reaction is shown.

Synthesis & characterization of anti-human CD44-functionalized GNPs loaded with everolimus

Our first goal was to synthesize an innovative nanocarrier targeting MCs and efficiently encapsulating and releasing everolimus, which should be optically detectable in order to monitor their distribution.

Hydrophobic GNPs (6 nm) were synthesized in organic solvents [46] and transferred to water phase by coating them with an amphiphilic polymer (PMA) [47]. The resulting GNP@PMAs were further functionalized with *N*-succinimidyl-3-[2-pyridyldithio]-propionate [52] (GNP-PDPs; hydrodynamic size = 24.7 ± 1.3 nm by dynamic light scattering). The resulting

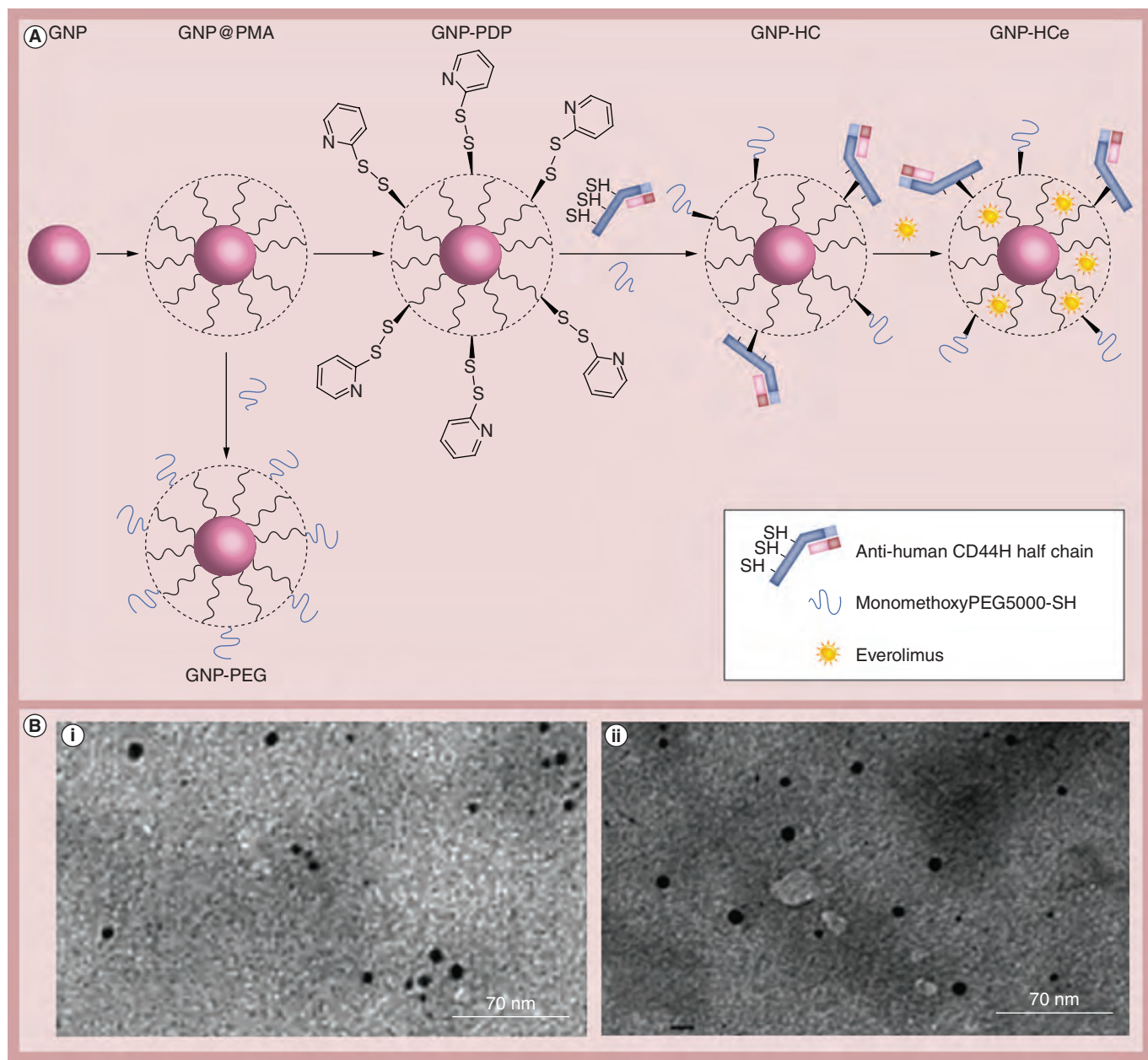


Figure 3. Synthesis of fully armed half-chain gold nanoparticles with everolimus, and PEGylated gold nanoparticles. (A) Hydrophobic GNPs were synthesized and coated with an amphiphilic polymer PMA. The resulting GNP@PMA were functionalized with *N*-succinimidyl-3-[2-pyridyldithio]-propionate (GNP-PDPs). The thiol-reactive PDP functionalities were exploited for the immobilization of heavy-chain CD44 monoclonal antibodies (GNP-HC) labeled with Alexa® (Invitrogen; CA, USA) Fluor 488 dye. As a control, we also synthesized fluorescently labeled, PEGylated GNPs. Finally, GNP-HCs were loaded with everolimus (GNP-HCe). (B) Transmission electron microscopy images showed that (i) GNP-HCs and (ii) GNP-HCe exhibited the same hydrodynamic size. GNP: Gold nanoparticle; HC: Half chain; HCe: Half chain with everolimus; PDP: 2-pyridylthiopropionate.

thiol-reactive PDP functionalities were exploited for the immobilization of two HCs of the anti-human CD44 antibody and the residual thiol-reactive groups on the polymer were saturated with monomethoxy-PEG-thiol (5 kDa), which acted as a colloidal stabilizer and reduced nonspecific interactions (GNP-HCs; hydrodynamic size = 47.3 ± 1.0 nm). As a control, we also synthesized fluorescently labeled, GNP-PEGs (hydrodynamic size = 29.8 ± 2.4 nm). The synthetic strategy is illustrated in Figure 3. Finally, GNP-HCs were loaded with everolimus by incubating overnight at 4°C (GNP-HCs) obtaining a loading efficiency of approximately 0.5 mg everolimus per mg of GNP-HCs. The hydrodynamic size measured by dynamic light scattering changed from 19.8 ± 2.6 nm (GNP@PMAs) to 47.3 ± 1.0 nm (GNP-HCs) and 46.7 ± 1.8 nm (GNP-HCs). Transmission electron microscope images confirmed the colloidal stability of GNP-HCs and GNP-HCs in aqueous dispersion and showed that no apparent changes in size and shape of the metal core were associated to the surface modifications of nanoparticles (Figure 3). As expected, GNP-HCs and GNP-HCs exhibited the same hydrodynamic size, corroborating the hypothesis that everolimus incorporated inside the polymer shell basically did not affect the overall colloidal stability of nanoparticles.

In vitro drug release kinetics

Figure 4 illustrates the release of everolimus from GNP-HCs into PBS buffer (pH 7.4) containing 2% bovine serum albumin. It could be noticed that the

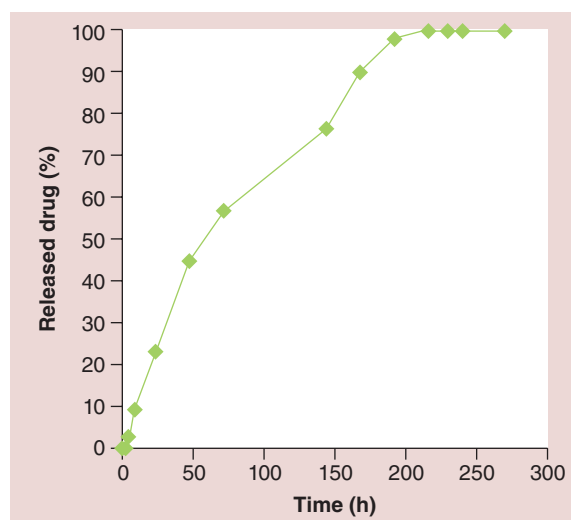


Figure 4. Curve of everolimus release from half-chain gold nanoparticles with everolimus into phosphate-buffered saline buffer. The loaded drug was released in a controlled way and 90% of half-chain gold nanoparticles with everolimus was dissolved in 8 days. A lag phase in everolimus release, approximately 3–5-h long, was recorded.

loaded drug was released in a controlled way and 90% of GNP-HCs were dissolved in 8 days. Surprisingly, the expected burst effect was not observed in this case, but a lag phase was detected. This retard in the everolimus release was approximately 3–5-h long and it could be ascribed to a sort of activation of the polymer due to the interaction with release medium; probably a process of PMA unfolding is necessary to permit the release of the entrapped drug. Based on these data, the drug release mechanism cannot be easily explained. For this reason, to interpret the release profile a Korsmeyer–Peppas model, suitable to describe different drug release profiles, has been applied:

$$ft = at^n \text{ (Equation 1)}$$

where ft is the cumulative percentage of drug released at time (t); a is a constant that incorporates structural and geometric characteristics of the drug dosage form; n is the release exponent, indicative of the drug release mechanism. To determine the exponent (n), the portion of the release curve where the amount of drug released after $t < 60\%$ was used [53]. Due to the presence of a lag time (l) in the first section of the release profile, a modified form of Korsmeyer–Peppas equation could be applied:

$$ft = a(t - l)^n \text{ (Equation 2)}$$

Fitting the data of the percentage of released drug and considering data up to 60% (72 h), the resulting equation is:

$$ft = 0.1863(t - l)^{0.8765} \text{ (} R^2 = 0.9895 \text{) (Equation 3)}$$

It interesting to note that exponent value is very close to 0.89, the value that, considering the structural and geometric characteristics of the dosage form, indicates a zero-order drug release. Equation fitting drug release data points using data up to 98% (192 h) is:

$$ft = 0.2719(t - l)^{0.7776} \text{ (} R^2 = 0.9813 \text{) (Equation 4)}$$

that surprisingly shows a very good fitting. Exponent value decreases with respect to the previous one, indicating a profile bending that is symptomatic of a moderate influence of drug amount remaining in the nanoparticles to the drug release rate.

GNP-HCe cell uptake

To evaluate nanoparticle uptake, experiments were performed adding GNP-HCs labeled with Alexa

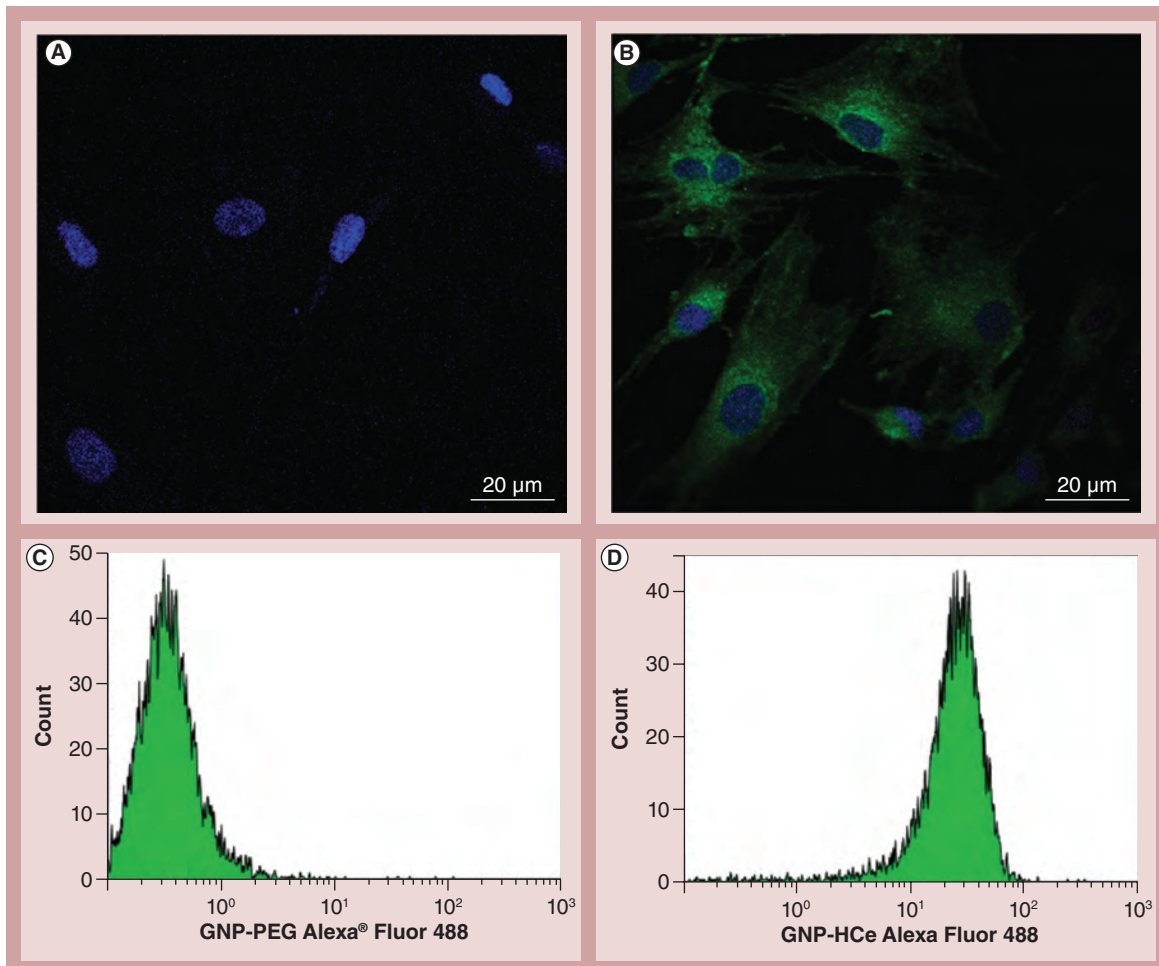


Figure 5. Half-chain gold nanoparticles with everolimus internalization in mesenchymal cells. To evaluate nanoparticle uptake and specificity, mesenchymal cells were incubated with GNP-HCe labeled with Alexa[®] (Invitrogen; CA, USA) Fluor 488 fluorescent dye. Internalization was detected by confocal microscopy along the z-axis and by flow cytometry. (B) Images showed that only functionalized nanoparticles were able to enter into mesenchymal cells within 1 h. (D) Scatter plots confirmed the positivity to fluorescence only in mesenchymal cells incubated with GNP-HCe. By contrast, (A & C) inert GNP-PEG, marked with the same fluorochrome, were not captured by the cells even after 8 h incubation. Original magnification: 60 \times . GNP: Gold nanoparticle; HCe: Half-chain with everolimus.

Fluor 488 fluorescent dye to the complete culture medium and observing their entrance from 15 min to 2 h. Internalization was detected by means of confocal microscopy along z-axis and by flow cytometry. Confocal microscopy images and scatterplot analysis showed that only HC-functionalized nanoparticles were able to enter into MCs within 1 h and remained inside, proving the uptake specificity (Figures 5B & 5D). By contrast, inert GNP-PEGs, marked with the same fluorochrome, were not captured by the cells even after 8 h incubation (Figures 5A & 5C). No differences were observed in particle uptake by different primary cells. For cell proliferation and apoptosis experiments, nanoparticles were left 2 h in culture to allow their full entrance into the cells.

Effect of GNP-HCes on MC proliferation & apoptosis

The inhibitory effect of GNP-HCes on MCs was assayed either by evaluating the inhibition of the proliferation rate or the increase in the percentage of apoptotic cells. To detect a possible toxic effect of functionalized GNPs without everolimus (GNP-HCs) inside the cells, GNP-HCs were used as control under the same experimental conditions. As further control, CD44 mAb alone was used to exclude an unspecific action of the antibody linked to the GNP surface on cell proliferation. MCs derived from three patients with different BOS grades (0p, 1 and 2), were analyzed to estimate whether BOS severity could influence GNP-HCe effectiveness. The results showed that GNP-HCes inhibited cell proliferation in all cells without significant differences between the three series.

In particular, the effect of the drug was significant at 24, 72 and 120 h after incubation while, in all experiments, proliferation rate invariably showed a tendency to increase at 48 h (Figure 6). As a result, no significant difference with control cells was detectable at this time point. Since this result was recovered in all MCs, we hypothesized that the interaction of CD44 mAb with CD44 could produce a remarkable biological effect, inducing cell proliferation.

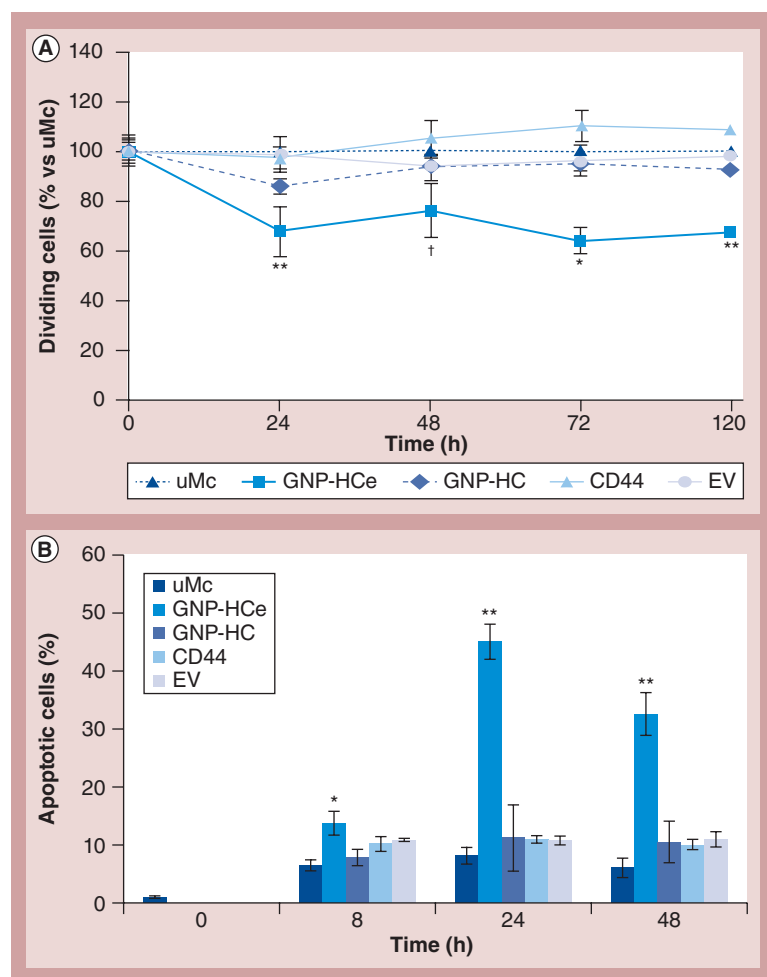


Figure 6. Effect of half-chain gold nanoparticles with everolimus on mesenchymal cell proliferation and apoptosis.

* $p < 0.05$ versus uMC, GNP-HC, CD44 and EV.

** $p < 0.01$ versus uMC, GNP-HC, CD44 and EV.

† $p < 0.05$ versus CD44.

(A) The proliferation rate was evaluated by carboxy-fluorescein succinimidyl ester at 24, 48, 72 and 120 h after 2 h incubation with GNP-HCe, GNP-HC, CD44 and EV. The results are referred to normal proliferation rate of uMCs cultured in the same experimental conditions.

(B) The apoptosis was evaluated by Annexin V incorporation at 8, 24 and 48 h after 2 h incubation with GNP-HCe, GNP-HC, CD44 and EV. The percentage of apoptotic cells is reported for uMCs cultured in the same experimental conditions. Curves and histograms are obtained from the means \pm standard error of three experiments. The error bars represent the standard error.

EV: Everolimus; GNP: Gold nanoparticle; HC: Half chain; HCe: Half-chain with everolimus; uMC: Untreated mesenchymal cell.

Indeed, a slight although not significant, increase in growth rate was recorded following the treatment of MC with anti-CD44 mAb (Figure 6). Accordingly, ICC experiments evidenced an increased expression of mTOR after 12 h incubation with functionalized GNPs (both GNP-HCs and GNP-HCes) (Figure 2B) or anti-CD44 mAb (Figure 2D), while no change in mTOR expression was detectable in the presence of MCs treated with GNP-PEGs (Figure 2C). In the same experimental conditions used for the treatment with GNP-HCes, everolimus did not significantly affect cell proliferation. Notably, the proliferation curve shows that the drug released by the uptaken GNP-HCes is effective overtime, as evidenced by the persistence of an inhibitory activity after 120 h from GNP incorporation and confirmed by *in vitro* drug release kinetic curve. MCs incubated with GNP-HCs or GNP-HCes were analyzed for Annexin V incorporation at 8, 24 and 48 h after GNP incubation. As further controls, we also studied apoptosis in presence of CD44 mAb and everolimus. Figure 6B shows a remarkable and significant increase of apoptosis: approximately 14% MC cells were apoptotic 8 h after GNP-HCe treatment. This percentage progressively increased up to approximately 42% after 24 h, and diminished at 48 h. The effect was due to the release of everolimus inside the cells, since the incubation with GNP-HCs (without everolimus) and CD44 mAb alone induced as much apoptosis as control untreated MCs. Of note MC treatment with everolimus alone for 2 h was unable to induce apoptosis, demonstrating the superiority of the drug carrier.

Effect of GNP-HCes on inflammatory cells

The uptake of fluorescent nanoparticles by inflammatory cells was demonstrated by flow cytometry (data not shown). The results summarized in Figure 7 showed that, after 24 h incubation, IL-8 secretion was not increased in the presence of GNP-HCes and GNP-PEGs (Figure 7A). Furthermore, both GNPs with or without functionalization did not activate neutrophils (Figure 7B).

Effect of GNP-HCes on bronchial epithelial cell line

In order to exclude a possible toxic effect of nanoparticles on epithelial cells, we studied the apoptotic and proliferation rate in presence of functionalized (GNP-HCes and GNP-HCs) and nonfunctionalized (GNP-PEGs) nanoparticles using the same experimental conditions and procedures. The results obtained by flow cytometry using Alexa Fluor 488 dye marked nanoparticles proved that 16HBE cells did not uptake either functionalized or nonfunctionalized nanoparticles from 1-h up to 8-h incubation. In addition, no significant differences were recorded in proliferation (GNP-PEGs: 100.8 ± 8.5 ;

GNP-HCs: 93 ± 10.8 ; GNP-HCs: 93.8 ± 9.2 after 72 h from incubation and expressed as percentage vs untreated 16HBE cells) or apoptosis rate (untreated 16HBE: 12.5 ± 1.4 ; GNP-PEGs: 11.4 ± 1.3 ; GNP-HCs: 12.8 ± 1.3 ; GNP-HCs: 16.35 ± 1.7 after 24 h from incubation and expressed as percentage).

Discussion

MCs are fibroblastoid-like cells and are the main responsible of the fibroproliferative process underlying BOS. In our study, we isolated MCs from BAL of BOS patients with the purpose to characterize them and identify a useful surface target necessary to functionalize drug-loaded GNPs. Our findings suggest that a consistent but variable fraction of cells express a mesenchymal phenotype but their phenotype does not provide conclusive information about their origin (i.e., from stromal niches, resident fibroblast transformation or a transition from epithelia). All primary cells were negative for CD34 and CD45, ruling out a hematopoietic origin [54,55], although a possible loss of expression of these two markers early in culture cannot be excluded [56]. Analogously, the absence of E-cadherin suggests that transitioned epithelia is not the main origin of these cells [57]. Whatever rising, their involvement in the fibroproliferative process has been proved by different authors [29–31,58]. On this basis, we selected as a possible initial marker for GNP functionalization CD44, which was found to be highly expressed by all primary MCs and was not detected on the surface of normal airway epithelium. The choice of a mTOR inhibitor was based on previously published data [36] and on the detection of a high expression of active phosphorylated form of mTOR in MC cytosol [59].

The synthetic strategy adopted in GNP preparation is illustrated in Figure 3. This strategy displays several advantages: the Fab portions of the antibodies are presented in an optimal orientation for antigen binding on the GNP surface; the use of an antibody fragment with a lower molecular weight, namely the HC, instead of the entire IgG results in a partially reduced immunogenicity of the whole hybrid nanoconstruct, while conserving remarkable binding affinity for the molecular counterpart; the approach with the HC fragment causes a reduced weight on the GNP surface, resulting in higher colloidal stability in aqueous environment.

In addition, the colloidal stability of our GNPs was not significantly affected by the everolimus-loading step inside the polymer shell, since GNP-HCs and GNP-HCs exhibited the same hydrodynamic size (Figure 3). Such designed GNPs were able to enter primary MCs, while inert unfunctionalized GNPs

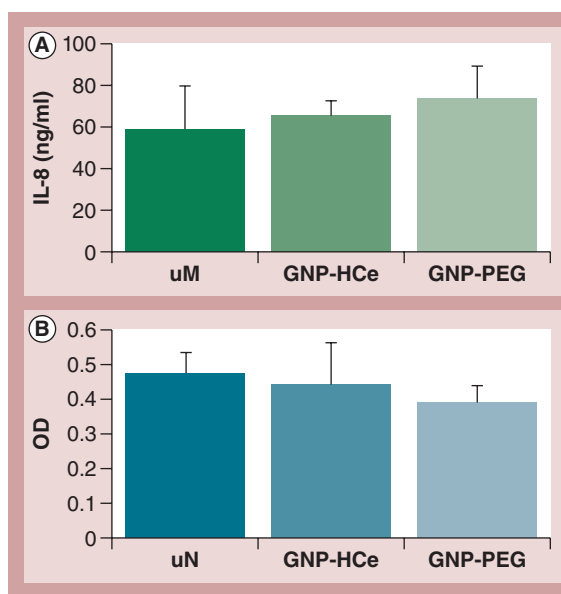


Figure 7. Effect of half-chain gold nanoparticles with everolimus on macrophage and neutrophil activation. (A) IL-8 secretion, evaluated by ELISA test and used to assay the macrophage activation, was not increased by 24 h incubation with GNP-HCe or GNP-PEG compared with untreated macrophages. (B) Elastase activity, evaluated by enzymatic assay to detect possible effects on neutrophils by incubation with GNP-HCe or GNP-PEG, was comparable to untreated neutrophils. The data represents the means \pm standard error of three experiments. The error bars represent the standard error. GNP: Gold nanoparticle; HCe: Half-chain with everolimus; OD: Optical density; uM: Untreated macrophage; uN: Untreated neutrophil.

did not penetrate into MCs. Biological activity of GNP-HCs was indeed clearly detectable in both apoptosis experiments and in cell proliferation assay. Some remarks can be drawn from these experiments. First of all, our targeted delivery system allowed the achievement of high intracellular drug levels, as demonstrated by the observation that GNP-HCe activity on primary MCs was significantly higher than that exerted by everolimus alone in the same experimental conditions. In addition, the experiments of *in vitro* drug-release kinetics suggest a potential use of these nanoparticles as prolonged-release vehicles for weekly administration, allowing good patient compliance. We could also exclude any possible toxic effect of GNPs inside the cells by testing GNPs without everolimus under the same experimental conditions. As further control, CD44 mAb alone proved the absence of unspecific inhibitory action of the antibody on cell proliferation. Interestingly, the link engagement of CD44 with its specific antibody (when MCs were incubated with either CD44 mAb-targeted GNPs or with CD44 mAb alone) heightened the expression of phospho-mTOR by

MCs and induced a slight but significant stimulation of cell proliferation at 48 h (Figure 2). This is not totally surprising since CD44 is implicated in tissue repair and present in the stem-cell phenotype [59]. However, this phospho-mTOR stimulatory effect was completely overcome by GNP-HCe treatment at 72 and 120 h, suggesting that everolimus might also exert its effect on downstream targets [60]. These findings open new interesting scenarios on the possibility of modulating mTOR activation and MC proliferation by interfering with CD44 and suggest that blocking CD44 mAb might be more effective in targeting GNPs.

The absence of inhibitory effect on bronchial epithelial cells that do not express CD44 state the suitability of our treatment, avoiding unspecific toxic effects on closely located epithelial cells.

Based on these data, GNP-HCes could represent an interesting tool in local treatment of BOS; however, one of the main issues in the field of nanotechnology is the possibility that GNPs might induce inflammation that could contribute to BOS evolution [32]. Since resident alveolar macrophages are an important source of profibrotic factors and neutrophils play a key role in BOS pathogenesis [26–28,32], we assessed nanoparticle activity on these two effectors. Dealing with phagocytes, we decided to also test nonfunctionalized GNPs (GNP-PEGs) to evaluate an unspecific stimulatory effect. We assayed *in vitro* IL-8 production by alveolar macrophages and elastase release by neutrophils since IL-8/neutrophil pathway is believed as crucial in BOS pathogenesis [61,62]. The results demonstrated the absence of a stimulating activity of GNPs on macrophages and neutrophils, indicating that their use would not exacerbate the inflammatory response.

Conclusion

We proved for the first time that specifically engineered GNPs could significantly inhibit MC proliferation *in vitro*. The functionalization opens the chance to avoid toxic effect on epithelial cells that otherwise would perpetuate the vicious cycle of epithelial damage/inflammatory response/uncontrolled repair/fibroproliferative process. Although CD44 seems a valuable marker for GNP targeting, further studies on MC characterization will allow us to identify other, even more specific, antigens preventing side effects due to CD44 engagement. As a corollary, yet relevant finding, the absence of proinflammatory activity of GNPs discloses the possibility to administrate functionalized drug-loaded GNPs by aerosolization without raising a further inflammatory response.

Future perspective

The fibrotic lung disorders include several clinical pictures (i.e., obliterans bronchiolitis following lung or bone-marrow transplant, primary or secondary interstitial lung fibrosis) all characterized by an adverse outcome due to our inability to hamper mesenchymal cell proliferation or reverse fibrosis once established. In recent years studies on the pathogenesis of these disorders have downsized the role of chronic inflammation as a trigger of the fibrosis process and focused on epithelial injury followed by a dysregulated fibro-reparative process. All newly developed therapeutic strategies are therefore directed toward an inhibition of MC proliferation. In this work, we directly targeted MCs and delivered a high concentration of an antiproliferative drug, thus increasing the efficacy of the treatment and limiting the potential toxic effect on near positioned cells. Future perspective studies, already in progress in our laboratory, are the *in vivo* administration by local route (i.e., inhalation) of GNPs to test their safety on normal mice and their efficacy on animal models of obliterative bronchiolitis. These key experiments will disclose the possibility to plan a new pharmacological treatment for patients affected by pulmonary fibroproliferative disorders.

Acknowledgements

The authors thank R Allevi (Centro di microscopia elettronica per lo studio) for transmission electron microscope images, M Agozzino for immunohistochemistry advice and the facility Grandi Strumenti of the University of Pavia (Italy), particularly P Vaghi for her helpful assistance.

Financial & competing interests disclosure

M Colombo acknowledges the research fellowships of the Centro di microscopia elettronica per lo studio (University of Milan, Italy). This work was partly supported by Fondazione Regionale per la Ricerca Biomedica and NanoMeDia Project. The authors have no other relevant affiliations or financial involvement with any organization or entity with a financial interest in or financial conflict with the subject matter or materials discussed in the manuscript apart from those disclosed.

No writing assistance was utilized in the production of this manuscript.

Ethical conduct of research

The authors state that they have obtained appropriate institutional review board approval or have followed the principles outlined in the Declaration of Helsinki for all human or animal experimental investigations. In addition, for investigations involving human subjects, informed consent has been obtained from the participants involved.

Executive summary

Background

- We synthesized an innovative nanotool for the selective targeting of ultimate fibroblastoid-like mesenchymal cells that drives fibrosis in chronic allograft dysfunction.

Results & discussion

- These gold nanoparticles can efficiently encapsulate and release the drug and also be optically detected in order to monitor the *in vivo* distribution.
- The nanoparticles maintained colloidal stability in aqueous dispersion and showed that no apparent changes in size and shape of the metal core were associated to the surface modifications.
- We characterized mesenchymal cells from patients with chronic lung allograft dysfunction and selected the surface glycoprotein CD44 as marker to specifically target the new engineered nanoparticles.
- We proved that drug-loaded nanoparticles selectively inhibit mesenchymal cell proliferation and induce apoptosis.
- The inhibitory effect was extended overtime and more effective compared with treatment with drug alone.
- We also proved the absence of a stimulating activity of our nanoparticles on macrophages and neutrophils, indicating that their use would not exacerbate the inflammatory response.

Conclusion

- This work opens new scenarios on the possibility to target a drug to specific cells involved in a pathological process avoiding systemic and side effects on nearby positioned cells.

References

Papers of special note have been highlighted as:

- of interest
 - of considerable interest
- 1 Giljohann DA, Seferos DS, Daniel WL, Massich MD, Patel PC, Mirkin CA. Gold nanoparticles for biology and medicine. *Angew. Chem. Int. Ed.* 49, 3280–3294 (2010).
 - **Describes the potential of gold nanoparticles for biomedical applications.**
 - 2 Lu Y, Chen W. Sub-nanometre sized metal clusters: from synthetic challenges to the unique property discoveries. *Chem. Soc. Rev.* 41, 3594–3623 (2012).
 - 3 Saha K, Agasti SS, Kim C, Li X, Rotello VM. Gold nanoparticles in chemical and biological sensing. *Chem. Rev.* 112, 2739–2779 (2012).
 - 4 Zijlstra P, Paulo PMR, Orrit M. Optical detection of single non-absorbing molecules using the surface plasmon resonance of a gold nanorod. *Nat. Nanotech.* 7, 379–782 (2012).
 - 5 Sperling RA, Rivera Gil P, Zhang F, Zanella M, Parak WJ. Biological applications of gold nanoparticles. *Chem. Soc. Rev.* 37, 1896–1908 (2008).
 - **Describes the potential of gold nanoparticles for biomedical applications.**
 - 6 Kim C, Favazza C, Wang LV. *In vivo* photoacoustic tomography of chemicals: high-resolution functional and molecular optical imaging at new depths. *Chem. Rev.* 110, 2756–2782 (2010).
 - 7 Choi MR, Stanton-Maxey KJ, Stanley JK *et al.* A cellular trojan horse for delivery of therapeutic nanoparticles into tumors. *Nano Lett.* 7, 3759–3765 (2007).
 - 8 Hamad-Schifferli K, Schwartz JJ, Santos AT, Zhang S, Jacobson JM. Remote electronic control of DNA hybridization through inductive coupling to an attached metal nanocrystal antenna. *Nature* 415, 152–155 (2002).
 - 9 Kim C, Agasti SS, Zhu Z, Isaacs L, Rotello VM. Recognition-mediated activation of therapeutic gold nanoparticles inside living cells. *Nat. Chem.* 2, 962–966 (2010).
 - 10 Mukherjee P, Bhattacharya R, Wang P *et al.* Antiangiogenic properties of gold nanoparticles. *Clin. Cancer. Res.* 1, 3530–3534 (2005).
 - 11 Kuriyama S, Mitoro A, Tsujinoue H *et al.* Particle-mediated gene transfer into murine livers using a newly developed gene gun. *Gene Ther.* 7, 1132–1136 (2000).
 - 12 Ghosh P, Han G, De M, Kim CK, Rotello VM. Gold nanoparticles in delivery applications. *Adv. Drug Delivery Rev.* 60, 1307–1315 (2008).
 - **Describes the concrete potential of gold nanoparticles as drug-delivery systems *in vivo*.**
 - 13 Cobley CM, Chen J, Chul Cho E, Wang LV, Xia Y. Gold nanostructures: a class of multifunctional materials for biomedical applications. *Chem. Soc. Rev.* 40, 44–56 (2011).
 - 14 Sandhu KK, McIntosh CM, Simard JM, Smith SW, Rotello VM. Gold nanoparticle-mediated transfection of mammalian cells. *Bioconjugate Chem.* 13, 3–6 (2002).
 - 15 Yavuz MS, Cheng Y, Chen J *et al.* Gold nanocages covered by smart polymers for controlled release with near-infrared light. *Nat. Mater.* 8, 935–939 (2009).
 - 16 Rothrock AR, Donkers RL, Schoenfisch MH. Synthesis of nitric oxide-releasing gold nanoparticles. *J. Am. Chem. Soc.* 127, 9362–9363 (2005).
 - 17 Chen YS, Hung YC, Liao I, Huang GS. Assessment of the *in vivo* toxicity of gold nanoparticles. *Nanoscale Res. Lett.* 4, 858–864 (2009).
 - 18 Longmire M, Choyke PL, Kobayashi H. Clearance properties of nano-sized particles and molecules as imaging agents: considerations and caveats. *Nanomedicine* 3, 703–717 (2008).
 - 19 Connor EE, Mwamuka J, Gole A, Murphy CJ, Wyatt MD. Gold nanoparticles are taken up by human cells but do not cause acute cytotoxicity. *Small* 1, 325–327 (2005).

- **Demonstrates that gold nanoparticles in the 10–20 size range are generally nondetrimental to cellular functions.**
- 20 Verleden GM, Vos R, De Vleeschauwer SI *et al.* Obliterative bronchiolitis following lung transplantation: from old to new concepts? *Transplant Int.* 22, 771–779 (2009).
- 21 Finlen Copeland CA, Snyder LD, Zaas DW, Turbyfill WJ, Davis WA, Palmer SM. Survival after bronchiolitis obliterans syndrome among bilateral lung transplant recipients. *Am. J. Respir. Crit. Care Med.* 182, 784–789 (2010).
- 22 Todd JL, Palmer SM. Bronchiolitis obliterans syndrome: the final frontier for lung transplantation. *Chest* 140, 502–508 (2011).
- **Highlights all main pathogenic mechanisms underlying bronchiolitis obliterans syndrome onset including allospecific and nonallospecific insults.**
- 23 Zheng L, Whitford HM, Orsida B *et al.* The dynamics and associations of airway neutrophilia post lung transplantation. *Am. J. Transplant.* 6, 599–608 (2006).
- 24 Vanaudenaerde BM, Verleden SE, Vos R *et al.* Innate and adaptive interleukin-17-producing lymphocytes in chronic inflammatory lung disorders. *Am. J. Respir. Crit. Care Med.* 183, 977–986 (2011).
- 25 Palmer SM, Burch LH, Trindade AJ *et al.* Innate immunity influences long-term outcomes after human lung transplant. *Am. J. Respir. Crit. Care Med.* 171, 780–785 (2005).
- 26 Ellsner A, Vogelmeier C. The role of neutrophils in the pathogenesis of obliterative bronchiolitis after lung transplantation. *Transplant. Infect. Dis.* 3, 168–176 (2001).
- 27 Hardison MT, Galin FS, Calderon CE *et al.* The presence of a matrix-derived neutrophil chemoattractant in bronchiolitis obliterans syndrome after lung transplantation. *J. Immunol.* 182, 4423–4431 (2009).
- 28 Khatwa UA, Kleibrink BE, Shapiro SD, Subramaniam M. MMP-8 promotes polymorphonuclear cell migration through collagen barriers in obliterative bronchiolitis. *J. Leukocyte Biol.* 87, 69–77 (2010).
- 29 Andersson-Sjoland A, Thiman L, Nihlberg K *et al.* Fibroblast phenotypes and their activity are changed in the wound healing process after lung transplantation. *J. Heart. Lung. Transplant.* 30, 945–954 (2011).
- 30 Lama VN, Smith L, Badri L *et al.* Evidence for tissue-resident mesenchymal stem cells in human adult lung from studies of transplanted allografts. *J. Clin. Invest.* 117, 989–996 (2007).
- **Represents the first evidence of mesenchymal cell involvement in chronic lung allograft dysfunction.**
- 31 Brocker V, Langer F, Fellous TG *et al.* Fibroblasts of recipient origin contribute to bronchiolitis obliterans in human lung transplants. *Am. J. Respir. Crit. Care Med.* 173, 1276–1282 (2006).
- 32 Sato M, Keshavjee S. Bronchiolitis obliterans syndrome: alloimmune-dependent and -independent injury with aberrant tissue remodeling. *Semin. Thorac. Cardiovasc. Surg.* 20, 173–182 (2008).
- 33 Ramirez AM, Nunley DR, Rojas M, Roman J. Activation of tissue remodeling precedes obliterative bronchiolitis in lung transplant recipients. *Biomarker Insights* 3, 351–359 (2008).
- 34 Hayes D Jr. A review of bronchiolitis obliterans syndrome and therapeutic strategies. *Cardiothorac. Surg.* 18, 86–92 (2011).
- 35 Bianco R, Garofalo S, Rosa R *et al.* Inhibition of mTOR pathway by everolimus cooperates with EGFR inhibitors in human tumours sensitive and resistant to anti-EGFR drugs. *Br. J. Cancer* 98, 923–930 (2008).
- 36 Azzola A, Havryk A, Chhajed P *et al.* Everolimus and mycophenolate mofetil are potent inhibitors of fibroblast proliferation after lung transplantation. *Transplantation* 77, 275–280 (2004).
- 37 Nashan B. Review of the proliferation inhibitor everolimus. *Expert. Opin. Invest. Drugs* 11, 1845–1857 (2002).
- **A thorough review on the cellular pathways targeted by everolimus.**
- 38 Budde K, Becker T, Arns W *et al.* Everolimus-based, calcineurin-inhibitor-free regimen in recipients of *de-novo* kidney transplants: an open-label, randomised, controlled trial. *Lancet* 377, 837–847 (2011).
- 39 Otton J, Hayward CS, Keogh AM, Glanville AR, Macdonald PS. Everolimus-associated pneumonitis in 3 heart transplant recipients. *J. Heart Lung. Transplant.* 28, 104–106 (2009).
- 40 Expósito V, de Prada JA, Gómez-Román JJ *et al.* Everolimus-related pulmonary toxicity in heart transplant recipients. *J. Heart Lung Transplant.* 27, 797–800 (2008).
- 41 Ponticelli C, Salvadori M, Scolari MP *et al.* Everolimus and minimization of cyclosporine in renal transplantation: 24-month follow-up of the EVEREST study. *Transplantation* 91, e72–e73 (2011).
- 42 Iacono AT, Johnson BA, Grgurich WF *et al.* A randomized trial of inhaled cyclosporine in lung-transplant recipients. *N. Engl. J. Med.* 354, 141–150 (2006).
- 43 Hayes D Jr, Zwischenberger JB, Mansour HM. Aerosolized tacrolimus: a case report in a lung transplant recipient. *Transplant. Proc.* 42, 3876–3879 (2010).
- 44 Dandel M, Lehmkühl HB, Knosalla C, Hetzer R. Impact of different long-term maintenance immunosuppressive therapy strategies on patients' outcome after heart transplantation. *Transplant. Immunol.* 23, 93–103 (2010).
- 45 Badri L, Murray S, Liu LX *et al.* Mesenchymal stromal cells in bronchoalveolar lavage as predictors of bronchiolitis obliterans syndrome. *Am. J. Respir. Crit. Care Med.* 183, 1062–1070 (2011).
- 46 Brust M, Walker M, Bethell D, Schiffrin DJ, Whyman RJ. Synthesis of thiol-derivatized gold nanoparticles in a two phase liquid-liquid system. *Chem. Commun.* 801–802 (1994).
- **Describing a universal protocol for the synthesis of organic soluble gold nanoparticles.**
- 47 Colombo M, Mazzucchelli S, Montenegro JM *et al.* Protein oriented ligation on nanoparticles exploiting O6-alkylguanine-DNA transferase (SNAP) genetically encoded fusion. *Small* 8, 1492–1497 (2012).
- **Describes the preparation and properties of an amphiphilic polymer that allows both for transfer of organic soluble nanoparticles to aqueous phase with minimal agglomeration and for surface functionalization with targeting ligands.**

- 48 Estenne M, Maurer JR, Boehler A *et al.* Bronchiolitis obliterans syndrome 2001: an update of the diagnostic criteria. *J. Heart Lung Transplant.* 21, 297–310 (2002).
- 49 Meloni F, Cascina A, Miserere S, Perotti C, Vitulo P, Fietta AM. Peripheral CD4(+)CD25(+) TREG cell counts and the response to extracorporeal photopheresis in lung transplant recipients. *Transplant. Proc.* 39, 213–217 (2007).
- 50 No authors listed. Technical recommendations and guidelines for bronchoalveolar lavage (BAL). Report of the European Society of Pneumology Task Group. *Eur. Respir. J.* 2, 561–585 (1989).
- 51 Mazzucchelli S, Colombo M, De Palma C *et al.* Single-domain protein A-engineered magnetic nanoparticles: toward a universal strategy to site-specific labeling of antibodies for targeted detection of tumor cells. *ACS Nano* 4, 5693–5702 (2010).
- 52 Cozens AL, Yezzi MJ, Kunzelmann K *et al.* CFTR expression and chloride secretion in polarized immortal human bronchial epithelial cells. *Am. J. Respir. Cell. Mol. Biol.* 10, 38–47 (1994).
- 53 Costa P, Sousa Lobo JM. Modeling and comparison of dissolution profiles. *Eur. J. Pharm. Sci.* 13, 123–133 (2001).
- 54 Bellini A, Mattoli S. The role of the fibrocyte, a bone marrow-derived mesenchymal progenitor, in reactive and reparative fibroses. *Lab. Invest.* 87, 858–870 (2007).
- 55 Nombela-Arrieta C, Ritz J, Silberstein LE. The elusive nature and function of mesenchymal stem cells. *Nat. Rev. Mol. Cell Biol.* 12, 126–131 (2011).
- 56 Andersson-Sjöland A, Nihlberg K, Eriksson L, Bjermer L, Westergren-Thorsson G. Fibrocytes and the tissue niche in lung repair. *Respir. Res.* 12, 76–83 (2011).
- 57 Zeisberg M, Neilson EG. Biomarkers for epithelial-mesenchymal transitions. *J. Clin. Invest.* 119, 1429–1437 (2009).
- 58 Walker N, Badri L, Wettlaufer S *et al.* Resident tissue-specific mesenchymal progenitor cells contribute to fibrogenesis in human lung allografts. *Am. J. Pathol.* 178, 2461–2469 (2011).
- 59 Zander DS, Baz MA, Massey JK. Patterns and significance of CD44 expression in lung allografts. *J. Heart Lung Transplant.* 18, 646–653 (1999).
- 60 Dancey J. mTOR signaling and drug development in cancer. *Nat. Rev. Clin. Oncol.* 7, 209–219 (2010).
- 61 Riise GC. On interleukin-8, neutrophil activation, and bronchiolitis obliterans syndrome in lung transplantation. *Transplantation* 70, 265–266 (2000).
- 62 Meloni F, Vitulo P, Cascina A *et al.* Bronchoalveolar lavage cytokine profile in a cohort of lung transplant recipients: a predictive role of interleukin-12 with respect to onset of bronchiolitis obliterans syndrome. *J. Heart Lung Transplant.* 23, 1053–1060 (2004).



ELSEVIER



POTENTIAL CLINICAL SIGNIFICANCE

Nanomedicine: Nanotechnology, Biology, and Medicine
11 (2015) 1387–1397



nanomedjournal.com

Feature Article

Nanoformulation of antiretroviral drugs enhances their penetration across the blood brain barrier in mice

Luisa Fiandra, PhD^b, Miriam Colombo, PhD^c, Serena Mazzucchelli, PhD^b, Marta Truffi, PhD^a,
Benedetta Santini, BPharm^c, Raffaele Allevi, CLT^a, Manuela Nebuloni, PhD^a,
Amedeo Capetti, MD^b, Giuliano Rizzardini, MD^b, Davide Prospero, PhD^{c,d}, Fabio Corsi, MD^{a,*}

^aDipartimento di Scienze Biomediche e Cliniche “Luigi Sacco”, Università di Milano, Milano, Italy

^bOspedale L. Sacco, Milano, Italy

^cDipartimento di Biotecnologie e Bioscienze, Università di Milano-Bicocca, Milano, Italy

^dLaboratorio di Biofisica e Nanomedicina, Polo Tecnologico, Fondazione Don Gnocchi IRCCS-ONLUS, Milan, Italy

Received 24 June 2014; accepted 19 March 2015

Abstract

Eradication of virus by sanctuary sites is a main goal in HIV management. The central nervous system (CNS) is a classic model of sanctuary where viral replication occurs despite a complete viral suppression in peripheral blood. In recent years, nanotechnologies have provided a great promise in the eradication of HIV from the CNS. We hereby demonstrate for the first time that the structurally complex antiretroviral drug enfuvirtide (Enf), which normally is unable to penetrate the cerebrospinal fluid, is allowed to cross the blood brain barrier (BBB) in mice by conjugation with a nanoconstruct. Iron oxide nanoparticles coated with an amphiphilic polymer increase Enf translocation across the BBB in both *in vitro* and *in vivo* models. The mechanism involves the uptake of nanoconjugated-Enf in the endothelial cells, the nanocomplex dissociation and the release of the peptide, which is eventually excreted by the cells in the brain parenchyma.

From the Clinical Editor: Despite the success of cocktail therapy of antiretroviral drugs, the complete eradication of HIV remains elusive, due to existence of viral sanctuary sites. The authors showed in this study that an antiretroviral drug complexed with iron oxide nanoparticles and coated with PMA amphiphilic polymer crosses the blood brain barrier. Furthermore, there was significant anti-viral activity. The results would aid further drug designs to eradicate HIV.

© 2015 Elsevier Inc. All rights reserved.

Key words: HIV sanctuaries; Enfuvirtide; Blood brain barrier; PMA-coated nanoparticles

Background

Current antiretroviral treatment regimens suppress plasma HIV-1 RNA and DNA below detectable levels in a consistent proportion of subjects.¹ However, functional cure and eradication are still beyond our possibilities. One obstacle to such goals is represented by the difficulty to achieve therapeutic antiretroviral concentrations within sanctuary sites where HIV-1 has been

shown to compartmentalize. Such sites include the genital tract, the gut-associated lymphoid tissue, the lymph nodes, tissue macrophages and the central nervous system (CNS).^{2–4} In particular, the CNS is considered one of the most important viral reservoirs. This is mainly due to the presence of macrophages that promote the inflammatory escalation with subsequent astrogliosis and neurodegeneration, thus establishing the so-called NeuroAIDS,⁵ responsible for neurocognitive disorders

Abbreviations: AF660, Alexa Fluor 660; BBB, blood brain barrier; CNS, central nervous system; DLS, dynamic light scattering; ECM, endothelial cell medium; Enf, enfuvirtide; Epf, epifluorescence; FI, fluorescence intensity; FD40, FITC-Dextran 40; FITC, fluoresceinamine; HAART, highly active anti-retroviral therapy; ICP-OES, inductively coupled plasma optical emission spectrometry; MRP, multidrug resistance-associated protein; P_{app} , apparent permeability coefficient; PBS, phosphate buffer saline; PFA, paraformaldehyde; PMA, poly(isobutylene-alt-1-tetradecene-maleic anhydride); RBMVECs, rat brain microvascular endothelial cells; RT, room temperature; SE, standard errors; SEM, scanning electron microscopy; TEM, transmission electron microscopy; TEER, transendothelial electrical resistance.

This work was supported by the Fondazione Regionale per la Ricerca Biomedica (FRRB), NanoMeDia Project (Regione Lombardia and “L. Sacco” Hospital), and by the “Fondazione Romeo ed Enrica Invernizzi”.

M.T. acknowledges “Centro di Microscopia Elettronica per lo sviluppo delle Nanotecnologie applicate alla medicina” (CMENA, University of Milan) for the postdoctoral fellowship.

*Corresponding author at: Dipartimento di Scienze Biomediche e Cliniche “Luigi Sacco”, Università di Milano, Milano, Italy.

E-mail address: fabio.corsi@unimi.it (F. Corsi).

<http://dx.doi.org/10.1016/j.nano.2015.03.009>

1549-9634/© 2015 Elsevier Inc. All rights reserved.

with different grades of severity (AIDS dementia complex). From a clinical point of view, NeuroAIDS is a real challenge since the blood brain barrier is poorly crossable by most antiretroviral drugs.²

In the effort toward viral eradication, one of the most promising strategies is to treat this latent-T cell reservoir, so that resting cells may be induced to release virions and reactivate,^{6–9} while preventing HIV-1 entry in uninfected CD4+ T cells. With this aim it would be important to design new therapeutic strategies to direct antiretroviral drugs in these HIV sanctuaries, both to reduce T-cell mediated delivery of the virus into the sanctuaries and to directly act on HIV-sensitive CD4+ cells inside these sites (*i.e.* microglial cells of brain)⁴.

Nanotechnology is an emerging multidisciplinary field that has the potential to offer a radical change in the treatment and monitoring of HIV/AIDS.^{10–13} The potential advantages in using nanoparticles for HIV infection treatment include the capacity to incorporate, encapsulate, or conjugate a variety of drugs in order to target specific cell populations, grant long-term drug release, and penetrate into sanctuary sites. With regard to the CNS, the employment of nanotechnology could allow antiretroviral drugs to effectively reach this reservoir,¹⁴ thus preventing the replication of the virus and reducing the damages induced by the infection.

In current clinical practice, the first-line antiretroviral therapy is generally constituted by a combination of two nucleoside reverse transcriptase inhibitors (NRTI) with a non-nucleoside reverse transcriptase inhibitor (NNRTI), such as a protease inhibitor or an integrase inhibitor. Conversely, fusion inhibitors are much less used because of some well-known limitations such as production time and costs, difficult administration (subcutaneous injection twice daily) and adverse effect profile.¹⁵ Therefore, fusion inhibitors are only used in case of resistance or failure of the HAART. Enfuvirtide (Fuzeon™ from Roche Laboratories Inc. and Trimeris Inc.) is a 36-amino acid peptide that targets multiple sites in gp41, a HIV glycoprotein responsible for the fusion with CD4+ cells.^{16–18} Enfuvirtide (Enf) inhibits HIV-1-mediated cell-cell fusion and transmission of cell-free virus while it does not have substantial activity against HIV-2.^{19–22} Because of its unfavorable pharmacological profile, with a half life of approximately 2 h and a high molecular weight (4.5 kDa), Enf is particularly indicated to provide a proof of concept of the improved access of antiretroviral drug to HIV sanctuaries by nanoformulation. Indeed, Enf does not penetrate the BBB because of its complex structure, and is therefore not detectable in cerebrospinal fluid (CSF).²³

Aim of our study is to demonstrate the ability of iron oxide nanoparticles coated with PMA amphiphilic polymer (MYTS) to enhance the permeation of a high-weighted molecule, such as Enf, across the BBB both in *in vitro* and *in vivo* models, and propose a mechanism for drug delivery across the endothelium.

Methods

Nanoparticle design

Magnetic nanoparticles (MNP) were synthesized by solvothermal decomposition in organic solvent from organometallic precursors according to Park et al. protocol.²⁴ MNP were transferred to water phase using a fluorescent labeled amphiphilic

polymer (PMA).²⁵ Fluorescent-PMA was obtained with fluoresceinamine 1.0 M (0.5 mL in DMSO) was added to a 0.5 M PMA in CHCl₃ (5 mL) and the mixture was left overnight at RT. Part of this solution (20 μL) was added to MNP (1.5 mg in CHCl₃). The organic solvent was evaporated and sodium borate buffer (SBB, pH 12, 20 mL) was added obtaining a stable nanoparticle dispersion which was concentrated in Amicon tubes (100 kDa filter cutoff) by centrifuging at 3500 rpm for 20 min. The nanoparticles were washed twice with water resulting in green labeled PMA-coated nanoparticles highly soluble in aqueous media (MYTS). MYTS were reacted with an amino-linker useful for Enf immobilization on the nanoparticles. Enf was previously labeled with AF660 dye (Invitrogen, Carlsbad, CA) according to manufacturer's protocol. The final double labeled Enf-MYTS are schematically represented in Figure 1, A.

Characterization of the BBB *in vitro* model

The setting of the BBB *in vitro* model, based on a co-culture of RBMVECs and astrocytes, is described in Supplementary materials. Before each experiment, we checked the trans-BBB electrical resistance by an EVOM2 Epithelial tissue Volt/Ohmmeter connected to an Endohm-24SNAP cup (WPI, Germany), obtaining a suitable value on 90% of the inserts. Moreover, the trans-BBB apparent permeability coefficient of FITC-Dextran 40 (FD40) was determined by measuring the flux of the molecule from the upper to the lower chamber of three BBB systems at 1 h, 2 h and 3 h from the addition of 1 mg mL⁻¹ FD40 in the upper compartment. The flux through the RBMVECs single layer or through the empty insert was used as control. The amount of FD40 recovered in the lower compartment was determined spectrofluorimetrically and the P_{app} was calculated from the mean flux (see Supplementary materials).

In vitro trans-BBB permeation

The permeation of (AF660)Enf, (FITC)MYTS or (AF660)Enf-MYTS(FITC) across the BBB was assessed on the *in vitro* model described above, using four inserts for each experimental condition. The two formulations were added to the upper chamber and, after 4 or 7 h of incubation, a defined volume of ECM was collected by both the upper and the lower chambers. The fluorescence intensity of the samples was measured spectrofluorimetrically. For an exact comparison between the trans-BBB permeation of free and MYTS-conjugated Enf (5 μg mL⁻¹), the FI of the two formulations was used for normalization, and the final amount of Enf-MYTS in the upper chamber was 0.1 mg mL⁻¹.

ICP-OES was also used to quantify the amount of MYTS iron in the collected samples.

Reported results are representative of one of three independent experiments.

Plasma concentration measurements in mice

Plasma concentration of free or conjugated Enf was determined upon intravenous injection of AF660-labeled Enf (0.2 μg g⁻¹ body weight) or Enf-MYTS (12.5 μg g⁻¹ body weight) in Balb/c mice. We treated four mice per experimental condition and repeated the experiment twice (for a total of eight

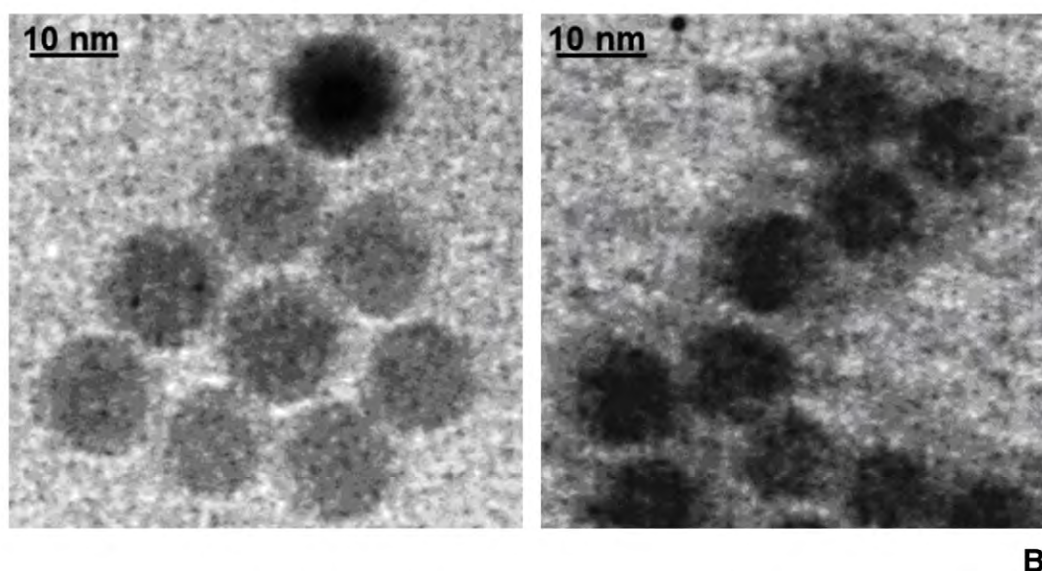
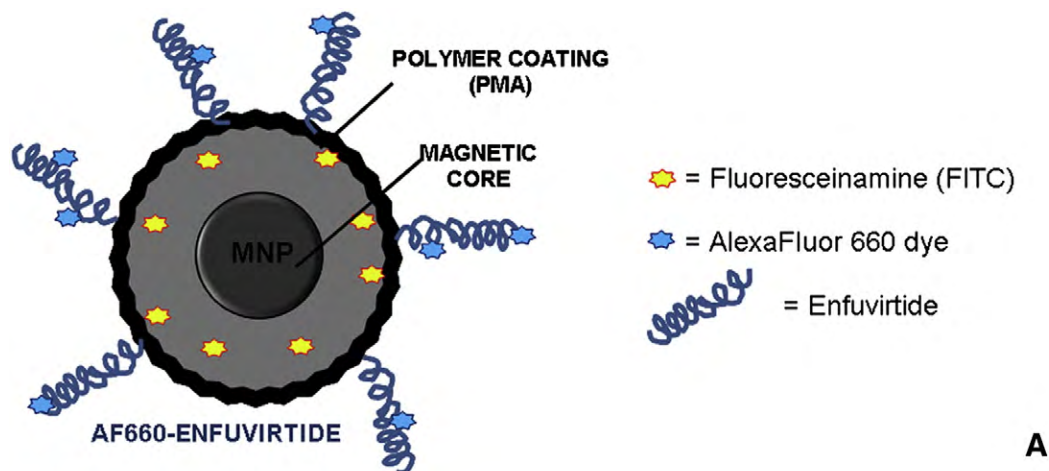


Figure 1. (A) Schematic representation of labeled Enf-MYTS. (B) TEM images of MNP in hexane (left) and MYTS in water (right).

animals per experimental condition). The amount of injected Enf-MYTS was calculated normalizing the fluorescence intensity of conjugated Enf to that of the free peptide. After 30 min, 1 h and 6 h postinjection, blood was collected and its fluorescence intensity was determined spectrofluorimetrically. After subtraction of background fluorescence, determined in samples collected from mice before treatment, the amount of Enf was calculated by using a calibration curve with known amounts of the compounds dissolved in control plasma samples.

Ex vivo IVIS imaging

Mice injected with (AF660)Enf or (AF660)Enf-MYTS (three animals for each experimental group) were employed in three different experiments, for a total of nine mice) were sacrificed 1 h after injection and dissected brains were analyzed in an IVIS Lumina II imaging system (Calipers Life Sciences, UK), together with the brains from three non-treated mice. Images were acquired with a Cy5 emission filter, while excitation was

scanned from 570 to 640 nm and tissue autofluorescence was removed by spectral unmixing.

Confocal laser scanning microscopy

For the confocal observations of brain cryosections, portions of the same tissues analyzed by IVIS or of additional tissues isolated from mice injected with $0.2 \mu\text{g g}^{-1}$ body weight (AF660)Enf, or $12.5 \mu\text{g g}^{-1}$ body weight (FITC)MYTS, (AF660)Enf-MYTS or (AF660)Enf-MYTS(FITC) (three animals for each experimental group), were fixed, frozen in liquid nitrogen and cryosectioned. Cryosections were counterstained with DAPI and NeuroTrace 530/615 fluorescent Nissl stain or immunodecorated with anti-CD31.

For the confocal microscopy of RBMVECs (three inserts for each experimental condition), cells on insert were fixed and immunodecorated with anti-CD31 and DAPI.

Images were acquired by a Leica TCS SPE confocal microscope and the intracellular distribution of AF660 and FITC signals was analyzed by ImageJ software.

Each image is representative of at least six images obtained from three inserts or mice brain sections for each experimental condition.

Scanning and transmission electron microscopy

For TEM analysis, MYTS were dispersed under sonication in water ($50 \mu\text{g mL}^{-1}$) and a drop of the resulting solution was placed on a formvar/carbon-coated copper grid and air-dried.

RBMVECs layered on inserts and exposed or not to 0.1 mg Enf-MYTS or MYTS, and sections of mice brains, exposed *in vivo* to the same nanoformulates ($12.5 \mu\text{g g}^{-1}$ body weight), were analyzed by TEM, by fixing small portions of cells-bearing inserts ($n = 3$) or tissues (pieces obtained from the same brains employed for confocal microscopy analyses) in 2.5% glutaraldehyde. For scanning electron microscopy analyses, other small portions of the RBMVECs-bearing inserts were fixed and processed as described in Supplementary materials.

Histopathology

Brain, liver, kidneys, spleen and lung samples obtained from three Balb/c mice, whose brains were analyzed by confocal microscopy, were fixed in 10% buffered formalin for at least 48 h and embedded in paraffin. Three μm sections were cut, stained with hematoxylin and eosin and examined blindly.

Statistical analysis

All mean values \pm SE reported in Results section and in Supplementary materials were compared by Student's *t* test.

Results

Nanoparticle characterization

MNP and the final Enf-MYTS, synthesized as described in Methods and Supplementary materials, were characterized in size and shape by DLS and TEM (Figure 1, B). MNP had a hydrodynamic diameter of $18.8 \text{ nm} \pm 2.1$ in hexane. After the phase transfer, MNP maintained the original average crystal size (8 nm by TEM), and the final nanoparticle shape was uniformly spherical, with a hydrodynamic diameter of $23.9 \pm 2.0 \text{ nm}$ (MYTS in water) as determined by DLS. After drug conjugation, the nanoparticle size increased up to $35.2 \pm 2.2 \text{ nm}$. The pH value of the suspension was around 5.5 and the zeta potential obtained at this pH value was $-29.58 \pm 1.90 \text{ mV}$, likely suggesting a high stability of Enf-MYTS with minimal aggregation in water medium at this pH. Indeed a zeta potential value higher than $\pm 30 \text{ mV}$ is generally required for a colloidal stable nanoparticle dispersion.^{26,27}

Nanoconjugated enfuvirtide crosses the *in vitro* BBB model

The efficiency of MYTS in increasing the trans-BBB permeation of Enf was first evaluated on an *in vitro* BBB model consisting of a double layer of astrocytes and RBMVECs. Before treatment, the integrity of our experimental model was validated by measuring TEER and by determining the trans-BBB apparent permeability of the Dextran 40. In all BBB models devoted to the subsequent experimental phase, we recorded a mean TEER value higher than $400 \Omega \text{ cm}^2$. BBB selectivity to the

Dextran 40 labeled with FITC (FD40) was assessed in some additional inserts by measuring the trans-BBB flux over 3 h (Figure S1). The resulting P_{app} ($0.10 \pm 0.03 \times 10^{-7} \text{ cm s}^{-1}$, mean \pm SE, $n = 6$) confirmed the production of a very tight barrier. SEM observations showed the presence of a uniform layer of endothelial cells (Figure S2A), and TEM images clearly demonstrated that cells were connected by well-structured tight junctions (Figure S2B).

The permeability of Enf, MYTS and Enf-MYTS across the BBB model was determined by labeling the peptide and the nanoparticle with AF660 and FITC, respectively (Figure 1, A). The nanoparticle suspensions were added in the upper chamber of the experimental apparatus and their passage through the BBB model was assessed after 4 and 7 h of incubation by measuring their fluorescence intensity (FI) into the lower chamber. We found that only a small fraction of free Enf was able to cross the BBB *in vitro*: after 4 h, Enf FI in the lower chamber was about 0,15 % of Enf FI added in the upper chamber, and the percentage increase of FI in the lower chamber over the subsequent 3 h of incubation was 30% (Figure 2, A). Conjugation of Enf to the nanoparticle did not significantly affect its FI in the lower chamber within the first four hours, but it was able to greatly increase its permeation across the BBB (by over 170%) between 4 and 7 h of incubation (Figure 2, A). Surprisingly, the percentage increase of the FITC FI in the lower chamber calculated between 4 and 7 h, which is associated to MYTS permeation across the BBB, was only 10%, and therefore much lower than that of the conjugated peptide in the same time span (Figure 2, B). The great difference between the % increase in lower chamber of AF660 (conjugated to Enf) and FITC (conjugated to MYTS) after incubation with the Enf-MYTS nanocomplex strongly suggested that the two components did not have the same fate when crossing the BBB, and that they likely dissociated into the barrier to be processed separately. The permeation of MYTS through the BBB was also assessed by measuring the iron content in the solution collected by the lower chamber by ICP-OES: we found that the percentage increase of iron recorded between 4 and 7 h was only 1.84 ± 0.04 (mean \pm SE, $n = 8$) for both MYTS and Enf-MYTS.

Then, we measured the FI of the three formulations in the lower chamber of the BBB apparatus after 24 h of incubation. We observed that the Enf trans-BBB permeation was enhanced between 7 and 24 h of incubation by 175% (Figure 2, A), likely because of increased leakage of the RBMVEC barrier over the time. However, the effect of the nanocomplexation on the permeation of Enf across the BBB was still remarkable: the percentage increase of AF660 FI in the lower chamber between 7 and 24 h of exposure to Enf-MYTS reached 745% (Figure 2, A). By contrast, the percentage increase of FITC FI in the lower chamber was about 20% for both MYTS and Enf-MYTS (Figure 2, B), thus underlining a discrepancy between the FI recorded for Enf and MYTS after incubation of the BBB with Enf-MYTS. The percentage increase of iron content in the lower chamber between 7 and 24 h was still negligible and comparable for both conjugated and unconjugated nanoparticles ($1.89\% \pm 0.03$, mean \pm SE, $n = 8$).

In parallel, we performed a confocal microscopy analysis of the upper side of the insert after 7 h of incubation with Enf or

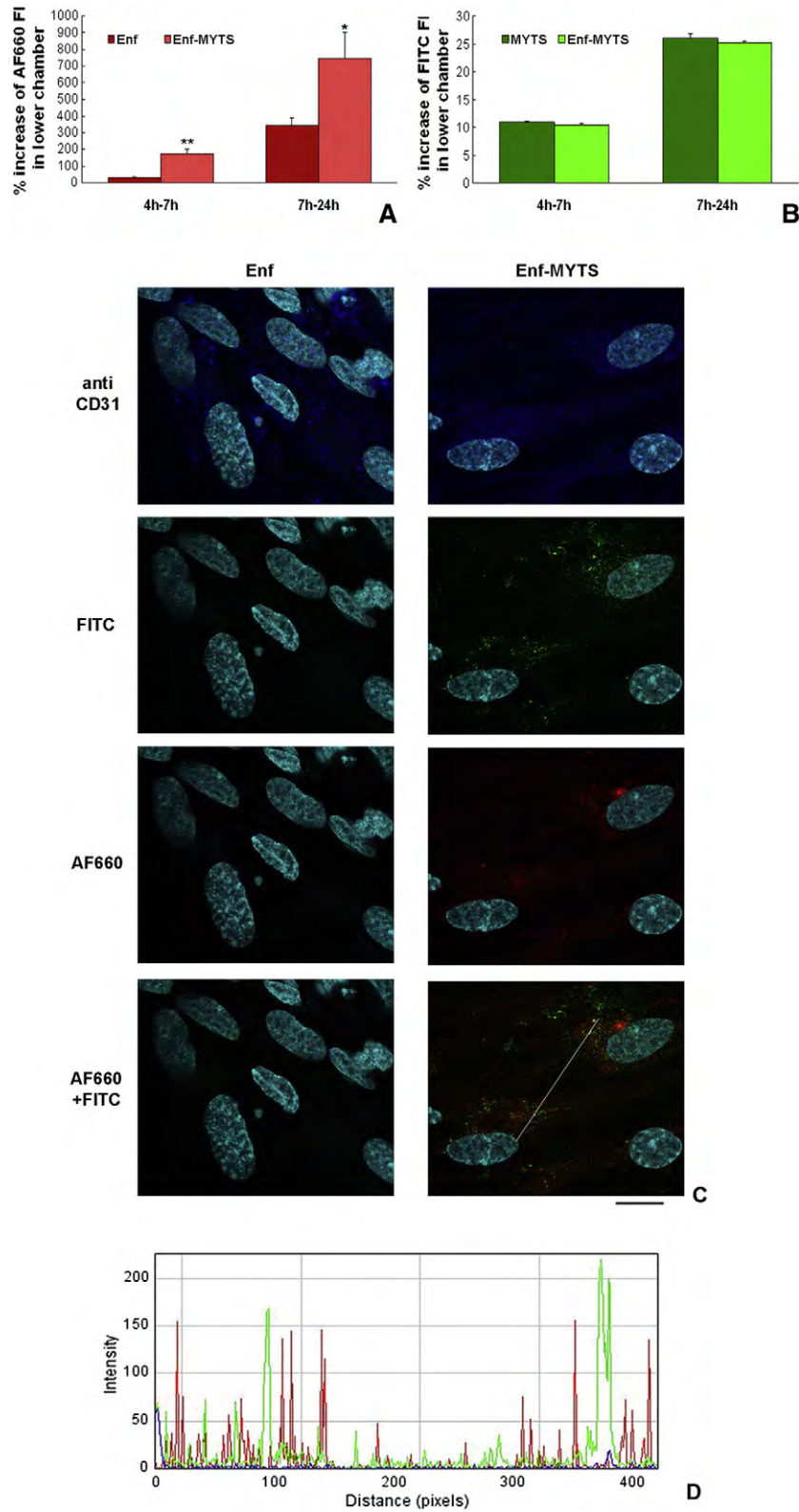


Figure 2. Percentage (%) increase of FI of free or conjugated (AF660)Enf (A) or (FITC)MYTS (B) in the lower chamber of the BBB *in vitro* system calculated between 4 and 7 h, and 7 and 24 h, from the addition of labeled Enf, MYTS and Enf-MYTS into the upper chamber. Mean \pm SE of 4 replicates; $**P < 0,001$ and $*P < 0,05$, Enf-MYTS vs Enf (Student's *t* test) (C) Confocal laser-scanning micrographs (single optical sections) of RBMVECs after 7 h of incubation with free Enf or Enf-MYTS. Enf and MYTS are labeled with AF660 (red) and FITC (green) respectively; nuclei are stained with DAPI (cyan) and endothelial cells are immunodecorated with anti-CD31 antibody (blue); scale bar: 10 μ m. (D) Overlay of the signal intensity plots of Enf and MYTS along a one-pixel line covering a cytoplasmic portion of the cells.

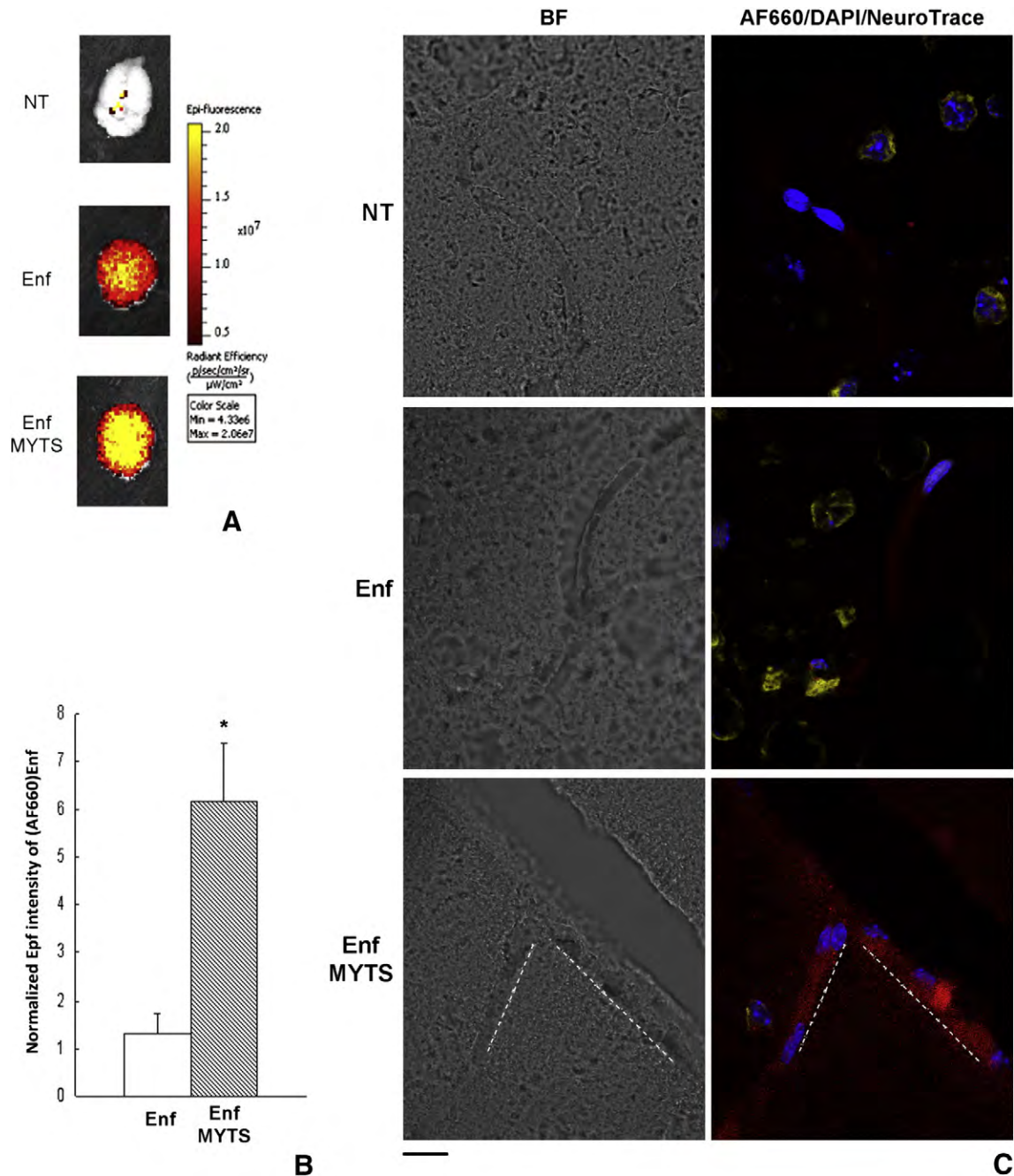


Figure 3. Analysis of brains isolated from non-treated mice (NT) or mice exposed for 1 h to free or conjugated AF660-labeled enfuvirtide. (A) Epf images of isolated brains, where Epf intensity is expressed as radiant efficiency. (B) Averaged Epf intensity of isolated brains where Epf values have been normalized on fluorescence intensity of injected solution in order to keep into account the differences in intrinsic fluorescence emission for each preparation; mean \pm SE of 9 different brains for each experimental condition; * $P < 0,01$ (Student's *t* test). (C) Confocal laser-scanning micrographs (single optical sections) of brain cryosections; images from control animals (NT) or from animals treated with free or nanocomplexed enfuvirtide (red) have been overlaid on the corresponding images reporting nuclei (blue) and neuronal cytoplasm (yellow), counterstained with DAPI and NeuroTrace 530/615, respectively (right column); brightfield (BF) images are reported on the left; dashed lines highlight the vessel boundaries; bar: 10 μm .

Enf-MYTS. Figure 2, C shows that while free Enf was not internalized by the RBMVECs, the conjugation of the peptide to the nanoparticles allowed it to deeply enter into the cells, confirming the enhanced permeability of Enf when nanoconjugated. The merge image of the cells incubated with Enf-MYTS revealed that the AF660 and the FITC fluorescence

were mostly non-overlapping (Figure 2, C and D). These image data, combined with the great difference in the trans-BBB permeation rate observed between the two components, strongly suggested that a dissociation of the peptide from the nanoparticle might have occurred in the endothelial layer.

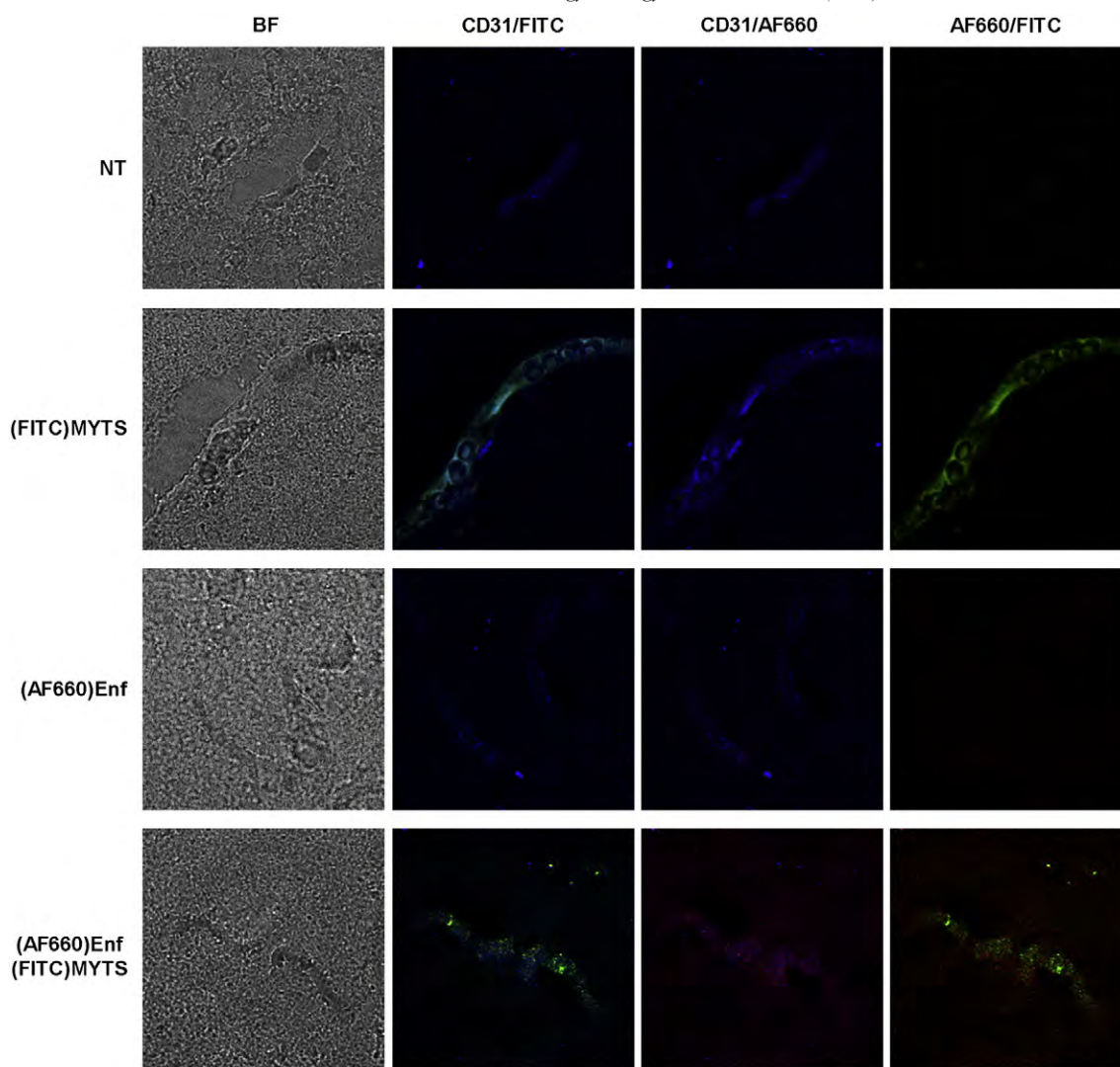


Figure 4. Confocal laser-scanning micrographs (single optical sections) of brain cryosections from non-treated mice (NT) or mice exposed for 1 h to (AF660)Enf, (FITC)MYTS or (AF660)Enf-MYTS(FITC); conjugated or free AF660-Enf (red) and FITC-MYTS (green) have been overlaid each other and with CD-31 stained endothelial cells (blue); brightfield (BF) images are reported on the left; bar: 10 μ m.

In vivo brain targeting and trans-BBB delivery of nanoconjugated enfuvirtide

Trans-BBB permeation of MYTS-conjugated Enf was then assessed *in vivo* in Balb/c mice intravenously injected with free Enf or with the same peptide conjugated to nanoparticles. We decided to follow the bioavailability and biodistribution of Enf, by labeling the peptide with AF660 whose efficiency as *in vivo* probe had been previously reported in mice.^{28,29} Firstly, plasma concentration of free or conjugated Enf was monitored at 30 min, 1 h and 6 h after injection in eight different animals for each experimental condition, to verify the effect of nanoconstruct on peptide bioavailability. We observed a maximal concentration of both free or conjugated drug in the blood stream within 1 h postinjection and a strong decrease over the following hours, up to negligible levels at 6 h postinjection. Moreover, Enf concentration in plasma appeared reduced by conjugation to MYTS and therefore less

available for the potentially infected organs, including brains (Figure S3). Other mice were injected with Enf or Enf-MYTS (nine for each experimental condition) to be sacrificed at 1 h postinjection, together with three untreated animals (controls). Fluorescence imaging of dissected brains revealed a significant accumulation of both free and nanoformulated Enf in this organ at 1 h postinjection, as pointed out by the strong Epf signal not observed in the brain of non-treated mice (Figure 3, A), feasibly due to the peptide content in the blood circulation of brain. Nevertheless, Epf intensity associated with nanoformulated Enf was stronger than that of free Enf (Figure 3, A, B), thus suggesting a higher accumulation of the nanoformulated peptide in this organ despite its lower bioavailability. To determine if the observed increased concentration of Enf in the brain was really associated to an increased permeation of the drug across BBB by effect of the nanocomplexation, we analyzed the interaction of Enf and Enf-MYTS with BBB cells and their localization in the

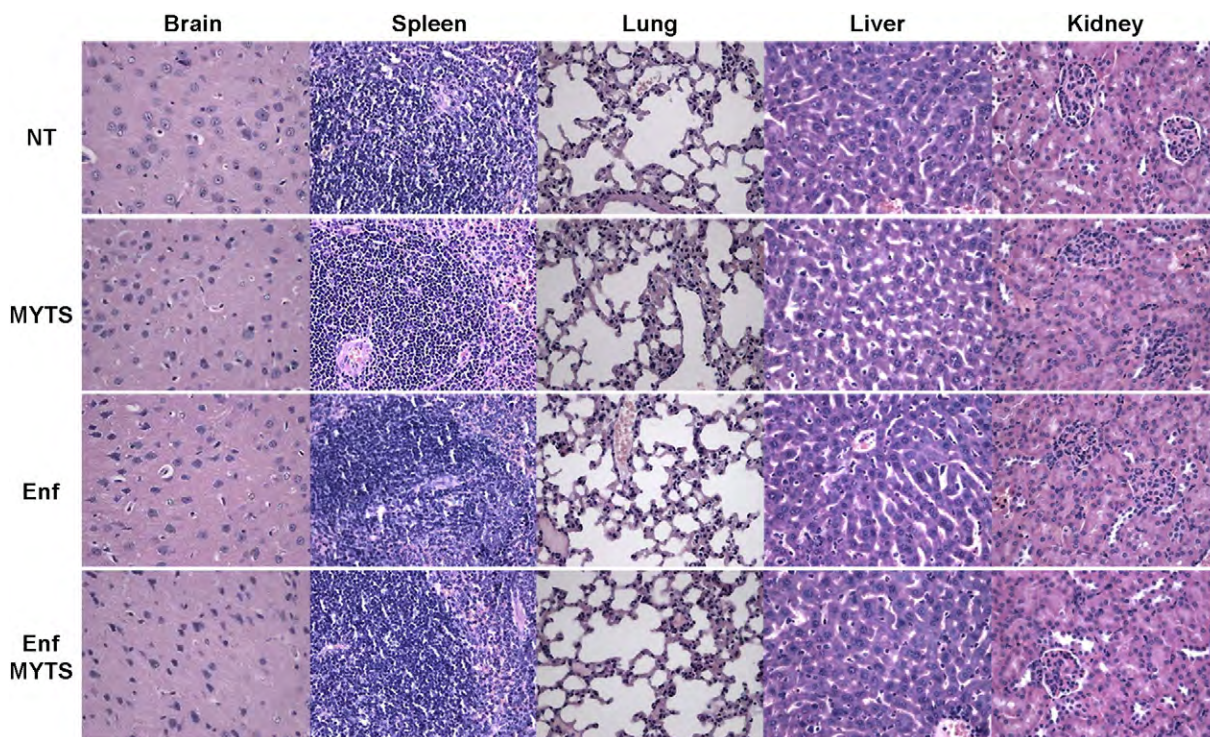


Figure 5. Histopathological analysis of brain, spleen, lung, liver and kidney dissected from non-treated (NT) mice, or from mice injected with MYTS, Enf and Enf-MYTS. Hematoxylin-eosin, OM $\times 40$.

perivascular space. Cryosections of mice brains excised 1 h postinjection of Enf or Enf-MYTS were analyzed by confocal microscopy. Figure 3, C shows enhanced fluorescence intensity in brain capillaries in samples treated with the nanoconjugated Enf when compared to the free peptide, where instead fluorescence was only slightly higher than control autofluorescence. In addition, nanocomplexation of Enf induced a spreading of fluorescence outside the boundaries of the vessel.

To confirm the efficacy of MYTS in driving Enf into the endothelial cells of brain capillaries and finally exerting an efficient trans-BBB permeation of the drug, we injected mice with MYTS, Enf or Enf-MYTS (three mice for each experimental condition) and analyzed the localization of the different compounds in brain sections after 1 h from injection, by means of the differential labeling of Enf and MYTS with AF660 and FITC, respectively (Figure 4). Immunodecoration of the endothelial cells with anti-CD31 antibody revealed a huge intracellular accumulation for MYTS. As expected, the ability of free Enf to enter BBB endothelial cells and reach brain parenchyma was negligible, while conjugation of the peptide to the nanoparticles allowed it to cross the barrier. Merge between Enf and MYTS signals in samples treated with Enf-MYTS clearly showed that only the peptide was able to diffuse outside the BBB, while nanoparticles were restricted to the vessel endothelium. This result, in agreement with *in vitro* observations, further suggested the dissociation of the nanocomplex within endothelial cells, with subsequent excretion of Enf.

The systemic toxicity of administered formulations was then assessed by histopathological examination of brain, liver, kidneys, spleen, and lungs isolated 1 h after Enf, MYTS or

Enf-MYTS injection. Analysis was performed on organs specimens from three different animals for each experimental condition. No histological lesions were observed in the analyzed organs (Figure 5).

Fate of MYTS in RBMVECs

The mechanism of MYTS entry and trafficking into the RBMVECs was investigated by TEM analysis on BBB-bearing inserts after 4, 7 or 24 h from the addition of Enf-MYTS in the upper chamber. Figure 6, A shows that, at 4 h of incubation, nanoparticles were either attached to the plasma membrane of the endothelial cells or internalized in the cytosol. The lack of membrane invaginations and the presence of free nanoparticles in the cytoplasm suggest that a non-endocytotic mechanism is involved in the internalization of MYTS by RBMVECs, as confirmed also by TEM images of brain samples exposed *in vivo* to the nanocomplex (Figure S4). Macropinocytosis rafts were also visible where a large number of nanoparticles came in contact with the cellular membrane. Once internalized, MYTS accumulated into large cellular compartments (Figure 6, A and B), and after 24 h of incubation, they were also detected into lysosomes (Figure 6, C). The same result was obtained by incubating the cells with the unconjugated MYTS.

Discussion

The BBB is the boundary that isolates brain tissues from the substances circulating in the blood and at the same time allows water and small lipophilic molecules to freely access the brain in

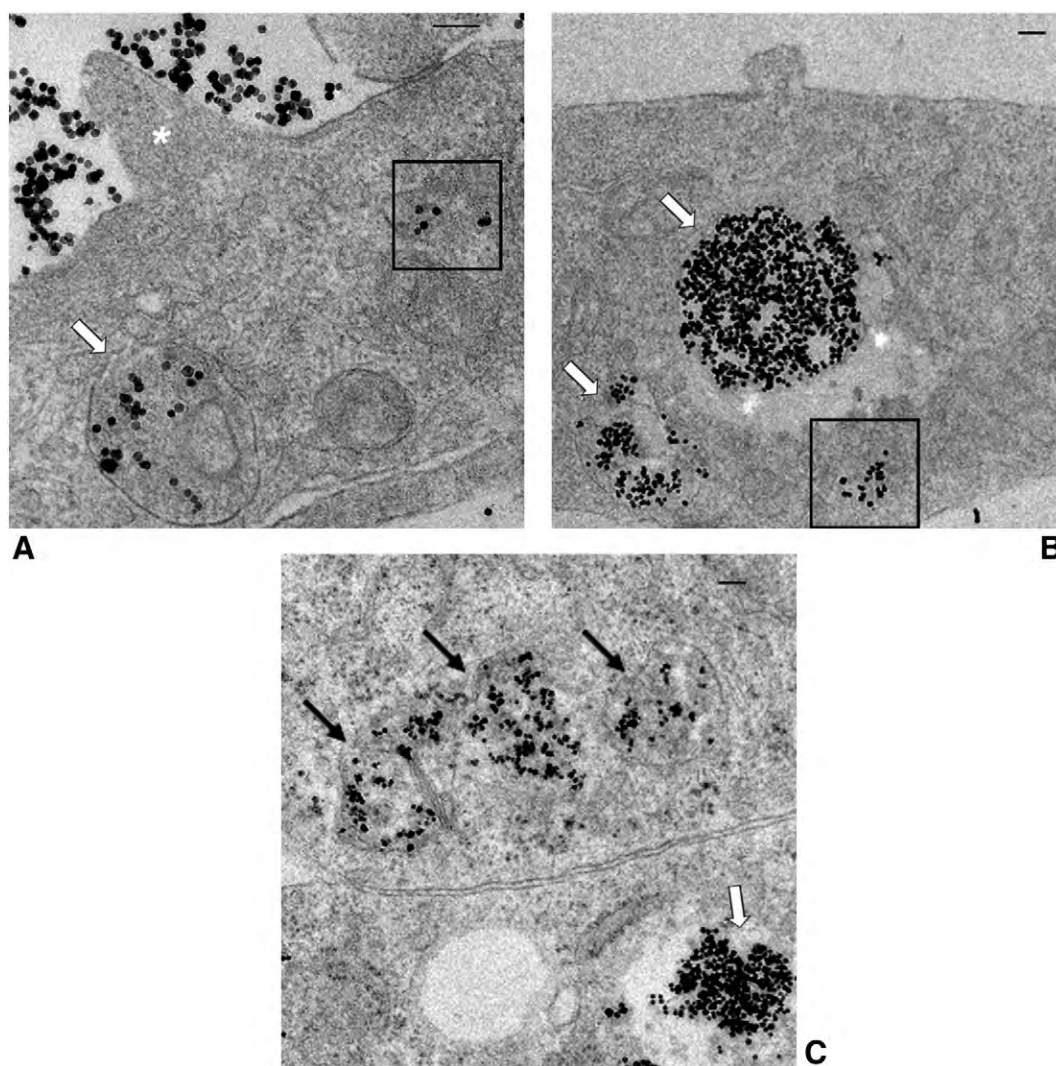


Figure 6. TEM images of RBMVECs in a BBB *in vitro* model exposed to 0.1 mg Enf-MYTS for 4 h (A), 7 h (B) and 24 h (C). MYTS are localized in big cell compartments (white arrows), in lysosomes (black arrows) or free into the cytosol (boxes); asterisk indicates a macropinosome raft; bars: 100 nm.

accordance with their concentration gradients. Within this barrier, the brain microvascular endothelial cells, phenotypically different from the endothelial cells of the peripheral circulation, hamper the filtration of therapeutic drugs, preventing them to reach the pathological tissues behind them. To permeate through the BBB, molecules need to be lipid soluble with a molecular weight <400 Da. Heavier and larger molecules, which are unable to diffuse through the BBB because of their size, weight and/or polarity, could cross the BBB only if transported by receptor-mediated transcytosis using ligands that bind specific BBB receptors. Therefore, drugs permeability across the BBB represents a clinical and biological challenge.

It is well established that a double correlation between HIV infection and the brain exists: HIV replication plays a major role in neurological diseases, and CNS is one of the main viral reservoir. During the acute phase of infection, HIV-1 rapidly infiltrates the CNS; there the viral replication can occur despite a complete drug-induced suppression of the virus in the peripheral blood. Noteworthy, while about 50% of HIV-infected patients are affected by neurological disease, evident morphological

alterations in CNS are observed in at least 80% of AIDS patients autopsies.³⁰ The acclaimed model for HIV-related injury of CNS involves the release from infected or activated glial cells (microglia and astrocytes) of numerous neurotoxic viral or cellular factors, which lead to neuronal damage and death, and of chemoattractants able to promote infiltration of infected and/or activated monocytes.⁴

In NeuroAIDS prevention, nanotechnology has been intensely explored with the aim to develop novel and promising drug delivery systems, and several experimental attempts have been carried out in last years in order to enhance the BBB permeability toward antiretroviral drugs. Indeed, BBB has been demonstrated to be impermeable to 98% of antiretroviral drugs.³¹ In 2006, Kuo and colleagues have incorporated two antiretroviral drugs, zidovudine and lamivudine, into polymeric polybutylcyanoacrylate (PBCA) nanoparticles, showing a 8-20 and 10-18 fold increase in BBB permeation, respectively.³² However, polymeric nanoparticles are not suitable as carriers for polar or ionic drugs, and degradation of PBCA can produce toxic formaldehyde by-products.³¹ Other biocompatible polymers, such as

polylactide, have been studied as novel nanocarriers for CNS drug delivery, but a transient inflammatory response has been reported.³¹ Conjugation of the protease inhibitor saquinavir with transferrin-conjugated quantum dots has shown improved BBB penetration *in vitro*, by exploiting an active transport mechanism mediated by transferrin receptors; nevertheless, *in vivo* results are still missing.¹⁴ Other nanocarriers such as liposomes are inefficient for loading with water-soluble drugs.³¹

In our study we have designed and developed a novel nanodrug consisting of an iron oxide nanoparticle coated with a suitable amphiphilic polymer and functionalized with the antiretroviral peptide enfuvirtide. Although rarely used in clinical practice, we selected Enf for two main reasons. First, it has proven effective as a non-selective inhibitor of HIV-1 fusion with cells, able to preclude virus entry regardless its co-receptor tropism. The blockade of virus entry into cells is relevant in view of the use of drugs that purge the latent reservoir, damming the circulating HIV-1 pool of virus that should not re-infect new cells. Secondly, Enf is one of the most structurally complex antiretroviral molecules, therefore ideal for testing the efficacy of our nanoconstruct as a drug delivery system to the brain.

So far, the use of iron oxide nanoparticles as antiretroviral carriers has been poorly investigated *in vivo*.³¹ In the present work, our polymer-coated iron oxide nanoparticles (namely MYTS) have proven to be promising as CNS drug delivery system for antiretroviral drugs, by taking advantage of their intrinsic propensity to cross the BBB. We observed *in vitro* an increased permeation of nanoformulated Enf across BBB up to 170% upon 3 h of incubation. Moreover, conjugated Enf showed increased epifluorescence intensity in mice brain, as a result of its huge CNS accumulation. Electron microscopy images suggested that endocytosis is not likely responsible for the internalization of MYTS in the endothelial cells, even though the presence of a large number of nanoparticles on the cell surface activated the production of macropinocytosis membrane ruffles. Rather, the presence of free nanoparticles in the cell cytoplasm strongly suggests that their internalization mainly occurred by a passive diffusion, probably mediated by the absorption of the amphiphilic coating on the cell membrane. In previous studies, it has been assumed that polymer aggregates carrying hydrophobic groups should have the same affinity for brain endothelial cell membranes of pluronic block copolymers³³, whose absorption on cell membrane induces a structural alteration of the lipid bilayer.³⁴ Membrane fluidization allows the pluronics micelles to enter the microvessel endothelial cells and deliver their cargo into the intracellular environment.³⁴ Once into the cell, MYTS were sequestered by huge endosome-like compartments and then directed to lysosomes. Our data indicate that Enf dissociated from MYTS in the endothelial cells to be efficiently excreted into the outside environment. The dissociation mechanism requires further studies to be elucidated, but it could involve the degradation of the PMA shells bearing the peptide. PMA degradation feasibly started into the more mature endosomal compartments, as an effect of the increased acidity and enzymatic activity of their inner environment, to be then completed within lysosomes. Concerning Enf efflux, it is known that foreign substances are usually rejected by the BBB through an efflux mechanism based on transporters such as P-glycoprotein and multidrug resistance-associated protein (MRP).³⁵ The brain-directed

efflux of Enf could occur via MRP4, a protein expressed on the abluminal membrane of the brain capillary endothelial cells, which were proven to mediate the excretion of different drugs, including some antiretrovirals.³⁶ Histopathological analysis of brain, spleen, lung, liver and kidneys dissected from mice upon Enf treatment, confirmed that this antiretroviral drug does not exert toxic effects. Moreover, the lack of any organ lesion in the presence of circulating MYTS is a clear evidence of the systemic safety of these nanoparticles at the experimental dosage, further supporting their great potential as drug delivery system across the BBB.

In conclusion, this is the first documented experience of a nanotechnological engineering of the complex antiretroviral drug enfuvirtide, which confers to this large peptide the capability to cross the BBB. Whether and how the propensity of Enf nanoconjugate to cross the BBB could affect the viral replication in the CNS sanctuary remain to be established, and further studies will be performed to assess the antiviral efficacy of Enf after trans-BBB permeation. However, at present, our results represent an important step forward toward HAART-mediated HIV eradication from the CNS reservoir. Since MYTS nanoparticles can be loaded with multiple drugs of different classes, the present study suggests a straightforward approach for targeting various phases of viral replication in the CNS.

Appendix A. Supplementary data

Supplementary data to this article can be found online at <http://dx.doi.org/10.1016/j.nano.2015.03.009>.

References

1. Sarmati L, Parisi SG, Montano M, Andreis S, Scaggiante R, Galgani A, et al. Nevirapine use, prolonged antiretroviral therapy and high CD4 nadir values are strongly correlated with undetectable HIV-DNA and -RNA levels and CD4 cell gain. *J Antimicrob Chemother* 2012;**67**:2932-8.
2. Cory TJ, Schacker TW, Stevenson M, Fletcher CV. Overcoming pharmacologic sanctuaries. *Curr Opin HIV AIDS* 2013;**8**:190-5.
3. Bunupuradah T, Bowonwattanuwoong C, Jirajariyavej S, Munsakul W, Klinbuaem V, Sophonphan J, et al. HIV-1 genital shedding in HIV-infected patients randomized to second-line lopinavir/ritonavir monotherapy versus tenofovir/lamivudine/lopinavir/ritonavir. *Antivir Ther* 2014;**24**. <http://dx.doi.org/10.3851/IMP2737>.
4. Kramer-Hämmerle S, Rothenaigner I, Wolff H, Bell JE, Brack-Werner R. Cells of the central nervous system as targets and reservoirs of the human immunodeficiency virus. *Virus Res* 2005;**11**:194-213.
5. Surdo M, Cortese MF, Perno CF, Aquaro S. NeuroAIDS: virological aspects of HIV infection. *J Biol Regul Homeost Agents* 2013;**27**:115-28.
6. Doyon G, Sobolewski MD, Huber K, McMahon D, Mellors JW, Cremer NS. Discovery of a small molecule agonist of phosphatidylinositol 3-kinase p110 α that reactivates latent HIV-1. *PLoS One* 2014;**29**. <http://dx.doi.org/10.1371/journal.pone.0084964>.
7. Wightman F, Lu HK, Solomon AE, Saleh S, Harman AN, Cunningham AL, et al. Entinostat is a histone deacetylase inhibitor selective for class I histone deacetylases and activates HIV production from latently infected primary T cells. *AIDS* 2013;**27**:2853-62.
8. Shan L, Xing S, Yang HC, Zhang H, Margolick JB, Siliciano RF. Unique characteristics of histone deacetylase inhibitors in reactivation of latent HIV-1 in Bcl-2-transduced primary resting CD4+ T cells. *J Antimicrob Chemother* 2014;**69**:28-33.

9. Kent SJ, Reece JC, Petravic J, Martyushev A, Kramski M, De Rose R, et al. The search for an HIV cure: tackling latent infection. *Lancet Infect Dis* 2013;**13**:614-21.
10. Parboosing R, Maguire GEM, Govender P, Kruger HG. Nanotechnology and the treatment of HIV infection. *Viruses* 2012;**4**:488-520.
11. Mamo T, Moseman EA, Kolishetti N, Salvador-Morales C, Shi J, Kuritzkes DR, et al. Emerging nanotechnology approaches for HIV/AIDS treatment and prevention. *Nanomedicine (Lond)* 2010;**5**:269-85.
12. Amiji MM, Vyas TK, Shah LK. Role of nanotechnology in HIV/AIDS treatment: potential to overcome the viral reservoir challenge. *Discov Med* 2006;**6**:157-62.
13. Mahajan SD, Aalinkeel R, Law WC, Reynolds JL, Nair BB, Sykes DE, et al. Anti HIV-1 nanotherapeutics: promises and challenges for the future. *Int J Nanomedicine* 2012;**7**:5301-14.
14. Mahajan SD, Roy I, Xu G, Yong KT, Ding H, Aalinkeel R, et al. Enhancing the delivery of anti retroviral drug "saquinavir" across the blood brain barrier using nanoparticles. *Curr HIV Res* 2010;**8**:396-404.
15. Trottier B, Walmsley S, Reynes J, Piliero P, O'Hearn M, Nelson M, et al. Safety of enfuvirtide in combination with an optimized background of antiretrovirals in treatment-experienced HIV-1-infected adults over 48 weeks. *J Acquir Immune Defic Syndr* 2005;**40**:413-21.
16. Liu S, Lu H, Niu J, Xu Y, Wu S, Jiang S. Different from the HIV fusion inhibitor C34, the anti-HIV drug Fuzeon (T-20) inhibits HIV-1 entry by targeting multiple sites in gp41 and gp120. *J Biol Chem* 2005;**280**:11259-73.
17. Patel IH, Zhang X, Nieforth K, Salgo M, Buss N. Pharmacokinetics, pharmacodynamics and drug interaction potential of enfuvirtide. *Clin Pharmacokinet* 2005;**44**:175-86.
18. Dando TM, Pery CM. Enfuvirtide. *Drugs* 2003;**63**:2755-66.
19. Borrego P, Calado R, Marcelino JM, Bártolo I, Rocha C, Cavaco-Silva P, et al. Baseline susceptibility of primary HIV-2 to entry inhibitors. *Antivir Ther* 2012;**17**:565-70.
20. Sista P, Melby T, Greenberg ML, Davison D, Jin J, Mosier S, et al. Characterization of baseline and treatment-emergent resistance to T-20 (enfuvirtide) observed in phase II clinical trials: substitutions in gp41 amino acids 36-45 and enfuvirtide susceptibility of virus isolates. *Antivir Ther* 2002;**7**:S16-7.
21. Cilliers T, Patience T, Pillay C, Papathanasopoulos M, Morris L. Sensitivity of HIV type 1 subtype C isolates to the entry inhibitor T-20. *AIDS Res Hum Retroviruses* 2004;**20**:477-82.
22. Derdeyn CA, Decker JM, Sfakianos JN, Zhang Z, O'Brien WA, Ratner L, et al. Sensitivity of human immunodeficiency virus type 1 to fusion inhibitors targeted to the gp41 first heptad repeat involves distinct regions of gp41 and is consistently modulated by gp120 interactions with the coreceptor. *J Virol* 2001;**75**:8605-14.
23. Price RW, Parham R, Kroll JL, Baker B, Sailstad J, Hoh R, et al. Enfuvirtide cerebrospinal fluid (CSF) pharmacokinetics and potential use in defining CSF HIV-1 origin. *Antivir Ther* 2008;**13**:369-74.
24. Park J, An K, Hwang Y, Park JG, Noh HJ, Kim JY, et al. Ultra-large-scale syntheses of monodisperse nanocrystals. *Nat Mater* 2004;**3**:891-5.
25. Pellegrino T, Manna L, Kudera S, Liedl T, Koktysh D, Rogach AL, et al. Hydrophobic nanocrystals coated with an amphiphilic polymer shell: a general route to water soluble nanocrystals. *Nano Lett* 2004;**4**:703-7.
26. Bazylińska U, Kulbacka J, Wilk WA. Dicarboxylic ionic surfactants in fabrication of biocompatible nanoemulsions: factors influencing droplet size and stability. *Colloids Surf A Physicochem Eng Asp* 2014;**460**:312-20.
27. Alkilany AM, Abulatefeh SR, Mills KK, Bani Yaseen AI, Hamaly MA, Alkhatib HS, et al. Colloidal stability of citrate and mercaptoacetic acid capped gold nanoparticles upon lyophilization: effect of capping ligand attachment and type of cryoprotectants. *Langmuir* 2014;**30**:13799-808.
28. Zaharoff DA, Hance KW, Rogers CJ, Schlom J, Greiner J. Intratumoral immunotherapy of established solid tumors with chitosan/IL-12. *J Immunother* 2010;**33**:697-705.
29. Fiandra L, Mazzucchelli S, De Palma C, Colombo M, Allevi R, Sommaruga S, et al. Assessing the in vivo targeting efficiency of multifunctional nanoconstructs bearing antibody-derived ligands. *ACS Nano* 2013;**7**:6092-102.
30. De Almeida SM, Letendre S, Ellis R. Human immunodeficiency virus and the central nervous system. *Braz J Infect Dis* 2006;**10**:41-50.
31. Sagar V, Pilakka-Kanthikeel S, Pottathil R, Saxena SK, Nair M. Towards nanomedicines for neuroAIDS. *Rev Med Virol* 2014;**24**:103-24.
32. Kuo YC, Chen HH. Effect of nanoparticulate polybutylcyanoacrylate and methylmethacrylate-sulfopropylmethacrylate on the permeability of zidovudine and lamivudine across the in vitro blood-brain barrier. *Int J Pharm* 2006;**327**:160-9.
33. Hemmelman M, Knoth C, Schmitt U, Allmeroth M, Moderegger D, Barz M, et al. HPMA based amphiphilic copolymers mediate central nervous effects of domperidone. *Macromol Rapid Commun* 2011;**32**:712-7.
34. Batrakova EV, Li S, Vinogradov SV, Alakhov VY, Miller DW, Kabanov AV. Mechanism of pluronic effect on P-glycoprotein efflux system in blood-brain barrier: contributions of energy depletion and membrane fluidization. *J Pharmacol Exp Ther* 2001;**299**:483-93.
35. Demeule M, Regina A, Jodoin J, Laplante A, Dagenais C, Berthelet F, et al. Drug transport to the brain: key roles for the efflux pump P-glycoprotein in the blood-brain barrier. *Vascul Pharmacol* 2002;**38**:339-48.
36. Löscher W, Potschka H. Drug resistance in brain disease and the role of drug efflux transporters. *Nat Rev Neurosci* 2005;**6**:591-602.

Delivering Colloidal Nanoparticles to Mammalian Cells: A Nano–Bio Interface Perspective

Paolo Verderio, Svetlana Avvakumova, Giulia Alessio, Michela Bellini, Miriam Colombo, Elisabetta Galbiati, Serena Mazzucchelli, Jesus Peñaranda Avila, Benedetta Santini, and Davide Prospero*

Understanding the behavior of multifunctional colloidal nanoparticles capable of biomolecular targeting remains a fascinating challenge in materials science with dramatic implications in view of a possible clinical translation. In several circumstances, assumptions on structure–activity relationships have failed in determining the expected responses of these complex systems in a biological environment. The present Review depicts the most recent advances about colloidal nanoparticles designed for use as tools for cellular nanobiotechnology, in particular, for the preferential transport through different target compartments, including cell membrane, cytoplasm, mitochondria, and nucleus. Besides the conventional entry mechanisms based on crossing the cellular membrane, an insight into modern physical approaches to quantitatively deliver nanomaterials inside cells, such as microinjection and electroporation, is provided. Recent hypotheses on how the nanoparticle structure and functionalization may affect the interactions at the nano–bio interface, which in turn mediate the nanoparticle internalization routes, are highlighted. In addition, some hurdles when this small interface faces the physiological environment and how this phenomenon can turn into different unexpected responses, are discussed. Finally, possible future developments oriented to synergistically tailor biological and chemical properties of nanoconjugates to improve the control over nanoparticle transport, which could open new scenarios in the field of nanomedicine, are addressed.

1. Introduction

1.1. Understanding Nanoparticle Properties at the Cellular Level

In the last decade, colloidal nanoparticles have been established as an emerging tool for the study of biological processes with an increasing number of possible applications in biotechnology and medicine.^[1–3] Depending on their constitutional materials, nanoparticles have different chemical–physical properties such as high electron density and strong optical absorption (e.g., gold nanoparticles, AuNPs), magnetic moment (e.g., iron oxide

nanoparticles, IONPs), and photoluminescence (e.g., semiconductor quantum dots, QDs). The complex interactions between nanoparticles and the cellular environment have been thoroughly examined, such that the knowledge of these relationships remains of fundamental attractiveness. This is the reason why the scientific community involved in nanomaterials evolution has raised numerous questions in order to understand the dynamic forces and the molecular components that shape these interactions. At the moment, several research groups are focusing on the creation of properly “designed” nanoparticles, as an essential prerequisite for each individual nano-biomedical and nano-biotechnological application. With a general impression of the biological interfaces that nanoparticles meet when interacting with living cells (i.e., membrane, cytoplasm, nucleus, and internal organelles), researchers have now the possibility to define how these interactions remodel the fundamental forces that govern the behavior of colloidal nanoparticles in a complex biological system. In addition, other works highlight the importance of

correlating nanoparticle fluid dynamics to their physicochemical features, which adds a basic but, at the same time, capital information to predict potential toxicological risks of such materials. Such correlations would help us to construct new materials and thus find the optimal mechanism of intracellular delivery of different nanoparticle platforms, evaluating and reducing their toxicity to the minimum level.^[4,5]

These basic issues, which can be collected in a unique concept that can be referred to as nano–bio interface, give rise to a very intricate system to investigate, as the nano–bio interface consists in a plethora of dynamic components. Most available

P. Verderio, Dr. S. Avvakumova, M. Bellini, Dr. M. Colombo, E. Galbiati, J. P. Avila, B. Santini, Dr. D. Prospero
Dipartimento di Biotecnologie e Bioscienze
Università di Milano-Bicocca
piazza della Scienza 2, 20126 Milano, Italy
E-mail: davide.prosperto@unimib.it

Dr. S. Avvakumova, G. Alessio, Dr. S. Mazzucchelli
Dipartimento di Scienze Biomediche e Cliniche “Luigi Sacco”
Università di Milano
Ospedale L. Sacco, via G. B. Grassi 74, 20157 Milano, Italy
Dr. D. Prospero
Laboratory of Nanomedicine and Clinical Biophotonics
Fondazione Don Carlo Gnocchi ONLUS
Via Capecelatro 66, 20148 Milan, Italy



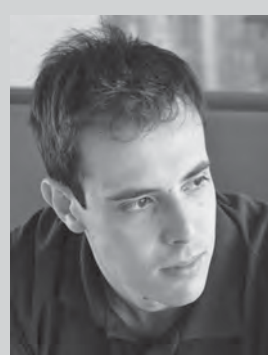
DOI: 10.1002/adhm.201300602

studies correlate these interactions with surface properties of nanomaterials, including size, shape, and curvature, roughness, porosity, and crystallinity.^[6–8] Other works deal with the properties of the solid–liquid interface originated when nanoparticles are suspended in the surrounding medium, including for instance the effective surface charge,^[9,10] the state of aggregation and the stability of the suspension over time and at different cellular pH values. Moreover, the solid–liquid contact zone with biological substrates might be influenced by the nature of surface ligands and chemical functionalization of nanoparticles.^[11,12] In particular, the contact with hydrophobic or charged regions of cells determines the nanoparticle preferential pathway of interaction with the cellular external environment and, later on, the formation of stable or transient complexes with their binding molecules and the route of internalization and metabolism of nanoparticles.^[13]

Another nanoscale engagement with biological processes is the identification of the biomolecular “protein corona” that provides the biological identity of nanomaterials.^[14] To better understand this concept, we should try to envision that when nanoparticles, which have higher free energy than the corresponding bulk materials, are suspended in a biological fluid, they are rapidly coated by a selected group of biomolecules to form a molecular corona essentially consisting in a layer of adsorbed proteins that represent the main biomolecular components of that fluid. Is this protein corona what the external biological environment actually “sees” when interacting with a suspended nanoparticle. As will be discussed below, this process leads to the formation of a near-monolayer of biomolecules, usually termed “hard” corona, which tightly, yet reversibly, binds to the nanoparticle surface. In addition, an exchangeable layer of biomolecules is formed as an outer shell over the hard corona; this process is more dynamic and reversible and this is the reason why it is called “soft” corona.^[15,16] Interestingly, from several specific analyses, it has been observed that only few molecules available in biological medium are found in the hard corona and they hardly correspond to the most abundant proteins in plasma. It is worth emphasizing that the protein corona is not only relevant in passive cellular adhesion and internalization (passive targeting), but is also relevant when antibodies or target molecules are immobilized on the nanoparticle surface with the aim of achieving a targeting action directed toward a selected molecular receptor (active targeting). In these cases, the corona may affect these specific interactions much more thoroughly than expected.^[17] For this reason, the surface modification with “bioinvisible” polymeric moieties (e.g., pegylation) is often required to reduce the formation of nonspecific bindings of biomolecules,^[18] thus making more relevant the role played by the active targeting component.

1.2. Designing the Nanoparticle “Framework”: A Progressive Evolution

Outcomes from studies of nano–bio interface have largely influenced nanomaterials design for biomedical applications. To date, three generations of nanoparticles can be recognized, which have been engineered to this purpose (Figure 1). The first generation is represented by nanomaterials functionalized



Paolo Verderio obtained his Master degree in 2009 in Industrial and Management Chemistry at University of Milano. Next, he worked as a research fellow at the Hosp. Luigi Sacco until 2011 focusing on iron oxide nanoparticles as contrast agents for early breast cancer diagnosis. He started the Ph.D. in Chemical Science at the University of Milano–Bicocca in 2011 where he is currently working. His scientific interests are based on synthesis and biofunctionalization of inorganic and organic nanoparticles for drug delivery applications.



Dr. Svetlana Avvakumova is a post-doc researcher in Department of Biomedical and Clinical Sciences at University of Milan. She graduated from Colloidal Chemistry at University of St. Petersburg in 2007. Prior to joining Dr. Prosperi's group, she obtained her Ph.D. degree in Chemistry at University of Milan in 2013. Her research interests have been focused on design and development of multifunctional nanoparticles for efficient targeting and drug delivery-based therapy of different tumors.



Dr. Davide Prosperi studied Chemistry at University of Milano, where he obtained his Master degree in 1998. He earned his Ph.D. degree at the same University in 2002. Subsequently, he was a Researcher in the Nanobiotechnology Unit at the ISTM-CNR until 2008. Next, he moved to his present position as an Assistant Professor of Biochemistry and Nanobiotechnology at the University of Milano–Bicocca, where he leads the NanoBioLab. His scientific interests concern the synthesis and biological investigation of colloidal and biomimetic nanoparticles for biomedical applications.

through basic surface chemistries to assess biocompatibility, enhance cellular uptake, and reduce toxicity. The second generation is focused on nanomaterials with optimized surface boundaries that improve stability and targeting in biological systems.^[19–23] These studies were characterized by two important

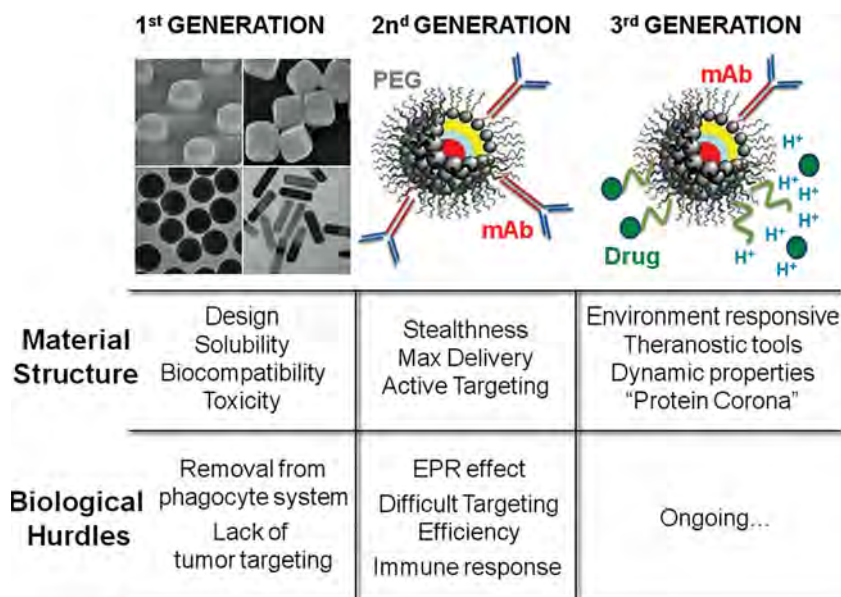


Figure 1. The evolution of nanomaterials and their biological challenges.

tasks: "stealthiness" and active targeting. The aim of developing "stealth" nanoparticles is to maximize blood circulation half-life to enhance the continuous delivery of nanoparticles into the target tissue via a leaky vasculature, exploiting the so-called tumor "enhanced permeability and retention" (EPR) effect. To gain this goal, chemistry has been evolved by adding an amphiphilic polymer coating capable of minimizing nonspecific interactions, such as polyethylene glycol (PEG), to the nanoparticle surface. In this context, the overall PEG chain length and its density on the surface strongly affect the nanoparticle stability over time.^[18] In addition, the main advantage of having a ligand bound to a nanoparticle, as opposed to the free molecule in solution, is that the nanoparticle surface creates a region of highly concentrated ligands, which is generally associated to an increase in the avidity for the membrane receptor resulting in clustering effects at the cell surface.^[24]

The third generation of nanomaterials, defined "environment-responsive," is in continuous evolution. These dynamic nanoparticles take advantage of a combination of physical, chemical, and biological properties, either deriving from intrinsic features or arising from the interaction of the nanoparticles with a specific environment they are in contact with, in order to maximize their effect into targeted sub-cellular compartments.^[25,26] Cellular delivery based on these more sophisticated nanomaterials remains a great challenge in the design of effective nanodrugs, while an understanding of how cells traffic their constituents to the appropriate place inside or outside the cell could provide valuable information to improve the targeting efficiency and to reduce the toxicity of the system.

Based on the above considerations, in this review we wish to provide a general overlook on the interaction processes at the nano-bio interface that mediate cellular internalization routes of nanoparticles and on their relevant outcomes. Next, we will describe recent advances in developing strategies for

nanoparticle sub-cellular targeting and delivery. Finally, we aim to shed a light on the future developments and long-term implications of these findings. This overview would enable researchers to restructure the assembly of composite nanovectors that is expected to afford the highest possible specific efficiency in targeted delivery of drugs and diagnostic agents.

2. Interactions of Nanoparticles with Mammalian Cells

2.1. Delivery Through the Cellular Membrane

At the cellular level, there are several biological barriers that nanoparticles must face to reach their destination: cell membrane is the first. Indeed, the hydrophobic nature of plasma membrane lipid bilayer prevents the diffusion of polar complexes larger than 1 kDa.^[27] Conveniently, nanoparticles are on the same size order of large proteins and of typical cellular and extracellular components, so that they can efficiently penetrate living cells by exploiting the ordinary cellular endocytic mechanisms.

Although small and positively charged nanoparticles can enter cells by passive diffusion through the plasma membrane,^[28] most of them are internalized by active processes, which could be subdivided into two broad categories: phagocytosis (or "cell eating") and pinocytosis (or "cell drinking"). Phagocytosis is conducted by specialized cells, including macrophages, monocytes, and neutrophils, whereas pinocytosis is more general and may occur in all cell types by at least four basic mechanisms: macropinocytosis, clathrin-mediated endocytosis (CME), caveolae-mediated endocytosis, and clathrin- and caveolae-independent endocytosis. Clathrin is a coat-protein exploited by the cell to assist the formation of endocytic vesicles to safely transport selected molecules within and between the cells, whereas caveolae are caveolin-1-enriched invaginations of the plasma membrane that form a 50–100 nm subdomain of lipid rafts. All of these processes have been already reviewed in detail (Figure 2).^[29,30]

Obviously, the pathway of entry is a crucial factor in orienting the subcellular trafficking and thereby the fate of a nanomaterial.^[31] Different inhibitors capable of interfering with the nanoparticle uptake can be used to study which pathways are preferentially chosen by the cell to internalize a certain nanoparticle. Example of such inhibitors include sucrose, which alters clathrin-mediated endocytosis, chlorpromazine, which disrupts the clathrin-coated pits, nystatin, which inhibits lipid-raft-dependent endocytosis, and dynasor, which interferes with dynamin-mediated pathways.^[32,33]

In recent years, great efforts have been spent to clarify the mechanisms behind cell-nanoparticle interactions. In order to try to elucidate the transport pathway of nanoparticles in epithelial cells, He et al. studied endocytosis, exocytosis,

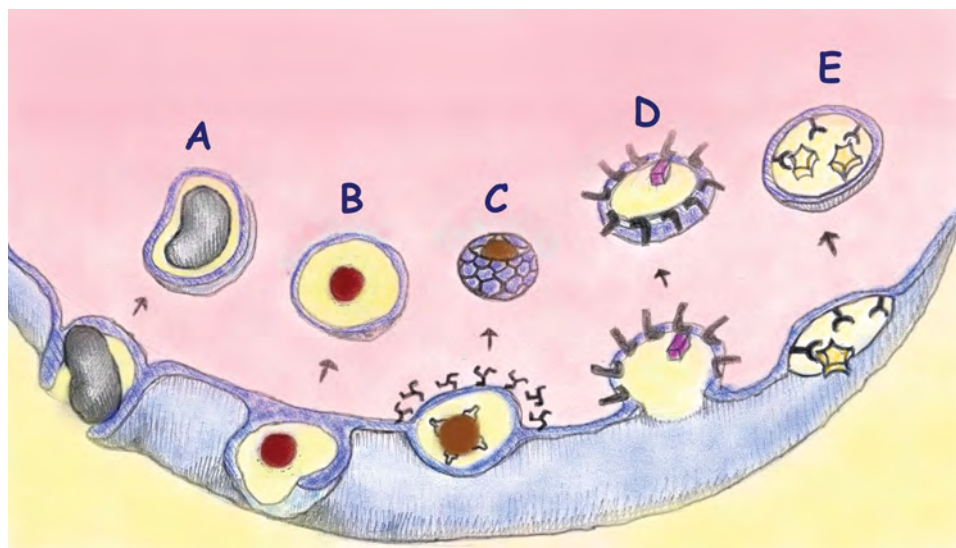


Figure 2. Cellular internalization models: A) phagocytosis; B) macropinocytosis; C) clathrin-mediated endocytosis; D) caveolae-mediated endocytosis; E) clathrin-independent and caveolin-independent endocytosis.

and transcytosis processes using MDCK epithelial cells and unmodified poly(lactide-co-glycolide) (PLGA) nanoparticles. By means of various endocytosis inhibitors, the authors demonstrated that nanoparticles could be endocytosed via multiple pathways involving both lipid raft and clathrin mechanisms, but not macropinocytosis.^[33] Binding and uptake of the same PLGA nanoparticles in Caco-2 cells proved to be either energy-dependent or independent and nanoparticles underwent multiple pathways including clathrin-mediated uptake, lipid raft/caveolae-mediated endocytosis, and macropinocytosis, thus displaying nonspecific endocytosis routes.^[34]

However, the use of targeting functionalities introduced in the nanoconstruct usually affects the internalization route. In a recent study, Huang et al. described the interaction between tumor cells and selenium (Se) nanoparticles functionalized with transferrin (Tf) as a targeting ligand. Tf significantly enhanced the cellular uptake of drug-loaded Se nanoparticles through clathrin-mediated and dynamin-dependent lipid-raft-mediated endocytosis in cancer cells over-expressing Tf receptors, concomitantly increasing their selectivity toward cancer cells compared with normal cells.^[32]

In accordance with the cellular equilibrium principles, as any type of molecules, nanoparticles can enter and distribute within cells by energy-dependent pathways.^[35–37] At the interface between nanomaterials and biological systems, nanoparticle uptake depends from several factors related to the nanoparticle properties, including size, shape, surface charge, and coating. Actually, size is a hot topic because a common predominant point of view about what dimension promotes cellular uptake is missing. However, it should be discussed that some types of nanoparticles that, due to their size, can cross the membrane in a receptor-mediated way under normal conditions, in a biological environment can be subjected to destabilizing forces and be endocytosed by the cells as aggregates.^[38,39] The effect of shape on cellular uptake is principally due to two different causes:

1) the specific functional groups protruding from the nanoparticle with directionalities that are affected by the surface geometry and 2) different surface geometries often lead to dissimilar uptake profiles, which may be due to the orientation of the nanoparticle at the cellular interface.^[40] The resulting variety of endocytic pathways can induce in turn different options to process the nanoparticles by the cell, usually dependent on the cell type and phenotype. For example, rod shape causes a lower uptake compared to spherical nanoparticles because the nanoparticle wrapping by the membrane requires a far longer process in the case of elongated shape.^[41] Finally, surface coating has a significant impact on nanomaterials translocation into cells especially in terms of charge. Verma et al. propose a model in which nanoparticles coated with amphiphilic molecules in an ordered ribbon-like alternating arrangement should be able to penetrate the cell membrane, whereas nanoparticles bearing molecules presented in a random arrangement are taken up by the endocytosis pathway.^[42] In a simplified model, due to the negative charge of phospholipids bilayer, nanoparticles with a surface charge of the same sign of the membrane basically present no contact, nanoparticles with a neutral surface show a minimal interaction with cells, while strong interaction is achieved using positively charged nanoparticles.^[43] However, further complexity originates from the patchiness and heterogeneity of the cell membrane,^[44] which is a 6-nm-thick soft interface consisting of a lipid bilayer incorporating variable distributions of proteins, lipids, and glycosylated architectures often containing portions on the extracellular side exploited by the cell to communicate with the external environment.^[30] Several cell features can affect the nanoparticle process of uptake. One such feature is the cell-type: uptake differences between polarized and non-polarized cells were recovered, caused by the respective different endocytic properties of their apical and basolateral side. In fact, while in non-polarized cells nanoparticles are mainly internalized via macropinocytosis, in polarized cells,

the same nanoparticles can be incorporated both by macropinocytosis and clathrin-mediated endocytosis.^[42,45] Nanoparticle entry is also dependent on the contingent state of the cell. For example, cells can be closely packed in a compact barrier rather than isolated or fluctuating in a medium. Also relevant is how old are cells and in which phase of the cell cycle they are,^[46] because, in each phase, protein and lipid expression can change significantly resulting in a dramatic alteration of the membrane structure and thus of nanoparticle interaction.

2.2. Influence of Protein Adsorption on the Biological Identity of Nanomaterials

The above arguments suggest that the interaction between nanomaterials and cells is of fundamental importance to understand and predict the fate of a composite hybrid nanoconstruct in a biological system. We mentioned that physicochemical properties of nanoparticles, as well as surface chemistry and functionalization, play a pivotal role in determining the modification of the physiology of interacting cells.^[28] Indeed, they can affect uptake (amount, ratio and mechanism), transportation (accumulation, localization and exclusion), and cytotoxicity (necrosis, apoptosis and reduced cell proliferation). This section is dedicated to discuss how the biological identity of a nanoparticle determines the physiological response, including signaling, kinetics, transport and accumulation.^[47]

As soon as a nanomaterial is introduced into a biological environment, proteins and other molecules from that media rapidly adsorb on its surface forming a biomolecular layer, essentially consisting of proteins.^[15,16] This phenomenon, mostly referred to as “protein corona,” alters the size and interfacial composition of that nanomaterial, giving it a biological identity that is distinct from its originally intended structure (Figure 3).

The structure of the protein corona is described by five parameters: i) thickness and density, ii) identity and quantity, iii) arrangement, orientation, iv) conformation, and v) affinity. Altogether, these parameters define the interaction of a nanomaterial within a specific biological environment. The thickness and density of the corona determine the overall size of the nanomaterial while the identity and number of adsorbed proteins affects the array of possible biological interactions according to their binding strengths. The orientation determines the accessibility of potential binding and/or catalytic domains, while protein conformation influences the activity of a protein and its interaction with other molecules. Finally, protein affinity to the nanomaterial surface regulates whether it adsorbs, remains bound, or dissociates during biophysical interactions or translocation to a new biological compartment.

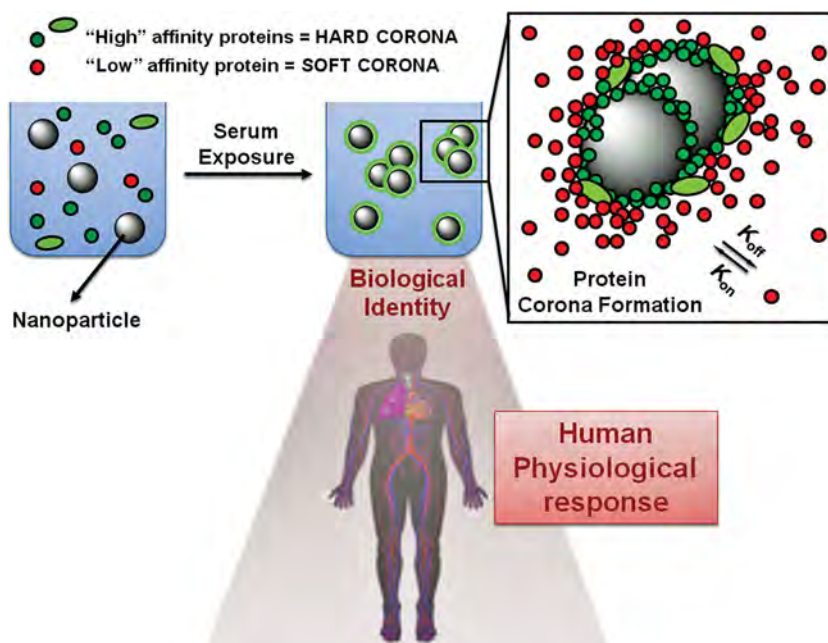


Figure 3. The formation of a protein corona occurs when a nanomaterial is soaked into a physiological environment. Biomolecules with high affinity (green) and low affinity (red) form a thin layer of molecules on the nanomaterial surface, which can be tightly bound (“hard” corona) and/or reversibly adsorbed (“soft” corona), or both. The formation of the protein corona is one of the key factors managing the cellular response in terms of uptake, accumulation, and elimination.

The mechanism of protein adsorption is mostly regulated by changes in Gibbs free energy:

$$\Delta G_{\text{ads}} = \Delta H_{\text{ads}} - T\Delta S_{\text{ads}} \leq 0 \quad (1)$$

where ΔG_{ads} , ΔH_{ads} , and ΔS_{ads} are free energy, enthalpy, and entropy, respectively, during adsorption, and T is the temperature. There are a number of interactions that contribute to favorable changes in enthalpy ($\Delta H_{\text{ads}} < 0$), or entropy ($\Delta S_{\text{ads}} > 0$), including the formation of covalent and noncovalent bonds, rearrangement of interfacial water molecules, or conformational changes in either the protein or the nanomaterial surface.

Protein adsorption does not necessarily involve direct interaction with the colloid surface, but may occur instead via protein–protein interactions, which could be either specific (complementary amino acid sequences) or nonspecific (conformational changes that expose charged or hydrophobic domains in a protein that interacts with other proteins). This highlights the fact that biological impact might be driven both by the composition of the biomolecular corona and by distortions conferred to the conformation of the proteins following adsorption on the nanoparticles. One example where the mechanism has been disclosed involves nanoparticle-induced protein unfolding leading to initiation of the nuclear factor- κ B (NF- κ B) pathway and inflammation.^[48]

Several recent works suggest that adsorbed proteins are not uniformly bound to the nanoparticle surface and the strength of the interaction is dependent on the protein affinity toward that material.^[49,50] Specifically, molecules adsorbed with high affinity form the “hard” corona, consisting of tightly bound

proteins that do not easily desorb, while molecules adsorbed with low affinity assemble the “soft” corona, consisting of loosely bound proteins. The general hypothesis defines that the hard corona binds directly with the nanoparticle surface, whereas the soft corona interacts preferentially with the hard corona via weak protein–protein interactions. Moreover, the corona probably consists of multiple layers: since most of plasma proteins have very small hydrodynamic size (range 3–15 nm), the average corona usually detected on nanoparticles is too thick to be accounted for by a single layer of adsorbed proteins.^[15,51]

At present, we can understand the complex role of the protein corona at the cellular level and we have means to investigate its possible outcomes when using nanomaterials in vivo. As a result, it has been suggested that the biological identity of a nanoparticle actually determines its interactions with biomolecules and biological barriers in a physiological environment. For example, there is a strong positive correlation between the plasma protein binding capacity of a nanomaterial and the rate at which it is taken up by cells in vitro.^[52] As a consequence, in vivo, nanoparticles that readily capture plasma proteins tend to interact strongly with tissue-resident macrophages of the reticuloendothelial system (RES), leading to a rapid blood clearance,^[49] whereas, in vitro, are often associated with cellular toxicity to some extent.^[53] In addition, a set of plasma proteins called *opsonins* promotes the phagocytosis of nanomaterials by macrophages. Adsorption of the major plasma opsonin IgG enhances the recognition and uptake of a number of nanoparticles by macrophages both in vitro and in vivo. In a recent work, it has been demonstrated that the interaction of adsorbed IgGs with CD64 (a high affinity IgG-Fc receptor) initiates the phagocytosis of carboxyl- and amino-functionalized polystyrene nanoparticles by human macrophages.^[54]

In certain cases, adsorbed plasma proteins do not act exclusively as opsonins. Cell uptake can occur in the absence of plasma proteins: this process, often referred to as “serum-independent uptake,” presumably results from direct recognition of the nanoparticle surface by cell-membrane receptors. Serum-independent cell uptake is typically observed in vitro using serum-free cell cultures. For instance, knocking down the expression of scavenger receptor A in RAW 264.7 cells significantly lowers the uptake of anionic silica nanoparticles.^[55]

In a recent study,^[53] the protein corona of lipid nanoparticles was investigated and the most enriched constituents were identified to be apolipoproteins (Apo A-I, Apo C-II, Apo D, and Apo E).^[56] As the total apolipoprotein content is relevant, nanoparticles with protein corona exhibit a propensity to target PC3 prostate carcinoma cell line that expresses high levels of scavenger receptor class B type 1 receptor, which mediates the bidirectional lipid transfer between low-density lipoproteins, high-density lipoproteins, and cells, thus enhancing the total amount of nanoparticles inside the cell. By contrast, the presence of serum can dramatically reduce the efficiency of cell uptake. For instance, uptake of oxidized silicon microparticles by human umbilical vein endothelial cells (HUVEC) in

serum is remarkably lower than in a serum-free medium.^[57] A possible strategy to overcome the effect of serum protein adsorption on cellular uptake, in this case, may reside in introducing targeting ligands onto the nanoparticle surface. These molecules enhance the specific cellular uptake concomitantly reducing nonspecific binding of proteins from the environment. However, in the presence of a biological *milieu*, it is likely that the interface they form with their biological target is much more complex than predicted, which may roughly explain the partial lack of success that sometimes occurs in targeting strategies.^[17]

Despite much progress has been made toward a comprehensive knowledge of biomolecular corona, several key problems still remain that need to be addressed. The macroscopic composition of molecules that form the hard corona could be investigated with a combination of complementary techniques, including: i) dynamic light scattering (DLS), differential centrifuge sedimentation (DCS), and size exclusion chromatography (SEC) to assess the shell thickness; ii) colorimetric assays to argue the protein density; iii) poly(acrylamide) gel electrophoresis (PAGE), liquid chromatography/mass spectroscopy (LC/MS) to determine the protein identity; iv) circular dichroism (CD) and computational simulations to predict the average protein conformation; v) surface plasmon resonance (SPR) and isothermal titration calorimetry (ITC) to quantify the affinity toward specific receptors. However, to fully understand the complex relationships between the properties of the corona and the biology of nanoparticles, more detailed information on the composition, structural organization, and dynamics of these phenomena is needed.^[58] A key challenge in the next future will be to determine the structure of the hard–soft corona interface in detail, for which researchers will require more sophisticated technologies and methods than those used at present in the field. All of these approaches could support the efforts to correlate and even predict aspects of the biological interactions of new materials, which are by now hidden behind a small layer of proteins.

2.3. Electroporation

Electroporation is a physical technique based on an electrical pulse for the active internalization of intrinsically charged extracellular materials into the cell cytosol through a temporary permeabilization of plasma membrane (Figure 4). This method

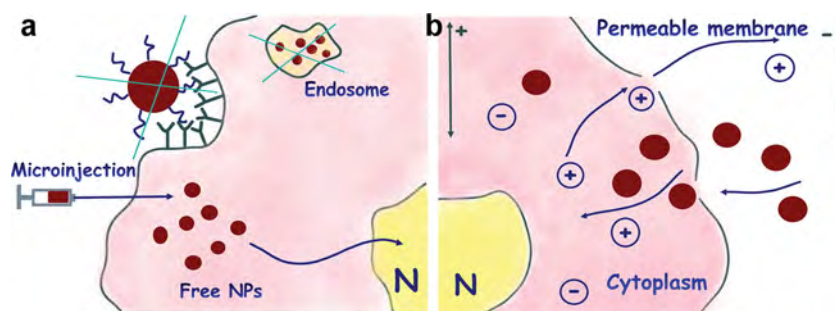


Figure 4. Physical methods to deliver colloidal nanoparticles inside cells: A) microinjection; B) electroporation.

is commonly used to transfect cells with nucleic acids, proteins, and peptides,^[59] and it has been adopted also for the controlled incorporation of different kinds of nanoparticles.^[60] The nanoparticles used for this approach should have appropriate size, because of the small pores generated, and good dispersion and stability in cell culture media to prevent the formation of aggregates.

Electroporation allows for a specific delivery in adherent and non-adherent cells and it is highly reproducible compared to other passive-targeting techniques, but it suffers from inability to tailor a specific cell type. In addition, it is not amenable for in vivo targeting and is used only in in vitro experiments with cells. Nanoparticles that are not able to cross the cell membrane can be internalized into the cellular cytosol with electroporation in a controlled and highly reproducible manner, which enables sensing and imaging of cell parameters. In a recent example, electroporation was exploited for the fast delivery of silver nanoparticles (AgNPs) into living cells for use as an intracellular signal amplification device for surface-enhanced Raman spectroscopy (SERS).^[61,62] Unfortunately, as well as other active delivery approaches, the cell physical manipulation is highly invasive and often results in compromising the cellular viability.^[63] Pack et al. showed that the diffusion and brightness of standard silica nanoparticles in solution were not affected by the electrical discharge necessary for electroporation and investigated their distribution in cell compartments after passive uptake following electroporation.^[64]

Electroporation is recommended for tagging cells or bacteria with nanoparticles when much higher loading efficiency is requested than it can be achieved by standard incubation. A typical example is the case in which high concentrations of incorporated nanoparticles as signal emitters are required to track labeled cells in vivo.^[65–67] Exploiting photoluminescent or magnetic properties of QDs and IONPs, respectively, it is possible to monitor the fate of transplanted cells, their targeting to solid tumors and to localize metastases. In addition, magnetic nanoparticles can be further utilized as mediators to modulate the cell membrane electroporation induced by an applied current, for cell tracking under various imaging modalities, and for facilitated drug delivery.^[68] The optimal condition to obtain a suitable level of poration efficiency maintaining good cell viability should be carefully adjusted depending on cell types and nanoparticle size. Moreover, Lee et al. investigated the effect of nanoparticle polarity on gene transfection in HeLa cells: this study suggested that anionic nanoparticles were more efficient as genetic material transporters compared to the cationic ones.^[69]

2.4. Microinjection

Microinjection is an alternative physical technique that allows nanoparticles to be injected directly inside the cytoplasm of the cells, without any residence time in the culturing medium. This novel approach avoids any possible effect related to receptor-mediated endocytosis. The interaction between cells and bare nanoparticles is straightforward and their access is consistent (Figure 4). In this way, the overall cellular response is not affected by the presence of proteins bound to the nanoparticles prior to the uptake. It is possible to deliver very small sample

volumes using a fine-tipped glass micro-capillary, thus guiding the cellular targeting with a fluorescent microscope. Microinjection enables nanoparticle delivery to the interior of the cell in a monodisperse form and it is the only technique that allows the target cell to be directly visualized first. On the other hand, it requires each cell to be individually selected, manipulated, and then injected. Thus, not all cells in a field of view will be successfully microinjected due to physical constraints, so it requires a well-trained operator. Moreover, microinjection is a very efficient technique but is also very expensive.

In a first seminal work, Dubertret et al. used QDs to revolutionize biological imaging: they injected into *Xenopus* embryos these fluorescent nanocrystals coated with a phospholipid block-copolymer to follow different evolutionary stages in embryogenesis.^[70] With this study, they demonstrated that QDs microinjected into cells allow fluorescence-based in vitro and in vivo studies. Candeloro et al. microinjected Ag and Fe₃O₄ nanoparticles inside HeLa cells.^[71] The aim of this work was to investigate the cytotoxic effects due to the interaction of nanoparticles with cells and the authors observed that microinjection allows that the effects observed were only due to the nanoparticles themselves and not to the solvents or the technique used. In fact, they put in evidence a different behavior of the cells treated with nanoparticles in comparison with the control cells. This is supposed to be generated by an emerging oxidative stress due to the nanoparticles. Derfus et al. also used microinjection as a means of introducing QDs into the cytoplasm.^[72] The authors used this technique to see a subcellular localization of QDs. QDs were endowed with an inert coating of PEG: in one case, a nuclear localization signal (NLS) peptide was added, in another case, a mitochondria localization sequence (MLS) peptide was used in place of NLS. The use of peptide localization sequences and PEG coating combined with microinjection allowed the delivery and subcellular localization of QDs in living cells. Medintz et al. used cellular microinjection of QD-fluorescent protein assemblies as an alternative strategy for intracellular delivery that could bypass the endocytic pathway.^[73] QDs functionalized with two different peptides were injected directly into COS-1 cells and this study demonstrated that cellular uptake is favored by the presence of cell-penetrating peptides within the QD–protein conjugates. Muro et al. investigated the intracellular stability and targeting of QDs that present three different surface chemistries using microinjection, electroporation, and pinocytosis to deliver them into the cytoplasm.^[74] In particular, QDs endowed with different surface chemistries were injected into *Xenopus laevis* embryos and their behavior was observed for a prolonged time. The authors concluded that the QD intracellular aggregation behavior is strongly dependent on the surface chemistry in all the delivery methods they used.

3. Delivering Nanoparticles to Selected Cellular Compartments

3.1. Targeting the Cellular Membrane

The interaction between nanobioconjugates and the cellular membrane starts with the particle adhesion to a cell-surface

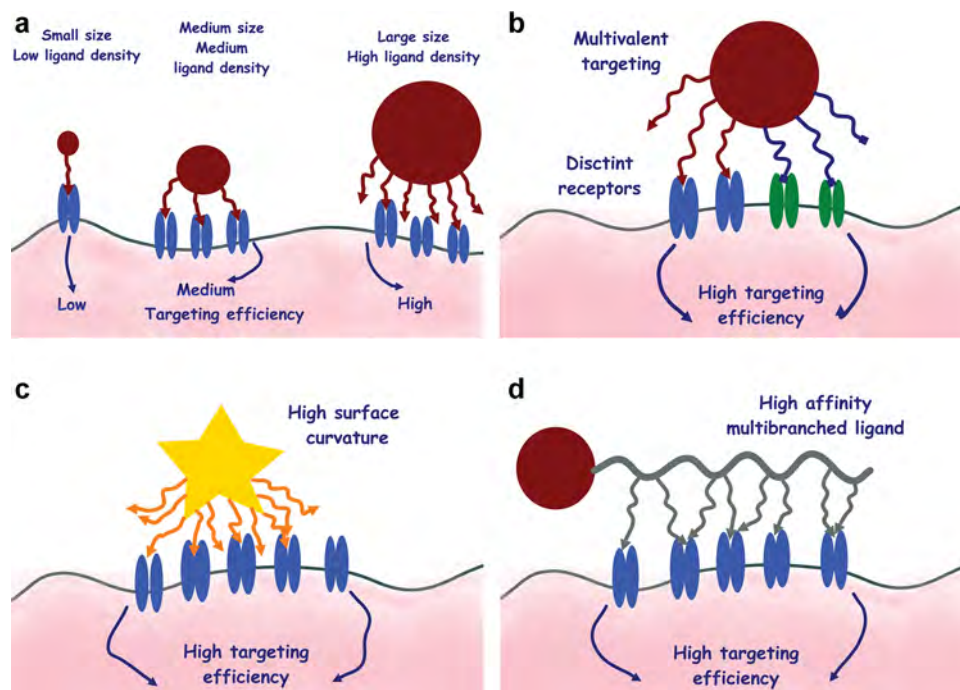


Figure 5. Properties of nanoparticles in correspondence of the cellular membrane: A) size-effect; B) multivalency effect; C) surface curvature effect; D) multibranching affinity ligand.

lipid bilayer or with a recognition event between a biomolecule exposed from the nanoparticle surface and a target receptors or a specific protein on the cell. Nanoparticle contact and membrane wrapping are dependent on different factors, such as the nanoparticle size and shape, the density and distribution of ligands on the nanoparticle surface. It has been established that particle adherence requires specific or nonspecific binding interactions to overcome the resistive forces that hinder particle uptake.^[30] On the other hand, the “wrapping time” by membrane is determined by the particle size and shape, rate of receptor diffusion and elasticity of the cell membrane (Figure 5).^[30]

One of the most commonly used approaches to target the cellular membrane is based on the bio-recognition between a receptor and antibody-bound nanoparticles.^[20,75–77] Importantly, the nanoconjugation was shown to affect both the mechanism of internalization and distribution inside the cell and the rate of endocytosis in a cell line characterized by a differential expression of a receptor.^[78] For example, it was found that gold nanoparticles conjugated with cetuximab were able to promote faster endocytosis of epidermal growth factor receptor (EGFR) compared to unconjugated antibody, due to enhanced clustering of EGFR induced by nanoconjugation. Moreover, it should be noticed that ligand tailoring on the nanoparticle surface by conjugating different amounts of antibody did not affect significantly the endocytosis pattern.^[79] Interestingly, the combination of two different antibodies, that is, farletuzumab and cetuximab, conjugated to AuNPs, drastically improved targeting efficiency of cancer cells expressing both folate receptor α and EGFR via dual targeting.^[79] To further understand the potential of nanoconjugation in improving the targeting efficiency

of specific molecular scaffolds, the selective targeting by using nanoparticles engaging two distinct receptors expressed in the same cell, namely androgen receptor and a novel G-protein coupled receptor, was shown to facilitate cell death in treatment-resistant cancer at nanomolar nanoparticle concentrations. Anti-androgen AuNPs were found to bind androgen receptor with 5 to 11 times higher affinity compared with free anti-androgen antibody and to bind androgen receptor with affinity superior to endogenous androgens, providing opportunities for further increased treatment efficacy via drug co-conjugation.^[80] Kim et al. have developed a nanoprobe for multimodal simultaneous targeting of three different proteins: nucleolin, integrin $\alpha_v\beta_3$, and tenascin-C. The nanoprobe, consisting of a cobalt ferrite core coated with a silica shell containing Rhodamine B isothiocyanate, was conjugated with AS1411 and TTA1 aptamers, as well as RGD peptide. Five different cancer cell lines, including C6 (brain tumor), NPA (thyroid papillary cancer), DU145 (prostate cancer), HeLa (cervical cancer), and A549 (non-small lung carcinoma), and two normal cell lines, including CHO (Chinese hamster ovary cell) and L132 (epithelial lung cell), were tested. Compared with the single cancer probe, the multitarget nanoprobe showed dramatically enhanced cancer targeting efficiency in all five cancer cell lines, whereas none of the multi-target conjugates demonstrated detectable fluorescence intensity in the normal healthy cells, and there was no significant difference in fluorescence when compared with single target probes, demonstrating the specificity of each of the multi-target conjugates. These findings demonstrate that the multi-target cancer probe with additional aptamers or other novel sets of cancer probes can be used to diagnose a variety of cancers as a master probe.^[80]

The presence of a targeting ligand is not always necessary for cellular labeling, as it was shown by Yan and co-workers. Having screened 474 clinical specimens from patients with nine types of cancer, the researchers established that magnetoferritin (M-HFn) nanoparticles generated by encapsulating IONPs inside a HFn shell were able to target transferrin receptor 1 (TfR1) without any additional recognition ligands on their surface, with high sensitivity (98%) and specificity (95%).^[81]

An interesting alternative strategy for cell membrane targeting was proposed by Stephan et al., in which liposome-like nanoparticles were directly bound to the plasma membrane of T cells, taking advantage from the fact that most cells have high levels of reduced thiol groups on their surfaces. The particles with a drug-loaded core and a phospholipid surface layer with exposed thiol-reactive maleimide headgroups were incubated with the cells to allow maleimide-thiol coupling, followed by in situ conjugation to thiol-terminated polyethylene glycol to quench residual reactive groups of the particles. The authors found that such a targeting did not induce toxicity or affect intrinsic cell functions. The particles followed the characteristic in vivo migration patterns of their cellular vehicles, endowing their carrier cells with substantially enhanced function using low drug doses that, by contrast, exhibited no effect when administered by traditional systemic routes.^[82]

Another kind of molecules able to interact with the cellular membrane via cationic groups, bringing about direct cellular entry due to so-called “proton sponge effect,” is such polymers as polyethyleneimine (PEI) and polyamidoamine.^[83,84] A careful control of the cationic density created by the polymers should be due in this case, as these interactions may compromise the cell membrane integrity, potentially leading to hole formation, membrane thinning or erosion and, thereby, cytotoxicity.^[85] Nel et al. have found that the cytotoxicity can be significantly reduced or even prevented by using shorter length polymers for nanoparticle fabrication.^[85] By contrast, conjugation of PEI with a targeting molecule such as folic acid allowed for the efficient receptor targeting and cellular uptake of nanoparticles into specific cancer cells.^[86]

Hydrophobicity and roughness also have a great influence on the interaction of nanoparticles with cellular membrane. Nanoparticles that are more hydrophobic than the surface membrane are more readily engulfed than their less-hydrophobic counterparts. Moreover, the number of contact sites between membrane and particle surface play an important role in nanoparticle wrapping. Therefore, such parameters as radius of curvature and ligand density influence the particle–membrane interaction.^[87–89] Chan et al. thoroughly studied the efficiency of ErbB2 tyrosine kinase receptor targeting and cellular uptake efficiency using AuNPs and AgNPs, in 2–100 nm range, conjugated with Herceptin (Her).^[88] The authors found the internalization of Her–GNPs to be highly dependent on size, with the most efficient uptake occurring within the 25–50 nm size range. Due to their inability to promote multivalent binding, smaller nanoparticles dissociate from the receptors before being engulfed by the membrane owing to a low-binding avidity. In contrast, extremely large nanoparticles possess a much higher antibody density on the particle surface, which, in turn, requires the involvement of more distant receptors causing a reduction

of membrane wrapping necessary for nanoparticle internalization.^[88] On the other hand, Johnson and co-workers have found a dependence of cellular uptake into EGFR⁺ A431 cancer cells on surface tailoring of nanoparticles, where the number of Clone 225 antibodies bound to gold coated iron oxide nanoroses was varied from 1 to 74, corresponding to either submonolayer or multilayer coverage. The nanoroses conjugated with 54 antibodies were found to show the most efficient cellular uptake (about 7000 nanoparticles per cell), compared to a much lower cellular uptake of spherical AuNPs, conjugated by the same protocol. The small overall hydrodynamic diameter, the high antibody density on the surface, and the orientation of the antibodies with respect to each other which is influenced by high local surface curvature do bring about, in turn, to the high cell uptake by antibody conjugated nanoroses.^[87]

Finally, the structure of targeting molecules and their valence also greatly contribute to the effectiveness of cellular targeting. In contrast to using low-affinity ligands for nanoparticle conjugation, the use of multivalent ligands can lead to enhanced affinities, engaging numerous receptors simultaneously to provide enhanced interactions. For example, Brown et al. have found how to improve the affinity of nanoparticles to a lung cancer cell line using liposomes conjugated with a H2009.1 tetrameric peptide: nanoparticles displaying this multivalent tetrameric peptide exhibited 5–10-fold higher delivery efficiency compared to liposomes displaying the lower affinity monomeric H2009.1 peptide, even when the same number of peptide subunits are displayed on the liposome.^[90]

3.2. Cytosolic Delivery

Nowadays, the identification of more effective strategies for a low toxic drug administration remains the main challenge in pharmacology and clinical practice.^[91] Therefore, increasing efforts are made to design and synthesize nanostructures able to efficiently deliver drugs to target tissues and to penetrate into the cellular environment.^[92] Before entering the cell, a nanoparticle has to cross the cell membrane. As mentioned previously, there are different strategies to overcome cell membrane barrier in order to deliver nanoparticles directly inside the cytoplasm avoiding the classical endocytotic pathway, including microinjection and electroporation. An additional approach exploits a passive diffusion through the phospholipid bilayer, which is usually achieved using cell-penetrating peptides (CPPs).^[93] CPPs present a great variety in terms of amino acid composition and 3D structure, with examples of cationic, anionic, and neutral sequences showing variable degrees of hydrophobicity and polarity. Over a hundred CPPs have been discovered so far, mostly bearing a net positive charge. Several peptides act as CPPs, including the transactivator of transcription (TAT peptide), an 11-amino-acid peptide of the HIV-1 TAT protein (YGRKKRRQRRR), the transcription factor from Antennapedia, and the VP22 protein from Herpes Simplex Virus 90. It was demonstrated that the amino acidic regions responsible for penetration in the cellular environment are either amphipathic sequences or arginine-containing stretches of 30 amino acids.^[93] On the other hand, the peptide secondary structure is of crucial importance for cell-penetration. Peptides conformation

can significantly change depending on whether they are free in solution, near the membrane interface, inside the membrane, or bound to a vehicle, thus affecting the mode of uptake. Finally, the heterogeneity of the cell membrane, including lipid composition, density, and dynamics, depends on different factors, such as the cell type, the specific region of the membrane, and a variety of signaling pathways. This results in different levels and modes of uptake depending on the conditions of each individual experiment.^[94]

Endocytosis and direct translocation through the cellular membrane are the major mechanisms used by CPPs to gain entry into the cell. Endocytosis pathway has been reported above, therefore, we will stress here the non-endocytic (i.e., energy independent) pathway. This may include different mechanisms that have been described, including inverted micelle formation, pore formation, the carpet-like model, and the membrane thinning model. The first stage in all of these mechanisms includes an interaction of the positively charged CPP with negatively charged components of membrane (heparan sulfate and phospholipid bilayer), which occurs involving stable or transient destabilization of the membrane associated with folding of the peptide on the lipid membrane. The interaction between hydrophobic residues, such as tryptophan, and the hydrophobic part of the membrane was shown to take part in the “inverted micelle” mechanism. The translocation via pore formation is explained by two alternative models: 1) the barrel stave model, possible for helical CPPs, suggesting a formation of a barrel by which hydrophobic residues are close to the lipid chains, and hydrophilic residues form the central pore; 2) the toroidal model, suggesting the lipids bending in a way to ensure CPP proximity to the headgroup: in this way, both CPP and lipids form a pore. Finally, in the carpet-like model and in the membrane thinning model, interactions between negatively charged phospholipid and cationic CPPs result in a carpeting and thinning of the membrane, respectively, facilitating the peptide translocation. Whatever the mechanism actually involved, one should take in mind that the translocation of the CPP is achieved when CPP concentration is above a certain concentration threshold.^[95]

Gold nanospheres conjugated with 17-amino acid α -helix peptides (P-GNS) show a different cell-penetrability upon changing just one amino acid in the peptide sequence. Moreover, the cytotoxic activity of an anti-cancer drug doxorubicin (DOX) conjugated to the P-GNS may strongly depend on the peptide sequence and penetrating capability.^[96] Pegylated PLGA nanoparticles modified with poly(arginine) enantiomers were found to exhibit significantly increased cellular uptake and transportation of insulin, thus improving the intestinal absorption of that protein.^[97] Nanoparticles unable to cross the cellular membrane are internalized by endocytosis mechanisms but remain entrapped inside the endosomal-lysosomal compartments, the main intracellular barrier that nanoparticles have to overcome to diffuse into the cytosol.^[98] However, it is widely accepted that an endocytosis process is involved in internalization of CPPs and CPP-conjugates, including CPP-nanoparticle conjugates, probably due to their large dimensions. Although the detailed mechanism of entry has not been fully elucidated, it is recognized that is dependent on CPP sequence, cell-type, size, shape, and charge of cargo moieties.^[92] Despite continuous

improvements in direct membrane translocation of CPPs and their cargoes, endosomal entrapment remains a major limitation to CPP-mediated cytoplasmic delivery.^[92] An important step forward in the cytosolic delivery of CPP-functionalized nanoparticles has been done by Delehanty and co-workers, who have developed a peptide sequence (JB829-JB826) that stimulates the initial endocytosis of peptide-QDs and then causes the QDs release to the cytosol within 48 h.^[99,100]

In the following, we describe a few strategies that have been explored to enhance nanoparticle endosomal escape. The first approach is based on a mechanism involving the formation of a cationic ion pair, which was originally proposed by Xu et al. to facilitate endosomal escape of nucleic acids.^[101] Endosome was destabilized by ion pair formation between cationic lipids and anionic lipids within the endosome membrane.^[102] Liposomes are the main example of nanoparticles able to escape from endosomes by this mechanism.^[103] However, pegylation, adopted to improve the systemic delivery, inhibited ion-pair formation.^[104] Thus, liposome-polycation-DNA (LPD) nanoparticles coated with a sheddable PEG were developed. PEG was arranged in the brush mode on the nanoparticle surface to protect the nanoparticle from the reticulo-endothelial system (RES) for an initial period of time and to favor the penetration into the tumor by EPR effect. After tumor penetration, nanoparticles were internalized by a ligand-induced endocytosis process, the shedding of PEG from LPD nanoparticles occurred by exposing the positive charges of the nanoparticles and allowing the charge-charge interaction with the endosomal membrane, which resulted in membrane fusion and endosomal escape.^[105,106]

Successful escape of nanoparticles from endosome and release of the payload into the cytoplasm is usually obtained by the so-called “proton-sponge” effect (Figure 6).^[98] pH-buffering agents are widely exploited to promote cargo release, due to the acidic nature of endosomal-lysosomal vesicles. Macromolecules with low pK_a amine groups, such as poly(ethyleneimine) (PEI), chitosan, poly(L-lysine) (PLL), poly(allylamine), poly(amidoamine) (PAMAM), dendrimers, and some cationic lipids, promote a proton-sponge effect under acidic conditions.^[107–109] Nanoparticles forming complexes with these macromolecules are internalized by the cell, then endosome buffering leads to the vesicle lysis, releasing the nanoparticles into the cytosol. For example, charge-reversal copolymers could shift their charge between positive and negative in a pH-dependent fashion.^[107,108,110] Charge conversion can occur at the endosome or lysosome stages (pH 5.6), next these copolymers facilitate the endosomal escape of nanoparticles enhancing the proton-sponge aptitude.

This nanoparticle escape mechanism has been reported in a recent work, in which PEG- and PEI-functionalized zinc(II) phthalocyanine (ZnPc)-loaded mesoporous silica nanoparticles (MSNs) exhibited a high escape efficiency from the lysosomes to the cytosol due to the proton-sponge effect of PEI.^[111] However, the mechanism of the proton-sponge effect as been questioned, as it has been demonstrated that there are no changes in lysosomal pH after PEI accumulation even in the presence of endosomal escape.^[112] Whatever the real mechanism that determines the endosomal escape after treatment with PEI or other similar macromolecules, this kind of strategy has a low

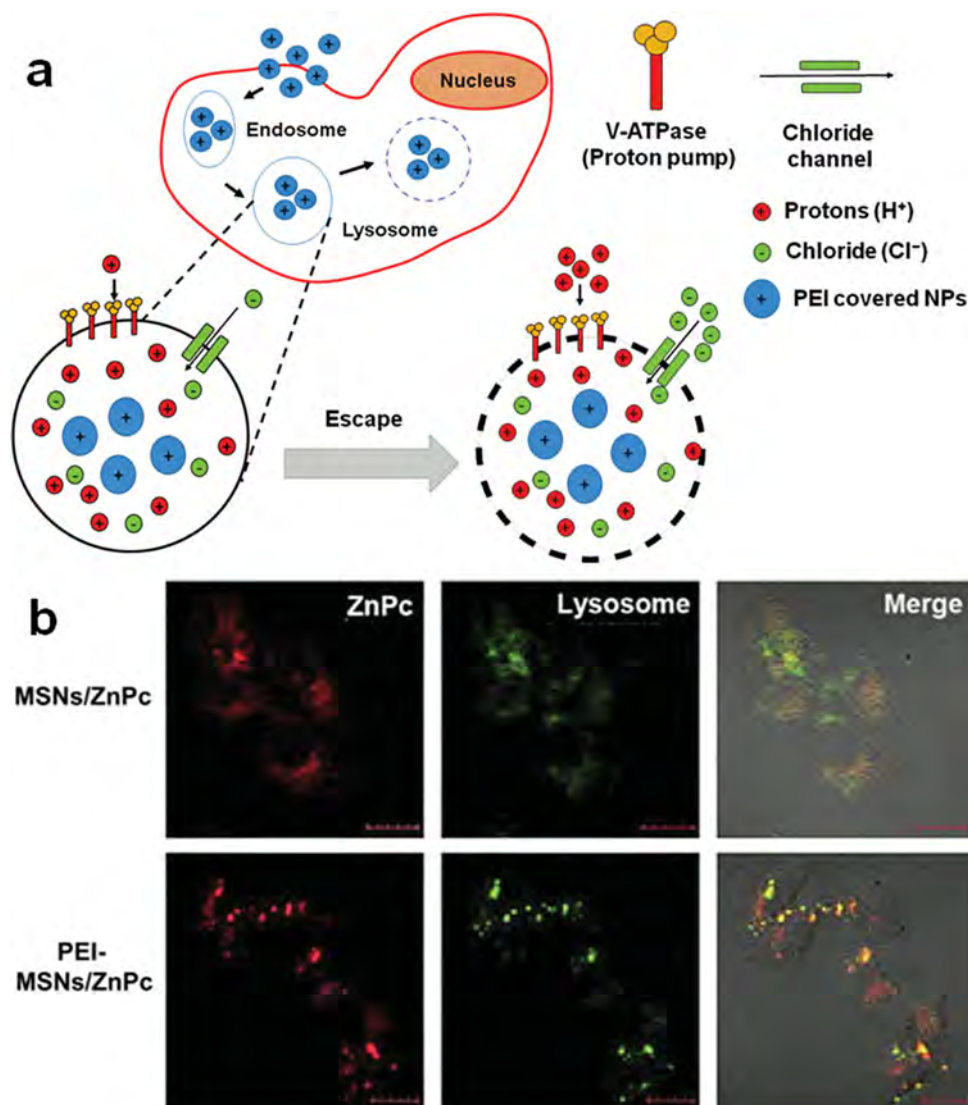


Figure 6. The “proton-sponge effect”. A) Cationic particles bind with high affinity to lipid groups on the plasma membrane and are endocytosed. Once these nanoparticles enter into a lysosomal compartment, the unsaturated amino groups are capable of sequestering protons that are supplied by the v-ATPase (proton pump). This process keeps the pump functioning and leads to the retention of one Cl⁻ ion and one water molecule per proton. Subsequent lysosomal swelling and rupture leads to nanoparticle release in the cytoplasm. B) Estimation of the lysosome disruption capability of MSNs/ZnPc, PEI-MSNs/ZnPc, by confocal microscopy. Representative confocal images showing colocalization of MSNs/ZnPc and PEI-MSNs/ZnPc (red) with late endosomes/lysosomes (green) after 24 h of exposition to nanoparticles. Scale Bar, 10 μm. Reproduced with permission.^[111] Copyright 2012, Elsevier Ltd.

efficiency in comparison with viral alternatives. This is probably due to the fact that an insufficient amount of nanocarrier actually accumulates in each endosome, thus preventing the achievement of the necessary buffering capacity in vivo. Moreover, cationic nanomaterials are usually associated to high toxicity and immunogenicity, which limit their clinical implementation.^[106] One promising approach to bypass these problems resides in the development of “synthetic viruses.” These structures consist of elements that mimic the delivery functions of viral particles and surface domains that prevent undesired biological interactions and enable specific cell receptor binding.^[113]

An alternative strategy to overcome endosomal accumulation takes advantage of the use of membrane-destabilizing macromolecules. These compounds mimic the action of viral hemagglutinin, which is a pH-sensitive and membrane-destabilizing protein that helps viral vectors to disrupt the endosome and enter the cytoplasm.^[114] Hemagglutinin acts by shifting from an ionized and hydrophilic conformation to a hydrophobic and membrane-active conformation in response to the environment changes from neutral to acidic, and this results in destabilization of the endosomal wall. Several peptides and polymers that simulate the function of hemagglutinin were synthesized. The incorporation of membrane-destabilizing peptides is another

strategy to utilize the low pH environment of endosomes-lysosomes.^[114] Among membrane destabilizing peptides, GALA (glutamic acid-alanine-leucine-alanine), a pH-sensitive fusogenic peptide, is the most studied. A multifunctional envelope nanodevice functionalized with GALA and an 8-arginine tail was developed, which led to an endosomal release of siRNA resulting in an efficient knockdown.^[115] Krpetic et al. reported on the intracellular trafficking of gold nanoparticles functionalized with Tat-peptide, showing their ability to overcome intracellular boundaries: unusually, the particles were initially found in the cytosol, in the nucleus and in mitochondria, and later within densely filled vesicles, from which they could be released again via an endosomal escape mechanism by penetration of the vesicle membrane followed by membrane rupture.^[116,117]

In addition to the ability to escape from endosomes, the ideal nanocarrier should be capable of releasing the drug into the cytoplasm. The design of polymeric micelles able to respond to the changes of intracellular environment has represented a promising strategy. To this purpose, an effective approach has been to incorporate cleavable links into the polymer structure, either to cause a structural change of the delivery systems, or to direct conjugate drug molecules, which could be released upon cleavage of the links.^[118]

Intelligent macromolecules or nanoparticles for drug delivery have been developed using acetal bond, that is the most widely used among pH-sensitive bonds due to its rapid degradation in endosomes.^[119–123] Nanoparticles containing acetal bonds are supposed to be degraded in endosomes, thus releasing their cargo. Hydrolysis of acetal bond is a hydrogen-consuming reaction, which also promotes cargo escape from endosome by increasing endosomal osmotic pressure. Endosomal escape of nanoparticles could be also achieved by stimulating membrane lysis through a hydrophobic modification of cationic polymers.^[124,125] Finally, membrane penetration can be promoted by means of a phage-mimetic carrier that takes advantage of the presentation of the scavenger receptor class B type I, a natural membrane channel that mediates the intracellular delivery of hydrophobic molecules,^[126] or exploiting isolated naturally produced exosomes for siRNA delivery into the cytosol.^[127]

3.3. Nuclear Preferential Transport

The nucleus is surrounded by a double membrane called nuclear envelope (NE). The communication between the nucleus and the cytoplasm is mediated by the nuclear pore complexes (NPCs). NPCs are specialized channels that allow passive diffusion of ions and small molecules (<40 kDa). Whereas the nucleus-cytoplasmic traffic of large molecules (>40 kDa) is regulated by specific nuclear import and export systems,^[128–132] the transport of these macromolecules requires a signal- and energy-dependent mechanism. The

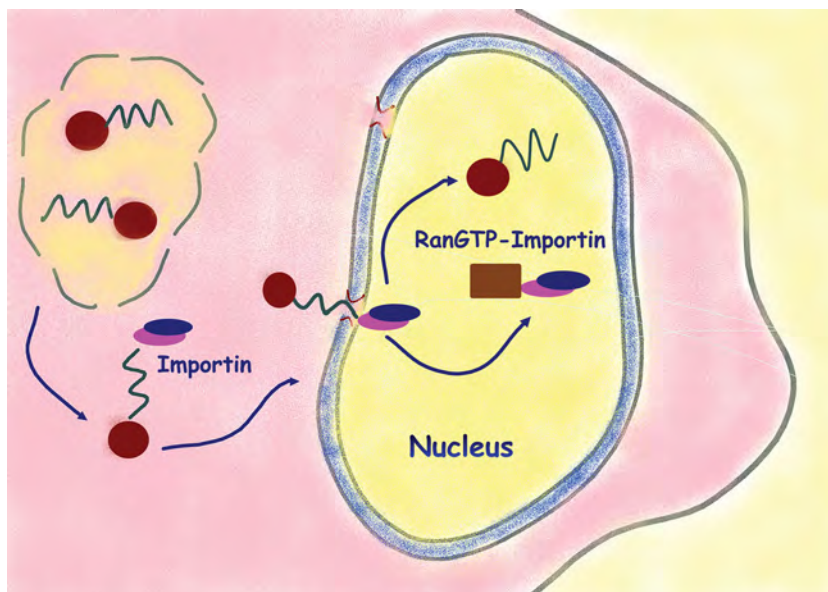


Figure 7. Nuclear preferential transport pathway. Nanoparticles with specific NLS peptide bind to an importin in order to achieve preferential transport inside the cell nucleus.

active transport is basically mediated by a specific molecule, usually referred to as the nuclear localization signal (NLS), which comprises a basic amino acid-rich short sequence. The energy-dependent step is mediated by a heterodimer of proteins called importin α (Imp- α) and importin β (Imp- β). Imp- α binds the NLS sequence, while Imp- β is responsible for the increase in the affinity of Imp- α toward the NLS and mediates the transfer of the cargo-Imp- α complex across the NPC. After passing through an NPC, the cargo of Imp- α is released inside the nucleus upon binding of the monomeric guanine nucleotide RAs related nuclease protein Ran-GTP to Imp- β (Figure 7). Once the dissociation of Imp- β and its cargo protein has occurred, Imp- β is recycled and sent back to the cytoplasm bound to Ran-GTP. The conversion of Ran-GTP to Ran-GDP releases the Imp- β protein that, in this form, is able to bind new cargoes. Ran-GDP is indeed transported into the nucleus by its own specific nuclear transporter in order to replenish its nuclear concentration.^[133]

These NLSs are divided in classical NLSs and non-classical sequences. Classical NLSs consist of one or two sequences of arginine and lysine: the most frequent classical monopartite NLS (PKKKRKV¹³²) has been found in the SV40 large tumor antigen (T-ag), while an example of bipartite NLS consisting of two sequences of basic amino acids separated by a spacer of 10–12 residues (KRPAATKKAGQAKKK¹⁷⁰) was isolated from the *Xenopus* nucleoplasm.

It has been shown that not only NLS peptide is used for nuclear transport, but also the HIV TAT peptide is able to transport cargoes across both the plasma membrane and the nuclear membrane. TAT peptide-mediated nuclear transport has different import properties if compared to NLS. Cardarelli et al. demonstrated that the dominant mechanism in live cells is the passive diffusion, whereas Truant et al. demonstrated that Imp- α is both necessary and sufficient for the nuclear translocation of TAT in the absence of Imp- β in vitro.^[131,132]

Table 1. Nuclear localization signals (NLSs) for nuclear transport and types of nanoparticles involved.

Nanoparticle type	Origin of peptide	Peptide sequence	Refs.
Polymeric micelles and iron oxide	Monopartite	PKKKRKV	142-149
Polymeric micelles and iron oxide	Nucleoplasmin NLS	KRPAATKAGQAKKKK	129,150
CdSe/ZnS QDs, Gold	SV40 large T NLS	CGGGPKKKRKVGG	138-142
Liposomes, Gold, QDs	SV40 NLS	PKKKRRV	140,151
Silica, Silver, CdSe/ZnS QDs	TAT peptide	YGRKKRRQRRR	132,137,141

The different classes of NLSs have been attached to different cargoes with the aim to enhance the nuclear transport and delivery: some examples are summarized in table (Table 1).

Also the cell cycle plays an important role in nuclear targeting. In non-dividing cells, vehicles must enter the nucleus through the NPCs. By contrast, in dividing cells, the majority of vehicles are supposed to enter the nucleus during mitosis. In a seminal study on the dependence of the efficiency of the delivery vehicle from the cell cycle, the highest level of transfection was obtained with cells that started in the G2 phase.^[134] However, more recently, it has been demonstrated that NLS sequence is necessary for nuclear proteins/nanoparticles retention after mitosis.^[135]

In order to enter the nucleus, nanoparticles have to cross the NPC and, for this reason, nanoparticles and vehicles must have specific requirements, including small size, cationic charge, proper shape, and surface functionalization.^[136] Moreover, they should be able to bind specific receptors on the plasma membrane, escape endosomal and lysosomal digestion, and help importins to cross the nuclear pore complex and to limit toxicity.

Nuclear targeting is exploited mainly for imaging (in diagnostic) and drug/gene delivery (in therapy). Nanoparticles can be effectively imaged by several techniques, including, for instance, surface-enhanced Raman scattering (SERS) spectroscopy, magnetic resonance imaging (MRI), and fluorescence. The use and the choice of one of these techniques depend on the variety of materials and on their physical and chemical skills. Gold and silver nanomaterials have unique optical properties, including the localized surface plasmon resonance (LSPR), which are leveraged in SERS. We can find examples of AuNPs and AgNPs functionalized with NLS or TAT for nuclear targeting and visualization/detection in single living cell.^[137-139] The AuNP LSPR adsorption is size-dependent: when nanoparticles are smaller than 3 nm, they lose their LSPR character, but they acquire photoluminescence properties. These kinds of nanoclusters are called gold quantum dots (GQDs), which might be very useful in cellular imaging. For example, by taking advantage of a combination of small size and intense emission, GQDs were functionalized with SV40 NLS and used for nuclear targeting and intracellular imaging.^[140] More in general, the brightness and the photostability of QDs, allow tracing the trajectories of individual QDs in living cells, using both confocal and internal reflection microscopes.^[141] The bio-functionalization of IONPs can be used to enhance the tissue contrast in MRI. For example, Xu et al. functionalized Fe₃O₄ SPIO with NLS to attempt nucleus targeting.^[142]

The second fundamental application of nuclear targeting is to produce nanoparticles/carriers for nuclear drug delivery. This function is very important because a large number of drugs exert the main cytotoxic action at the nucleus. Yu et al. have produced glycol chitosan micelles for doxorubicin nuclear delivery,^[129] whereas Misra et al. developed doxorubicin-loaded PLGA nanoparticles for this purpose.^[143] A poly(2-(pyridin-2-yl-disulfanyl)ethyl acrylate (PDS) delivery system, a novel redox stimulus-responsive nanoparticle system conjugated with RGD peptide, was designed to enhance the nuclear drug delivery of doxorubicin.^[144]

It is also possible to combine two or more applications in the same construct to create a multifunctional nanoparticle. Liu et al. developed multifunctional nanoparticles that targeted cell nuclei, delivering the drug and at the same time detecting cell nucleus by a dual imaging modality including MRI and fluorescence.^[145]

Finally, the literature reports several examples of different nanoparticles that have been used for studying nuclear mechanisms of targeting and uptake, with special focus on the effect of nanoparticle morpho-structural characteristics, including charge and size, on nuclear uptake,^[126] but also for investigating the cytotoxicity caused by the chemical nature of nanoparticles. For instance, Austin and co-workers revealed the difference between AuNPs and AgNPs for nuclear targeting during cell cycle.^[139,146]

3.4. Mitochondrial Targeting

Mitochondria can be considered the powerhouse of the cell because they act as the site for the production of high-energy compounds (e.g., ATP), which are the vital energy source for several cellular processes. Mitochondria play important roles in a variety of vital cellular processes, most of which are related to cell disease. For this reason, targeting of this organelle may present a few important benefits.^[27] The relationship between mitochondrial DNA (mtDNA) mutations and human myopathies indicates that the delivery of nucleic acids plays a vital role that will be analyzed. Another important reason for targeting the mitochondria arises from its ability to propagate reactive oxygen species and oxidative stress signaling,^[152] which is one of the main causes of cellular toxicity.

In order to attempt the identification of mitochondria-specific targeting is necessary to stand out the main compartments in which they are divided, that is, the outer mitochondrial membrane (OMM), the inner membrane space (IMS), the inner mitochondrial membrane (IMM), and the mitochondrial matrix. There are several strategies for the targeting of mitochondria.^[153] In a first example, the electrochemical potential maintained across the IMM is exploited for the confined delivery using some molecules, also referred to as delocalized lipophilic cations (DLCs), that are particularly effective in crossing the hydrophobic membrane layers and, hence, that preferentially accumulate in mitochondria. Studies on dibenzylammonium cation in isolated mitochondria and on the

fluorescent dye rhodamine in cultured cells suggest that DLCs actively accumulate in mitochondria in a potential-dependent manner. Indeed, DLCs, including the commercial Mitotracker, tetraphenylphosphonium (TPP), and 5,5'-6,6'-tetrachloro-1,1',3,3'-tetra-ethylbenzimidazolcarbocyanine iodide (JC-1), are commonly used as mitochondria-specific dyes for staining and studying mitochondrial physiology.^[153] Another strategy, used to selectively target mitochondria, takes advantage of the mitochondrial protein import machinery, which is naturally utilized by cells for the delivery of nuclear-encoded mitochondrial proteins. These proteins are directed to the mitochondria post-translationally through cleavable *N*-terminal peptide sequences. Mitochondrial targeting sequences (MTSs) are basically 20–40 amino acids in length with structural motifs recognized by the mitochondrial import machinery. When an MTS is recognized by a specific receptor on the outer membrane, the attached protein is transported into the IMS by threading through the pore of the outer mitochondrial membrane. Once entered the matrix, the MTS is cleaved in one or two proteolytic steps by mitochondrial processing peptidases, and, with the help of matrix-localized chaperones, such as mhs70, the protein refolds into its mature form.^[153] This approach has been used successfully with a variety of molecules like proteins, nucleic acids, and endonucleases. The use of vesicle-based transporter for the mitochondrial targeting has also shown good efficiency in transporting large or impermeable cargoes, such as drug molecules. This strategy is based on the use of surface-bound cationic peptides to deliver a liposome-based carrier for macromolecular delivery to the mitochondria.^[154]

Various tailoring nanocarriers for the intracellular transport of biological cargoes, including DNA, proteins, and drug molecules have been actively investigated.^[155] To target the acidic endosomal/lysosomal compartments, nanovectors with pH-cleavable linkers were reported to improve payload bioavailability. In 2011, Zhou et al. reported a set of tunable, pH-activatable micellar (pHAM) nanoparticles based on the supramolecular self-assembly of ionizable block copolymer micelles.^[156] Despite these significant advances, specific transport and activation of nanoparticles in different organelles during endocytosis in living cells is not well documented.

From a medical point of view, targeting of mitochondria using engineered nanovectors is gaining interest in chemotherapy, as mitochondria are key regulators of cell death and their functions are often altered in neoplasia. For this reason, the development of mitochondria-targeted drugs represents a promising approach for eradicating chemotherapy-refractory cancer cells.^[156] Promising strategies are based on electrostatic interactions between the engineered nanoparticles and the mitochondrial membrane, which has a membrane potential in the 130–150 mV range that is lower than other membranes in the cell and can be exploited by grafting cationic species, such as triphenylphosphonium (TPP) cations, to the surface of the nanocarrier.^[153] In particular, cationic TPP has been applied in various studies for mitochondrial targeting of antioxidants with the aim of protecting them from oxidative damage.^[157] Peptide ligands provide an alternative method for targeting mitochondria. For instance, Yamamoto and co-workers made an approach by conjugating a peptide-based mitochondrial targeting sequence to QDs.^[157] The sequence was attached to

n-trioctylphosphine oxide-capped QDs in a multi-step process by a thiol-exchange method. In order to generate carboxyl-QDs, a 3-mercaptopropanoic acid was used and then coupled with a cysteine to get free sulfhydryl groups on the surface of QDs. The amino group of the mitochondrial targeting sequence Mito-8 (NH₂-MSVLTPLLRGLTGSAARRLPVPRAKIHWLCCOOH) was then attached using sulfo-SMCC. Results showed that QD520-Mito8 exhibited a strong mitochondrial localization in living cells compared to QDs modified with a control peptide, which was assessed by mitochondrial staining using confocal microscopy.^[157]

Another interesting application of nanoparticles for mitochondrial targeting has been recently explored by Chou et al., who have demonstrated the induction of cell death by physical trapping of mitochondria using bacterial-derived magnetic nanoparticles (BMPs) labeled with cytochrome *c* (Cyt *c*)-specific binding aptamers, combined with an applied external static magnetic field.^[155] Cyt-*C* has an important role in the life-supporting function of ATP synthesis. In this way, the authors demonstrated that the method might be useful for targeted cell therapy, with the advantage of conferring remote control over subcellular elements by means of a magnetic field.

Finally, Chamberlain et al. reported the targeting of doxorubicin into mitochondria using mitochondria-penetrating peptides (MPPs) formed by cationic sequences that can deliver cargoes into the mitochondrial matrix (Figure 8).^[158] Doxorubicin, an inhibitor of DNA topoisomerase II (TopoII), is used in the treatment of a wide range of cancers, and its principal mechanism of action is the generation of TopoII-mediated lesions in nuclear DNA leading to cell apoptosis.^[158] A mitochondrially targeted version of doxorubicin (mtDox) was synthesized by coupling the primary amine of the sugar motif to a succinic anhydride conjugated to the *N*-terminus of the MPP. This compound was shown to maintain the ability to inhibit TopoII and to induce damage to mtDNA selectively. At the same time, the potency of mtDox is somewhat diminished compared with the parent drug in sensitive cells, which may indicate that TopoII is not as essential in mitochondria as in the nucleus. For that reason, mtDox may also find application in the study of the enzyme mtTopoII.

In another work, mitochondria-targeted nanoparticles based on PLGA-*b*-PEG and a lipophilic triphenyl phosphonium (TPP) cation were used for the delivery of a therapeutic payload, specifically, a zinc phthalocyanine photosensitizer.^[159] The action of these nanoparticles upon light activation inside the mitochondria was shown to produce reactive oxygen species (ROS), which caused cell death via apoptosis and necrosis. The authors demonstrated that tumor antigens generated from the treatment of breast cancer cells with these nanoparticles activate dendritic cells (DCs) upon light stimulation to produce high levels of interferon-gamma (IFN- γ). The advantages of this activation process are: 1) activated DCs can be produced in bulk quantities, 2) *ex vivo* culture conditions can be carefully controlled, and 3) DC quality can be controlled before the cells are administered to the patient. These results open the possibility of using mitochondria-targeted nanoparticles, light-activated cancer cell supernatants as possible vaccines and the approach has the potential to be readily transferred to the clinical practice.

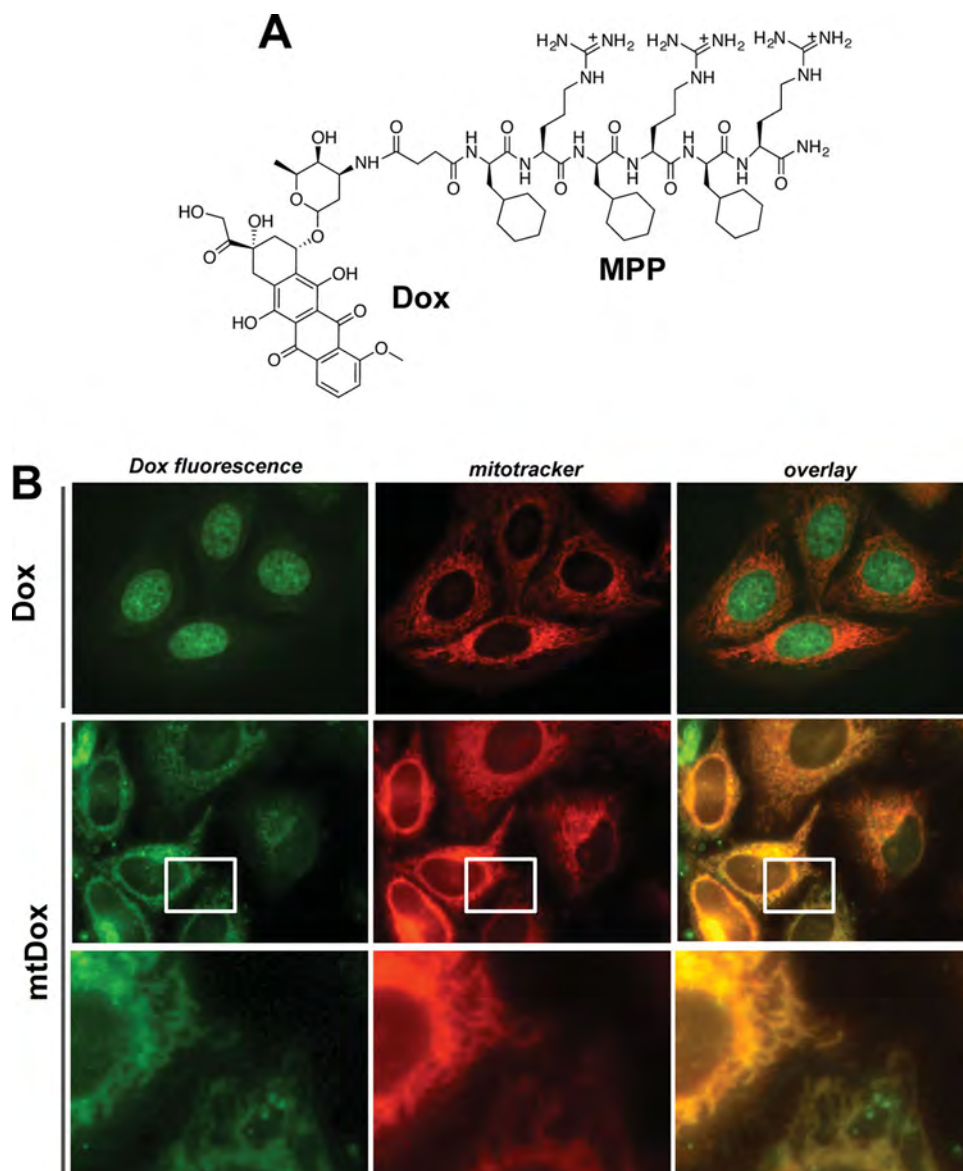


Figure 8. Mitochondrial targeting by mitochondria-penetrating peptides. A) Structure of doxorubicin (Dox) conjugated to a mitochondria-penetrating peptide (MPP) (mtDox conjugate). B) Subcellular localization of mtDox. Top row: Dox (green channel) demonstrates strong nuclear staining as monitored using its intrinsic fluorescence and no colocalization with Mitotracker 633 (red channel) as shown in overlay image (right). Middle row: mtDox (red channel) shows a high level of mitochondrial accumulation with a staining pattern that matches Mitotracker 633 (green channel). The high degree of colocalization can be visualized in the bottom row close-up images. Reproduced with permission.^[158] Copyright 2013, ACS American Chemical Society.

4. Perspectives: Future Developments in Nanoparticle Delivery

In the last decade, a lot of research work has been devoted to the development of nanoconjugates able to penetrate the cells both for drug delivery application and intracellular targeting. Although nanotechnology combined with bioscience has been developing rapidly with new bioconjugation approaches to be discovered, the guided nanoparticle delivery inside the cell remains a challenging task.^[160–163] Recently, a new modern approach, so-called Halo Tag technology, has been designed to

provide new options for rapid, site-specific labeling of proteins in living cells and in vitro, and based on the efficient formation of a covalent bond between the Halo Tag protein and synthetic ligands (Figure 9a).^[164–166] Besides being used in biology for protein expression studies, this technology has been gaining a lot of interest in nanobiotechnology as well. At the moment, there are only few examples reporting the Halo tag use in nanoparticle studies. In a recent research from our group, Halo tag was used as nanoparticle capture module, taking advantage of a new covalent bond formation by site-specific reaction with a chloro-alkane linker immobilized on the surface of an

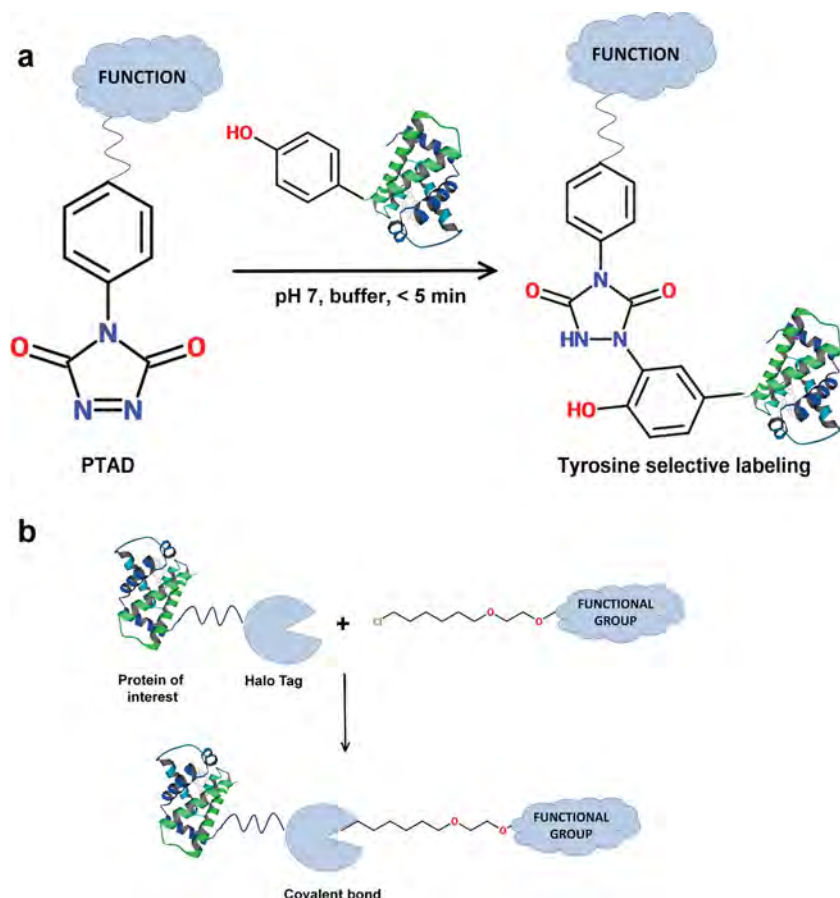


Figure 9. Orientation controlled site-specific labeling of proteins via a) Halo tag covalent bond formation, and b) tyrosine selective conjugation.

IONP. Expressing Halo Tag in fusion with a small peptide of 11 amino acids (U11) with a high affinity for urokinase plasminogen activator receptor (uPAR), we were able to successfully label cancer cells in an orientation-controlled manner.^[23] Similarly, Ting and co-workers used Halo tag-conjugated QDs for labeling of specific membrane proteins in living cells. In this case, the protein of interest was genetically fused to a 13 amino acid recognition sequence and subsequently conjugated with 10-bromodecanoic acid for site-specific attachment of a lipophilic acid ligase enzyme.^[167] Another useful, highly efficient, and chemoselective strategy for the conjugation of small molecules, peptides, and entire proteins involves the tyrosine “click” reaction of 4-phenyl-3H-1,2,4-triazol-3,5(4H)-diones (PTAD) derivatives (Figure 9b). While tyrosine residues are commonly found in proteins, surface accessible tyrosines only seldom occur and provide attractive opportunities for minimal labeling. The reaction is selective for the phenolic side chain of tyrosine and occurs in buffered aqueous media over a broad pH range without the requirement of added heavy metals or other reagents, resulting in a C–N linkage, which is significantly more stable to extreme pH, high temperatures, and in human serum for extended periods of time in comparison with the more popular maleimide-based methods.^[168]

Beyond their use as tumor targeting platforms, nanoparticles are attracting much interest as potential cancer vaccines.

Recently, several reviews describing some recent advances in nanoscale systems designed for cancer immunotherapy, as well as the potential for these systems to translate into clinical cancer vaccines, have been reported.^[169,170] For instance, Cameron et al. have used small AuNPs decorated with Tn-antigen (truncated core 1 mucin-type) glycans in a “multicopy-multivalent” manner, giving rise to a nanoparticle with a surface that mimics much more closely the surface of cancer cells. Immunological studies successfully proved that these nanoparticles were able to generate strong and long-lasting production of antibodies that were selective to the Tn-antigen glycan and cross-reactive toward mucin proteins displaying Tn, thus demonstrating the possibility to use glycosylated AuNPs as an anticancer vaccine even in the absence of a typical vaccine protein component.^[169,170] In another example, Barchi et al. have used AuNPs coated with both the tumor-associated glycopeptides antigens containing the cell surface mucin MUC4 with Thomsen Friedenreich (TF) antigen attached at different sites and a 28-residue peptide from the complement-derived protein C3d to act as a B-cell activating “molecular adjuvant.” As a result, the authors obtained nanoparticles that could act both as immunogens and immune system stimulants, showing statistically significant antibody response in mice to each glycopeptide antigen.^[171,172] Finally, it was also found

elsewhere that nanoparticle shape and size greatly influence the immune response both in vivo and in vitro.^[173] In conclusion, although several advantages in subcellular targeting by nanoconjugates have been observed, many challenges still need to be overcome to increase the targeting efficiency and reduce the overall cytotoxicity. For this reason, an ad hoc design of nanoconjugates, including studies on their morphological properties and choice of the proper targeting ligands, is needed to drive the uptake efficiency and pathway of entry. These studies are expected to take advantage of modern simulation methods, which could provide researcher with new predictive tools for the de novo design of more efficient, high-affinity molecular nanoconjugates.^[174,175] Moreover, the combination of targeting and therapeutic functions to create an “ideal” theranostic nanoparticle platform for tumor treatment will be of great utility in the purpose to improve tumor treatment efficiency on earlier stages.

5. Conclusions and Outlooks

In the present review, we have provided the most recent advances and challenges on the use of nanoparticles designed ad hoc for cellular nanobiotechnology. In particular, we have pointed out different strategies for delivering nanoparticles through the targeting of different cellular compartments such

as cellular membrane, cytoplasm, nucleus, and mitochondria, which are intended to meet the medical needs emerging by the modern challenges in the diagnosis and therapy of highly threatening human diseases.

Besides the well-documented internalization mechanisms based on the crossing of cellular membrane, we have described also the physical approaches that have been used to deliver nanoparticles inside the cellular matrix. A few examples using advanced techniques, such as microinjection and electroporation, have been illustrated. However, at present, incubation remains by far the preferred strategy to investigate the biological interactions between nanoparticles and cells reproducing the ordinary living conditions avoiding invasive destabilization of the cellular environment. From this rapid overview, it appears how the nanoparticle nature and functionalization could affect the interaction at the nano-bio interface, which, in turn, mediates nanoparticle internalization routes. In addition, we have discussed some hurdles occurring when this small interface faces the physiological environment and how this phenomenon can turn into different unexpected responses. Eventually, we have concluded with a picture of future perspectives on new possible improvements and developments, which could open new directions towards potential applications in nanomedicine.

Once fully mapped, the relationships between synthetic nanoparticle chemistry, molecular recognition, and cellular biology will converge and could enable researchers to predict the physiological response of colloidal nanoparticles. These concepts will also help the researchers to design “ideal” and rational conjugate nanosystems, which could be used as nanovector to ensure the efficient and selective delivery of a specific agent to a specific cellular compartment, with the aim of an in vitro screening of its efficacy and possible toxicity, prior to an in vivo validation. Disclosing these relationships will require an extensive research and we would expect that also new experimental techniques and strategies will be the major driving forces directing the progress in the future of nanomedicine.

Acknowledgements

P.V. and S.A. contributed equally to this work. This work was supported by Fondazione Regionale per la Ricerca Biomedica (FRRB), NanoMeDia Project (A. O. “L. Sacco” and Regione Lombardia), the “NanoBioSense” Project (Sardegna-Lombardia), and Cariplo Foundation (“The MULAN program”, Project N° 2011–2096). S.A. and G.A. acknowledge a research fellowship from “Fondazione Romeo ed Enrica Invernizzi” and CMENA.

Received: October 31, 2013

Revised: December 5, 2013

Published online: January 20, 2014


- [1] S. Dufort, L. Sancey, J. L. Coll, *Adv. Drug. Delivery Rev.* **2012**, *64*, 179.
- [2] J. B. Haun, N. K. Devaraj, S. A. Hilderbrand, H. Lee, R. Weissleder, *Nat. Nanotechnol.* **2010**, *5*, 660.
- [3] K. Prapainop, D. P. Witter, P. A. Wentworth, *J. Am. Chem. Soc.* **2012**, *134*, 4100.
- [4] G. L. Pilar, D. J. De Aberasturi, V. Wulf, B. Pelaz, P. Del Pino, Y. Zhao, J. M. De La Fuente, I. R. De Larramendi, T. Rojo, X. J. Liang, W. J. Parak, *Acc. Chem. Soc.* **2013**, *6*, 743.
- [5] C. Luccardini, A. Yakovlev, S. Gaillard, M. van't Hoff, A. P. Alberola, J. M. Mallet, W. J. Parak, A. Feltz, M. Oheim, *J. Biomed. Biotechnol.* **2007**, *7*, 68973.
- [6] A. Albanese, P. S. Tang, W. C. W. Chan, *Annu. Rev. Biomed. Eng.* **2012**, *14*, 1.
- [7] W. K. Oh, S. Kim, O. Kwon, J. Jang, *J. Nanosci. Nanotechnol.* **2011**, *11*, 4254.
- [8] L. Florez, C. Herrmann, J. M. Cramer, C. P. Hauser, K. Koynov, K. Landfester, D. Crespy, V. Mailänder, *Small* **2012**, *8*, 2222.
- [9] D. Hühn, K. Kantner, C. Geidel, S. Brandhold, I. De Cock, S. J. H. Soenen, P. R. Gil, J. M. Montenegro, K. Braekmans, K. Müllen, G. U. Nienhaus, M. Klapper, W. J. Parak, *ACS Nano* **2013**, *7*, 3253.
- [10] C. Sweigher, R. Hartmann, F. Zhang, W. J. Parak, T. H. Kissel, *J. Nanobiotechnol.* **2012**, *10*, 10.
- [11] K. E. Sapsford, W. R. Algar, L. Berti, K. B. Gemmill, B. J. Casey, E. Oh, M. H. Steward, I. L. Medintz, *Chem. Rev.* **2013**, *113*, 1904.
- [12] S. Fraga, H. Faria, M. E. Soares, J. A. Duarte, J. P. Soares, M. L. Bastos, H. Carmo, *J. Appl. Toxicol.* **2013**, *33*, 1111.
- [13] W. J. Stark, *Angew. Chem. Int. Ed.* **2011**, *50*, 1242.
- [14] M. P. Monopoli, C. Åberg, A. Salvati, K. A. Dawson, *Nat. Nanotechnol.* **2012**, *7*, 779.
- [15] M. P. Monopoli, D. Walczyk, A. Campbell, G. Elia, I. Lynch, F. Baldelli Bombelli, K. A. Dawson, *J. Am. Chem. Soc.* **2011**, *133*, 2525.
- [16] A. Lesniak, F. Fenaroli, M. P. Monopoli, C. Åberg, K. A. Dawson, A. Salvati, *ACS Nano* **2012**, *6*, 5845.
- [17] A. Salvati, A. S. Pitek, M. P. Monopoli, K. Prapainop, F. Baldelli Bombelli, D. R. Hristov, P. M. Kelly, C. Åberg, E. Mahon, K. A. Dawson, *Nat. Nanotechnol.* **2013**, *8*, 137.
- [18] J. V. Jokerst, T. Lobovkina, R. N. Zare, S. S. Gambhir, *Nanomedicine* **2011**, *6*, 715.
- [19] E. Occhipinti, P. Verderio, A. Natalello, E. Galbiati, M. Colombo, S. Mazzucchelli, A. Salvadè, P. Tortora, S. M. Doglia, D. Prospero, *Nanoscale* **2011**, *3*, 387.
- [20] F. Corsi, L. Fiandra, C. De Palma, M. Colombo, S. Mazzucchelli, P. Verderio, R. Allevi, A. Tosoni, M. Nebuloni, E. Clementi, D. Prospero, *ACS Nano* **2011**, *8*, 6383.
- [21] M. Colombo, S. Sommaruga, S. Mazzucchelli, L. Polito, P. Verderio, P. Galeffi, F. Corsi, P. Tortora, D. Prospero, *Angew. Chem. Int. Ed.* **2012**, *51*, 496.
- [22] F. Danhier, F. Ansorena, J. M. Silva, R. Coco, A. Le Breton, V. Preat, *J. Controlled Release* **2012**, *161*, 505.
- [23] S. Mazzucchelli, M. Colombo, P. Verderio, E. Rozek, F. Andreato, P. Tortora, F. Corsi, D. Prospero, *Angew. Chem. Int. Ed.* **2013**, *52*, 3121.
- [24] S. Mazzucchelli, P. Verderio, S. Sommaruga, M. Colombo, A. Salvadè, F. Corsi, P. Galeffi, P. Tortora, D. Prospero, *Bioconjugate Chem.* **2011**, *22*, 2296.
- [25] S. Huang, K. Shao, Y. Kuang, Y. Liu, J. Li, S. An, Y. Guo, H. Ma, X. He, C. Jiang, *Biomaterials* **2013**, *34*, 5294.
- [26] P. Kocbek, S. Kralj, M. E. Kreft, J. Kristl, *Eur. J. Pharm. Sci.* **2013**, *50*, 130.
- [27] R. A. Petros, J. M. De Simone, *Nat. Rev. Drug Discovery* **2010**, *9*, 615.
- [28] L. Treuel, X. Jiang, G. U. Nienhaus, *J. R. Soc. Interface* **2013**, *10*, 20120939.
- [29] S. D. Conner, S. L. Schmid, *Nature* **2003**, *422*, 37.
- [30] A. E. Nel, L. Mädler, D. Velegol, D. Xia, E. M. V. Hoek, P. Somasundaran, F. Klaessig, V. Castranova, M. Thompson, *Nat. Mater.* **2009**, *8*, 543.
- [31] J. V. Georgieva, D. Kalicharan, P. O. Couraud, I. A. Romero, B. Weksler, D. Hoekstra, I. S. Zuhorn, *Mol. Ther.* **2011**, *19*, 318.

- [32] Y. Huang, L. He, W. Liu, C. Fan, W. Zheng, Y. S. Wong, T. Chen, *Biomaterials* **2013**, *34*, 7106.
- [33] B. He, Z. Jia, W. Du, C. Yu, Y. Fan, W. Dai, L. Yuan, H. Zhang, X. Wang, J. Wang, X. Zhang, Q. Zhang, *Biomaterials* **2013**, *34*, 4309.
- [34] B. He, P. Lin, Z. Jia, W. Du, W. Qu, L. Yuan, W. Dai, H. Zhang, X. Wang, J. Wang, X. Zhang, Q. Zhang, *Biomaterials* **2013**, *34*, 6082.
- [35] V. E. Kagan, J. Shi, W. Feng, A. A. Shvedova, B. J. Fadeel, *Occup. Environ. Med.* **2010**, *52*, 943.
- [36] G. Oberdörster, *J. Intern. Med.* **2010**, *267*, 89.
- [37] A. Salvati, C. Åberg, T. Dos Santos, J. Varela, P. Pinto, I. Lynch, K. A. Dawson, *Nanomedicine* **2011**, *7*, 818.
- [38] S. J. H. Soenen, U. Himmelreich, N. Nuytten, T. R. Pisanic, A. Ferrari, M. De Cuyper, *Small* **2010**, *6*, 2136.
- [39] D. A. Heller, R. Sharma, M. S. Strano, *ACS Nano* **2009**, *3*, 149.
- [40] H. Herd, N. Daum, A. T. Jones, H. Huwer, H. Ghandehari, C. M. Lehr, *ACS Nano* **2013**, *7*, 1961.
- [41] E. C. Cho, L. Au, Q. Zhang, Y. Xia, *Small* **2010**, *6*, 517.
- [42] A. Verma, O. Uzun, Y. Hu, Y. Hu, H. S. Han, N. Watson, S. Chen, D. J. Irvine, F. Stellacci, *Nat. Mater.* **2008**, *7*, 588.
- [43] A. Verma, F. Stellacci, *Small* **2010**, *6*, 12.
- [44] T. Hamada, M. Morita, M. Miyakawa, R. Sugimoto, A. Hatanaka, M. C. Vestergaard, M. Takagi, *J. Am. Chem. Soc.* **2012**, *134*, 13990.
- [45] T. Fujiwara, H. Akita, H. Harashima, *Int. J. Pharm.* **2010**, *386*, 122.
- [46] J. A. Kim, C. Åberg, A. Salvati, K. A. Dawson, *Nat. Nanotech.* **2011**, *7*, 62.
- [47] M. Rahman, in *Springer Series in Biophysics*, Springer-Verlag Berlin, Heidelberg, Germany **2013**, Vol. 15, p. 21.
- [48] Z. J. Deng, M. Liang, M. Monteiro, I. Toth, R. F. Minchin, *Nat. Nanotechnol.* **2011**, *6*, 39.
- [49] W. Liu, J. Rose, S. Plantevin, M. Auffan, J. Bottero, C. Vidaud, *Nanoscale* **2013**, *5*, 1658.
- [50] D. Dell'Orco, M. Lundqvist, C. Oslakovic, T. Cedervall, S. Linse, *PLoS ONE* **2010**, *5*, e10949.
- [51] M. A. Dobrovolskaia, A. K. Patri, J. W. Zheng, J. D. Clogston, N. Ayub, P. Aggarwal, B. W. Neun, Hall, S. B. McNeil, *Nanomedicine* **2009**, *5*, 106.
- [52] M. S. Ehremer, E. Freidman, J. N. Finkelstein, G. Oberdoster, J. L. McGrath, *Biomaterials* **2009**, *30*, 603.
- [53] M. J. D. Clift, S. Bhattacharjee, D. M. Brown, V. Stone, *Toxicol. Lett.* **2010**, *198*, 358.
- [54] O. Lunov, T. Syrovets, C. Loos, J. Beil, M. Delacher, K. Tron, G. U. Nienhaus, A. Musyanovych, V. Mailander, K. Landefester, T. Simmet, *ACS Nano* **2011**, *5*, 1657.
- [55] G. A. Orr, W. B. Chrisler, K. J. Cassens, R. Tan, V. J. Tarasevich, L. M. Markillie, R. C. Zangar, B. D. Thrall, *Nanotoxicology* **2011**, *5*, 296.
- [56] A. L. Barràn-Berdòn, D. Pozzi, G. Caracciolo, A. L. Capriotti, G. Caruso, C. Cavaliere, A. Riccioli, S. Palchetti, A. Laganà, *Langmuir* **2013**, *29*, 6485.
- [57] R. E. Serda, J. H. Go, R. C. Bhavane, X. Liu, C. Chiappini, P. Decuzzi, M. Ferrari, *Biomaterials* **2009**, *30*, 2440.
- [58] P. Sandin, L. W. Fitzpatrick, J. C. Simpons, K. A. Dawson, *ACS Nano* **2012**, *6*, 1513.
- [59] J. A. Stolwijk, C. Hartmann, D. Balani, S. Albermann, C. S. Keese, I. Giaever, J. Wegener, *Biosens. Bioelectron.* **2011**, *26*, 4720.
- [60] J. B. Delehanty, H. Mattoussi, I. L. Medintz, *Anal. Bioanal. Chem.* **2009**, *393*, 1091.
- [61] X. D. Wang, J. A. Stolwijk, T. Lang, M. Sperber, R. J. Meier, J. Wegener, O. S. Wolfbeis, *J. Am. Chem. Soc.* **2012**, *134*, 17011.
- [62] J. Lin, R. Chen, S. Feng, Y. Li, Z. Huang, S. Xie, Y. Yu, M. Cheng, H. Zeng, *Biosens. Bioelectron.* **2009**, *25*, 388.
- [63] J. B. Delehanty, C. E. Bradburne, K. Boeneman, K. Susumu, D. Farrell, B. C. Mei, J. B. Blanco-Canosa, G. Dawson, P. E. Dawson, H. Mattoussi, I. L. Medintz, *Integr. Biol.* **2010**, *2*, 265.
- [64] C. G. Pack, M. R. Song, E. L. Tae, M. Hiroshima, K. H. Byun, J. S. Kim, Y. Sako, *J. Controlled Release* **2012**, *163*, 315.
- [65] Y. Liu, M. Zhou, D. Luo, L. Wang, Y. Hong, Y. Yang, V. Y. Sha, *Biochem. Biophys. Res. Commun.* **2012**, *425*, 769.
- [66] T. Kim, E. Momin, J. Choi, K. Yuan, H. Zaidi, J. Kim, M. Park, N. Lee, M. T. McMahon, A. Quinones-Hinojosa, J. W. Bulte, T. Hyeon, A. A. Gilad, *J. Am. Chem. Soc.* **2011**, *133*, 2955.
- [67] J. S. Yoo, H. B. Kim, N. Won, J. Bang, S. Kim, S. Ahn, B. C. Lee, K. S. Soh, *Mol. Imaging Biol.* **2011**, *13*, 471.
- [68] Y. C. Liu, P. C. Wu, D. B. Shieh, S. N. Wu, *Int. J. Nanomed.* **2012**, *7*, 1687.
- [69] J. A. Kim, W. G. Lee, *Nanoscale* **2011**, *3*, 1526.
- [70] B. Dubertret, P. Skourides, D. J. Norris, V. Noireaux, A. H. Brivanlou, A. Libchaber, *Science* **2002**, *298*, 1759.
- [71] A. Candeloro, L. Tirinato, N. Malara, A. Fregola, E. Casals, V. Puntès, G. Perozziello, F. Gentile, M. L. Coluccio, G. Das, C. Liberale, F. De Angelis, E. Di Fabrizio, *Analyst* **2011**, *136*, 4402.
- [72] A. M. Derfus, W. C. W. Chan, S. N. Bhatia, *Adv. Mater.* **2004**, *16*, 961.
- [73] I. L. Medintz, T. Pons, J. B. Delehanty, K. Susumu, F. M. Brunel, P. E. Dawson, H. Mattoussi, *Bioconjugate Chem.* **2008**, *19*, 1785.
- [74] E. Muro, T. Fragola, N. Pons, N. Lequeux, A. Ioannou, P. Skouridies, B. Dubertret, *Small* **2012**, *8*, 1029.
- [75] F. M. Kievit, Z. R. Stephen, O. Veisheh, H. Arami, T. Wang, V. P. Lai, J. O. Park, R. G. Ellenbogen, M. L. Disis, M. Zhang, *ACS Nano* **2012**, *6*, 2591.
- [76] P. A. McCarron, W. M. Marouf, D. J. Quinn, F. Fay, R. E. Burden, S. A. Olwill, C. J. Scott, *Bioconjugate Chem.* **2008**, *19*, 1561.
- [77] L. W. Chan, Y. N. Wang, L. Y. Lin, M. P. Upton, J. H. Hwang, S. H. Pun, *Bioconjugate Chem.* **2013**, *67*, 167.
- [78] S. Bhattacharyya, R. Bhattacharya, S. Curley, M. A. McNiven, P. Mukherjee, *Proc. Nat. Am. Soc.* **2010**, *107*, 14541.
- [79] S. Bhattacharyya, J. A. Khan, G. L. Curran, J. D. Robertson, R. Bhattacharya, P. Mukherjee, *Adv. Mater.* **2011**, *23*, 5034.
- [80] H. Y. Ko, K. J. Choi, C. H. Lee, S. Kim, *Biomaterials* **2011**, *32*, 1130.
- [81] K. Fan, C. Cao, Y. Pan, D. Lu, D. Yang, J. Feng, L. Song, M. Liang, X. Yan, *Nat. Nanotechnol.* **2012**, *7*, 459.
- [82] M. T. Stephan, J. J. Moon, S. H. Um, A. Bershteyn, D. J. Irvine, *Nat. Med.* **2010**, *16*, 1035.
- [83] F. N. Al-Deen, J. Ho, C. Selomulya, C. Ma, R. Coppel, *Langmuir* **2011**, *27*, 3703.
- [84] C. Xu, D. Yang, L. Mei, B. Lu, L. Chen, Q. Li, H. Zhu, T. Wang, *ACS Appl. Mater. Interfaces* **2013**, *5*, 2715.
- [85] T. Xia, M. Kovochich, M. Liang, H. Meng, S. Kabehie, S. George, J. I. Zink, A. E. Nel, *ACS Nano* **2009**, *3*, 3273.
- [86] H. Yoo, S. K. Moon, T. Hwang, Y. S. Kim, H. J. Kim, S. W. Choi, J. K. Kim, *Langmuir* **2013**, *29*, 5962.
- [87] L. L. Ma, J. O. Tam, B. W. Willsey, D. Rigdon, R. Ramesh, K. Sokolov, K. P. Johnston, *Langmuir* **2011**, *27*, 7681.
- [88] W. Jiang, B. Y. S. Kim, J. T. Rutka, W. C. W. Chan, *Nat. Nanotechnol.* **2008**, *3*, 145.
- [89] Y. W. Huang, H. Liu, X. Xiong, Y. Chen, W. Tan, *J. Am. Chem. Soc.* **2009**, *131*, 17328.
- [90] B. P. Gray, S. Li, K. C. Brown, *Bioconjugate Chem.* **2013**, *24*, 85.
- [91] M. Youns, J. D. Hoheisel, T. Efferth, *Curr. Drug Targets* **2011**, *12*, 357.
- [92] J. G. Huang, T. Leshuk, F. X. Gu, *Nanotoday* **2011**, *6*, 478.
- [93] L. Rajendran, H. J. Knölker, K. Simons, *Nat. Rev. Drug Discovery* **2010**, *9*, 29.
- [94] F. Milletti, *Drug Discovery Today* **2012**, *17*, 850.

- [95] F. Madani, S. Lindberg, U. Langel, S. Futaki, A. Graslund, *J. Biophys.* **2011**, 414729.
- [96] H. Park, H. Tsutsumi, H. Mihara, *Biomaterials* **2013**, *34*, 4872.
- [97] X. Liu, C. Liu, W. Zhang, C. Xie, G. Wei, W. Lu, *Int. J. Pharm.* **2013**, *448*, 159.
- [98] S. Guo, L. Huang, *J. Nanomater.* **2011**, 742895
- [99] J. B. Delehanty, J. B. Blanco-Canosa, C. E. Bradbourne, K. Susumu, M. H. Stewart, D. E. Prasuhn, P. E. Dawson, I. L. Mednitz, *Chem. Commun.* **2013**, 49, 7878.
- [100] K. Bohenenman, J. B. Delehanty, J. B. Blanco-Canosa, K. Susumu, M. H. Stewart, E. Oh, A. L. Huston, G. Dawson, S. Ingale, R. Walters, M. Domowicz, J. R. Deschamps, W. R. Algar, S. DiMaggio, J. Manono, C. M. Spillmann, D. Thompson, T. L. Jennings, P. E. Dawson, I. L. Mednitz, *ACS Nano* **2013**, *7*, 3778.
- [101] Y. Xu, F. C. Szoka, *Biochemistry* **1996**, *37*, 5616.
- [102] I. M. Hafez, N. Maurer, P. R. Cullis, *Gene Ther.* **2001**, *8*, 1188.
- [103] S. D. Li, L. Huang, *Biochim. Biophys. Acta* **2009**, 1788, 2259.
- [104] S. D. Li, L. Huang, *J. Controlled Release* **2010**, *145*, 178.
- [105] H. Hatakeyama, H. Akita, H. Harashima, *Adv. Drug Delivery Rev.* **2011**, *63*, 152.
- [106] Z. Rehman, I. S. Zuhom, D. Hoekstra, *J. Controlled Release* **2013**, *166*, 46.
- [107] R. R. Sawant, S. K. Sriraman, G. Navarro, S. Biswas, R. A. Dalvi, V. P. Torchilin, *Biomaterials* **2012**, *33*, 3942.
- [108] F. Pittella, M. Zhang, Y. Lee, H. J. Kim, T. Tockary, K. Osada, T. Ishii, K. Miyata, N. Nishiyama, K. Kataoka, *Biomaterials* **2011**, *32*, 3106.
- [109] H. C. Kang, H. J. Kang, Y. K. Bae, *Biomaterials* **2011**, *32*, 1193.
- [110] X. Liu, J. Zhang, D. M. Lynn, *Soft Matter* **2008**, *4*, 1688.
- [111] J. Tu, T. Wang, W. Shi, G. Wu, X. Tian, Y. Wang, D. Ge, L. Ren, *Biomaterials* **2012**, *33*, 7903.
- [112] R. V. Benjaminsen, M. A. Matthebjerg, J. R. Henriksen, S. M. Moghimi, T. L. Andresen, *Mol. Ther.* **2013**, *1*, 149.
- [113] E. Wagner, *Acc. Chem. Soc.* **2012**, *45*, 1005.
- [114] I. Nakase, S. Kobayashi, S. Futaki, *Peptide Sci.* **2010**, *94*, 763.
- [115] N. Toriyabe, Y. Haiashi, H. Harashima, *Biomaterials* **2013**, *34*, 1337.
- [116] Z. Krpetic, S. Saleemi, I. A. Prior, V. See, R. Qureshi, M. Brust, *ACS Nano* **2011**, *5*, 5195.
- [117] P. Nativo, I. A. Prior, M. Brust, *ACS Nano* **2008**, *2*, 1639.
- [118] H. Wei, R. X. Zhuo, X. Z. Zhang, *Prog. Polym. Sci.* **2013**, *3*, 503.
- [119] M. S. Shim, Y. J. Kwon, *Biomaterials* **2010**, *31*, 3404.
- [120] M. S. Shim, C. S. Kim, Y. C. Ahn, Z. Chen, Y. J. Kwon, *J. Am. Chem. Soc.* **2010**, *132*, 8316.
- [121] M. S. Shim, Y. J. Kwon, *Biomaterials* **2011**, *32*, 4009.
- [122] S. C. Semple, A. Akinc, J. Chen, A. P. Sandhu, B. L. Mui, C. K. Cho, D. W. Sah, D. Stebbing, E. J. Crosley, E. Yaworski, I. M. Hafez, J. R. Dorkin, J. Qin, K. Lam, K. G. Rajeev, K. F. Wong, L. B. Jeffs, L. Nechev, M. L. Eisenhardt, M. Jayaraman, M. Kazem, M. A. Maier, M. Srinivasulu, M. J. Weinstein, Q. Chen, R. Alvarez, S. A. Barros, S. De, S. K. Klimuk, T. Borland, V. Kosovrasti, W. L. Cantley, Y. K. Tam, M. Manoharan, M. A. Ciufolini, M. A. Tracy, A. de Fougères, I. MacLachlan, P. M. Cullis, T. D. Madden, M. J. Hope, *Nat. Biotechnol.* **2010**, *28*, 172.
- [123] M. S. Shim, Y. J. Kwon, *Bioconjugate Chem.* **2009**, *20*, 488.
- [124] S. Guo, Y. Huang, T. Wei, W. Zhang, W. Wang, D. Lin, H. Zhang, A. Kumar, Q. Du, J. Xing, L. Deng, Z. Liang, P. C. Wang, L. Dong, X. J. Liang, *Biomaterials* **2011**, *32*, 879.
- [125] A. Dehshahri, R. K. Oskuee, W. T. Shier, A. Hafezi, M. Ramezani, *Biomaterials* **2009**, *30*, 4187.
- [126] Z. Zhang, W. Coa, H. Jin, J. F. Lovell, M. Yang, L. Ding, J. Chen, I. Corbin, Q. Luo, G. Zheng, *Angew. Chem. Int. Ed.* **2009**, *48*, 9171.
- [127] J. G. van der Boorn, M. Schlee, C. Coch, G. Hartmann, *Nat. Biotechnol.* **2011**, *29*, 325.
- [128] D. Drescher, J. Kneipp, *Chem. Soc. Rev.* **2012**, *41*, 5780.
- [129] Y. Yu, X. Xie, M. Zheng, L. Yu, L. Zhang, J. Zhao, D. Jiang, X. Che, *Int. J. Nanomed.* **2012**, *7*, 5079.
- [130] P. L. Mallet, F. Bachand, *Traffic* **2013**, *14*, 282.
- [131] F. Cardarelli, M. Serresi, A. Albanese, R. Bizzarri, F. Beltram, *J. Biol. Chem.* **2011**, 286, 12292.
- [132] L. Pan, J. Liu, Q. He, L. Wang, J. Shi, *Biomaterials* **2013**, *34*, 2719.
- [133] M. Nagai, Y. Yoneda, *Biochim. Biophys. Acta.* **2013**, 1830, 2813.
- [134] S. Brunner, T. Sauer, S. Carotta, M. Cotten, M. Saltik, E. Wagner, *Gene Ther.* **2000**, *7*, 401.
- [135] J. D. Larsen, N. L. Ross, M. O. Sullivan, *J. Gene Med.* **2012**, *14*, 580.
- [136] I. Ojea-Jiménez, L. García-Fernández, L. Lorenzo, V. F. Puentes, *ACS Nano* **2012**, *6*, 7692.
- [137] M. K. Gragas, J. P. Scaffidi, B. Lauly, T. Vo-Dinh, *App. Spect.* **2010**, *64*, 858.
- [138] W. Xie, L. Wang, Y. Zhang, L. Su, A. Shen, J. Tan, J. Hu, *Bioconjugate Chem.* **2009**, *20*, 768.
- [139] L. A. Austin, B. Kang, C. W. Yen, M. A. El-Sayed, *J. Am. Chem. Soc.* **2011**, *133*, 17594.
- [140] S. Y. Lin, N. T. Chen, S. P. Sum, L. Lo, C. S. Yang, *Chem. Commun.* **2008**, *21*, 4762.
- [141] C. W. Kuo, D. Y. Chueh, N. Singh, F. C. Chien, P. Chen, *Bioconjugate Chem.* **2011**, *22*, 1073.
- [142] C. Xu, J. Xie, N. Kohler, E. G. Walsh, Y. E. Chinand, S. Sun, *Chem. Asian. J.* **2008**, *3*, 548.
- [143] R. Misra, S. K. Sahoo, *Eur. J. Pharm. Sci.* **2010**, *39*, 152.
- [144] R. Bahadur, B. Thapa, P. Xu, *Mol. Pharm.* **2012**, *9*, 2719.
- [145] J. N. Liu, W. Bu, L. M. Pan, S. Zhang, F. Chen, L. Zhou, K. L. Zhao, W. Peng, J. Shi, *Biomaterials* **2012**, *33*, 7282.
- [146] L. A. Austin, B. Kang, C. W. Yen, M. A. El-Sayed, *Bioconjugate Chem.* **2011**, *22*, 2324.
- [147] L. Yong-Yong, D. Hai-Qing, C. Xiao-Jun, R. Tian-Bin, *Mater. Sci. Eng. C. Mater. Biol. Appl.* **2013**, *33*, 2698.
- [148] R. Tian-Bin, X. Wen-Juan, D. Hai-Qing, L. Yong-Yong, *Polymer* **2011**, *52*, 3580.
- [149] L. Yong-Yong, H. Shou-Hu, X. Wang, W. Hui-Yuan, L. Xiao-Hua, L. Cao, C. Si-Xue, Z. Xian-Zheng, Z. Ren-Xi, *J. Mater. Chem.* **2011**, *21*, 3100.
- [150] L. C. Knight, J. E. Romano, B. Krynska, S. Faro, F. B. Mohamed, J. J. Gordon, *Mol. Biomark. Diagn.* **2010**, *1*, 1.
- [151] D. Kurihara, M. Akita, A. Kudo, T. Masuda, S. Futaki, H. Harashima, *Biol. Pharm. Bull.* **2009**, *3*, 1303.
- [152] D. M. Hockenbery, *Environ. Mol. Mutagen.* **2010**, *51*, 486.
- [153] L. F. Yousif, K. M. Stewart, S. O. Kelley, *ChemBioChem* **2009**, *10*, 1939.
- [154] Y. Yamada, H. Harashima, *Adv. Drug Delivery Rev.* **2008**, *60*, 1439.
- [155] J. Choi, J. Shin, J. Lee, M. Cha, *Chem. Commun.* **2012**, *48*, 7474.
- [156] K. Zhou, Y. Wang, X. Huang, K. Luby-Phelps, B. D. Sumer, J. Gao, *Angew. Chem. Int. Ed.* **2012**, *123*, 6233.
- [157] M. Breunig, S. Bauer, A. Goepferich, *Eur. J. Pharm. Biopharm.* **2008**, *68*, 112.
- [158] G. Chamberlain, D. Tulumello, S. Kelley, *ACS Chem. Biol.* **2013**, *8*, 1389.
- [159] S. Marrache, S. Tundup, D. Harn, S. Dhar, *ACS Nano* **2013**, *7*, 7392.
- [160] M. Colombo, S. Mazzucchelli, V. Collico, S. Avvakumova, L. Pandolfi, F. Corsi, F. Porta, D. Prosperi, *Angew. Chem. Int. Ed.* **2012**, *10*, 9272.
- [161] S. Mazzucchelli, S. Sommaruga, M. O'Donnell, P. Galeffi, P. Tortora, D. Prosperi, M. Colombo, *Biomater. Sci.* **2013**, *1*, 728.
- [162] M. Colombo, S. Mazzucchelli, J. M. Montenegro, E. Galbiati, F. Corsi, W. J. Parak, D. Prosperi, *Small* **2012**, *21*, 1492.

- [163] S. Mazzucchelli, M. Colombo, C. De Palma, A. Salvadé, P. Verderio, M. D. Coghi, E. Clementi, P. Tortora, F. Corsi, D. Proserpi, *ACS Nano* **2010**, *4*, 5693.
- [164] G. V. Los, L. P. Encell, M. G. McDougall, D. D. Hartzell, N. Karassina, C. Zimprich, M. G. Wood, R. Learish, R. Friedman Ohana, M. Uhr, D. Simpson, J. Mendez, K. Zimmermann, P. Otto, G. Vidugiris, Zhu, A. Darzins, D. H. Klaubert, R. F. Bulleit, K. V. Wood, *ACS Chem. Biol.* **2008**, *3*, 373.
- [165] S. N. Peterson, K. Kwon, *Current. Chem. Genomics* **2012**, *6*, 8.
- [166] T. K. Neklesa, H. S. Tae, A. R. Schneekloth, M. J. Stulberg, *Nat. Chem.* **2011**, *7*, 538.
- [167] D. S. Liu, W. S. Phipps, K. H. Loh, M. Howarth, A. Y. Ting, *ACS Nano* **2012**, *6*, 11080.
- [168] H. Ban, M. Nagano, J. Gavriluyuk, W. Hakamata, T. Inokuma, C. F. Barbas, *Bioconjugate Chem.* **2013**, *24*, 520.
- [169] J. M. Silva, M. Videira, R. Gaspar, V. Prêt, H. F. Florindo, *J. Controlled Release* **2013**, *168*, 179.
- [170] Y. Krishnamachari, S. M. Geary, C. D. Lemke, A. K. Salem, *Pharm. Res.* **2011**, *28*, 215.
- [171] A. L. Parry, N. A. Clemson, J. Ellis, S. R. Bernhard, B. G. Davis, N. R. Cameron, *J. Am. Chem. Soc.* **2013**, *135*, 9362.
- [172] R. P. Brinãs, A. Sundgren, P. Sahoo, S. Morey, K. Rittenhouse-Olson, G. E. Wilding, W. Deng, J. J. Barchi, *Bioconjugate Chem.* **2012**, *23*, 1513.
- [173] K. Nikura, T. Matsunaga, T. Suzuki, S. Kobayashi, H. Yamaguchi, Y. Orba, A. Kawaguchi, H. Hasegawa, K. Kajino, T. Ninomiya, K. Ijjiro, H. Sawa, *ACS Nano* **2013**, *7*, 3926.
- [174] F. Ding, S. Radic, R. Chen, P. Y. Chen, N. K. Geitner, J. M. Brown, P. C. Ke, *Nanoscale* **2013**, *5*, 9162.
- [175] Jie Feng, J. M. Slocik, M. Sarikaya, R. R. Naik, B. L. Farmer, H. Heinz, *Small* **2012**, *8*, 1049.

SCIENTIFIC REPORTS



OPEN

Digital Detection of Exosomes by Interferometric Imaging

George G. Daaboul^{1,*}, Paola Gagni^{2,*}, Luisa Benussi³, Paolo Bettotti⁴, Miriam Ciani³, Marina Cretich², David S. Freedman¹, Roberta Ghidoni³, Ayca Yalcin Ozkumur⁵, Chiara Piotta⁴, Davide Prospero⁶, Benedetta Santini⁶, M. Selim Ünlü⁷ & Marcella Chiari²

Received: 20 June 2016

Accepted: 26 October 2016

Published: 17 November 2016

Exosomes, which are membranous nanovesicles, are actively released by cells and have been attributed to roles in cell-cell communication, cancer metastasis, and early disease diagnostics. The small size (30–100 nm) along with low refractive index contrast of exosomes makes direct characterization and phenotypical classification very difficult. In this work we present a method based on Single Particle Interferometric Reflectance Imaging Sensor (SP-IRIS) that allows multiplexed phenotyping and digital counting of various populations of individual exosomes (>50 nm) captured on a microarray-based solid phase chip. We demonstrate these characterization concepts using purified exosomes from a HEK 293 cell culture. As a demonstration of clinical utility, we characterize exosomes directly from human cerebrospinal fluid (hCSF). Our interferometric imaging method could capture, from a very small hCSF volume (20 µL), nanoparticles that have a size compatible with exosomes, using antibodies directed against tetraspanins. With this unprecedented capability, we foresee revolutionary implications in the clinical field with improvements in diagnosis and stratification of patients affected by different disorders.

Exosomes are a class of membranous extracellular vesicles (EV) that originate from inward budding of the endosomal compartment within a cell¹. The interest of scientists and physicians in EVs has grown dramatically over the past decade in response to the discovery that these vesicles transfer mRNA, miRNA, and protein from the cell of origin to recipient cells², serving a new route for cell-to-cell communication. Presence of exosomes in circulating bodily fluids, including blood³, urine⁴ and saliva⁵, suggests that minimally-invasive diagnosis of a number of diseases can be achieved through detection of these vesicles^{6–9}. In particular, EVs are considered valuable for liquid biopsies in cancer diagnosis since they carry molecular and proteomic cargo from their tumour cell of origin¹⁰. In human CSF, EVs are rich reservoirs of biomarkers for neurological disorders and there is increasing evidence that deregulation of EVs secretion play a pathological role in neurodegenerative diseases such as Alzheimer's disease (AD) and Frontotemporal dementia (FTD)^{11–15}.

The limited utility of exosomes in diagnostics is mainly due to difficulties in specifically characterizing them using a scalable phenotyping method. Exosomes have diameters in the range from 30–100 nanometers, i.e., which is too small to be accurately sized by conventional methods such as optical microscopy and flow cytometry (FC) without labels. Alternatively, immunocapturing of exosomes on antibody coated beads¹⁶ facilitates analysis by FC. However, such indirect detection is not quantitative and measurements are further complicated due to aggregation of exosome-bead complexes. A number of references report on the direct visualization of exosomes with electron microscopy¹⁷ but this technique is not suitable for large scale application due to its complexity and low-throughput. Western blot is currently used to verify that isolated vesicles are indeed exosomes through characterization of exosomal proteins. However, even the analysis for a single antigen demands large amounts of purified exosomal proteins isolated by extensive and time-consuming (hours to days) procedures. Such requirements limit the throughput and substantially increase the cost for multi-parameter measurements.

¹Nexgen Arrays, Boston, Massachusetts 02215, USA. ²Consiglio Nazionale delle Ricerche, Istituto di Chimica del Riconoscimento Molecolare (ICRM), Milano, Italy. ³Molecular Markers Laboratory, IRCCS Istituto Centro San Giovanni di Dio Fatebenefratelli, Brescia, Italy. ⁴Nanoscience Laboratory, Department of Physics, University of Trento, Povo (TN) Italy. ⁵Department of Electrical and Electronics Engineering, Bahçeşehir University, Istanbul, Turkey. ⁶Dipartimento di Biotecnologie e Bioscienze, Università di Milano-Bicocca, Milano, Italy. ⁷Department of Electrical and Computer Engineering, Boston University, Boston, Massachusetts 02215, USA. *These authors contributed equally to this work. Correspondence and requests for materials should be addressed to G.G.D. (email: gdaaboul@nexgenarrays.com) or M. Chiari (email: marcella.chiari@icrm.cnr.it)

The efforts in development of new tools for analysis of exosomes have led to a number of innovative technologies with potential clinical applications. Two recently commercialized nanoparticle detection technologies are typically utilized in characterization of exosomes: Nanoparticle Tracking Analysis (NTA) (NanoSight) and conductivity measurements across a porous membrane (qNano by Izon Science Ltd). NTA is the most commonly used method for determining size distribution and concentration of isolated exosomes in suspension where particle size is calculated based on Brownian motion¹⁸. In order to overcome the limitations of conventional NTA to determine the cell of origin and to distinguish between different vesicles types (i.e. EVs, lipids and protein aggregates), a short wavelength (405-nm blue-violet) laser and a high sensitivity camera to detect fluorescent particles¹⁹ are incorporated to the optical system. In this modality, combining NTA with fluorescence measurements, only exosomes labeled with specific fluorescent antibodies are detected, thus allowing their phenotype to be determined. Despite this improvement, challenges persist due to the difficulty in multiplexing and large volume requirements. TRPS measures the size and concentration of a nanoparticle suspension through conductivity changes through a porous membrane²⁰, but no information is provided on the nature of the protein expressed on the surface. Both techniques provide valuable information but they cannot identify and simultaneously phenotype exosomes, which is an important limitation, as the actual presence of certain surface proteins would allow the identification of exosomes originating from different cell sources.

There are several emerging new techniques for label-free detection of exosomes. Recently, a real-time, label-free sensing of single exosomes in serum using antibody functionalized micro-toroid optical resonators has been introduced²¹. Although highly sensitive, such high-Q optical resonators have significant challenges of identifying size of captured particles in a complex solution and difficulty of multiplexing.

Another real-time, label-free exosome assay based on surface plasmon resonance (SPR) has been demonstrated²². The plasmonic sensor comprises of an array of periodic nanoholes patterned in a metal film. Binding to the sensor surface is monitored through change in optical transmission due to change of refractive index at the sensor surface. The technology offers high sensitivity and enables continuous and real-time monitoring of molecular binding. However, this sensor technology does not provide any information about the size of the captured target to indicate if the signal is due to capture of intact vesicles or soluble proteins.

The study presented in this paper demonstrates a label-free detection platform for routine analysis of exosomes using antibody-based exosome arrays and interferometric digital detection of individual nanoparticles (NPs). The technique enables the fractionation of populations of exosomes that exhibit specific surface proteins allowing better understanding of EV heterogeneity. By comparing the phenotype and size of EVs present in body fluids of healthy donors and patients with different diseases, the platform is expected to accelerate the translation of exosome studies from research into clinics. The technology proposed in this article, based on interferometric imaging, can detect individual nanovesicles on a capture surface in a microarray format and, potentially, assess their size. The principle of Single Particle Interferometric Reflectance Imaging Sensor (SP-IRIS) technology is the enhanced contrast in the scattering signal from nanoparticles that is generated using a layered substrate. The technology has so far mostly been applied to the simultaneous detection of multiple viruses in serum or whole blood²³. By employing affinity-based capture, size discrimination, and a digital detection scheme to count single virus particles, a robust and sensitive virus/nanoparticle sensing assay was established for targets in complex samples. The SP-IRIS platform has been previously shown to count and size individual viruses from complex solutions at low concentrations down to 5×10^3 PFU/mL in serum²³. In this work, we demonstrate that the SP-IRIS platform can count and phenotype multiple types of exosomes from a single sample. The contrast of the detected nanovesicles in the SP-IRIS image can be used to estimate the relative size of the nanovesicles, while their spatial location in the array provides information on the exosomes' phenotype. The novelty of this work is that a single instrument provides the size and multi-phenotype information from the same exosome preparation.

Materials and Methods

Materials. Phosphate buffered saline (PBS), Trizma base (Tris), HCl, ethanolamine, ammonium sulphate, and Tween-20 were purchased from Sigma-Aldrich (St. Louis, MO, USA). Copoly(DMA-NAS-MAPS) (MCP-2) was purchased from Lucidant Polymers Inc. (Sunnivale, CA, USA). SP-IRIS printed microarrays were provided by nanoView Diagnostics Inc.

Monoclonal antibodies against the human tetraspanins CD63, CD81, CD9, and CD171 were purchased from Nexgenarrays LLC (Boston, MA). Pure whole molecules IgG from Goat (R&D Biosystems) or Rabbit (Jackson ImmunoResearch, West Grove, PA, USA) were used as negative controls.

Artificial cerebrospinal fluid was composed of NaCl (120 mM), NaHCO₃ (25 mM), KCl (2.5 mM), NaH₂PO₄ (1 mM), CaCl₂ (2.5), MgCl₂ · 6 H₂O (1 mM), Glucose (20 mM) and Human Serum Albumin (0.4 mg/mL), all purchased from Sigma-Aldrich (St. Louis, MO, USA).

Exosome isolation from human biological samples. HEK 293 (Human Embryonic Kidney 293) cell line were cultured in Minimum Essential Medium (MEM, Life Technologies) supplemented with 10% Fetal Bovine Serum (EuroClone S.p.A.), 1% Penicillin/Streptomycin solution (Carlo Erba Reagents), 2 mM L-glutamine (Carlo Erba Reagents), 1% MEM non-essential Amino Acids solution (Carlo Erba Reagents), at 37 °C in 5% CO₂/95% air. Cells were grown to complete confluence and incubated in serum-free medium for 72 h. Conditioned media were pooled and centrifuged to obtain exosomes according to a standard protocol²⁴. Briefly, conditioned media were collected and spun at $300 \times g$ for 10 min three times. The supernatants were then sequentially centrifuged at $1200 \times g$ for 20 min and again at $10,000 \times g$ for 30 min followed by ultracentrifugation at $110,000 \times g$ for 60 min (T-8100 rotor) (Sorvall). All centrifugations were performed at 4 °C. The $110,000 \times g$ pellet was then resuspended in PBS (5 μ L per Petri 100 mm dish) and then serially diluted for NTA and SP-IRIS analyses.

Human cerebrospinal fluid (hCSF) samples were obtained from patients affected by neuropsychiatric disorders, selected from the Fatebenefratelli Biobank. All experiments were performed in accordance with the rules of the local ethical committee of Fatebenefratelli Hospital (Brescia Italy) that approved the study (Prot. N. 2/92/p/rm; Prot. N. 52/2014; Prot. N. 44/2016).

Informed consent was obtained from all subjects. For Western blot analysis exosomes were isolated from 1.8 mL hCSF by serial centrifugation as described above; for further characterization, the $110,000 \times g$ pellet obtained from 12 mL of hCSF was loaded into a continuous 0.25–2 M sucrose gradient and after 16 h of centrifugation at $200,000 \times g$ (TH-641 rotor) (Sorvall), fractions were collected from the top of the gradient, diluted with PBS and spun at $110,000 \times g$ for 70 min. All centrifugations were performed at 4 °C. The pelleted fractions were analyzed by Western Blot using the TSG101 monoclonal antibody (4A10) (Abcam), the Flotillin-2/ESA antibody (BD Biosciences), the cystatin C polyclonal antibody (Upstate Biotechnology), and monoclonal calnexin antibody (Transduction Laboratories).

Nanoparticle Tracking Analysis (NTA). Nano-Sight LM10 instrument (Malvern, Worcestershire, UK) was used to analyze suspensions containing vesicles. The diluted samples were illuminated by a monochromatic laser beam at 532 nm to register a 60 second video taken with a mean frame rate of 30 frames/s. The NTA software (version 3.0, NanoSight) was used to analyze EVs samples, optimized to first identify and then track each particle on a frame-by-frame basis, and its Brownian movement is tracked and measured from frame to frame. Particle size was determined applying the two-dimensional Stokes–Einstein equation based on the velocity of particle movement. From each video, the mean, mode, and median EVs size was used to calculate samples concentration expressed in nanoparticles/mL.

Coating of microarray silicon chips with copoly-(DMA-NAS-MAPS). Silicon chips were coated according to the protocol described by M. Cretich *et al.*²⁵. Briefly, silicon chips were immersed in a copoly-(DMA-NAS-MAPS)²⁶ solution (1% w/v in 0.9 M $(\text{NH}_4)_2\text{SO}_4$) for 30 min. The chips were then rinsed with water, dried under nitrogen and cured for 15 min under vacuum at 80 °C.

Brief description of the SP-IRIS platform. SP-IRIS measurements were carried out using a NVDX10 reader (Nexgenarrays LLC, Boston, MA). The reader automatically acquires interferometric images of the microarray. Nanoparticles bound to the surface of the sensor appear as bright diffraction limited spots that are quantified using the NVDX10 analysis software. NVDX10 software counts nanoparticles captured on the antibody spots within a user defined particle contrast window. For exosome analysis the size window was selected as 1–20% to include particle sizes from 50–200 nm.

Digital detection of exosomes either from HEK cell line and hCSF using SP-IRIS. Capture antibodies against human CD63, CD81, CD9, CD171 together with negative controls IgG (Goat or Rabbit, pure whole molecules) were arrayed on copoly-(DMA-NAS-MAPS)-coated SP-IRIS patterned silicon chips, with 100 nm oxide layer thickness, using a SciFlexArrayer S5 spotter from Scienion (Berlin, Germany). Antibodies were printed at 1–2 mg/mL in 4 replicates, using PBS as printing buffer; the volume of spotted drops was 265 pL. Printed chips were placed in a humid chamber and incubated overnight at room temperature. Then they were blocked with 50 mM ethanolamine solution in 1 M TRIS/HCl pH 9, for 1 h, washed with pure water and dried under a nitrogen stream. Antibody arrays were first characterized by quantifying the immobilization density of the antibody probes using label-free film thickness measurement using IRIS²⁷. IRIS images were taken and analyzed by Nexgenarrays LLC (Boston, MA) QC10 software. The QC software reports the probe density for the immobilized antibodies on the array. According to NanoSight quantifications, vesicles standard preparations were diluted in PBS to a concentration of 6.75×10^6 and 0 particles/mL and then 20 μL of each sample was incubated overnight in static conditions on printed chips. Similarly, 20 μL of hCSF was incubated overnight at room temperature without any dilution. After incubation, chips were washed on a shaker with PBST (PBS with 0.05% Tween-20), PBS and pure water, rinsed in pure water and dried. Label-free SP-IRIS post-incubation scans were acquired and compared to previous corresponding detections using NVDX10 analysis software. The effective vesicle binding to the capture antibodies was obtained subtracting the signals measured after and before sample incubation. Net values from four spot replicates were averaged. Statistical analysis was performed with GraphPad Prism software.

SEM analysis of SP-IRIS substrates incubated with exosomes. For SEM imaging of captured exosomes the chips were fixed and stained after regular washing procedure but before final drying step. First, the exosomes were fixed with 0.1% glutaraldehyde in PBS for 15 minutes, then rinsed in Millipore water and dried. The chips were then stained in 1% osmium tetroxide in PBS for 30 minutes, then washed three times in Millipore water and dried under pure nitrogen stream. The stained chips were imaged using side scatter detector on a Zeiss Supra 55vp.

AFM analysis of SP-IRIS substrates incubated with exosomes. AFM measurements were performed on an NT-MDT instrument (SMENA head) working in tapping mode, in air and using a NSG-10 tip (240 kHz resonant frequency, 11.8 N/m force constant). Images of $20 \times 20 \mu\text{m}$ were acquired at 1024 points (19.5 nm step) to assure a proper mapping of the EVs. Images acquired at 2048 points showed an increase of nanoparticle size of less than 10%. The software Nova Px 3.4.0 and Gwyddion 2.44 were used for data analysis: for each acquired image, after its planarization, a proper mask was constructed to mark particles higher than 15 nm. The instrument was calibrated with a grating of 19 ± 1 nm height, thus the height accuracy of the nanoparticles mapped in the images is approximately 1 nm.

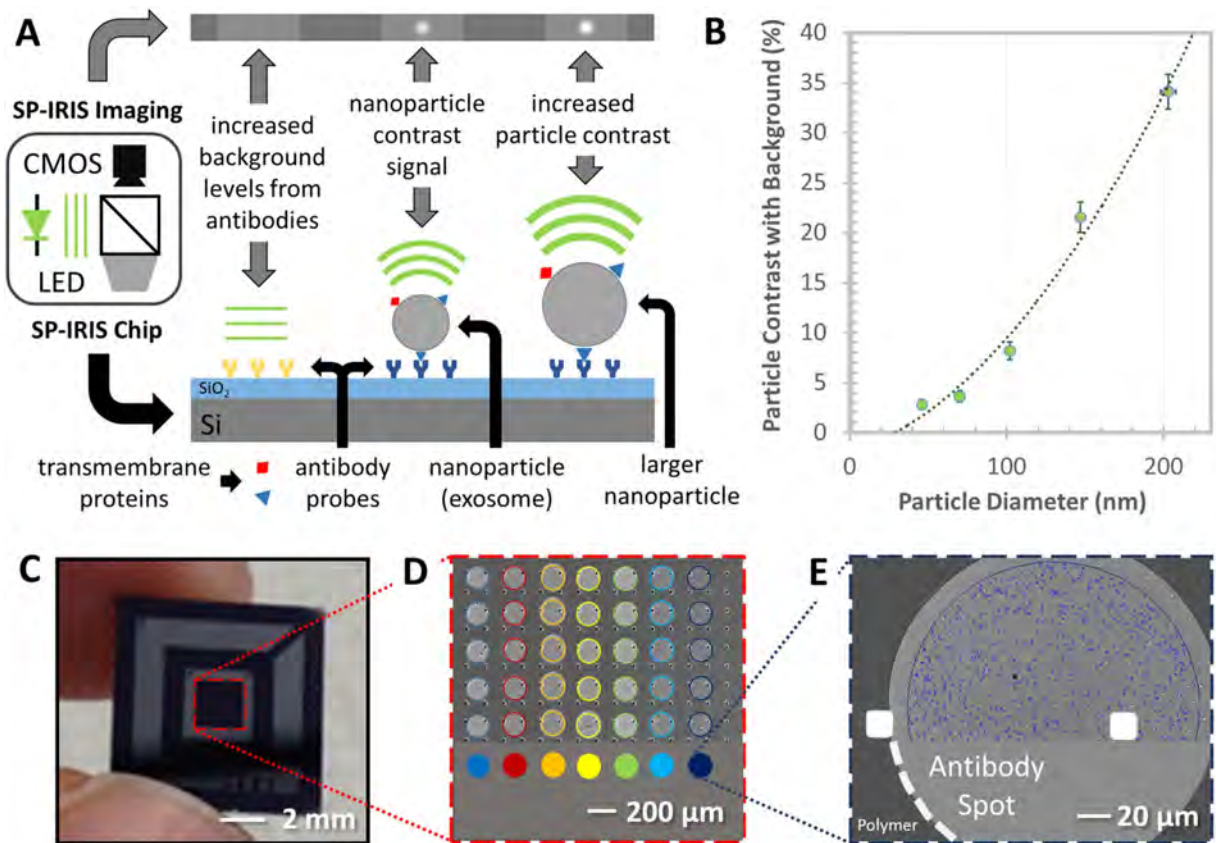


Figure 1. Schematic representation of the SP-IRIS detection process. (A) SP-IRIS detection principle, monochromatic LED light illuminates the sensor surface and the interferometrically enhanced nanoparticle scattering signature is captured on a CMOS camera. (B) Demonstrates SP-IRIS signal for polystyrene nanoparticles with a diameter from 50–200 nm which can be used to infer size of captured EVs. (C) Image of the SP-IRIS chip. (D) Low-magnification interferometric image showing microarray of immobilized capture probes. (E) SP-IRIS image of a capture probe. NVDX analysis software recognize capture spot and detects nanoparticles captured.

Results and Discussion

Exosomes detection with SP-IRIS, SEM and AFM. The lack of high-throughput methods to assess EVs' phenotype and determine their size and concentration in biological fluids inhibits progress in the validation and clinical use of this class of biomarkers. Standardization and consolidation of methods and protocols that display high feasibility, reliability and reproducibility would speed up the translation of basic scientific findings in clinically relevant applications. In this work we demonstrate the use of an innovative technological platform termed Single Particle Interferometric Reflectance Imaging Sensor (SP-IRIS) for the high-throughput characterization of exosome concentration, relative size distribution and phenotyping in biological fluids²⁸. The detection principle for SP-IRIS is based on the enhanced contrast in the scattering signal from particles captured on a silicon substrate with a thin silicon dioxide layer (Fig. 1).

To detect and size nanoparticles, IRIS shines light from visible LED source onto nanoparticles bound to the sensor surface, which consists of a silicon dioxide layer on top of a silicon substrate. Interference of light reflected from the sensor surface is modified by the presence of particles producing a distinct signal that correlates to the size of the particle (Fig. 1A,B). The detection of low-index dielectric particles with diameters of 50 nm to 200 nm is shown in Fig. 1B²⁸ demonstrating that the SP-IRIS signal correlates with the size of the particle.

In this work, EVs are captured on the surface of silicon chips through antibodies targeting exosomal markers. The chip's glass surface is similar to that of a standard microarray slide and is coated with a functional polymer, copoly-(DMA-NAS-MAPS)²⁶, on which antibodies, specific for exosome surface antigens, are spotted in a microarray format. In Fig. 1 the analysis steps are shown. The process can be divided into three phases: antibody spotting, exosome capturing and image analysis (Fig. 1C–E). To demonstrate exosome capture and digital counting, exosomes purified by ultracentrifugation from HEK 293 cell line cultures and characterized by NanoSight (Supporting Information, Figure S11) were captured on anti-CD81 capture antibody spots. Dots of different contrast were clearly distinguished from the background after the chips were incubated with the HEK 293 exosome sample. EVs that, upon incubation, became visible on the spot surface, as shown in Fig. 2, were individually counted by an automated software and surrounded by circles which correspond to an area with contrast higher than the background and represent countable unlabeled individual exosomes (Fig. 2C–F). In the analysis phase particle counts are plotted as a function of their contrast and the distribution is shown in Fig. 2E,F.

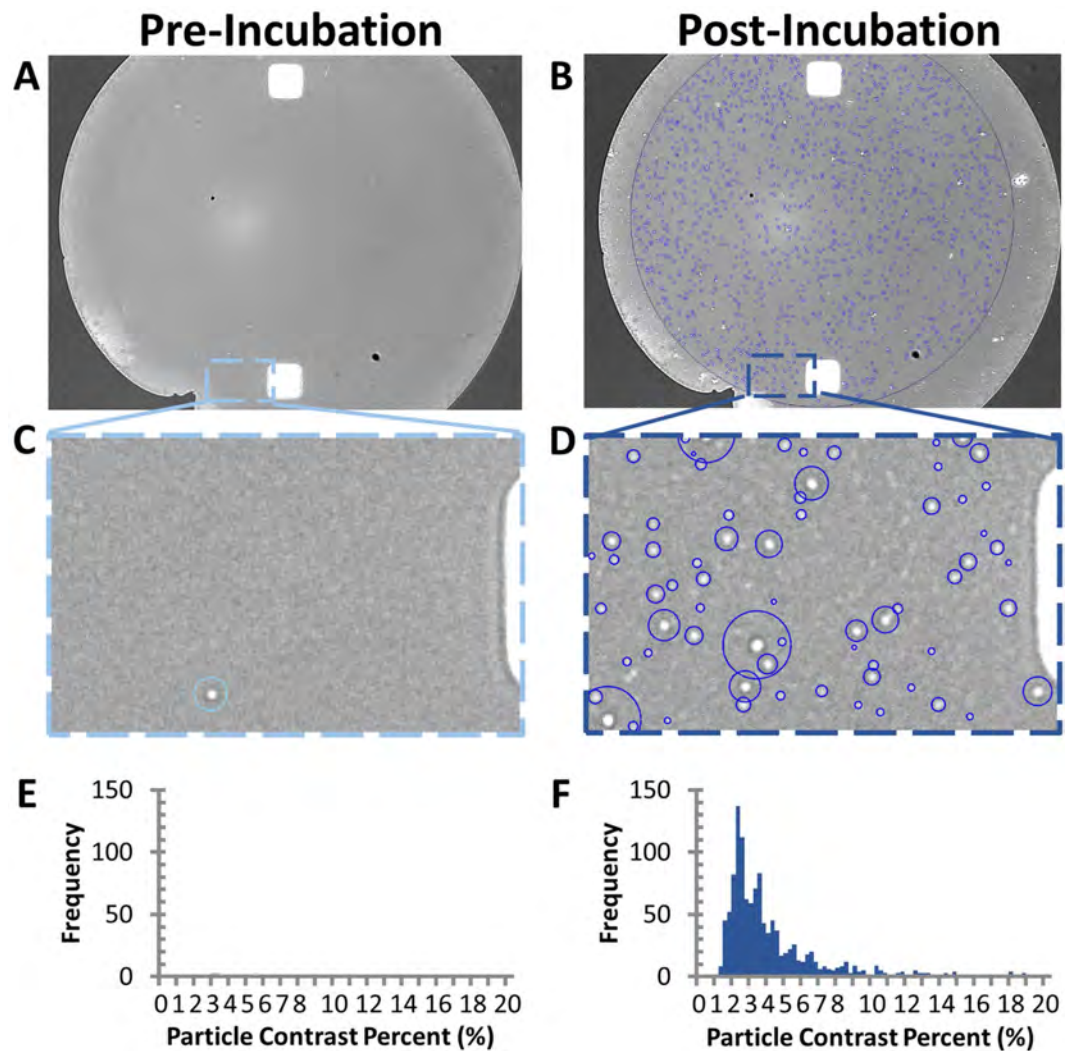


Figure 2. Exosome capture, digital counting, and relative sizing. (A,B) Anti-CD81 capture probe image acquired before and after incubation with purified HEK293 cells derived exosomes. (C,D) Zoom-box of particles detected pre- and post-incubation. (E–F) Particle contrast histogram pre- and post-incubation.

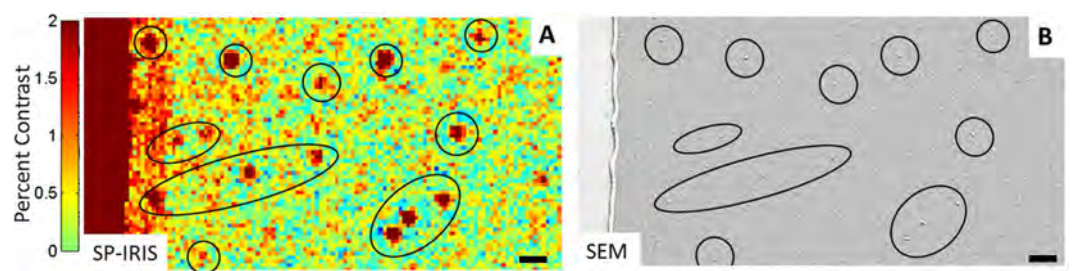


Figure 3. Nanoparticle capture validation with SEM. (A) SP-IRIS image of exosomes being captured by anti-CD81 antibody. (B) Exosomes visualized by SEM of the same field-of-view for comparison. Scale bar is 1 micron.

To demonstrate that high contrast dots correspond to exosomes, scanning electron microscopy (SEM) and atomic force microscopy (AFM) images of the chip were taken and aligned with SP-IRIS images collected in dry conditions at end-point. In Fig. 3, a portion of capture antibody spot against CD81, after incubation with exosomes purified from HEK cell line ($5.27E + 10$ particles/mL) and analyzed in SP-IRIS, is compared to the same area observed in SEM. Nanoparticles (NPs) detected with SP-IRIS (Fig. 3A) are circled and correlate with the circles on the SEM image (Fig. 3B). SP-IRIS and SEM showed perfect correspondence for particles larger than

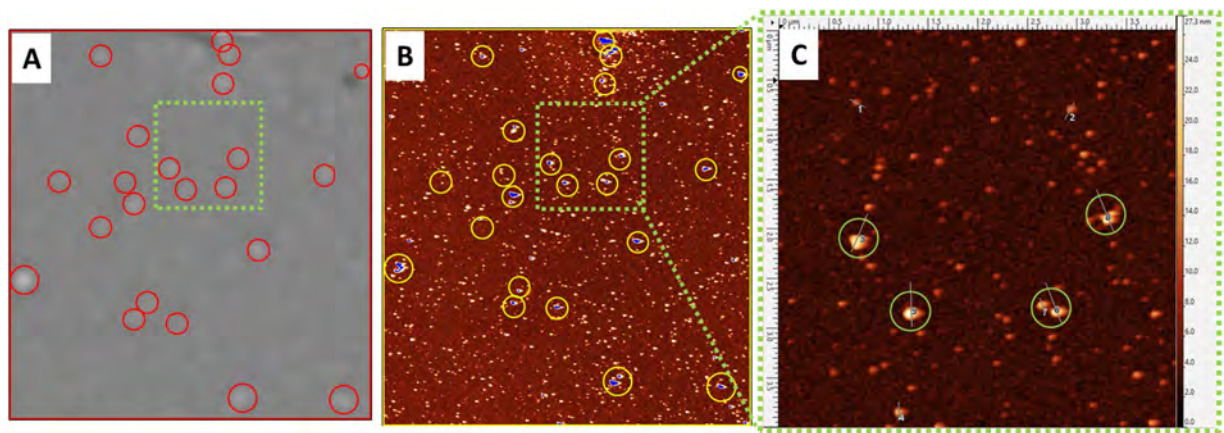


Figure 4. Exosomes purified from HEK cell line, captured with anti-CD81 antibody on silicon chip and detected by SP-IRIS (A) and AFM (B,C). (A) SP-IRIS Image of the anti-CD81 spot incubated with a suspension of exosomes ($6.75E + 10$ exosomes/mL), the red circles highlight the countable nanoparticles. (B) AFM image of the same spot area: the blue dots identify particles larger than 15 nm; the yellow circles show in image (B) perfectly match the particles detected by SP-IRIS in image (A). (C) Zoom in area of the anti-CD81 spot shown in the green frame highlights the particles larger than 15 nm in height detected by AFM and SP-IRIS. Particles smaller than 15–10 nm are detectable only with AFM as they are below SP-IRIS detection limit.

65 nm, while smaller particles are detectable only with electron microscopy, which is consistent with detection limits of both analytical techniques. The particle sizes detected by SP-IRIS ranged between 65–85 nm as measured using the SEM image. No particles were detected with either SP-IRIS or SEM on CD81 antibody spot incubated with exosome depleted HEK293 culture media (Supporting Information, Figure SI2).

In Fig. 4, a part of anti-CD81 spot is analyzed by SP-IRIS and aligned with an AFM image of the same area. SP-IRIS images were acquired before (Supporting Information, Figure SI3) and after (Fig. 4A) incubation with exosomes purified from HEK cell line. Red circles in Fig. 4A correspond to vesicles detected after sample incubation. Figure 4B shows the same spot area imaged with AFM.

In a number of publications^{29,30}, the height of exosomes measured by AFM is as low as 10–20 nm. The size of vesicles on images performed on dry chips (nanoparticles are surrounded by air) may be an underestimation of the real size due to the drying process. Particles with a height profile in excess of 15 nm in the AFM image are considered exosomes and lateral dimension was measured to be between 80–140 nm \pm 20 nm. In the image of Fig. 4B the particles higher than 15 nm, marked in blue coincide with the spots of higher contrast, surrounded by yellow circles, detected by SP-IRIS (red circles). The close up of the area in the green square, shown in Fig. 4C provides a higher resolution AFM image of the surface. SP-IRIS detects vesicles that appear to be higher than 15 nm (Supporting Information SI4), whereas smaller particles go undetected in SP-IRIS. No particles were detected on CD81 antibody spot incubated with exosome depleted HEK293 culture media (Supporting Information, Figure SI5).

SP-IRIS phenotyping of exosomes purified from HEK cell. Three capture antibodies against the exosomal biomarkers CD81, CD63 and CD9 were arrayed on the same chip together with a negative control IgG in order to evaluate the vesicle tetraspanin expression profile (Supporting Information, Figure SI6). Exosomes purified from HEK cell line and the EV depleted supernatant (SN, as negative control) were analyzed with NTA (Supporting Information, Figure SI1) to determine the particle concentration in each sample. Exosomes were diluted in PBST at 5.27 and $2.64E + 10$ particles/mL. In Fig. 5, the histogram reports the number of vesicles, per square millimeter, detected by SP-IRIS. The results indicate higher expression of CD81 tetraspanin compared to CD63 and CD9. As expected, the EVs depleted SN showed no binding to CD81 and CD9, but low binding to CD63. No significant particles were counted on control IgG spots. The relative size of the exosomes captured by CD81, CD9, and CD63 was measured using SP-IRIS through particle contrast quantification (Supporting Information, Figure SI6). Based on polystyrene nanoparticle response (Fig. 1B), the estimated mean diameter of the exosomes is 55–65 nm. Also much larger particles were observed whose diameter is comparable to that measured by AFM and SEM.

By establishing a dilution curve with exosome standards the user can determine the EVs concentration for different surface phenotype using a single microarray. The exosomes detected by the tetraspanin probes showed similar size distribution as inferred by the measured contrast distribution of the particle in the SP-IRIS image (Supporting Information, Figure SI6).

Dilution curves of exosomes purified from HEK cell line and assay limit of detection. Exosomes purified from HEK cell line and EV depleted supernatant (SN, negative control) were characterized by NTA (Supporting Information, Figure SI1) in order to evaluate the particle content in each sample. Several dilutions ranging from $6.8E + 10$ to $9E + 09$ particles/mL were incubated on silicon chips where capture antibodies against CD81 and CD63 as well as Rabbit IgG (R IgG, as negative control) were arrayed. As NTA was unable to detect any particle in the SN, this sample was used as control.

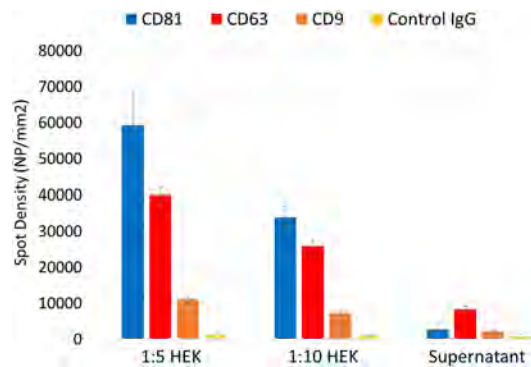


Figure 5. Exosome Phenotyping. Exosomes, isolated from HEK fibroblast cells and EV depleted supernatant, captured with antibodies against CD81, CD63, CD9 and IgG negative control and detected by SP-IRIS.

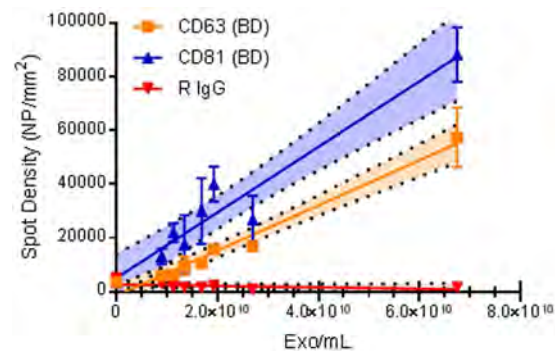


Figure 6. Dilution curve of exosomes purified from HEK cell line and detected with SP-IRIS. A good correlation can be observed for both capture antibodies CD63 (yellow line, R^2 0.97) and CD81 (blue line, R^2 0.93); no particles were detected on the negative control R IgG (red line). The bright area around the regression line corresponds to the 95% confidence interval. Based on line equations, limits of detection (LOD) were calculated, resulting in $5.07E + 09$ particles/mL for CD63 antibody and $3.94E + 09$ particles/mL for CD81 antibody.

Figure 6 shows the dose-response curves for particles counted on each antibody by SP-IRIS. The regression area around each line corresponds to 95% confidence interval of the data. As expected, no particles were detected on the negative control R IgG. A linear correlation was observed between exosome concentration and particle counts with excellent correlation coefficients (R^2) for both capture antibodies: CD81 (0.93) and CD63 (0.97). By using the equations of the extrapolated lines, detection limits were calculated for both tetraspanins: $3.94E + 09$ and $5.07E + 09$ particles/mL, respectively for CD81 and CD63.

Detection limit comparison between SP-IRIS target specific capture and NTA warrants further investigation. NTA measures non-specifically all particles in a solution, while SP-IRIS is only measuring the subpopulation based on the capture antibody target on the sensor's surface. It has been reported in the literature that exosome preparations by pelleting through ultracentrifugation contain a heterogeneous population of exosomes with different proteomic and molecular composition³¹. Further experiments are required using exosome standard with known surface marker composition to allow direct comparison of analytical sensitivity between NTA and SP-IRIS.

SP-IRIS detection and quantification of exosomes in human cerebrospinal fluid (hCSF). As exosomes are vesicles released by every kind of cell, they have been found in several human biological fluids, such as urine, saliva, blood as well as cerebrospinal fluid (CSF)³². Determining the concentration and size of exosomes in human CSF (hCSF) is not trivial, because the available sample volume is usually too small to allow analysis either with NTA or ELISA. In this work, hCSF has been used to demonstrate the potential of clinical utility of the technique. A conventional way to characterize exosomes in hCSF requires serial centrifugations in a density gradient followed by a characterization by Western blot. We first characterized exosomes in hCSF by a conventional approach and the results are shown in Fig. 7A,B. The exosomal proteins TSG101 and flotillin were present in the exosomal fractions and not in CSF depleted of exosomes (Neat CSF) while cystatin C (CysC), a soluble protein which is also secreted in association with exosomes¹¹, was present in both fractions. Conversely, calnexin, an endoplasmic reticulum residential protein, was absent from both fractions indicating the absence of cell fragments contamination (Fig. 7A). Furthermore TSG101 was used as a marker to identify the fractions containing exosomes in a sucrose gradient. The results of Fig. 7B confirm that the 1.13 and 1.14 g/mL sucrose fractions are enriched in exosomes.

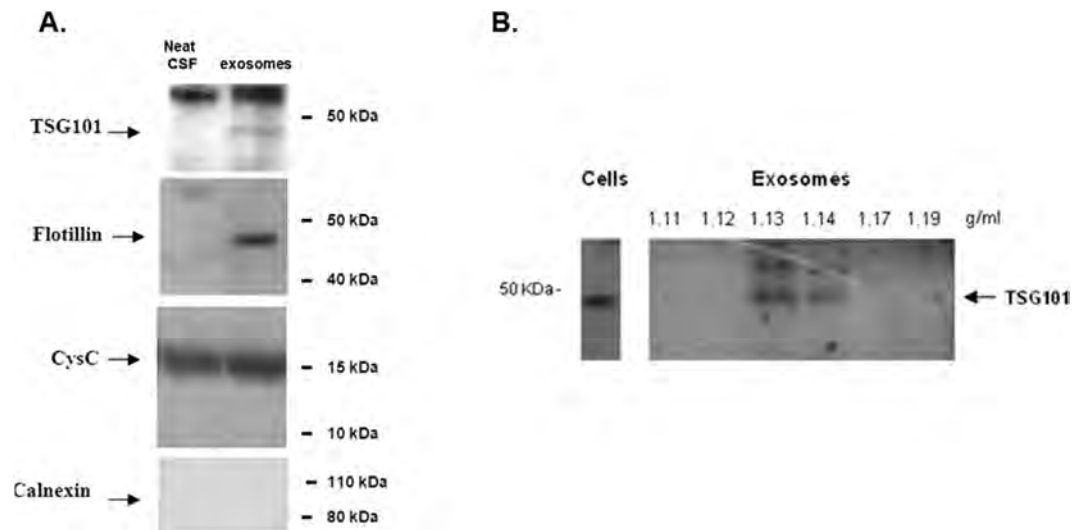


Figure 7. (A) Western blot analysis of exosomes isolated from 1.8 ml of hCSF and neat hCSF: the exosomal markers TSG101 and flotillin marked the exosomes fraction and not neat CSF, cystatin C marked both fractions and calnexin was not detected. (B) Sucrose gradient fractions of exosomal preparations from hCSF were immunoblotted with the TSG101 monoclonal antibody. TSG101 marked the exosomes-positive fractions (corresponding to 1.13 and 1.14 g/mL sucrose). HEK cells lysate was used as positive control. Western blot gels have been cropped to show only the relevant protein bands. Complete figures can be found as Supplementary, Figure SI 7.

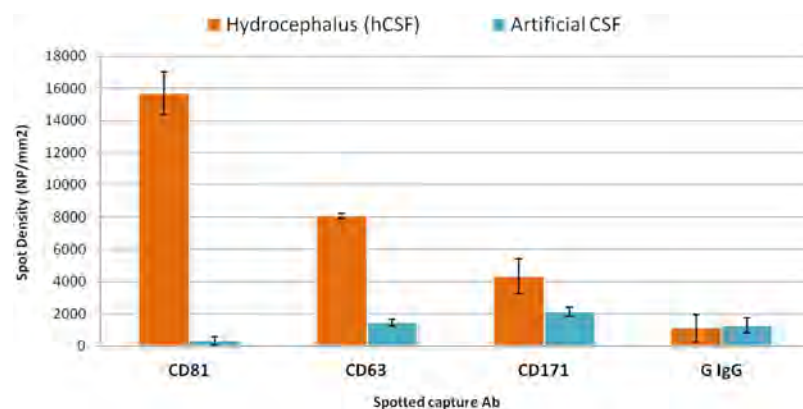


Figure 8. SP-IRIS label-free assay on human hydrocephalus CSF sample and artificial CSF. The expression of the typical exosomal biomarkers CD81 CD63 as well as the neural adhesion protein CD171 is significantly different than in the artificial CSF, negative control. An additional negative control, a non correlated IgG, shows a low level of non-specific binding. Each multiplexed chip was run in duplicate independent replicate tests.

While the analysis reported above, required 1.8 mL of hCSF, only 20 μ L of sample were required by SP-IRIS. The 20 μ L of hCSF were incubated over-night, without any dilution, on chips multiplexed with antibodies against tetraspanins (CD81 and CD63) as exosome markers and CD171, a cell adhesion molecule highly expressed by neuronal cells commonly used to capture exosomes of neural sources from blood³³, together with a control IgG antibody. As negative control, an artificial CSF was used. SP-IRIS images after hCSF incubation were compared with pre-scan acquisitions and the data analyzed by NVDX10 Analysis Software. Figure 8 reports the results of the SP-IRIS label-free assay on hCSF. Signals on CD81 and CD63 are different, indicating that not all tetraspanins are expressed equally. Also CD171 showed higher binding in hCSF than negative control sample.

Considering the average particle densities on CD81 and using the calibration curves previously obtained for each capture antibody (Fig. 6), an average concentration of about $2E + 10$ particles/mL in hCSF was extrapolated.

Conclusions

The characterization and quantification of circulating as well as cell culture-derived exosomes based on expression of specific exosomal biomarkers (e.g. tetraspanins, annexins and heat shock proteins) is currently performed by running size and concentration measurements on vesicles and immunoproteomic analyses in parallel and then correlating the results. Size and concentration measurements are performed with Electron Microscopy,

Nanoparticle Tracking Analysis (NTA) (NanoSight) or qNano (Izon Science Ltd). However, these techniques can only be used to characterize pure EVs as they do not discriminate nanoparticles of different origin, for instance exosomes from protein aggregates or lipids of the same size. Even though they can objectively define the EVs size range and concentration, they are restricted in their ability to simultaneously phenotype them. Therefore, phenotyping is done in parallel using immunoproteomic techniques like immunoblotting or by a novel, high resolution, flow cytometric analysis where exosomes are captured on antibody-coated latex beads¹⁶. This latter type of analysis allows the simultaneous evaluation of multiple parameters on single exosomes by a multicolor labeling strategy. However, conventional flow cytometry and Western Blotting demand large amounts of proteins isolated by extensive and time-consuming standard isolation procedures.

Therefore, direct counting, sizing and phenotyping of EVs will streamline both analysis and characterization. SP-IRIS platform can perform phenotyping and, potentially, sizing at the single exosome level without the need to correlate two separate measurements, which could be inaccurate, especially when done on non-purified samples because exosomal marker targets could be in soluble form not associated with nanoparticles. SP-IRIS can enumerate, estimate particle size, and phenotype exosomes from purified samples from cell culture, or directly from just 20 μ L of a clinical sample such as hCSF. A detection limit of $3.94E + 09$ particles/mL was achieved for purified nanoparticles from HEK 293 cell lines, as quantified using NTA. Exosome quantification by NTA is non-specific and therefore concentration of nanoparticles measured is an overestimate of the exosome concentration. Therefore, further experiments need to be done to understand the detection limits differences. In addition, we demonstrated that SP-IRIS can potentially phenotype exosomes directly from hCSF, employing a very small sample volume.

References

1. Beaudoin, A. R. & Grondin, G. Shedding of vesicular material from the cell surface of eukaryotic cells: different cellular phenomena. *Biochim. Biophys. Acta - Rev. Biomembr.* **1071**, 203–219 (1991).
2. Zhang, J. *et al.* Exosome and exosomal microRNA: Trafficking, sorting, and function. *Genomics, Proteomics and Bioinformatics* **13**, 17–24 (2015).
3. Orozco, A. F. & Lewis, D. E. Flow cytometric analysis of circulating microparticles in plasma. *J. Int. Soc. Adv. Cytom.* **77**, 502–514 (2010).
4. Gonzales, P. A. *et al.* Large-scale proteomics and phosphoproteomics of urinary exosomes. *J. Am. Soc. Nephrol.* **20**, 363–379 (2009).
5. Sharma, S., Gillespie, B. M., Palanisamy, V. & Gimzewski, J. K. Quantitative nanostructural and single-molecule force spectroscopy biomolecular analysis of human-saliva-derived exosomes. *Langmuir* **27**, 14394–14400 (2011).
6. Skog, J. *et al.* Glioblastoma microvesicles transport RNA and proteins that promote tumour growth and provide diagnostic biomarkers. *Nat. Cell Biol.* **10**, 1470–1476 (2008).
7. Lv, L.-L. *et al.* MicroRNA-29c in urinary exosome/microvesicle as a biomarker of renal fibrosis. *Am. J. Physiol. Renal Physiol.* **305**, F1220–F1227 (2013).
8. Alvarez, S. *et al.* Urinary exosomes as a source of kidney dysfunction biomarker in renal transplantation. *Transplant. Proc.* **45**, 3719–3723 (2013).
9. Duijvesz, D., Luiders, T., Bangma, C. H. & Jenster, G. Exosomes as biomarker treasure chests for prostate cancer. *Eur. Urol.* **59**, 823–831 (2011).
10. Brock, G., Castellanos-Rizaldos, E., Hu, L., Cotichia, C. & Skog, J. Liquid biopsy for cancer screening, patient stratification and monitoring. *Transl. Cancer Res.* **4**, 280–290 (2015).
11. Ghidoni, R., Paterlini, A. & Benussi, L. Circulating progranulin as a biomarker for neurodegenerative diseases. *Am. J. Neurodegener. Dis.* **1**, 180–190 (2012).
12. Joshi, R. S., Tanpure, R. S., Singh, R. K., Gupta, V. S. & Giri, A. P. Resistance through inhibition: ectopic expression of serine protease inhibitor offers stress tolerance via delayed senescence in yeast cell. *Biochem. Biophys. Res. Commun.* **452**, 361–368 (2014).
13. Joshi, P., Benussi, L., Furlan, R., Ghidoni, R. & Verderio, C. Extracellular vesicles in Alzheimer's disease: friends or foes? Focus on abeta-vesicle interaction. *Int. J. Mol. Sci.* **16**, 4800–4813 (2015).
14. Rajendran, L. *et al.* Emerging Roles of Extracellular Vesicles in the Nervous System. *J. Neurosci.* **34**, 15482–15489 (2014).
15. Benussi, L. *et al.* Loss of exosomes in progranulin-associated frontotemporal dementia. *Neurobiol. Aging* **40**, 41–49 (2016).
16. Lässer, C., Eldh, M. & Lötvall, J. Isolation and characterization of RNA-containing exosomes. *J. Vis. Exp.* e3037, doi: 10.3791/3037 (2012).
17. Raposo, G. *et al.* B lymphocytes secrete antigen-presenting vesicles. *J. Exp. Med.* **183**, 1161–1172 (1996).
18. Filipe, V., Have, A. & Jiskoot, W. Critical Evaluation of Nanoparticle Tracking Analysis (NTA) by NanoSight for the Measurement of Nanoparticles and Protein Aggregates. *Pharm. Research* **27**, 796–810 (2010).
19. Dragovic, R. A. *et al.* Sizing and phenotyping of cellular vesicles using Nanoparticle Tracking Analysis. *Nanomedicine* **7**, 780–788 (2011).
20. Lane, R. E., Korbie, D., Anderson, W., Vaidyanathan, R. & Trau, M. Analysis of exosome purification methods using a model liposome system and tunable-resistive pulse sensing. *Sci. Rep.* **5**, 7639 (2015).
21. Su, J. Label-Free Single Exosome Detection Using Frequency-Locked Microtoroid Optical Resonators. *ACS Photonics* **2**, 1241–1245 (2015).
22. Im, H. *et al.* Label-free detection and molecular profiling of exosomes with a nano-plasmonic sensor. *Nat. Biotechnol.* **32**, 490–495 (2014).
23. Daaboul, G. G. *et al.* Digital sensing and sizing of vesicular stomatitis virus pseudotypes in complex media: a model for Ebola and Marburg detection. *ACS Nano* **8**, 6047–6055 (2014).
24. Théry, C., Amigorena, S., Raposo, G. & Clayton, A. Isolation and characterization of exosomes from cell culture supernatants and biological fluids. *Curr. Protoc. Cell Biol.* Chapter 3, Unit 3.22 (2006).
25. Cretich, M. *et al.* Silicon biochips for dual label-free and fluorescence detection: Application to protein microarray development. *Biosens. Bioelectron.* **26**, 3938–3943 (2011).
26. Cretich, M., Pirri, G., Damin, F., Solinas, I. & Chiari, M. A new polymeric coating for protein microarrays. *Anal. Biochem.* **332**, 67–74 (2004).
27. Daaboul, G. G. *et al.* LED-based Interferometric Reflectance Imaging Sensor for quantitative dynamic monitoring of biomolecular interactions. *Biosens. Bioelectron.* **26**, 2221–2227 (2011).
28. Yurt, A., Daaboul, G. G., Connor, J. H., Goldberg, B. B. & Selim Ünü, M. Single nanoparticle detectors for biological applications. *Nanoscale* **4**, 715 (2012).
29. Hardij, J. *et al.* Characterisation of tissue factor-bearing extracellular vesicles with AFM: comparison of air-tapping-mode AFM and liquid Peak Force AFM. *J. Extracell. Vesicles* **2** (2013).

30. Yuana, Y. *et al.* Atomic force microscopy: A novel approach to the detection of nanosized blood microparticles. *J. Thromb. Haemost.* **8**, 315–323 (2010).
31. Bobrie, A., Colombo, M., Krumeich, S., Raposo, G. & Théry, C. Diverse subpopulations of vesicles secreted by different intracellular mechanisms are present in exosome preparations obtained by differential ultracentrifugation. *J. Extracell. Vesicles* **1**, 1–11 (2012).
32. Chiasserini, D. *et al.* Proteomic analysis of cerebrospinal fluid extracellular vesicles: A comprehensive dataset. *J. Proteomics* **106**, 191–204 (2014).
33. Goetzl, E. J. *et al.* Altered lysosomal proteins in neural-derived plasma exosomes in preclinical Alzheimer disease. *Neurology* **85**, 40–47 (2015).

Acknowledgements

This work was supported by Regione Lombardia and Fondazione Cariplo through POR-FESR, project MINER (ID 46875467); Italian Ministry of Health, Ricerca Corrente. This work was partially supported by The Scientific and Technological Research Council of Turkey (grant #113E643).

Author Contributions

M. Chiari, M. Cretich, S.M.U., G.G.D. and A.Y.O. designed the study; P.G. and G.G.D. equally contributed to the obtained results; M. Ciani, R.G. and L.B. provided CSF and purified exosome samples; D.P. and B.S., made NTA measurements. G.G.D. and D.F. made SEM analysis; P.B. and C.P. conducted AFM analysis. P.G., G.G.D. and M. Chiari wrote the article; all authors reviewed the manuscript.

Additional Information

Supplementary information accompanies this paper at <http://www.nature.com/srep>

Competing financial interests: The authors declare the following competing financial interest(s): George G. Daaboul is the chief scientific officer of Nexgenarrays LLC. David Freedman is the chief executive officer of NexgenArrays LLC. All remaining contributing authors declare no competing financial interests.

How to cite this article: Daaboul, G. G. *et al.* Digital Detection of Exosomes by Interferometric Imaging. *Sci. Rep.* **6**, 37246; doi: 10.1038/srep37246 (2016).

Publisher's note: Springer Nature remains neutral with regard to jurisdictional claims in published maps and institutional affiliations.



This work is licensed under a Creative Commons Attribution 4.0 International License. The images or other third party material in this article are included in the article's Creative Commons license, unless indicated otherwise in the credit line; if the material is not included under the Creative Commons license, users will need to obtain permission from the license holder to reproduce the material. To view a copy of this license, visit <http://creativecommons.org/licenses/by/4.0/>

© The Author(s) 2016



Loss of exosomes in progranulin-associated frontotemporal dementia



Luisa Benussi^{a,1}, Miriam Ciani^{a,1}, Elisa Tonoli^a, Michela Morbin^b, Luisa Palamara^b, Diego Albani^c, Federica Fusco^c, Gianluigi Forloni^c, Michela Glionna^a, Monika Baco^a, Anna Paterlini^a, Silvia Fostinelli^a, Benedetta Santini^d, Elisabetta Galbiati^d, Paola Gagni^e, Marina Cretich^e, Giuliano Binetti^a, Fabrizio Tagliavini^b, Davide Prospero^d, Marcella Chiari^e, Roberta Ghidoni^{a,*}

^a Molecular Markers Laboratory, IRCCS Istituto Centro San Giovanni di Dio- Fatebenefratelli, Brescia, Italy

^b Division of Neuropathology and Neurology 5, Fondazione IRCCS Istituto Neurologico Carlo Besta, Milano, Italy

^c Department of Neuroscience, IRCCS - Istituto di Ricerche Farmacologiche Mario Negri, Milano, Italy

^d NanoBioLab, Dipartimento di Biotecnologie e Bioscienze, Università di Milano-Bicocca, Milano, Italy

^e Consiglio Nazionale delle Ricerche, Istituto di Chimica del Riconoscimento Molecolare, Milano, Italy

ARTICLE INFO

Article history:

Received 11 August 2015

Received in revised form 4 December 2015

Accepted 2 January 2016

Available online 7 January 2016

Keywords:

Progranulin

GRN

Null mutations

Human primary fibroblasts

Exosomes

Extracellular vesicles

ABSTRACT

Many cells of the nervous system have been shown to release exosomes, a subclass of secreted vesicles of endosomal origin capable of transferring biomolecules among cells: this transfer modality represents a novel physiological form of intercellular communication between neural cells. Herein, we demonstrated that progranulin (PGRN), a protein targeted to the classical secretory pathway, is also secreted in association with exosomes by human primary fibroblasts. Moreover, we demonstrated that null mutations in the progranulin gene (*GRN*), a major cause of frontotemporal dementia, strongly reduce the number of released exosomes and alter their composition. In vitro *GRN* silencing in SHSY-5Y cells confirmed a role of PGRN in the control of exosome release. It is believed that depletion of PGRN in the brain might cause neurodegeneration in *GRN*-associated frontotemporal dementia. We demonstrated that, along with shortage of the circulating PGRN, *GRN* null mutations alter intercellular communication. Thus, a better understanding of the role played by exosomes in *GRN*-associated neurodegeneration is crucial for the development of novel therapies for these diseases.

© 2016 Elsevier Inc. All rights reserved.

1. Introduction

Frontotemporal lobar degeneration (FTLD) is the second most common cause of dementia after Alzheimer's disease (AD) mainly affecting individuals younger than 65 years and accounts for 5%–15% of all dementias (Neary et al., 1998; Ratnavalli et al., 2002; Riedl et al., 2014). The term FTLD defines a heterogeneous group of disorders characterized by a degeneration of the frontal and anterior temporal lobes and that differs at the clinical, genetic, and pathological level (Mackenzie et al., 2014; The Lund and Manchester Groups, 1994). Genetic factors are the only cause of FTLD so far identified and up to 50% of patients have a family history of disease (Goldman et al., 2007; Rademakers et al., 2012; Sieben et al., 2012).

* Corresponding author at: Molecular Markers Laboratory, IRCCS Istituto Centro San Giovanni di Dio Fatebenefratelli, Brescia; via Pilastroni 4, 25125 Brescia, Italy. Tel.: +39 030 3501725; fax: +39 030 3533513.

E-mail address: rghidoni@fatebenefratelli.eu (R. Ghidoni).

¹ Equal contribution.

Until now, 7 disease-causing genes have been discovered (Riedl et al., 2014; van der Zee and Van Broeckhoven, 2014), including *GRN* (Baker et al., 2006; Cruts et al., 2006), which is one of the most frequent genetic determinants. In fact, in patients with familial FTLD, the *GRN* mutation frequency can be up to 26% (Benussi et al., 2009, 2010; Chen-Plotkin et al., 2011; Gijssels et al., 2008; Schlachetzki et al., 2009; Yu et al., 2010). The most common *GRN* mutations worldwide are the *GRN* p.Arg493X (c.1477C>T) (Rademakers et al., 2007), the Belgian *GRN* p.0 (c.138+1G>C) (Cruts et al., 2006; van der Zee et al., 2006), and the *GRN* p.Leu271LeufsX10 (c.813-816delCTCA), which was shown to be the most frequent mutation in Italy (Benussi et al., 2008, 2009, 2010; Bagnoli et al., 2012; Tremolizzo et al., 2009). All the known *GRN* mutations cause disease through the loss of functional progranulin protein (PGRN) or haploinsufficiency (Baker et al., 2006; Cruts et al., 2006), leading to the reduction of circulating progranulin in *GRN*-mutated subjects (Ghidoni et al., 2008a, 2012a, 2012b; Finch et al., 2009; Sleegers et al., 2009).

It has been demonstrated that some pathogenic proteins involved in neurodegenerative disorders can be released from cells in association with exosomes (Emmanouilidou et al., 2010; F evrier et al., 2004; Ghidoni et al., 2011; Gomes et al., 2007; Perez-Gonzalez et al., 2012; Rajendran et al., 2006), a specific subclass of small secreted vesicles (30–120 nm in diameter) derived from the intraluminal membranes of multivesicular bodies of the endocytic pathway (El Andaloussi et al., 2013; Vlassov et al., 2012). Exosomes are biologically active entities, important for intercellular communication and transfer of specific molecular constituents, including nucleic acids such as micro RNAs and noncoding RNAs, lipids, and proteins, from one cell to another (Rajendran et al., 2014; Raposo and Stoorvogel, 2013; Valadi et al., 2007). Herein, we analyzed PGRN protein trafficking and release in human primary fibroblasts both in physiological and pathological (i.e., presence of *GRN* null mutations) conditions. Moreover, we performed in vitro *GRN* silencing in SH-SY5Y cells to further study the effect of loss of progranulin on exosome release.

2. Methods

2.1. Human primary skin fibroblasts and SH-SY5Y cell culture and treatment

Skin fibroblasts primary cultures were selected from the tissue repository of the IRCCS Istituto Centro San Giovanni di Dio Fatebenefratelli (approved by the local ethical committee, CEIOC Prot. N. 2/92/p/rm) on the bases of their *GRN* genotypes: we cultured cells derived from 16 donors, 8 being carriers of null mutations in *GRN* gene (*GRN* mut) ($n = 5$ p. Leu271LeufsX10; $n = 1$ p. Gln341X; $n = 1$ p. Thr276SerfsX7; $n = 1$ p. c.709-3C>G carriers), 8 age- and gender-matched cognitively intact subjects (CTR) (mean age \pm standard deviation: *GRN* mut = 55.8 ± 9.6 years; CTR = 58.6 ± 4.2 years; $p = 0.4$, Student *t*-test; % of female: *GRN* mut = 62.5%; CTR = 75%; $p = 0.5$, Fisher exact test). Establishment of fibroblast cultures, growth, storage conditions, and lysis protocol for Western blot analysis are described elsewhere (Benussi et al., 2003). The different fibroblast cell cultures (600,000 cells/plate), each at the same passage number, were grown to 80% confluence and incubated in serum-free medium for 72 hours. For Western blot analyses, we loaded—for each fibroblast cell line—exosome pellets obtained from medium conditioned from 2 plates.

The study was approved by the local ethical committee (Prot. N. 52/2014).

Cells proliferation and viability were measured by the trypan blue exclusion method and MTT (3, (4,5-dimethylthiazol-2)2,5 difeniltetrazoliumbromide) assay. Briefly, fibroblasts were plated at density of 3×10^3 cells and harvested immediately after cells attachment and after 3, 5, and 7 days in vitro. An equal volume of trypan blue dye (Sigma, USA) was added to the cell suspension to a final concentration of 0.04% 5 minutes before counting; all dead trypan blue positive cells were excluded. MTT (300 μ L; 0.5 mg/mL phosphate-buffered saline [PBS]; Sigma-Aldrich, Steinheim, Germany) was added to each well of culture plate, incubated for 3 hours in a humidified atmosphere at 37 °C in 5% CO₂. Then, MTT-containing medium was removed, and the insoluble formazan blue was dissolved in 100 μ L DMSO. The absorbance of the samples was measured at 570 nm using a spectrophotometer (Bio-Tek Power Wave XS Spectrophotometer, Fisher Scientific).

SH-SY5Y cells were cultured at 37 °C, 5% CO₂ in DMEM medium (Invitrogen, Carlsbad, CA, USA) supplemented with 10% FCS (Sigma, St Louis, MO, USA), 2-mM L-glutamine (Invitrogen, Carlsbad, CA, USA) 100 UI/mL penicillin, and 100 μ g/mL streptomycin (Invitrogen, Carlsbad, CA, USA) in humidified atmosphere.

2.2. RNA interference

RNA interference setup was performed as follows: 75×10^3 SH-SY5Y cells were seeded in a 24-well plate and grown overnight. Then, commercially available pre-designed double-strand small-interfering RNA (siRNA) against PGRN mRNA sequence (Ambion, Austin, TX, USA) was added in serum-free Optimem (Invitrogen, Carlsbad, CA, USA) at 100-nM final concentration, using as vehicle SilentFect liposome formulation (BioRad Laboratories, Hercules, CA, USA). To prove specific silencing, a negative control siRNA was used (CT-), comprised of a 19-bp scrambled sequence with 3' dT overhangs that has no significant homology to any known human gene sequence (Ambion, Austin, TX, USA). Forty-eight hours after silencing, serum-free media were collected and processed for exosome isolation as described. For large-scale exosome preparation, RNA interference was scaled up and performed in at least 2 T75 plates, starting from around 6×10^6 cells/plate.

2.3. Exosome isolation from cell culture media

Conditioned media from human primary fibroblasts and SH-SY5Y cells were pooled and centrifuged to obtain exosomes according to the standard protocol (Thery et al., 2006). Briefly, conditioned media were collected and spun at $300 \times g$ for 10 minutes for 3 times. The supernatants were then sequentially centrifuged at $1200 \times g$ for 20 minutes (P2 fraction) and $10,000 \times g$ for 30 minutes (P3 fraction) followed by ultracentrifugation at $110,000 \times g$ for 60 minutes (P4 fraction) (T-8100 rotor) (Sorvall). The $110,000 \times g$ pellet was then resuspended in 12.5 μ L of RIPA lysis buffer (150-mM NaCl, 1.0% IGEPAL CA-630, 0.5% sodium deoxycholate, 0.1% SDS, and 50 mM Tris, pH 8.0) or loaded into a continuous 0.25–2 M sucrose gradient: after 16 hours of centrifugation at $200,000 \times g$ (TH-641 rotor) (Sorvall), fractions were collected from the top of the gradient, diluted with PBS, and spun at $110,000 \times g$ for 70 minutes. All centrifugations were performed at 4 °C. The pelleted fractions were then analyzed.

2.4. Western blotting

Western blot analyses were performed using the progranulin anti-PCDGF polyclonal antiserum (Invitrogen), the antitumor susceptibility gene 101 (TSG101) mouse monoclonal antibody (4A10) (Abcam-Cambridge, UK), antilyosomal-associated membrane protein (LAMP1) (Abcam) mouse monoclonal antibody (Abcam-Cambridge, UK) and anti- α -tubulin monoclonal antibody (Abcam, Cambridge, UK). Human recombinant progranulin (R&D Systems, Inc, Minneapolis, MN, USA) was produced in mouse myeloma cell lines. For the enzymatic deglycosylation of progranulin, 1- μ L (50,000 U) of peptide-N-glycosidase F (PNGase F) enzyme (New England Biolabs-Ipswich, MA, USA) was added to each sample and incubated 1 hour at 37 °C. Sample aliquots incubated without the deglycosylation enzyme were used as controls. Means of densitometric measurements, normalized on respect to the lowest densitometric signal for each experiment, were compared by Student *t*-test in normally distributed continuous variables. When normality was not confirmed, the Mann-Whitney *U* test was used. Two-tailed *p* value equal or less than 0.05 was considered statistically significant. All calculations were performed using SPSS 22.0 for Windows.

2.5. Immunoelectron Microscopy

Exosomes isolated from fibroblast culture media by differential centrifugation as described previously were suspended in 2% paraformaldehyde (Merk). Exosomes preparations were used for

electron microscopy and immunoelectron microscopy examination using a modified previously described protocol (Thery et al., 2006). Five microliter of exosome preparation was placed on 200-mesh formvar-carbon-coated nickel grids for 20 minutes at room temperature (RT), and then grids were washed in 1× PBS solution pH 7.4. For morphological examination, grids were fixed in 1% glutaraldehyde diluted in PBS for 5 minutes at RT. After 2 washings of 2 minutes each in distilled water, grids were negatively stained by oversaturated uranyl-acetate aqueous solution for 10 minutes at RT. The excess fluid was gently removed using Whatman no.1 filter paper, and grids were observed under transmission electron microscope (EM 109, ZEISS, Oberkochen, Germany). To verify the exosomal nature of vesicles and the presence of progranulin, a double immunogold labeling was performed using as primary antibodies either monoclonal 4A10 antibody (Mouse anti-TSG101, Abcam) as marker of exosomes or polyclonal antibody PCDGF (Rabbit anti-PGRN C-term, Zymed) as markers for progranulin. Immunoreaction was evidenced with the secondary antibody 6-nm gold-conjugated GAM (Goat Anti-Mouse, Aurion) and 10-nm gold-conjugated GAR (Goat Anti-Rabbit, Aurion), respectively. Briefly, grids were submerged in blocking buffer (PBS and/or bovine serum albumin [BSA] 5%) for 15 minutes at RT and then incubated with primary antibody 4A10 (1:50) and PCDGF (1:12.5) diluted in PBS and/or 1% BSA for 2 hours at RT. After 3 washings of 3 minutes each in PBS and/or 0.1% BSA, grids were incubated with appropriate secondary antibody 6-nm gold GAM or 10-nm gold GAR diluted 1:10 in 10% BSA for 30 minutes at RT. After 3 washings of 3 minutes each in PBS and/or 0.1% BSA, grids were fixed, washed, and counterstained for viewing under electron microscope as reported previously for morphological studies.

2.6. Surface-enhanced laser desorption/ionization time-of-flight mass spectrometry

Three microliter of the polyclonal anti-PCDGF (0.25 µg/µL) antiserum was incubated in a humidity chamber for 3 hours at RT to allow covalent binding to the PS20 ProteinChip Array (Bio-Rad Laboratories, Inc.). Unreacted sites were blocked with Tris-HCl 0.5 M, pH 8 in a humid chamber at RT for 30 minutes. Each spot was washed first 3 times with PBS containing 0.5% (v/v) TritonX-100 and then twice with PBS. The spots were coated with 5 µL of sample and incubated in a humid chamber at RT for 3 hours. Each spot was washed first 3 times with PBS containing 0.1% (v/v) TritonX-100, twice with PBS, and finally with deionized water. One microliter of sinapinic acid (Bio-Rad Laboratories, Inc.) was added to each spot. Mass identification was made using the ProteinChip SELDI System, Enterprise Edition (Bio-Rad Laboratories, Inc.).

2.7. Nanoparticle tracking analysis

Suspensions containing exosomes from CTR and *GRN* mutant fibroblasts as well as from SH-SY5Y treated and/or untreated (liposome only) cells were analyzed using a Nano-Sight LM10 instrument (Malvern, Worcestershire, UK). A monochromatic laser beam at 532 nm was applied to the dilute suspension of vesicles and a video of 90 seconds duration was taken with a mean frame rate of 30 frames/s. Each particle movement was analyzed by nanoparticle tracking analysis (NTA) software (version 2.2, NanoSight), which identify and track vesicles on its Brownian movement. The velocity of particle movement is used to calculate particle size by applying the 2-dimensional Stokes-Einstein equation. NTA postacquisition settings were optimized and kept constant between samples, and each video was then analyzed to give the mean, mode, and median vesicle size together with an estimate of the concentration.

2.8. Sandwich fluorescence immunoassay

Copoly(DMA-NAS-MAPS) was synthesized as described in Cretich et al. (2004). Silicon chips were coated according to the protocol described in Cretich et al. (2011). Briefly, silicon chips were immersed in a copoly(DMA-NAS-MAPS) solution (1% w/v in 0.9 M (NH₄)₂SO₄) for 30 minutes. Then, the chips were rinsed with water, dried under nitrogen, and cured for 15 minutes under vacuum at 80°C. Capture antibody against hCD63, clone H5C6, and Cy3-labeled streptavidin (as positional reference) were arrayed on copoly(DMA-NAS-MAPS)-coated silicon chips using a SciFlexArrayer S5 spotter from Scienion (Berlin, Germany). Antibodies were printed at 1 mg/mL in 64 replicates; the volume of spotted drops was 400 µL. Printed chips were placed in a humid chamber and incubated overnight at RT. Then, they were blocked with 50-mM ethanolamine solution in 1-M TRIS/HCl pH 9 for 1 hour, washed with water, and dried under a stream of nitrogen. Exosome samples (20 µL of PBS-suspension per chip) were incubated for 2 hours at RT. After incubation, chips were washed with PBS under stirring, rinsed in water, and dried under a nitrogen stream. Subsequently, all chips were incubated for 1 hour, with the biotin-labeled detection antibody against hCD63 at 1 µg/mL in incubation buffer (50-mM Tris/HCl, 150-mM NaCl, and 0.02% Tween-20). Chips were then washed with PBS for 10 minutes, rinsed with water, and incubated for 1 hour with Cy3-labelled streptavidin (SA-Cy3) at 2 µg/mL in PBS. Chips were washed with PBS and water for 10 minutes each, rinsed with water, and dried under a nitrogen stream. Fluorescence was detected by a ProScanArray scanner (PerkinElmer, Boston, MA), and silicon chips were analyzed using 70%, 80%, or 90% photomultiplier gain and laser power. The fluorescence intensities of replicate spots were averaged.

3. Results

3.1. Glycosylated progranulin is released in association with exosomes

Enzymatic deglycosylation with PNGase F (N-glycosidase) enzyme of human recombinant progranulin followed by immunoproteomic analysis, using surface-enhanced laser desorption/ionization time-of-flight mass spectrometry, showed that progranulin is N-glycosylated: after PNGase F enzyme digestion, we detected a shift in the molecular weight of progranulin from 72,861 Da to 62,898 Da that was evident also by Western blot (Fig. 1A). The full-length progranulin was also present mainly as a glycosylated form in human fibroblasts lysates from healthy control subjects: as observed using the recombinant PGRN, after PNGase F treatment of human fibroblast lysates, PGRN was detected as a band of 60 kDa, corresponding to the expected MW of the native form of the protein (Fig. 1B).

To explore if progranulin is released in association with exosomes, we isolated these vesicles from conditioned media of primary human fibroblasts from healthy donors through serial centrifugations and density gradient centrifugation. TSG101 was used as marker protein to identify exosome-containing fraction and PGRN antibody to detect if progranulin is transported by exosomes (Fig. 2A). Western blot analysis showed that exosomes are enriched in the 1.17 g/mL fraction and revealed the presence in these vesicles of progranulin (Fig. 2A). Moreover, ultracentrifuge-purified exosomes were analyzed by using Western blot assay after PNGase F treatment: exosomes contain mainly the glycosylated form of progranulin (Fig. 2B). Electron microscopy ultrastructural examination of fraction enriched in exosomes released from fibroblasts showed the presence of both single (Fig. 2C) and aggregated vesicles (Fig. 2D). Exosomes appeared as 40- to 100-nm diameter vesicles surrounded by a lipid layer with a cup-shaped morphology.

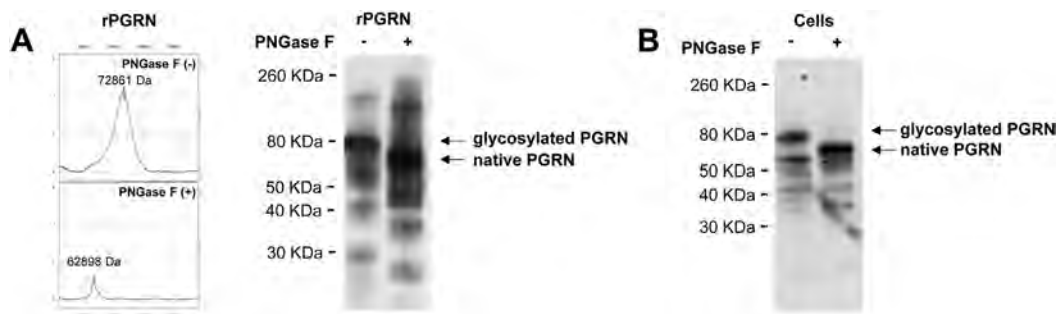


Fig. 1. Deglycosylation of human progranulin as a result of treatment with PNGase F. (A) SELDI-TOF MS on PS20 chip array and Western blot assay detected a molecular mass shift from 72,861 Da to 62,898 Da of glycosylated recombinant PGRN (rPGRN) after deglycosylation reaction. (B) After PNGase F treatment of human fibroblast lysates, PGRN was detected as a band of 60 kDa in Western blot, corresponding to the expected MW of the native form of the protein. Abbreviations: PNGase F, peptide-N-glycosidase F; SELDI-TOF MS, surface-enhanced laser desorption/ionization time-of-flight mass spectrometry.

Immunoelectron microscopy revealed that progranulin, recognized by 10-nm gold-particle 4A10 antibody (Fig. 2E, red arrows), colocalized with vesicles immunodecorated with 6-nm gold particles recognizing TSG101 antibody, a specific marker for exosomes (Fig. 2E, blue arrows).

3.2. Low progranulin levels in GRN-mutated human fibroblasts

To evaluate the impact of *GRN* gene mutations on protein expression and trafficking, we analyzed PGRN protein levels in lysates (Lys), conditioned media (CM) and exosomes (Exo) of *GRN* mut (n = 5 p. Leu271LeufsX10; n = 1 p. Gln341X; n = 1 p. Thr276SerfsX7; n = 1 p. c.709-3C>G carriers) and control subjects

(CTR) fibroblasts. PGRN levels were significantly decreased in lysates of *GRN* mut cells with respect to controls (% of PGRN level \pm SEM. CTR: 15.27 ± 3.09 ; *GRN* mut: 2.71 ± 0.65 ; $p < 0.001$ with respect to CTR; Mann-Whitney test) (Fig. 3A and C). As shown in Fig. 3A, PGRN levels were significantly decreased in CM of *GRN* MUT fibroblasts with respect to controls (% of PGRN level \pm SEM. CTR: 7.05 ± 1.66 ; *GRN* mut: 1.28 ± 0.32 ; $p < 0.001$ with respect to CTR; Mann-Whitney test) (Fig. 3C). In parallel, a strong reduction of PGRN was observed in exosomes released by *GRN* mut cells (% of PGRN level \pm SEM. CTR: 6.14 ± 0.69 ; *GRN* mut: 1.60 ± 0.27 ; $p < 0.001$ with respect to CTR; Mann-Whitney test) (Fig. 3A and C). We then calculated the ratio between PGRN level measured in CM versus lysates (CM/Lys) and in exosomes versus lysates (Exo/Lys):

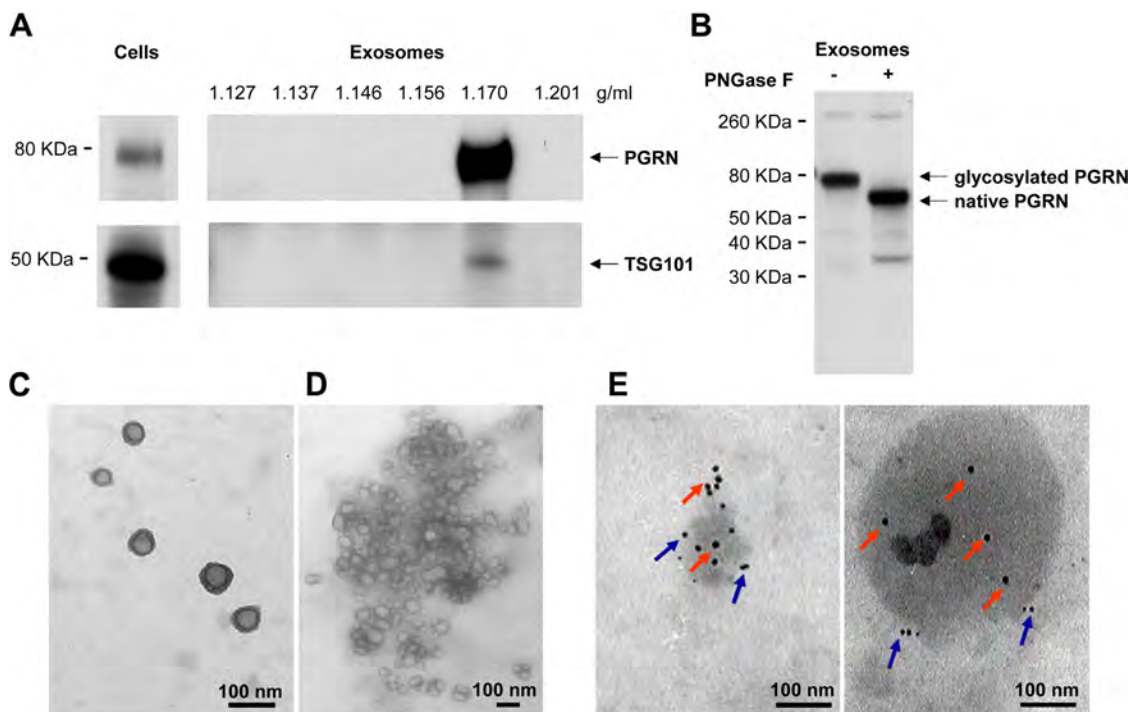


Fig. 2. Exosomes released by human primary fibroblasts contain glycosylated progranulin. (A) Immunoblotting of sucrose gradient fractions with exosomal preparations from conditioned media of human primary fibroblasts using antibodies directed against TSG101 and PGRN. TSG101 marked the fraction positive in exosomes, and PGRN was enriched in this fraction. (B) PNGase F enzymatic deglycosylation of PGRN glycoforms demonstrated that progranulin in this fraction is N-glycosylated. Electron microscopy: ultrastructural examination of fraction enriched in exosomes released from fibroblasts showed the presence of both single (C) and aggregated vesicles (D). Exosomes appeared as 40- to 100-nm diameter vesicles surrounded by a lipid layer with a cup-shaped morphology. Immunoelectron microscopy: ultrastructural examination of the same fraction revealed that progranulin, recognized by 10-nm gold-particles PCDGF antibody, recognizing PGRN (E, red arrows), colocalized with vesicles immunodecorated with 6-nm gold-particles 4A10 antibody, recognizing TSG101 a specific marker for exosomes (E, blue arrows). The morphology of the exosomes was probably influenced by immunolabeling procedures (scale bars, 100 nm each photo). Abbreviation: PNGase F, peptide-N-glycosidase F. (For interpretation of the references to color in this figure legend, the reader is referred to the Web version of this article.)

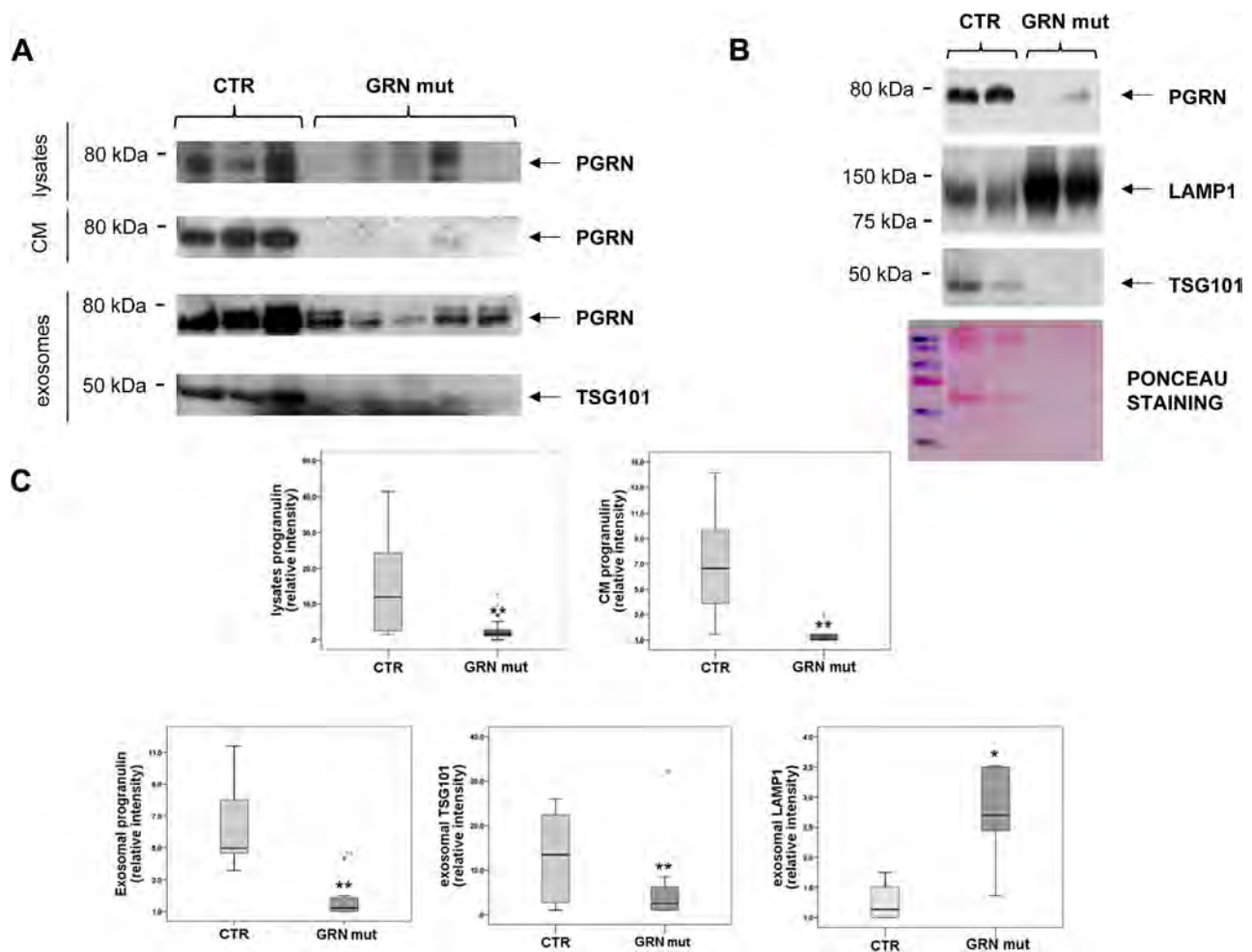


Fig. 3. Progranulin mutations alter PGRN levels in mutated human fibroblasts. (A) Western blot analysis showed a decrease of PGRN levels in lysates and conditioned media and a decrease of both PGRN and TSG101 levels in exosomes of *GRN* mut fibroblasts. (B) In contrast to PGRN and TSG101 protein trend, Western blot analysis revealed an increase of LAMP1 in *GRN* mut exosomes. Moreover, Ponceau staining showed a reduction of the whole protein content in exosomes released by *GRN* mut fibroblasts. (C) Densitometric analyses of lysates, conditioned media, and exosomal levels of PGRN, TSG101, and LAMP1. Mean values, presented as relative intensity \pm SEM, were normalized relative to the lowest protein level; * $p < 0.05$, Student *t*-test; ** $p < 0.001$, Mann-Whitney test. Abbreviation: SEM, standard error of the mean.

comparing *GRN* mut and controls, we found no difference in the CM/Lys ratios (CTR: 0.46 ± 0.15 ; *GRN* mut: 0.47 ± 0.14 , $p = 0.07$ Student *t*-test) and in the Exo/Lys ratios (CTR: 0.40 ± 0.34 , *GRN* mut: 0.59 ± 0.12 , $p = 0.75$ Student *t*-test): the % of PGRN released in association with exosomes in *GRN* mut and CTR is comparable.

Of note, the level of the exosomal marker TSG101 (Fig. 3B and C) as well as the total protein cargo, as revealed by Ponceau staining (Fig. 3B), were strongly reduced in exosomes released by *GRN* mut fibroblasts (% of TSG101 level \pm SEM. CTR: 13.24 ± 2.65 ; *GRN* mut: 5.43 ± 2.25 ; $p < 0.001$ with respect to CTR; Mann-Whitney test). Because of this reduction, a trend toward an increased ratio of exosomal PGRN level versus exosomal TSG101 level in *GRN* mut was observed, even if not statistically significant (CTR: 4.36 ± 1.68 , *GRN* mut: 8.11 ± 7.41 , $p = 0.07$; Student *t*-test). Conversely, Western blot analyses with antibody directed against LAMP1 showed a strong enrichment of its level in the exosomal fraction from *GRN* mut cells (% of LAMP1 level \pm SEM. CTR: 1.26 ± 0.18 ; *GRN* mut: 2.70 ± 0.40 ; $p < 0.05$ with respect to CTR; Student *t*-test) (Fig. 3B and C).

Cells proliferation and viability were measured by the trypan blue exclusion method and MTT assay. By using Trypan blue exclusion method, we found no significant changes in the number of viable cells between CTR fibroblasts ($n = 4$) and *GRN* mut ($n = 4$) (assorbance [mean \pm SEM]: plating day, CTR: 2850 ± 63.2397 ; *GRN*

mut: 2725 ± 188.7459 ; $p = 0.56$; day 3. CTR: 7132.5 ± 187.7257 ; *GRN* mut: 6012.5 ± 583.2291 ; $p = 0.12$; day 5. CTR: 9810.75 ± 661.3026 ; *GRN* mut: 9920.5 ± 492.7925 ; $p = 0.90$; day 7. CTR: $12,137.75 \pm 930.0776$; *GRN* mut: $11,970 \pm 1013.4471$; $p = 0.92$). In addition, MTT viability assay did not reveal significant differences between CTR and *GRN* mut fibroblasts (absorbance [mean \pm SEM]: plating day, CTR: 0.04 ± 0.0048 ; *GRN* mut: 0.03 ± 0.0030 ; $p = 0.55$; day 3, CTR: 0.08 ± 0.0039 ; *GRN* mut: 0.08 ± 0.0019 ; $p = 0.56$; day 5, CTR: 0.10 ± 0.00651 ; *GRN* mut: 0.09 ± 0.0068 ; $p = 0.41$; day 7, CTR: 0.12 ± 0.0075 ; *GRN* mut: 0.10 ± 0.0185 ; $p = 0.50$) (Fig. 4). All these data prove that mutations in *GRN* gene do not alter cell proliferation and viability.

3.3. Decreased exosome concentrations in media conditioned by *GRN* mut human fibroblasts

To clarify if the decrease in exosomal proteins observed in *GRN* mut cells was due to a decrease in the exosomes total amount, we analyzed intact vesicles solutions using NTA and a high-sensitivity sandwich fluorescence assay on a microarray. A sandwich immunoassay was developed using the same monoclonal antibody for both capture and detection purposes using antibody to human CD63. Exosomes were purified from pooled conditioned media

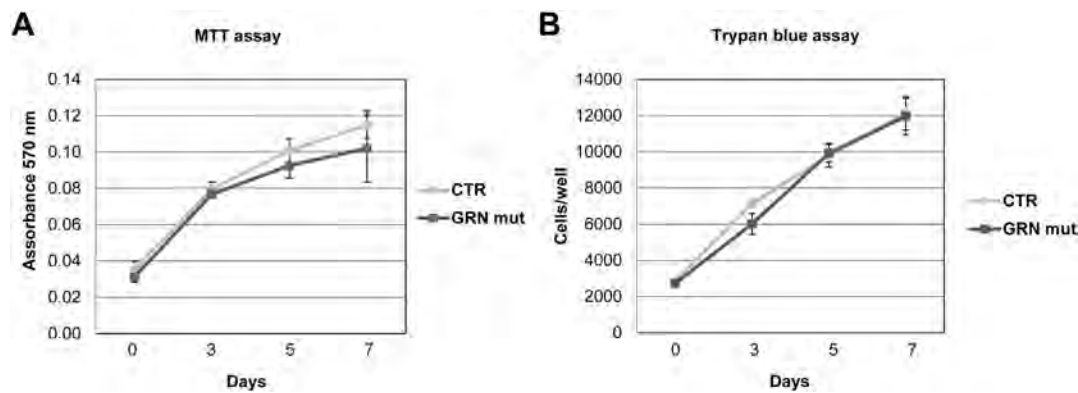


Fig. 4. Progranulin mutations do not alter cells proliferation and viability. Assessment of cell proliferation and viability by trypan blue exclusion (A) and MTT assay (B) after cell attachment and 3, 5, and 7 days after plating demonstrates that there are no significant variations in cell viability of *GRN*-mutated fibroblasts with respect to the control group. In the graphics, mean values \pm SEM are presented. Abbreviation: SEM, standard error of the mean.

from CTR and *GRN* mut human fibroblasts, resuspended in PBS, and analyzed in parallel using the 2 quantification methods. NTAs showed a decrease in the total number of extracellular vesicles (Fig. 5A) from *GRN* mut human fibroblasts with respect to controls. The immunoassay revealed a specific reduction of CD63 positive vesicles (Fig. 5B) (relative fluorescence intensity of CD63 \pm SEM: CTR: 30,871.526 \pm 575.70; *GRN* mut: 20,460.16 \pm 638.81, $p < 0.001$, Student *t*-test).

3.4. Increased exosome concentration after *in vitro* *GRN* silencing

To further explore the role of PGRN in exosome release, we performed *GRN* silencing experiments in SH-SY5Y cells. In cell lysates, PGRN protein level downregulation (as compared to alpha-tubulin) was confirmed after 48 hours of cell treatment (Fig. 6A and B). Exosomes were then isolated from SH-SY5Y untreated (liposomes only) and PGRN siRNA-treated cells and assessed for the presence of PGRN (Fig. 6C and D). All exosome preparations were normalized for protein concentration before Western blot analyses. The exosomal marker TSG101 was used as loading control and to normalize protein levels. As expected, following PGRN down-regulation, we observed a very strong decrease in exosomal PGRN (Fig. 6E). We then performed NTAs to analyze the concentration of exosomes released by SH-SY5Y in both conditions. Surprisingly, we detected an increased number of exosomes released after PGRN silencing (Fig. 6F).

4. Discussion

In this study, we analyzed PGRN protein trafficking and release in human primary fibroblasts both in physiological and pathological (i.e., presence of *GRN* null mutations) conditions. We made several novel observations. We showed that (1) PGRN is secreted in association with exosomes, mainly in its N-glycosylated form; (2) the level of exosomal PGRN released by *GRN* mut human fibroblasts is strongly reduced; (3) the whole release of exosomes by *GRN* mut cells is impaired; (4) and exosomes released by *GRN* mut cells are enriched in Lamp1. Because the presence of *GRN* mutations does not affect cells viability and proliferation, cell death is not responsible for the observed biological effects. This is confirmed also by *GRN* silencing in SH-SY5Y that does not affect cell viability and proliferation (data not shown).

Most *GRN* mutations cause frame shifts, premature terminations, or affect initiation of translation in case of mutations within the Kozak consensus sequence: these mutations result in a reduction of the PGRN protein levels because of nonsense-mediated mRNA decay (Baker et al., 2006; Cruts et al., 2006). Few missense mutations were demonstrated to be pathogenic: those mutations impact on PGRN N-glycosylation and secretion (Mukherjee et al., 2006; Shankaran et al., 2008). Thus, apparently all pathogenic *GRN* mutations cause reduced protein expression or secretion, although by different cellular mechanisms. Because progranulin is a secreted neurotrophic factor that can promote neuronal survival and enhance neurite outgrowth (Ryan et al.,

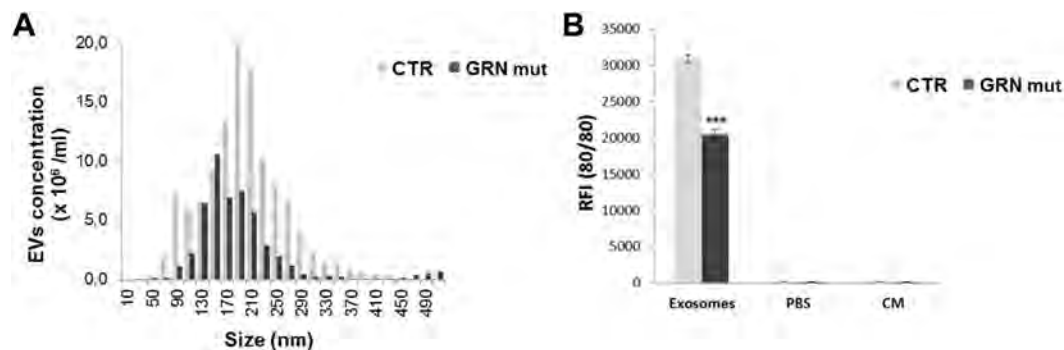


Fig. 5. Progranulin mutations alter exosomes number in *GRN* mut human fibroblasts. (A) Nanoparticle tracking analysis (NanoSight LM10 instrument) quantification of extracellular vesicles (EVs) revealed a decrease in the total amount of vesicles isolated from *GRN* mut human fibroblast. (B) Fluorescence detection of CD63-positive vesicles on a Si/SiO₂ interferometric platform showed a decrease in the content of exosomes in *GRN* mut human fibroblasts. Mean values are presented as relative fluorescence intensity (RFI) \pm SEM; *** $p < 0.001$, Student *t*-test. Abbreviation: SEM, standard error of the mean.

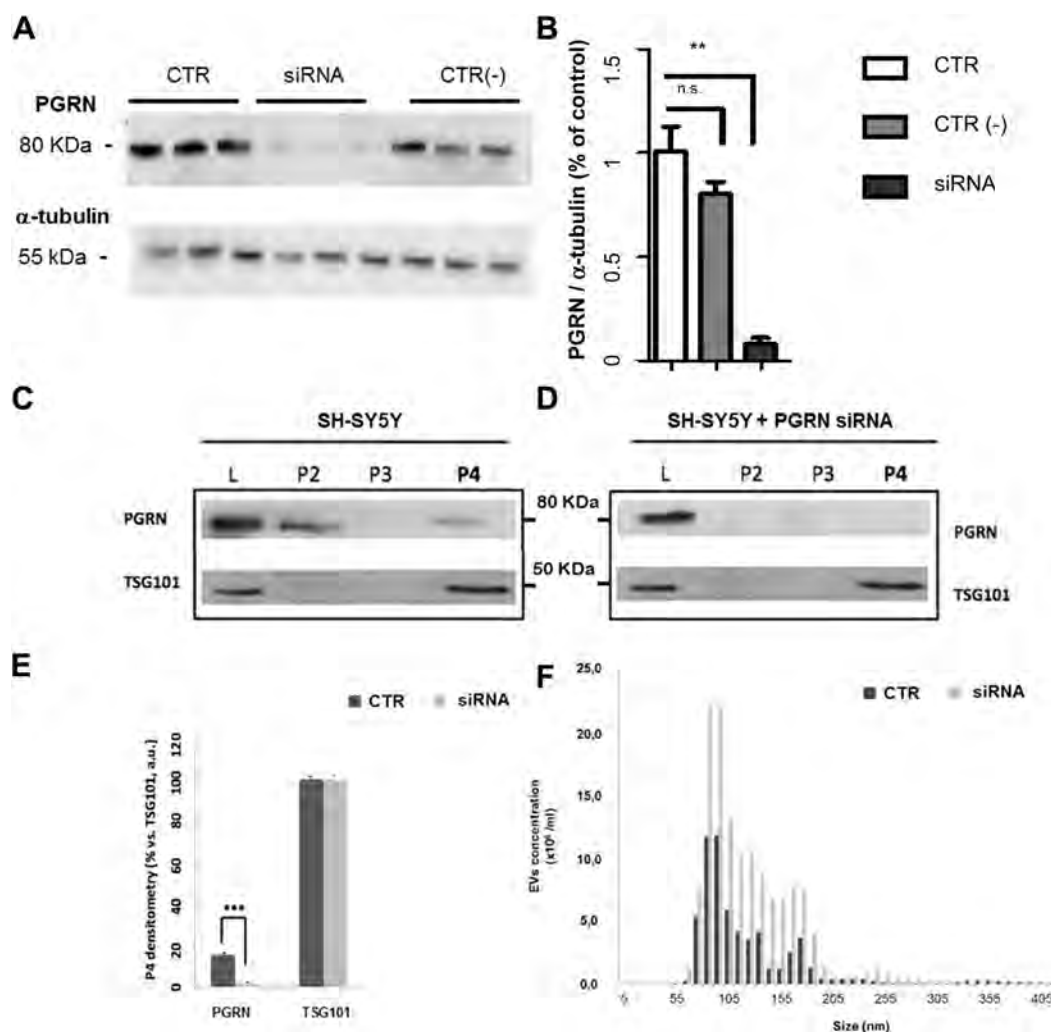


Fig. 6. Progranulin silencing alters exosome release. (A) Representative Western blotting showing PGRN downregulation at 24 hours; the bar graph (B) is the densitometric quantification (3 independent samples for each point). CTR: control; CTR (–): siRNA negative control; siRNA: small interfering RNA. (C) Control condition: exosomes released from cells expressing basal level of PGRN; (D) silenced condition: exosomes released from SH-SY5Y cells after 48 hours of PGRN silencing. In both conditions, the TSG101 antibody was used to show the exosomal enrichment in P4 fraction after serial centrifugation at increasing speed. (E) Densitometric quantification of the P4 lanes of the Western blotting experiments. The densitometric values of the exosome-enriched fractions were normalized for TSG101 signal and are the mean \pm standard deviation from 3 independent experiments. (F) Nanoparticle tracking analysis of EVs released by SH-SY5Y in both conditions revealed an increased number of exosomes released after PGRN silencing. L: total cell lysate before centrifugation; P2 \rightarrow P4: protein extract from the pellet obtained at different centrifugation step. $**p < 0.01$, $***p < 0.001$ 1-way ANOVA and post-hoc test. Abbreviations: ANOVA, analysis of variance; n.s., not significant.

2009; Van Damme et al., 2008), it is believed that depletion of PGRN in the brain might cause neurodegeneration, but the mechanism by which it leads to neuronal death remain unclear.

Previous studies described that PGRN is secreted by the classical ER and/or Golgi secretory pathway (Ryan et al., 2009); once it is secreted, PGRN is actively internalized by sortilin and sorted to early endosomes and then to lysosomes (Hu et al., 2010; Tanimoto et al., 2015). Herein, we demonstrated that progranulin is secreted not only as soluble protein, but it is also incorporated into exosomes in a highly glycosylated form.

Many cells of the nervous system have been shown to release exosomes, implicating their active roles in development, function, and pathologies of this system: because exosomes are capable of transferring biomolecules among cells without direct cell-to-cell contact, this transfer modality represents a novel physiological form of intercellular communication between neural cells (Agnati and Fuxe, 2014; Fauré et al., 2006; Fruhbeis et al., 2013; Lachenal et al., 2011). In physiological conditions, exosomes have been demonstrated to promote neuronal survival

(Wang et al., 2011). In neurodegenerative disorders, exosomes have been suggested as potential carriers of misfolded toxic proteins, such as the amyloid-beta peptide in AD (Rajendran et al., 2014). However, controversial data have been published on their role in AD pathogenesis and whether they promote or counteract the toxic action of the amyloid-beta peptide is still a matter of debate (Joshi et al., 2015). We previously demonstrated that the presence of AD-associated presenilin-2 mutations results in a loss of exosomal glycosylated-cystatin C, a neuroprotective growth factor (Ghidoni et al., 2011). In the presence of GRN null mutations, we observed not only a loss of exosomal glycosylated-PGRN, but also a loss of exosomes.

As we previously hypothesized, we might speculate that during aging, characterized by progressive loss of neurons, exosomes could become the key player of neuronal communication: in this view, survival of neurons could be easily affected by factors modulating exosomes release and/or composition, such as the presence of pathogenic mutations (Ghidoni et al., 2008b). We demonstrated that in GRN-associated frontotemporal dementia, this shuttle

system is strongly impaired: thus, along with shortage of the circulating PGRN, *GRN* null mutations alter intercellular communication.

The molecular mechanism underlying this effect deserves further investigations. Our data suggest that the loss of PGRN might impact on cellular protein sorting and degradation. Several studies have now implicated PGRN in lysosomal functions (Belcastro et al., 2011; Götzl et al., 2014; Smith et al., 2012; Zhou et al., 2015). Of interest, *GRN* null mutation in homozygosity was described to cause the neuronal ceroid lipofuscinoses, a lysosomal storage disorder (Smith et al., 2012). *GRN* silencing experiment in SH-SY5Y cells confirmed a direct role of PGRN in the control of exosome release. The differential effect of the loss of PGRN on exosomes release in the 2 cellular disease models (i.e., silenced cells and mutated fibroblasts from patients) may be due to the fact that we are comparing an acute versus a chronic lifelong PGRN deprivation: in humans, loss of PGRN could first upregulate exosome release and then result in a downregulation of this pathway. In this view, the observed enrichment of exosomal Lamp1 in human diseased cells might attest an activation of the lysosomal pathway in the attempt to rebalance exosome release. As a matter of fact, *GRN*-associated neurodegeneration is pathologically characterized by intracellular protein accumulation.

The ideal time to treat neurodegenerative disease is before clinical presentation, at a point when the minimum of irreversible neuronal loss has occurred and cognitive function is still preserved. At present, this could be achieved in genetically determined forms of neurodegenerative disease, such as *GRN*-associated frontotemporal dementia: in presymptomatic *GRN* mutation carriers, markers of neurodegeneration (i.e., structural imaging changes) can be detected even a decade before the expected onset of clinical symptoms (Pievani et al., 2014; Rohrer et al., 2015). Because all pathogenic *GRN* mutations are associated with a strong reduction of extracellular PGRN protein, drug discovery effort aimed at enhancing extracellular PGRN levels is of great interest to the scientific community (Almeida et al., 2012; Capell et al., 2011; Cenik et al., 2011; Lee et al., 2014). A better understanding of the role played by exosomes in *GRN*-associated neurodegeneration is crucial for the development of novel therapies targeting exosomes release.

Disclosure statement

The authors have no actual or potential conflicts of interest.

Acknowledgements

This work was supported by Regione Lombardia and Fondazione Cariplo through POR-FESR, project MINER (ID 46875467); Italian Ministry of Health, Ricerca Corrente.

References

- Agnati, L.F., Fuxe, K., 2014. Extracellular-vesicle type of volume transmission and tunnelling-nanotube type of wiring transmission add a new dimension to brain neuro-glial networks. *Philos. Trans. R. Soc. Lond. B Biol. Sci.* 369.
- Almeida, S., Zhang, Z., Coppola, G., Mao, W., Futai, K., Karydas, A., Geschwind, M.D., Tartaglia, M.C., Gao, F., Gianni, D., Sena-Esteves, M., Geschwind, D.H., Miller, B.L., Farese, R.V., Gao, F.B., 2012. Induced pluripotent stem cell models of progranulin-deficient frontotemporal dementia uncover specific reversible neuronal defects. *Cell Rep.* 2, 789–798.
- Bagnoli, S., Piaceri, I., Tedde, A., Piacentini, S., Nannucci, S., Bracco, L., Sorbi, S., Nacmias, B., 2012. Progranulin genetic screening in frontotemporal lobar degeneration patients from central Italy. *Cell Mol. Neurobiol.* 32, 13–16.
- Baker, M., Mackenzie, I.R., Pickering-Brown, S.M., Gass, J., Rademakers, R., Lindholm, C., Snowden, J., Adamson, J., Sadovnick, A.D., Rollinson, S., Cannon, A., Dwosh, E., Neary, D., Melquist, S., Richardson, A., Dickson, D., Berger, Z., Eriksen, J., Robinson, T., Zehr, C., Dickey, C.A., Crook, R., McGowan, E., Mann, D., Boeve, B., Feldman, H., Hutton, M., 2006. Mutations in progranulin cause tau-negative frontotemporal dementia linked to chromosome 17. *Nature* 442, 916–919.
- Belcastro, V., Siciliano, V., Gregoret, F., Mithbaokar, P., Dharmalingam, G., Berlingieri, S., Iorio, F., Oliva, G., Polishchuck, R., Brunetti-Pierri, N., di Bernardo, D., 2011. Transcriptional gene network inference from a massive dataset elucidates transcriptome organization and gene function. *Nucleic Acids Res.* 39, 8677–8688.
- Benussi, L., Binetti, G., Sina, E., Gigola, L., Bettecken, T., Meitinger, T., Ghidoni, R., 2008. A novel deletion in progranulin gene is associated with FTDP-17 and CBS. *Neurobiol. Aging* 29, 427–435.
- Benussi, L., Ghidoni, R., Binetti, G., 2010. Progranulin mutations are a common cause of FTLD in Northern Italy. *Alzheimer Dis. Assoc. Disord.* 24, 308–309.
- Benussi, L., Ghidoni, R., Pegoiani, E., Moretti, D.V., Zanetti, O., Binetti, G., 2009. Progranulin Leu271LeufsX10 is one of the most common FTLD and CBS associated mutations worldwide. *Neurobiol. Dis.* 33, 379–385.
- Benussi, L., Ghidoni, R., Steinhoff, T., Alberici, A., Villa, A., Mazzoli, F., Nicosia, F., Barbiero, L., Broglio, L., Feudatari, E., Signorini, S., Finckh, U., Nitsch, R.M., Binetti, G., 2003. Alzheimer disease-associated cystatin C variant undergoes impaired secretion. *Neurobiol. Dis.* 13, 15–21.
- Capell, A., Liebscher, S., Fellerer, K., Brouwers, N., Willem, M., Lammich, S., Gijssels, I., Bittner, T., Carlson, A.M., Sasse, F., Kunze, B., Steinmetz, H., Jansen, R., Dormann, D., Sleegers, K., Cruts, M., Hermis, J., Van Broeckhoven, C., Haass, C., 2011. Rescue of progranulin deficiency associated with frontotemporal lobar degeneration by alkalinizing reagents and inhibition of vacuolar ATPase. *J. Neurosci.* 31, 1885–1894.
- Cenik, B., Sephton, C.F., Dewey, C.M., Xian, X., Wei, S., Yu, K., Niu, W., Coppola, G., Coughlin, S.E., Lee, S.E., Dries, D.R., Almeida, S., Geschwind, D.H., Gao, F.B., Miller, B.L., Farese, R.V., Posner, B.A., Yu, G., Herz, J., 2011. Suberoylanilide hydroxamic acid (vorinostat) up-regulates progranulin transcription: rational therapeutic approach to frontotemporal dementia. *J. Biol. Chem.* 286, 16101–16108.
- Chen-Plotkin, A.S., Martinez-Lage, M., Sleiman, P.M., Hu, W., Greene, R., Wood, E.M., Bing, S., Grossman, M., Schellenberg, G.D., Hatanpaa, K.J., Weiner, M.F., White, C.L., Brooks, W.S., Halliday, G.M., Kril, J.J., Gearing, M., Beach, T.G., Graff-Radford, N.R., Dickson, D.W., Rademakers, R., Boeve, B.F., Pickering-Brown, S.M., Snowden, J., van Swieten, J.C., Heutink, P., Seelaar, H., Murrell, J.R., Ghetti, B., Spina, S., Grafman, J., Kaye, J.A., Woltjer, R.L., Mesulam, M., Bigio, E., Lladó, A., Miller, B.L., Alzualde, A., Moreno, F., Rohrer, J.D., Mackenzie, I.R., Feldman, H.H., Hamilton, R.L., Cruts, M., Engelborghs, S., De Deyn, P.P., Van Broeckhoven, C., Bird, T.D., Cairns, N.J., Goate, A., Frosch, M.P., Riederer, P.F., Bogdanovic, N., Lee, V.M., Trojanowski, J.Q., Van Deerlin, V.M., 2011. Genetic and clinical features of progranulin-associated frontotemporal lobar degeneration. *Arch. Neurol.* 68, 488–497.
- Cretich, M., Pirri, G., Damin, F., Solinas, I., Chiari, M., 2004. A new polymeric coating for protein microarrays. *Anal. Biochem.* 332, 67–74.
- Cretich, M., Reddington, A., Monroe, M., Bagnati, M., Damin, F., Sola, L., 2011. Silicon biochips for dual label-free and fluorescence detection: application to protein microarray development. *Biosens. Bioelectron.* 26, 3938–3943.
- Cruts, M., Gijssels, I., van der Zee, J., Engelborghs, S., Wils, H., Pirici, D., Rademakers, R., Vandenberghe, R., Dermaut, B., Martin, J.J., van Duijn, C., Peeters, K., Sciot, R., Santens, P., De Pooter, T., Matheijssens, M., Van den Broeck, M., Cuijt, I., Vennekens, K., De Deyn, P.P., Kumar-Singh, S., Van Broeckhoven, C., 2006. Null mutations in progranulin cause ubiquitin-positive frontotemporal dementia linked to chromosome 17q21. *Nature* 442, 920–924.
- El Andaloussi, S., Mager, I., Breakefield, X.O., Wood, M.J., 2013. Extracellular vesicles: biology and emerging therapeutic opportunities. *Nat. Rev. Drug Discov.* 12, 347–357.
- Emmanouilidou, E., Melachroinou, K., Roumeliotis, T., Garbis, S.D., Ntzouni, M., Margaritis, L.H., Stefanis, L., Vekrellis, K., 2010. Cell-produced alpha-synuclein is secreted in a calcium-dependent manner by exosomes and impacts neuronal survival. *J. Neurosci.* 30, 6838–6851.
- Fauré, J., Lachenal, G., Court, M., Hirrlinger, J., Chatellard-Causse, C., Blot, B., Grange, J., Schoehn, G., Goldberg, Y., Boyer, V., Kirchhoff, F., Raposo, G., Garin, J., Sadoul, R., 2006. Exosomes are released by cultured cortical neurons. *Mol. Cell Neurosci.* 31, 642–648.
- Février, B., Vilette, D., Archer, F., Loew, D., Faigle, W., Vidal, M., Laude, H., Raposo, G., 2004. Cells release prions in association with exosomes. *Proc. Natl. Acad. Sci. U. S. A.* 101, 9683–9688.
- Finch, N., Baker, M., Crook, R., Swanson, K., Kuntz, K., Surtees, R., Bisceglia, G., Rovelet-Lecrux, A., Boeve, B., Petersen, R.C., Dickson, D.W., Younkin, S.G., Deramecourt, V., Crook, J., Graff-Radford, N.R., Rademakers, R., 2009. Plasma progranulin levels predict progranulin mutation status in frontotemporal dementia patients and asymptomatic family members. *Brain* 132, 583–591.
- Fruhbeis, C., Frohlich, D., Kuo, W.P., Kramer-Albers, E.M., 2013. Extracellular vesicles as mediators of neuron-glia communication. *Front. Cell Neurosci.* 7, 182.
- Ghidoni, R., Benussi, L., Binetti, G., 2008b. Exosomes: the Trojan horses of neurodegeneration. *Med. Hypotheses* 70, 1226–1227.
- Ghidoni, R., Benussi, L., Glionna, M., Franzoni, M., Binetti, G., 2008a. Low plasma progranulin levels predict progranulin mutations in frontotemporal lobar degeneration. *Neurology* 71, 1235–1239.
- Ghidoni, R., Paterlini, A., Albertini, V., Binetti, G., Benussi, L., 2012b. Losing protein in the brain: the case of progranulin. *Brain Res.* 1476, 172–182.
- Ghidoni, R., Paterlini, A., Albertini, V., Glionna, M., Monti, E., Schiaffonati, L., Benussi, L., Levy, E., Binetti, G., 2011. Cystatin C is released in association with

- exosomes: a new tool of neuronal communication which is unbalanced in Alzheimer's disease. *Neurobiol. Aging* 32, 1435–1442.
- Ghidoni, R., Stoppani, E., Rossi, G., Piccoli, E., Albertini, V., Paterlini, A., Glionna, M., Pegoiani, E., Agnati, L.F., Fenoglio, C., Scarpini, E., Galimberti, D., Morbin, M., Tagliavini, F., Binetti, G., Benussi, L., 2012a. Optimal plasma progranulin cutoff value for predicting null progranulin mutations in neurodegenerative diseases: a multicenter Italian study. *Neurodegener. Dis.* 9, 121–127.
- Gijselink, I., Van Broeckhoven, C., Cruts, M., 2008. Granulin mutations associated with frontotemporal lobar degeneration and related disorders: an update. *Hum. Mutat.* 29, 1373–1386.
- Goldman, J.S., Adamson, J., Karydas, A., Miller, B.L., Hutton, M., 2007. New genes, new dilemmas: FTL genetics and its implications for families. *Am. J. Alzheimers Dis. Other Demen.* 22, 507–515.
- Gomes, C., Keller, S., Altevogt, P., Costa, J., 2007. Evidence for secretion of Cu, Zn superoxide dismutase via exosomes from a cell model of amyotrophic lateral sclerosis. *Neurosci. Lett.* 428, 43–46.
- Götzl, J.K., Mori, K., Damme, M., Fellerer, K., Tahirovic, S., Kleinberger, G., Janssens, J., van der Zee, J., Lang, C.M., Kremmer, E., Martin, J.J., Engelborghs, S., Kretschmar, H.A., Arzberger, T., Van Broeckhoven, C., Haass, C., Capell, A., 2014. Common pathobiochemical hallmarks of progranulin-associated frontotemporal lobar degeneration and neuronal ceroid lipofuscinosis. *Acta Neuropathol.* 127, 845–860.
- Hu, F., Padukkavidana, T., Vaegter, C.B., Brady, O.A., Zheng, Y., Mackenzie, I.R., Feldman, H.H., Nykjaer, A., Strittmatter, S.M., 2010. Sortilin-mediated endocytosis determines levels of the frontotemporal dementia protein, progranulin. *Neuron* 68, 654–667.
- Joshi, P., Benussi, L., Furlan, R., Ghidoni, R., Verderio, C., 2015. Extracellular vesicles in Alzheimer's disease: friends or foes? Focus on abeta-vesicle interaction. *Int. J. Mol. Sci.* 16, 4800–4813.
- Lachenal, G., Pernet-Gallay, K., Chivet, M., Hemming, F.J., Belly, A., Bodon, G., Blot, B., Haase, G., Goldberg, Y., Sadoul, R., 2011. Release of exosomes from differentiated neurons and its regulation by synaptic glutamatergic activity. *Mol. Cell Neurosci* 46, 409–418.
- Lee, W.C., Almeida, S., Prudencio, M., Caulfield, T.R., Zhang, Y.J., Tay, W.M., Bauer, P.O., Chew, J., Sasaguri, H., Jansen-West, K.R., Gendron, T.F., Stetler, C.T., Finch, N., Mackenzie, I.R., Rademakers, R., Gao, F.B., Petrucelli, L., 2014. Targeted manipulation of the sortilin-progranulin axis rescues progranulin haploinsufficiency. *Hum. Mol. Genet.* 23, 1467–1478.
- Mackenzie, I.R., Frick, P., Neumann, M., 2014. The neuropathology associated with repeat expansions in the C9ORF72 gene. *Acta Neuropathol.* 127, 347–357.
- Mukherjee, O., Pastor, P., Cairns, N.J., Chakraverty, S., Kauwe, J.S., Shears, S., Behrens, M.L., Budde, J., Hinrichs, A.L., Norton, J., Levitch, D., Taylor-Reinwald, L., Gitcho, M., Tu, P.H., Tenenholz Grinberg, L., Liscic, R.M., Armendariz, J., Morris, J.C., Goate, A.M., 2006. HDDD2 is a familial frontotemporal lobar degeneration with ubiquitin-positive, tau-negative inclusions caused by a missense mutation in the signal peptide of progranulin. *Ann. Neurol.* 60, 314–322.
- Neary, D., Snowden, J.S., Gustafson, L., Passant, U., Stuss, D., Black, S., Freedman, M., Kertesz, A., Robert, P.H., Albert, M., Boone, K., Miller, B.L., Cummings, J., Benson, D.F., 1998. Frontotemporal lobar degeneration: a consensus on clinical diagnostic criteria. *Neurology* 51, 1546–1554.
- Perez-Gonzalez, R., Gauthier, S.A., Kumar, A., Levy, E., 2012. The exosome secretory pathway transports amyloid precursor protein carboxyl-terminal fragments from the cell into the brain extracellular space. *J. Biol. Chem.* 287, 43108–43115.
- Pievani, M., Paternicò, D., Benussi, L., Binetti, G., Orlandini, A., Cobelli, M., Magnaldi, S., Ghidoni, R., Frisoni, G.B., 2014. Pattern of structural and functional brain abnormalities in asymptomatic granulin mutation carriers. *Alzheimers Dement.* 10, 354–363.
- Rademakers, R., Baker, M., Gass, J., Adamson, J., Huey, E.D., Momeni, P., Spina, S., Coppola, G., Karydas, A.M., Stewart, H., Johnson, N., Hsiung, G.Y., Kelley, B., Kuntz, K., Steinbart, E., Wood, E.M., Yu, C.E., Josephs, K., Sorenson, E., Womack, K.B., Weintraub, S., Pickering-Brown, S.M., Schofield, P.R., Brooks, W.S., Van Deerlin, V.M., Snowden, J., Clark, C.M., Kertesz, A., Boylan, K., Ghetti, B., Neary, D., Schellenberg, G.D., Beach, T.G., Mesulam, M., Mann, D., Grafman, J., Mackenzie, I.R., Feldman, H., Bird, T., Petersen, R., Knopman, D., Boeve, B., Geschwind, D.H., Miller, B., Wszolek, Z., Lipka, C., Bigio, E.H., Dickson, D., Graff-Radford, N., Hutton, M., 2007. Phenotypic variability associated with progranulin haploinsufficiency in patients with the common 1477C>T (Arg493X) mutation: an international initiative. *Lancet Neurol.* 6, 857–868.
- Rademakers, R., Neumann, M., Mackenzie, I.R., 2012. Advances in understanding the molecular basis of frontotemporal dementia. *Nat. Rev. Neurol.* 8, 423–434.
- Rajendran, L., Bali, J., Barr, M.M., Court, F.A., Kramer-Albers, E.M., Picou, F., Raposo, G., van der Vos, K.E., van Niel, G., Wang, J., Brakefield, X.O., 2014. Emerging roles of extracellular vesicles in the nervous system. *J. Neurosci.* 34, 15482–15489.
- Rajendran, L., Honscho, M., Zahn, T.R., Keller, P., Geiger, K.D., Verkade, P., Simons, K., 2006. Alzheimer's disease beta-amyloid peptides are released in association with exosomes. *Proc. Natl. Acad. Sci. U. S. A.* 103, 11172–11177.
- Raposo, G., Stoorvogel, W., 2013. Extracellular vesicles: exosomes, microvesicles, and friends. *J. Cell Biol.* 200, 373–383.
- Ratnavalli, E., Brayne, C., Dawson, K., Hodges, J.R., 2002. The prevalence of frontotemporal dementia. *Neurology* 58, 1615–1621.
- Riedl, L., Mackenzie, I.R., Forstl, H., Kurz, A., Diehl-Schmid, J., 2014. Frontotemporal lobar degeneration: current perspectives. *Neuropsychiatr. Dis. Treat* 10, 297–310.
- Rohrer, J.D., Nicholas, J.M., Cash, D.M., van Swieten, J., Dopfer, E., Jiskoot, L., van Minkelen, R., Rombouts, S.A., Cardoso, M.J., Clegg, S., Espak, M., Mead, S., Thomas, D.L., De Vita, E., Masellis, M., Black, S.E., Freedman, M., Keren, R., Macintosh, B.J., Rogaeva, E., Tang-Wai, D., Tartaglia, M.C., Laforce, R., Tagliavini, F., Tiraboschi, P., Redaelli, V., Prioni, S., Grisoli, M., Borroni, B., Padovani, A., Galimberti, D., Scarpini, E., Arighi, A., Fumagalli, G., Rowe, J.B., Coyle-Gilchrist, I., Graff, C., Fallström, M., Jelic, V., Ståhlbom, A.K., Andersson, C., Thonberg, H., Lilius, L., Frisoni, G.B., Pievani, M., Bochetta, M., Benussi, L., Ghidoni, R., Finger, E., Sorbi, S., Nacmias, B., Lombardi, G., Polito, C., Warren, J.D., Ourselin, S., Fox, N.C., Rossor, M.N., 2015. Presymptomatic cognitive and neuroanatomical changes in genetic frontotemporal dementia in the Genetic Frontotemporal Dementia Initiative (GENFI) study: a cross-sectional analysis. *Lancet Neurol.* 14, 253–262.
- Ryan, C.L., Baranowski, D.C., Chitramuthu, B.P., Malik, S., Li, Z., Cao, M., Minotti, S., Durham, H.D., Kay, D.G., Shaw, C.A., Bennett, H.P., Bateman, A., 2009. Progranulin is expressed within motor neurons and promotes neuronal cell survival. *BMC Neurosci.* 10, 130.
- Schlachetzki, J.C., Schmidtke, K., Beckervordersandforth, J., Borozdin, W., Wilhelm, C., Hull, M., Kohlhaase, J., 2009. Frequency of progranulin mutations in a German cohort of 79 frontotemporal dementia patients. *J. Neurol.* 256, 2043–2051.
- Shankaran, S.S., Capell, A., Hruscha, A.T., Fellerer, K., Neumann, M., Schmid, B., Haass, C., 2008. Missense mutations in the progranulin gene linked to frontotemporal lobar degeneration with ubiquitin-immunoreactive inclusions reduce progranulin production and secretion. *J. Biol. Chem.* 283, 1744–1753.
- Sieben, A., Van Langenhove, T., Engelborghs, S., Martin, J.J., Boon, P., Cras, P., De Deyn, P.P., Santens, P., Van Broeckhoven, C., Cruts, M., 2012. The genetics and neuropathology of frontotemporal lobar degeneration. *Acta Neuropathol.* 124, 353–372.
- Sleegers, K., Brouwers, N., Van Damme, P., Engelborghs, S., Gijselink, I., van der Zee, J., Peeters, K., Mattheijssens, M., Cruts, M., Vandenbergh, R., De Deyn, P.P., Robberecht, W., Van Broeckhoven, C., 2009. Serum biomarker for progranulin-associated frontotemporal lobar degeneration. *Ann. Neurol.* 65, 603–609.
- Smith, K.R., Damiano, J., Franceschetti, S., Carpenter, S., Canafoglia, L., Morbin, M., Rossi, G., Pareyson, D., Mole, S.E., Staropoli, J.F., Sims, K.B., Lewis, J., Lin, W.L., Dickson, D.W., Dahl, H.H., Bahl, M., Berkovic, S.F., 2012. Strikingly different clinicopathological phenotypes determined by progranulin-mutation dosage. *Am. J. Hum. Genet.* 90, 1102–1107.
- Tanimoto, R., Morcavallo, A., Terracciano, M., Xu, S.Q., Stefanello, M., Buraschi, S., Lu, K.G., Bagley, D.H., Gomella, L.G., Scotlandi, K., Belfiore, A., Iozzo, R.V., Morriane, A., 2015. Sortilin regulates progranulin action in castration-resistant prostate cancer cells. *Endocrinology* 156, 58–70.
- The Lund and Manchester Groups, 1994. Clinical and neuropathological criteria for frontotemporal dementia. *J. Neurol. Neurosurg. Psychiatry* 57, 416–418.
- Thery, C., Amigorena, S., Raposo, G., Clayton, A., 2006. Isolation and characterization of exosomes from cell culture supernatants and biological fluids. *Curr. Protoc. Cell Biol.* Chapter 3, Unit 3.22.
- Tremolizzo, L., Gelosa, G., Galbusera, A., Isella, V., Arosio, C., Bertola, F., Casati, G., Piperno, A., Ferrarese, C., Appollonio, I., 2009. Higher than expected progranulin mutation rate in a case series of Italian FTL patients. *Alzheimer Dis. Assoc. Disord.* 23, 301.
- Valadi, H., Ekstrom, K., Bossios, A., Sjostrand, M., Lee, J.J., Lotvall, J.O., 2007. Exosome-mediated transfer of mRNAs and microRNAs is a novel mechanism of genetic exchange between cells. *Nat. Cell Biol.* 9, 654–659.
- Van Damme, P., Van Hoecke, A., Lambrechts, D., Vanacker, P., Bogaert, E., van Swieten, J., Carmeliet, P., Van Den Bosch, L., Robberecht, W., 2008. Progranulin functions as a neurotrophic factor to regulate neurite outgrowth and enhance neuronal survival. *J. Cell Biol.* 181, 37–41.
- van der Zee, J., Rademakers, R., Engelborghs, S., Gijselink, I., Bogaerts, V., Vandenbergh, R., Santens, P., Caekebeke, J., De Pooter, T., Peeters, K., Lübke, U., Van den Broeck, M., Martin, J.J., Cruts, M., De Deyn, P.P., Van Broeckhoven, C., Dermaut, B., 2006. A Belgian ancestral haplotype harbours a highly prevalent mutation for 17q21-linked tau-negative FTL. *Brain* 129, 841–852.
- van der Zee, J., Van Broeckhoven, C., 2014. Dementia in 2013: frontotemporal lobar degeneration-building on breakthroughs. *Nat. Rev. Neurol.* 10, 70–72.
- Vlassov, A.V., Magdaleno, S., Setterquist, R., Conrad, R., 2012. Exosomes: current knowledge of their composition, biological functions and diagnostic and therapeutic potentials. *Biochim. Biophys. Acta* 1820, 940–948.
- Wang, S., Cesca, F., Loers, G., Schweizer, M., Buck, F., Benfenati, F., Schachner, M., Kleene, R., 2011. Synapsin I is an oligomannose-carrying glycoprotein, acts as an oligomannose-binding lectin, and promotes neurite outgrowth and neuronal survival when released via glia-derived exosomes. *J. Neurosci.* 31, 7275–7290.
- Yu, C.E., Bird, T.D., Bekris, L.M., Montine, T.J., Leverenz, J.B., Steinbart, E., Galloway, N.M., Feldman, H., Woltjer, R., Miller, C.A., Wood, E.M., Grossman, M., McCluskey, L., Clark, C.M., Neumann, M., Danek, A., Galasko, D.R., Arnold, S.E., Chen-Plotkin, A., Karydas, A., Miller, B.L., Trojanowski, J.Q., Lee, V.M., Schellenberg, G.D., Van Deerlin, V.M., 2010. The spectrum of mutations in progranulin: a collaborative study screening 545 cases of neurodegeneration. *Arch. Neurol.* 67, 161–170.
- Zhou, X., Sun, L., Bastos de Oliveira, F., Qi, X., Brown, W.J., Smolka, M.B., Sun, Y., Hu, F., 2015. Prosaoposin facilitates sortilin-independent lysosomal trafficking of progranulin. *J. Cell Biol.* 210, 991–1002.



Combined mass quantitation and phenotyping of intact extracellular vesicles by a microarray platform



Paola Gagni^a, Marina Cretich^{a,*}, Luisa Benussi^b, Elisa Tonoli^b, Miriam Ciani^b,
Roberta Ghidoni^b, Benedetta Santini^c, Elisabetta Galbiati^c, Davide Prosperi^c,
Marcella Chiari^a

^a Consiglio Nazionale delle Ricerche, Istituto di Chimica del Riconoscimento Molecolare (ICRM), Italy

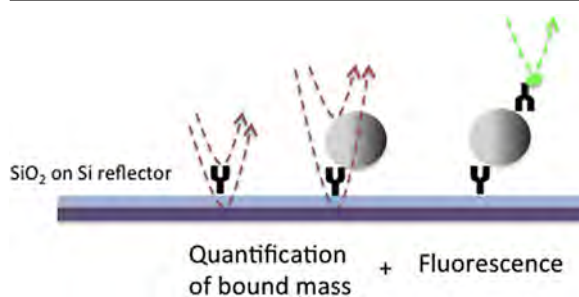
^b Molecular Markers Laboratory, IRCCS Istituto Centro San Giovanni di Dio Fatebenefratelli, Brescia, Italy

^c NanoBioLab, Dipartimento di Biotecnologie e Bioscienze, Università di Milano-Bicocca, Milano, Italy

HIGHLIGHTS

- Extracellular vesicles (EVs) have a great potential for liquid biopsy development.
- Isolation and characterization of EVs present unique challenges due to their small size, low refractive index, and polydispersity.
- We propose, for the first time, the use of a Si/SiO₂ interferometric platform for multiparameter intact EVs analysis combining EVs mass quantitation and phenotyping.
- Successful fluorescence detection of EVs from plasma samples opens the way to the use of the platform in diagnostic applications.

GRAPHICAL ABSTRACT



ARTICLE INFO

Article history:

Received 16 July 2015

Received in revised form 8 October 2015

Accepted 14 October 2015

Available online 26 October 2015

Keywords:

Extracellular vesicles
Exosomes
Biomarkers
Interferometry
Fluorescence
Microarrays

ABSTRACT

The interest towards extracellular vesicles (EVs) has grown exponentially over the last few years; being involved in intercellular communication and serving as reservoirs for biomarkers for tumors, they have a great potential for liquid biopsy development, possibly replacing many costly and invasive tissue biopsies.

Here we propose, for the first time, the use of a Si/SiO₂ interferometric, microarray platform for multiparametric intact EVs analysis combining label-free EVs mass quantitation and high sensitivity fluorescence based phenotyping. Label free interferometric measurement allows to quantify the amount of vesicles captured by printed antibodies while, on the same chip, EVs are also detected by fluorescence in a sandwich immunoassay. The proposed method simultaneously detects, quantify and phenotype intact EVs in a microarray format.

© 2015 Elsevier B.V. All rights reserved.

1. Introduction

Cells release into the extracellular environment a variety of membrane vesicles of endosomal and membrane origin called

* Corresponding author. ICRM, CNR, Via Mario Bianco, 9, 20131 Milano, Italy.

E-mail address: marina.cretich@icrm.cnr.it (M. Cretich).

exosomes and microvesicles/ectosomes, respectively. The interest towards extracellular vesicles (EVs) has grown exponentially over the last few years following the discovery that they are involved in intercellular communication by serving as transfer vehicles of proteins, lipids, DNA and RNA between cells [1–3], furthermore, EVs are reservoirs for biomarkers for neurological disorders and tumors [4–6]. A major driver of translational interest in EV classes remains their potential for liquid biopsy development. The presence of EVs in body fluids including blood, urine, and saliva allows the non-invasive detection of biomarkers from easily obtained samples and the improved access to the benefits of personalized medicine, potentially replacing many costly and invasive tissue biopsies [7,8].

In general, the isolation and characterization of EVs present unique challenges due to their small size, low refractive index, and polydispersity [9]. Since they are too small for direct analysis by flow cytometry or other conventional state-of-the-art techniques for the analysis of nanoparticles, new methods are needed to successfully quantify EVs and to identify their cellular origin [10].

Currently, EVs are mostly isolated from the supernatant of cultured cells grown in fetal calf serum by performing differential ultracentrifugation [11]. Although it is possible to detect EVs in any given preparation through qualitative analysis, their quantification still remains an issue and only one approach is widely used: quantification of the amount of an EV's associated protein using ELISA or immunoblotting. The main limitation of this approach is that it is very hard to distinguish between a modification of the number of expressed proteins per EV and a real modification in the amount of EVs in the sample. An alternative approach takes advantage of measuring the total protein concentration in the EV preparations. However, all of these protocols require the disruption of the vesicle membranes and the release of internal proteins into the sample buffer.

The main methods used to characterize intact EVs are: 1) Electron Microscopy (EM), 2) Nanoparticle Tracking Analysis (NTA) (NanoSight) and 3) qNano (Izon Science Ltd). NTA is a special optical microscopy technique complementary to electron microscopy, which allows determination of the size distribution of isolated EVs based on the Brownian motion of vesicles in suspension (www.nanosight.com). qNano is based on a technique known as Tunable Resistive Pulse Sensing (TRPS), and utilizes dynamically resizable nanopores for real-time particle detection, quantitation and characterization. A significant limitation of these techniques is that while they can objectively define the vesicle size range and concentration, they are restricted in their ability to simultaneously phenotype vesicles by identification of their expressed proteins.

An emerging technique is flow cytometry of exosomes captured on antibody-coated latex beads [12] on a novel high resolution flow cytometer analysis of individual (immunolabeled) nano-sized vesicles [13]. This type of test allows the simultaneous evaluation of multiple parameters on single vesicles by a multi-color labeling strategy. In general, the analysis of a single, specific EV's antigen using conventional flow cytometry and Western blotting demands 10–30 μg of EV's total protein content, isolated by extensive and time-consuming standard extraction procedures. In order to obtain that amount of purified exosomal material, large quantities of cells producing the exosomes are needed (3×10^7 – 4×10^8 cells).

Recently, a high-throughput fluorescence microarray able to efficiently capture and phenotype EVs was developed based on the use of 21 [14] or 60 [15] antibodies for different surface antigens. The array uses a cocktail of antibodies against tetraspanins CD9, CD63 and CD81 to profile the captured vesicles but an absolute quantitation of the EVs mass present in the sample is not yet implemented.

In summary, to use exosomes in diagnostic tests, new quantitative and high-throughput methods for assessing their concentration and phenotype in biological fluids are needed with capability beyond the state-of-the-art technologies.

Here we propose, for the first time, the use of a Si/SiO₂ interferometric platform [16,17], for multiparameter intact EVs analysis combining label-free EVs mass quantitation and high sensitivity, fluorescence based phenotyping. The scheme of the assay is reported in Fig. 1. In the proposed method, EVs are captured by antibody spots on Si/SiO₂ chip displaying regions with a dual SiO₂ thickness: 500 nm and 100 nm. The vesicle mass quantitation is based on the use of the Interferometric Reflectance Imaging Sensor (IRIS) [18] which utilizes optical interferometry to detect biomolecular binding on the 500 nm SiO₂ surface through an optical phase shift, sampling the reflectivity of the surface with a camera and multiple wavelength sources. IRIS is a label-free and quantitative technique, directly relating the measured optical thickness of the bilayers (providing an optical phase shift) to the absolute amount of molecules on the surface [19]. On the same silicon chip, the phenotyping of EVs is allowed by fluorescence immuno-labeling of vesicle protein biomarkers. High sensitivity is provided by the use of chip areas coated by a 100 nm SiO₂ layer for the selective enhancement of fluorophores [20–22]. Fig. 1b–d, show typical microarray images after each step of the proposed assay.

The combination of the dual detection scheme (label-free and fluorescence) on the same silicon chip was demonstrated in the past for protein microarrays [17,23,24]. Here, this innovative platform is applied to detect, quantify and phenotype EVs without disrupting their membranes. A correlation between the total amount of vesicles, purified from human fibroblast cell culture, and the mean content of a specific biomarker was demonstrated. The ability to phenotype these EVs samples by fluorescence antibody microarray is also proved. Moreover, the successful fluorescence detection of EVs from plasma samples without the use of time-consuming purification steps opens the way to the use of the platform in diagnostic applications.

2. Experimental section

2.1. Materials

Phosphate buffered saline (PBS), Trizma base (Tris), HCl, ethanolamine, Bovine Serum Albumin (BSA), ammonium sulfate, N,N'-dymethylacrylamide (DMA), Tween-20 and 3-(trimethoxysilyl)propylmethacrylate (MAPS) were purchased from Sigma–Aldrich (St. Louis, MO, USA). Either unmarked and biotin-labeled mouse monoclonal antibodies, clone H5C6, against the human tetraspanin CD63 (hCD63) were purchased from BioLegend (San Diego, CA, USA).

Cy3-labeled streptavidin (SA-Cy3) was obtained from Jackson ImmunoResearch (West Grove, PA, USA). Antibodies against human tetraspanins CD9 and CD81, against Rab5, HSP70 and Flotillin1 were purchased from Hansabiomed Ltd (Tallin, Estonia).

Silicon chips with a 100 nm and 500 nm thermal oxide layer [17] were a kind gift from Prof. Selim M. Unlu from Boston University, MA (USA).

2.2. EVs isolation from human biological samples

Skin fibroblasts primary cultures were selected from the tissue repository of the IRCCS Istituto Centro San Giovanni di Dio Fatebenefratelli (approved by the local ethical committee, CEIOC Prot. N. 2/92/p/rm). Establishment of fibroblast cultures, growth, storage conditions and lysis protocol for Western blot analysis

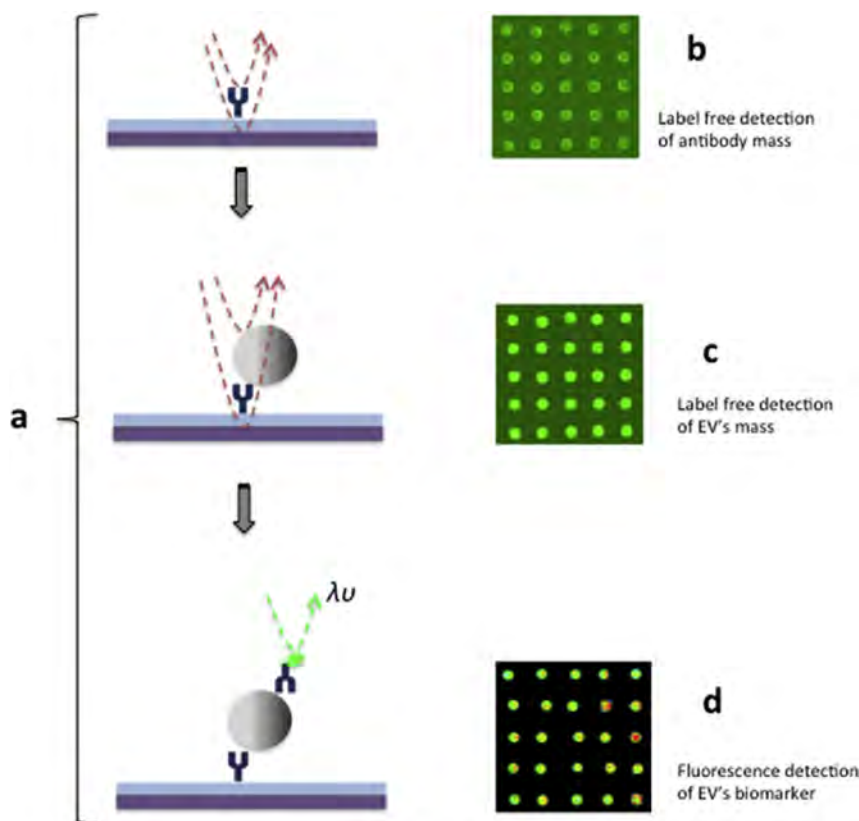


Fig. 1. a) Scheme of the assay: EVs are captured by antibody spots on Si/SiO₂ chip. The vesicle mass quantitation is based on the use of the interferometric reflectance imaging sensor (IRIS) which utilizes optical interferometry to detect biomolecular binding on chip. On the same silicon chip, the phenotyping of EVs is allowed by fluorescence immuno-labeling of vesicle protein biomarkers. b) Typical IRIS image of the anti-CD63 antibody array (before EVs capture). c) Typical IRIS image of the array after EVs capture. The total amount of captured EVs was calculated subtracting the measurements after the EV's sample incubation from the one corresponding to the anti-CD63 antibody spots only. d) Typical fluorescence image of the array after immunostaining with biotinylated anti-CD63 antibody and CY3-streptavidin.

are described elsewhere [25]. HEK 293 (Human Embryonic Kidney 293) cells were cultured in Minimum Essential Medium (MEM, Life Technologies) supplemented with 10% Fetal Bovine Serum (EuroClone S.p.A.), 1% Penicillin/Streptomycin solution (Carlo Erba Reagents), 2 mM L-glutamine (Carlo Erba Reagents), 1% MEM non Essential Amino Acids solution (Carlo Erba Reagents), at 37 °C in 5% CO₂/95% air. The different fibroblast cell cultures (obtained from cognitively intact subjects), each at the same passage number were plated at 300,000 cells/100 mm Petri dish, grown to 80% confluence and then incubated in serum-free medium for 72 h (3 mL/100 mm Petri dish). HEK 293 cells were grown to 80% confluence and then incubated in serum-free medium for 72 h (3 mL each 100 mm Petri dish). Conditioned media were pooled (~48 mL of conditioned media/experiment) and centrifuged to obtain exosomes according to the standard protocol [26]. Briefly, conditioned media were collected and spun at 300 × g for 10 min for three times. The supernatants were then sequentially centrifuged at 1200 × g for 20 min and again at 10,000 × g for 30 min followed by ultracentrifugation at 1,10,000 × g for 60 min (T-8100 rotor) (Sorvall). According to [26], the discarded pellet contains cell debris. All centrifugations were performed at 4 °C. The 1,10,000 × g pellet was then resuspended in PBS (5 μL per Petri 100 mm dish) and then serially diluted for NTA and IRIS analyses.

Human plasma samples were isolated according to standard procedure and centrifuged at 3000 × g for 5 min before undergoing NTA and IRIS analyses. For Western blot analysis, exosomes were purified from 125 μL of plasma by ultracentrifugation

(1,10,000 × g for 120 min) after a dilution step with PBS (final volume: 6 mL) and a filtration step (syringe filter 0.2 μm).

Study protocol was approved by the local ethical committee (Prot. N. 52/2014).

2.3. Western blotting

Ultracentrifuge-purified exosomal pellets were resuspended in 12.5 μL RIPA lysis buffer (150 mM NaCl, 1.0% IGEPAL® CA-630, 0.5% sodium deoxycholate, 0.1% SDS and 50 mM Tris, pH 8.0) and then analyzed by Western blot using the anti-tetraspanin CD63 SC5275 monoclonal antibody (Santa Cruz Biotechnology, Inc.).

2.4. Nanoparticle tracking analysis (NTA)

Nano-Sight LM10 instrument (Malvern, Worcestershire, UK) was selected to analyze suspensions containing vesicles. The dilute samples were illuminated by a monochromatic laser beam at 532 nm to register a 60 s video taken with a mean frame rate of 30 frames/s. The NTA software (version 2.2, NanoSight) was used to analyze EV samples, optimized to first identify and then track each particle on a frame-by-frame basis, and its Brownian movement is tracked and measured from frame to frame. Particle size was determined applying the two-dimensional Stokes–Einstein equation based on the velocity of particle movement. From each video was elaborated the mean, mode and median EV size to calculate samples concentration expressed in nanoparticles per mL.

2.5. Coating of microarray silicon chips with poly(DMA-NAS-MAPS)

Copoly(DMA-NAS-MAPS) was synthesized as described in Ref. [27]. Silicon chips were coated according to the protocol described in Ref. [17]. Briefly, silicon chips were immersed in a copoly(DMA-NAS-MAPS) solution (1% w/v in 0.9 M $(\text{NH}_4)_2\text{SO}_4$) for 30 min. The chips were then rinsed with water, dried under nitrogen and cured for 15 min under vacuum at 80 °C.

2.6. Sandwich immunoassays using IRIS and fluorescence-based detection platforms

Capture antibody against hCD63, clone H5C6, PBS and BSA as negative controls and Cy3-labeled streptavidin (as reference) were arrayed on copoly(DMA-NAS-MAPS)-coated silicon chips, with 100 and 500 nm oxide layer thickness, using a SciFlexArrayer S5 spotter from Scienion (Berlin, Germany). Antibodies were printed at 1 mg/mL in 25 or 32 replicates; the volume of spotted drops was 400 μL . Printed chips were placed in a humid chamber and incubated overnight at room temperature. Then they were blocked with 50 mM ethanolamine solution in 1 M TRIS/HCl pH 9 for 1 h, washed with water and dried under a stream of nitrogen.

Antibody arrays were first characterized with the label-free IRIS platform. Images of printed capture antibodies were acquired with Zoiray Acquire software and quantified according to [19], before any incubation with samples.

According to NanoSight quantifications, EV standard preparations were diluted in PBS to a concentration of 16, 4, 2, 1.6, 0.6, 0.4 and 0 E+10 particles/mL and then 20 μL of each sample was incubated in static conditions for 2 h on printed chips. Human plasma samples (20 μL) were incubated overnight at room temperature without any dilution.

After incubation, chips were washed with PBS under stirring, rinsed in water and dried under a nitrogen stream. Post-incubation label-free IRIS images were then acquired as described above. All IRIS files were fitted and processed using Zoiray Process software. The effective mass increase from captured EVs on printed antibodies was obtained subtracting the signals measured before and after sample incubation. Net values from 25 spots were averaged to design a calibration curve.

Subsequently, all chips were incubated for 1 h, with the biotin-labeled detection antibody against hCD63 at 1 $\mu\text{g}/\text{mL}$ in incubation buffer (50 mM Tris/HCl, 150 mM NaCl and 0.02% Tween-20). As vesicles display several tetraspanins on their membrane, a sandwich immunoassay is possible even when using the same monoclonal antibody for both capture and detection purposes. Chips were then washed with PBS for 10 min, rinsed with water and incubated, for 1 h, with Cy3-labeled streptavidin (SA-Cy3) at 2 $\mu\text{g}/\text{mL}$ in PBS. Chips were washed with PBS and water for 10 min each, rinsed with water and dried under a nitrogen stream. Fluorescence was detected by a ProScanArray scanner (PerkinElmer, Boston, MA), and silicon chips were analyzed using 70, 80 or 90% photomultiplier (PMT) gain and laser power. The fluorescence intensities of 25 or 32 replicate spots were averaged.

3. Results and discussion

3.1. Label free measurements

EVs from human fibroblasts cell culture were purified according to the ultracentrifugation protocol described in the experimental section. The suspension of EVs was then analyzed by Nanoparticle Tracking to estimate the number of particles contained in the preparation: in a typical experiment such preparations provided 1.6×10^{11} particles/mL. Six dilutions of the characterized

suspension in the range 4×10^9 – 4×10^{10} particles/mL were then incubated on the surface of the antibody array displaying the anti-hCD63 antibody, being CD63 a marker generally present in EVs and overexpressed in exosomes [28–30]; all preparations were CD63 positive, as demonstrated by Western blot (Fig. 1S). Silicon chips were then analyzed by the label-free IRIS platform to detect the increase in the mass generated by the binding of vesicles to the anti-hCD63 antibody spots. The binding provided an optical phase shift in the range 0.5–3 nm. The net signals originated by EVs captured by the antibody spots were calculated subtracting the measurements after the sample incubation from the one corresponding to the anti-hCD63 antibody spots only. Typical IRIS images are reported in Fig. 1(b,c). A calibration curve was then generated correlating the number of particles estimated by Nanoparticle Tracking in the incubated suspensions with the mean optical phase shift values originated by the captured vesicles (Fig. 2a). Samples ranging from 0 to 1.6×10^{10} particles/mL showed a linear correlation between the number of incubated vesicles and the biomass measured on the capture antibodies, demonstrating the capability to capture and quantify CD63-positive vesicles (Fig. 2b). On the contrary, samples with more than 1.6×10^{10} particles/mL did not provide any further optical phase shift. This is likely due to the saturation of printed capture antibodies, as a consequence of steric hindrance or depletion of available binding sites. These data suggest the possibility to use the IRIS label-free platform and a calibration curve as a method to quantify the amount of CD63-positive EVs in a given sample. The method provided a dynamic range (0– 1.6×10^{10} particles/mL) which allows the quantification of EVs when extracted from plasma samples by established protocols [31,32], without any pre-quantification.

3.2. Sandwich fluorescence assay

As vesicles display several CD63 tetraspanins on their membranes, a sandwich immunoassay was developed using the same monoclonal antibody for both capture and detection purposes. After label-free IRIS analysis of chips, they were further incubated with a biotin-labeled anti-hCD63 antibody; fluorescence detection was allowed by a Cy3-labeled streptavidin. Fluorescence spots were revealed and quantified by a microarray fluorescence scanner. A calibration curve was obtained in a linear range from 0 to 4.0×10^{10} particles/mL (Fig. 3). Furthermore, the fact that human CD63 was detectable, by the same monoclonal antibody, in a sandwich assay, strongly suggests that the captured vesicles maintained their integrity during the assay.

3.3. Correlation between label free and fluorescence assay

The signals from label free and fluorescence measurements, in the common range from 0 to 1.6×10^{10} particles/mL, were plotted on a single graph (Fig. 4), demonstrating a correlation factor ($R^2 = 0.99208$) between data originating from the two combined detection methods.

These proof-of-principle experiments demonstrated for the first time the use of a microarray based dual detection platform to quantify the amount of intact vesicles while simultaneously providing information on their phenotypes. We anticipate the great potential of this tool by exploiting the multiplexing capabilities of antibody microarrays either using several different capturing antibodies for biomarkers of interest or by printing a cocktail of capture antibodies followed by incubation with different detection antibodies. This would enhance the vesicle capturing yield in a given sample, allowing the detection of the total amount of bound biomaterial as well as to phenotype it by incubating with differen-

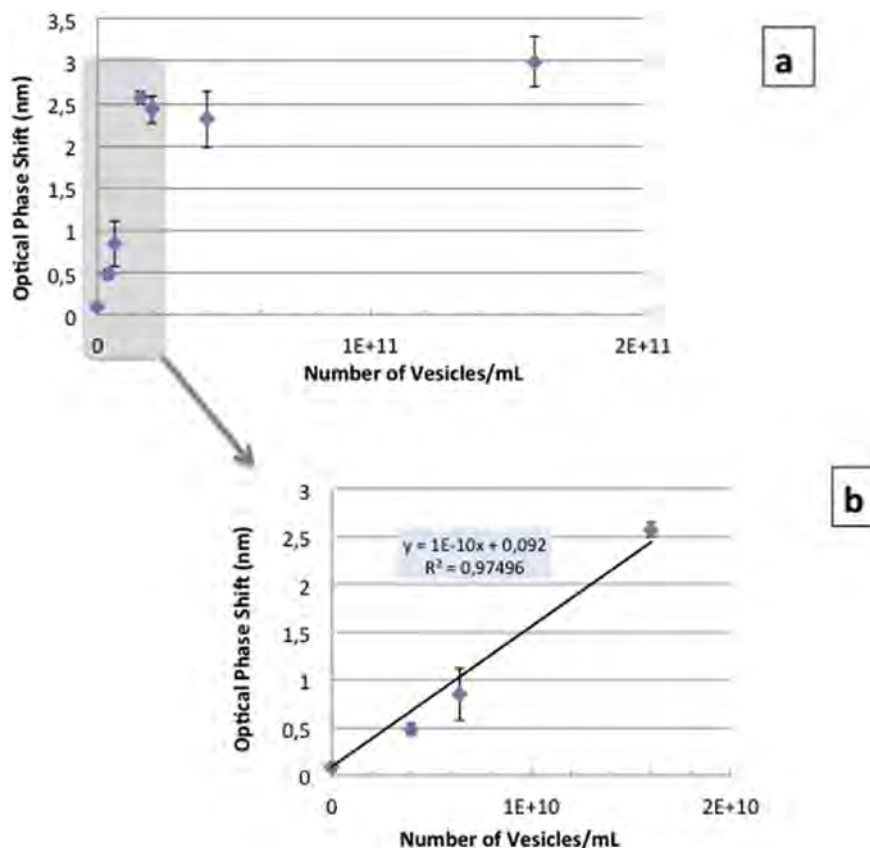


Fig. 2. IRIS measurements and calibration curve of EVs bound to anti-CD63 capture antibodies printed on silicon chips. a) Signals from samples with more than 1.6×10^{10} particles/mL reach a plateau as a consequence of saturation of binding sites on each spot of interest. b) Close-up of the linear range of IRIS measurements from 0 to 1.6×10^{10} particles/mL.

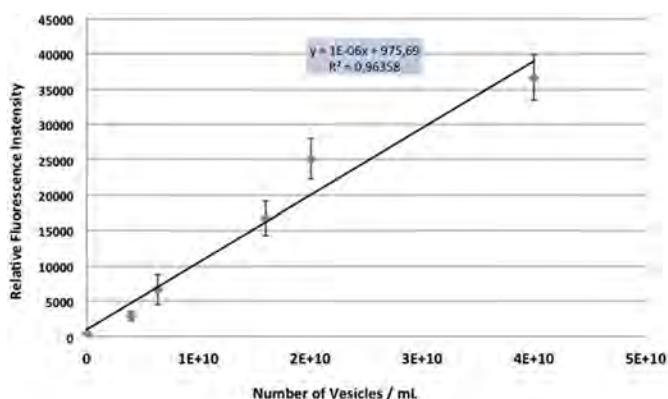


Fig. 3. Fluorescence signals (70% laser power and PMT gain) from EVs captured and detected using antibodies against hCD63 in a sandwich immunoassay format.

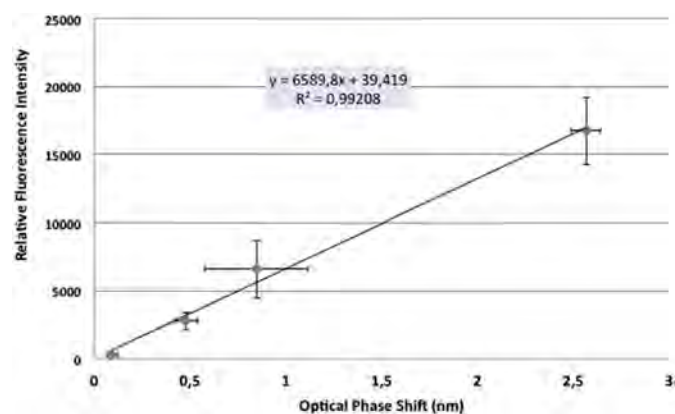


Fig. 4. Correlation between IRIS measurements (x axis) and fluorescence (at 70% laser power and PMT gain, y axis) detection in the common range from 0 to 1.6×10^{10} particles/mL.

tial detection antibodies, specific for a given tissue or pathology biomarker.

3.4. Vesicles phenotyping

The feasibility of the workflow for combined mass quantitation and phenotyping was verified using two preparations of EVs from fibroblasts and HEK 293 (Human Embryonic Kidney 293) cells. All preparations were CD63 positive, as demonstrated by Western blot (Fig. 1S). An array of antibodies to human CD63, CD81, CD9, Rab5, HSP70, Flotillin1 and negative controls was spotted on Si/SiO₂ chips and incubated with EVs from the two cell cultures

purified according to the ultracentrifugation protocol. Both mass quantitation by IRIS and fluorescence analysis using anti-hCD63 detection antibody were performed. The mass quantitation by IRIS on the hCD63 antibody spots provided optical phase shift values of 0.437 ± 0.11 and 0.376 ± 0.17 for the fibroblast and HEK cells respectively, revealing very similar purification yields (as also demonstrated by NTA measurements: $1.75 \times 10^9 \pm 5.68 \times 10^7$ and $1.6 \times 10^9 \pm 4.57 \times 10^6$ particles/mL). On the contrary, the fluorescence based phenotyping performed on the array of antibodies revealed differences in the pattern of expressed biomarkers in the two cell lines as demonstrated by the fluorescence values as

reported in Fig. 5. The HEK cells EVs preparation showed a higher fluorescence intensity for CD9, fibroblast revealed a higher intensity for CD63 whereas the expression of CD81 was comparable for the two cell lines. Fluorescence for Rab5, HSP70 and Flotillin1 was undetectable in these samples. The negative control spots (BSA and PBS) and supernatant solutions (data not shown) provided negligible signals.

3.5. Analysis of EVs from human plasma

The sandwich immunoassay described above using anti-CD63 antibody was applied to human plasma samples to verify the feasibility of the detection of EVs directly in biological fluids without the need of time-consuming purification protocols. Plasma samples were in fact simply centrifuged at $3000 \times g$. Nanoparticle Tracking measurements typically estimated the EVs content in these samples in 1.3×10^{10} particles/mL. Vesicles captured on spotted antibodies were then detected by fluorescence using the anti-hCD63 biotin-labeled antibody, coupled with Cy3-labeled streptavidin. Microarray experiments required the overnight incubation of $20 \mu\text{L}$ of undiluted plasma. Table 1 reports the comparison of fluorescence intensity detected for both plasma and EVs preparations purified by ultracentrifugation. A comparison of the typical fluorescence images for the two types of sample preparations are reported in Fig. 2S in the Supplementary Information. Notably, at comparable EVs concentration of about 10^{10} particles/mL, the fluorescence signals originated by EVs from plasma are lower than the signals detected for samples purified from cell culture and resuspended in PBS. To detect plasma samples it was necessary to extend the incubation time and to increase the laser power in order to improve the signal-to-noise ratio. This is most likely due to the presence of many lipoproteins in plasma samples, as suggested by previous studies [31]. We may also speculate that a lower expression of CD63 in plasma EVs compared to fibroblast vesicles could give a contribution to the observed underestimate in fluorescence signal. The purification procedure applied to fibroblast cell culture was tested on plasma as well; however, to obtain comparable fluorescence signals it would be necessary to use a 10 times higher plasma volume ($200 \mu\text{L}$) making this approach not applicable for use in routine diagnostics.

To check non-specific binding on the microarray we used spotted BSA and PBS as negative control spots [14,15]. Negligible non-

Table 1

Relative fluorescence intensity of EVs from human plasma (1.31×10^{10} particles/mL) and EVs from fibroblast cell culture followed by standard purification (6.38×10^9 particles/mL). Samples were incubated overnight and analyzed at 90% laser power and PMT gain.

	Human plasma	Fibroblast cell culture
Number of vesicles in 1 mL	1.31×10^{10}	6.38×10^{10}
Relative fluorescence intensity	4414 ± 1392	$60,966 \pm 1980$

specific binding was detected on the control spots as shown in Fig. 3S in the Supplementary Information which reports fluorescence intensities for three plasma samples analyzed. A further specificity control is the absence of fluorescence signals on anti-hCD63 spots when incubating the supernatant solution collected after ultracentrifugation of fibroblast culture (data not shown).

Inter and intra-assay reproducibility of the fluorescence microarray analysis of three different human plasma samples performed in triplicate are reported in Table 2. The fluorescence assay provided an intra-assay coefficient of variation (CV%) ranging from 15% to 19% and an inter-assay CV% ranging from 17% to 19%. These reproducibility ranges are not uncommon in protein microarrays [32,33], and mostly depend on manufacturing (spotting) variability and non homogeneous surface [34]. The use of internal calibration methods by quantitation of the absolute amount of immobilized bioprobes (antibodies) can improve reproducibility of results [23]. For comparison, reproducibility of the measurement of nanoparticles number by NTA are reported in Table 1S in the Supplementary Information.

The corresponding fluorescence images of the microarrays are reported in Fig. 6. The fluorescence enhancing properties of the 100 nm SiO_2 chip layer coupled to the non-fouling properties of the polymeric coating [35] provided a good signal to noise ratio for all the analyzed samples even when using undiluted complex sample matrices. Notably, in this system, sensitivity can be enhanced and consequently, incubation time reduced, by introducing agitation of the sample to overcome mass transport limitations [22]. Further studies are necessary to understand the reason of the apparent impaired binding of vesicles derived from plasma with respect to samples purified by centrifugation. Nonetheless this result paves the way to the use of the dual-detection microarray platform in diagnostic assays directly on clinical samples and without the use of time consuming ultracentrifugation protocols.

4. Conclusions

In this work, a method to simultaneously detect, quantify and phenotype intact EVs by combining qualitative and quantitative analysis was introduced. The proposed microarray platform aims at surpassing the main limitation of current approaches for EVs characterization that is the inability to distinguish between a modification of the number of expressed proteins per EV and a real modification in the amount of EVs in the sample. Furthermore, the technique ensures the phenotyping of vesicles based on the biomarkers that they expose on the membrane surface and not on the protein total content as in Western blot or ELISA.

Label free IRIS measurements allowed to quantify the amount of vesicles captured on the printed antibodies by detection of optical phase shifts originating from accumulation of biomaterial on antibody spots. Simultaneously, EVs were also detected by fluorescence in a sandwich immunoassay using human CD63 biomarker, proving identity and vesicle integrity. Multiplexed fluorescence detection (phenotyping) was also verified on a panel of capturing antibodies. Further studies will aim at fur-

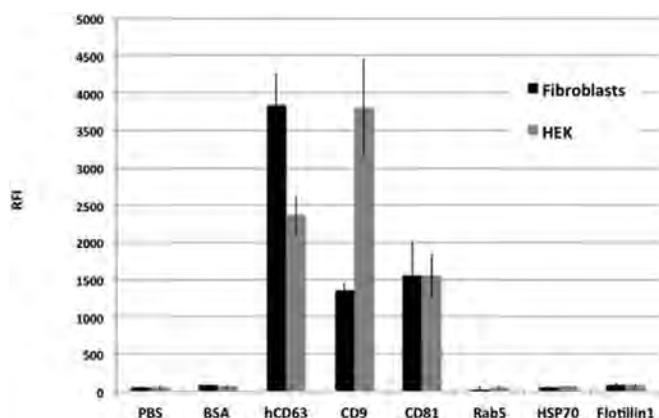


Fig. 5. Comparison of fluorescence detection (at 70% laser power and PMT) of the phenotyping of EVs purified by ultracentrifugation from two cell lines: fibroblast and HEK. The detection antibody used was a labeled anti-CD63 antibody. Error bars represent the standard deviation of medium fluorescence intensity of 32 spots. Fluorescence on non-correlated antibody spots used as negative controls (anti Beta-Lactoglobulin and anti Alfa-Lactalbumin) was negligible (data not shown).

Table 2
Reproducibility of the EV's microarray analysis of centrifuged plasma. Three plasma samples (A, B and C) were analyzed in triplicate. Fluorescence intensity over the anti-human CD63 spots is averaged, values and standard deviations are reported. Intra-assay reproducibility is expressed as the coefficient of variation (CV%) on 32 replicated anti-hCD63 spots; inter-assay reproducibility is expressed as the coefficient of variation (CV%) on 3 analysis of the same plasma sample, see Fig. 6.

	Plasma A			Plasma B			Plasma C		
	Run 1	Run 2	Run 3	Run 1	Run 2	Run 3	Run 1	Run 2	Run 3
Average fluorescence	9584	10,297	9612	7096	6725	7558	11,598	12,534	10,406
St. dev.	1729	1928	1762	1354	1294	1442	1876	1928	1680
CV% intra	18%	19%	18%	19%	19%	19%	16%	15%	16%
Average fluorescence	9875			7215			11,589		
St. dev.	1818			1393			2000		
CV% inter	18%			19%			17%		

CV% are in bold.

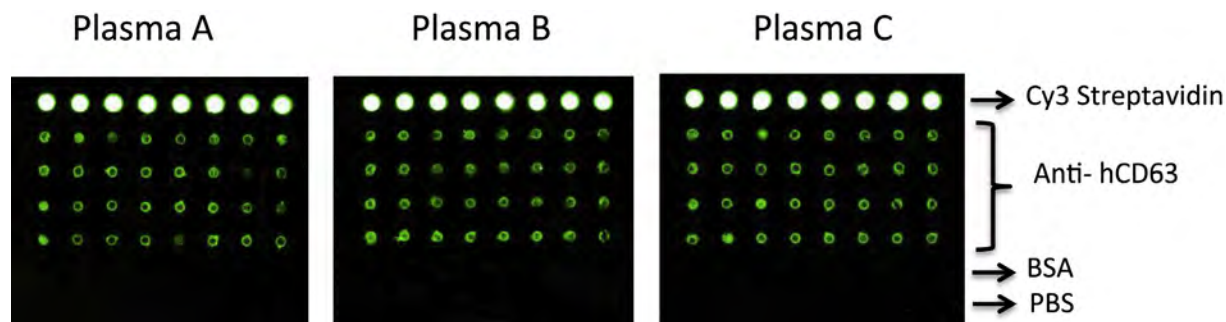


Fig. 6. Fluorescence images (90% laser power and PMT) of the analysis of three plasma samples (A, B and C). The spotting scheme is identical for all the images: Cy3 labeled streptavidin is used as positional control, an array of 8x4 anti human CD63 antibody is used to selectively capture EVs, lines of 8 BSA and 8 PBS spots are used as negative controls. Fluorescence intensity for the anti-human CD63 spots is averaged and values are reported in Table 2 together with intra and inter-assay reproducibility.

ther multiplexing the assay and improving detection of EVs directly in complex matrices avoiding time consuming purification protocols.

Acknowledgments

This work was partially supported by Regione Lombardia & Fondazione Cariplo through POR-FESR, project MINER (ID 46875467) and by CNR-TUBITAK bilateral agreement.

Appendix A. Supplementary data

Supplementary data related to this article can be found at <http://dx.doi.org/10.1016/j.aca.2015.10.017>.

References

- [1] H. Valadi, K. Ekström, A. Bossios, M. Sjöstrand, J.J. Lee, J.O. Lötvall, Exosome-mediated transfer of mRNAs and microRNAs is a novel mechanism of genetic exchange between cells, *Nat. Cell Biol.* 9 (2007) 654–659, <http://dx.doi.org/10.1038/ncb1596>.
- [2] G. Raposo, W. Stoorvogel, Extracellular vesicles: exosomes, microvesicles, and friends, *J. Cell Biol.* 200 (2013) 373–383, <http://dx.doi.org/10.1083/jcb.201211138>.
- [3] C. Tetta, E. Ghigo, L. Silengo, M.C. Deregibus, G. Camussi, Extracellular vesicles as an emerging mechanism of cell-to-cell communication, *Endocrine* 44 (2013) 11–19, <http://dx.doi.org/10.1007/s12020-012-9839-0>.
- [4] G. Lachenal, K. Pernet-Gallay, M. Chivet, F.J. Hemming, A. Belly, G. Bodon, et al., Release of exosomes from differentiated neurons and its regulation by synaptic glutamatergic activity, *Mol. Cell. Neurosci.* 46 (2011) 409–418, <http://dx.doi.org/10.1016/j.mcn.2010.11.004>.
- [5] J.L. Hood, S. San Roman, S.A. Wickline, Exosomes released by melanoma cells prepare sentinel lymph nodes for tumor metastasis, *Cancer Res.* 71 (2011) 3792–3801, <http://dx.doi.org/10.1158/0008-5472.CAN-10-4455>.
- [6] Y. Yuana, A. Sturk, R. Nieuwland, Extracellular vesicles in physiological and pathological conditions, *Blood Rev.* 27 (2013) 31–39, <http://dx.doi.org/10.1016/j.blre.2012.12.002>.
- [7] P.D. Robbins, A.E. Morelli, Regulation of immune responses by extracellular vesicles, *Nat. Rev. Immunol.* 14 (2014) 195–208, <http://dx.doi.org/10.1038/nri3622>.
- [8] Y. Yoshioka, N. Kosaka, Y. Konishi, H. Ohta, H. Okamoto, H. Sonoda, et al., Ultra-sensitive liquid biopsy of circulating extracellular vesicles using ExoScreen, *Nat. Commun.* 5 (2014) 3591, <http://dx.doi.org/10.1038/ncomms4591>.
- [9] Z. Varga, Y. Yuana, A.E. Grootemaat, E. van der Pol, C. Gollwitzer, M. Krümey, et al., Towards traceable size determination of extracellular vesicles, *J. Extracell. Vesicles* 3 (2014) 1–10, <http://dx.doi.org/10.3402/jev.v3.23298>.
- [10] F. Momen-Heravi, L. Balaj, S. Alian, J. Tigges, V. Toxavidis, M. Ericsson, et al., Alternative methods for characterization of extracellular vesicles, *Front. Physiol.* (2012) 3 SEP, <http://dx.doi.org/10.3389/fphys.2012.00354>.
- [11] R. Wubbolts, R.S. Leckie, P.T.M. Veenhuizen, G. Schwarzmann, W. Möbius, J. Hornschmeyer, et al., Proteomic and biochemical analyses of human B cell-derived exosomes: potential implications for their function and multivesicular body formation, *J. Biol. Chem.* 278 (2003) 10963–10972, <http://dx.doi.org/10.1074/jbc.M207550200>.
- [12] C. Lässer, M. Eldh, J. Lötvall, Isolation and characterization of RNA-containing exosomes, *J. Vis. Exp.* (2012), <http://dx.doi.org/10.3791/3037>.
- [13] E.J. van der Vlist, E.N.M. Nolte-t Hoen, W. Stoorvogel, G.J.A. Arkesteijn, M.H.M. Wauben, Fluorescent labeling of nano-sized vesicles released by cells and subsequent quantitative and qualitative analysis by high-resolution flow cytometry, *Nat. Protoc.* 7 (2012) 1311–1326, <http://dx.doi.org/10.1038/nprot.2012.065>.
- [14] M. Jørgensen, R. Bæk, S. Pedersen, E.K.L. Søndergaard, S.R. Kristensen, K. Varming, Extracellular vesicle (EV) array: microarray capturing of exosomes and other extracellular vesicles for multiplexed phenotyping, *J. Extracell. Vesicles* 2 (2013) 1–9, <http://dx.doi.org/10.3402/jev.v2i0.20920>.
- [15] M.M. Jørgensen, R. Bæk, K. Varming, Potentials and capabilities of the extracellular vesicle (EV) array, *J. Extracell. Vesicles* 4 (2015), http://www.journalofextracellularvesicles.net/index.php/jev/article/view/26048/xml_7.
- [16] M. Cretich, M.R. Monroe, A. Reddington, X. Zhang, G.G. Daaboul, F. Damin, et al., Interferometric silicon biochips for label and label-free DNA and protein microarrays, *Proteomics* 12 (2012) 2963–2977, <http://dx.doi.org/10.1002/pmic.201200202>.
- [17] M. Cretich, A. Reddington, M. Monroe, M. Bagnati, F. Damin, L. Sola, et al., Silicon biochips for dual label-free and fluorescence detection: application to protein microarray development, *Biosens. Bioelectron.* 26 (2011) 3938–3943, <http://dx.doi.org/10.1016/j.bios.2011.03.016>.
- [18] E. Ozkumur, J.W. Needham, D.A. Bergstein, R. Gonzalez, M. Cabodi, J.M. Gershoni, et al., Label-free and dynamic detection of biomolecular interactions for high-throughput microarray applications, *Proc. Natl. Acad. Sci. U. S. A.* 105 (2008) 7988–7992, <http://dx.doi.org/10.1073/pnas.0711421105>.
- [19] E. Ozkumur, A. Yalçin, M. Cretich, C.A. Lopez, D.A. Bergstein, B.B. Goldberg, et al., Quantification of DNA and protein adsorption by optical phase shift, *Biosens. Bioelectron.* 25 (2009) 167–172, <http://dx.doi.org/10.1016/j.bios.2009.06.033>.
- [20] M. Cretich, G. Di Carlo, R. Longhi, C. Gotti, N. Spinella, S. Coffa, et al., High sensitivity protein assays on microarray silicon slides, *Anal. Chem.* 81 (2009) 5197–5203, <http://dx.doi.org/10.1021/ac900658c>.
- [21] M. Cretich, D. Breda, F. Damin, M. Borghi, L. Sola, S.M. Unlu, et al., Allergen microarrays on high-sensitivity silicon slides, *Bioanal. Chem.* 398 (2010) 1723–1733, <http://dx.doi.org/10.1007/s00216-010-4077-x>.

- [22] M. Cretich, M. Bagnati, F. Damin, L. Sola, M. Chiari, Overcoming mass transport limitations to achieve femtomolar detection limits on silicon protein microarrays, *Anal. Biochem.* 418 (2011) 164–166.
- [23] M.R. Monroe, A.P. Reddington, A.D. Collins, C. Laboda, M. Cretich, M. Chiari, et al., Multiplexed method to calibrate and quantitate fluorescence signal for allergen-specific IgE, *Anal. Chem.* 83 (2011) 9485–9491, <http://dx.doi.org/10.1021/ac202212k>.
- [24] P. Gagni, L. Sola, M. Cretich, M. Chiari, Development of a high-sensitivity immunoassay for amyloid-beta 1–42 using a silicon microarray platform, *Biosens. Bioelectron.* 47 (2013) 490–495.
- [25] L. Benussi, R. Ghidoni, T. Steinhoff, A. Alberici, A. Villa, F. Mazzoli, et al., Alzheimer disease-associated cystatin C variant undergoes impaired secretion, *Neurobiol. Dis.* 13 (2003) 15–21, [http://dx.doi.org/10.1016/S0969-9961\(03\)00012-3](http://dx.doi.org/10.1016/S0969-9961(03)00012-3).
- [26] C. Théry, S. Amigorena, G. Raposo, A. Clayton, Isolation and characterization of exosomes from cell culture supernatants and biological fluids, *Curr. Protoc. Cell Biol.* (2006) Unit 3.22, <http://dx.doi.org/10.1002/0471143030.cb0322s30>.
- [27] M. Cretich, G. Pirri, F. Damin, I. Solinas, M. Chiari, A new polymeric coating for protein microarrays, *Anal. Biochem.* 332 (2004) 67–74.
- [28] S.S. Kanwar, C.J. Dunlay, D.M. Simeone, S. Nagrath, Microfluidic device (ExoChip) for on-chip isolation, quantification and characterization of circulating exosomes, *Lab. Chip* 14 (2014) 1891–1900, <http://dx.doi.org/10.1039/c4lc00136b>.
- [29] M. Record, C. Subra, S. Silvente-Poirot, M. Poirot, Exosomes as intercellular signalosomes and pharmacological effectors, *Biochem. Pharmacol.* 81 (2011) 1171–1182, <http://dx.doi.org/10.1016/j.bcp.2011.02.011>.
- [30] J. Van Deun, P. Mestdagh, R. Sormunen, V. Cocquyt, K. Vermaelen, J. Vandesompele, et al., The impact of disparate isolation methods for extracellular vesicles on downstream RNA profiling, *J. Extracell. Vesicles* 3 (2014). (accessed 23.04.15) <http://www.journalofextracellularvesicles.net/index.php/jev/article/view/24858/35788>.
- [31] R.A. Dragovic, C. Gardiner, A.S. Brooks, D.S. Tannetta, D.J.P. Ferguson, P. Hole, et al., Sizing and phenotyping of cellular vesicles using nanoparticle tracking analysis, *Nanomedicine Nanotechnol. Biol. Med.* 7 (2011) 780–788, <http://dx.doi.org/10.1016/j.nano.2011.04.003>.
- [32] T. Bacarese-Hamilton, L. Mezzasoma, a. Ardizzoni, F. Bistoni, a. Crisanti, Serodiagnosis of infectious diseases with antigen microarrays, *J. Appl. Microbiol.* 96 (2004) 10–17, <http://dx.doi.org/10.1046/j.1365-2672.2003.02111.x>.
- [33] T. Anderson, J. Wulfkuhle, L. Liotta, R.L. Winslow, E. Petricoin, Improved reproducibility of reverse-phase protein microarrays using array microenvironment normalization, *Proteomics* 9 (2009) 5562–5566, <http://dx.doi.org/10.1002/pmic.200900505>.
- [34] M. Cretich, F. Damin, M. Chiari, Protein microarray technology: how far off is routine diagnostics? *Analyst* 139 (2014) 528–542, <http://dx.doi.org/10.1039/c3an01619f>.
- [35] G.W. Platt, F. Damin, M.J. Swann, I. Metton, G. Skorski, M. Cretich, et al., Allergen immobilisation and signal amplification by quantum dots for use in a biosensor assay of IgE in serum, *Biosens. Bioelectron.* 52 (2014) 82–88, <http://dx.doi.org/10.1016/j.bios.2013.08.019>.